



**ΟΝΟΜΑΤΕΠΩΝΥΜΟ:** Ευσταθία Μπουραντά

**A.M. :** 219003

**ΤΙΤΛΟΣ:** Ιδιότητες των σεισμικών κυμάτων ουράς (S coda), που έχουν δημιουργηθεί από ισχυρά σεισμικά γεγονότα στην κεντρική Ελλάδα, χρησιμοποιώντας την μέθοδο της μη εκτατικής στατιστικής φυσικής (Non-Extensive Statistical Physics, NESP).

**Ειδίκευση:** Εφαρμοσμένη Γεωλογία και Γεωφυσική

Στην παρούσα διατριβή θα μελετήσουμε σεισμικά κύματα ουράς (S coda), που έχουν δημιουργηθεί από ισχυρά σεισμικά γεγονότα στην κεντρική Ελλάδα. Τα κύματα ουράς ερμηνεύονται ως σκεδασμένα σεισμικά κύματα που δημιουργούνται από ετερογένειες εντός της Γης, δηλαδή από ρήγματα, δομές ρωγμών, μικρορωγμές, όρια ταχύτητας ή/και πυκνότητας/ανωμαλίες κ. λπ. Λόγω της φύσης και της πολυπλοκότητας της διαδρομής των κυμάτων coda θα χρησιμοποιήσουμε την μη εκτατική στατιστική φυσική (Non-Extensive Statistical Physics, NESP) για να μελετήσουμε τις συναρτήσεις πυκνότητας πιθανότητας (probability density functions or pdfs) των μεταβολών (fluctuations) των σεισμικών κυμάτων ουράς. Ο σκοπός της ανάλυσης είναι να δείξει ότι οι χρονοσειρές που περιγράφουν τις μεταβολές (fluctuations) στα σεισμικά κύματα ουράς αποκλίνουν από την Gaussian περιγραφή και οι αντίστοιχες συναρτήσεις πυκνότητας πιθανότητας τους θα μπορούσαν επαρκώς να περιγραφούν από την κατανομή q-Gaussian. Θα δοθεί μια προσπάθεια ερμηνείας των αποτελεσμάτων με βάση τη θεωρία για την δημιουργία των κυμάτων ουράς όπως έχει περιγραφεί σε σειρά εργασιών του Sato και συνεργατών για τη μορφή των κυμάτων ουράς που δημιουργεί μια κατανομή σκεδαστών που ακολουθεί ασυμπτωτικό νόμο δύναμης

**Τριμελής Εξεταστική Επιτροπή**

- Καθηγητής Βαλλιανάτος Φ. (Επιβλέπων)
- Αναπλ. Καθηγητής Καβύρης Γ.
- ΕΔΙΠ. Παύλου Κ.



ΕΛΛΗΝΙΚΗ ΔΗΜΟΚΡΑΤΙΑ  
Εθνικόν και Καποδιστριακόν  
Πανεπιστήμιον Αθηνών  
— ΙΔΡΥΘΕΝ ΤΟ 1837 —

Τμήμα Γεωλογίας και Γεωπεριβάλλοντος



Πρόγραμμα  
Μεταπτυχιακών  
Σπουδών

Επιστήμες Γης  
και Περιβάλλον

**NAME/SURNAME:** Efstathia Bouranta

**REGISTRATION NUMBER:** 219003

**TITLE:** Properties of seismic S coda waves from strong events in central Greece using the method of non – extensive statistical physics.

*Specialisation: Applied Geology - Geophysics*

In this thesis we will study seismic coda waves (S coda), created by strong seismic events in central Greece. Wave surges are interpreted as scattered seismic waves created by heterogeneities within the Earth, i.e. fault lines, crack structures, micro cracks, speed and/or density limits/anomalies, etc. Due to the nature and complexity of the path of the coda waves we will use non-Extensive Statistical Physics (NESP) to study the probability density functions (probability density functions or pdfs) of the coda seismic wave flows. The purpose of the analysis is to show that the time series describing the fluctuations in the seismic coda waves diverge from the Gaussian description and their corresponding probability density functions could be adequately described by the q-Gaussian distribution. An attempt will be made to interpret the results based on the theory of coda wave generation as described in a series of work by Sato and collaborators on the form of coda waves that creates a scattering distribution that follows an asymptotic force law.

### *Three-member Committee of Examination*

- Professor Vallianatos F. (Supervisor)
- Assoc. Professor Kaviris G.
- Laboratory Teaching Staff Pavlou K.

ATHENS 2023

## ΔΗΛΩΣΗ ΠΕΡΙ ΜΗ ΠΡΟΣΒΟΛΗΣ ΠΝΕΥΜΑΤΙΚΗΣ ΙΔΙΟΚΤΗΣΙΑΣ

---

Προσβολή πνευματικής ιδιοκτησίας θεωρείται η ολική ή η μερική αναπαραγωγή του έργου άλλου προσώπου ή η παρουσίαση του έργου κάποιου άλλου ως προσωπικού του γράφοντος. Το Τμήμα Γεωλογίας και Γεωπεριβάλλοντος λαμβάνει πολύ σοβαρά υπόψη και καταδικάζει την προσφυγή σε τέτοιου είδους πρακτικές από τους Μεταπτυχιακούς Φοιτητές. Σε περιπτώσεις πρόδηλης ή εκ προθέσεως προσβολής πνευματικής ιδιοκτησίας, τα αρμόδια όργανα του Τμήματος δύνανται να επιβάλουν ως κύρωση έως και την οριστική διαγραφή από το ΠΜΣ. Κατά την εκπόνηση, υποβολή, εξέταση και δημοσίευση της Διπλωματικής Εργασίας Ειδίκευσης οι Μεταπτυχιακοί Φοιτητές οφείλουν να τηρούν τις ακόλουθες κατευθυντήριες οδηγίες:

1. Η Διπλωματική Εργασία Ειδίκευσης πρέπει να αποτελεί έργο του υποβάλλοντος αυτήν φοιτητή.
2. Η αντιγραφή ή η παράφραση έργου τρίτου προσώπου αποτελεί προσβολή πνευματικής ιδιοκτησίας και συνιστά σοβαρό αδίκημα. Στο αδίκημα αυτό περιλαμβάνεται τόσο η προσβολή πνευματικής ιδιοκτησίας άλλου φοιτητή όσο και η αντιγραφή από δημοσιευμένες πηγές, όπως βιβλία, εισηγήσεις ή επιστημονικά άρθρα. Το υλικό που συνιστά αντικείμενο λογοκλοπής μπορεί να προέρχεται από οποιαδήποτε πηγή. Η αντιγραφή ή χρήση υλικού προερχόμενου από το διαδίκτυο ή από ηλεκτρονική εγκυκλοπαίδεια είναι εξίσου σοβαρή με τη χρήση υλικού προερχόμενου από τυπωμένη πηγή ή βάση δεδομένων.
3. Η χρήση αποσπασμάτων από το έργο τρίτων είναι αποδεκτή εφόσον, αναφέρεται η πηγή του σχετικού αποσπάσματος. Σε περίπτωση αυτολεξί μεταφοράς αποσπάσματος από το έργο άλλου, η χρήση εισαγωγικών ή σχετικής υποσημείωσης είναι απαραίτητη, ούτως ώστε η πηγή του αποσπάσματος να αναγνωρίζεται.
4. Η παράφραση κειμένου, αποτελεί προσβολή πνευματικής ιδιοκτησίας.
5. Οι πηγές των αποσπασμάτων που χρησιμοποιούνται θα πρέπει να καταγράφονται πλήρως σε πίνακα βιβλιογραφίας στο τέλος της εργασίας.
6. Η προσβολή πνευματικής ιδιοκτησίας επισύρει την επιβολή κυρώσεων. Κατά την απόφαση επί των ενδεδειγμένων κυρώσεων, τα αρμόδια όργανα του Τμήματος θα λαμβάνουν υπόψη παράγοντες όπως το εύρος και το μέγεθος του τμήματος της εργασίας που οφείλεται σε προσβολή πνευματικής ιδιοκτησίας. Οι κυρώσεις θα επιβάλλονται σύμφωνα με το Άρθρο 7 Παράγραφος 7 του Κανονισμού Σπουδών.

**Βεβαιώνω ότι η Διπλωματική Εργασία Ειδίκευσης, την οποία υποβάλλω, δεν περιλαμβάνει στοιχεία προσβολής πνευματικής ιδιοκτησίας, όπως αυτά προσδιορίζονται από την παραπάνω δήλωση, τους όρους της οποίας διάβασα και αποδέχομαι.**

**Παρέχω τη συναίνεσή μου, ώστε ένα ηλεκτρονικό αντίγραφο της διπλωματικής εργασίας μου να υποβληθεί σε ηλεκτρονικό έλεγχο για τον εντοπισμό τυχόν στοιχείων προσβολής πνευματικής ιδιοκτησίας.**

Ημερομηνία  
13/09/2023

Υπογραφή Υποψηφίου



# Table of Contents

<b>Abstract</b> .....	5
<b>Περίληψη</b> .....	6
<b>1. Introduction</b> .....	7
1.1 Lithosphere's inhomogeneity.....	7
1.2 Geological processes that reveal heterogeneity .....	8
1.3 Fractal nature of the inhomogeneities.....	10
<b>2. Coda Waves</b> .....	11
2.1 Definition of Coda waves.....	11
2.2 Composition and frequency characteristics of Coda waves.....	12
2.3 Duration of Coda waves .....	13
2.4 The decay rate of Coda attenuation.....	14
<b>3. Parameters</b> .....	14
3.1 Frequency dependence of S-wave attenuation $Q_S^{-1}$ .....	15
3.2 Spatial variation of $Q_c^{-1}$ .....	15
3.3 Isotropic scattering coefficient $g_{iso}$ .....	16
<b>4. Measurement models</b> .....	16
4.1 Single Scattering Model.....	17
4.2 Single Backscattering Model for a common source and receiver location .....	18
4.3 Single Isotropic Scattering Model for general source and receiver locations.....	20
4.4 Diffusion Model .....	22
4.5 Energy-Flux Model.....	23
<b>5. Radiative Transfer Theory</b> .....	24
5.1 Introduction in Radiative Transfer Theory .....	24
5.2 Application of the Radiative Transfer Theory.....	26
5.3 Fractal distribution of scatterers and absorbers .....	27
5.4 Equations in Radiative Transfer Theory .....	28
5.5 Method of Coda normalization .....	30
5.6 Equations in the non-dimensional form.....	31
5.7 The ballistic term .....	32
<b>6. Statistical Analysis</b> .....	34
6.1 Introduction to statistical parameters .....	34
6.2 Gaussian (Normal) distribution .....	35
6.3 Measures of Skewness and Kurtosis .....	36
6.4 Power law in nature .....	37
6.5 Power law in seismology .....	38

<b>7. Entropy and statistical mechanics</b> .....	39
7.1 Introduction.....	39
7.2 Boltzmann Gibbs statistical mechanics .....	41
7.3 The q – Functions .....	43
7.4 Non-extensive statistical mechanics .....	45
<b>8. Area of study and data selection</b> .....	49
8.1 Geological background.....	49
8.2 Seismic Data Selection.....	50
<b>9. Discussion and conclusions</b> .....	64
<b>Appendix A</b> .....	65
<b>Appendix B</b> .....	74
<b>References</b> .....	169

## Abstract

In this thesis we will study seismic coda waves (S coda), created by strong seismic events in central Greece. S coda waves are interpreted as scattered seismic waves created by heterogeneities within the Earth, i.e. fault lines, crack structures, micro cracks, speed and/or density variations/anomalies, etc. Due to the nature and complexity of the path of the coda waves we will use non-Extensive Statistical Physics (NESP) to study the probability density functions (probability density functions or pdfs) of the S coda seismic wave. The purpose of the analysis is to show that the time series describing the fluctuations in the seismic coda waves diverge from the Gaussian description and their corresponding probability density functions could be adequately described by the q-Gaussian distribution. An attempt will be made to interpret the results based on the theory of coda wave generation as described in a series of work by Sato and collaborators on the form of coda waves that creates a scattering distribution that follows an asymptotic power law.

Keywords: S coda, earthquake, heterogeneities, distribution, scattering

## Περίληψη

Στην παρούσα διατριβή θα μελετήσουμε σεισμικά κύματα ουράς (S coda), που έχουν δημιουργηθεί από ισχυρά σεισμικά γεγονότα στην κεντρική Ελλάδα. Τα κύματα ουράς ερμηνεύονται ως σκεδασμένα σεισμικά κύματα που δημιουργούνται από ετερογένειες εντός της Γης, δηλαδή από ρήγματα, δομές ρωγμών, μικρορωγμές, μεταβολές ταχύτητας ή/και πυκνότητας/ανωμαλίες κ. λπ. Λόγω της φύσης και της πολυπλοκότητας της διαδρομής των κυμάτων coda θα χρησιμοποιήσουμε την μην εκτατική στατιστική φυσική (Non-Extensive Statistical Physics, NESP) για να μελετήσουμε τις συναρτήσεις πυκνότητας πιθανότητας (probability density functions or pdfs) των μεταβολών (fluctuations) των σεισμικών κυμάτων ουράς. Ο σκοπός της ανάλυσης είναι να δείξει ότι οι χρονοσειρές που περιγράφουν τις μεταβολές (fluctuations) στα σεισμικά κύματα ουράς αποκλίνουν από την Gaussian περιγραφή και οι αντίστοιχες συναρτήσεις πυκνότητας πιθανότητας τους θα μπορούσαν επαρκώς να περιγραφούν από την κατανομή q-Gaussian. Θα δοθεί μια προσπάθεια ερμηνείας των αποτελεσμάτων με βάση τη θεωρία για την δημιουργία των κυμάτων ουράς όπως έχει περιγραφεί σε σειρά εργασιών του Sato και συνεργατών για τη μορφή των κυμάτων ουράς που δημιουργεί μια κατανομή σκεδαστών που ακολουθεί ασυμπτωτικό νόμο δύναμης.

Λέξεις κλειδιά: κύματα ουράς, σεισμός, ετερογένειες, κατανομή, σκεδασμός

## 1. Introduction

In seismology the seismic waves that are caused either by earthquakes or by manmade sources are used in order to study the structure of the earth. After studies that have been done over the years, the theory that has prevailed is that the earth consists of a sequence of horizontal layers that have different elastic properties. This is a consideration that is dominant in the classical seismology, along with the fact that this structure is determined by the travel-time readings of body waves and the dispersion of surface waves. Classical seismic methods have also characterized three dimensional heterogeneities with a scale larger than the predominant seismic wavelength, by using travel-time data with velocity tomography. Thus, there are classical methods which can be used in order to model complicated structures, such as explaining many features of complex waveforms. Those methods are using forward and inverse waveforms for deterministic models.

However, it was observed in seismograms of local earthquakes that after the S waves, there were some continuous wave trains, which could not be explained by the determinist models of classical seismology. Those waves are named 'coda waves' and after observations they seem to be incoherent, with random sizes and contrasts of physical properties. They occur after scattering in randomly distributed inhomogeneities in the earth's medium. Each heterogeneity has a characteristic scale which is very important for the waves, but it is not much longer than the wavelength, as most of the times it has the same scale with it. There was found strong random fluctuations in seismic velocity and density having short wavelengths in well logs of boreholes drilled even in old crystalline rocks located in stable tectonic environments. Those observations have led us to believe that the earth is a random medium with a broad spectrum of spatial velocity fluctuations and the resulting importance of seismic wave scattering. After these depictions of the earth, there were investigations that could connect the seismogram envelopes and the spectral structure of the random inhomogeneity in the earth. At first scientists tried to find the connection by phenomenological description of the scattering process. After some observations, theoretical studies have been proposed, which use perturbation methods, the parabolic approximation, the phase screen method, and another phenomenological method known as the Radiative transfer theory. After this method was proposed and applied, the scattering process of the seismic waves has been described in the inhomogeneous earth and a detailed characterization of the statistical properties of the inhomogeneity has been able to be made.

### 1.1 Lithosphere's inhomogeneity

Before defining coda waves and how we can obtain useful information about the scattering process through the Radiative transfer theory, we will refer to the earth's structure. It is known that the first 100 km under the surface is the so called lithosphere. This region is solid and the velocity at this part is low. The thickness of the lithosphere is not the same and has many variations from place to place, as it is connected to the tectonic setting. In this study when we refer to the term lithosphere, we mean the crust and the upper mantle. At the base of the crust there is the Mohorovicic discontinuity or Moho (Mohorovicic 1909) and in the mid-crust there is another discontinuity, the Conrad. There have been many studies after the Moho has been discovered, most of them using layered models. Those studies have led to the belief that the Moho is not only a simple discontinuity, but it really works as a transition zone, as it consists of

many segments of small reflectors. As far as the crust is concerned, the use of the regional velocity tomography has shown that the crust is heterogeneous on scales from a few meters to a few tens of kilometers in many regions of the world.

Apart from investigating the earth's heterogeneity by using the coda waves and the scattering process, there are also other ways that can be used in order to study and identify the earth's medium and its characteristics. In geology, the measurements include mineralogical composition and grain size distribution. Geology is based on the observation of the surface, since rock samples that originate from within the earth are being studied, in order to obtain any signs that will declare heterogeneity. Those rocks are mostly being found after the eruption of volcanoes and they offer geochemical and geological evidence of heterogeneity within the earth. Also, rocks are being found in boreholes and they present wide variation and rapid changes in chemical composition with depth. However, as rock samples are being involved, those methods are being affected by the evolution of the rock. Inhomogeneity of the lithosphere is partially being caused by tectonical processes associated with plate tectonics such as folding, faulting, and large scale crustal movements.

On the other hand, geophysical research is based on measurements of physical properties, such as seismic velocities and density of rocks. The physical properties of rocks cannot only be controlled by the mineral composition, as, after measurements that were made in wells, show correlation and lack of correlation with chemical composition of the rocks. Elastic properties within the lithosphere are revealed to indicate wide spatial variation, after the realization of deterministic seismic studies. In those studies, lithosphere's small scale heterogeneities are revealed to exist by the scattering of seismic waves with high frequency.

## **1.2 Geological processes that reveal heterogeneity**

As we have mentioned above, the lithosphere presents inhomogeneities which are being revealed to us by different methods. A very popular method that is used in order to identify the heterogeneity is by studying the various types of the rocks. Seismic velocities are different for each rock type. Since rocks have crystals whose sizes vary from fractions of mm to a few cm in scale, they can be very helpful for the numerous scales of the earth's heterogeneities. The mineral's properties that create the rocks in the crust are very different from one another, thus the abundance of each mineral in a rock's configuration can influence its elastic properties.

Significant role to the earth's geology and to its study play the fractures. They have various sizes that can be from submicroscopic to many tens of meters. They influence the rock's elastic properties, as their spatial variation in size and content can affect more the elastic properties of a crystal rock than the mineral composition. The presence of a fracture has also effect on the velocity of the P and S waves. The velocity of P waves is more sensitive to the presence of fluids in a fracture comparing to the velocity of the S waves. This happens as fluids transmit compressional waves but not shear waves.

Another significant fact in understanding the inhomogeneities of the earth is anisotropy of rock properties. It has variation according to location and increases rock inhomogeneity. Fractures can also lead to anisotropy of the elastic properties of the bulk rock. Some fractures have an alignment as a function of orientation that is the result of the way their formation was made or due to the variation of a stress magnitude and that is the reason some cracks are open and

some others are closed. The layering of rocks is another anisotropy type and it is found in many sedimentary formations. As it is known the layering is being rotated by tectonic processes, thus the horizontal and vertical directions are not aligned with the preferential orientation of fast and slow directions of anisotropic media.

Since we discuss about geological processes, we could not proceed without referring to the intrusions of magma. Those intrusions into country rock that was already there, led to the creation of dikes and sills that have different composition from the country rock. The size of those dikes and sills can be as small as a few mm wide and this leads to a spatial variation that is quick in rock properties. In volcanic regions, the rock properties have multiple variations created by the different composition of the magma that was erupted at different stages of a volcano's life. The variations of the rock properties can be on a large scale from a few meters to a few kilometers. In multiple tectonic provinces the variation is over tens to hundreds of kilometers. For example, in the Western U.S.A. the Cascade range is mostly created from young volcanic rocks, while in the central U.S.A. there are mainly old Precambrian rocks. The elastic properties in those two areas are dramatically different.

Magmatic processes have created a large part of the crust. There are some large silicic batholiths, like in Sierra Nevada, U.S.A. that constitute the intrusive remains of eroded away volcanic complexes. Geochemists insist that silicic rocks that intrude into the shallow crust and erupt at volcanoes were formed either by the transfer of heat from intruded iron-rich mantle rocks to silicic rocks in the deep crust or by fractionation of iron-rich rocks that intrude into the lower crust from the mantle. In both cases, high velocity material will remain within the silicic crust. The high density material's velocity can be as high as 7.5 km/s (Fountain and Christensen 1989). If there is heat transfer from mantle-derived magmas, the velocity of the resulting magmas could be 7.0 km/s. As a result, the process of the intrusion causes heterogeneity in the earth's crust.

Sedimentary formations have a huge importance, as the sedimentary rocks contain the majority of the world's hydrocarbons. Heterogeneity in those formations created by sedimentation has many causes, as there are variations in the cementing rocks together, as well as in porosity and pore fluids, the source rocks that the sediments were formed from have changed and there is influence by the tectonic processes that act on the rocks after deposition. Heterogeneity in sedimentary rocks has been extensively studied by seismic imaging of various types, borehole logging and geological characterization that was held for the exploration and development of hydrocarbon resources.

There are also other geological processes that have an impact on the inhomogeneity of the lithosphere, such as erosion and metamorphism that transport rocks or change their character in place. Faulting and folding, are included in the tectonic processes that move relative rocks to one another and create heterogeneity. Lithospheric plates and their large scale movements contribute to common origin rock's distribution over a wide range. Lastly, different types of rocks came into contact by the collision of tectonic plates at plate boundaries, such as subduction zones or collision zones.

## 1.2 Fractal nature of the inhomogeneities

As discussed, the inhomogeneities of the earth medium have been showing a fractal nature. More specific to that is the relation between the fractal dimension of the 3D inhomogeneities of the earth and that of the fault surfaces that has been studied by the scattering of the seismic waves. In order to proceed with the measurement of the heterogeneity spectrum of a random medium, there have been introduced two methods. The first method is the coda excitation spectrum method, and the second one is the method of measuring the frequency dependence of scattering attenuation. The heterogeneity spectrum of the medium can lead us to the fractal dimension. The first method of the coda excitation has been applied to data that have been taken from the Hindu-Kush mountain in Asia. The observed coda excitation spectra for frequencies between 1-25 Hz, in accordance with the frequency dependence of scattering attenuation, we come to the conclusion that the lithospheres' inhomogeneities are multiple scaled and can be modeled as a bandlimited fractal random medium (BLFRM) with an outer scale of about 1 km.

'Fractal' is a term coined by Mandelbrot to denote a mathematical set or a concrete object whose form is extremely irregular and/or fragmented at all scales' (MANDELBROa" 1977, p. 294). Fractal is a geometrical description of objects having self-similar hierarchical structure down to arbitrarily small scales. Mathematically a fractal set is defined as a set whose Hausdorff - Besicovitch dimension is greater than its topological dimension. As a mathematical object, a fractal is an idealization and simplification of a variety of highly irregular but self similar natural phenomena. All real objects or process in the nature consist of a maximum scale, that can be the outer scale, and a minimum scale, that is the inner scale. Therefore all fractals in nature are bandlimited. Whether the fractal is bandlimited or not, is of no importance if the scale range of the observations is within the scale range of a bandlimited fractal. Then the object that is observed can be treated as a fractal.

For the propagation of the wave we assume that the medium is random, continuous and differentiable. We make this speculation, in order to be able to set up a system of differential equations for acoustic or elastic vibrations in the medium. So, we consider that the inhomogeneities or irregularities of the medium have a minimum scale, thus the inner scale. Therefore, the medium can be treated as a bandlimited fractal random medium. If the length of the waves that we test is larger than the inner scale and smaller than the outer scale of the bandlimited fractal medium, then we say that the propagation of the wave is in the fractal regime. If the shortest wavelength of the studying waves is longer than the length of the outer scale heterogeneities of the medium we say that the wave propagation is in the Rayleigh regime. Additionally, if the longest wavelength of the observed waves is shorter than the length of the inner scale, we say that the propagation of the wave is in the short wave regime. Rayleigh or short wave regime can never be reached for ideal fractal medium.

On the other hand the fractal regime of wave propagation and scattering is interesting, as the fractal's mathematical treatment can be used for the simplicity of the study and it can also advance it. Diffractals we call the waves that have been diffracted in the fractal regime, as the name given by Berry (1979) suggests. From the diffraction of the diffractals, we have obtained statistical properties of waves passing through a one-dimensional random phase screen or from the reflection by a fractal random surface. So, the bandlimited fractal random medium has proved to be useful for modeling multi scale media that are inhomogeneous and similar to

one another. We can determine its fractal dimension by measuring the inhomogeneity spectrum, which we obtain from experiments on wave scattering.

## **2. Coda Waves**

### **2.1 Definition of Coda waves**

In seismology the coda waves are defined as waves that occur after backscattering in the numerous heterogeneities distributed in the earth. After an earthquake happens, the first waves to observe are the P and S waves. There are also other surface waves that follow them, but all those waves propagate away from the seismic source. Nonetheless, the area around the source of the earthquake is still vibrating. This motion of the ground around the earthquake's source has a slow decay rate, leaving a tail following the passage of the P and S waves. Those continuous wave trains we call coda waves.

Historically, the first who not only just noticed, but also paid attention and showed interest in those continuous wave trains in the tail portion of the seismograms in local earthquakes, was Aki (1969). Aki named those random signals coda waves. They have envelope amplitudes that decrease as the lapse time increases. The lapse time is measured from the origin time of the earthquake. Rautian and Khalturin (1978) observed that the envelopes of coda waves that originate from local earthquakes have a steady decay and there are independent from the epicentral distance and they are only dependent from the lapse time.

If we go back to the first seismograms, we will understand that they were used in order to record the first arrival and locate the earthquake. The regional networks that the seismograms were located relied on analog transmission from stations over phone lines and radio links, the recordings had a limited dynamic range.

Due to the analog transmission that caused the limited dynamic range, the stations should be working in high-gain, in order to have the ability to record the P waves that are the first arriving. Working in high-gain, resulted in clipping the early part of the seismogram. Thus, the analysis of seismograms was first developed on working on seismograms that their first part was clipped, especially in large earthquakes. So the analysis of the coda waves at first was based in those small dynamic range networks and it focused on obtaining information about the seismic source and the medium of the earth.

As the years passed, the seismic network became digital and it allowed the increase of the dynamic range. This, in combination with the placement of the seismograms in boreholes, where the noise of the ambience was significantly reduced compared to that on the surface of the ground, led to recording seismogram envelopes, both with their maximum amplitude part and their last part, where the coda appear, in order to model the heterogeneities of the earth's medium. The frequencies used were between 1-30 Hz. Since the coda are not regular plain waves originated from the epicenter, but are composed of scattered waves coming from all directions, the theoretical and deterministic studies are not suitable for them. After 1970, the study of the coda waves started being based on the single scattering approximation, which has been used to the explanation of three component seismogram envelopes characteristics.

## 2.2 Composition and frequency characteristics of Coda waves

There are P and S coda waves, that as the name suggests are the result of the P waves and S waves scattering to earth inhomogeneities. P coda waves are the ones to be seen first in seismograms and S coda waves, are sometimes twice the travel time of P waves. After analysis on the spectral ratios of P and S coda waves, it has been observed that the S coda waves have similar frequency content to those of S waves rather than P waves. This means that S coda waves are mainly composed of scattered S waves.

The excitation of S coda waves constitutes evidence that there is indeed random inhomogeneity in the lithosphere. Aki and Chouet (1975) were the first to collect the characteristics of high frequency S coda waves of local earthquakes. Those characteristics are the following. At first if we compare the spectral contents of the later portions of S coda of local earthquakes, but from different stations, we will realize that it is the same. A reliable measure of the magnitude of an earthquake is the total duration of a seismogram, that is it defined as the length of time from the appearance of the P waves to the time when the amplitude of the coda is the same level of microseisms. If we have records of local earthquakes within a certain region, the S coda bandpass filtered traces we obtain from them have a common envelope shape and its time is independent from the epicentral distance. The coda amplitudes have a temporal decay that is independent of the earthquake's magnitude at least for  $M_L < 6$ . However, the S coda amplitude is affected by the local geology of the recording site. Aki and Tsujiura (1959) after proceeding with array measurements have shown that S coda are not just regular plane waves originated from the epicenter. Observations in boreholes and at sites with different rock types have led to the fact that S coda waves and direct S waves have the same site amplification factor which confirms that S coda waves are composed of scattered S waves. Also, there have been identified S coda waves, even on seismograms that were recorded at the bottom of deep boreholes drilled in hard rock beneath soft deposits. The meaning of this is that S coda waves are not dominated by near surface scattering.

The last few years the studies that have been performed approach the S coda waves in more detail based on higher quality digital seismic wave data. Spudich and Bostwick (1987) proposed an array analysis technique with using data obtained at a station from an earthquake cluster. After analyzing the S coda waves they came to the result that those S coda waves before 1.5-2 times the S wave travel time are caused by multiple scattering close to the recording site or by small angle forward multiple scattering along the ray path of direct waves since these waves arrive to the seismic array, which is actually the earthquake cluster, from almost the same direction as direct waves.

The later part of coda waves is composed of S waves incoherently arriving from scatterers distributed in all directions. Su et al. (1991), compared the amplitude of the decay of coda waves originated from quarry blasts with that of earthquakes. He observed that in the later part of coda waves, the decay rate was similar. The amplitudes of those coda waves from quarry blasts are affected by surface waves in the early part of the record at lower frequencies, only for this contribution to disappear while lapse time is increasing. Following this result, a quarry blast-earthquake discrimination method has been proposed in order to analyze the rate of the decay of the early part of coda waves at lower frequencies. It is generally believed that the radiated source energy from quarry blast is not dominated by S wave energy, but by P wave energy. Therefore, the decay of S coda of quarry blasts is similar to that of earthquakes, and

that fact suggests that P to S converted energy strongly contributes to the energy of the S coda part.

Studies have been also performed on P coda waves as well. It seems that those waves also arrive to the station from various directions. P wave scattering occurs in very close proximity to the array that is not strong developed. Nikoraev and Troitskiy (1987), after studying P-coda waves, observed that they contain coherent phases continuously arriving at therecording sites from specific scatterers. They showed that coherent signals found in P coda waves arrived at stations from the upper mantle scatterers at a depth of about 116 km.

P coda wave data obtained from quarry blasts have been studied and the result has shown that the frequency wave number spectral analysis that P coda waves at 2.4 Hz propagate from the direction of a hypocenter with a diversified phase velocity.

Kuwahara et al. (1992) obtained similar results for P coda waves at 2.5 Hz by applying a semblance analysis to small aperture array data of explosions. However, it has been shown that P-coda waves at frequencies higher than 5 Hz arrive various directions. Kuwahara et al. (1990, 1991) also applied the semblance analysis technique to P coda waves from regional earthquakes and came to the conclusion that the arrival direction of P-coda waves is restricted to a narrow range centered on the direction of the direct wave. Scherbaum et al. (1991) obtained similar characteristics of P coda waves from a slowness analysis. There have been suggested three possibilities for the generation of P coda waves, by the results mentioned: P coda waves are composed of P to P, P to S or S to P scattered energy around a direct wave path. Essentially, the radiated S wave energy is much larger than P wave energy from a double couple source. Moreover, it is considered that S to P wave scattering becomes strong for regional distance earthquakes compared with teleseismic ones, because the contribution of teleseismic S-P converted energy to the early P coda part is weak due to propagation through the mantle, which is considered to be relatively uniform. P-S converted waves dominate in the P coda part for teleseismic events. To the contrary, S-P converted waves greatly contribute to the P-coda waves of regional earthquakes.

Matsumoto and Hasegawa (1989, 1991), took the data from a controlled P wave source, like an airgun and came to the conclusion that the amplitude of P waves is independent of the hypocentral distance. The amplification factors that are used among the stations correlate well to the amplitudes of P waves in the records of distant earthquakes. Those results lead us to the fact that the energy from coda waves is distributed uniformly in the earth, thus beneath the stations too, and the site factors can be corrected by their amplitudes, if we have a P wave source. Another fact that we obtain from those measurements is that there has to be a convert from P to S energy which has a peak at the arrival time of S wave we have calculated. Sato (1997) has predicted this appearance of the energy peak. Besides him, many other researchers have studied the coda waves and have managed to understand them and come to some conclusions about them. However, some problems remain, such as the quantity of the energy that converts from P to S and from S to P scattered waves.

### **2.3 Duration of Coda waves**

Coda wave duration was initially determined by the sample point in time domain, where the decay of the amplitude starts to behave non-exponentially. Later, a more quantitative

approach was used, as the travel time between the origin time and the S phase onset was being measured. After we multiply this duration by a factor of two or in some cases by a factor of three, it is considered to be the start point of the coda wave. We consider the end of the coda wave duration to be set by the user, when the signal to noise ratio reaches the value that the user has set, which is normally between 1 and 3. This specific value is not being set randomly. In order to set the value, the local geotectonic regime, the background noise and any kind of in-situ physical site properties need to be taken into consideration.

The duration of the coda waves has also been found to be related with the magnitude of the earthquake. However, for earthquakes of small magnitude, the length of the coda waves cannot be considered as a stable estimation, due to the fact that the measurement of backscattered energy from large distances is not possible to be made (Aki and Chouet 1975). However, if the case is ideal and the coda waves envelope is characterized with monotonic decay, and seismic stations are located upon bedrock with little to none sedimentary cap, there could be an empirical relation as an index of a coda wave duration.

## **2.4 The decay rate of Coda attenuation**

There is evidence that the origin of coda waves is connected with the lateral heterogeneities in the interior of the earth, as close to the surface the scatterers show high density and this density decreases with not only with depth but also to the consequences of the overall tectonic dynamics. Attenuation is a physical process which refers to the rate that the seismic amplitude and energy content decays and is associated with the processes of multiple scattering and intrinsic phenomena, as the intrinsic attenuation due to the transversion of elastic energy into heat and other forms of energy. The physical procedure of the scattering of a seismic wavefront is the result of the existence of irregularities, discontinuities, fractures, faults, fissures, microcracks and a variety of randomly distributed scatterers, within the rigid layer of the lithosphere, as well as of the fluctuations of the elastic properties of the Earth's materials. On the other hand, another effect that contributes to the attenuation mechanics is the absorption effect, which is connected with the anelastic properties of the Earth's interior. There can be also other phenomena that contribute to the absorption of seismic energy, such as fluid migrations and energy viscous dissipation in a wider area of fissile materials and crack like structures.

## **3. Parameters**

As it can be easily understood, there should be some parameters that explain and define the S coda waves. Two of them are the total scattering coefficient  $g_0$  and S coda attenuation  $Q_c^{-1}$  that have been measured in many regions and they have been compared with seismotectonic settings. The parameter  $Q_c^{-1}$  of S-coda attenuation describes how the S coda envelope decays exponential, while the lapse time increases, after the geometrical decay has been corrected. The total scattering coefficient  $g_0$  is used to describe how the power of the scattering per unit volume. It has been observed that the prices of those parameters are slightly different when they refer to a large earthquake (e.g. Gusev and Lemzikov 1985; Jin and Aki 1986).

### 3.1 Frequency dependence of S wave attenuation $Q_s^{-1}$

As a result of the energy conservation, due to the excitation of coda waves in scattering media, there is a loss of energy at the direct wave, as the distance of propagation is increasing. Until the 1970s, there was not enough knowledge of how and whether there was contribution by the energy loss due to scattering, to the attenuation of the amplitude of the seismic wave with travel distance. On the other hand, there was the belief that the dominant process was the intrinsic absorption and was considered also to be frequency independent. Thus, the frequency dependence of S wave attenuation  $Q_s^{-1}$  has been introduced. This parameter was first measured in the USA and in Japan, where the seismic networks are dense and the purpose of their construction was to record microearthquakes. When we have frequencies higher than 1 Hz and they keep increasing, the frequency dependence  $Q_s^{-1}$  decreases. After measurements on low frequency attenuation on surface waves Aki (1980a) proposed that  $Q_s^{-1}$  has a peak frequency around 0.5 HZ. If we take as granted that attenuation has as a dominant mechanism the scattering, the ordinary stochastic field theory for wave propagation through random media is not capable of explaining the observed frequency dependence, as this theory predicts that scattering attenuation increases with frequency. For this reason, some improvements were made at the stochastic theory, in order to become more realistic concerning the measurements of amplitude attenuation. There were two improvements made. The first one, proposed by Wu (1982), was to calculate the loss caused from scattering, only from scattered waves with scattering angles larger than  $90^\circ$ . The second one was to subtract the travel time fluctuation caused by the slowly varying velocity fluctuation before using the stochastic averaging procedure in the mean field theory (Sato 1982a). These improvements have an impact on the scattering, as they propose that scattering has a peak and then decreases with frequency on both sides. In addition, those models in combination with the observed frequency dependence of  $Q_s^{-1}$  were the base for studying the spectral structure of the random inhomogeneity.

### 3.2 Spatial variation of $Q_c^{-1}$

The value of  $Q_c^{-1}$  has been measured in many regions around the world and it constitutes a parameter that is well connected with the tectonic activity. In general, high values of  $Q_c^{-1}$  have been measured in regions with high seismic activity. What is important to mention about the values of  $Q_c^{-1}$  is that those values obtained by different regions cannot be compared as they depend on the hypocenter's location and the lapse time window they were estimated. In general, the values of  $Q_c^{-1}$  are smaller for large time windows. We also cannot be aware if those values are more affected by multiple scattering, by the depth of by the scattering coefficient. Spatial correlation between  $Q_c^{-1}$  and lapse time window was studied by Peng (1989) in order to estimate  $Q_c^{-1}$ . There is a function of  $Q_c^{-1}$  of a spatial auto correlation and it is estimated from a map, where  $Q_c^{-1}$  is in the middle of the epicenter and the station and is considered as an average in a small area.

Several researchers have studied the  $Q_c^{-1}$  and its values, as it is believed that it is connected with the lapse time window. The two dimensional  $Q_c^{-1}$  structure was estimated by Matsumoto and Hasegawa (1989) from a method that was spatial weighting and averaging for grip points that were spatially distributed. They used a time window where the minimum travel time of the waves that are scattered from scatterers at a depth of 60 km, was the end time.

Gagnepain-Beyneix (1987), made their measurements in the western Pyreneas, using a frequency range of 4-20 Hz and data from local earthquakes, in order to set the depth dependence of  $Q_c^{-1}$ . The same procedure was used by Kanao and Ito (1990) in the Kinki district of Japan and by Kosuga (1992) in Nagano Prefecture. All those surveys had in common that they set the depth distribution with the assumption that the energy originated from coda is mostly composed of scattered waves travelling in the vertical direction. In addition, the dependence of  $Q_c^{-1}$  with lapse time is not due to multiple scattering.

### 3.3 Isotropic scattering coefficient $g_{iso}$

Another parameter that is widely used in the study of the inhomogeneities of the earth and as a result in the model we will analyze below is the isotropic scattering coefficient  $g_{iso}$ . The isotropic scattering coefficient of the heterogeneous solid earth has been measured in many different regions such as the lower and upper mantle, the crust, volcanoes, sediments, mines and rock samples. Recent reviews have shown that the transport scattering coefficient increases with frequency, which explains the observed isotropic scattering coefficients for a wide range of frequencies. Meanwhile, it has been noticed that some isotropic scattering coefficients show unusual behavior. There are measurements that show the isotropic scattering coefficient increasing as the depth decreases in the crust and the upper mantle of the earth and the moon. The isotropic scattering coefficients beneath volcanoes are larger than those in the lithosphere and those in a sandstone sample with a large porosity are larger than those in a gabbro sample with little porosity. These differences observed in the isotropic scattering coefficient suggest possible scattering contribution of pores and cracks widely distributed in addition to the scattering by random velocity fluctuations.

## 4. Measurement models

As it is mentioned above, the seismic coda waves are the result of the body waves that have been scattered in the heterogeneities of the earth. We may also define the whole train wave that follows the P and S waves as the "coda wave". The part of the coda waves that has been mostly studied is that part that is the result of the scattered S waves of small local earthquakes. The latter part of the coda waves is being created by backward scattering and is independent of the asymmetry of the radiation of the source. On the contrary, if we wish to study the early part of the coda wave, we need to take into consideration the angular dependence of scattering and the pattern of the source's radiation.

In order to explain the temporal and the spatial changes of the energy density of the coda waves, there have been two models proposed. The first model is the single isotropic scattering and the second one is a diffusion model. Those two models have in common the assumption that the scattering is isotropic, the distribution of the scatterers is homogenous, isotropic and random, and the radiation of the source is spherical, while there is no conversion. The major difference the two models have, relates to the mean free time. The diffusion model is based on multiple scattering process, thus the mean free time is considerably shorter than the lapse time. On the other hand, the single isotropic scattering model is based, according to its name, on a single scattering process. This leads to the assumption that the hypocentral distance and

the lapse time measured from the earthquake origin time are shorter than the mean free path and the mean free time, respectively.

It is easy to understand that if we restrict the study of the coda waves in the case that the mean free time is longer than the lapse time, then the single scattering model will be used. The assumptions of spherical radiation of the source and isotropic scattering are simple and appropriate for analytical calculation. However, they are not appropriate for studying in the real earth the scattering process and the energy radiation that is caused by earthquakes. For this reason, researchers have tried to make the single isotropic model more realistic. There are four ways that this can be achieved. First is isotropic to non-isotropic scattering, second spherical to non-spherical source radiation, third including conversion scattering between S and P waves and fourth homogeneous to inhomogeneous distribution of scatterers.

There have been many studies of the angular dependence of scattering for various types of inclusions and random fluctuations of the velocity structure. The scattering can be isotropic only when the length of the wave is essentially longer than the characteristic length of the scatterer. The degree of scattering anisotropy usually depends on the frequency of seismic waves. As it is known, seismic waves are radiated by a shear dislocation and the pattern of the radiation that is created is not even close to a spherical symmetry. Another important thing to inhomogeneous elastic media is the conversion scattering between the P and S waves. The effect of this conversion of the P and S waves has been studied for some particular kinds of inclusions and randomness to a two layer structure in order to help with the explanation of the coda waves of the moon.

#### 4.1 Single Scattering Model

We will now discuss the energy density of coda waves according to an observer located, along with a hypocenter at the origin and on the z axis. The distance between the hypocenter and the observer is  $r$ , as illustrated in the picture below. We assume that the coordinate vector of a scatterer, that is point like, is  $x$  and  $r$  is that of the observer. The distance between the scatterer and the hypocenter is  $r_1 = |x|$  and the distance between the scatterer and the observer is  $r_2 = |r - x|$ .

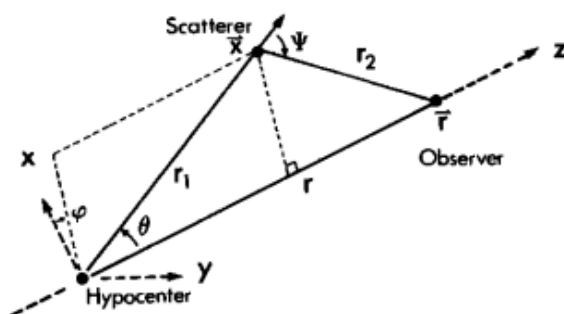


Figure 4.1.1 Geometry of a hypocenter, an observer and a scatterer

If we choose to use the spherical polar coordinate system, the polar coordinates  $(r_1, \theta, \phi)$  will represent the scatterer. We call  $\theta$  and  $\phi$  radiation angles.  $W$  denotes the total energy radiated, while  $R(\theta, \phi)$  denotes the radiation pattern and in the case of spherical source radiation  $R(\theta, \phi) = 1$ . If we measure the lapse time from the origin time of the earthquake, we can write as

$W(4\pi)^{-1}R(\theta, \phi) \delta(t)$  the energy spread from a source to the direction  $(\theta, \phi)$ , within a unit solid angle. The function  $R$  is normalized as  $(4\pi)^{-1} \int R(\theta, \phi) d\Omega = 1$ , where  $d\Omega$  is an infinite solid angle element.

In the meantime, we use the symbol  $\psi$  to represent a scattering angle of a propagation direction, of a direct and a scattered wave. The direct wave is given by vector  $x$  and the scattered wave is given by the vector  $r - x$ , as shown in the above picture. Of course, we suppose that the scattering is axially symmetrical around propagation direction of direct wave. The scattering that follows every scatterer is characterized by  $d\sigma(\psi)/d\Omega$  that is called differential scattering cross section, where  $d\sigma(\psi)$  gives energy per unit time of waves scattered into an infinitesimal solid angled  $\Omega$  to a direction  $\psi$  per unit energy flux density of the incident direct plane wave.

For all the above we assume that the distribution of scatterers is homogeneous, isotropic and random in a three dimensional medium. This medium has a density number  $n$ . The random distribution has a result of mutual incoherency of waves scattered by different scatterers, thus we can sum up the energy density that comes from the scattered waves at the observer. We come up with the result of the energy density by dividing the energy flux density by the wave velocity  $V$  for each scattered wave. Summation over distributing scatterers is substituted by an integral over a three-dimensional space.

#### 4.2 Single Backscattering Model for a common source and receiver location

We have already explained that the coda waves are being scattered in the earth's medium multiple times, until they reach to us. We suppose that the distribution of the scatterers is fractally homogeneous, with the fractal dimension being three, in a three dimension medium. If the scattering is taking place in a sphere of radius  $r$ , then the number of the scatterers is proportional to  $r^D$ . Since we have multiple scattering, the decay of the energy density of the  $k$  order scattering is given by  $[(D - 2)k - 3]$  power of lapse time. There are three different options for the type of scattering happening in the lithosphere, depending on the fractal dimension. When the fractal dimension is  $D=3$ , the distribution of the scatterers is uniform. When we have  $2 < D \leq 3$ , there is multiple scattering occurring with order  $k \geq 2$ , that dominates over the single scattering with order  $k=1$  at long lapse time. When  $D=2$ , the decay of energy density is according to the - 3rd power of lapse time. Thus, we conclude that the single scattering model survives on condition  $D < 2$ , that the single scattering dominates over the multiple scattering, even on long lapse time.

When we are on a three dimensional infinity space and we are working on point like isotropic scatterers in a homogenous distribution and the spherical radiation from the hypocenter, the energy density for scattered waves at the hypocenter at lapse time  $t$ , can be calculated as power series of scattering cross-section  $\sigma$ :

$$E^s(t) = W [n\sigma/(2\pi V^2 t^2) + \pi(n\sigma^2)/(16Vt) + \dots C_k (n\sigma)^k (Vt)^{k-3} + \dots] \quad (4.2.1)$$

The parameters are the following:  $W$ , the radiated energy;  $n$ , the number density of scatterers being constant;  $V$ , wave velocity;  $C_k$ , the coefficient of the  $k$  power of  $\sigma$  (cf, KOPNICHEV, 1977; GAO et al., 1983). The first term originally obtained by AKI and CHOJET (1975) is called the single scattering model for the coda excitation. The power of the lapse time for the  $k$  order

multiple scattering is  $k=3$ . Thus, we believe that the terms  $k \geq 2$  of multiple scattering are stronger than the single scattering of the order  $k=1$ , as lapse time increases. We should now search of the parameters that determine the power of the lapse time and if this theory of the single scattering model is valid at long lapse time.

As we already know, the high frequency coda waves are mainly composed of S scattered waves (AKI and CHOUET, 1975) and this means that the geometrical spreading of the seismic energy is inversely proportional to the second power of distance. If we follow the global density of matter in Astronomy and the mass is proportional to  $r^D$ , then the global density is proportional to  $r^{D-3}$ , where  $D$  is of course the fractal dimension. The spatial distribution of the earthquake epicenters with  $D = 1.0 \sim 1.6$  in two dimensional space, have stochastic self similarities (SADOVSKIY et al., 1984; KAGAN and KNOPOFF, 1980). In addition, the distribution of acoustic emission hypocenters in a rock sample under a uniaxial loading has a fractal structure with  $D = 2.25 \sim 2.75$  for granite (HIRATA et al., 1987a) and  $D = 1.47 \sim 2.0$  for andesite (HIRATA et al., 1987b). It has been also reported that in France there is a decrease of  $Q_c^{-1}$  with the depth, which it is not necessarily referring to the fractal structure, but it is related to the non-uniform distribution of scatterers. Thus, we can say that we possess a few observations for the constant number density of scatterers and all this can lead us to conclude that the distribution of scatterers, such as cracks and inclusions of various kinds, is not uniform but fractally homogeneous in the lithosphere.

For fractal homogeneity, we can assume that the number density of scatterers at coordinate  $x$  is not constant, but it is a function of distance  $r = |x|$  from the origin as  $n(r) = F r^{D-3}$ , where the dimension of coefficient  $F$ ,  $[F] = L^{-D}$  and  $L$  is the dimension of length. The number of scatterers  $n(r)$  in a sphere of radius  $r$  is

$$n(r) = \int_0^r n(r) 4\pi r^2 dr = \left(\frac{4\pi F}{D}\right) r^D \quad (4.2.2)$$

The wave energy is supposed to be spherically radiated from the source. Following this assumption, the single scattering energy density from the origin is given by

$$E_1^S(t) = W\sigma \iint_{-\infty}^{\infty} \int d^3x \left[ \frac{n(r)}{(4\pi r^2)^2} \delta(Vt - 2r) \right] = \frac{W\sigma F}{\pi 2^{D-2} (Vt)^{5-D}} \text{oc } W(\sigma F)^1 (Vt)^{D-5} \quad (4.2.3)$$

If we use  $[(D - 2)k - 3]$  we will find the power of lapse to be  $-2$  for  $D=3$ ,  $-3$  for  $D=2$  and  $-4$  for  $D=1$ .

If we have double scattering energy density  $k=2$  with the scatterers located the first at  $x_1$  and the second at  $x_2$ , we have the function

$$E_2^S(t) = W\sigma^2 \iint_{-\infty}^{\infty} \int d^3x_1 n(r_1) \iint_{-\infty}^{\infty} \int d^3x_2 n(r_2) \cdot \left\{ \delta \frac{Vt - r_1 - r_{1,2} - r_2}{(4\pi r_1^2)(4\pi r_{1,2}^2)(4\pi r_2^2)} \right\} =$$

$$\left[ \frac{W\sigma^2}{4\pi Vt} \right] \cdot \int_0^1 dz \frac{n \frac{Vtz}{z}}{z} \cdot \int_{1-z}^1 dy \cdot \left\{ \frac{n \frac{Vty}{z}}{y(2-z-y)} \right\} = \left\{ \frac{W(\sigma F)^2}{\pi 4^{D-2} (Vt)^{7-2D}} \right\} \cdot \int_0^1 dz (z^{D-4}) \cdot \int_{1-z}^1 dy \frac{y^{D-4}}{2-z-y} \quad (4.2.4)$$

where  $r_1 = |x_1|$  and  $r_2 = |x_2|$  and  $r_{1,2} = |x_1 - x_2|$ .

In general, we can write the energy density of a  $k$  order scattering as a multiple integral as

$$E_k^S(t) = W\sigma^k \iint_{-\infty}^{\infty} \int d^3x_1 n(r_1) \iint_{-\infty}^{\infty} \int d^3x_2 n(r_2) \dots \iint_{-\infty}^{\infty} \int d^3x_k n(r_k) \cdot$$

$$\delta(Vt - r_1 - r_{1,2} \dots - r_{k-1} - r_k) \cdot \{(4\pi)^{-k-1} \cdot r_1^{-2} \cdot r_{1,2}^{-2} \cdot r_{2,3}^{-2} \dots \cdot r_{k-1}^{-2} \cdot r_k^{-2}\} \quad (4.2.5)$$

where  $r_1 = |x_1|$ ,  $r_k = |x_k|$  and  $r_{i-1,i} = |x_{i-1} - x_i|$  for  $i=2, \dots, k$

$$\text{The total scattering energy density at the origin is written as a sum: } E^S(t) = \sum_{k=1}^{\infty} E_k^S(t) \quad (4.2.6)$$

As said previously, when  $2 < D \leq 3$  the multiple scattering of order  $k \geq 2$  is stronger and dominates over the single scattering with order  $k=1$  at long lapse time. For  $D=2$ , the energy density of every order has a decay of -3rd power of lapse time. Thus, when we have the condition of  $D < 2$ , the decay gradient for the single scattering energy has the smallest price of all. So, in the case of  $D < 2$ , the single scattering dominates over the multiple scattering at long lapse time.

An important thing we have to note here is that we have not taken into account that there could be scattering energy loss. We are not able to assure about the energy conservation of the sum of the scattered and the direct wave energy density. Only in the case of single scattering, energy conservation was proven (SATO, 1977, Appendix B). We should also add that AKI and CHOUET (1975), as they assumed the distribution of the scatterers' density was a constant number, they interpreted that the power of lapse time for the geometrical factor depends on whether the coda waves are composed of scattered body waves or scattered surface waves. Since we follow the determination that coda waves are the outcome of scattered body waves, the power of lapse time for the geometrical factor is deeply affected by the fractal dimension  $D$  of the scatterers' distribution in three dimensional space.

As a conclusion, Wu and AKI (1985) studied the fractal nature of the lithosphere as an inhomogeneous elastic medium from the spectral structure of coda excitation strength and scattering attenuation. It is left to examine whether the structure of the scatterers' distribution in the lithosphere is indeed fractal and also the regional differences and the frequency dependences of the power of lapse time. We should examine theoretically the scattering attenuation in fractal structure and observationally the change in scattering attenuation with travel distance, as in the case of a small fractal dimension we expect decreasing of scattering attenuation with distance.

### 4.3 Single Isotropic Scattering Model for general source and receiver locations

Now, we will try to calculate the spatiotemporal change in the single scattering energy density at a receiver locate in a position  $x$  which has a distance  $r$  from a point source at the origin in case of isotropic scattering.

First we will proceed with the 3 dimensional space. The scattering is isotropic, the radiation of total energy  $W$  from the source to the origin is spherical, the scatterer is located in a position  $z$  and the receiver is located in a position  $x$ . The energy-flux density is given by

$$\frac{W}{4\pi r_1^2} \delta\left(t - \frac{r_1+r_2}{V_0}\right) \frac{1}{r_2^2} \cdot \frac{\sigma_0}{4\pi} \quad (4.3.1)$$

where  $r_1 = |z|$  is the distance from the source to the scatterers and  $r_2 = |x-z|$  is the distance from the scatterer to the receiver. If we divide by  $V_0$  and then multiply the equation 4.3.1 with the number density of scatterers  $n$ , the energy density will be given by the following

$$E^1(x,t) = \sum \frac{W}{4\pi r_1^2} \delta\left(t - \frac{r_1+r_2}{V_0}\right) \frac{1}{r_2^2} \cdot \frac{\sigma_0}{4\pi V_0} = \frac{W g_0}{(4\pi)^2} \iiint_{-\infty}^{\infty} \frac{\delta(r_1+r_2-V_0 t)}{r_1^2 r_2^2} dz \quad (4.3.2)$$

where  $g_0 = n\sigma_0$ .

Since we have placed the source and the receiver at a distance  $r$  on the third axis, we shall integrate the above equation 4.3.2 by inserting the spheroidal coordinates  $(w, v, \phi)$ . We see the geometry in the following figure.

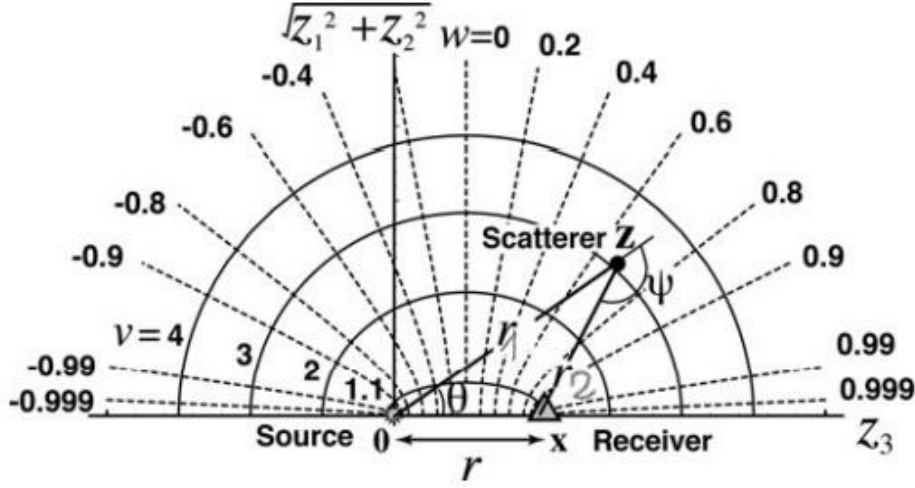


Figure 4.3.1  
Geometry of the single scattering process at a spherical coordinate system

The spheroidal coordinates  $(w, v, \phi)$  are associated with the axis  $z$  by the following equations:

$$\begin{aligned} z_1 &= \frac{r}{2} \sqrt{(v^2 - 1)(1 - w^2)} \cos \phi \\ z_2 &= \frac{r}{2} \sqrt{(v^2 - 1)(1 - w^2)} \sin \phi \\ z_3 &= \frac{r}{2} (1 + vw) \end{aligned} \quad (4.3.3)$$

We will remind that  $r \equiv |x|$  is the distance between the source and the receiver which are chosen focused on the spheroidal coordinates. The ranges of the coordinate are  $1 \leq v < \infty$ ,  $-1 \leq w \leq 1$  and  $0 \leq \phi < 2\pi$ . The receiver and the source locations are given by  $w = -1$  and  $v = 1$  and  $w = 1$  and  $v = 1$  respectively. In addition, we also note that

$$\begin{aligned} r_1 &\equiv \sqrt{z_1^2 + z_2^2 + z_3^2} = \frac{1}{2} r (v + w) \\ r_2 &\equiv \sqrt{z_1^2 + z_2^2 + (z_3 - r)^2} = \frac{1}{2} r (v - w) \end{aligned} \quad (4.3.4)$$

As far as the volume element is concerned, it is infinitesimal and it is given by

$$dz = \left| \frac{\partial(z_1, z_2, z_3)}{\partial(w, v, \phi)} \right| dv dw d\phi = \left( \frac{r}{2} \right)^3 (v^2 - w^2) dv dw d\phi = \frac{r \cdot r_1 \cdot r_2}{2} dv dw d\phi \quad (4.3.5)$$

In figure 4,3,1, there are also  $\psi$  and  $\theta$ , which are the scattering angle and the radiation angle respectively. Those are defined by the equations

$$\psi = \cos^{-1} \frac{r^2 - r_1^2 - r_2^2}{2r_1 r_2} = \cos^{-1} \frac{2 - v^2 - w^2}{v^2 - w^2} \quad (4.3.6)$$

$$\theta = \cos^{-1} \frac{z_3}{r_1} = \cos^{-1} \frac{1 + vw}{v + w} \quad (4.3.7)$$

If we have a given lapse time  $t$  and the velocity is given by  $v = \frac{V_0 t}{r}$  over the spheroidal surface (Sato 1977a) the integral 4.3.2 can be written:

$$E^1(x,t) = \frac{Wg_0}{(4\pi)^2} \int_0^{2\pi} d\varphi \int_1^\infty dv \int_{-1}^1 dw \left(\frac{r}{2}\right)^3 (v^2-w^2) \frac{\delta\left(\frac{v-V_0 t}{r}\right)}{r\left(\frac{r}{2}\right)^4 (v^2-w^2)^2} = \frac{Wg_0}{4\pi r^2} \int_1^\infty dv \cdot \delta\left(v - \frac{V_0 t}{r}\right) \int_{-1}^1 dw \frac{1}{v^2-w^2} = \frac{Wg_0}{4\pi r^2} K\left(\frac{V_0 t}{r}\right) H(V_0 t-r) \quad (4.3.8)$$

Thus, a new function has been introduced:

$$K(v) = \int_{-1}^1 dw \frac{1}{v^2-w^2} = \frac{2}{v} \tanh^{-1} \frac{1}{v} = \begin{cases} \frac{1}{v} \ln \frac{v+1}{v-1} & \text{for } v > 1 \\ \frac{2}{v^2} & \text{for } v \gg 1 \end{cases} \quad (4.3.9)$$

where  $\tanh^{-1} x \equiv \frac{1}{2} \ln \frac{1+x}{1-x}$  for  $|x| < 1$ . This  $K(v)$  function diverges logarithmically as  $v \rightarrow 1_+$  and decays according to the inverse square of  $v$  with increasing  $v$ . The asymptotic time dependence of singly scattered energy density is given by

$$E^1(x,t) \approx \frac{Wg_0}{2\pi V_0^2 t^2} \quad \text{for } V_0 t \gg r \quad (4.3.10)$$

For the case of two dimensional space, Kopnichev (1975) derived the energy density for isotropic scattering, in order for the surface wave scattering to be studied. If there is a receiver located at  $x$  and the source is located at the origin, for impulsive circular radiation  $W$ , the singly scattered energy density is given by the following:

$$E^1(x,t) = \frac{Wg_0}{2\pi r} \frac{H(V_0 t-r)}{\sqrt{\left(\frac{V_0 t}{r}\right)^2 - 1}} \approx \frac{Wg_0}{2\pi V_0 t} \quad \text{for } V_0 t \gg r \quad (4.3.11)$$

where again  $r=|x|$ . The energy density diverges at the direct arrival time and decreases with the inverse power of lapse time near the source location.

#### 4.4 Diffusion Model

The integral  $\iiint_{-\infty}^{\infty} E^1(x,t) dx = Wg_0 V_0 t$  shows the single scattering energy and shows a monotonously increase while the lapse time also increases. Since we have the total energy conservation happening and we have to maintain it, we will multiply by the exponential scattering attenuation  $e^{-g_0 V_0 t}$  to account for the loss of energy, since the loss of energy is happening due to scattering by the direct energy propagation term. In addition, as in large lapse times multiple scattering is dominant over single scattering, if we have a large lapse time we can assume that the direct energy is being reduced and at the same time the multiple scattering creates a smooth spatial distribution of energy density. It can explain a medium's distribution that is homogeneous and isotropic, the scatterers are also isotropic and the energy  $W$  is radiated spherically from a source located at the origin and is delta function in time. The following diffusion function can well describe the strong process of the multiple scattering

$$(\partial_1 - D\Delta) E(x,t) = W\delta(x)\delta(t) \quad (4.4.1)$$

where diffusivity is  $D = \frac{V_0}{3g_0} = \frac{V_0 l}{3}$ . The analytical for equation 4.4.1 is the following and is called the diffusion solution

$$E^D(x,t) = \frac{W}{(4\pi Dt)^{\frac{3}{2}}} e^{-\frac{r^2}{4Dt}} H(t) \text{ oct }^{-\frac{3}{2}} \quad \text{for } r=0 \quad (4.4.2)$$

Energy density decreases with the – 1.5th power of lapse time near the source location, which is slower than that of the single scattering model. As we said, we also have to satisfy the conservation of the total energy and it is given by the spatial integral of the energy density

$$\iiint_{-\infty}^{\infty} E^D(x,t) dx = W \quad (4.4.3)$$

For the intrinsic attenuation  $Q_c^{-1}$  at an angular frequency  $\omega$ , we can write the function 4.4.2 as:

$$E^D(x,t) = \frac{W}{(4\pi Dt)^{\frac{3}{2}}} H(t) e^{-\frac{r^2}{4Dt} - Q_c^{-1}\omega t} \quad (4.4.4)$$

This model has great and effective use in the analysis of late coda of earthquakes, as well as of coda of lunar earthquakes.

#### 4.5 Energy-Flux Model

This model was proposed by Frankel and Clayton (1986) that in randomly inhomogeneous media used 2D finite difference (FD) simulations of wave propagations and managed to investigate the excitation of coda waves in numerical way. The numerical simulations' results showed that the waves being scattered from the direct wave spread all over the space that is behind the wavefront, quickly. Frankel and Wennerberg (1987), in order to measure the energy density that distributes spatiotemporally proposed a model that is phenomenological. The observations recorded by seismograph envelopes at different distances should be in consistency with the proposed model. Those seismogram envelopes approach asymptotically a decay curve and are consistent with the amplitude of the coda waves that are recorded in large lapse times and in the space behind the S wavefront.

In 1987 Frankel and Wennerberg assumed that if the total energy  $W$  is radiated spherically from the source to the origin, then the scattering has an impact on the distribution of the coda energy density, which is symbolized  $E^{EF}(x,t)$ , as the distribution is spatially uniform within a spherical volume of radius  $V_0t$ . The scattering attenuation has an exponential decay rate of  $e^{S_c} Q^{-1}\omega$  and along with the lapse time increasing, they cause decrease of the direct energy. The model has a strict discrimination between scattered and direct waves. If in this model we are studying there is no intrinsic absorption, then we have conservation of the energy density at angular frequency  $\omega$  that is written

$$We^{-S_c} Q^{-1}\omega t + \frac{4\pi}{3} (V_0t)^3 E^{EF}(x,t) = W \quad \text{for } V_0t > r \text{ and } r=|x| \quad (4.5.1)$$

On this equation, the left part refers to energy that comes from the direct wave, while the right part refers to the energy coming from the scattered wave within a volume and behind the direct wavefront. Thus, the energy density after all is written

$$E^{EF}(x,t) = \frac{3W(1-e^{-S_c Q^{-1}\omega t})}{4\pi(V_0t)^3} H\left(t - \frac{r}{V_0}\right) \approx \frac{3W\omega^{S_c} Q^{-1}}{4\pi V_0^3 t^2} H\left(t - \frac{r}{V_0}\right) \quad \text{for } S_c Q^{-1}\omega t \ll 1 \quad (4.5.2)$$

At small lapse times, the energy density decreases with the inverse square of lapse time in agreement with the single backscattering model solution. The duration of the source is the one that affects the direct wave energy density at the wavefront.

If we insert intrinsic absorption  $lQ^{-1}$ , then we can modify the equation 4.5.2 as:

$$E^{EF}(x,t) = \frac{3W(1-e^{-ScQ^{-1}\omega t})e^{-lQ^{-1}\omega t}}{4\pi(V_0t)^3} H\left(t - \frac{r}{V_0}\right) \quad (4.5.3)$$

It was pointed out by Frankel and Wennerberg (1987), that the  $Q_c^{-1}$ , which is the phenomenological exponential decay factor of coda amplitude is not a simple combination of scattering and intrinsic attenuation, but is closer to the  $lQ^{-1}$  than the  $^{Sc}Q^{-1}$ .

## 5. Radiative Transfer Theory

### 5.1 Introduction in Radiative Transfer Theory

This study is about how we can obtain useful information of the Earth's heterogeneities, by studying coda waves and how their amplitude decreases with the travel time.

Coda waves, as it has been mentioned above, are short period seismic waves that are created by an earthquake source and after they are scattered by heterogeneities in the earth and distributed in the earth medium. Its characteristic is that although their faces are complex, they have smooth and systematic amplitude envelope at a given central frequency. The ballistic term amplitude decay with travel time and the coda amplitude decay with lapse time are measured from the earthquake.

As for the power law characteristics, there is another way to explain what we observe. It has been proposed a concept of a fractal distribution of points, which means that the number density of origin time is enough to describe very sufficiently the medium heterogeneities and absorption properties.

For the study of the distribution of the small-scale heterogeneities, the Radiative transfer theory has been used. However, the conventional theory supports that the scattered waves seen on seismograms are the outcome of scatterers that are uniformly distributed in the Earth. In order to explain their characteristics, as the ballistic term and the coda wave amplitude decreases with time, we will use the Radiative transfer theory of a distribution of isotropic scatterers and intrinsic absorbers with fractal dimension. This fractal dimension should be  $D \leq 3$  in the 3D space.

There are many structures that are fractal-like and can be created by many ways such as fracturing, diffusion, aggregation and dissolution. Many faults, crack systems, surfaces with fragmentations and stratification have fractal structures. Fractals have been used to describe cracks in rocks as well as shear zones and fault systems. As fractals can be also assumed inhomogeneities in the earth, there is a relation between the 3D inhomogeneities in the earth and that of the fault surfaces.

The Radiative transfer theory has been used to synthesize seismogram envelopes in short periods. The conventional theory is based on a distribution of scatterers which is random and homogeneous in space and is characterized by the volume independent scattering coefficient

g<sub>50</sub>. In case of no intrinsic absorption, at large lapse times measured from the earthquake origin time, it leads to the -1.5th power of lapse time for the energy density of coda waves, which corresponds to the mean square (MS) coda envelope.

The ballistic term peak amplitude, as it often takes the maximum amplitude, decreases according to an inverse power of travel distance, the travel time of the wave. We usually use this decay of the amplitude according to travel time to determinate the magnitude of the earthquake. If we use the conventional single scattering model on coda, which predicts the mean square coda amplitude, we can measure the attenuation of coda. Measures that have been done around the world show that the coda attenuation decreases when the lapse time increases. Those measurements also imply that when the depth increases, the intrinsic absorption decreases. Also, after making the logarithm of coda amplitude against lapse time, we have concluded that the decay of coda amplitude can be represented by power law decay. The power law decay of the amplitude by the scattering coefficient decreases with depth. The most important thing that we focus on after those measurements is the power law characteristics of the ballistic and coda wave amplitude increases with time, even though we have noticed there is some scatter in the reported power values in relation with lapse time.

The method that was used traditionally in order to build up the structure of the earth medium was to suppose the velocity's variation of depth, the intrinsic attenuation and the strength of the scattering. However, we have now proposed a new way to suppose what exists underneath the surface. Since we expect a fractal structure behind distributed points depends on the size of a sampled volume. If we have a sphere of radius  $r$  and we are in a 3D space, then the number of points is proportional to  $r^{D-3}$ , where  $D$  is the fractal dimension. If the fractal dimension  $D$  is equal to the Euclidean dimension of the space, then the distribution is homogenous. If the fractal dimension is smaller than the Euclidean dimension of space, this parameter characterizes the clustering nature of points.

There have also been studies that use the hypocenters of microearthquakes as a distribution of cracks that have various sizes. Those cracks and cavities are believed to cause the scattering and there have been theoretical studies around that. Yamashita (1990), while he was trying to explain the observed frequency dependence of  $Q_s^{-1}$  for S waves, proposed randomly oriented cracks characterized by a power law size distribution. Benites (1997) studied scattering by a cluster of many cavities, Murai (1995) studied scattering not by one but by several clusters with thin cracks, while Robertson the same year reported  $D \approx 1.82-2.01$  for the microearthquake hypocenter distribution in southern California. Hirata and Imoto (1991) had analyzed the hypocenter distribution in Kanto Japan and their estimation about the dimension was  $D \approx 2.2$  for the distance range from 1 to 10 km. A decade later, Nogushi (2001) used another method at the same area and estimated  $D \approx 2.3$  for the distance range from 10 to 100 km. The region beneath the area studied is heterogeneous and as the Pacific and Philippine plates collide and subduct under the North American plate. All those studies lead us to believe that there is a fractal distribution of scatterers and absorbers in the earth medium with a dimension smaller than the Euclidean one.

Sato (1988) proposed a mathematical model that is applied in a 3D medium and for the power law decay of amplitude with travel distance through a fractal distribution of absorbers/scatterers. This model was applied by Godano et al. (1994) in the areas of Italy and New Mexico to short period seismic data and he concluded that the range of  $D$  is between 2 and 3. Rastogi & Scheucher (1990) observed the above results in the atmosphere, as from

some atmospheric radar experiments, they studied back scattered radio-coda waves by a fractal distribution of meteorological turbulences. Another formulation of this theory was on a fractal distribution of isotropic scatterers by Sato & Fehler (1998, p. 186). However, their research was focusing on the spatial distribution that occurred on the energy density of coda waves by the inhomogeneities and the intrinsic absorption was left aside.

We are about to present a formulation of the Radiative transfer theory for the propagation of energy density through a fractal distribution of isotropic scatterers and intrinsic absorbers. If we proceed with solving it for the instant spherical radiation from a point source, we examine the space time distribution of the synthesized energy density. We will show that this model for  $D \leq 2$  well predicts a power law decay of the ballistic and coda wave amplitudes with time.

## 5.2 Application of the Radiative Transfer Theory

In the previous chapters, we have made an introduction to the theory that we will use, in order to analyze our data and come to the results. The distribution of scatterers we will be using, is fractally random and homogeneous, and consists of isotropic scatterers and intrinsic absorbers. Their fractal dimension should be  $D \leq 3$ , in a 3 dimensional space.

If we suppose that we have a sphere of radius  $r$ , the number density of scatterers or absorbers is proportional to  $r^{D-3}$  for a distance  $r \gg r_c$ , which is constant for  $r \ll r_c$ , where  $r_c$  is the corner distance. The purpose of the corner distance is to avoid divergence at a small  $r$ . The fractal dimension can be between  $D=1$  and  $D=3$ . In the case of  $D=3$ , the distribution is the conventional uniform one. In the case of  $D=2$ , which is the one we are studying, we will figure out that the mean square amplitude of coda waves decreases according to a power of lapse time measured from the origin time and the mean square amplitude of the ballistic wave decreases according to a power of travel time. The powers of lapse and travel time are both controlled by the scattering coefficient, intrinsic absorption coefficient and corner distance. In the last case of  $D=1$ , the mean square amplitude of the of the ballistic wave decays according to the inverse square of time, when the decay of the coda energy is much faster.

Another important parameter we can measure regarding the coda waves, when the conventional single scattering model is applied to them is the coda attenuation  $Q_c^{-1}$ . It has been shown that at an angular frequency  $\omega$ , the mean square amplitude decreases according to  $t^{-2} \exp [Q_c^{-1} \omega t]$  (e.g. Aki & Chouet 1975; Sato 1977). Observations have shown that the coda attenuation  $Q_c^{-1}$  decreases as the lapse time increases (Rautian & Khalturin 1978; Roecker et al. 1982; Kosuga 1992). This phenomenon has been compared to the decrease of the intrinsic absorption with the increasing of the depth. Later, Gusev (1995) proposed that the coda amplitude decay can be represented by power law decay. He came to this conclusion, as he plotted the logarithm of coda amplitude against that of lapse time.

After the data of local earthquakes in the former Soviet Union, he reported that at a 1.3 Hz band for a wide lapse time range, their mean square amplitudes decay according to the 4–6th inverse power of lapse time. From the analysis of IRIS (Incorporated Research Institutions for Seismology) data, Lee & Sato (2006) observed that at a 1 Hz band the mean square amplitude decays according to the 6–10th inverse power of lapse time. At these observations there is some scatter happening, which is related with lapse time ranges, however we focus on the

alteration of the power law characteristics of the ballistic and coda wave amplitudes with the increase of the time.

### 5.3 Fractal distribution of scatterers and absorbers

Regarding the implement of the Radiative transfer theory, we will now present the equations and the process we followed in order to find the results that will be shown next. We have already explained that in the conventional radiative transfer theory, the distribution both of the intrinsic absorbers and the isotropic scatterers is random and homogenous (Sato 1977; Hoshiba 1991; Zeng et al. 1991). When we are in a Euclidian dimension of space and more specific in a 3D space, the number density of scatterers is independent of volume size. If there is a sphere in this 3D space, that its radius is  $r$ , then the number of the scatterers is proportional to  $r^3$ , where 3 is the number of the space. However, we don't study the distribution in a Euclidian dimension, we are studying the distribution of scatterers, which are isotropic, in a fractal distribution that is random and homogeneous with fractal dimension  $D$  in a 3D space. Thus, if we are again in a sphere radius  $r$ , the total number of the scatterers will now be proportional to  $r^D$  and the number density will be proportional to  $r^{D-3}$ , where  $D$  can be any value less or equal to 3, so  $D \leq 3$ . Since the fractal dimension we are working on is supposed to be homogeneous, we can consider any point of the radius to be its center.

We first mathematically define a function of  $r$ :

$$f(r) = \frac{1}{\sqrt{1 + \left(\frac{r}{r_c}\right)^2}}^{3-D} \approx \begin{cases} 1 & \text{for } r \ll r_c \\ \frac{r_c}{r} & \text{for } r \gg r_c \end{cases} \quad (5.3.1)$$

where  $r_c$  is the corner distance and it is introduced in order to avoid divergence at  $r=0$ . This function  $f(r)$  shows the power law decay at large distances and the corner distance  $r_c$  is the lower bound of the fractal structure. In the power law range,  $r_c$  gives the absolute value of the  $f(r)$  function. We will also introduce some other coefficients, in order to better describe the function, as well as the scattering process. We have the scattering cross-section  $\sigma_{s0}$ , the total scattering coefficient  $g_s(r)$ , the total scattering coefficient  $g_{s0}$  for  $r \ll r_c$  and we will define by those the number density function of isotropic scatterers  $n_s(r)$ :

$$n_s(r) \equiv n_{s0} f(r) \quad (5.3.2)$$

$$g_s(r) \equiv g_{s0} f(r) = \sigma_{s0} n_{s0} f(r) \quad (5.3.3)$$

$$g_{s0} = \sigma_{s0} n_{s0} \quad (5.3.4)$$

The  $n_s(r)$  and  $f_s(r)$  show differences depending on the distance. For distances shorter than the corner distance  $r_c$  they are uniform but for distances larger than  $r_c$  they are fractal with a fractal dimension  $D$ .

Since we have defined the coefficients for the isotropic scatterers, we will now do the same for the intrinsic absorbers. We will use the same function  $f(r)$  and we have the coefficient  $g_i(r)$ , which is the intrinsic absorption coefficient and  $b_i0$  which is the ratio of intrinsic absorption coefficient to scattering coefficient.

$$g_i(r) = g_{i0} f(r) = \sigma_{i0} n_{i0} f(r) = b_i0 g_s(r) \quad (5.3.5)$$

$$b_i0 = g_{i0} / g_{s0} \quad (5.3.6)$$

We will also define  $B_0$  as the seismic albedo that is the ratio of scattering coefficient to the sum of scattering and intrinsic absorption coefficients.

$$B_0 = g_s / (g_s + g_i) = 1 / (1 + b_i) \quad (5.3.7)$$

In the following figure, we can examine how the function  $f(r)$  changes for different fractal dimensions. We will set the corner distance  $r_c = 1$  and we will study the region between  $0.1 \leq r \leq 100$  for the fractal dimensions  $D=1, D=1.5, D=2, D=2.5$  and  $D=3$ .

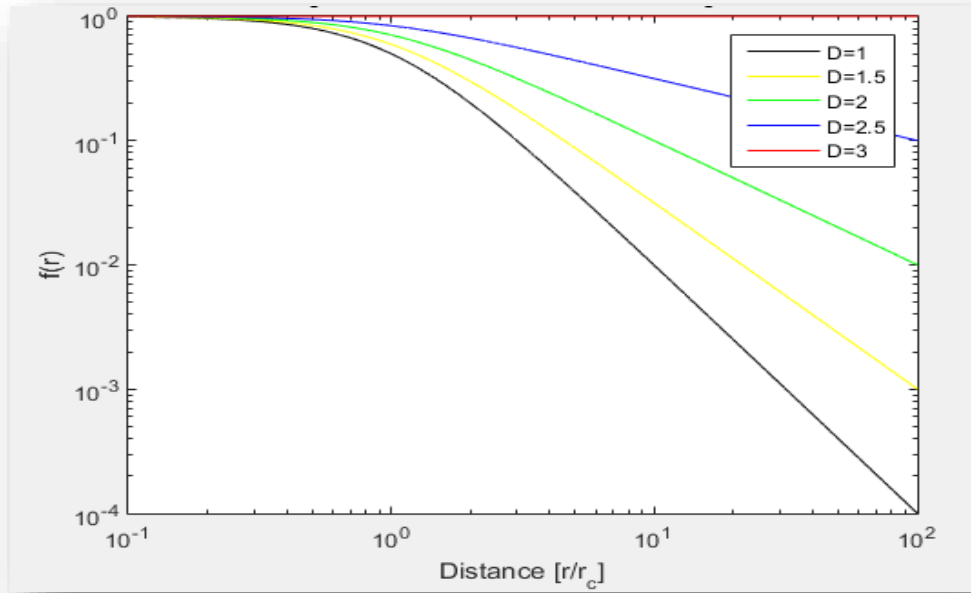


Figure 5.3.1 Plot of  $f(r)$  against  $r/r_c$  for various  $D$  values, where  $r_c$  is the corner distance

As it is seen from the figure, for the fractal dimension  $D=3$  the price of the function  $f(r)$  is steady at 10, and is independent of the price of the distance  $r$  and corner distance  $r_c$ . For the other dimensions  $D=1, D=1.5, D=2$  and  $D=2.5$ , the prices begin to decrease steeper as we are closer to  $D=1$  and smoother as we get closer to  $D=3$ .

#### 5.4 Equations in Radiative Transfer Theory

One of the most important things to measure after the scattering of seismic waves in the fractal medium, is the propagation of the energy density  $E(x,t)$ , where  $x$  is the position vector. The following figure 5.4.1 shows the propagation of the energy density from the source to various directions. We consider that the vectors  $x_1, x_2, x_3$  depict the different directions of the energy propagation and the vector  $x$  is the one depicting the position of the observer, thus it is the position that we make the measurements. If we consider that  $x'$  is the point that the last scattering occurred, we will take into consideration the distance  $|x-x'|$  for the following equation:

$$E(x, t) = WG(x, t) + V\sigma_{s0}n_{s0} \int \iiint_{-\infty}^{\infty} G(x - x', t - t') xf(|x - x'|) E(x', t') dx' dt' \quad (5.4.1)$$

where  $V_0$  is the background velocity and  $n_{s0}|x-x'|$  the number density of the isotropic scatterers that we find in the distance  $|x-x'|$ .

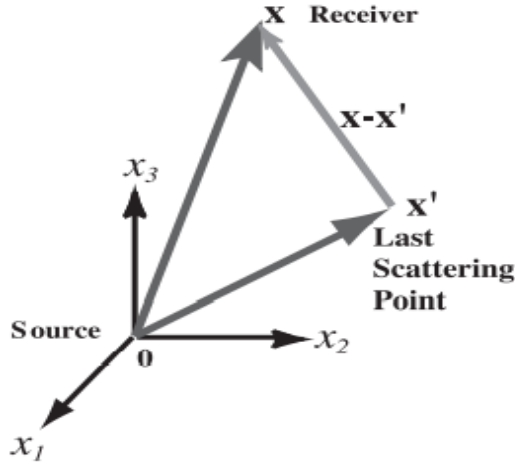


Figure 5.4.1 Geometry of the scattering process for spherical radiation from the source at the origin.

Now, if we wish to define the ballistic term, we have to take into consideration, in order to proceed with an equation, the geometrical factor, causality, scattering and intrinsic loss term. We have the following, where  $r=|x|$ :

$$G(x,t) = \frac{1}{4\pi V_0 r^2} \delta\left(t - \frac{r}{v_0}\right) e^{-U(r)} \quad (5.4.2)$$

The function  $U(r)$  on the exponent of the previous equation is given by a line integral along the ray and we can use Gauss's hypergeometric function  ${}_2F_1$  on it.

$$U(r) = \int_0^r [g_s(r') + g_i(r')] dr' = (\sigma_{s0} + \sigma_{i0}) n_{s0} \int_0^r f(r') dr' = (1+b_{i0}) g_{s0} \int_0^r \left[1 + \left(\frac{r'}{r_c}\right)^2\right]^{\frac{D-3}{2}} dr' =$$

$$(1+b_{i0}) g_{s0} r^{\frac{1}{2}} \int_0^1 t^{-1/2} \left[1 - t \left(-\frac{r^2}{r_c^2}\right)\right]^{\frac{3-D}{2}} dt = (1+b_{i0}) g_{s0} r {}_2F_1\left(\frac{3-D}{2}, \frac{1}{2}; \frac{3}{2}; -\frac{r^2}{r_c^2}\right) \quad (5.4.3)$$

In this equation we have used the transform  $r' = r\sqrt{t}$  (Gradshteyn & Ryzhik 2007, p. 1005) and in differential form it is written:

$$\frac{dU(r)}{dr} = g_s(r) + g_i(r) = (1+b_{i0}) g_{s0} f(r) \quad (5.4.4)$$

After defining the above equations, we will now move them in the Fourier space. If we suppose that  $G_F(x,t) = G(x,t)f(|x|)$  (5.4.5)

then we can write the integral equation 5.4.1 accordingly as

$$E(x,t) = WG(x,t) + V_0 g_{s0} \int \int \int_{-\infty}^{\infty} G_F(x-x', t-t') x E(x', t') dx' dt' \quad (5.4.6)$$

The above equation 5.4.6 in the Fourier domain it is written as:

$$\hat{\tilde{E}}(k,\omega) = \frac{W\hat{\tilde{G}}(k,\omega)}{1 - V_0 g_{s0} \hat{\tilde{G}}_F(k,\omega)} \quad (5.4.7)$$

We should mention that the tilde and the over hat mean the Fourier transform with respect to space and time coordinates, respectively. If we perform on 5.4.7 the integral over time and solid angle we will obtain the following:

$$\hat{G}(k, \omega) = \int \int \int_{-\infty}^{\infty} G(x, t) e^{-ikx + i\omega t} dx dt = \frac{1}{V_0} \int_0^{\infty} e^{-U(r) + i\omega r/V_0} \frac{\sin kr}{kr} dr \quad (5.4.8)$$

$$\hat{G}_F(k, \omega) = \frac{1}{V_0} \int_0^{\infty} f(r) e^{-U(r) + i\omega r/V_0} \frac{\sin kr}{kr} dr \quad (5.4.9)$$

In order to continue, we an inverse Fourier transform will be used and the integral equation of the energy density will be getting

$$E(r, t) = \frac{1}{(2\pi)^4} \int \int \int_{-\infty}^{\infty} \hat{E}(k, \omega) e^{-ikx - i\omega t} dk d\omega = \frac{1}{2\pi} \int_{-\infty}^{\infty} d\omega e^{-i\omega t} \frac{1}{2\pi^2 r} \int_0^{\infty} dk k \sin kr \hat{E}(k, \omega) \quad (5.4.10)$$

## 5.5 Method of Coda normalization

The idea of coda normalization is based on the necessity to make the assessment of seismic risk more accurate. In order to achieve that, it is needed to take into consideration the parameter's frequency dependence. We have to quantify the seismic source radiation, the effects of the propagation and the receiver site amplification. This is usually achieved by eliminating the two of them, so that the one that we wish to study is being left alone and we can evaluate it in more detail. The seismic source radiation estimations are more important than the others for quantifying the size of earthquakes and explosions. The effects of the propagation include the influence of the deterministic velocity structure, among other effects, as the attenuation along the source receiver path. The amplification of the receiver site is being influenced by the geology of the near surface that can alter the recorded waveform's character only near the place of the recording. Near surface geology can cause other influences too, such as reverberation, local amplification of signal or even add more complexity in the waveform, that cannot be modeled deterministically from information that are available at the moment. In order to make the measurements more accurate, building codes is needed to be established, in order to estimate which areas are being more affected by seismic hazards. For establishing these codes, there have to be reliable estimates of the relative ground motion in seismically active zone as a function of spatial location. Since those estimate's purpose is to be aware of the areas with more seismic phenomena, in order to provoke hazards and be prepared, they will be more helpful, if they can be given as a function of frequency, as the buildings respond to the ground motion according to frequency.

The method of coda normalization is based on the uniform distribution of seismic energy at a certain lapse time, normally for long lapse times, in some volume that is around the source. Some empirical observations have indicated that from records of regional seismic networks, the length of the seismogram is proportional to the magnitude of the event. In addition, for some local earthquakes recorder at times greater than almost twice the travel time of an S wave from a source to a receiver, the seismograms with bandpass filter have an envelope shape that is common and is independent of the distance between the source and the receiver. However, the envelope's maximum amplitude varies according to the size of the source and the recording amplification of the site. Its primary use is to give us the opportunity to estimate the difference of site amplification factors as a function of frequency, to remove differences in source spectral characteristics and to use data from only a single station in order to measure attenuation.

## 5.6 Equations in the non-dimensional form

Since we have represented the equations that are used in order to explain the energy density and its propagation, we will now represent those equations by using normalized quantities, in order to understand the theoretical solutions. We will normalize length, time and all the quantities that are related to  $W$ ,  $g_{s0}$  and  $V_0$ . The normalized quantities will be

$$\bar{t} = V_0 g_{s0} t, \quad \bar{x} = g_{s0} x, \quad \bar{G} = \frac{G}{g_{s0}^3}, \quad \bar{G}_F = \frac{G_F}{g_{s0}^3}, \quad \bar{E} = \frac{E}{W g_{s0}^3}, \quad \bar{r}_c = g_{s0} r_c = \frac{r_c}{g_{s0}^{-1}} \quad (5.6.1)$$

As we have now the quantities in the normalized form, the Radiative transfer equation for the normalized energy density will be:

$$\bar{E}(\bar{x}, \bar{t}) = \bar{G}(\bar{x}, \bar{t}) \int \iiint_{-\infty}^{\infty} \bar{G}_F(\bar{x} - \bar{x}', \bar{t} - \bar{t}') \bar{E}(\bar{x}', \bar{t}') d\bar{x}' d\bar{t}' \quad (5.6.2)$$

We should also mention:

$$\bar{G}(\bar{x}, \bar{t}) = \frac{1}{4\pi\bar{r}^2} \delta(\bar{t} - \bar{r}) e^{-U(\bar{r})} \quad (5.6.3)$$

$$\bar{G}_F(\bar{x}, \bar{t}) = \bar{G}(\bar{x}, \bar{t}) f(\bar{r}) \quad (5.6.4)$$

$$U(\bar{r}) = (1 + b_{i0}) \int_0^{\bar{r}} f(\bar{r}') d\bar{r}' = (1 + b_{i0}) \bar{r}_2 F_1 \left[ \frac{3-D}{2}, \frac{1}{2}; \frac{3}{2}; -\left(\frac{\bar{r}}{\bar{r}_c}\right)^2 \right] \quad (5.6.5)$$

In figure 5.6.1 that we see below, for  $\bar{r} \gg \bar{r}_c$  the function is curved for  $D < 2$  and as it approaches to  $D=2$  it becomes a straight line. As the fractal dimension approaches to  $D=1$ , the curve is becoming a straight line for large distances.

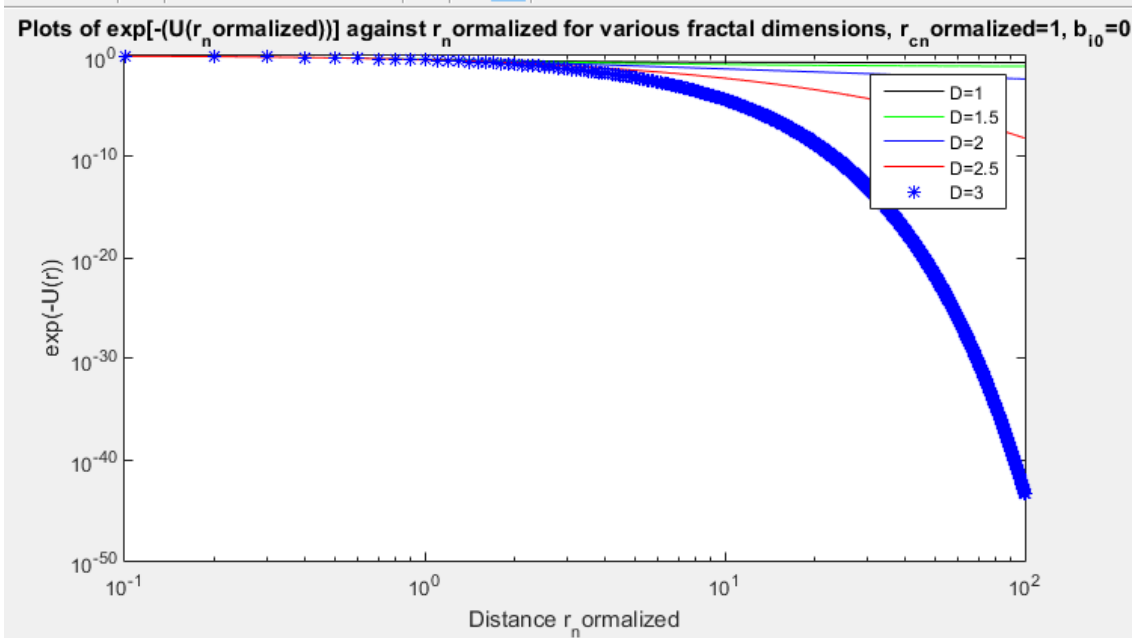


Figure 5.6.1 Plots of  $e^{-U(\bar{r})}$  against normalized travel distance  $\bar{r} = \bar{t}$  for various fractal dimensions, where  $\bar{r}_c = 1$  and  $b_{i0} = 0$

## 5.7 The ballistic term

In this section we will study the ballistic term and especially how it decays with travel time. In function 5.4.2 that we defined previously, we used the delta function to present the propagator of the ballistic energy. With the use of equation 5.4.2 the distance dependence of the energy density of the ballistic term is  $\frac{W e^{-U(r)}}{4\pi r^2 V_0} \delta\left(\frac{t-r}{V}\right)$ . (5.7.1)

If we choose a short duration distance from the source compared to the traveltime, which we will symbolize  $\bar{T}_w \ll 1$ , in this time window of the length  $\bar{T}_w$  with  $r=V_0 t$ , the ballistic energy density will be  $\frac{W e^{-U(r)}}{4\pi r^2 V_0 \bar{T}_w}$ . (5.7.2)

In the specific case of  $D=3$  the energy density if the ballistic term is:

$$E^0(r=V_0 t) = \frac{W e^{-(1+b_{i0})g_{s0}V_0 t}}{4\pi T_w V_0^3 t^2} \quad (5.7.3)$$

If the fractal dimension is  $D=2$ , we can approximately define that

$$U(r) \approx (1+b_{i0})g_{s0}r_c \ln\left(\frac{2r}{r_c}\right) \text{ for } r \gg r_c \quad (5.7.4)$$

$$as_2F_1\left(\frac{1}{2}, \frac{1}{2}, \frac{3}{2}; -z^2\right) = \frac{\sinh^{-1}z}{z} = \frac{[\ln(z+\sqrt{1+z^2})]}{z} \approx \frac{\ln 2z}{z} \text{ for } z \gg 1$$

$$\text{For } r=V_0 t \text{ we have } E^0(r=V_0 t) = \frac{W}{\pi T_w r_c^2 V_0} \left(\frac{r_c}{2V_0 t}\right)^{2+(1+b_{i0})g_{s0}r_c} \quad (5.7.5)$$

where the inverse power of traveltime is larger than 2 and it depends on the scattering, the absorption and the corner distance.

If now the fractal dimension is  $D=1$ , and  ${}_2F_1\left(1, \frac{1}{2}, \frac{3}{2}; -z^2\right) = \frac{\tan^{-1}z}{z} \approx \frac{\pi}{2z}$  for  $z \gg 1$  then

$U(r) \approx (1+b_{i0})\pi g_{s0}r_c$  for  $r \gg r_c$  which leads to the traveltime's inverse square

$$E^0(r=V_0 t) = \frac{W e^{-(1+b_{i0})\pi g_{s0}r_c}}{4\pi T_w V_0^3 T^2} \quad (5.7.6)$$

If we are about to measure the ballistic energy in the non-dimensional form, again at a time window  $\bar{T}_w \ll \bar{t}$  and for  $\bar{r} \gg \bar{r}_c$  we will have the energy density

$$\bar{E}^0(r=V_0 t) = \frac{e^{-(1+b_{i0})\bar{t}}}{4\pi \bar{T}_w \bar{t}^2} \text{ for } D=3 \quad (5.7.7)$$

$$= \frac{1}{\pi \bar{T}_w \bar{r}_c^2} \left(\frac{\bar{r}_c}{2\bar{t}}\right)^{2+(1+b_{i0})\bar{r}_c} \text{ for } D=2 \quad (5.7.8)$$

$$= \frac{e^{-(1+b_{i0})\pi \bar{r}_c}}{4\pi \bar{T}_w \bar{t}^2} \text{ for } D=1 \quad (5.7.9)$$

In the following figure 5.7.1, we see log-log plots of the normalized ballistic energy density  $\bar{E}^0(\bar{t})$  for various  $D$  values. It is obvious that the decay of the ballistic energy density is affected by the fractal dimension, thus fractal dimension is the most important parameter for the amplitude decay of the ballistic term with travel distance. When  $D \leq 2$ , the curve of the decay is almost straight, while as we move to  $D=3$ , the curve becomes steeper. The case of  $D=2$ , is special, as the curve of decay is affected by scattering, corner distance and intrinsic absorption.

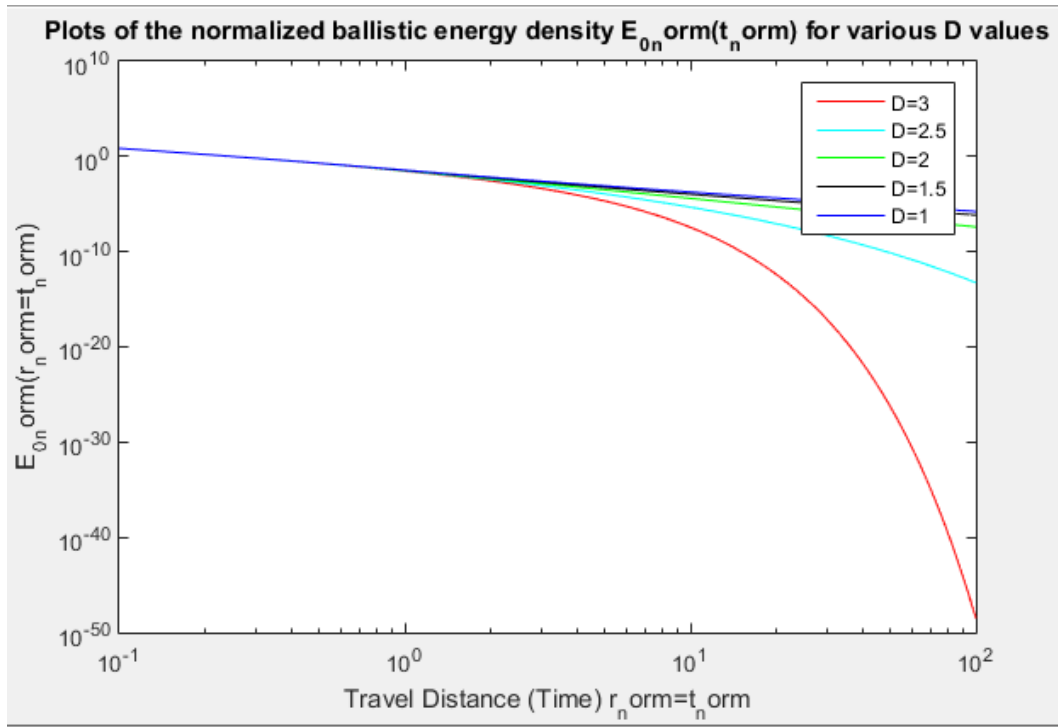


Figure 5.7.1 Plot of the normalized ballistic energy density  $\bar{E}^0(\bar{t})$  in time window  $\bar{T}_w$  against normalized travel distance  $\bar{r} = \bar{t}$  for various fractal dimensions, where  $\bar{r}_c = \bar{T}_w = 1$  and  $b_{i0} = 0$ .

The next figure 5.7.2, refers to the special case of fractal dimension  $D=2$ , for various values of  $b_{i0}$  of the normalized ballistic energy density  $\bar{E}^0(\bar{t})$  in a time window  $\bar{T}_w = 1$  and corner distance  $\bar{r}_c = 1$ . The conclusion is that as the intrinsic absorption increases according to the inverse power of  $2 + (1 + b_{i0}) \bar{r}_c$ , the decay gradient becomes steeper.

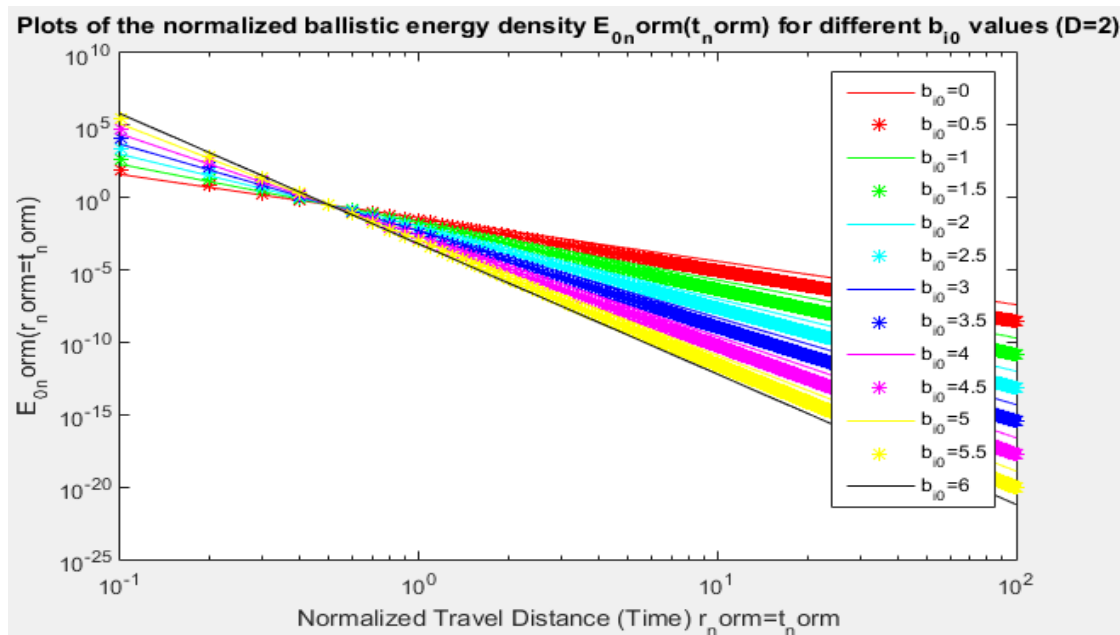


Figure 5.7.2 Plot of the normalized ballistic energy density in the time window  $\bar{T}_w$  against normalized travel distance  $\bar{r} = \bar{t}$  for various intrinsic absorption parameter for the fractal dimension  $D=2$ , where  $\bar{r}_c = \bar{T}_w = 1$

## 6. Statistical Analysis

In the present study, we focus on the dynamical evolution through the natural processes of the area of central Greece, by instrumental seismological observations. Thus, it is necessary to understand the connection between the basic concepts of statistics with the wider study of seismology, along with the transition from statistical mechanics to the generalized framework of non-extensive statistical mechanics-physics (NESM theory).

### 6.1 Introduction to statistical parameters

In statistics, when we are working with population and sample data, there are two different ways to approach the result. In order for each data point to be well determined, the whole population must be given. If we are working on a sample of the whole population, each data point is an approximation of the population parameter. As a result, all formulas are algebraically adjusted to reflect this statistical issue.

The parameters that are used in the statistics and provide us with numerical information about the distribution of the dataset we are working on are the mode, median, mean, range, variance and standard deviation. The parameters of range, variance and standard deviation provide measurements of spread, while the parameters of the mode, median and mean refer to the central tendency. In order to be more specific, the mode refers to the data value that is presented most frequently, the median refers to the value that is positioned in the middle of the given ordered dataset and the mean is referred to the arithmetic average, while the range can be calculated as the difference between the maximum and the minimum value. The variance measures the dispersion around the mean value. Population variance, denoted as  $\sigma^2$ , is given by the equation:

$$\sigma^2 = \frac{\sum_{i=1}^N (x_i - \mu)^2}{N} \quad (6.1.1)$$

where N and  $\mu$  refer to the total number of observations.

The sample variance, which is denoted by  $s^2$  is given by the equation:

$$s^2 = \frac{\sum_{i=1}^n (x_i - \bar{x})^2}{n-1} \quad (6.1.2)$$

where n and  $\bar{x}$  refer to sample observations.

Since there are two types of variance, population and sample, there are also population and sample standard deviation. Those two are given by the square root of the population variance and square root of the sample variance respectively.

The equation for the standard deviation is:

$$s = \sqrt{\frac{\sum (x_i - \bar{x})^2}{n-1}} \quad (6.1.3)$$

## 6.2 Gaussian (Normal) distribution

The Gaussian distribution is also called the “bell shaped curve”, due to its symmetric curve, which means that is symmetrical about the mean. In this distribution, the relative probability of an independent variable, which variable is always centered on the average value, is represented by the y axis. The standard deviation defines any curve’s width. When the shape of the curve bell is narrow, then the value of the standard deviation is small. When the shape of the curve bell is wide, then its value is big. Lastly, the centered curve bell refers to a normal distribution.

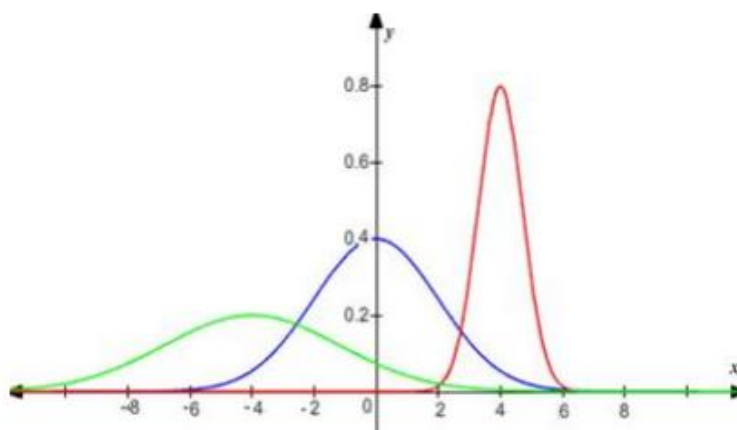


Figure 6.2.1 The three different types of normal distribution, depicted with different colors. The green line, which has a wide curve, refers to a distribution with mean value equal to -4 and standard deviation 2. The blue line refers to a normal distribution with mean value 0 and standard deviation 1 and the red line, which is a narrow curve, refers to a distribution with a mean value of 4 and standard deviation equal to 0.5.

The normal distribution is being depicted in the behavior of many physical phenomena. This is a result of the central limit theorem and of the normal distribution of the mean values, no matter how many measurements are being conducted. Also, even other means that were calculated from samples which were taken from a specific distribution are normally distributed.

The mean’s normal distribution can be also used to conduct the student’s test to find a potential difference between the means between two samples, to make confidence intervals and ANOVA (analysis of variance) in order to find differences among three or more samples.

In the theory of probability, the Gaussian distribution, which is also known as normal or Laplace-Gaussian distribution, is a type of a continuous probability distribution and has the equation:

$$f(x) = \frac{1}{\sigma\sqrt{2\pi}} e^{-\frac{1}{2}\left(\frac{x-\mu}{\sigma}\right)^2} \quad (6.2.1)$$

where  $\mu$  is the mean, median and mode of the distribution and  $\sigma$  represents the standard deviation.

A random variable can have a specific value of  $x_i$  or exist within an interval of  $dx$ . The probability of those is given by the functions of the random variable  $X$ . There are two cases: the discrete and continuous case. For the discrete case the function is:

$$f_x(x_i) = P(X=x_i) \quad (6.2.2)$$

$$\text{with } f_x(x_i) \geq 0 \quad (6.2.3)$$

$$\text{and } \sum_{i=1}^m f_x x_i = 1 \quad (6.2.4)$$

The above function is known as as probability mass function.

For the continuous case, the function is known as probability density function and the conditions are:

$$f_x(x) \geq 0 \quad (6.2.5)$$

$$\text{and } \int_{-\infty}^{\infty} f_x(x) dx = 1 \quad (6.2.6)$$

The cumulative distribution function  $F_x(x)$  can determine a random variable's X probability distribution. That indicates the probability of the random variable X to get equal or smaller values to a specific x value. For the case of a discrete variable X we have:

$$F_x(x_i) = P(X \leq x_i) = \sum_{x \leq x_i} f_x(x) \quad (6.2.7)$$

For the case of a continuous random variable X we have:

$$F_x(x) = P(X \leq x) = \int_{-\infty}^{\infty} f_x u du \quad (6.2.8)$$

A characteristic of the normal distribution is that is universally unimodal. It is fully characterized by the parameters  $\mu$  and  $\sigma$  and its curve is symmetric around the mean value. Another characteristic of the normal distribution that is universal is that within one standard deviation away from the mean value, 68% is approximately the area covered. For two standard deviations, within this range, the covered area is about 95%. Within three standard deviations, the percentage of the covered area is 99.7%. If course we can continue increasing the range of standard deviation along with the covered area respectively. As it is known, the normal distribution never touches the x-axis, thus it will continue to infinity with an arbitrary standard deviation. In this case, the probability of the existence of outlier data point will end up close to zero, which is not happening in many natural systems.

### 6.3 Measures of Skewness and Kurtosis

When we need to analyze data, we need first to understand the shape of data, in order to observe where the most information lies and analyze the outliers. Thus, it is crucial to make a reference to the importance of skewness and kurtosis in statistics.

Skewness is a measure that is commonly used in statistics and characterizes the asymmetry of any unimodal curve and the distribution of data. It is given by the following relation:

$$Sk = \frac{\frac{1}{n} \sum_{i=1}^n (x_i - \bar{x})^3}{\sqrt{\frac{1}{n-1} \sum_{i=1}^n (x_i - \bar{x})^2}} \quad (6.3.1)$$

The direction of the skew reflects on which side the tails are leaning to, thus it can be also abstract, since it does not show the side that the line is leaning to. It is considered to be the degree of distortion, as it is deviating from the normal distribution's initial, symmetrical bell-

like curve and it also differentiates the outliers on the right side as a function to the left tail and on the left side as a function to the right tail respectively.

In the following figure 6.3.1, we can see the three cases of skewness. To the left, we have the case of the positive or right skewness. The tail on the right is either fatter or longer. In this case the mean value is bigger than the median and at the peak of the distribution the mode is located. The central distribution is a symmetrical one with ideal symmetrical tails. To the right side, we have a negative or left skewness, where the tail on the left is fatter or longer.

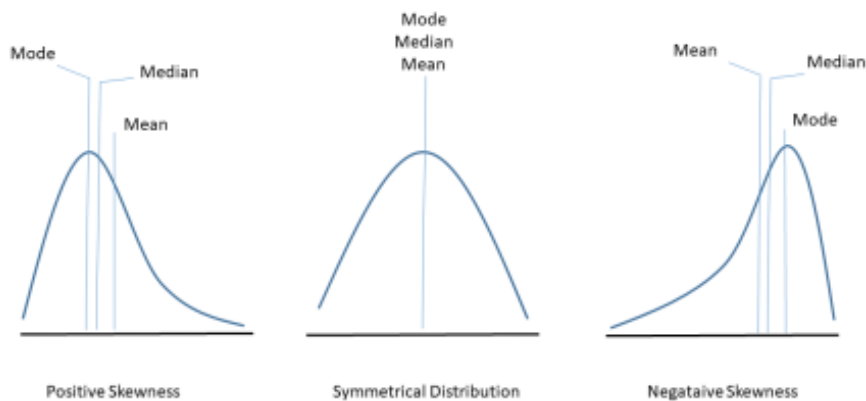


Figure 6.3.1 The three different types of skewness.

Moving to the kurtosis, we should firstly refer that it determines the heaviness of the distribution tails. It constitutes a mean to measure the behavior of flatness of any given distribution, while taking into consideration the extreme values within the tails. In kurtosis, we observe three different types. At a normal distribution, the kurtosis is called Mesokurtic curve. When we have a distribution that is lower peaked than Mesokurtic and has shorter tails, the kurtosis is called Platykurtic curve. Lastly, when the peak is higher than Mesokurtic, the kurtosis is called Leptokurtic curve. Kurtosis is given by the following relation:

$$Ku = \frac{\frac{\sum_{i=1}^N (y_i - \bar{y})^4}{N}}{\sqrt{\frac{1}{n-1} \sum_{i=1}^n (x_i - \bar{x})^2}} \quad (6.3.2)$$

## 6.4 Power law in nature

Power law is a distribution that is applied in many scientific areas, such as physical, chemical, social as well as biological phenomena. It has been observed that many irrelevant phenomena have similar statistical behavior. Among those phenomena are the frequency of words we use in our lifetime (oral and written), similarity of protein structure sequences, gamma-ray intensity of solar flares, city populations, the scale (diameter) distribution of Lunar craters, normal immune receptors, forage pattern in many different species, predator strategies, road and websites traffic, engaging neural patterns, the loss of souls in wars, the frequency at which our complex structured brain forgets, citation number of academic researches, the popularity of opening chess strategies and of course in earthquake magnitudes and the dissipated release of energy.

Those systems might be natural or human made and sometimes they can even be biased, however they present every time the power law behavior. George Kingsley Zipf was the first who introduced this characteristic. His distribution, which is named after him, Zipf distribution, is related to the discrete power law Pareto distribution and the Riemann zeta distribution. The first one, Pareto distribution, which is also known as power law distribution is given by the following relation:

$$\Pr(X>x) = \bar{F}(x) = \left(\frac{x_{min}}{x}\right)^{\alpha} \quad \text{when } x \geq x_{min} \quad (6.4.1)$$

## 6.5 Power law in seismology

Power law distribution is also being noticed in seismology. At an earthquake population, if we apply the empirical Gutenberg and Richter (G-R distribution) scaling relation, a power law behavior will be indicated, as we can see in the equation below:

$$\log N (N>M) = a - bM \quad (6.4.2)$$

where  $N (N> M)$  is the sum of all the earthquakes with magnitude equal or greater than  $M$ , while the value of  $a$  indicates the total seismicity rate of the region that is being investigated. The  $-a-$  value is associated as the intersection of the linear regression model with  $y$ -axis ( $\log N$ ). The  $b$  value is a parameter that shows the proportion of small to large earthquake events. The equation that follows gives the maximum likelihood solution of the  $b$  value:

$$b = 1/\log(10)(\bar{M} - M_c) \quad (6.4.3)$$

where  $\bar{M}$  is the mean magnitude that has been observed and  $M_c$  is the completeness magnitude. The equation below represents the generalization form:

$$\log N > m = \log N + \left(\frac{2-q}{1-q}\right) \log \left[1 - \left(\frac{1-q}{2-q}\right) \left(\frac{10^{2m}}{a^{2/3}}\right)\right] \quad (6.4.4)$$

where  $N$  is as said before, the total number of events,  $q$  is the non extensivity parameter and  $a$  is a proportional constant. Thus, the equivalent power law expression of the G–R distribution is:

$$N (> M) = 10^{a-bM} \quad (6.4.5)$$

The result is that the Gutenberg and Richter law indicates a dependence of power law between the magnitude and the number of earthquakes. Gutenberg and Richter law in terms of energy can be written as:

$$N (> E) \sim E^{-\beta-1} \quad (6.4.6)$$

The parameter  $\beta$  has been calculated and was found to be the  $2/3$  of the  $b$  value. This equation is an expression of the magnitude and the seismic energy distribution. Also, the seismic energy expressed with the seismic moment, is related to the surface fault area and the equation is the following:

$$M_0 = \mu \Delta A \quad (6.4.7)$$

In the above equation, the  $M_0$  is the seismic moment,  $\mu$  represents the shear modulus or the rigidity,  $\Delta$  expresses the average relative slip of the fault plane and  $A$  is the fault's surface area. Those equations have a physical approach, which implies that if we have a number of seismic events, that their rupture surfaces are bigger than a specific size  $A$ , then the population of those events is power law dependent with that area. This mentioned dependence displays that the law of Gutenberg and Richter shows a behavior of fractal distribution.

An indication of the scale invariant property is the fact that both the fault structures and fault distributions depict self-similarity. This scale invariance, however, is restrained into a narrow range of scales, which is finite. That range of scales is connected strongly with the size of the volume under stressed. Therefore, the evolution of fault – population is dynamical and shows a transition from behavior of power law and fractal, without losing the memory property to exponential behavior and memory-lessness. The non – linearity arises as a function of the accumulated stress. In this evolution and transition, the faults can be large scaled or even fractures and microcracks. The behavior of exponential and power law is expressed by the relations:

$$N(> L) = AL^{-D} \text{ and} \tag{6.4.8}$$

$$N(> L) = Ae^{\left(\frac{-L}{L_0}\right)} \tag{6.4.9}$$

In both of them  $N$  represents the number of liner faults that have a size bigger than  $L$ ,  $D$  is the power law exponent and  $A$  represents the scaling constant. At the relation 6.4.9,  $L_0$  represents a specific length.

Moreover, the attenuation of the amplitude of the coda waves decreases as a power law function, as coda waves show that that the time lapse depends on the origin time. This coda wave amplitude attenuation exhibits a power law behavior, which is the result of the scattering coefficient decreasing with depth. The dependence of the amplitude decay of coda waves with frequency can be explained by the scatterers' power law sized distribution. These properties have been originated by observational methods and constitute indications that nonlinear dynamical procedures are taking place throughout the evolution of earthquakes phenomena.

## 7. Entropy and statistical mechanics

### 7.1 Introduction

Entropy is a scientific concept that is often used for the measurement of disorder, randomness, or uncertainty. It was first recognized in classical thermodynamics; however, it is now used in different fields, as the microscopic description of nature, and in many more applications in the fields of physics and chemistry. According to Boltzmann, entropy can be defined as the number of the possible arrangements, on microscopic level, of individual atoms and molecules of a system that are in accordance with the macroscopic condition of the system. With this definition of entropy, he introduced a new field of thermodynamics, named statistical mechanics, with the concept of statistical disorder and probability distributions.

Statistical mechanics can be described as a mean used to understand and explain the dynamical evolution of complex systems. According to it, every set of properties, which are

large scale, has a configuration of particles. Every probable configuration of those particles that can result those properties has the same probability. Configuration as a term, is to define the exact arrangement of any physical characteristic, for example velocity, position and momentum spin of the microscopic particles. We call microstates, every possible distributed configurations of energy. We call macrostates, a combination of large scale macroscopic properties. The combination of the macroscopic properties is defined by the properties of thermodynamics, such as temperature, pressure and volume. As a result of all the above, most of the times for every potential microstate configuration that statistically comes as a result of a specific macrostate configuration, there is the same probability to be observed.

The second law of thermodynamics explains why it is inevitable for every system to maximize its entropy and why that is fundamental in statistical mechanics. Specifically, entropy is associated with the second law of thermodynamics in the way the particles are distributed under the laws of motion. Thus, entropy is able to give an explanation of a system's thermodynamic behavior, as the motion of individual particles can give a summed up result, according to Newton's motion laws.

Newton's second law is given by the well known equation:

$$F = ma \quad (7.1.1)$$

Also, Newton's law of universal gravitation is given by the below relation:

$$F_G = \frac{Gm_1m_2}{r^2} \hat{r} \quad (7.1.2)$$

The Schrödinger equation is a linear partial differential function that represents the quantum wave function and is given by the following relation:

$$i\hbar \frac{\partial}{\partial t} \Psi = \frac{-\hbar^2}{2m} \nabla^2 \Psi \quad (7.1.3)$$

where  $\Psi$  represents the value of the wave function throughout space and time, the constant  $i$  is the imaginary unit, and  $\hbar$  is the reduced Planck constant.

In the 3D dimensional space the complex number  $\nabla^2 \Psi$  at each point is given by the equation:

$$\nabla^2 \Psi = \frac{\partial^2 \Psi}{\partial x^2} + \frac{\partial^2 \Psi}{\partial y^2} + \frac{\partial^2 \Psi}{\partial z^2} \quad (7.1.4)$$

All subatomic particles have an inherently probabilistic behavior; however, the relation 7.1.3 does not lie in probabilities. The wave function evolves and changes in a deterministic way and determines the probability of every possible observation. After all this behavior cannot present the way the energy scatters and diffuses in space time.

Thus, we can suggest that entropy can be used to measure each energy configuration's probability and can be instinctively used as a measurement of the energy distribution. When we detect concentrated energy, then the entropy is low. On the other hand, when the energy is distributed to the maximum, entropy it detected in high amount. The best way to understand the definition of entropy and its consequences, is by giving an example of a dynamical system that changes in time. For example, energy distribution in the earth's medium is being triggered by an earthquake. The energy that emerges from the earthquake is being continuously transferred between bonds, due to the propagation of the P and S body waves, through the

materials of the earth, via the crystal lattice and atomic bonds. So, its configuration is constantly changing, as the energy's transfer continues. The probability that is most likely to happen, is the dispersion of the energy distribution, due to the scattered microstates, that leads to higher entropy for the system. As a result, higher entropy is more likely to happen statistically in a large scale system.

The aftershock sequence that follows a seismic event presents a spatial distribution that can assist in understanding the concepts of microstate and macrostate. The seismic events recorded either follow a random spatially distribution or a fractal like geometry. The microstate of the system is represented by individual events of the aftershock sequence that take place and the macro state of the system is represented by the density of the spatial cumulative number of event distribution. Thus, if we consider all the random possible configuration of seismicity, the potential macro states and microstates should correspond to each other, while any clustered distribution that does not follow existing or preexisting tectonic features, like seismicity which is narrow scattered, should not. This results to high entropy distributed hypocenters within the rupture area.

Statistics is the mean by which we can better understand and gain a better overview of the observable microstates of an existing system. Each physical system's normal outcome is that the majority of any possible microstate distribution will leave the system very close to a single macro-state, the state of thermal equilibrium. The microstate is well defined by the fact of how the energy is distributed through phase space, instead on focusing on the distribution of the particle in the three dimensional space. As a result, in a given system its thermodynamic properties are defined by the average distribution of particles in phase space.

## 7.2 Boltzmann Gibbs statistical mechanics

When we examine a system which is large in size, we observe a transform of the small scale exact states to large scale average states. This happens by assigning probabilities to the system being in different states. Founder of the statistical mechanics is Ludwig Boltzmann, who introduced a different approach of thermodynamics, instead of what was believed until then. The relation between the macroscopic and microscopic states is displayed by entropy, which is based on the second law of thermodynamics. Entropy is given by the following equation:

$$S = -k \sum_i p_i \log p_i \quad (7.2.1)$$

The  $p_i$  represents the state probabilities and is  $0 \leq p \leq 1$ , the  $S$  is their sum and  $k$  is a positive constant, which is known as the Boltzmann's constant in the field of thermodynamics ( $k_B = 1.38 \cdot 10^{-23} \text{ J/k}$ ). The equation 7.2.1 is the Boltzmann's Gibbs' entropy  $S_{BG}$ .

If all probabilities  $p_i$  are equal, which means:  
 $p_i = \frac{1}{W}, \forall i \quad (7.2.2)$

the relation 7.2.1 is as follows:

$$S = k \ln W \quad (7.2.3)$$

This relation of entropy is used in the case of a given system, where the probability of all the microstates is equal to happen and as the microstates increase, the entropy will be higher.

In the case of a continuous variable  $x$ , the relation 7.2.1 will be:

$$S = -k \int_0^{\infty} p(x) dx = 1 \quad (7.2.4)$$

The most likely macroscopic state can be retrieved by the maximization of entropy, subject to the normalization of  $p(x)$  constraints:

$$\int_0^{\infty} p(x) dx = 1 \quad (7.2.5)$$

The following relation gives us the average  $x$  value:

$$\langle x \rangle = \int_0^{\infty} xp(x) dx \quad (7.2.6)$$

If we use the Lagrange multiplier method along with the previous defined constraints, the probability that maximizes the Boltzmann's Gibbs, takes the following form, which is the Boltzmann distribution:

$$p(x) = \frac{e^{-\beta x}}{\int_0^{\infty} e^{-\beta x} dx} \quad (7.2.7)$$

where  $e^{-\beta x}$  is the Boltzmann factor and  $\beta$  represents the Lagrange multiplier.

If we have two independent sub systems A and B along with its states, represented as  $W_A$  and  $W_B$ , and we combine them in a way that their conjugated probabilities satisfy the below relation, the entropy  $S_{BG}$  is called additive.

$$p_{ij}^{A+B} = p_i^A p_j^B, \quad \forall i, j \quad (7.2.8)$$

The entropy  $S_{BG}$  can be mathematically expressed by the relations below:

$$S_{BG} (A + B) = -k \sum_{i=1}^{W_A} \sum_{j=1}^{W_B} p_{ij}^{A+B} \ln p_{ij}^{A+B} \quad (7.2.9)$$

$$S_{BG} (A) = -k \sum_{i=1}^{W_A} p_i^A \ln p_i^A \quad (7.2.10)$$

$$S_{BG} (B) = -k \sum_{j=1}^{W_B} p_j^B \ln p_j^B \quad (7.2.11)$$

The Boltzmann-Gibbs classical statistical mechanics is based on the entropy of Boltzmann–Gibbs, and from the classical Boltzmann-Gibbs statistical mechanics the Boltzmann distribution emerges for the case of thermal equilibrium. Thus, for statistical mechanics, the Boltzmann-Gibbs entropy and distribution constitute guidelines for plenty of procedures, as well as natural phenomena.

$S_{BG}$  entropy has an important property that is the non – negativity. From an assumption of a specific probability then we can conclude to the assumption:

$$\lim_{x \rightarrow 0} (x \ln x) = 0 \quad (7.2.12)$$

$$S_{BG} = -k \langle \ln p_i \rangle = k \ln \left\langle \frac{1}{p_i} \right\rangle \quad (7.2.13)$$

The  $\ln p_i$  and  $\ln \left( \frac{1}{p_i} \right)$  represent the mean value of the under examination probabilities.

As we said the entropy has the important property of non – negativity. It is always positive since:

$$\ln\left(\frac{1}{p_i}\right) > 0, \forall i \quad (7.2.14)$$

The entropy is being maximized by the  $S_{BG}$ , which will reach its maximum state when:

$$S_{BG}(\{p_i''\}) > \lambda S_{BG}(\{p_i\}) + (1 - \lambda)S_{BG}(\{p_i'\}) \quad (7.2.15)$$

In order for this to be functioning, the set  $p_i''$  has the following property:

$$p_i'' = \lambda p_i + (1 - \lambda)p_i' \forall i \text{ and } 0 < \lambda < 1 \quad (7.2.16)$$

The  $p_i$  and  $p_i'$  are given set of probabilities, connected with a system of  $W$  state. The 7.2.16 relation occurs from the second law of thermodynamics and indicates that the entropy gains its maximum value, when the studied system is under equilibrium.

The Boltzmann Gibbs entropy is considered extensive, when the limit below exists:

$$\lim_{N \rightarrow \infty} \frac{X(N)}{N} \quad (7.2.17)$$

$$\text{with } X(N) \propto N(N \rightarrow \infty) \quad (7.2.18)$$

In the above equation,  $X$  is a physical quantity and is proportional to the system size. In the case that the elements of a system are not associated with each other, the entropy of Boltzmann – Gibbs is considered as extensive, thus we have:

$$S_{BG}(N) \propto N \quad (7.2.19)$$

$$\text{with } 0 < \lim_{N \rightarrow \infty} \frac{S_{BG}(N)}{N} < \infty \quad (7.2.20)$$

### 7.3 The q – Functions

Previously, we spoke and explained the case of a system that its elements are not correlated. Now, we will study and explain the opposite case, where the elements of the system we examine are strongly correlated, such as long range interaction, long memory etc. In this case, we cannot characterize the entropy as extensive. In addition, the Boltzmann-Gibbs entropy is not valid for system with correlated elements, thus it is not a universal form. Since there are different data that apply in that case, we will expand the  $S_{BG}$  and we will have the following differential equations, along with their solution of  $f(x)$ :

$$\frac{dy}{dx} = 0, y(0) = 1, y=1 \quad (7.3.1)$$

$$\frac{dy}{dx} = 1, y(0) = 1, y = 1 + x \quad (7.3.2)$$

$$\frac{dy}{dx} = y, y(0) = 1, y = e^x \quad (7.3.3)$$

The  $q$  – parameter is the result of the combination of those three differential equations, 7.3.1, 7.3.2 and 7.3.3, taking into consideration the concept of linearity.

The following relation is a mathematical approach of the Cauchy problem:

$$\frac{dy}{dx} = y^q, y(0) = 1 \quad (7.3.4)$$

In the above relation 7.3.4, in the case of  $q \neq 1$ , there is the following analytical solution:

$$\begin{aligned} \frac{dy}{dx} = y^q &\Leftrightarrow \frac{dy}{y^q} = dx \Leftrightarrow \int \left(\frac{1}{y^q}\right) dy = \int dx + c \Leftrightarrow \int y^{-q} dy = x + c \Leftrightarrow \\ \frac{1}{1-q} \int (1-q)y^{-q} dy &= x + c \Leftrightarrow \frac{y^{1-q}}{1-q} = x + c \Leftrightarrow y^{1-q} = (1-q)(x + c) \Leftrightarrow \\ y(x) &= [(1-q)(x + c)]^{\frac{1}{1-q}} \end{aligned}$$

If we assume  $y(0) = 1$ , we have:

$$[(1-q)c]^{\frac{1}{1-q}} = 1 \Leftrightarrow (1-q)c = 1 \Leftrightarrow c = \frac{1}{1-q} \quad (7.3.5)$$

Thus, since  $c = \frac{1}{1-q}$  the solution for the equation 7.3.4 is:

$$y(x) = [1 + (1-q)x]^{\frac{1}{1-q}}, \quad y(0) = 1, \quad q \in \mathbb{R}, \quad q \neq 1 \quad (7.3.6)$$

These functions, after an analysis of their properties can lead to the well known functions of  $q$  – exponential,  $q$  – logarithmic and  $q$  – gaussian.

First, we will analyze the  $q$  – exponential parameter. In order to proceed we will assume that the limit of the  $q$  index tends to 1, and with the function of 7.3.6, the equation 7.3.4 will be analyzed as following:

$$\begin{aligned} \lim_{q \rightarrow 1} e_q^x &= \lim_{q \rightarrow 1} [1 + (1-q)x]^{\frac{1}{1-q}} = \lim_{q \rightarrow 1} e^{\ln[1+(1-q)x]^{\frac{1}{1-q}}} = \lim_{q \rightarrow 1} e^{(1-q)^{-1} \ln[1+(1-q)x]} = \\ e^{\left[ \lim_{q \rightarrow 1} (1-q)^{-1} \ln(1+(1-q)x) \right]} &= e^{\left[ \lim_{q \rightarrow 1} \frac{\ln(1+(1-q)x)}{1-q} \right]} = e^{\left[ \lim_{q \rightarrow 1} \frac{\frac{d}{dq} \ln(1+(1-q)x)}{\frac{d}{dq} (1-q)} \right]} = e^{\left[ \lim_{q \rightarrow 1} \frac{\frac{1}{1+(1-q)x} \cdot \frac{d}{dq} [1+(1-q)x]}{-1} \right]} = \\ e^{\left( \lim_{q \rightarrow 1} -\frac{x}{-1} \right)} &= e^{\lim_{q \rightarrow 1} x} = e^x \end{aligned}$$

Hence, for the case of  $q \rightarrow 1$  we have:

$$e_q^x = e_1^x = e^x \quad (7.3.7)$$

The  $q$  – exponential class is being represented by this type of functions  $e_q^x$  and a unique  $q$  – exponential function is given for every single value of  $q$ . Moreover, the probability density function can describe the  $q$  – exponential distribution, as below:

$$p(x) = p_0 \left[ 1 - (1-q) \frac{x}{x_0} \right]^{\frac{1}{1-q}} \quad (7.3.8)$$

The relation 7.3.8 will take the simple form of the exponential distribution, for the case of  $q \rightarrow 1$ , as when the limit is  $q \rightarrow 1$ , the  $q$  – exponential function takes the form of the exponential function.

The inverse solution of equation 7.3.6 emerges the  $q$ -logarithmic functions class. We assume the relation:

$$y = [1 + (1-q)x]^{\frac{1}{1-q}} \Leftrightarrow y^{1-q} = 1 + (1-q)x \Leftrightarrow x = \frac{y^{(1-q)} - 1}{1-q} \quad (7.3.9)$$

the inverse of the equation 7.3.6 will be:

$$y^{-1}(x) = \frac{x^{1-q} - 1}{1-q} \equiv \ln_q x, \quad \text{where } x > 0 \text{ and } q \in \mathbb{R} \quad (7.3.10)$$

Moving with the analyzation of the case  $q \rightarrow 1$ , the inverse we get for  $e_q^x$  is as follows:

$$\begin{aligned} \lim_{q \rightarrow 1} \ln_q x &= \lim_{q \rightarrow 1} \frac{x^{1-q} - 1}{1-q} = \lim_{q \rightarrow 1} \frac{e^{\ln x^{1-q}} - 1}{1-q} = \lim_{q \rightarrow 1} \frac{(e^{\ln x^{1-q}} - 1) \ln x}{(1-q) \ln x} = \ln x \left[ \lim_{q \rightarrow 1} \frac{(e^{\ln x^{1-q}} - 1)}{(1-q) \ln x} \right] = \\ \ln x \left[ \lim_{q \rightarrow 1} \frac{\frac{d}{dq}(e^{\ln x^{1-q}} - 1)}{\frac{d}{dq}(1-q) \ln x} \right] &= \ln x \left[ \lim_{q \rightarrow 1} \frac{-(1-q) \ln x e^{1-q \ln x}}{-\ln x} \right] = \ln x \left[ \lim_{q \rightarrow 1} (1-q) e^{\ln x^{1-q}} \right] = \ln x, \end{aligned}$$

where  $x > 0$  and  $\ln_1 x = \ln x$

The  $q$  – logarithm function is non-additive because of the mixing terms that appear in the case of summation of two independent  $q$  – logarithms of  $A$  and  $B$  terms. This property is called pseudo – additivity.

$$\ln_q x_A x_B = \ln_q x_A + \ln_q x_B + (\ln_q x_A \ln_q x_B) \quad (7.3.11)$$

## 7.4 Non-extensive statistical mechanics

Classical thermodynamics and the kinetic theory of gases, where the only fields that entropy and the associated field of statistical mechanics were used exclusively at the beginning. As the years passed, it expanded to other scientific fields, in order to obtain the least biased probability distribution from limited information. The collective properties of earthquakes or fault populations seem to correspond well to the empirical laws, where simple forms are used, after scientific research. If in these two specific fields of earthquake and fault population we apply the theory of statistical mechanics, the approach will be considered as the link between the micro cracking and fracturing that is experienced in the upper, rigid crust, to the genesis of a significant earthquake event that is expressed by a fault rupture.

There are certain complex seismological dynamic processes, which have been explained by a generalized form and use of the non extensive statistical physics based on the concept of entropy. Those seismological processes can be the change of local scattering evolution by analyzing coda waves and seismic noise of seismographic stream records. It can also be used in a more general form, in order for the macroscopic configuration of the seismological occurrences to be estimated by the specification of the relevant microscopic components and their interactions. Such seismological occurrences are earthquakes, evolution of faulting, time intervals of aftershock sequences, time domain samples increment etc. In such complex systems, the occurrence of an individual constituent is strongly correlated with the state and the occurrence of some other micro-constituent.

The statistical mechanics of Boltzmann-Gibbs is well suited for physical systems, that have the characteristics of presenting interactions of short range and their memory is also short. Such physical systems with these characteristics where found in Markovian chain processes. On the other hand, the Boltzmann-Gibbs-Shannon approach is not that functional when used in physical systems with macroscopic behavior and weak chaotic dynamics. These systems follow distributions with asymptotic power law behavior, that present long memory along with heavy

tails and long range interactions, enhanced by multi-fractal geometries. This behavior of those physical systems violates essential properties of the Boltzmann's Gibb's distribution.

What we call heavy tail distributions, are distributions with a tail heavier than a tail of an exponential distribution. They exhibit relatively many high valued outliers, and there are three categories of them, fat tailed, long tailed and sub exponential distribution. Known distributions that present heavy tails are cauchy, log normal, Pareto, Zipf and Students t-distributions.

The non extensive statistical mechanics, known as NESM, is a generalized framework proposed by Tsallis, which is used in order to achieve the statistical mechanics description of such systems. Non extensive statistical mechanics has the advantage of taking into account the correlations of all scales between the elements of a system. To quantify the non-extensivity, the concept of entropy is used to infer the least biased distribution via the concept of maximum entropy principle.

The non-additive entropy  $S_q$  is central for the non extensive statistical mechanics and for discrete cases is given by the relation:

$$S_q = k \frac{1 - \sum_{i=1}^W p_i^q}{q-1} \quad (7.4.1)$$

where  $q \in \mathbb{R}$

$W$  represents the number of microscopic configurations,  $k$  is a positive constant, which we assume it is the Boltzmann's constant, and  $q$  represents the entropic index.

Taking into consideration the relation of non-addictive entropy below:

$$S_q = k \ln_q \left( \frac{1}{p_i} \right) \quad (7.4.2)$$

Along with the equation of  $q$  logarithmic as we presented at the relation 7.3.10:

$$y^{-1}(x) = \frac{x^{1-q} - 1}{1-q} \equiv \ln_q x, \quad \text{where } x > 0 \text{ and } q \in \mathbb{R}$$

we get the relation below:

$$\ln_q p_i = \frac{p_i^{1-q} - 1}{1-q} \Leftrightarrow \ln_q \left( \frac{1}{p_i} \right) = \frac{\left( \frac{1}{p_i} \right)^{1-q} - 1}{1-q} = \frac{\left( \frac{1}{p_i^{1-q}} - 1 \right)}{1-q} = \frac{\left( \frac{1 - p_i^{1-q}}{p_i^{1-q}} \right)}{1-q} \quad (7.4.3)$$

and finally we have

$$\ln_q \left( \frac{1}{p_i} \right) = \frac{1 - p_i^{1-q}}{(1-q)p_i^{1-q}} \quad (7.4.4)$$

Now, in the equation 7.4.3 we replace the equation 7.4.4 and after we impose the normalization constraint:

$$\sum_{i=1}^W p_i = 1 \quad (7.4.5)$$

we retrieve the equation:

$$\begin{aligned}
S_q &= k \left( \ln_q \frac{1}{p_i} \right) = k \sum_{i=1}^W \frac{\ln_q \left( \frac{1}{p_i} \right)}{p_i} = k \sum_{i=1}^W \frac{1}{p_i} \left( \frac{1-p_i^{1-q}}{(1-q)p_i^{1-q}} \right) = k \sum_{i=1}^W \left( \frac{1-p_i^{1-q}}{(1-q)p_i^{-q}} \right) = \\
&= k \left( \frac{1}{1-q} \right) \sum_{i=1}^W \frac{1-p_i^{1-q}}{p_i^{-q}} = k \left( \frac{1}{1-q} \right) \sum_{i=1}^W p_i^q (1-p_i^{1-q}) = k \left( \frac{1}{1-q} \right) \sum_{i=1}^W (p_i^q - p_i) = \\
&= k \left( \frac{1}{1-q} \right) \left( \sum_{i=1}^W p_i^q - \sum_{i=1}^W p_i \right) = \\
&= k \left( \frac{1}{1-q} \right) \sum_{i=1}^W p_i^{q-1}
\end{aligned} \tag{7.4.6}$$

Thus, the equation 7.4.6 is equivalent to the entropy of Tsallis, as shown in the relation below:

$$S_q = k \frac{1 - \sum_{i=1}^W p_i^q}{q-1} \tag{7.4.7}$$

The equation of the  $S_q$  for continuous variables is given by:

$$S_q[p] = k \frac{1}{q-1} (1 - \int p(x)^q dx) \tag{7.4.8}$$

This form represents the case of the ordinary  $S_{BG}$  when the limit is  $\lim_{q \rightarrow 1}$ , which means the generalized framework of the classical Boltzmann-Gibbs entropy of statistical mechanics. If we apply the limit  $\lim_{q \rightarrow 1}$ , when the  $q$  approaches the value of 1 to the relation 7.4.7, we have the following:

$$\begin{aligned}
\lim_{q \rightarrow 1} S_q &= \lim_{q \rightarrow 1} k \frac{1 - \sum_{i=1}^W p_i^q}{q-1} = k \lim_{q \rightarrow 1} \frac{1 - \sum_{i=1}^W p_i^q}{q-1} = k \lim_{q \rightarrow 1} \frac{1 - \sum_{i=1}^W p_i p_i^{q-1}}{q-1} = k \lim_{q \rightarrow 1} \frac{1 - \sum_{i=1}^W p_i e^{(q-1) \ln p_i}}{q-1} \\
&= k \lim_{q \rightarrow 1} \frac{1 - \sum_{i=1}^W p_i (1 - (q-1) \ln p_i + \frac{(q-1)^2 \ln^2 p_i}{2!} - \dots)}{q-1}
\end{aligned} \tag{7.4.9}$$

If we apply at  $e^{(q-1) \ln p_i}$  an expansion of Taylor series we have:

$$e^{(q-1) \ln p_i} = \sum_{n=0}^{\infty} \frac{(q-1)^n \ln^n p_i}{n!} \tag{7.4.10}$$

For the case of  $n = 0$  we get:

$$e^{(q-1) \ln p_i} = \frac{(q-1)^0 \ln^0 p_i}{0!} + \frac{(q-1)^1 \ln^1 p_i}{1!} + 0 (\ln^2 p_i) = \sum_{n=0}^{\infty} \binom{q-1}{n} (p_i - 1)^n \tag{7.4.11}$$

With the implement of equation 7.4.11 on 7.4.10 we have:

$$\begin{aligned}
e^{(q-1) \ln p_i} &\approx 1 + (q-1) \ln p_i = \lim_{q \rightarrow 1} S_q \approx k \lim_{q \rightarrow 1} \frac{1 - \sum_{i=1}^W p_i [1 + (q-1) \ln p_i]}{q-1} = \\
&= k \lim_{q \rightarrow 1} \frac{1 - \sum_{i=1}^W p_i + \sum_{i=1}^W (q-1) p_i \ln p_i}{q-1} = k \lim_{q \rightarrow 1} \frac{(q-1) \sum_{i=1}^W p_i \ln p_i}{q-1} = k \lim_{q \rightarrow 1} \sum_{i=1}^W p_i \ln p_i = \\
&= k \sum_{i=1}^W p_i \ln p_i = k \frac{S_{BG}}{k_B}
\end{aligned} \tag{7.4.12}$$

From the relation that we have analyzed above, we can clearly express that the Boltzmann-Gibbs entropy and the generalized form of Tsallis entropy are equivalent to each other, in the case of  $\lim_{q \rightarrow 1}$  and  $k = k_B$ .

The potential cases for the entropic index  $q$  are three. The first one, which is called super-additivity, is when  $q < 1$ . The second case, which is the one that retrieves the Boltzmann-Gibbs entropy, is called additivity and is recovered when  $q = 1$ . This case is actually the limit of the  $q$  index as it approaches the value 1 ( $\lim_{q \rightarrow 1}$ ). The third case is called sub-additivity and emerges when  $q > 1$ . Even though that Boltzmann-Gibbs entropy and Tsallis entropy have the

majority of the properties the same, Tsallis  $q$  entropy is non – additive, while Boltzmann-Gibbs entropy is additive.

$$S_{BG} = (A + B) = S_{BG}(A) + S_{BG}(B) \quad (7.4.13)$$

This behavior introduces the non-additivity concept for the NESM theory. The main difference between  $S_{BG}$  and  $S_q$  entropy is generated by the concept that instead of summing the entropy of the two probabilistically independent subsystems, A and b, to obtain the total entropy of the main system (A, B), the non-additive entropy approaches the main system entropy via the formula of:

$$\frac{S_q(A+B)}{k} = \frac{S_q(A)}{k} + \frac{S_q(B)}{k} + (1 - q) \frac{S_q(A)}{k} \frac{S_q(B)}{k} \quad (7.4.14)$$

Tsallis (1998) was the one who first introduced that the generalized framework of Boltzmann – Gibbsof statistical mechanics initiates bias in probabilities. This concept of Tsallis was influenced by multifractality physics.

We retrieve the conditions below by taking into consideration the maximization of  $S_q$ :

$$\int p(x)dx = 1 \quad (7.4.15)$$

and

$$\int p_q(x)U(x)dx = U_q \quad (7.4.16)$$

The  $p_q$  is given by the equation below:

$$p_q(x) = \frac{p_q(x)}{\int p_q(x)dx} \quad (7.4.17)$$

The value  $p_q$  represents the escort probability; the system under examination is represented by the function  $U(x)$  and  $U_q$  represents the  $q$  – average.

The escort distribution is a simple parameter deformation of the original distribution and is the result of the maximum entropy theory, which is applied between the uniform distribution and the one under examination.

Complex systems have mandatory and critical existence of custom long tailed probability distribution. A custom made probability distribution has an essential role due to distributions that can be either a sequence of escort distributions or a generalized one. Those two last types of distributions are considered to be useful, as they are in accordance with the conditions of the respective statistical analysis and can be successfully applied into complex and anomalous statistical physics.

The escort distribution procedure can also be considered as a fundamental approach of giving suitable weight for individual fat tailed constituents. The mentioned approach is assigned to the multi-fractal attributes of nonlinear dynamic systems. In the case of a parabolic function, the  $U(x)$  is given by:

$$U(x) = x^2 \quad (7.4.18)$$

In the relation above the  $U_q$  as presented in the formula 7.4.16, behaves as a fluctuation intensity index. If we implement the method of Lagrange Multiplier to the relation 7.4.8 the

outcome will be the probability distribution function and under the constraints of the relations 7.4.15 and 7.4.16, we will have the relation:

$$p(x) = \frac{1}{Z_q(B)} [1 + B(q - 1)U(x)]^{-\frac{1}{q-1}} \text{ where } q > 1 \quad (7.4.19)$$

The  $Z_q$  is given by:

$$Z_q(B) = [B(q - 1)]^{-\frac{1}{2}} \frac{\Gamma(\frac{1}{2})\Gamma(\frac{1}{q-1})}{\Gamma(\frac{1}{q-1})} \quad (7.4.20)$$

The above equation is known as a generalized  $q$  – partition function and  $\Gamma$  is a gamma function. It is considered as a generalized canonical distribution under the frame of Tsallis statistics.

In the case of a parabolic function and the relation 7.4.18 the distribution becomes:

$$p(x) = \frac{1}{Z_q(B)} [1 + B(q - 1)q^2]^{-\frac{1}{q-1}} \quad (7.4.21)$$

The formulation 7.4.21 is the famous  $q$  – Gaussian distribution, which in the specific case of  $\lim_{q \rightarrow 1}$  it becomes a normal Gaussian distribution.

## 8. Area of study and data selection

### 8.1 Geological background

The data are about to be studied in this paper, were obtained by local earthquakes that occurred in the area of central Greece. In order to have a better understanding on the results that are going to come up, we must take in mind the geotectonic setting of the studying area.

As it is known, central Greece is part of the Greek peninsula, more specific of its continental, massif part, thus it is on the Aegean microplate, which is the most seismically active area of Europe, and of the Mediterranean as well. The Aegean continental crust is located between the North Anatolian fault's extension to the west, which is found at the north of the Aegean continental crust, and the Hellenic Trench, which is found at the west and south of it. Central Greece, in general, is found in the back arc part of the Hellenic Arc and since the early Miocene has experienced extension. Due to this constant extension, many grabens have been formatted. Some of those grabens that have been created in the central Greece are the gulfs of Maliakos, Korinthiakos, North and South Evoikos, and also the graben of Sperchios River. Those grabens are located between the right-lateral Cephalonia Transform Fault (CTF) and the North Aegean Trough (NAT). The North Aegean Trough is a west oriented prolongation of the right-lateral strike-slip North Anatolian Fault (NAF).

So, one very important graben, for the area we are studying, is the fault system of Sperchios River. This fault system can be divided in two parts; the one is in the west and is the Sperchios-Ipati fault zone and the other is in the east and is the Kamena Vourla-Arkitsa fault zone. The fault zone of Sperchios-Ipati has a south border of the Quaternary narrow valley of the Sperchios River and the fault zone of Kamena Vourla-Arkitsa has a south border of the Maliakos Basin, which has a width of 12 km and is bounded from faults. This Basin has been filled with Neogene sediments prior to the Quaternary ones (Galanakis 1997).

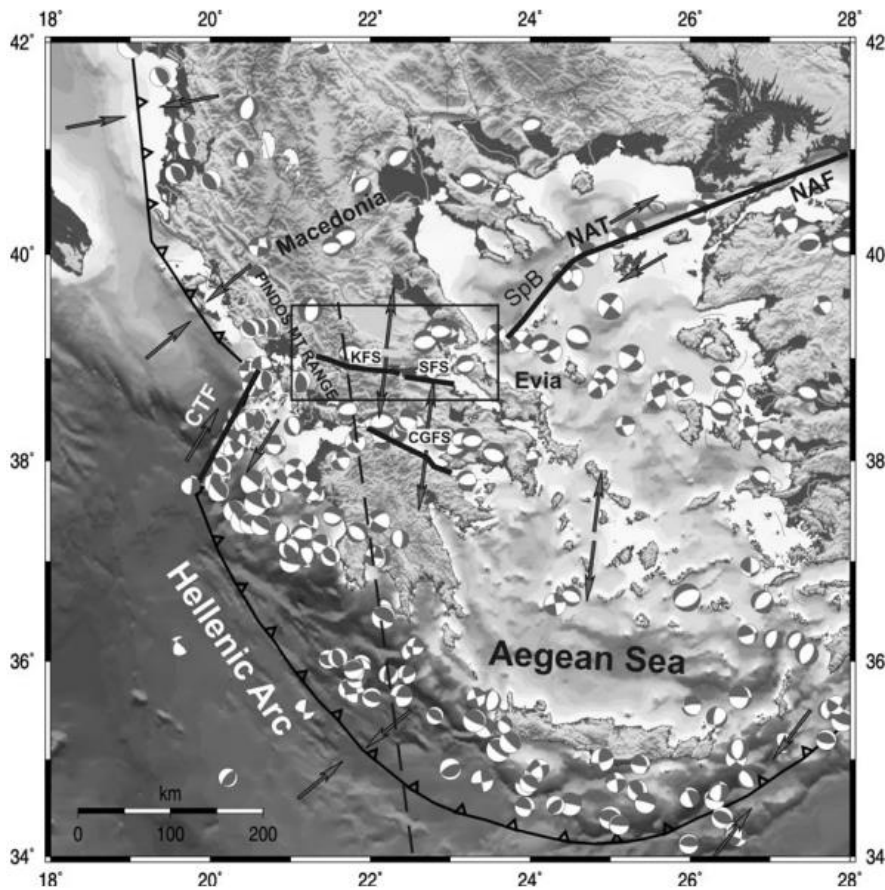


Figure 8.1.1 A map of the main structural features and the focal mechanisms of the earthquakes that have happened the last decades. The arrows show the different kinematics (contractional, strike-slip and extensional). CTF = Cephalonia Transform Fault, NAT = North Aegean Trough, NAF = North Anatolian Fault, SpB = Sporades Basin

In the southern Thessaly, the 80 km southern Thessaly fault zone is found. It is consisted by ENE–WSW striking steeply dipping faults. It can also be divided in two parts (Mountrakis et al. 1993a); the western part, which is consisted by normal faults that dip towards the north and is limiting the Thessaly Basin and the eastern part, which is consisted by the fault of Nea Aghialos, that is seismically active, dips towards the south and is the limit of the Almyros Basin and Pagasitikos Gulf.

## 8.2 Seismic Data Selection

Following the previous theory, we will now proceed with the selection of the data that are going to be used and their analysis. They are 200 S coda waveforms within the frequency range 1-30Hz and with magnitude range between 3.1 and 5.2. Those events took place during the period from 01-01-2010 to 30-12-2019 and were recorder by a station in Athens, which belongs to the National Observatory of Athens Network (HL), part of the Hellenic Unified Seismic Network (HUSN). The station is located in Athens and it code name is “ATH\_HL”. The geographical coordinates of the station are 37.97384°N and 23.71767°E and its elevation reaches the 93m. The station is equipped with a STS-2 High-Gain broadband-seismometer and a DR24-SC datalogger with sampling frequency  $F_s = 100$  Hz.

Below there is a list of the seismic events used, along with their origin time, their latitude and longitude, their depth, their magnitude and the area of their location. They are sorted from the one with the biggest magnitude to the one with the smallest.

Table 8.2.1. List of the 200 seismic events, with origin time, latitude, longitude, depth, magnitude and location.

Origin Time (GMT)	Latitude	Longitude	Depth (km)	Magnitude	Location
2014-11-17T23:05:55.000000Z	38.64	23.4	24	5.2	26.2 km NW of Chalkida
2014-11-17T23:09:03.000000Z	38.64	23.41	23	5.2	25.6 km NW of Chalkida
2010-03-09T02:55:00.000000Z	38.87	23.65	22	5.1	36.0 km SSE of Skiathos
2010-07-16T18:53:10.000000Z	39.32	24.02	34	5.1	49.3 km ENE of Skiathos
2012-09-22T03:52:24.000000Z	38.09	22.74	25	4.9	23.9 km NW of Korinthos
2013-09-16T15:01:14.000000Z	38.72	22.74	17	4.9	23.8 km WNW of Atalanti
2014-04-30T04:03:32.000000Z	38.23	25.13	32	4.9	47.4 km NNE of Andros
2013-11-12T18:09:28.000000Z	38.92	23.1	17	4.8	31.2 km NNE of Atalanti
2013-08-07T13:44:32.000000Z	38.69	22.66	15	4.7	29.8 km W of Atalanti
2013-08-09T13:10:10.000000Z	38.69	22.65	17	4.7	30.0 km SE of Lamia
2014-06-27T16:14:27.000000Z	38.24	25.13	30	4.7	48.4 km NNE of Andros
2012-10-26T23:16:44.000000Z	38.96	22.91	26	4.6	35.2 km NNW of Atalanti
2010-07-17T02:30:35.000000Z	39.33	24.02	34	4.5	49.7 km ENE of Skiathos
2013-09-16T14:42:39.000000Z	38.7	22.73	20	4.5	24.0 km WNW of Atalanti
2014-02-01T08:14:03.000000Z	38.7	22.75	18	4.5	22.3 km WNW of Atalanti
2011-02-22T20:37:02.000000Z	38.86	24.95	37	4.4	33.9 km E of Skyros
2013-09-20T02:05:18.000000Z	38.18	23.13	23	4.4	32.0 km NNE of Korinthos
2013-11-27T14:21:15.000000Z	37.33	23.01	25	4.4	22.6 km NE of Leonidhion
2014-06-06T12:21:03.000000Z	39.17	23.71	23	4.4	19.5 km E of Skiathos
2014-07-11T09:46:04.000000Z	38.45	23.71	26	4.4	9.7 km E of Chalkida
2014-10-04T00:12:01.000000Z	37.41	22.2	20	4.4	19.3 km SW of Tripolis
2015-10-27T01:25:51.000000Z	38.92	24.33	25	4.4	20.2 km W of Skyros
2017-03-24T04:24:30.000000Z	37.5705	23.8847	165	4.4	47.8 km SSE of Athens
2010-08-29T00:51:57.000000Z	38.66	23.38	22	4.3	29.0 km NW of Chalkida
2010-09-02T03:53:04.000000Z	38.22	23.17	26	4.3	35.2 km SE of Levadhia
2010-10-09T19:04:49.000000Z	38.15	22.72	20	4.3	30.0 km NW of Korinthos
2011-08-21T06:14:18.000000Z	37.63	23.32	115	4.3	45.8 km E of Nafplio
2012-06-28T13:11:29.000000Z	39.01	23.17	25	4.3	32.2 km WSW of Skiathos
2013-04-28T16:31:04.000000Z	37.45	22.7	61	4.3	15.8 km SW of Nafplio
2013-06-04T01:56:53.000000Z	37.98	24.01	24	4.3	24.3 km E of Athens
2014-02-06T07:58:26.000000Z	38.71	22.77	22	4.3	20.9 km WNW of Atalanti
2014-05-20T23:30:44.000000Z	39.53	24.2	30	4.3	73.7 km ENE of Skiathos
2019-07-19T12:11:54.000000Z	38.0956	23.5808	15	4.3	18.3 km NW of Athens
2010-05-11T07:03:36.000000Z	38.62	23.77	24	4.2	22.9 km NE of Chalkida
2012-02-17T08:05:04.000000Z	37.87	23.02	17	4.2	10.8 km SE of Korinthos
2013-04-28T04:49:55.000000Z	38.26	22.25	55	4.2	14.7 km E of Aegion
2013-11-22T15:12:03.000000Z	39.05	22.41	21	4.2	16.8 km N of Lamia
2016-06-11T08:29:45.000000Z	39.23	23.73	15	4.2	22.4 km ENE of Skiathos
2019-11-29T20:46:40.000000Z	39.0482	22.3178	77	4.2	19.3 km NNW of Lamia
2010-04-04T22:05:56.000000Z	38.42	22.32	17	4.1	12.6 km SSW of Amfissa
2010-06-27T13:10:09.000000Z	37.52	22.94	79	4.1	12.6 km ESE of Nafplio
2011-09-06T04:14:13.000000Z	37.88	23.1	104	4.1	16.1 km ESE of Korinthos
2012-08-02T10:30:39.000000Z	39.27	23.72	25	4.1	23.4 km ENE of Skiathos
2012-08-06T15:22:11.000000Z	38.75	24.83	29	4.1	28.8 km SE of Skyros
2012-12-09T01:23:05.000000Z	37.93	22.59	24	4.1	30.0 km W of Korinthos
2014-05-10T03:04:50.000000Z	38.42	22.46	20	4.1	13.9 km SSE of Amfissa

2014-12-19T22:40:32.000000Z	39.33	22.62	19	4.1	28.3 km W of Volos
2015-04-13T03:49:02.000000Z	39.13	24.46	17	4.1	26.6 km NNW of Skyros
2019-12-11T02:29:27.000000Z	37.5504	24.0079	142	4.1	53.9 km SSE of Athens
2011-07-14T08:41:55.000000Z	37.83	22.62	82	4	29.9 km WSW of Korinthos
2013-01-30T04:27:25.000000Z	38.78	23.37	22	4	35.2 km ENE of Atalanti
2016-09-16T06:55:13.000000Z	38.89	23.33	25	4	33.5 km SSW of Skiathos
2016-09-29T01:17:36.000000Z	39.53	24.1	30	4	66.7 km NE of Skiathos
2011-04-22T01:20:24.000000Z	38.37	23.62	23	3.9	10.6 km S of Chalkida
2012-09-24T19:18:37.000000Z	39.03	23.16	23	3.9	31.8 km WSW of Skiathos
2013-09-17T05:46:52.000000Z	38.72	22.77	17	3.9	21.3 km WNW of Atalanti
2013-11-04T22:09:17.000000Z	38.91	23.1	23	3.9	30.1 km NNE of Atalanti
2014-09-29T08:15:07.000000Z	39.31	24.04	32	3.9	50.5 km ENE of Skiathos
2014-11-18T01:13:47.000000Z	38.64	23.41	23	3.9	25.6 km NW of Chalkida
2014-11-19T00:37:26.000000Z	38.64	23.42	24	3.9	25.1 km NW of Chalkida
2014-12-31T04:49:58.000000Z	38.19	22.51	20	3.9	38.0 km E of Aegion
2015-11-17T03:00:09.000000Z	39.51	24.07	43	3.9	63.3 km NE of Skiathos
2016-05-20T20:00:20.000000Z	38.59	24.47	15	3.9	35.9 km SSW of Skyros
2018-01-19T10:10:07.000000Z	37.5118	23.7805	137	3.9	52.6 km S of Athens
2010-03-12T03:34:37.000000Z	38.12	22.63	20	3.8	33.3 km NW of Korinthos
2011-01-17T22:27:10.000000Z	38.78	23.45	23	3.8	37.5 km NNW of Chalkida
2011-02-09T08:13:10.000000Z	38.63	22.49	21	3.8	15.5 km NE of Amfissa
2011-05-19T09:05:38.000000Z	38.43	23.86	24	3.8	23.0 km E of Chalkida
2012-08-25T06:17:44.000000Z	38.89	23.22	25	3.8	32.7 km NE of Atalanti
2014-05-13T01:24:10.000000Z	38.24	25.13	32	3.8	48.4 km NNE of Andros
2014-05-27T11:21:30.000000Z	37.54	22.86	78	3.8	5.3 km ESE of Nafplio
2014-11-17T23:40:36.000000Z	38.65	23.37	21	3.8	28.8 km NW of Chalkida
2016-04-09T01:36:11.000000Z	38.63	24.45	26	3.8	32.0 km SSW of Skyros
2016-05-09T17:29:19.000000Z	38.85	23.62	19	3.8	37.1 km SSE of Skiathos
2016-05-09T22:57:01.000000Z	39.14	24.15	15	3.8	44.3 km NW of Skyros
2018-12-23T22:34:10.000000Z	37.3258	23.945	28	3.8	50.4 km WNW of Seriphos
2019-11-24T18:34:57.000000Z	39.4579	24.0852	15	3.8	61.1 km ENE of Skiathos
2011-01-11T15:46:45.000000Z	38.75	22.2	23	3.7	26.2 km SW of Lamia
2011-02-13T00:17:22.000000Z	38.71	22.81	17	3.7	17.7 km WNW of Atalanti
2011-09-12T14:29:22.000000Z	38.72	23.39	21	3.7	33.8 km NNW of Chalkida
2013-03-13T23:09:01.000000Z	39.19	23.47	15	3.7	2.8 km NNW of Skiathos
2014-04-28T03:49:50.000000Z	38.69	22.81	23	3.7	17.0 km WNW of Atalanti
2014-06-28T19:09:47.000000Z	37.46	22.85	20	3.7	12.1 km SSE of Nafplio
2014-10-30T06:09:08.000000Z	38.14	22.63	15	3.7	34.7 km NW of Korinthos
2014-11-05T20:51:39.000000Z	39.14	24.19	25	3.7	41.5 km NW of Skyros
2014-11-15T08:11:31.000000Z	38.99	23.7	24	3.7	27.1 km SE of Skiathos
2014-11-18T00:53:59.000000Z	38.63	23.43	23	3.7	23.7 km NW of Chalkida
2014-12-14T08:16:33.000000Z	38.62	22.88	18	3.7	10.9 km WSW of Atalanti
2015-03-09T03:24:41.000000Z	39.31	24.02	16	3.7	48.9 km ENE of Skiathos
2016-07-28T16:17:29.000000Z	38.17	22.94	15	3.7	25.8 km N of Korinthos
2010-03-11T09:54:08.000000Z	38.12	23.26	21	3.6	35.1 km NE of Korinthos
2010-05-12T06:59:22.000000Z	38.62	23.78	25	3.6	23.4 km NE of Chalkida
2010-07-28T13:55:27.000000Z	37.47	23.32	29	3.6	46.4 km ESE of Nafplio
2010-09-06T19:20:42.000000Z	37.59	22.61	56	3.6	17.7 km W of Nafplio
2010-10-28T04:04:46.000000Z	38.36	22.25	20	3.6	19.2 km NE of Aegion

2010-12-14T13:58:52.000000Z	38.06	22.78	19	3.6	19.0 km NW of Korinthos
2011-01-31T17:23:13.000000Z	37.87	22.7	26	3.6	21.7 km WSW of Korinthos
2012-08-16T21:22:53.000000Z	38.28	22.55	24	3.6	31.3 km SSE of Amfissa
2013-09-08T06:22:10.000000Z	38.59	23.76	23	3.6	19.8 km NE of Chalkida
2014-02-12T07:41:00.000000Z	37.93	22.6	16	3.6	29.1 km W of Korinthos
2014-06-09T22:02:57.000000Z	39.17	23.75	24	3.6	23.0 km E of Skiathos
2014-07-30T00:55:04.000000Z	38.04	24.12	19	3.6	34.5 km E of Athens
2016-07-26T16:59:47.000000Z	37.63	23.5	15	3.6	44.3 km SSW of Athens
2016-08-26T07:47:24.000000Z	38.6	24.47	21	3.6	34.8 km SSW of Skyros
2017-06-23T22:26:17.000000Z	38.4549	23.53	17	3.6	6.1 km W of Chalkida
2019-08-03T17:17:09.000000Z	38.1404	22.7019	15	3.6	30.2 km NW of Korinthos
2010-06-05T05:12:40.000000Z	38.13	23.18	18	3.5	30.5 km NE of Korinthos
2010-06-16T15:11:21.000000Z	37.41	23.58	28	3.5	65.2 km SSW of Athens
2011-03-07T17:10:53.000000Z	38.25	22.55	15	3.5	34.2 km SSE of Amfissa
2011-08-16T20:22:22.000000Z	38.15	22.71	22	3.5	30.6 km NW of Korinthos
2011-10-24T09:24:37.000000Z	37.61	23.51	27	3.5	45.9 km SSW of Athens
2011-11-20T22:14:14.000000Z	38.17	22.56	21	3.5	40.2 km SW of Levadhia
2013-06-11T19:36:16.000000Z	38.17	23.23	23	3.5	36.7 km NE of Korinthos
2013-10-27T13:53:37.000000Z	38.64	23.61	22	3.5	19.6 km N of Chalkida
2013-12-22T18:04:02.000000Z	37.85	22.76	27	3.5	18.0 km WSW of Korinthos
2014-04-10T17:40:44.000000Z	37.93	22.61	24	3.5	28.3 km W of Korinthos
2014-11-17T23:18:45.000000Z	38.66	23.4	23	3.5	27.9 km NW of Chalkida
2014-11-20T16:26:22.000000Z	38.65	23.36	24	3.5	29.4 km NW of Chalkida
2015-06-09T02:31:27.000000Z	38.63	23.4	16	3.5	25.4 km NW of Chalkida
2015-06-09T03:04:41.000000Z	38.63	23.42	15	3.5	24.2 km NW of Chalkida
2016-05-28T21:00:10.000000Z	37.57	23.57	16	3.5	48.1 km SSW of Athens
2016-06-03T01:28:49.000000Z	38.62	24.45	16	3.5	33.1 km SSW of Skyros
2019-07-19T11:42:19.000000Z	38.1248	23.5158	16	3.5	24.7 km NW of Athens
2010-08-27T11:23:20.000000Z	37.86	22.98	19	3.4	9.6 km SSE of Korinthos
2010-09-21T08:02:11.000000Z	38.15	23.32	24	3.4	40.7 km WNW of Athens
2010-12-12T08:19:31.000000Z	38.11	23.55	18	3.4	21.4 km NW of Athens
2011-06-26T06:31:10.000000Z	38.88	23.69	22	3.4	36.5 km SSE of Skiathos
2011-12-01T01:17:43.000000Z	38.76	23.44	25	3.4	35.8 km NNW of Chalkida
2013-08-15T01:03:30.000000Z	38.7	22.67	19	3.4	29.1 km W of Atalanti
2013-12-21T05:50:39.000000Z	38.23	22.21	50	3.4	11.4 km E of Aegion
2014-02-28T22:13:54.000000Z	38.2	22.53	21	3.4	38.6 km SSE of Amfissa
2014-03-30T20:31:03.000000Z	37.58	23.45	20	3.4	51.3 km SSW of Athens
2014-11-18T01:16:19.000000Z	38.63	23.4	19	3.4	25.4 km NW of Chalkida
2014-11-18T03:18:49.000000Z	38.64	23.41	23	3.4	25.6 km NW of Chalkida
2014-11-18T23:44:40.000000Z	38.64	23.36	21	3.4	28.6 km NW of Chalkida
2015-10-27T01:52:29.000000Z	38.94	24.3	16	3.4	23.1 km W of Skyros
2016-01-14T00:27:57.000000Z	38.95	24.08	16	3.4	42.1 km W of Skyros
2016-02-06T02:23:31.000000Z	38.42	23.99	26	3.4	34.4 km E of Chalkida
2016-08-22T13:24:10.000000Z	38.33	24.06	15	3.4	42.8 km ESE of Chalkida
2016-09-09T14:07:49.000000Z	37.57	23.58	17	3.4	47.9 km SSW of Athens
2017-06-04T00:07:21.000000Z	38.1495	24.0802	20	3.4	35.5 km ENE of Athens
2017-09-02T04:21:05.000000Z	38.4229	23.5107	23	3.4	9.0 km WSW of Chalkida
2017-10-29T20:35:32.000000Z	37.5146	22.6611	30	3.4	14.0 km WSW of Nafplio
2012-03-15T23:47:48.000000Z	38.14	22.67	20	3.3	32.1 km NW of Korinthos

2012-04-14T20:19:18.000000Z	38.11	22.71	15	3.3	27.3 km NW of Korinthos
2012-09-30T05:19:37.000000Z	38.1	22.7	15	3.3	27.2 km NW of Korinthos
2013-09-26T00:49:53.000000Z	38.44	23.81	24	3.3	18.5 km E of Chalkida
2013-12-26T13:51:58.000000Z	38.6	23.95	28	3.3	34.1 km ENE of Chalkida
2014-01-13T03:08:12.000000Z	38.86	23.39	24	3.3	35.0 km SSW of Skiathos
2014-06-23T01:47:01.000000Z	38.69	23.56	15	3.3	25.4 km N of Chalkida
2014-11-18T00:35:38.000000Z	38.65	23.41	21	3.3	26.5 km NW of Chalkida
2014-11-18T00:47:48.000000Z	38.66	23.41	24	3.3	27.4 km NW of Chalkida
2015-05-06T19:05:01.000000Z	38.43	23.9	17	3.3	26.4 km E of Chalkida
2015-06-10T18:46:41.000000Z	38.66	23.42	17	3.3	26.8 km NW of Chalkida
2016-06-23T12:10:57.000000Z	38.16	22.68	16	3.3	33.1 km NW of Korinthos
2016-07-04T05:42:46.000000Z	37.54	23.63	16	3.3	50.1 km S of Athens
2016-09-07T09:34:15.000000Z	38.4	23.92	18	3.3	28.8 km ESE of Chalkida
2019-10-01T01:23:57.000000Z	39.521	23.5826	17	3.3	40.3 km NNE of Skiathos
2011-05-29T22:23:19.000000Z	38.16	23.95	18	3.2	27.3 km NE of Athens
2011-08-05T05:49:59.000000Z	38.72	23.71	25	3.2	30.1 km NNE of Chalkida
2012-09-30T02:41:34.000000Z	38.11	22.7	20	3.2	27.9 km NW of Korinthos
2013-07-27T06:46:52.000000Z	38.6	23.94	28	3.2	33.3 km ENE of Chalkida
2013-11-15T18:11:03.000000Z	37.54	22.9	76	3.2	8.6 km ESE of Nafplio
2014-10-11T01:53:35.000000Z	37.88	22.55	19	3.2	34.1 km W of Korinthos
2014-10-21T17:46:25.000000Z	38.59	22.99	23	3.2	6.8 km S of Atalanti
2014-11-19T16:32:28.000000Z	38.65	23.42	24	3.2	25.9 km NW of Chalkida
2015-05-06T18:05:31.000000Z	38.43	23.9	16	3.2	26.4 km E of Chalkida
2015-11-05T14:27:53.000000Z	38.62	24.46	24	3.2	32.8 km SSW of Skyros
2016-03-31T04:43:29.000000Z	37.54	23.57	21	3.2	51.3 km SSW of Athens
2016-05-04T23:03:37.000000Z	37.53	23.58	15	3.2	52.2 km SSW of Athens
2016-07-02T23:46:09.000000Z	37.55	23.59	15	3.2	49.8 km SSW of Athens
2016-10-29T11:52:42.000000Z	38.91	23.92	26	3.2	47.3 km SE of Skiathos
2017-05-10T12:44:01.000000Z	38.7763	23.358	25	3.2	34.1 km ENE of Atalanti
2010-03-24T20:15:18.000000Z	38.87	23.63	21	3.1	35.3 km SSE of Skiathos
2010-05-15T12:10:02.000000Z	38.13	23.17	19	3.1	29.8 km NE of Korinthos
2011-01-28T01:36:06.000000Z	38.21	23.16	17	3.1	35.3 km SE of Levadhia
2011-05-20T23:36:21.000000Z	38.44	23.88	24	3.1	24.6 km E of Chalkida
2011-05-24T10:27:50.000000Z	37.88	22.98	16	3.1	7.7 km SSE of Korinthos
2011-09-13T02:13:33.000000Z	38.72	23.38	22	3.1	33.9 km ENE of Atalanti
2011-11-06T07:38:21.000000Z	39.1	23.28	22	3.1	19.0 km WSW of Skiathos
2012-01-18T17:53:18.000000Z	37.72	23.04	24	3.1	26.0 km SSE of Korinthos
2012-02-20T00:51:46.000000Z	38.19	24.1	21	3.1	39.5 km NE of Athens
2012-05-16T00:00:01.000000Z	37.81	22.91	22	3.1	14.3 km S of Korinthos
2013-06-25T20:25:24.000000Z	38.17	23.22	15	3.1	36.1 km NE of Korinthos
2013-09-08T06:28:10.000000Z	38.61	23.76	24	3.1	21.4 km NE of Chalkida
2013-11-08T20:01:57.000000Z	38.65	24.61	26	3.1	28.6 km S of Skyros
2014-08-11T00:25:29.000000Z	38.41	22.5	19	3.1	16.9 km SE of Amfissa
2014-11-18T01:19:37.000000Z	38.65	23.41	25	3.1	26.5 km NW of Chalkida
2014-11-21T10:37:59.000000Z	38.66	23.39	25	3.1	28.4 km NW of Chalkida
2015-06-06T00:40:19.000000Z	38.79	23.46	15	3.1	38.3 km NNW of Chalkida
2015-07-23T16:05:50.000000Z	38.6	23.42	15	3.1	21.8 km NW of Chalkida
2016-01-21T03:14:49.000000Z	37.51	22.62	76	3.1	17.6 km WSW of Nafplio
2016-03-19T08:17:32.000000Z	37.52	23.61	18	3.1	52.6 km SSW of Athens

2016-04-22T13:33:20.000000Z	37.54	23.6	19	3.1	50.7 km SSW of Athens
2016-05-28T20:18:58.000000Z	37.56	23.57	15	3.1	49.2 km SSW of Athens
2016-07-06T16:26:12.000000Z	37.55	23.6	15	3.1	49.6 km SSW of Athens
2017-05-18T08:14:16.000000Z	38.0013	23.9545	17	3.1	19.5 km E of Athens
2017-06-06T08:01:33.000000Z	38.4808	23.3872	20	3.1	18.6 km W of Chalkida
2018-08-23T02:30:42.000000Z	37.5758	22.626	64	3.1	16.1 km W of Nafplio
2019-07-15T20:28:24.000000Z	37.9047	22.6447	16	3.1	25.5 km W of Korinthos
2014-11-17T23:05:55.000000Z	38,64	23,4	24	5,2	26.2 km NW of Chalkida
2014-11-17T23:09:03.000000Z	38,64	23,41	23	5,2	25.6 km NW of Chalkida
2010-03-09T02:55:00.000000Z	38,87	23,65	22	5,1	36.0 km SSE of Skiathos
2010-07-16T18:53:10.000000Z	39,32	24,02	34	5,1	49.3 km ENE of Skiathos
2012-09-22T03:52:24.000000Z	38,09	22,74	25	4,9	23.9 km NW of Korinthos
2013-09-16T15:01:14.000000Z	38,72	22,74	17	4,9	23.8 km WNW of Atalanti
2014-04-30T04:03:32.000000Z	38,23	25,13	32	4,9	47.4 km NNE of Andros
2013-11-12T18:09:28.000000Z	38,92	23,1	17	4,8	31.2 km NNE of Atalanti
2013-08-07T13:44:32.000000Z	38,69	22,66	15	4,7	29.8 km W of Atalanti
2013-08-09T13:10:10.000000Z	38,69	22,65	17	4,7	30.0 km SE of Lamia
2014-06-27T16:14:27.000000Z	38,24	25,13	30	4,7	48.4 km NNE of Andros
2012-10-26T23:16:44.000000Z	38,96	22,91	26	4,6	35.2 km NNW of Atalanti
2010-07-17T02:30:35.000000Z	39,33	24,02	34	4,5	49.7 km ENE of Skiathos
2013-09-16T14:42:39.000000Z	38,7	22,73	20	4,5	24.0 km WNW of Atalanti
2014-02-01T08:14:03.000000Z	38,7	22,75	18	4,5	22.3 km WNW of Atalanti
2011-02-22T20:37:02.000000Z	38,86	24,95	37	4,4	33.9 km E of Skyros
2013-09-20T02:05:18.000000Z	38,18	23,13	23	4,4	32.0 km NNE of Korinthos
2013-11-27T14:21:15.000000Z	37,33	23,01	25	4,4	22.6 km NE of Leonidhion
2014-06-06T12:21:03.000000Z	39,17	23,71	23	4,4	19.5 km E of Skiathos
2014-07-11T09:46:04.000000Z	38,45	23,71	26	4,4	9.7 km E of Chalkida
2014-10-04T00:12:01.000000Z	37,41	22,2	20	4,4	19.3 km SW of Tripolis
2015-10-27T01:25:51.000000Z	38,92	24,33	25	4,4	20.2 km W of Skyros
2017-03-24T04:24:30.000000Z	37,5705	23,8847	165	4,4	47.8 km SSE of Athens
2010-08-29T00:51:57.000000Z	38,66	23,38	22	4,3	29.0 km NW of Chalkida
2010-09-02T03:53:04.000000Z	38,22	23,17	26	4,3	35.2 km SE of Levadhia
2010-10-09T19:04:49.000000Z	38,15	22,72	20	4,3	30.0 km NW of Korinthos
2011-08-21T06:14:18.000000Z	37,63	23,32	115	4,3	45.8 km E of Nafplio
2012-06-28T13:11:29.000000Z	39,01	23,17	25	4,3	32.2 km WSW of Skiathos
2013-04-28T16:31:04.000000Z	37,45	22,7	61	4,3	15.8 km SW of Nafplio
2013-06-04T01:56:53.000000Z	37,98	24,01	24	4,3	24.3 km E of Athens
2014-02-06T07:58:26.000000Z	38,71	22,77	22	4,3	20.9 km WNW of Atalanti
2014-05-20T23:30:44.000000Z	39,53	24,2	30	4,3	73.7 km ENE of Skiathos
2019-07-19T12:11:54.000000Z	38,0956	23,5808	15	4,3	18.3 km NW of Athens
2010-05-11T07:03:36.000000Z	38,62	23,77	24	4,2	22.9 km NE of Chalkida
2012-02-17T08:05:04.000000Z	37,87	23,02	17	4,2	10.8 km SE of Korinthos
2013-04-28T04:49:55.000000Z	38,26	22,25	55	4,2	14.7 km E of Aegion
2013-11-22T15:12:03.000000Z	39,05	22,41	21	4,2	16.8 km N of Lamia
2013-12-11T13:00:53.000000Z	39,01	22,29	21	4,2	17.4 km NW of Lamia
2014-05-06T02:00:00.000000Z	39,35	23,88	29	4,2	39.8 km ENE of Skiathos
2016-06-11T08:29:45.000000Z	39,23	23,73	15	4,2	22.4 km ENE of Skiathos
2019-11-29T20:46:40.000000Z	39,0482	22,3178	77	4,2	19.3 km NNW of Lamia
2010-04-04T22:05:56.000000Z	38,42	22,32	17	4,1	12.6 km SSW of Amfissa

2010-06-27T13:10:09.000000Z	37,52	22,94	79	4,1	12.6 km ESE of Nafplio
2011-09-06T04:14:13.000000Z	37,88	23,1	104	4,1	16.1 km ESE of Korinthos
2012-08-02T10:30:39.000000Z	39,27	23,72	25	4,1	23.4 km ENE of Skiathos
2012-08-06T15:22:11.000000Z	38,75	24,83	29	4,1	28.8 km SE of Skyros
2012-12-03T21:40:15.000000Z	39,53	23,51	27	4,1	40.5 km N of Skiathos
2012-12-09T01:23:05.000000Z	37,93	22,59	24	4,1	30.0 km W of Korinthos
2014-05-10T03:04:50.000000Z	38,42	22,46	20	4,1	13.9 km SSE of Amfissa
2014-12-19T22:40:32.000000Z	39,33	22,62	19	4,1	28.3 km W of Volos
2015-04-13T03:49:02.000000Z	39,13	24,46	17	4,1	26.6 km NNW of Skyros
2016-08-26T13:37:32.000000Z	38,57	24,51	17	4,1	37.4 km S of Skyros
2019-12-11T02:29:27.000000Z	37,5504	24,0079	142	4,1	53.9 km SSE of Athens
2011-07-14T08:41:55.000000Z	37,83	22,62	82	4	29.9 km WSW of Korinthos
2013-01-30T04:27:25.000000Z	38,78	23,37	22	4	35.2 km ENE of Atalanti
2016-09-16T06:55:13.000000Z	38,89	23,33	25	4	33.5 km SSW of Skiathos
2016-09-29T01:17:36.000000Z	39,53	24,1	30	4	66.7 km NE of Skiathos
2018-12-11T04:11:43.000000Z	39,5152	24,249	41	4	73.1 km NNW of Skyros
2010-03-12T07:23:27.000000Z	37,76	22,76	80	3,9	22.2 km N of Nafplio
2010-03-20T20:24:48.000000Z	39,53	23,47	28	3,9	40.4 km N of Skiathos
2011-04-22T01:20:24.000000Z	38,37	23,62	23	3,9	10.6 km S of Chalkida
2011-11-29T16:55:57.000000Z	37,56	24,05	161	3,9	54.7 km SSE of Athens
2012-09-24T19:18:37.000000Z	39,03	23,16	23	3,9	31.8 km WSW of Skiathos
2013-09-17T05:46:52.000000Z	38,72	22,77	17	3,9	21.3 km WNW of Atalanti
2013-11-04T22:09:17.000000Z	38,91	23,1	23	3,9	30.1 km NNE of Atalanti
2014-09-29T08:15:07.000000Z	39,31	24,04	32	3,9	50.5 km ENE of Skiathos
2014-11-18T01:13:47.000000Z	38,64	23,41	23	3,9	25.6 km NW of Chalkida
2014-11-19T00:37:26.000000Z	38,64	23,42	24	3,9	25.1 km NW of Chalkida
2014-12-07T12:59:53.000000Z	39,35	22,63	18	3,9	27.2 km W of Volos
2014-12-31T04:49:58.000000Z	38,19	22,51	20	3,9	38.0 km E of Aegion
2015-11-17T03:00:09.000000Z	39,51	24,07	43	3,9	63.3 km NE of Skiathos
2016-05-20T08:45:33.000000Z	39,27	22,93	15	3,9	10.8 km S of Volos
2016-05-20T20:00:20.000000Z	38,59	24,47	15	3,9	35.9 km SSW of Skyros
2018-01-19T10:10:07.000000Z	37,5118	23,7805	137	3,9	52.6 km S of Athens
2019-10-14T09:24:32.000000Z	38,167	22,657	18	3,9	35.1 km NW of Korinthos
2010-03-12T03:34:37.000000Z	38,12	22,63	20	3,8	33.3 km NW of Korinthos
2010-07-05T08:37:58.000000Z	38,86	23,6	24	3,8	35.6 km SSE of Skiathos
2010-07-18T05:00:19.000000Z	39,32	24,02	29	3,8	49.3 km ENE of Skiathos
2011-01-17T22:27:10.000000Z	38,78	23,45	23	3,8	37.5 km NNW of Chalkida
2011-01-20T11:39:36.000000Z	39,55	23,51	25	3,8	42.7 km N of Skiathos
2011-01-23T13:06:34.000000Z	39,54	23,5	29	3,8	41.5 km N of Skiathos
2011-02-09T08:13:10.000000Z	38,63	22,49	21	3,8	15.5 km NE of Amfissa
2011-05-19T09:05:38.000000Z	38,43	23,86	24	3,8	23.0 km E of Chalkida
2011-07-12T08:00:14.000000Z	39,39	24	27	3,8	50.9 km ENE of Skiathos
2011-10-04T06:12:13.000000Z	37,33	23,28	96	3,8	41.7 km ENE of Leonidhion
2012-08-25T06:17:44.000000Z	38,89	23,22	25	3,8	32.7 km NE of Atalanti
2012-12-04T09:41:14.000000Z	39,53	23,52	28	3,8	40.5 km N of Skiathos
2013-08-14T17:12:57.000000Z	38,7	22,66	19	3,8	29.7 km SE of Lamia
2014-05-13T01:24:10.000000Z	38,24	25,13	32	3,8	48.4 km NNE of Andros
2014-05-27T11:21:30.000000Z	37,54	22,86	78	3,8	5.3 km ESE of Nafplio
2014-07-11T10:47:01.000000Z	38,45	23,71	25	3,8	9.7 km E of Chalkida

2014-09-03T09:40:48.000000Z	38,61	24,53	27	3,8	32.8 km S of Skyros
2014-11-17T23:13:29.000000Z	38,65	23,45	24	3,8	24.5 km NNW of Chalkida
2014-11-17T23:40:36.000000Z	38,65	23,37	21	3,8	28.8 km NW of Chalkida
2016-04-09T01:36:11.000000Z	38,63	24,45	26	3,8	32.0 km SSW of Skyros
2016-05-09T17:29:19.000000Z	38,85	23,62	19	3,8	37.1 km SSE of Skiathos
2016-05-09T22:57:01.000000Z	39,14	24,15	15	3,8	44.3 km NW of Skyros
2018-12-16T19:21:58.000000Z	39,5338	24,283	17	3,8	74.1 km NNW of Skyros
2018-12-23T22:34:10.000000Z	37,3258	23,945	28	3,8	50.4 km WNW of Seriphos
2019-03-14T10:37:09.000000Z	39,5215	24,1113	15	3,8	66.9 km NE of Skiathos
2019-11-24T18:34:57.000000Z	39,4579	24,0852	15	3,8	61.1 km ENE of Skiathos
2011-01-11T15:46:45.000000Z	38,75	22,2	23	3,7	26.2 km SW of Lamia
2011-02-13T00:17:22.000000Z	38,71	22,81	17	3,7	17.7 km WNW of Atalanti
2011-09-12T14:29:22.000000Z	38,72	23,39	21	3,7	33.8 km NNW of Chalkida
2012-01-05T20:25:49.000000Z	38,99	22,26	22	3,7	18.0 km NW of Lamia
2013-03-13T23:09:01.000000Z	39,19	23,47	15	3,7	2.8 km NNW of Skiathos
2013-08-10T07:09:33.000000Z	38,7	22,67	18	3,7	29.1 km W of Atalanti
2014-04-17T07:04:04.000000Z	38,42	22,47	15	3,7	14.4 km SE of Amfissa
2014-04-28T03:49:50.000000Z	38,69	22,81	23	3,7	17.0 km WNW of Atalanti
2014-06-28T19:09:47.000000Z	37,46	22,85	20	3,7	12.1 km SSE of Nafplio
2014-10-30T06:09:08.000000Z	38,14	22,63	15	3,7	34.7 km NW of Korinthos
2014-11-05T20:51:39.000000Z	39,14	24,19	25	3,7	41.5 km NW of Skyros
2014-11-15T08:11:31.000000Z	38,99	23,7	24	3,7	27.1 km SE of Skiathos
2014-11-18T00:53:59.000000Z	38,63	23,43	23	3,7	23.7 km NW of Chalkida
2014-12-14T08:16:33.000000Z	38,62	22,88	18	3,7	10.9 km WSW of Atalanti
2015-03-09T03:24:41.000000Z	39,31	24,02	16	3,7	48.9 km ENE of Skiathos
2015-07-02T13:15:29.000000Z	39,51	24,22	44	3,7	73.6 km NNW of Skyros
2016-07-28T16:17:29.000000Z	38,17	22,94	15	3,7	25.8 km N of Korinthos
2016-08-26T17:23:37.000000Z	39,28	22,94	24	3,7	9.7 km S of Volos
2010-03-11T09:54:08.000000Z	38,12	23,26	21	3,6	35.1 km NE of Korinthos
2010-04-15T18:51:43.000000Z	38,81	23,43	20	3,6	39.9 km S of Skiathos
2010-05-12T06:59:22.000000Z	38,62	23,78	25	3,6	23.4 km NE of Chalkida
2010-07-28T13:55:27.000000Z	37,47	23,32	29	3,6	46.4 km ESE of Nafplio
2010-08-03T00:07:37.000000Z	38,73	22,54	21	3,6	21.0 km SSE of Lamia
2010-09-06T19:20:42.000000Z	37,59	22,61	56	3,6	17.7 km W of Nafplio
2010-10-28T04:04:46.000000Z	38,36	22,25	20	3,6	19.2 km NE of Aegion
2010-12-14T13:58:52.000000Z	38,06	22,78	19	3,6	19.0 km NW of Korinthos
2011-01-31T17:23:13.000000Z	37,87	22,7	26	3,6	21.7 km WSW of Korinthos
2012-02-13T09:40:42.000000Z	38,88	24,14	26	3,6	36.7 km W of Skyros
2012-08-16T21:22:53.000000Z	38,28	22,55	24	3,6	31.3 km SSE of Amfissa
2013-08-07T10:02:33.000000Z	38,68	22,65	18	3,6	29.6 km NE of Amfissa
2013-09-08T06:22:10.000000Z	38,59	23,76	23	3,6	19.8 km NE of Chalkida
2014-02-07T06:59:59.000000Z	38,7	22,78	18	3,6	19.8 km WNW of Atalanti
2014-02-12T07:41:00.000000Z	37,93	22,6	16	3,6	29.1 km W of Korinthos
2014-06-09T22:02:57.000000Z	39,17	23,75	24	3,6	23.0 km E of Skiathos
2014-07-30T00:55:04.000000Z	38,04	24,12	19	3,6	34.5 km E of Athens
2014-09-18T07:24:25.000000Z	37,7	23,09	25	3,6	29.1 km ENE of Nafplio
2016-07-26T16:59:47.000000Z	37,63	23,5	15	3,6	44.3 km SSW of Athens
2016-08-26T07:47:24.000000Z	38,6	24,47	21	3,6	34.8 km SSW of Skyros
2017-06-23T22:26:17.000000Z	38,4549	23,53	17	3,6	6.1 km W of Chalkida

2018-12-11T04:01:21.000000Z	39,5293	24,2372	35	3,6	75.0 km NNW of Skyros
2018-12-18T16:29:08.000000Z	39,5654	24,2725	15	3,6	76.1 km S of Kariai
2019-02-26T14:31:17.000000Z	38,1885	23,4521	20	3,6	33.2 km SSW of Chalkida
2019-08-03T17:17:09.000000Z	38,1404	22,7019	15	3,6	30.2 km NW of Korinthos
2010-04-30T21:47:55.000000Z	38,88	23,62	22	3,5	34.0 km SSE of Skiathos
2010-05-13T21:49:45.000000Z	38,61	23,63	23	3,5	16.5 km N of Chalkida
2010-06-05T05:12:40.000000Z	38,13	23,18	18	3,5	30.5 km NE of Korinthos
2010-06-16T15:11:21.000000Z	37,41	23,58	28	3,5	65.2 km SSW of Athens
2010-11-09T12:04:59.000000Z	38,67	23,31	24	3,5	27.1 km E of Atalanti
2010-12-21T21:52:14.000000Z	39,23	23,55	24	3,5	9.1 km NE of Skiathos
2011-01-30T09:32:38.000000Z	37,86	23,1	18	3,5	17.1 km ESE of Korinthos
2011-02-24T03:48:52.000000Z	39,56	23,45	26	3,5	43.8 km N of Skiathos
2011-03-07T17:10:53.000000Z	38,25	22,55	15	3,5	34.2 km SSE of Amfissa
2011-07-08T10:13:23.000000Z	39,47	23,73	29	3,5	39.8 km NNE of Skiathos
2011-08-16T20:22:22.000000Z	38,15	22,71	22	3,5	30.6 km NW of Korinthos
2011-08-18T09:47:40.000000Z	38,91	24,15	27	3,5	35.7 km W of Skyros
2011-10-24T09:24:37.000000Z	37,61	23,51	27	3,5	45.9 km SSW of Athens
2011-11-03T13:06:33.000000Z	39,1	23,29	22	3,5	18.2 km WSW of Skiathos
2011-11-20T22:14:14.000000Z	38,17	22,56	21	3,5	40.2 km SW of Levadhia
2012-01-18T19:49:23.000000Z	38,95	22,46	24	3,5	6.0 km NNE of Lamia
2013-06-11T19:36:16.000000Z	38,17	23,23	23	3,5	36.7 km NE of Korinthos
2013-10-27T13:53:37.000000Z	38,64	23,61	22	3,5	19.6 km N of Chalkida
2013-11-13T06:50:23.000000Z	38,92	23,1	21	3,5	31.2 km NNE of Atalanti
2013-12-22T18:04:02.000000Z	37,85	22,76	27	3,5	18.0 km WSW of Korinthos
2014-03-17T17:40:53.000000Z	39,16	22,37	92	3,5	29.4 km N of Lamia
2014-04-04T05:00:01.000000Z	39,02	23,39	24	3,5	18.2 km SSW of Skiathos
2014-04-10T17:40:44.000000Z	37,93	22,61	24	3,5	28.3 km W of Korinthos
2014-06-27T16:44:38.000000Z	38,24	25,13	32	3,5	48.4 km NNE of Andros
2014-11-17T23:18:45.000000Z	38,66	23,4	23	3,5	27.9 km NW of Chalkida
2014-11-18T00:18:27.000000Z	38,65	23,41	21	3,5	26.5 km NW of Chalkida
2014-11-19T19:54:08.000000Z	38,64	23,43	23	3,5	24.5 km NW of Chalkida
2014-11-20T16:26:22.000000Z	38,65	23,36	24	3,5	29.4 km NW of Chalkida
2015-06-09T02:31:27.000000Z	38,63	23,4	16	3,5	25.4 km NW of Chalkida
2015-06-09T03:04:41.000000Z	38,63	23,42	15	3,5	24.2 km NW of Chalkida
2015-06-09T06:51:04.000000Z	38,6	23,44	15	3,5	20.6 km NW of Chalkida
2015-11-10T06:53:47.000000Z	39,39	23,95	32	3,5	47.2 km ENE of Skiathos
2016-02-25T12:06:09.000000Z	39,21	22,32	22	3,5	35.8 km NNW of Lamia
2016-04-07T05:56:22.000000Z	38,65	22,5	80	3,5	17.7 km NE of Amfissa
2016-05-28T21:00:10.000000Z	37,57	23,57	16	3,5	48.1 km SSW of Athens
2016-06-03T01:28:49.000000Z	38,62	24,45	16	3,5	33.1 km SSW of Skyros
2019-07-19T11:42:19.000000Z	38,1248	23,5158	16	3,5	24.7 km NW of Athens
2010-04-10T11:03:28.000000Z	38,43	22,29	16	3,4	12.8 km SW of Amfissa
2010-08-05T13:37:26.000000Z	39,32	24,02	28	3,4	49.3 km ENE of Skiathos
2010-08-26T09:09:48.000000Z	39,53	23,47	30	3,4	40.4 km N of Skiathos
2010-08-27T11:23:20.000000Z	37,86	22,98	19	3,4	9.6 km SSE of Korinthos
2010-09-21T08:02:11.000000Z	38,15	23,32	24	3,4	40.7 km WNW of Athens
2010-12-12T08:19:31.000000Z	38,11	23,55	18	3,4	21.4 km NW of Athens
2011-03-26T08:21:43.000000Z	39,32	24,02	29	3,4	49.3 km ENE of Skiathos
2011-04-21T05:17:25.000000Z	38,76	22,21	23	3,4	24.8 km SW of Lamia

2011-06-26T06:31:10.000000Z	38,88	23,69	22	3,4	36.5 km SSE of Skiathos
2011-12-01T01:17:43.000000Z	38,76	23,44	25	3,4	35.8 km NNW of Chalkida
2011-12-08T20:59:34.000000Z	38,08	23,53	20	3,4	20.8 km WNW of Athens
2012-10-20T23:28:49.000000Z	38,82	24,91	32	3,4	31.5 km ESE of Skyros
2013-03-06T14:55:34.000000Z	38,75	23,92	27	3,4	42.3 km NE of Chalkida
2013-05-31T16:18:00.000000Z	37,36	23,17	18	3,4	35.1 km NE of Leonidhion
2013-08-15T01:03:30.000000Z	38,7	22,67	19	3,4	29.1 km W of Atalanti
2013-12-21T05:50:39.000000Z	38,23	22,21	50	3,4	11.4 km E of Aegion
2014-01-25T19:13:39.000000Z	38,37	22,27	16	3,4	19.4 km SSW of Amfissa
2014-02-28T22:13:54.000000Z	38,2	22,53	21	3,4	38.6 km SSE of Amfissa
2014-03-30T20:31:03.000000Z	37,58	23,45	20	3,4	51.3 km SSW of Athens

After the selection of the seismic events that are going to be used, we are processing them with the program of SeisComplex, which is based on matlab and is made for editing waveforms. The feature that we want to study and understand its variations is the  $q$  – Gaussian distribution, which is dependent on the value of the  $q$  index.

In the following figures we may find the results from editing some of the coda waveforms, along with their characteristics, which will be their origin time at GMT, their latitude and longitude, their depth, their magnitude (ML) and the area of their location. The rest of them will be found in the appendix B.

In figure 8.2.1 the time origin of the earthquake is 17/11/2014 at 23:05:55, latitude 38.64, longitude 23.4, depth 24 km, magnitude 5.2 at 26.2 km NW of Chalkida. The value of the index  $q$  is 1.8.

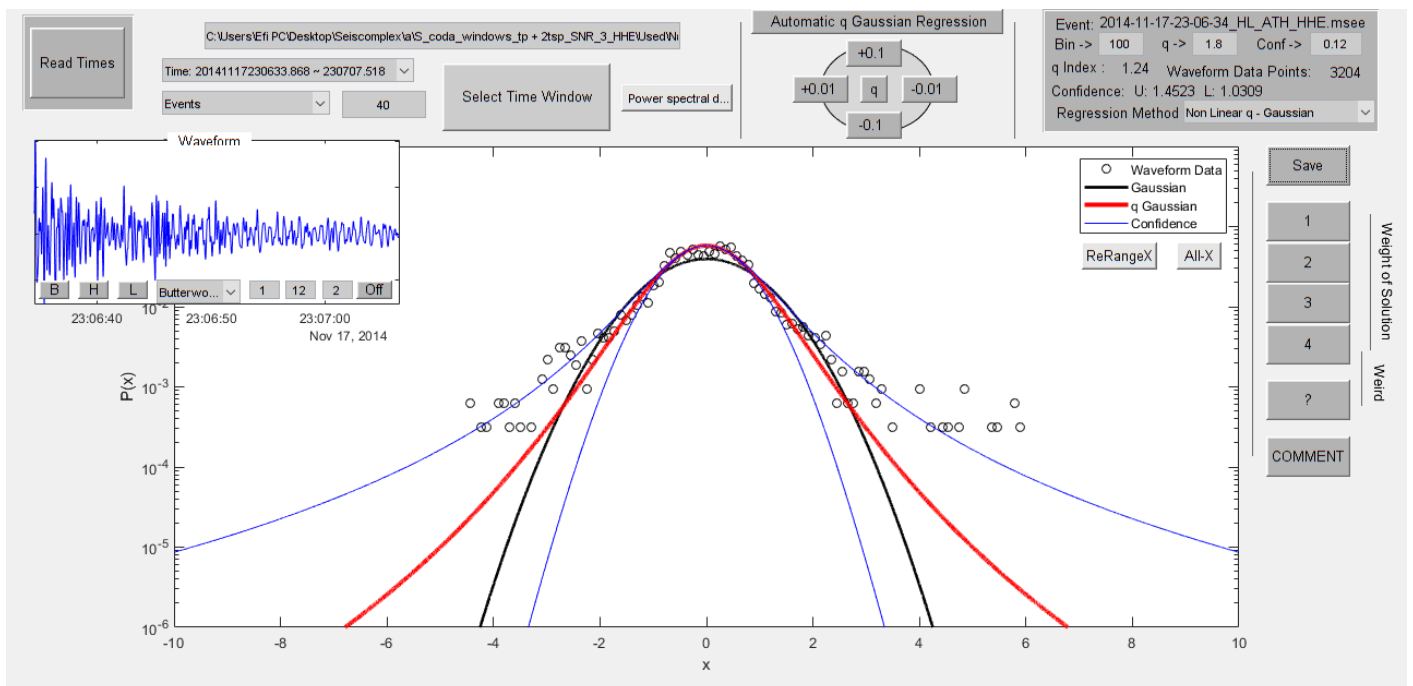


Figure 8.2.1.

In figure 8.2.2 the time origin of the earthquake is 17/11/2014 at 23:09:03, latitude 38.64, longitude 23.41, depth 23 km, magnitude 5.2 at 25.6 km NW of Chalkida, following the previous seismic event. The value of the index  $q$  is 1.8.

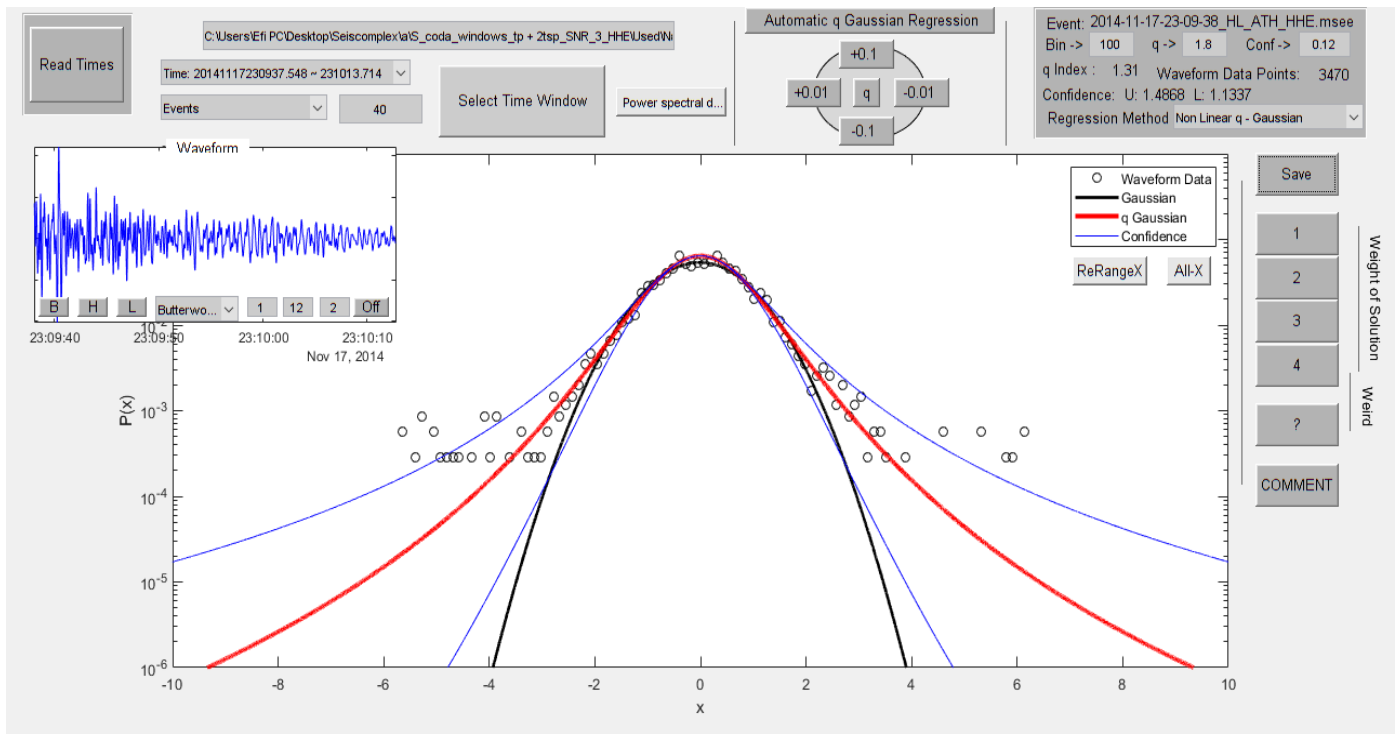


Figure 8.2.2

In figure 8.2.3 the time origin of the earthquake is 09/03/2010 at 02:55:00, latitude 38.87, longitude 23.65, depth 22 km, magnitude 5.1 at 36.0 km SSE of Skiathos. The value of the index  $q$  is 1.6.

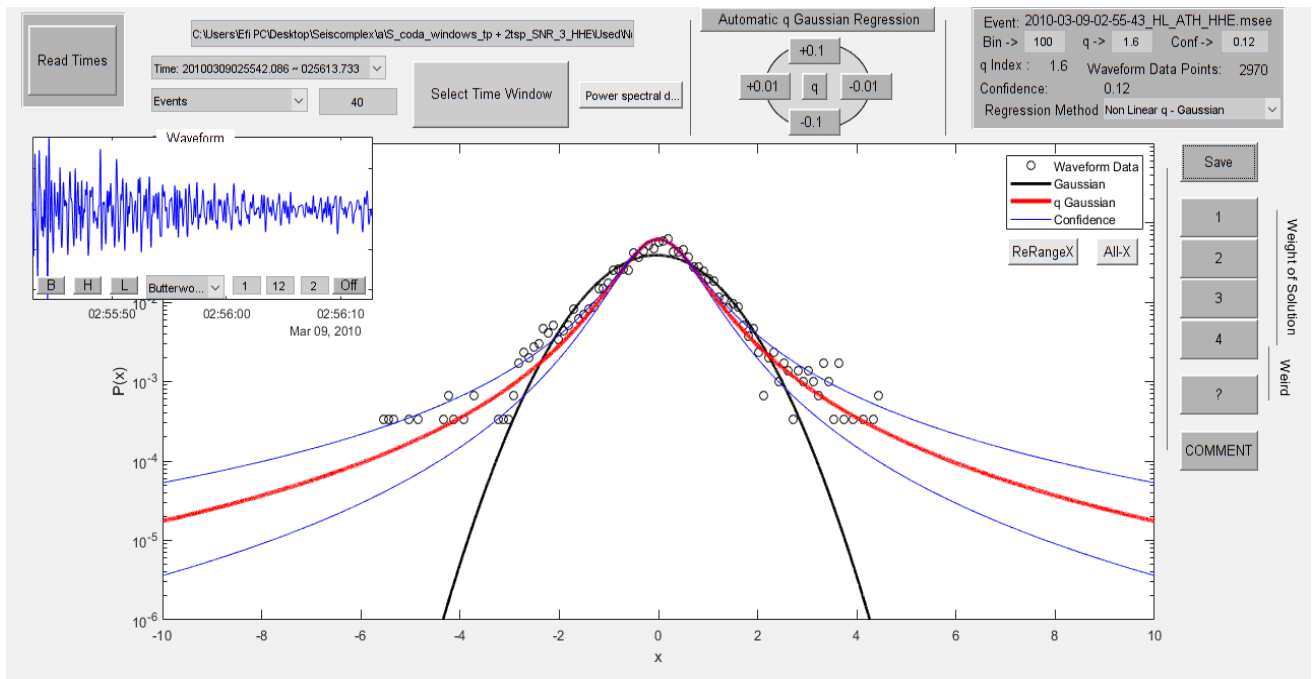


Figure 8.2.3

In figure 8.2.4 the time origin of the earthquake is 16/07/2010 at 18:53:10, latitude 39.32, longitude 24.02, depth 34 km, magnitude 5.1 at 49.3 km ENE of Skiathos. The value of the index  $q$  is 1.72.

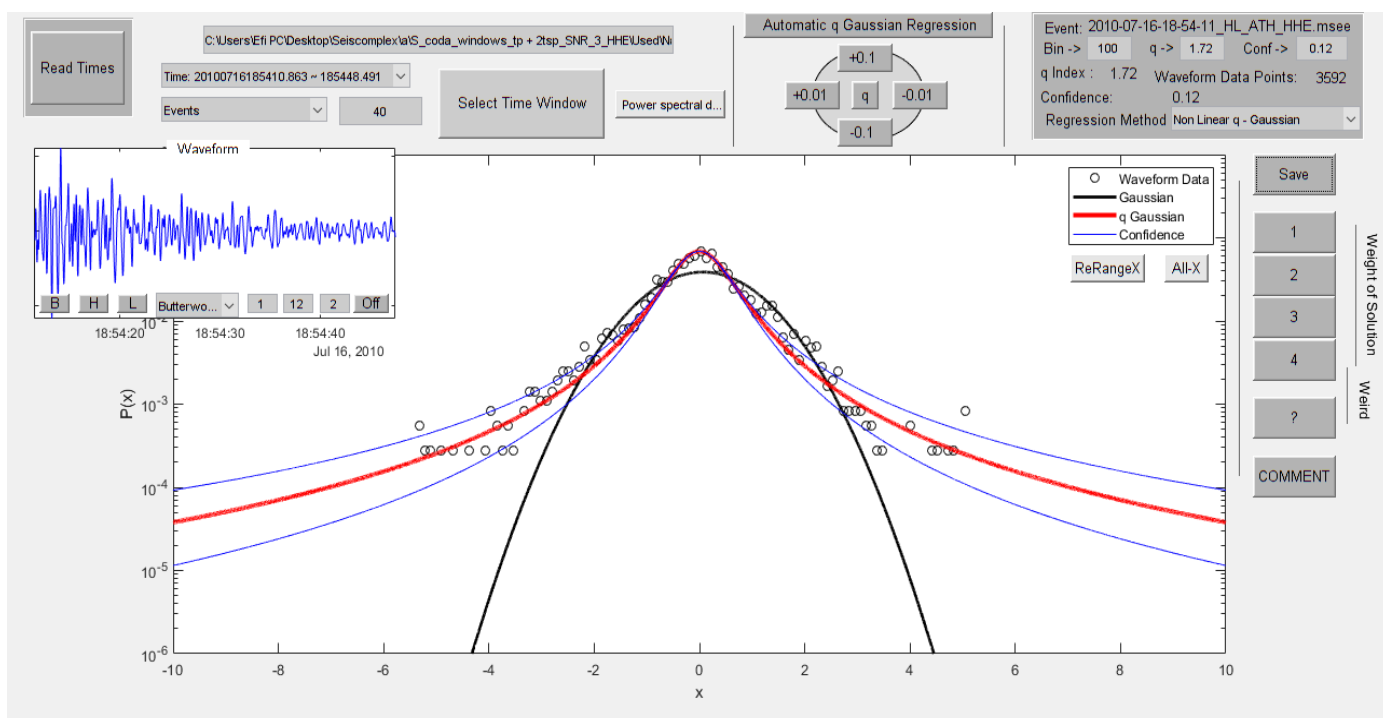


Figure 8.2.4

In figure 8.2.5 the time origin of the earthquake is 22/09/2012 at 03:52:24, latitude 38.09, longitude 22.74, depth 25 km, magnitude 4.9 at 23.9 km NW of Korinthos. The value of the index  $q$  is 1.8.

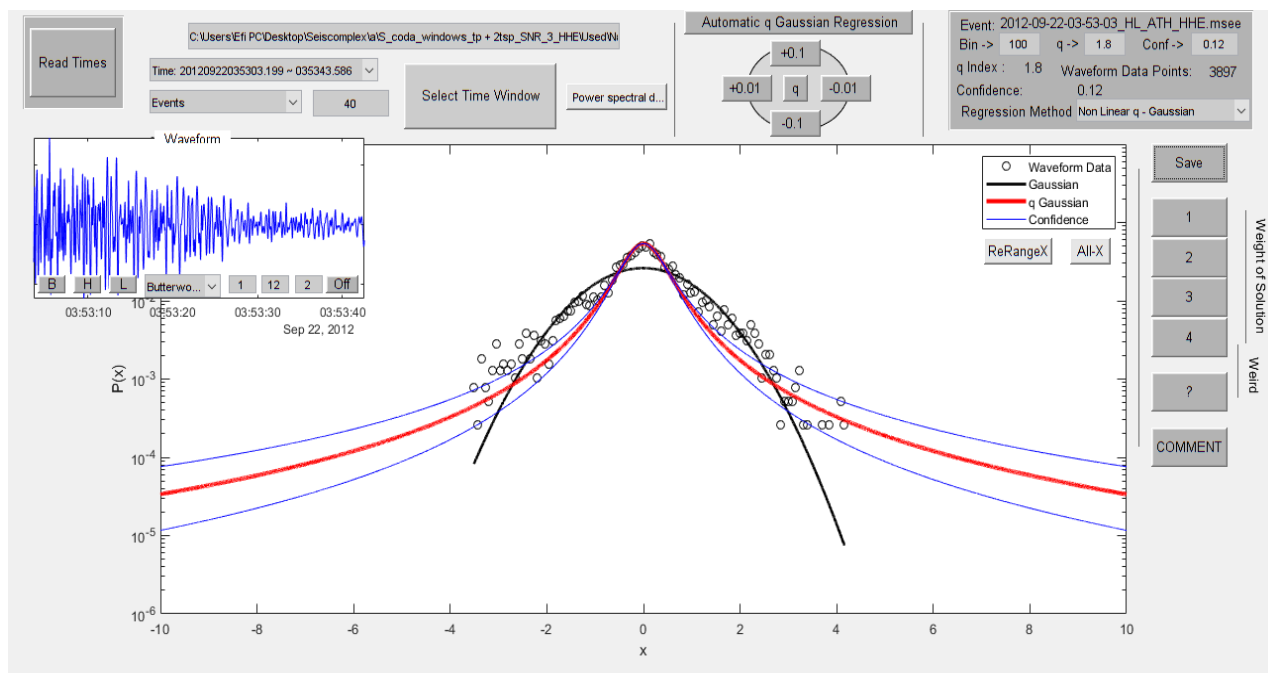


Figure 8.2.5

In figure 8.2.6 the time origin of the earthquake is 30/04/2014 at 04:03:32, latitude 38.23, longitude 25.13, depth 32 km, magnitude 4.9 at 47.4 km NNE of Andros. The value of the index  $q$  is 1.8.

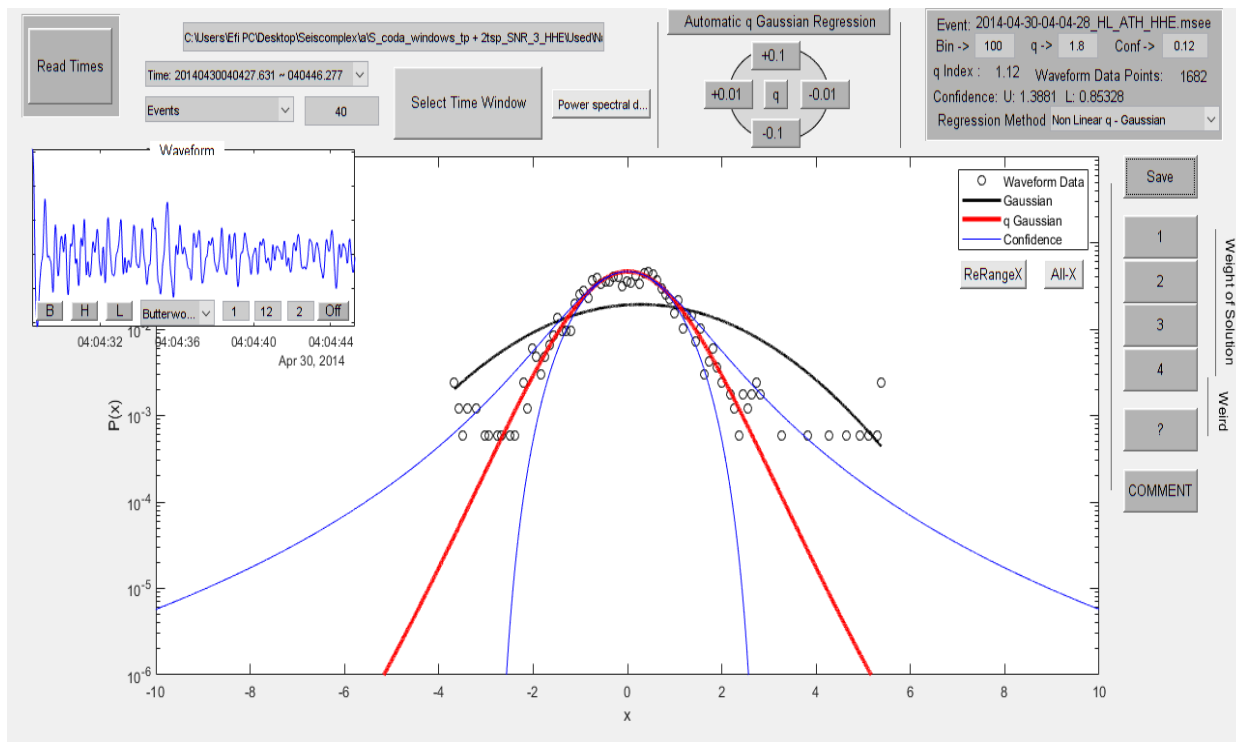


Figure 8.2.6

In figure 8.2.7 the time origin of the earthquake is 26/10/2012 at 23:16:44, latitude 38.96, longitude 22.91, depth 26 km, magnitude 4.6 at 35.2 km NNW of Atalanti. The value of the index  $q$  is 1.72.

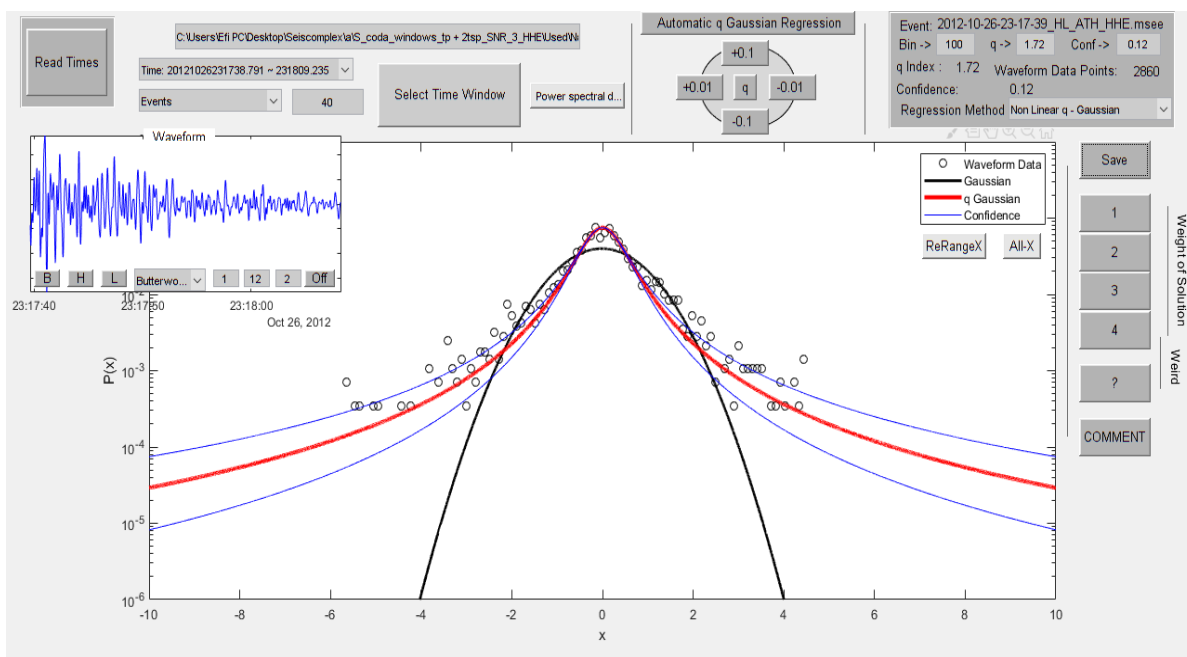


Figure 8.2.7

In figure 8.2.8 the time origin of the earthquake is 17/07/2010 at 02:30:35, latitude 39.33, longitude 24.02, depth 34 km, magnitude 4.5 at 49.7 km ENE of Skiathos. The value of the index  $q$  is 1.82.

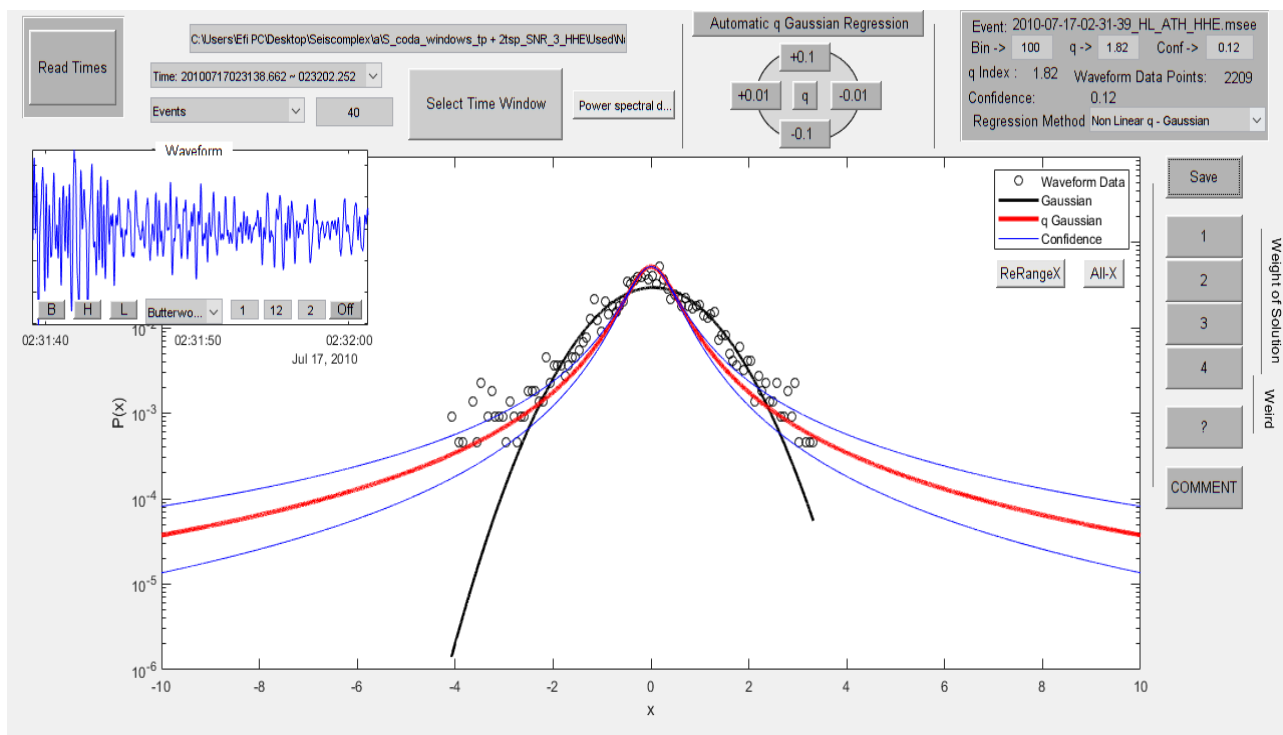


Figure 8.2.8

In figure 8.2.9 the time origin of the earthquake is 20/09/2013 at 02:05:18, latitude 38.18, longitude 23.13, depth 23 km, magnitude 4.4 at 32.0 km NNE of Korinthos. The value of the index  $q$  is 1.8.

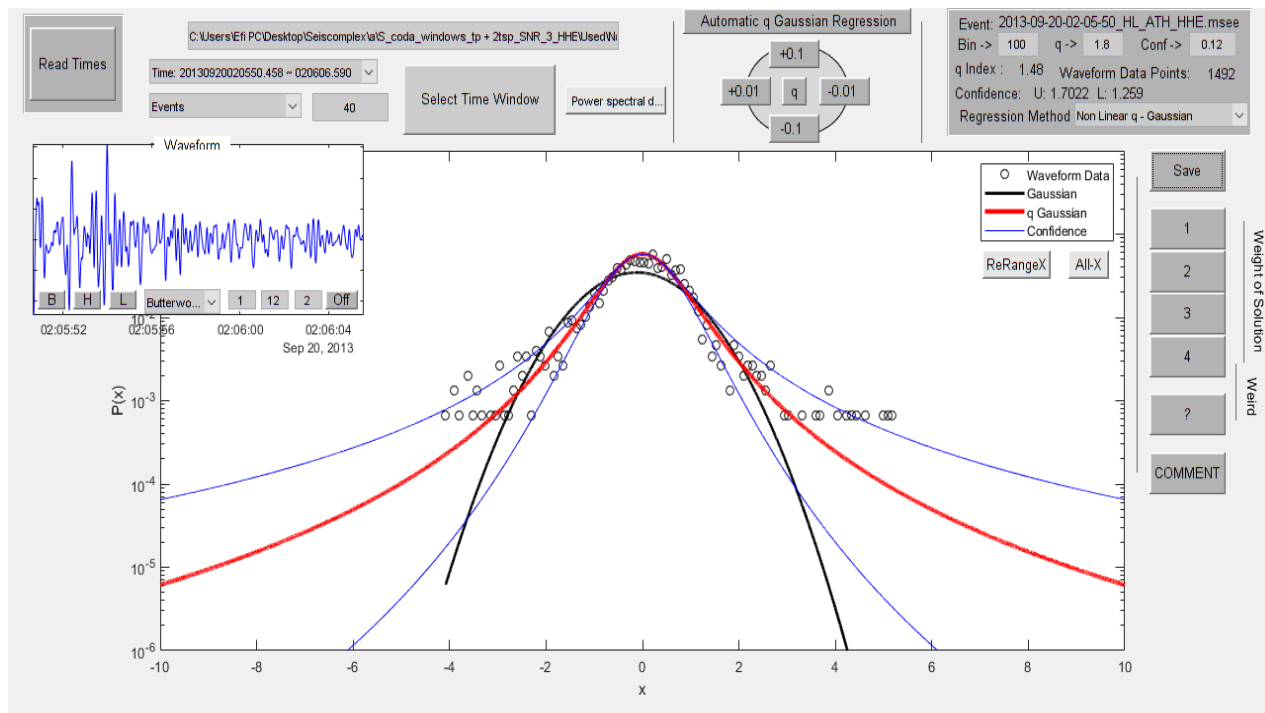


Figure 8.2.9

In figure 8.2.10 the time origin of the earthquake is 27/11/2013 at 14:21:15, latitude 37.33, longitude 23.01, depth 25 km, magnitude 4.4 at 22.6 km NE of Leonidhion. The value of the index  $q$  is 1.8.

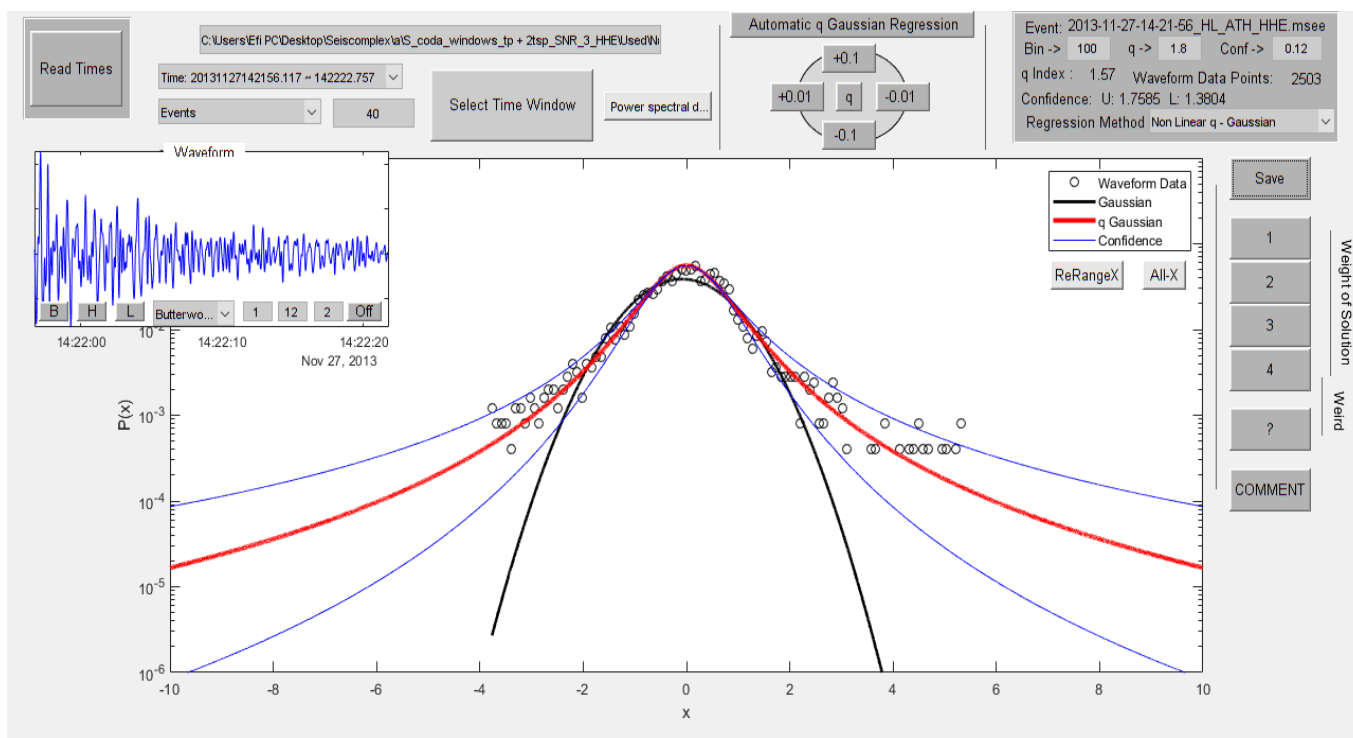


Figure 8.2.10

## 9. Discussion and conclusions

After the previous studies that we have presented, we will make some conclusions based on them. The recent theoretical studies which have been applied to Radiative energy transfer theory in a medium with uniformly distributed scatterers have made clearer the process of multiple isotropic scattering. Although the experimental study of Matsunami (1991) supports this theory, there are many limitations on isotropic scattering and homogenous distribution of scatterers that have come from the observations. Sato has created a theory of strong forward scattering that is opposite the isotropic scattering. Scherbaum and Sato (1991) proposed a full seismogram envelope inversion method based on this theory. This method does not take into consideration the effects of inhomogeneity of scatterer distribution, radiation pattern and wave conversion. Frankel and Clayton (1986) and Gusev and Abubakirov (1987) have many theories and approaches for anisotropic multiple scattering. A multiple scattering model has been developed by Sato according to the P to S and S to P-wave mode conversions. In addition he has also developed a multiple scattering model according to anisotropic scattering. Both models are based on the energy transfer theory.

In order to clear the composition of coda, array analyses using high quality digital data have been used. Those studies had the intension to understand the effects of P-S and S-P conversions, scatterers' distribution and topographic relief using the coda wave composition. Analyses of P-coda waves are useful to evaluate the contribution of conversion scattering to the total scattering. If P coda waves are mainly composed of S-P scattered waves, the conversion rate of S-P scattered waves estimated from P coda waves may become an indicator

of S wave velocity perturbation. Three component array observations and detailed analyses are very important for the above purposes.

For the second part of this thesis, we used S coda waveforms from seismic events that took place in central Greece, within the frequency range 1-30Hz and with magnitude range between 3.1 and 5.2. The time period of those seismic events was from 01-01-2010 to 30-12-2019 and were recorder by a station in Athens. After analyzing the S- coda waveforms with the method of non-extensive statistical mechanics, using the SeisComplex program, we can see from the figures 8.2.1 to 8.2.200 that the value of the q index is not far from the value of 1.8. This leads us to the conclusion that the time series describing the fluctuations in the seismic coda waves diverge from the Gaussian description and their corresponding probability density functions could be adequately described by the q-Gaussian distribution.

## Appendix A

### Function f(r)

```
function f1 = f_r_1(r,r_c,D)
% H function douleuei kai me orismata eisodou - dianusmata timwn:
f1=1./(((sqrt(1+(r./r_c).^2))).^(3-D));
end
```

### Function G(x,t)

```
function Gxt = G_x_t(x_vector3,t,d,V0,U1)
r=norm(x_vector3); % r=|x|, opws lee i thewria
Gxt=(1/(4*pi*V0*r^2))*d*(t-r/V0)*exp(-U1);
end
```

### Function U(r)

```
function U1 = U_r_1(r,r_c,D,b_i_0,g_s_0)
% Sto script tha einai r=|x| (opws lee i thewria)
U1=(1+b_i_0)*g_s_0*r*hypergeom([(3-D)/2,1/2],3/2,-r^2/r_c^2); % hypergeom([a,b],c,z) is
the Gauss hypergeometric function 2F1(a,b;c;z)
end
```

### Function G<sub>F</sub>(x,t)

```
function GFxt = G_F_x_t(x_vector3,t,d,V0,U1,f1)
r=norm(x_vector3); % r=|x|, opws lee i thewria
GFxt=((1/(4*pi*V0*r^2))*d*(t-r/V0)*exp(-U1)) *f1;
end
```

### Function $\widehat{E}(k, \omega)$

```
function [Ehatkw,Ehatkw_no1] = E_hat_k_w(V0,b_i_0,g_s_0,D,r_c,W)
```

```
% H en logw function epistrefei 2 orismata: 1) ton tupo, dil tin sunartisi Ehatkw(k,w) kai,
% 2) tin timi tis sunartisis autis gia sugkekrimena k kai w pou eisagei
% o xristis (edw, oxi sto script)
```

```
syms r_var
syms k
syms w
```

```
expr1=exp(-((1+b_i_0)*g_s_0*r_var*hypergeom([(3-D)/2,1/2],3/2,-r_var^2/r_c^2))) +
((1i*w*r_var/V0)*(sin(k*r_var)/(k*r_var)));
Ghatkw=(1/V0)* int(expr1,r_var,[0,Inf]) ;
expr2=(1./(((sqrt(1+(r_var/r_c).^2))).^(3-D))) * exp(-((1+b_i_0)*g_s_0*r_var*hypergeom([(3-
D)/2,1/2],3/2,-r_var^2/r_c^2))) + ((1i*w*r_var/V0)*(sin(k*r_var)/(k*r_var)));
GFhatkw=(1/V0)* int(expr2,r_var,[0,Inf]) ;
Ehatkw = (W*Ghatkw)/(1-V0*g_s_0*GFhatkw);
```

```

syms Ghatkw_no(k,w)

Ghatkw_no(k,w)=Ghatkw;

% Specific value (for specific k, w):
condition=false;
while condition==false
    k_no=input('Eisagete k number: ');
    if k_no>=0 % Prepei k_no>=0
        condition=true;
    else
        disp('PROSOXH: eisagete apodekti timi k number (megaluteri /isi tou 0) !')
        disp(' ')
    end
end

condition=false;
while condition==false
    w_no=input('Eisagete w number : ');
    if w_no>0 % Prepei w_no>0
        condition=true;
    else
        disp('PROSOXH: eisagete apodekti timi w number (megaluteri tou 0) !')
        disp(' ')
    end
end

Ghatkw_no1=Ghatkw_no(k_no,w_no); % Ghatkw_no1=Ghatkw_no(1,2);

syms GFhatkw_no(k,w)

GFhatkw_no(k,w)=GFhatkw;

GFhatkw_no1=GFhatkw_no(k_no,w_no); % Ghatkw_no1=Ghatkw_no(1,2);

Ehatkw_no1=(W*Ghatkw_no1)/(1-V0*g_s_0*GFhatkw_no1);

end

```

### Function $\widehat{G}(k, \omega)$

```

function [Ghatkw,Ghatkw_no1] = G_hat_k_w(V0,b_i_0,g_s_0,D,r_c)

% H en logw function epistrefei 2 orismata: 1) ton tupo, dil tin sunartisi Ghatkw(k,w) kai,
% 2) tin timi tis sunartisis autis gia sugkekrimena k kai w pou eisagei
% o xristis (edw, oxi sto script)

% Ypologismos definite integral:
syms r_var
syms k
syms w

```

```

    expr=exp(-((1+b_i_0)*g_s_0*r_var*hypergeom([(3-D)/2,1/2],3/2,-r_var^2/r_c^2))) +
    ((1*i*w*r_var/V0)*(sin(k*r_var)/(k*r_var))); % expr=b*r_var^2+r_var*k*w*b;
    Ghatkw=(1/V0)*int(expr,r_var,[0,Inf]);

syms Ghatkw_no(k,w)

Ghatkw_no(k,w)=Ghatkw;

% Specific value (for specific k, w):
condition=false;
while condition==false
    k_no=input('Eisagete k number: ');
    if k_no>=0 % Prepei k_no>=0
        condition=true;
    else
        disp('PROSOXH: eisagete apodekti timi k number (megaluteri / isi tou 0) ! ')
        disp(' ')
    end
end

condition=false;
while condition==false
    w_no=input('Eisagete w number : ');
    if w_no>0 % Prepei w_no>0
        condition=true;
    else
        disp('PROSOXH: eisagete apodekti timi w number (megaluteri tou 0) ! ')
        disp(' ')
    end
end

Ghatkw_no1=Ghatkw_no(k_no,w_no);

end

Function  $\widehat{G}_F(k, \omega)$ 

function [GFhatkw,GFhatkw_no1] = G_F_hat_k_w(V0,b_i_0,g_s_0,D,r_c) %
G_F_hat_k_w(k,w,V0,b_i_0,g_s_0,D,r_c)

% H en logw function epistrefei 2 orismata: 1) ton tupo, dil tin sunartisi GFhatkw(k,w) kai,
% 2) tin timi tis sunartisis autis gia sugkekrimena k kai w pou eisagei
% o xristis (edw, oxi sto script)

% Ypologismos definite integral:
syms r_var
syms k
syms w

expr=(1./(((sqrt(1+(r_var/r_c).^2))).^(3-D))) * exp(-((1+b_i_0)*g_s_0*r_var*hypergeom([(3-
D)/2,1/2],3/2,-r_var^2/r_c^2))) + ((1*i*w*r_var/V0)*(sin(k*r_var)/(k*r_var)));
GFhatkw=(1/V0)*int(expr,r_var,[0,Inf]);

```

```

syms GFhatkw_no(k,w)

GFhatkw_no(k,w)=GFhatkw;

% Specific value (for specific k, w):
condition=false;
while condition==false
    k_no=input('Eisagete k number: ');
    if k_no>=0 % Prepei k_no>=0
        condition=true;
    else
        disp('PROSOXH: eisagete apodekti timi k number (megaluteri / isi tou 0) ! ')
        disp(' ')
    end
end

condition=false;
while condition==false
    w_no=input('Eisagete w number : ');
    if w_no>0 % Prepei w_no>0
        condition=true;
    else
        disp('PROSOXH: eisagete apodekti timi w number (megaluteri tou 0) ! ')
        disp(' ')
    end
end

GFhatkw_no1=GFhatkw_no(k_no,w_no);

end

Function E(r,t)

function [Ert,Ert_no1] = E_r_t(V0,b_i_0,g_s_0,D,r_c,W)

% H en logw function epistrefei 2 orismata: 1) ton tupo, dil tin sunartisi Ert(r,t) kai,
% 2) tin timi tis sunartisis autis gia sugkekrimena r kai t pou eisagei
% o xristis (edw, oxi sto script - - alla mporei na epanalabei ta r, t pou briskontai sto C.W. so
far)

syms r_var
syms k
syms w

syms r
syms t

expr1=exp(-((1+b_i_0)*g_s_0*r_var*hypergeom([(3-D)/2,1/2],3/2,-r_var^2/r_c^2))) +
((1i*w*r_var/V0)*(sin(k*r_var)/(k*r_var)));
Ghatkw=(1/V0)* int(expr1,r_var,[0,Inf]) ;
expr2=(1./(((sqrt(1+(r_var/r_c).^2))).^(3-D))) * exp(-((1+b_i_0)*g_s_0*r_var*hypergeom([(3-
D)/2,1/2],3/2,-r_var^2/r_c^2))) + ((1i*w*r_var/V0)*(sin(k*r_var)/(k*r_var)));

```

```
Gfhatkw=(1/V0)*int(expr2,r_var,[0,Inf]);
Ehatkw=(W*Ghatkw)/(1-V0*g_s_0*Gfhatkw);
```

```
% Sto dia tauta:
expr3=k*sin(k*r)*Ehatkw;
I1_function_of_omega_and_r=int(expr3,k,[0,Inf]);
expr4=exp(-1i*w*t)*(1/(2*pi^2*r))*I1_function_of_omega_and_r;
Ert=(1/(2*pi))*int(expr4,w,[-Inf,Inf]);
```

```
syms Ert_no(r,t)
Ert_no(r,t)=Ert;
```

```
% Specific value (for specific r, t):
condition=false;
while condition==false
    r_no=input('Eisagete r number: ');
    if r_no>0 % Prepei r_no>0
        condition=true;
    else
        disp('PROSOXH: eisagete apodekti timi r number (megaluteri tou 0) !')
        disp(' ')
    end
end
```

```
condition=false;
while condition==false
    t_no=input('Eisagete t number : ');
    if t_no>0 % Prepei t_no>0
        condition=true;
    else
        disp('PROSOXH: eisagete apodekti timi t number (megaluteri tou 0) !')
        disp(' ')
    end
end
```

```
Ert_no1=Ert_no(r_no,t_no);
```

```
end
```

### Function $\bar{t}$

```
function t_normalized = t_normal(V0,g_s_0,t)
    t_normalized=V0*g_s_0*t;
end
```

### Function $\bar{x}$

```
function x_normalized = x_normal(g_s_0,x_vector)
    x_normalized=g_s_0*x_vector;
end
```

### Function $\bar{G}$

```
function G_normalized = G_normal(x_vector3,t,d,V0,U1,g_s_0)
```

```
    r=norm(x_vector3); % r=|x|, opws leei i thewria
    Gxt=(1/(4*pi*V0*r^2))*d*(t-r/V0)*exp(-U1);
    G_normalized = Gxt/g_s_0^3;
    %end
```

```
end
```

### Function $\bar{G}_F$

```
function G_F_normalized = G_F_normal(x_vector3,t,d,V0,U1,f1,g_s_0)
```

```
    r=norm(x_vector3); % r=|x|, opws leei i thewria
    GFxt=((1/(4*pi*V0*r^2))*d*(t-r/V0)*exp(-U1)) *f1;
    G_F_normalized = GFxt/g_s_0^3;
```

```
end
```

### Function $\bar{E}$

```
function E_normalized = E_normal(V0,b_i_0,g_s_0,D,r_c,W)
```

```
syms r_var
syms k
syms w
```

```
syms r
syms t
```

```
    expr1=exp(-((1+b_i_0)*g_s_0*r_var*hypergeom([(3-D)/2,1/2],3/2,-r_var^2/r_c^2))) +
    ((1i*w*r_var/V0)*(sin(k*r_var)/(k*r_var)));
    Ghatkw=(1/V0)*int(expr1,r_var,[0,Inf]);
    expr2=(1./(((sqrt(1+(r_var/r_c).^2)).^(3-D))) * exp(-((1+b_i_0)*g_s_0*r_var*hypergeom([(3-
    D)/2,1/2],3/2,-r_var^2/r_c^2))) + ((1i*w*r_var/V0)*(sin(k*r_var)/(k*r_var)));
    GFhatkw=(1/V0)*int(expr2,r_var,[0,Inf]);
    Ehatkw = (W*Ghatkw)/(1-V0*g_s_0*GFhatkw);
```

```
    expr3=k*sin(k*r)*Ehatkw;
    I1_function_of_omega_and_r=int(expr3,k,[0,Inf]);
    expr4= exp(-1i*w*t)* (1/(2*pi^2*r))* I1_function_of_omega_and_r;
    Ert=(1/(2*pi))*int(expr4,w,[-Inf,Inf]);
```

```
    % Twra:
    E_normalized=Ert/(W*g_s_0^3);
```

```
end
```

### Function $\bar{r}_c$

```
function r_c_normalized = r_c_normal(g_s_0,r_c)
```

```
    r_c_normalized=g_s_0*r_c;
```

```
end
```

### Function $\bar{G}(\bar{x}, \bar{t})$

```
function G_normalized_function =  
G_normal_function(t_normalized,r_normalized,d,r_c_normalized,D,b_i_0)  
    U2=(1+b_i_0)*r_normalized*hypergeom([(3-D)/2,1/2],3/2,-  
((r_normalized/r_c_normalized)^2));  
    G_normalized_function=(1/(4*pi*r_normalized^2))*d*(t_normalized-r_normalized)*exp(-  
U2);  
end
```

```
%function U2 = U_r_2(r_normalized,r_c_normalized,D,b_i_0)  
% U2=(1+b_i_0)*r_normalized*hypergeom([(3-D)/2,1/2],3/2,-  
((r_normalized/r_c_normalized)^2)); % hypergeom([a,b],c,z) is the Gauss hypergeometric  
function 2F1(a,b;c;z)  
%end
```

### Function $\bar{G}_F(\bar{x}, \bar{t})$

```
function G_F_normalized_function =  
G_F_normal_function(t_normalized,r_normalized,d,r_c_normalized,D,b_i_0)  
    U2=(1+b_i_0)*r_normalized*hypergeom([(3-D)/2,1/2],3/2,-  
((r_normalized/r_c_normalized)^2));  
    G_normalized_function=(1/(4*pi*r_normalized^2))*d*(t_normalized-r_normalized)*exp(-  
U2); % EIPAME STO SCRIPT: EBALA OTI TO delta einai noumero --  
    G_F_normalized_function=G_normalized_function*  
1./(((sqrt(1+(r_normalized./r_c_normalized).^2))).^(3-D));% swstos o tupos ?? : r_c_normalized  
h' r_c ??  
end
```

```
%function U2 = U_r_2(r_normalized,r_c_normalized,D,b_i_0)  
% U2=(1+b_i_0)*r_normalized*hypergeom([(3-D)/2,1/2],3/2,-  
((r_normalized/r_c_normalized)^2)); % hypergeom([a,b],c,z) is the Gauss hypergeometric  
function 2F1(a,b;c;z)  
%end
```

```
%function f1 = f_r_1(r,r_c,D)  
% H function douleuei kai me orismata eisodou - dianusmata timwn:  
% f1=1./(((sqrt(1+(r./r_c).^2))).^(3-D));  
%end
```

### Function $U(\bar{r})$

```
function U2 = U_r_2(r_normalized,r_c_normalized,D,b_i_0)  
    U2=(1+b_i_0)*r_normalized*hypergeom([(3-D)/2,1/2],3/2,-  
((r_normalized/r_c_normalized)^2)); % hypergeom([a,b],c,z) is the Gauss hypergeometric  
function 2F1(a,b;c;z)  
end
```

### Function $e^{-U(\bar{r})}$

```
function e_U2 = e_U_r_2(r_normalized,r_c_normalized,D,b_i_0)
```

```
e_U2=exp(-((1+b_i_0).*r_normalized.*hypergeom([(3-D)/2,1/2],3/2,-  
((r_normalized/r_c_normalized).^2))))); % hypergeom([a,b],c,z) is the Gauss hypergeometric  
function 2F1(a,b;c;z)  
end
```

## Appendix B

In figure 8.2.11 the time origin of the earthquake is 16/09/2013 at 15:01:14, latitude 38.72, longitude 22.74, depth 17 km, magnitude 4.9 at 23.8 km WNW of Atalanti. The value of the index  $q$  is 1.61.

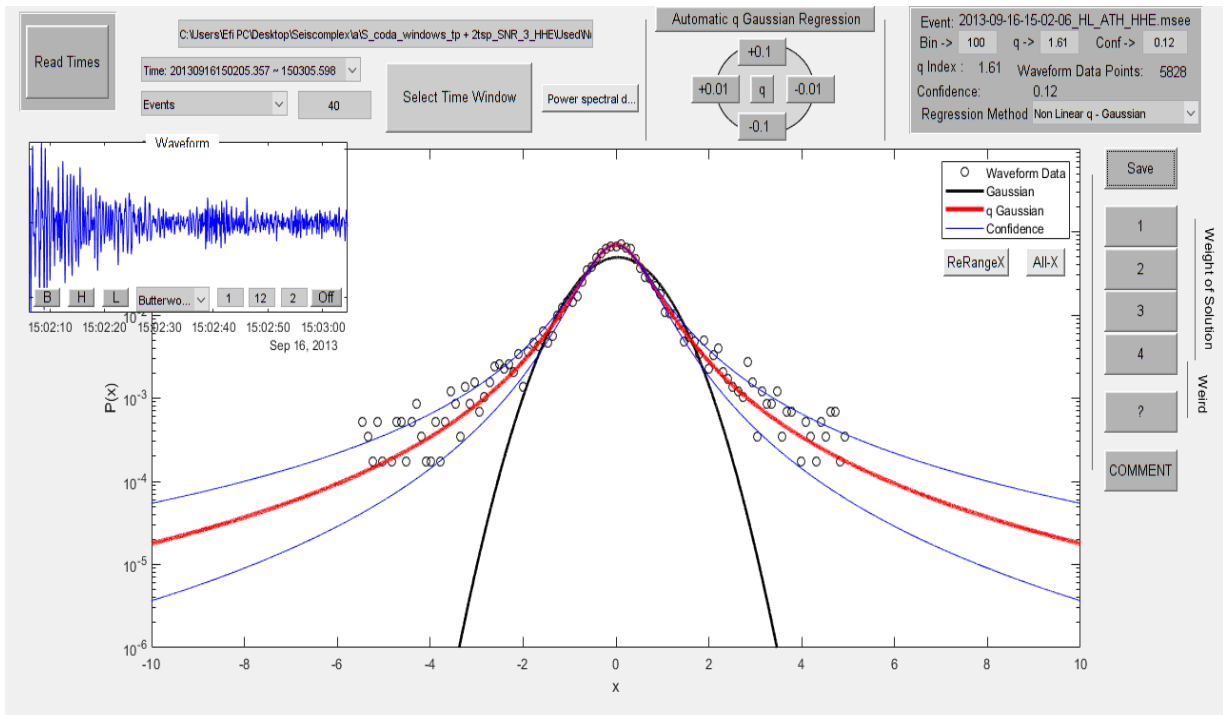


Figure 8.2.11

In figure 8.2.12 the time origin of the earthquake is 12/11/2013 at 18:09:28, latitude 38.92, longitude 23.1, depth 17 km, magnitude 4.8 at 31.2 km NNE of Atalanti. The value of the index  $q$  is 1.58.

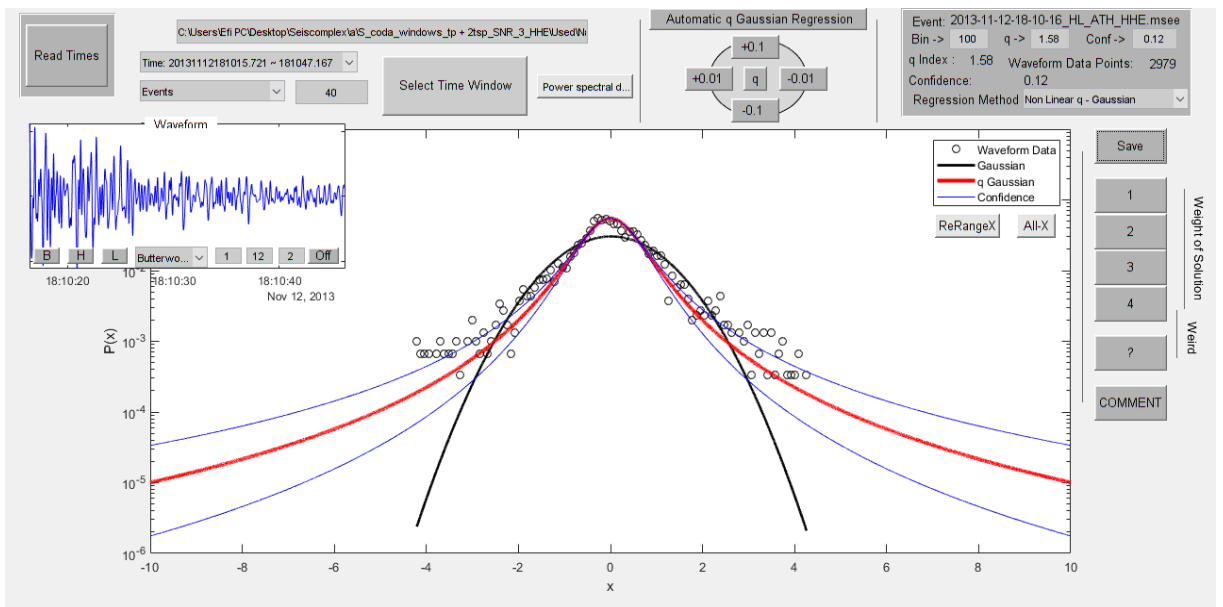


Figure 8.2.12

In figure 8.2.13 the time origin of the earthquake is 07/08/2013 at 13:44:32, latitude 38.69, longitude 22.66, depth 15 km, magnitude 4.7 at 29.8 km W of Atalanti. The value of the index  $q$  is 1.59.

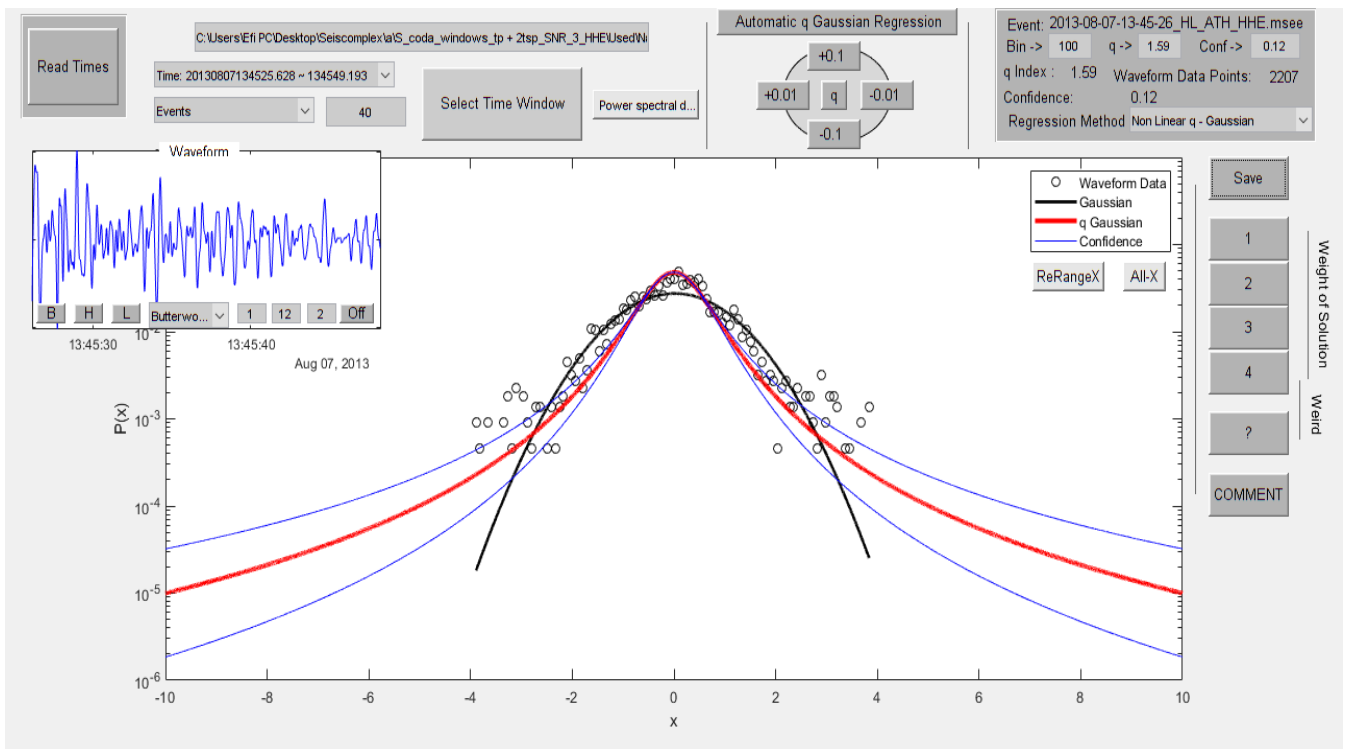


Figure 8.2.13

In figure 8.2.14 the time origin of the earthquake is 09/08/2013 at 13:10:10, latitude 38.69, longitude 22.65, depth 17 km, magnitude 4.7 at 30.0 km SE of Lamia. The value of the index  $q$  is 1.59.

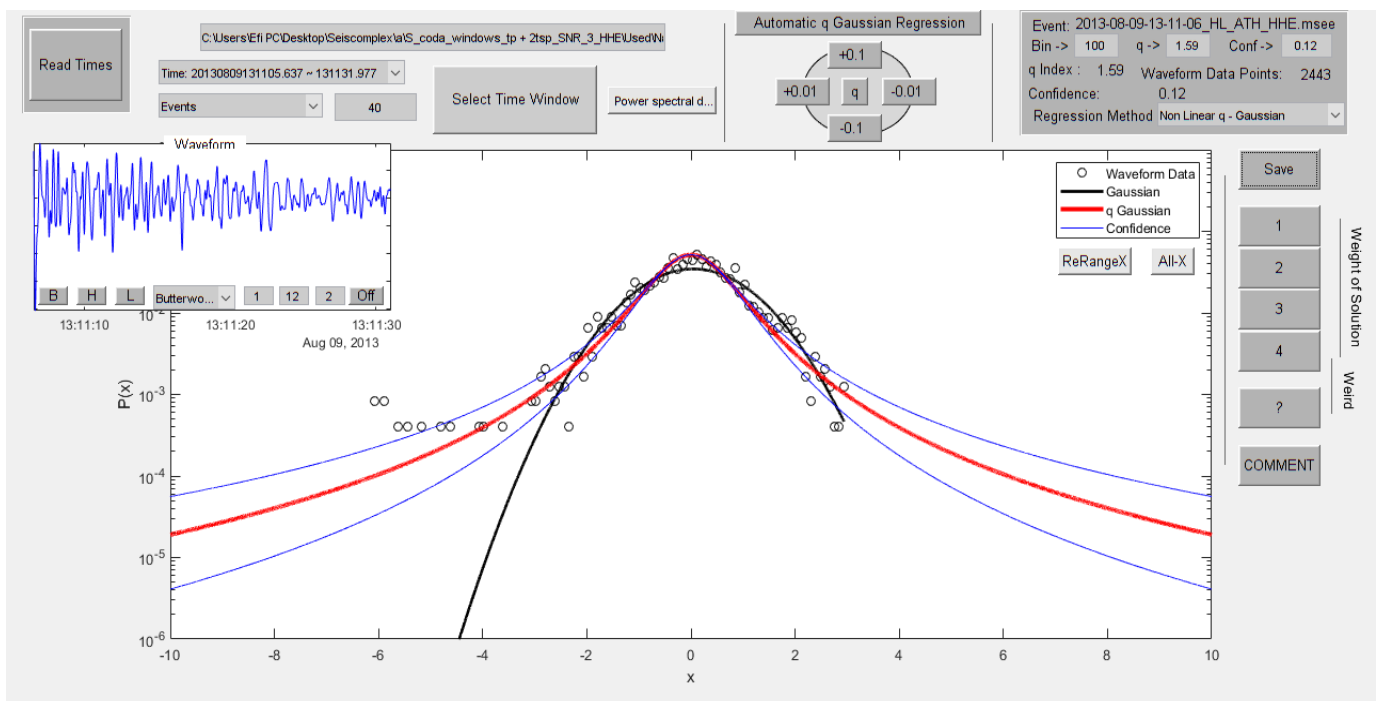


Figure 8.2.14

In figure 8.2.15 the time origin of the earthquake is 27/06/2014 at 16:14:27, latitude 38.24, longitude 25.13, depth 30 km, magnitude 4.7 at 48.4 km NNE of Andros. The value of the index  $q$  is 1.61.

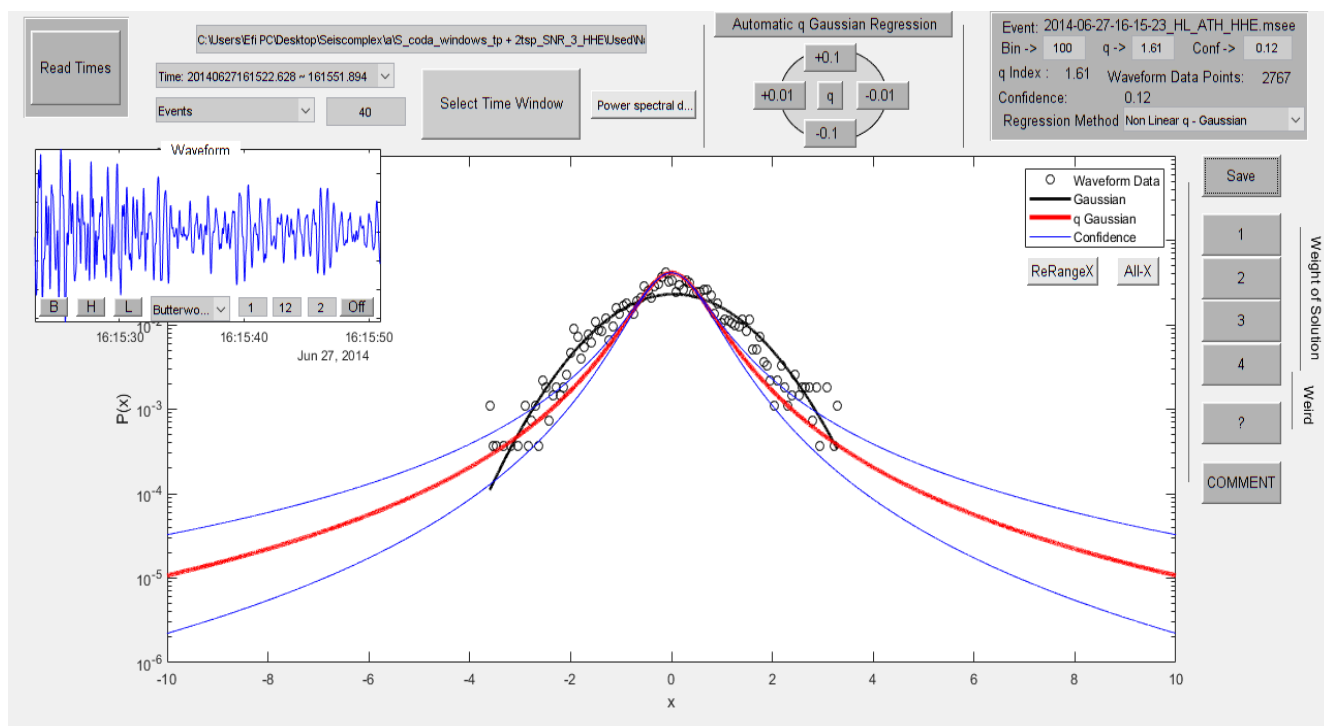


Figure 8.2.15

In figure 8.2.16 the time origin of the earthquake is 16/09/2013 at 14:42:39, latitude 38.7, longitude 22.73, depth 20 km, magnitude 4.5 at 24.0 km WNW of Atalanti. The value of the index  $q$  is 1.71.

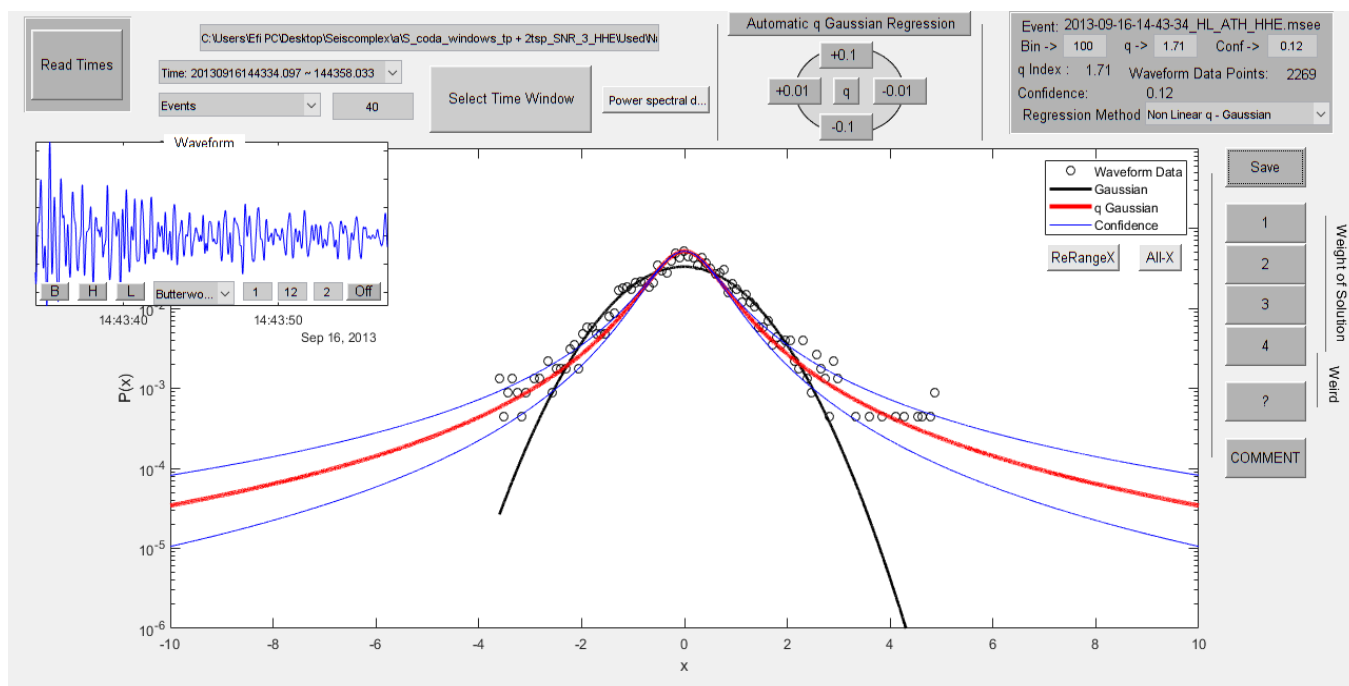


Figure 8.2.16

In figure 8.2.17 the time origin of the earthquake is 01/02/2014 at 08:14:03, latitude 38.7, longitude 22.75, depth 18 km, magnitude 4.5 at 22.3 km WNW of Atalanti. The value of the index  $q$  is 1.62.

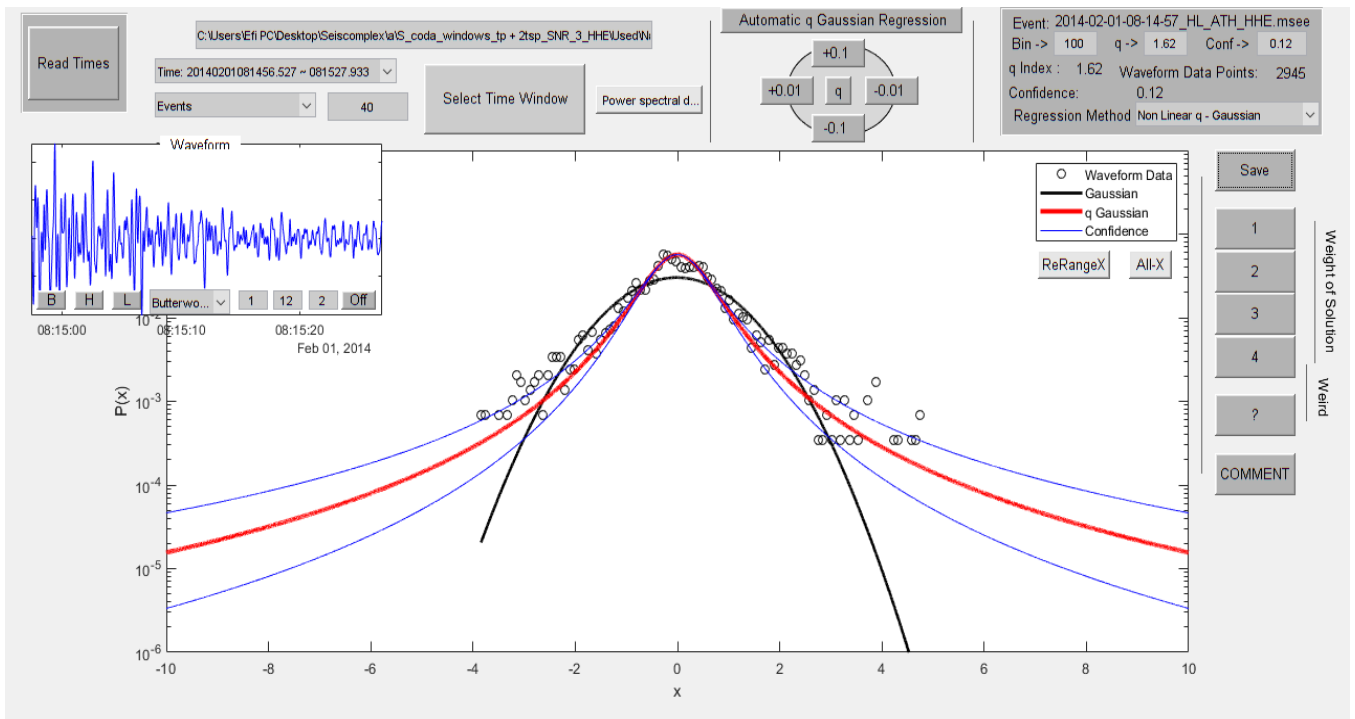


Figure 8.2.17

In figure 8.2.18 the time origin of the earthquake is 22/02/2011 at 20:37:02, latitude 38.86, longitude 24.95, depth 37 km, magnitude 4.4 at 33.9 km E of Skyros. The value of the index  $q$  is 1.73.

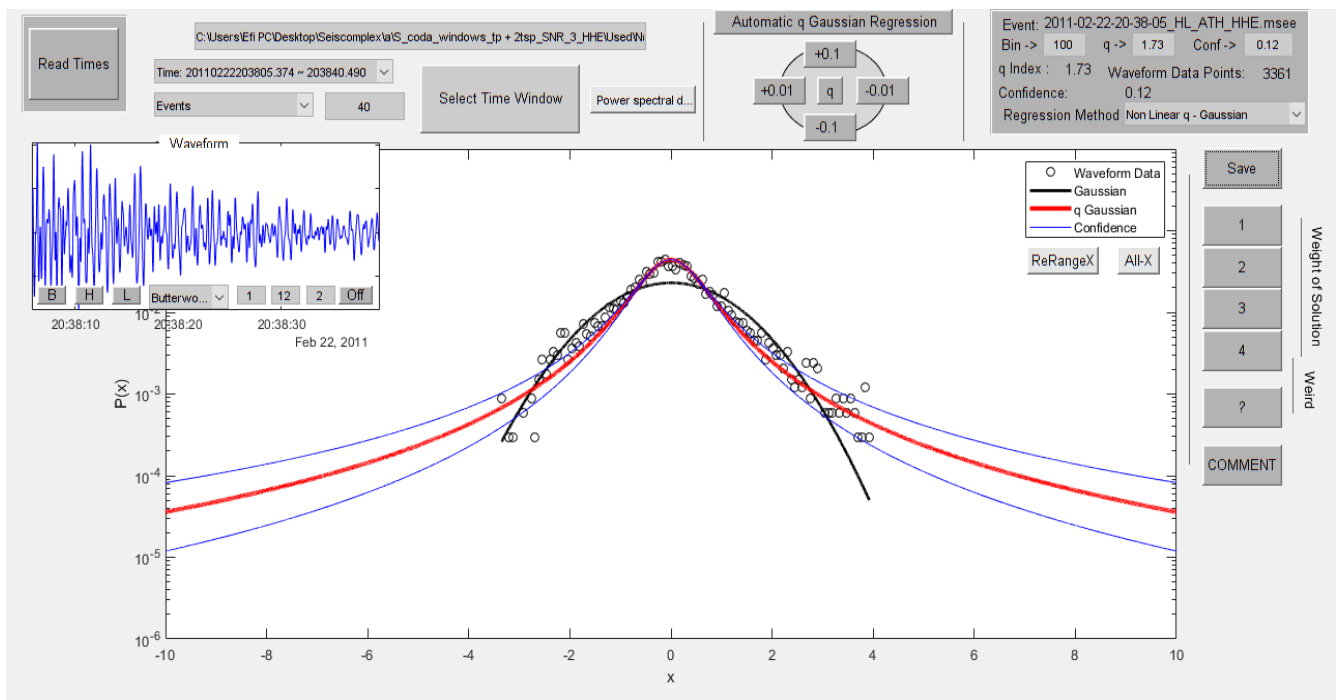


Figure 8.2.18

In figure 8.2.19 the time origin of the earthquake is 06/06/2014 at 12:21:03, latitude 39.17, longitude 23.71, depth 23 km, magnitude 4.4 at 19.5 km E of Skiathos. The value of the index  $q$  is 1.47.

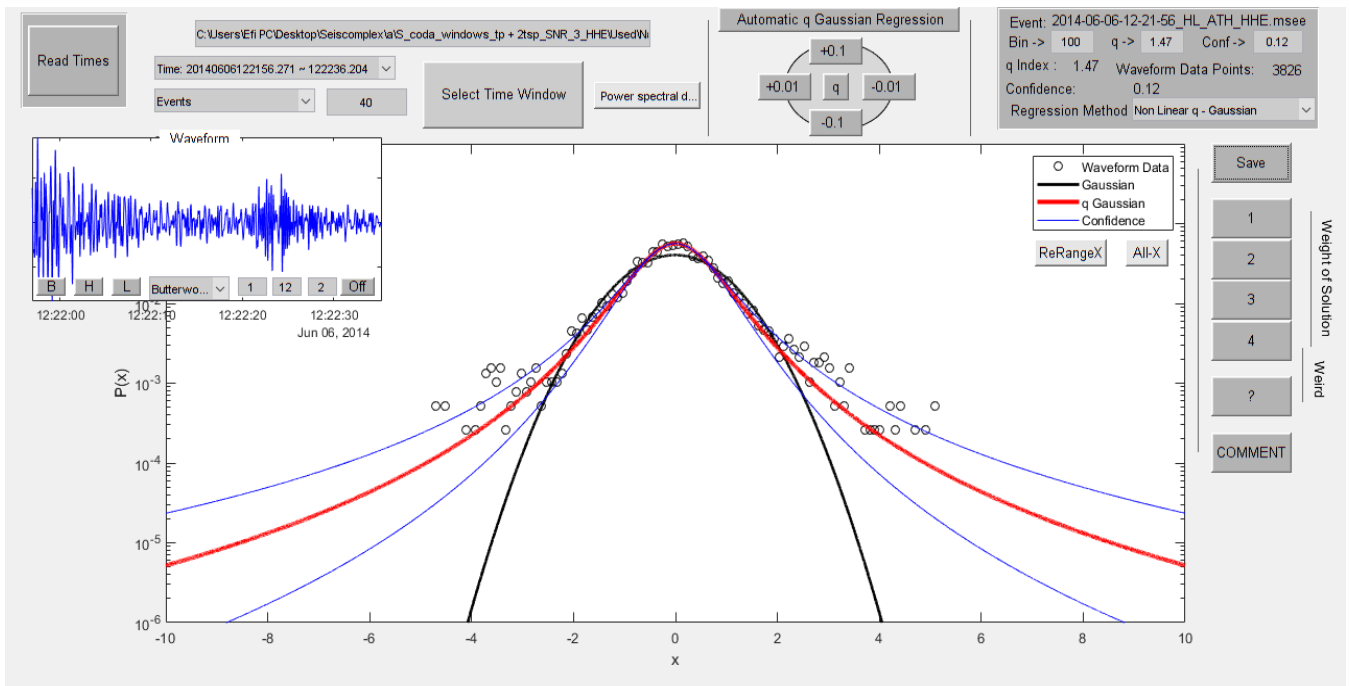


Figure 8.2.19

In figure 8.2.20 the time origin of the earthquake is 11/07/2014 at 09:46:04, latitude 38.45, longitude 23.71, depth 26 km, magnitude 4.4 at 9.7 km E of Chalkida. The value of the index  $q$  is 1.53.

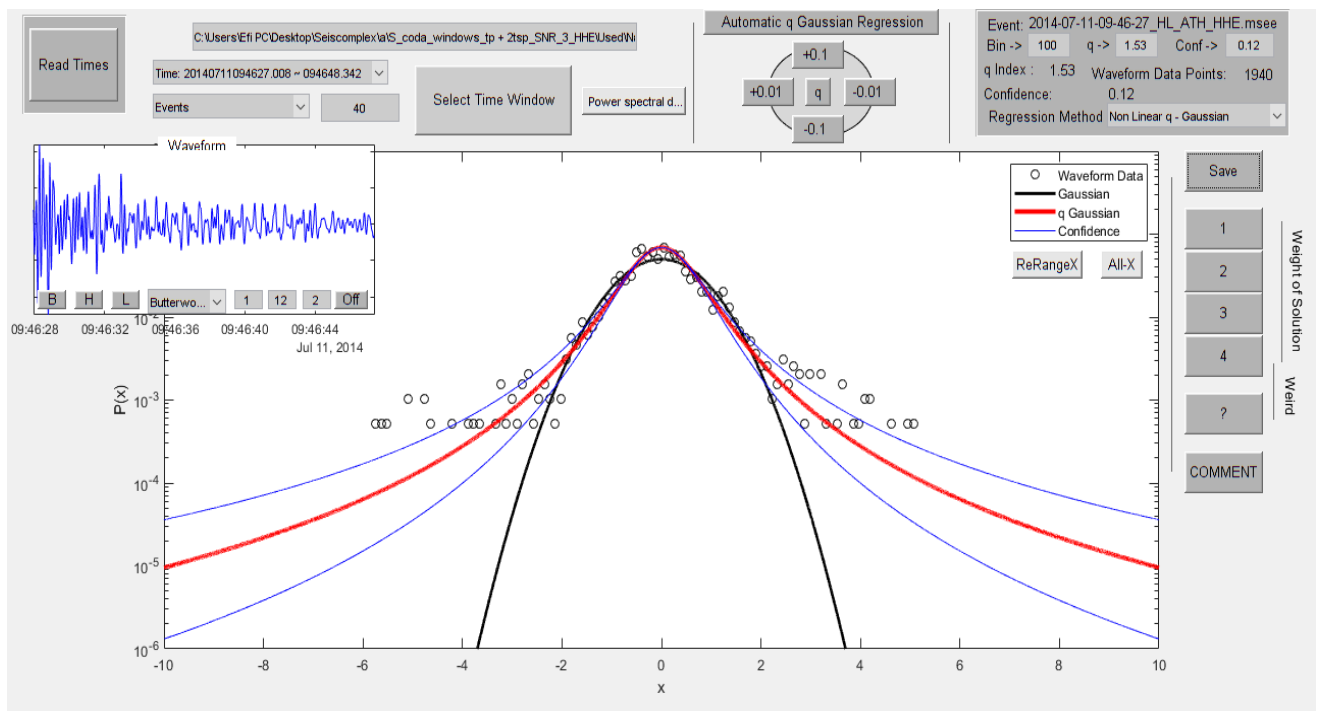


Figure 8.2.20

In figure 8.2.21 the time origin of the earthquake is 04/10/2014 at 00:12:01, latitude 37.41, longitude 22.2, depth 20 km, magnitude 4.4 at 19.3 km SW of Tripolis. The value of the index  $q$  is 1.78.

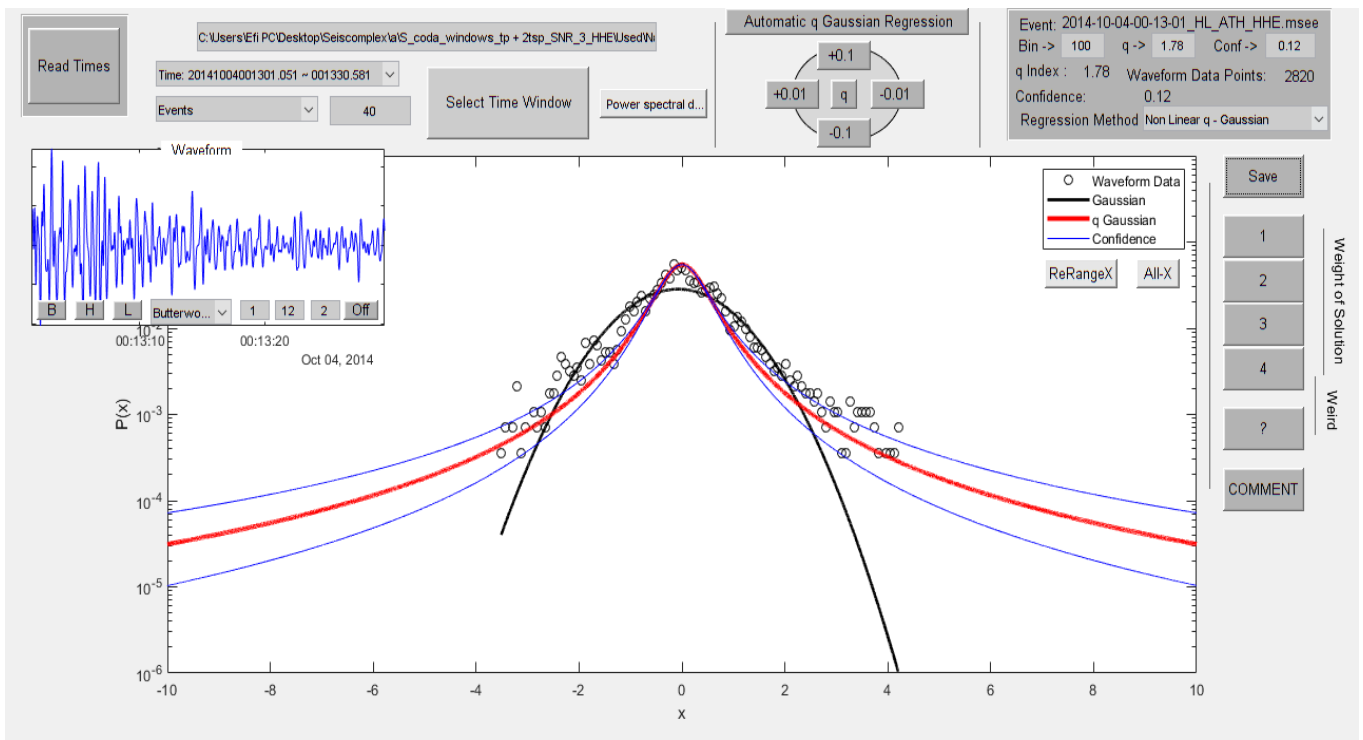


Figure 8.2.21

In figure 8.2.22 the time origin of the earthquake is 27/10/2015 at 01:25:51, latitude 38.92, longitude 24.33, depth 25 km, magnitude 4.4 at 20.2 km W of Skyros. The value of the index  $q$  is 1.57.

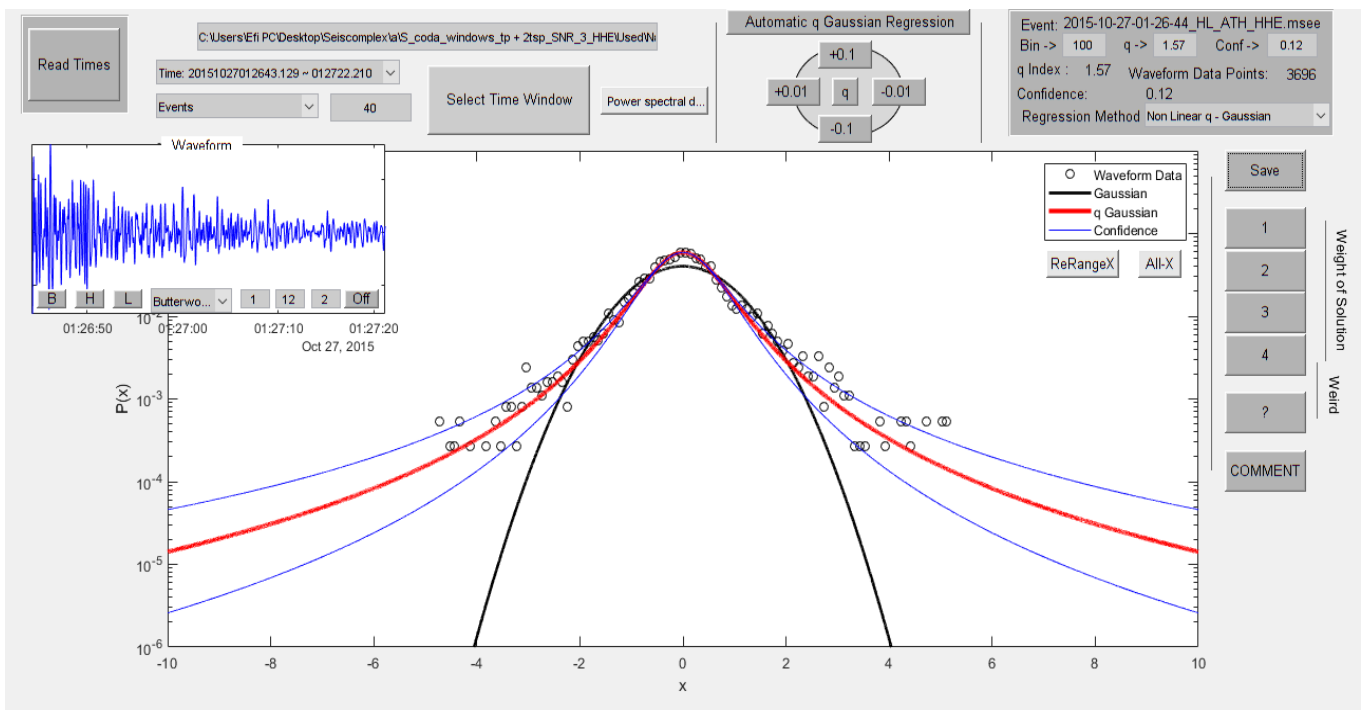


Figure 8.2.22

In figure 8.2.23 the time origin of the earthquake is 24/03/2017 at 04:24:30, latitude 37.5705, longitude 23.8847, depth 165 km, magnitude 4.4 at 47.8 km SSE of Athens. The value of the index  $q$  is 1.61.

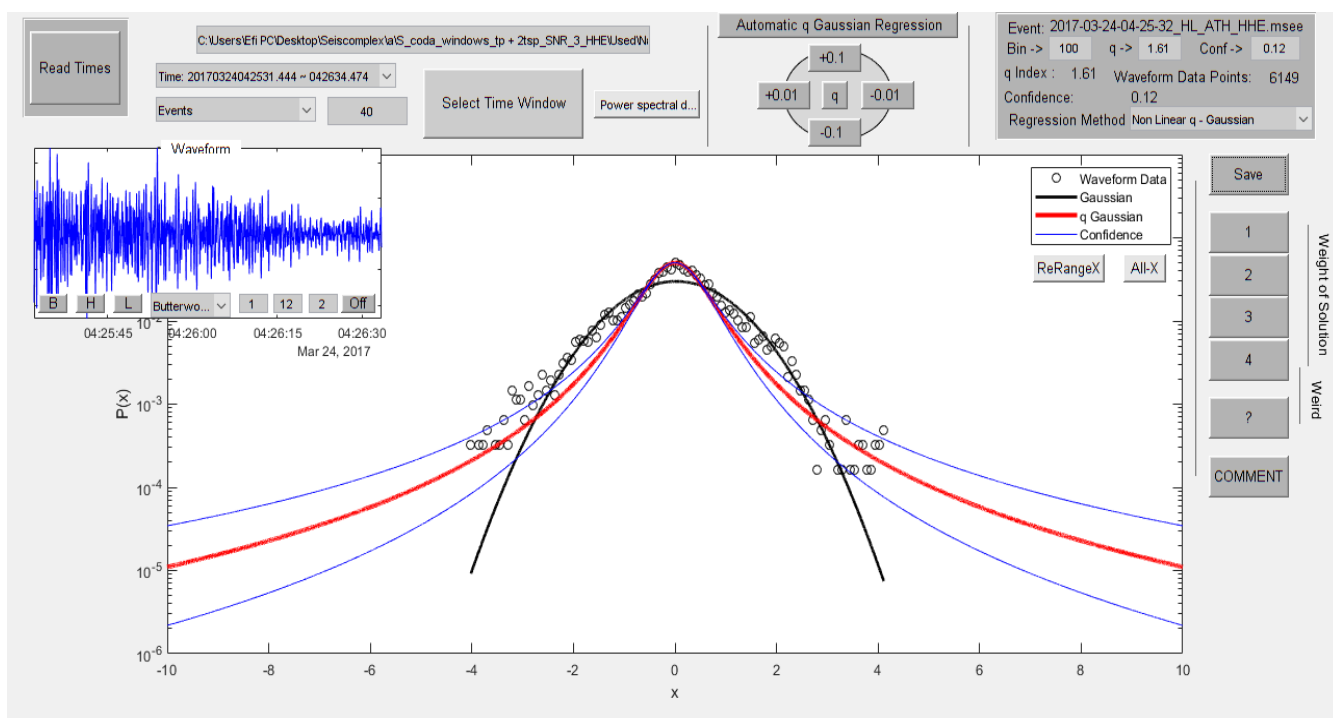


Figure 8.2.23

In figure 8.2.24 the time origin of the earthquake is 29/08/2010 at 00:51:57, latitude 38.66, longitude 23.38, depth 22 km, magnitude 4.3 at 29.0 km NW of Chalkida. The value of the index  $q$  is 1.56.

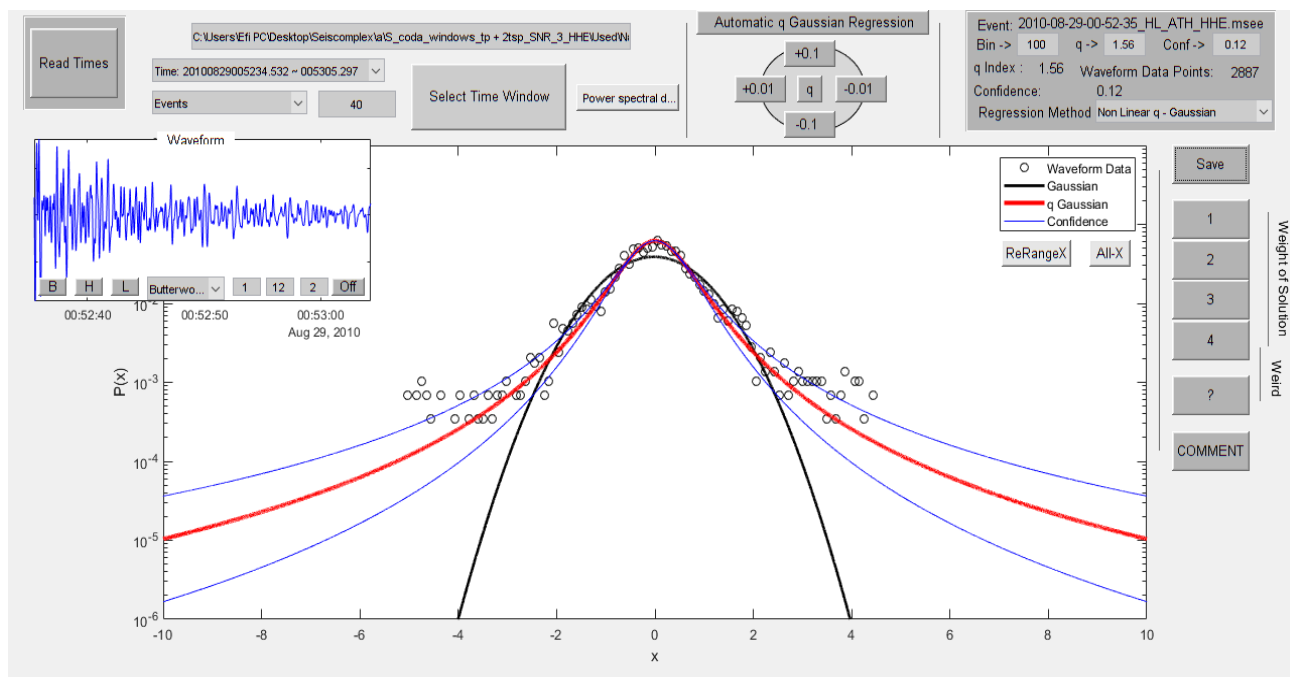


Figure 8.2.24

In figure 8.2.25 the time origin of the earthquake is 02/09/2010 at 03:53:04, latitude 38.22, longitude 23.17, depth 26 km, magnitude 4.3 at 35.2 km SE of Levadhia. The value of the index  $q$  is 1.8.

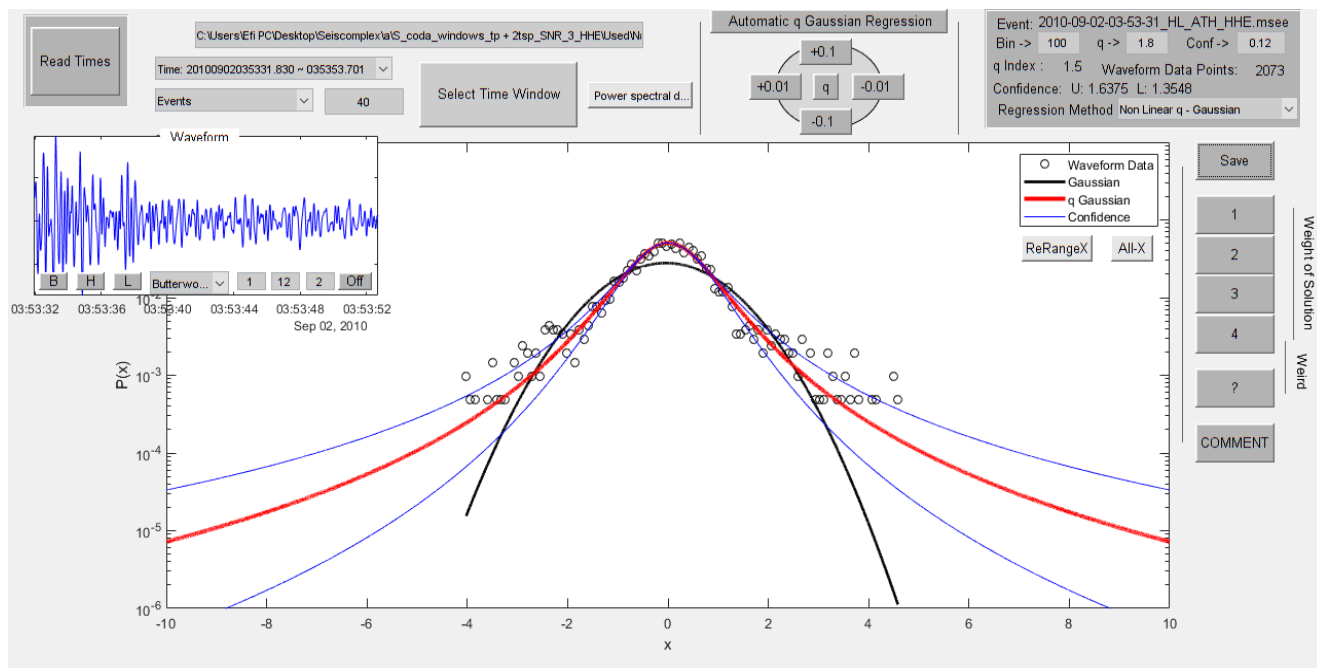


Figure 8.2.25

In figure 8.2.26 the time origin of the earthquake is 09/10/2010 at 19:04:49, latitude 38.15, longitude 22.72, depth 20 km, magnitude 4.3 at 30.0 km NW of Korinthos. The value of the index  $q$  is 1.52.

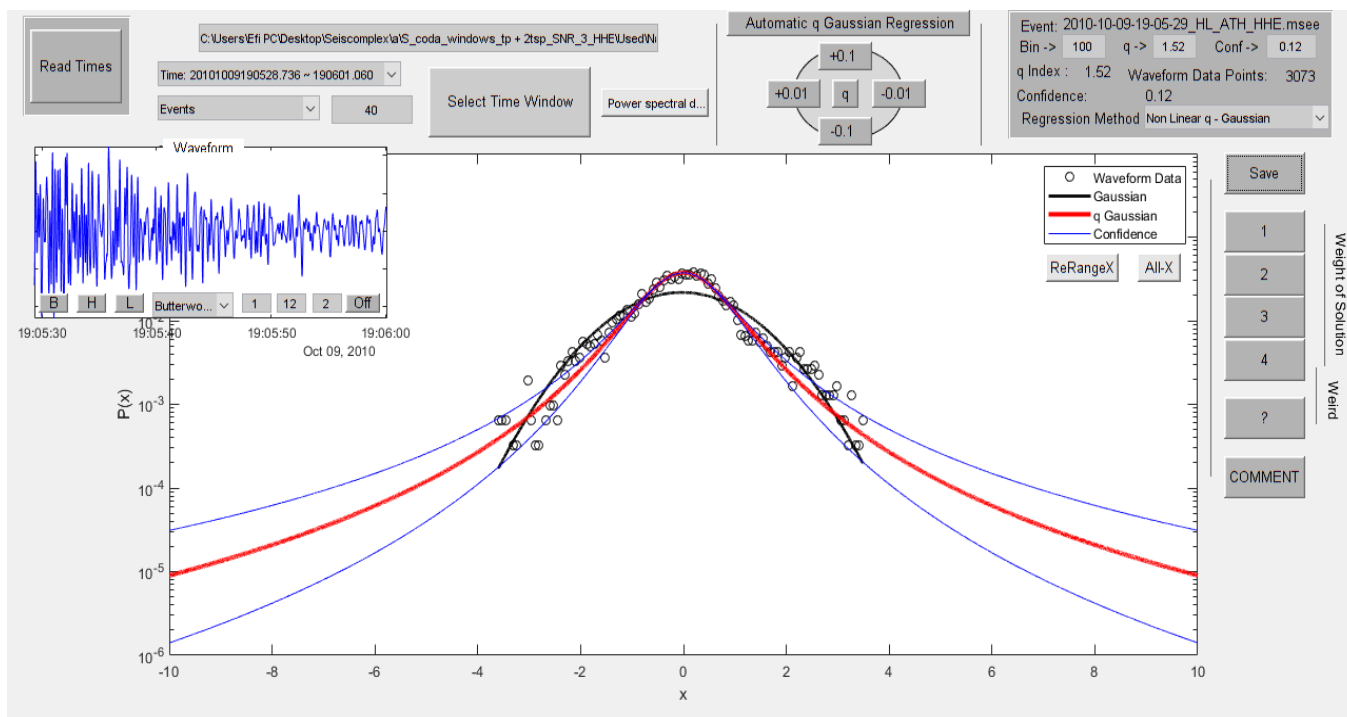


Figure 8.2.26

In figure 8.2.27 the time origin of the earthquake is 21/08/2011 at 06:14:18, latitude 37.63, longitude 23.32, depth 115 km, magnitude 4.3 at 45.8 km E of Nafplio. The value of the index  $q$  is 1.56.

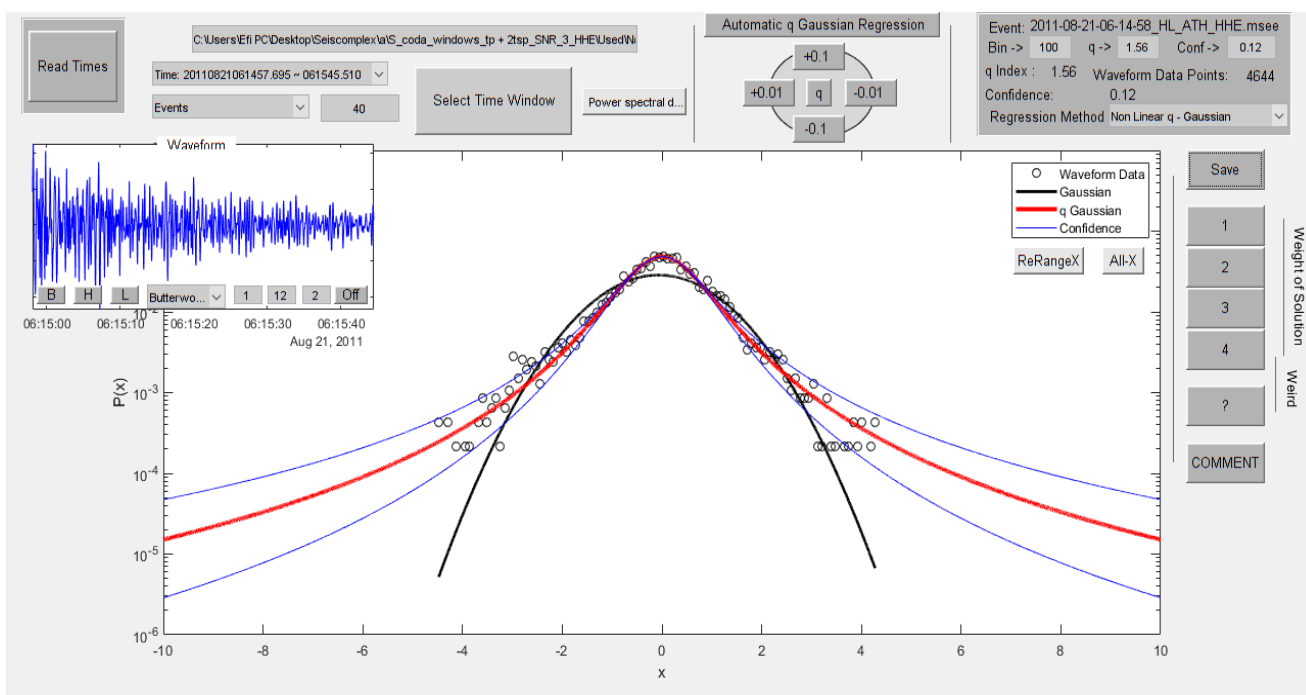


Figure 8.2.27

In figure 8.2.28 the time origin of the earthquake is 28/06/2012 at 13:11:29, latitude 39.01, longitude 23.17, depth 25 km, magnitude 4.3 at 32.2 km WSW of Skiathos. The value of the index  $q$  is 1.6.

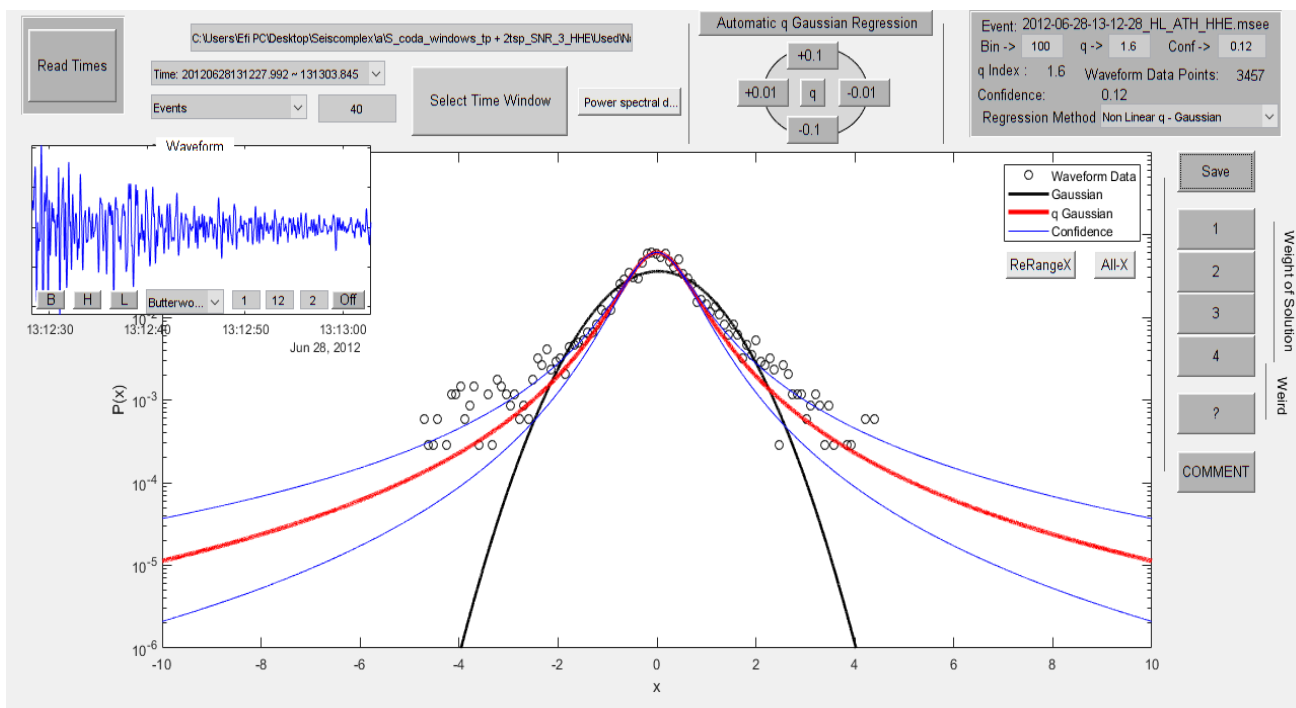


Figure 8.2.28

In figure 8.2.29 the time origin of the earthquake is 28/04/2013 at 16:31:04, latitude 37.45, longitude 22.7, depth 61 km, magnitude 4.3 at 15.8 km SW of Nafplio. The value of the index  $q$  is 1.59.

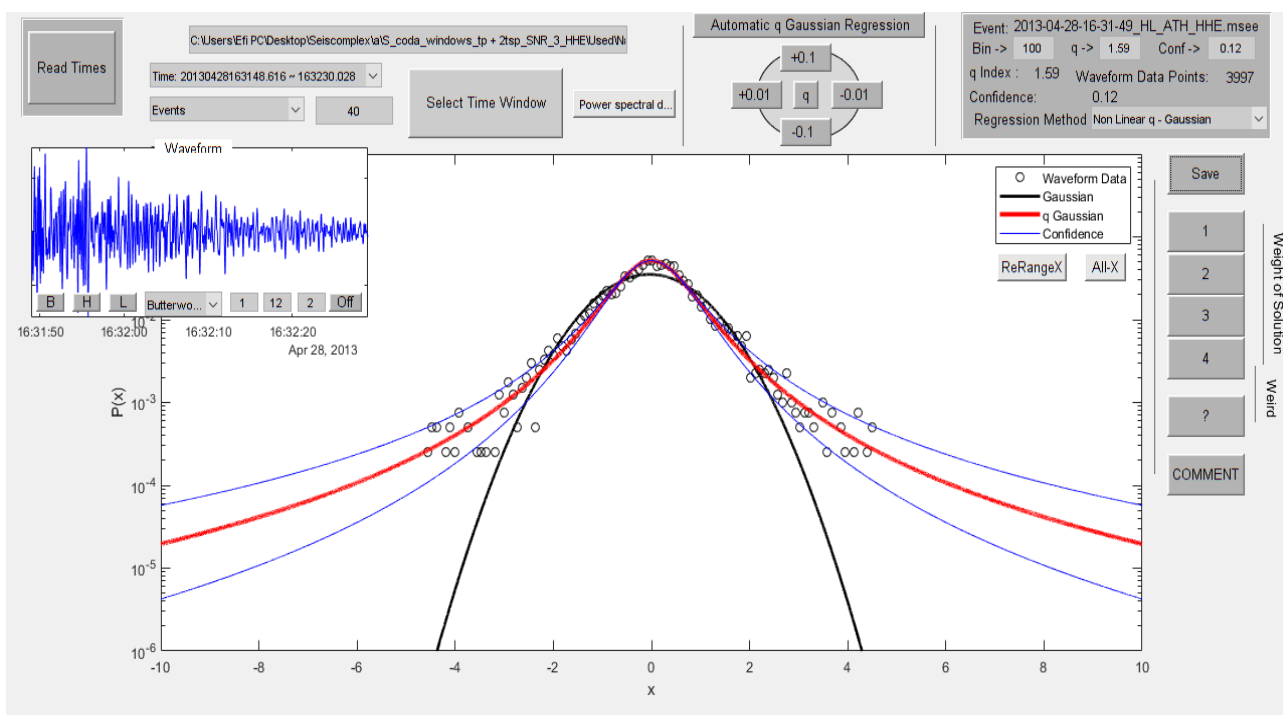


Figure 8.2.29

In figure 8.2.30 the time origin of the earthquake is 04/06/2013 at 01:56:53, latitude 37.98, longitude 24.01, depth 24 km, magnitude 4.3 at 24.3 km E of Athens. The value of the index  $q$  is 1.86.

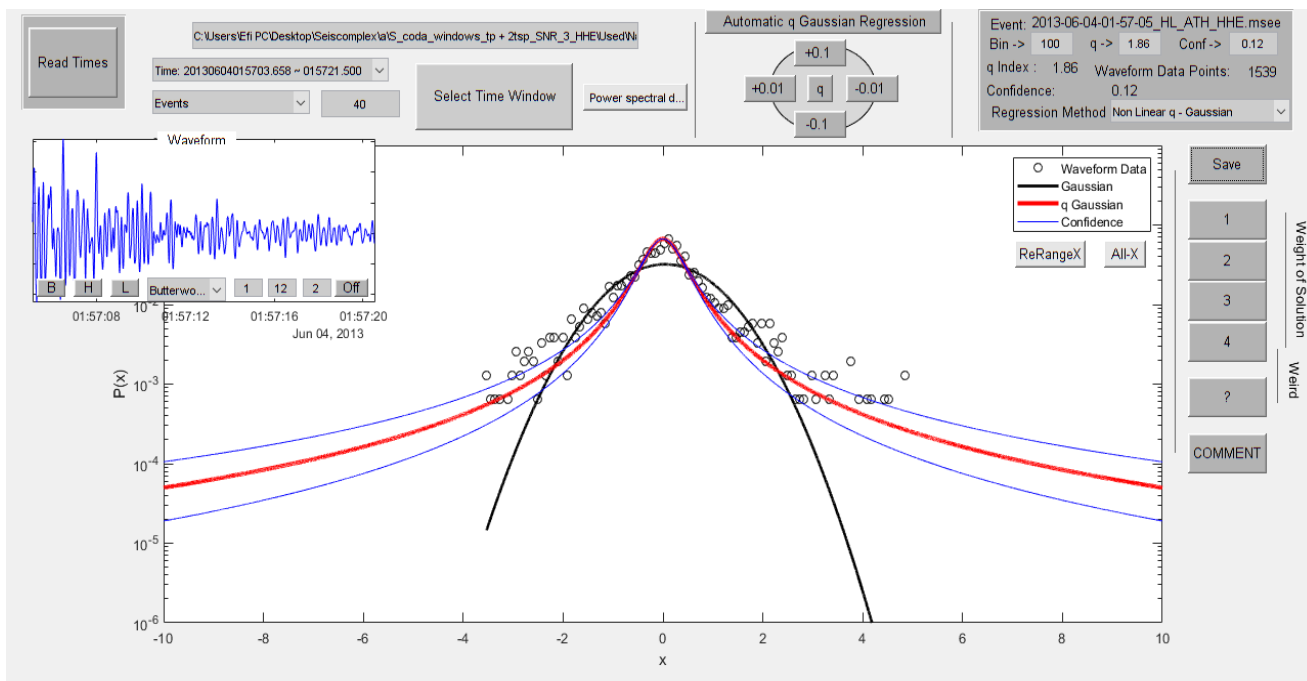


Figure 8.2.30

In figure 8.2.31 the time origin of the earthquake is 06/02/2014 at 07:58:26, latitude 38.71, longitude 22.77, depth 22 km, magnitude 4.3 at 20.9 km WNW of Atalanti. The value of the index  $q$  is 1.73.

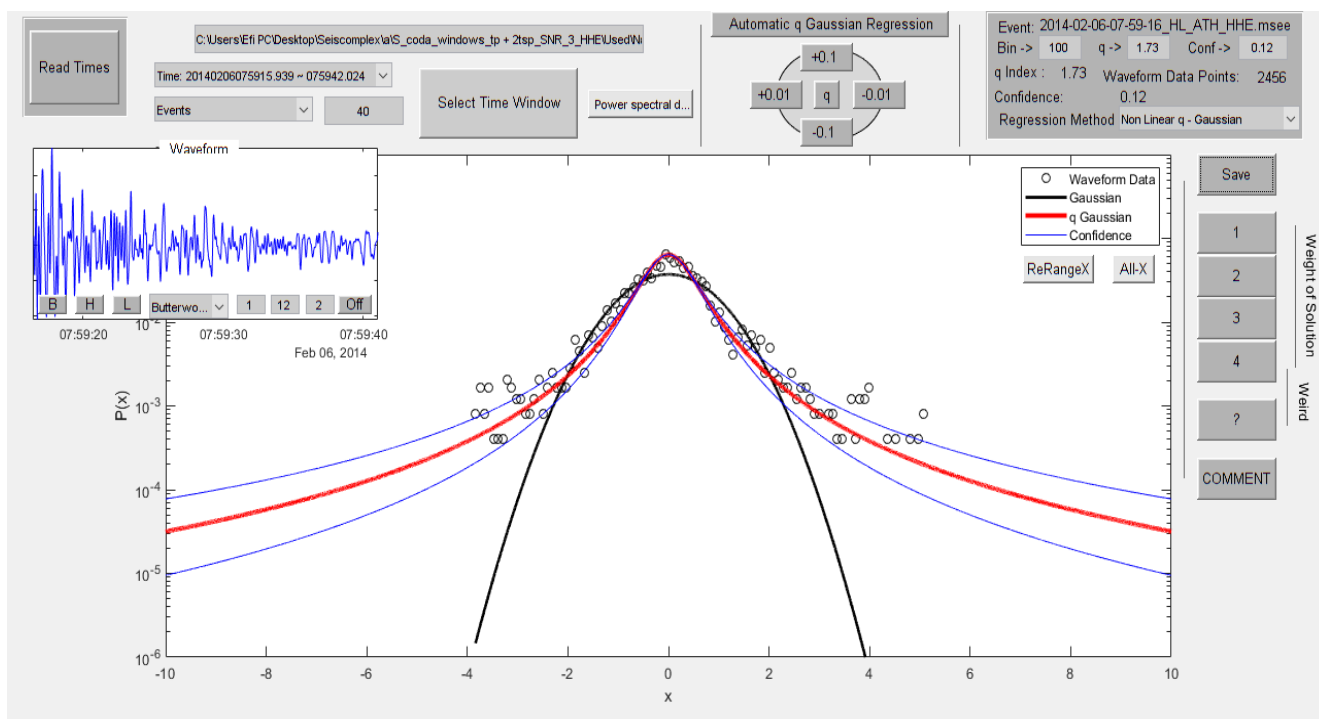


Figure 8.2.31

In figure 8.2.32 the time origin of the earthquake is 20/05/2014 at 23:30:44, latitude 39.53, longitude 24.2, depth 30 km, magnitude 4.3 at 73.7 km ENE of Skiathos. The value of the index  $q$  is 2.14.

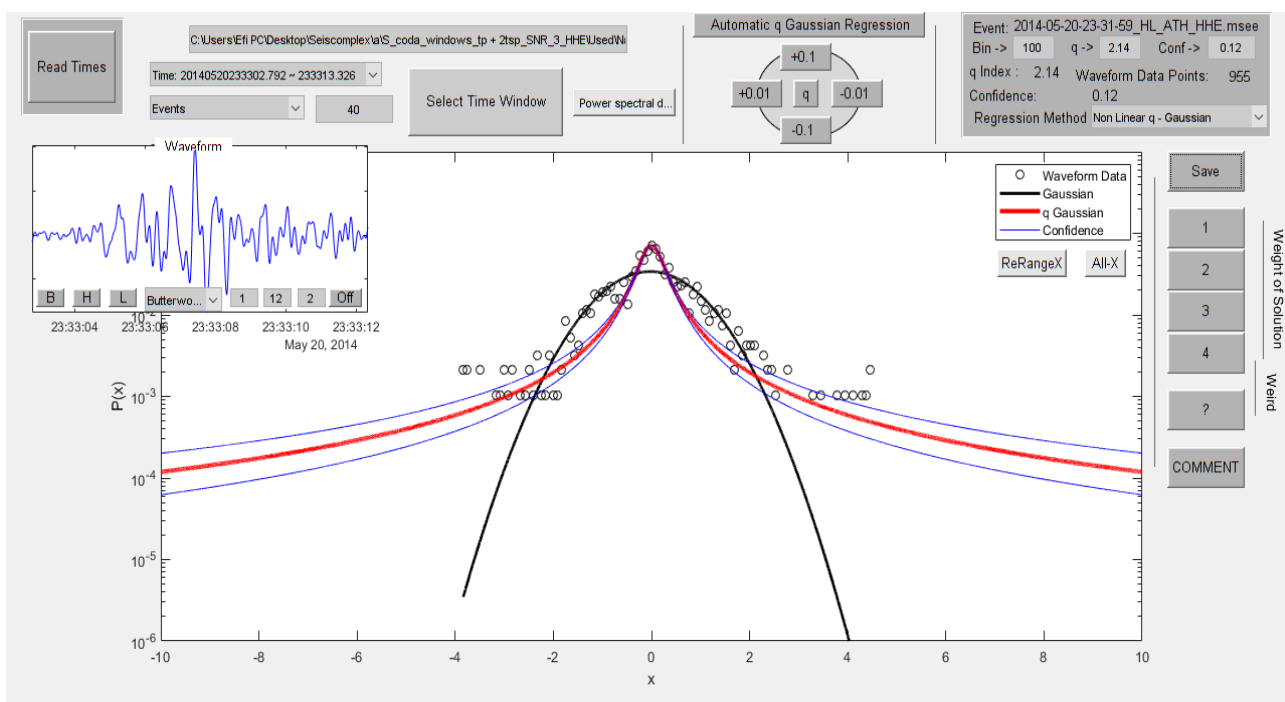


Figure 8.2.32

In figure 8.2.33 the time origin of the earthquake is 19/07/2019 at 23:30:44, latitude 38.0956, longitude 23.5808, depth 15 km, magnitude 4.3 at 18.3 km NW of Athens. The value of the index  $q$  is 1.91.

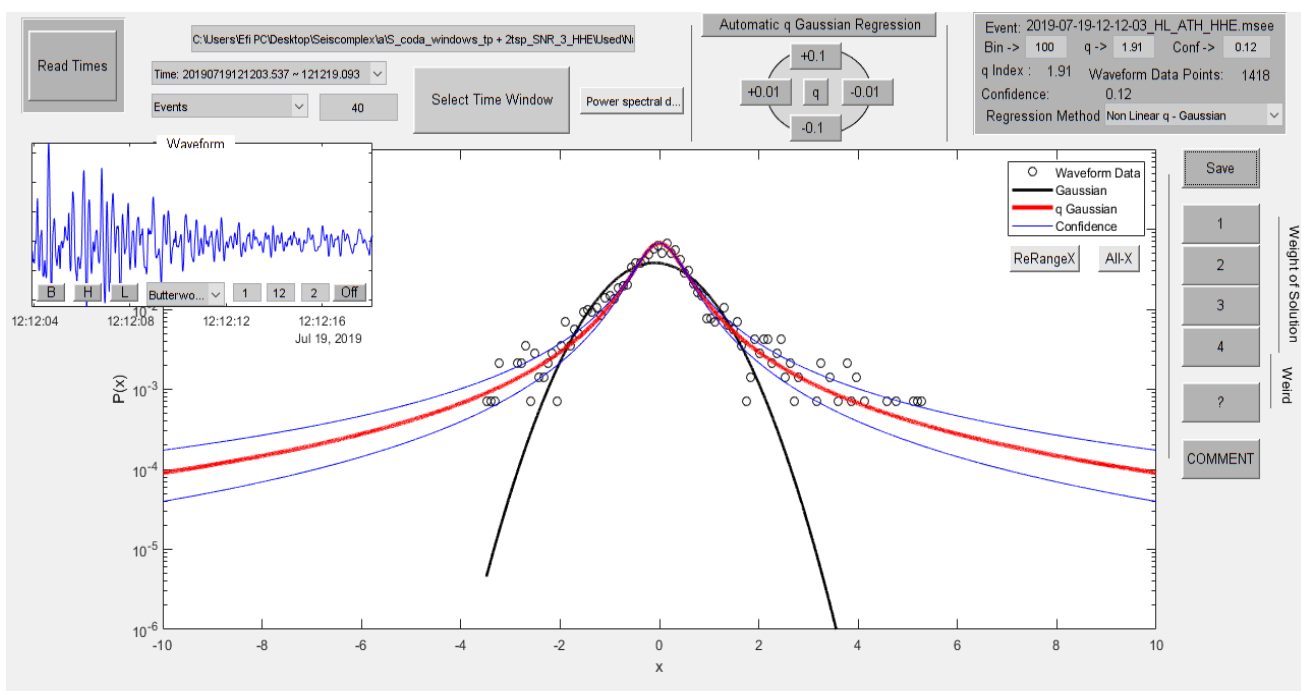


Figure 8.2.33

In figure 8.2.34 the time origin of the earthquake is 11/05/2010 at 07:03:36, latitude 38.62, longitude 23.77, depth 24 km, magnitude 4.2 at 22.9 km NE of Chalkida. The value of the index  $q$  is 1.61.

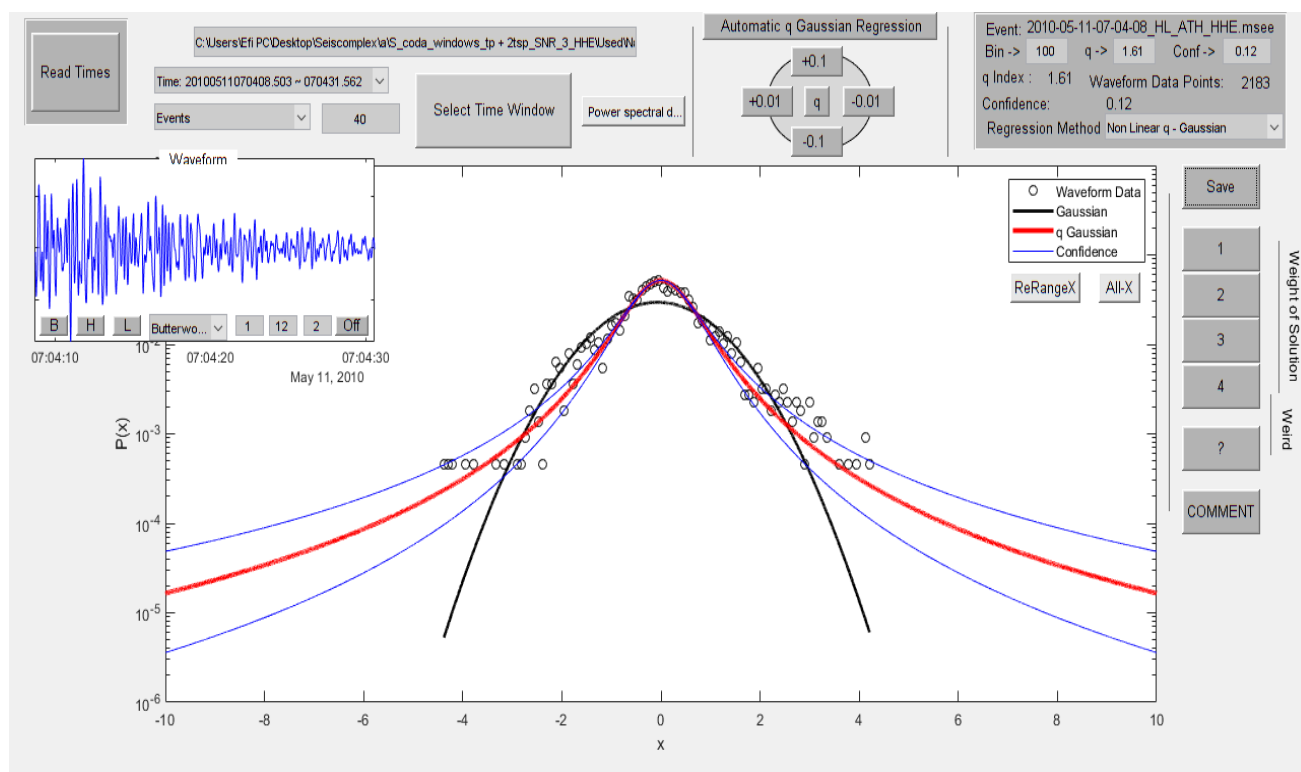


Figure 8.2.34

In figure 8.2.35 the time origin of the earthquake is 17/02/2012 at 08:05:04, latitude 37.87, longitude 23.02, depth 17 km, magnitude 4.2 at 10.8 km SE of Korinthos. The value of the index  $q$  is 1.89.

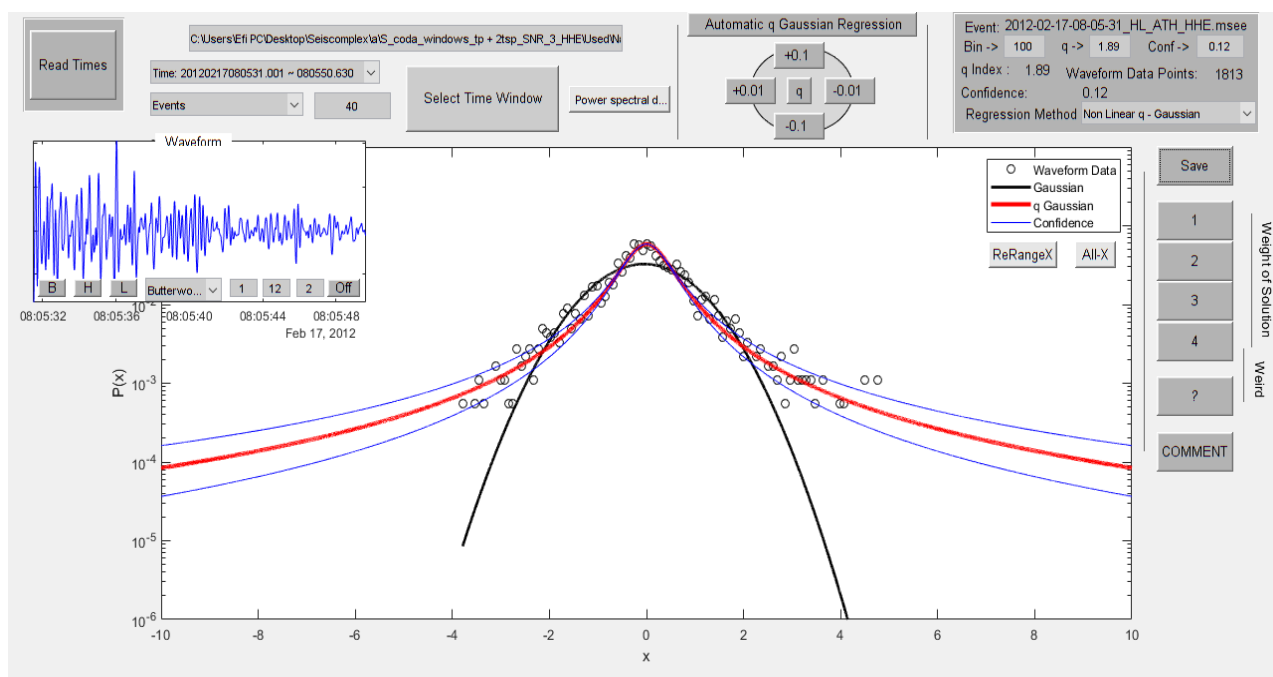


Figure 8.2.35

In figure 8.2.36 the time origin of the earthquake is 28/04/2013 at 04:49:55, latitude 38.26, longitude 22.25, depth 55 km, magnitude 4.2 at 14.7 km E of Aegion. The value of the index  $q$  is 1.55.

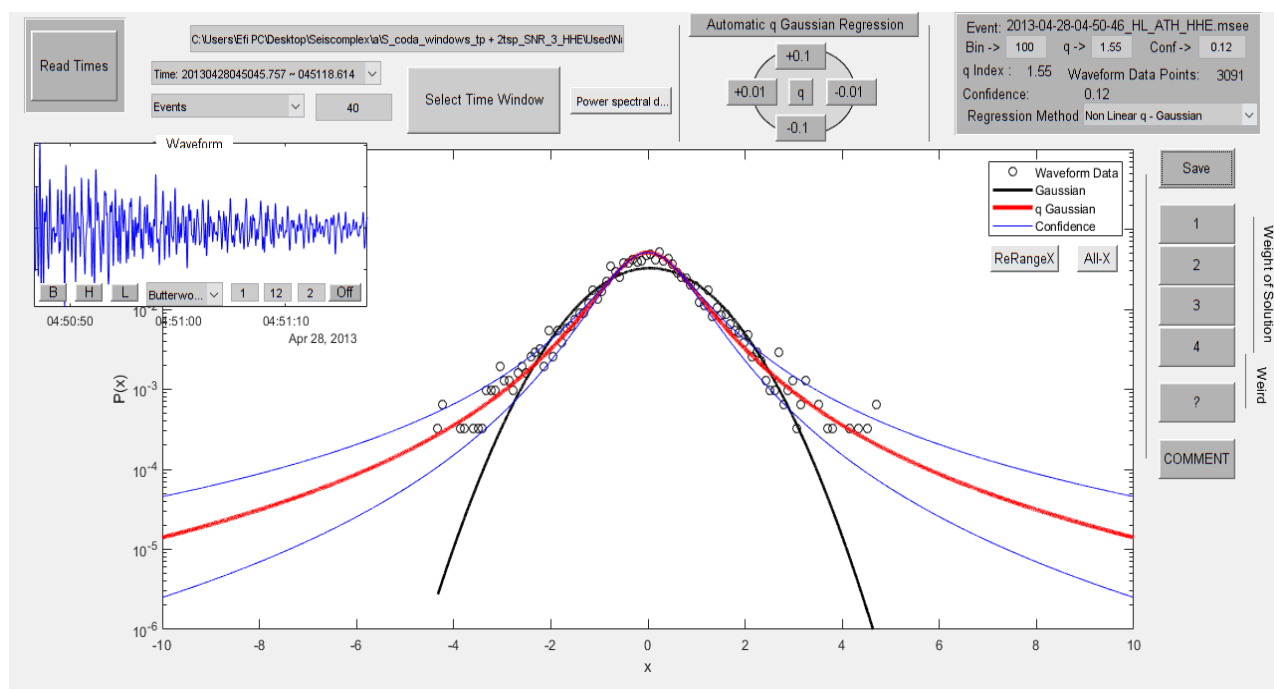


Figure 8.2.36

In figure 8.2.37 the time origin of the earthquake is 22/11/2013 at 15:12:03, latitude 39.05, longitude 22.41, depth 21 km, magnitude 4.2 at 16.8 km N of Lamia. The value of the index  $q$  is 1.78.

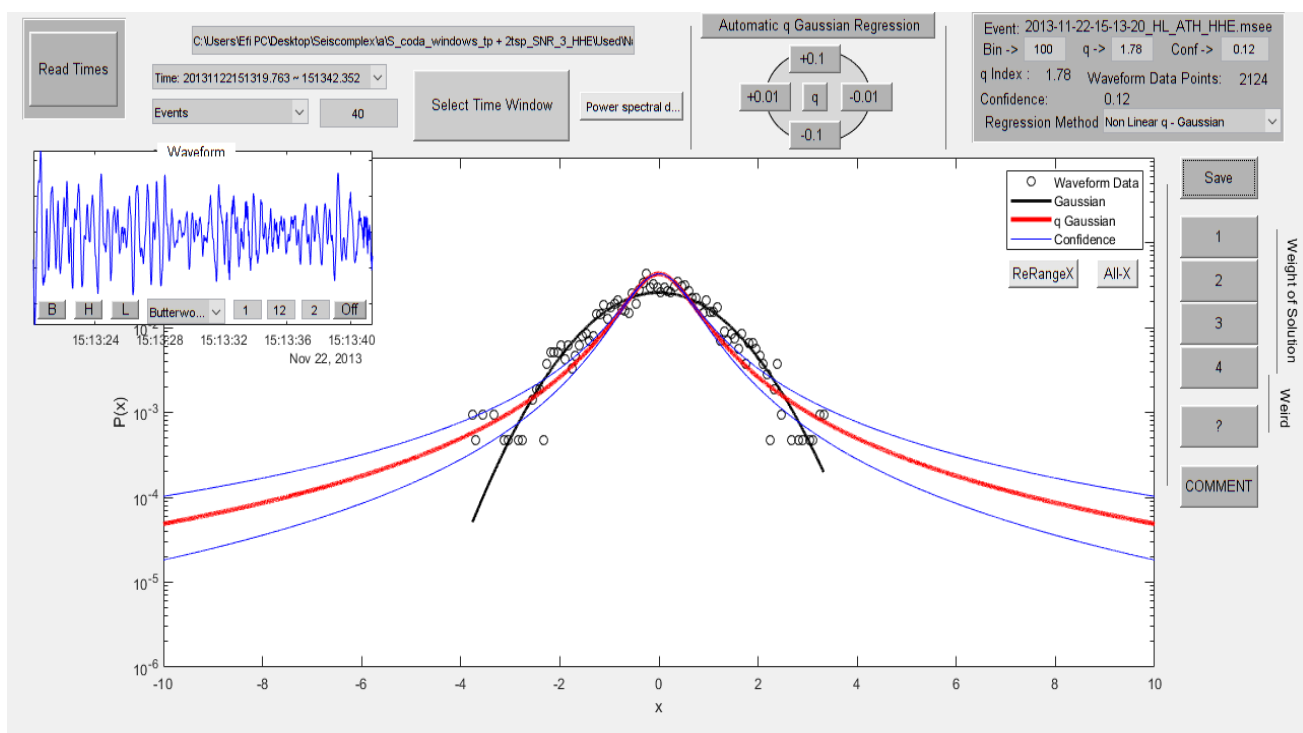


Figure 8.2.37

In figure 8.2.38 the time origin of the earthquake is 11/06/2016 at 08:29:45, latitude 39.23, longitude 23.73, depth 15 km, magnitude 4.2 at 22.4 km ENE of Skiathos. The value of the index  $q$  is 1.76.

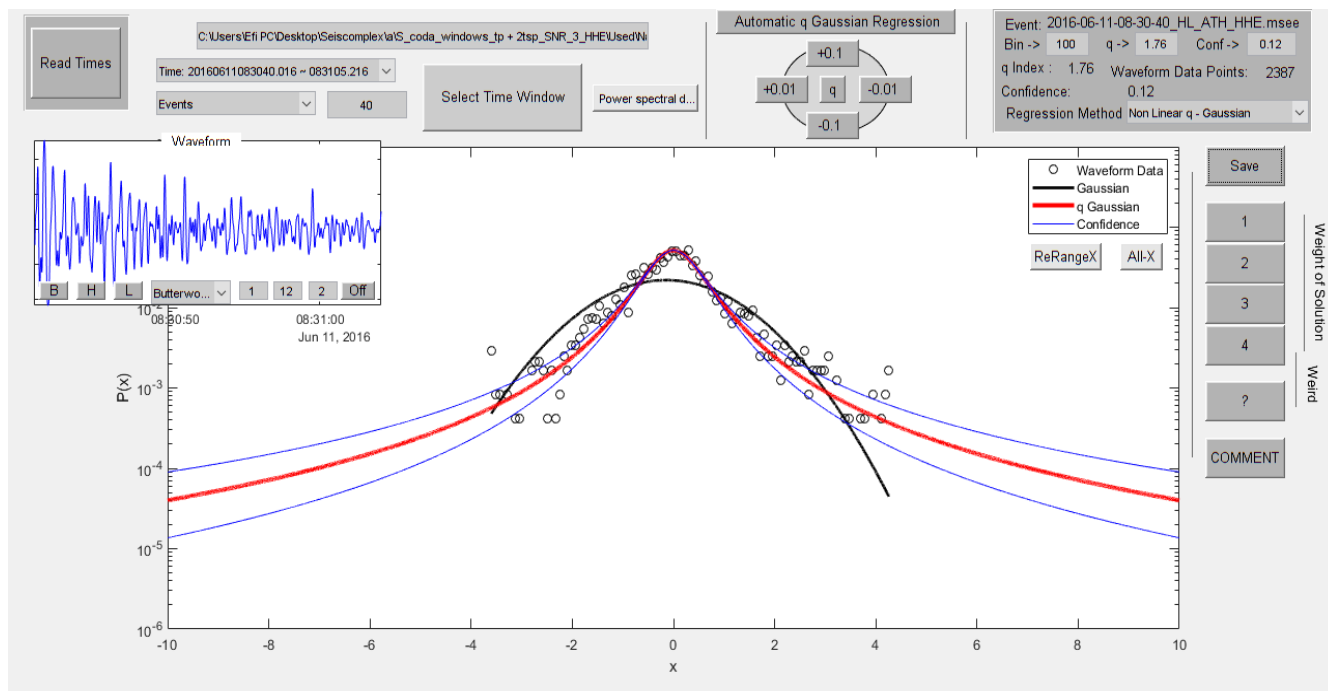


Figure 8.2.38

In figure 8.2.39 the time origin of the earthquake is 29/11/2019 at 20:46:40, latitude 39.0482, longitude 22.3178, depth 77 km, magnitude 4.2 at 19.3 km NNW of Lamia. The value of the index  $q$  is 1.65.

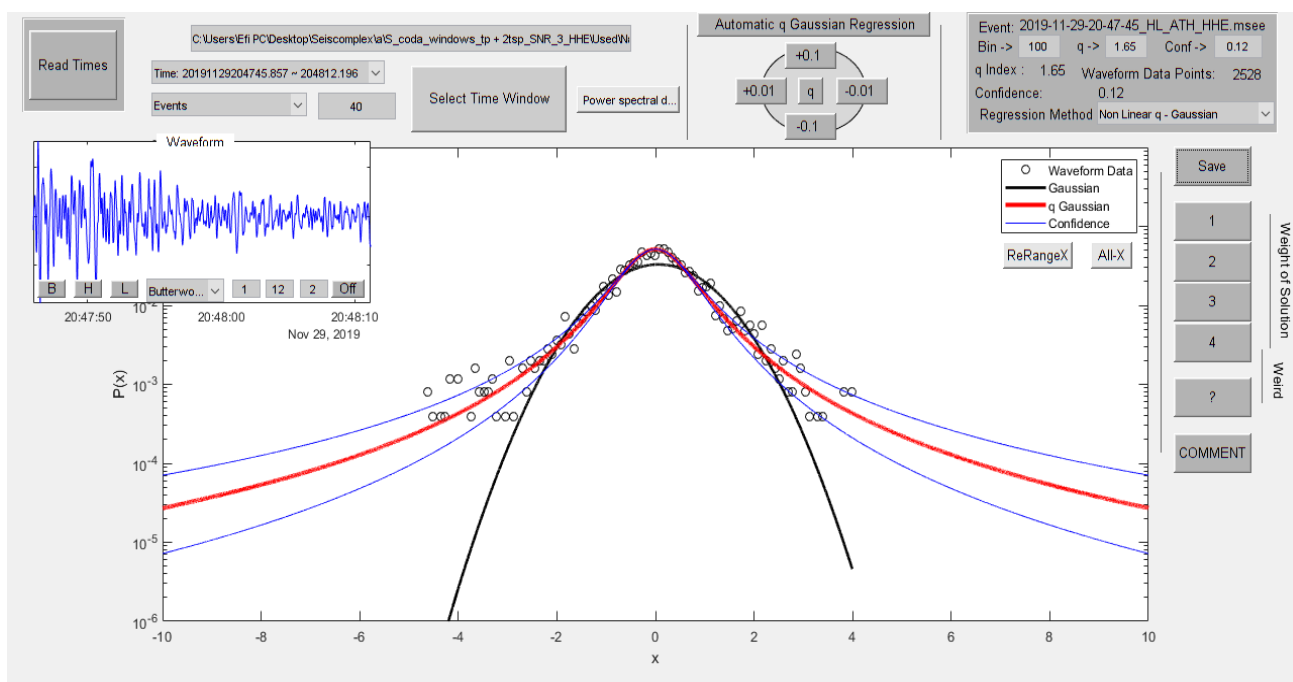


Figure 8.2.39

In figure 8.2.40 the time origin of the earthquake is 04/04/2010 at 22:05:56, latitude 38.42, longitude 22.32, depth 17 km, magnitude 4.1 at 12.6 km SSW of Amfissa. The value of the index  $q$  is 1.74.

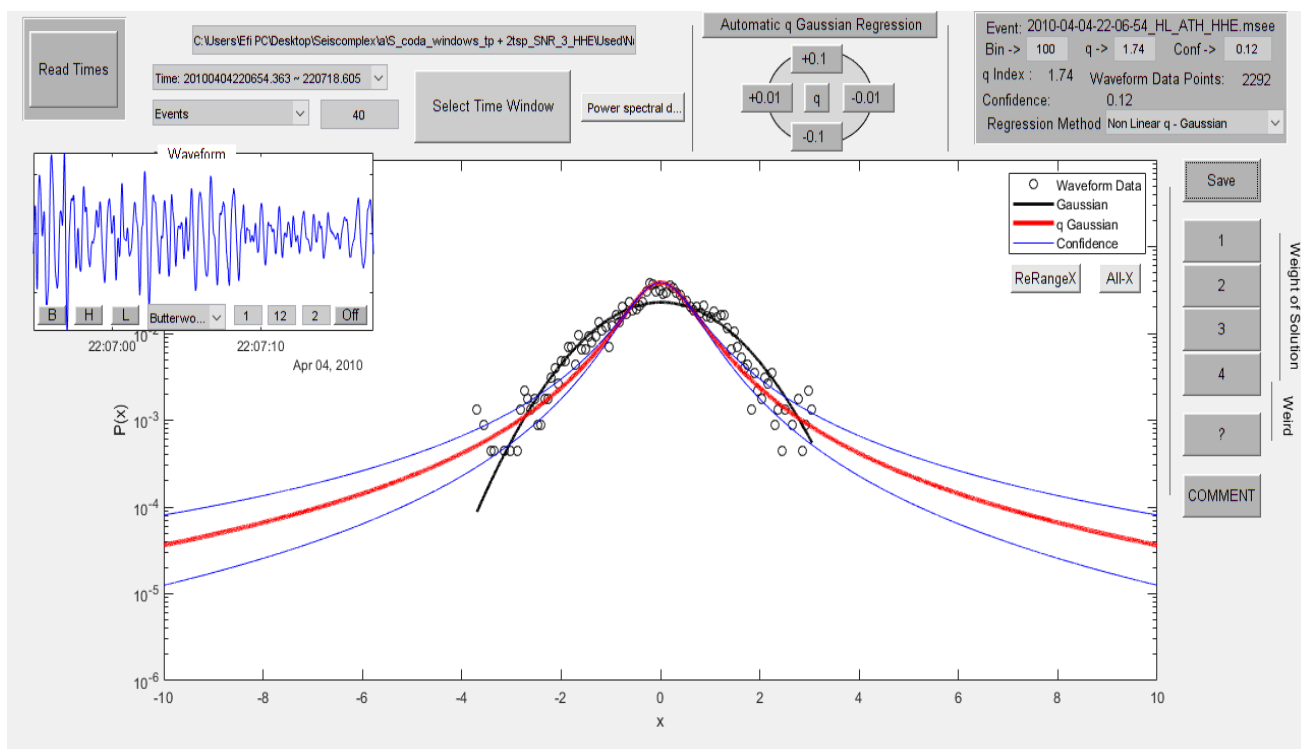


Figure 8.2.40

In figure 8.2.41 the time origin of the earthquake is 27/06/2010 at 13:10:09, latitude 37.52, longitude 22.94, depth 79 km, magnitude 4.1 at 12.6 km ESE of Nafplio. The value of the index  $q$  is 1.63.

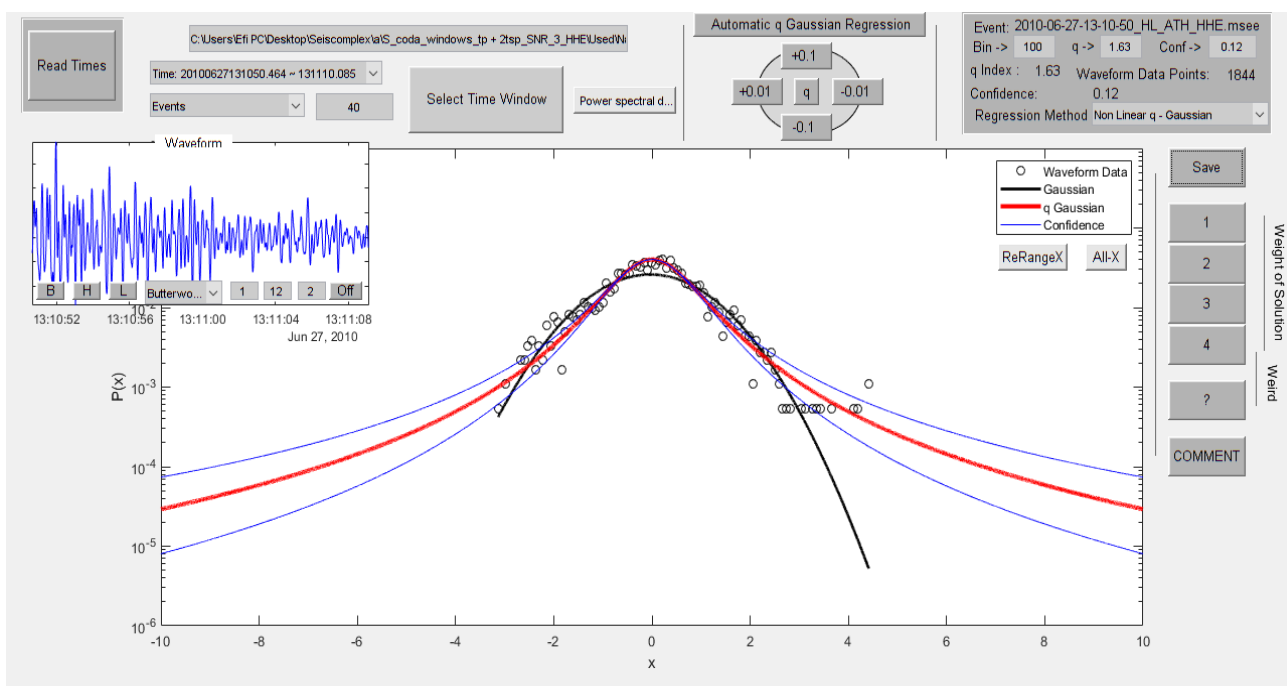


Figure 8.2.41

In figure 8.2.42 the time origin of the earthquake is 06/09/2011 at 04:14:13, latitude 37.88, longitude 23.1, depth 104 km, magnitude 4.1 at 16.1 km ESE of Korinthos. The value of the index  $q$  is 1.8.

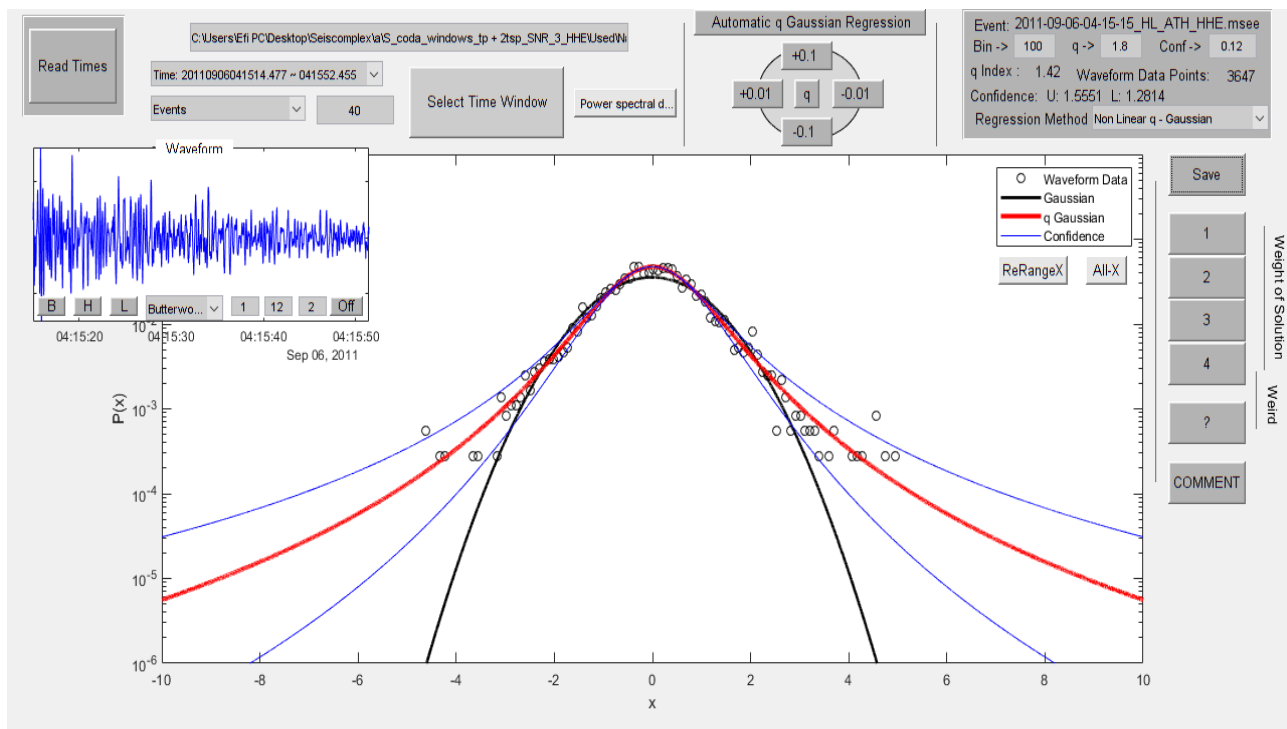


Figure 8.2.42

In figure 8.2.43 the time origin of the earthquake is 02/08/2012 at 10:30:39, latitude 39.27, longitude 23.72, depth 25 km, magnitude 4.1 at 23.4 km ENE of Skiathos. The value of the index  $q$  is 1.51.

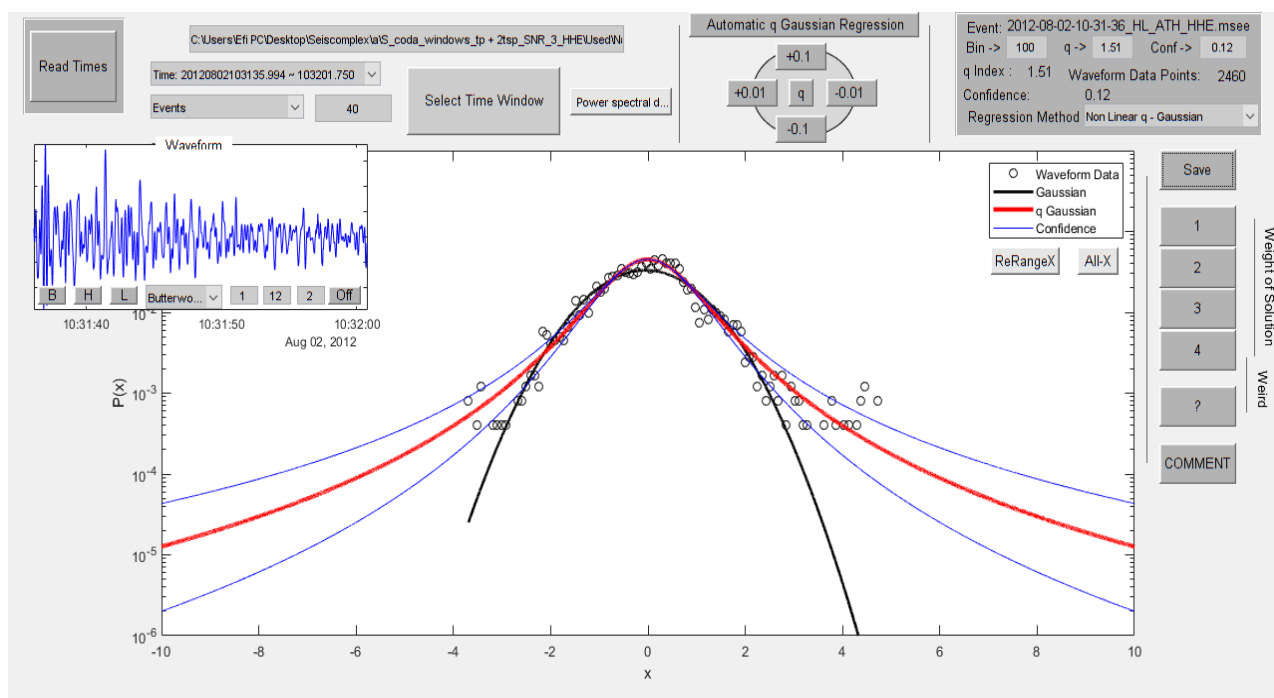


Figure 8.2.43

In figure 8.2.44 the time origin of the earthquake is 06/08/2012 at 15:22:11, latitude 38.75, longitude 24.83, depth 29 km, magnitude 4.1 at 28.8 km SE of Skyros. The value of the index  $q$  is 1.8.

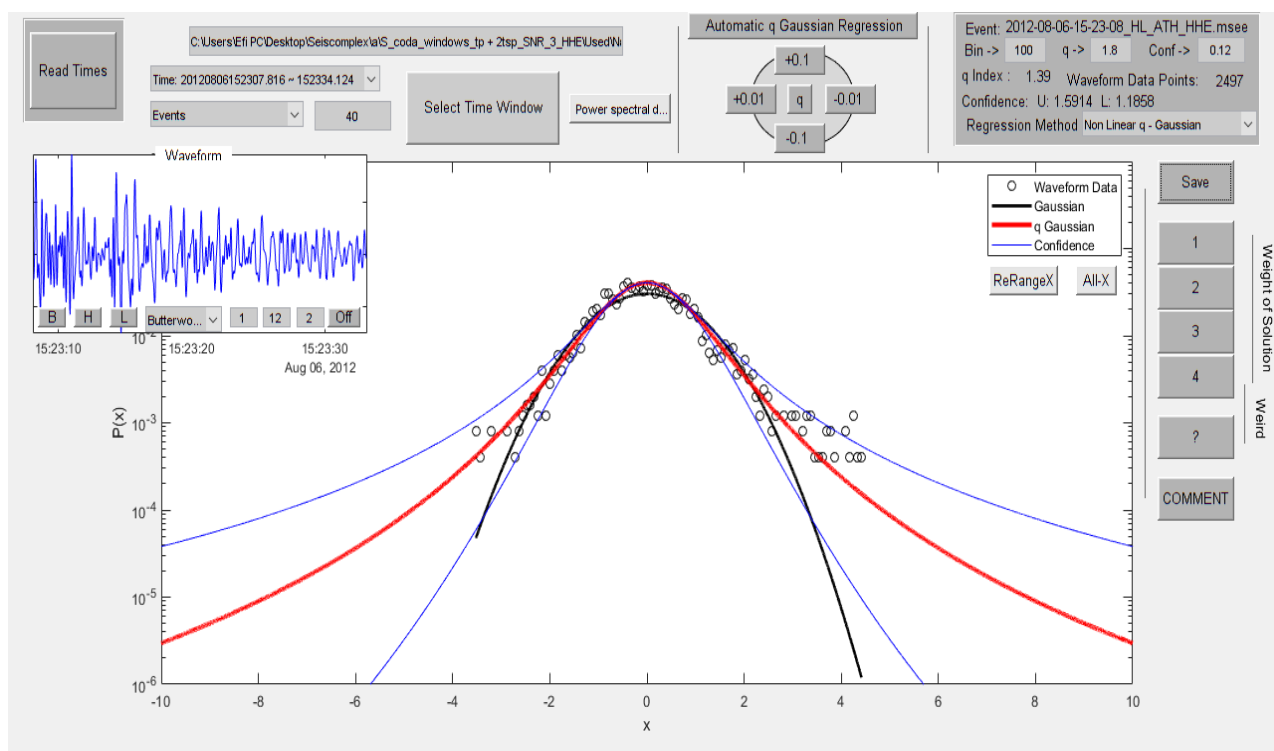


Figure 8.2.44

In figure 8.2.45 the time origin of the earthquake is 09/12/2012 at 01:23:05, latitude 37.93, longitude 22.59, depth 24 km, magnitude 4.1 at 30.0 km W of Korinthos. The value of the index  $q$  is 1.73.

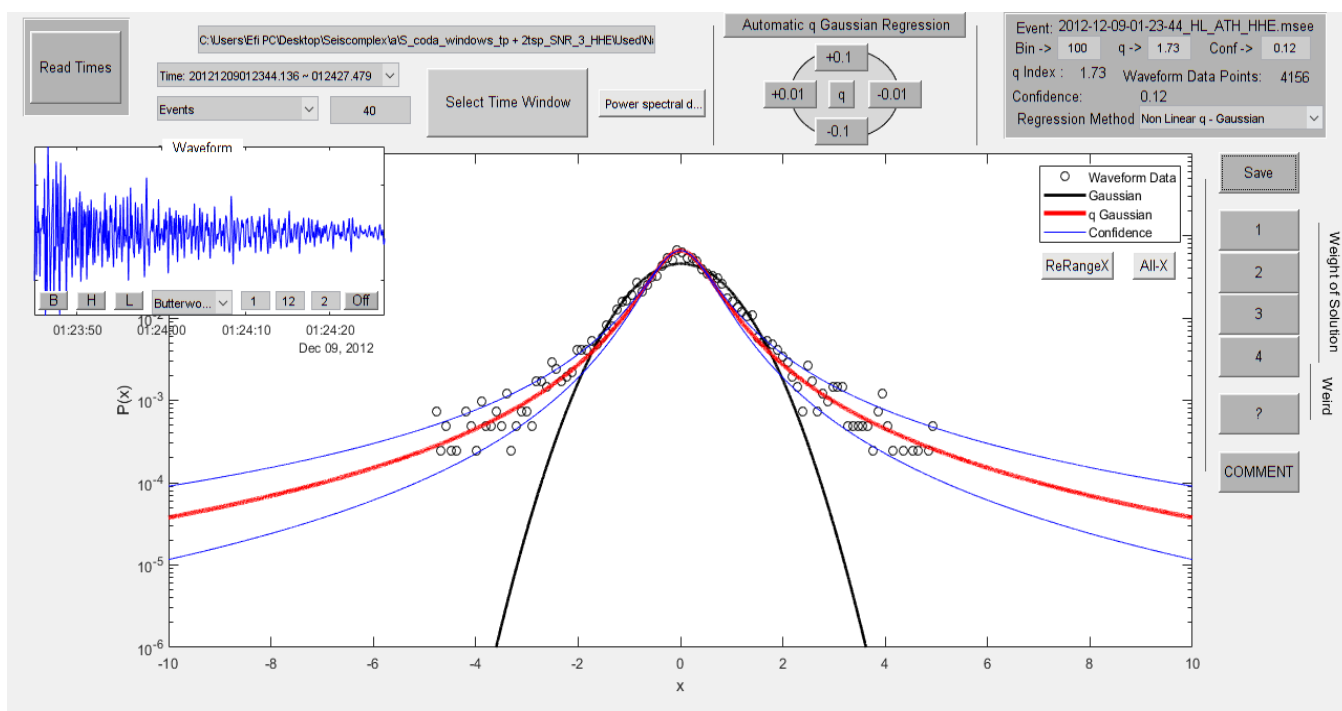


Figure 8.2.45

In figure 8.2.46 the time origin of the earthquake is 10/05/2014 at 03:04:50, latitude 38.42, longitude 22.46, depth 20 km, magnitude 4.1 at 13.9 km SSE of Amfissa. The value of the index  $q$  is 1.67.

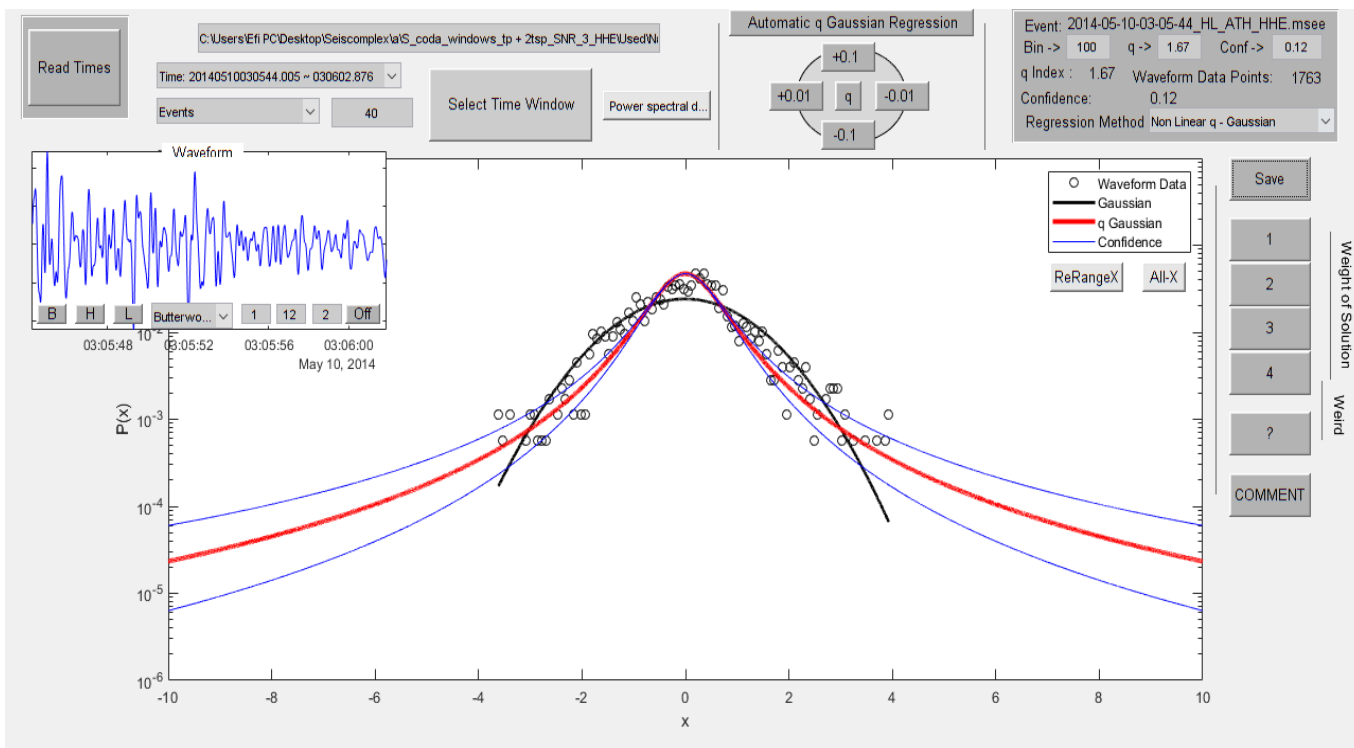


Figure 8.2.46

In figure 8.2.47 the time origin of the earthquake is 19/12/2014 at 22:40:32, latitude 39.33, longitude 22.62, depth 19 km, magnitude 4.1 at 28.3 km W of Volos. The value of the index  $q$  is 1.69.

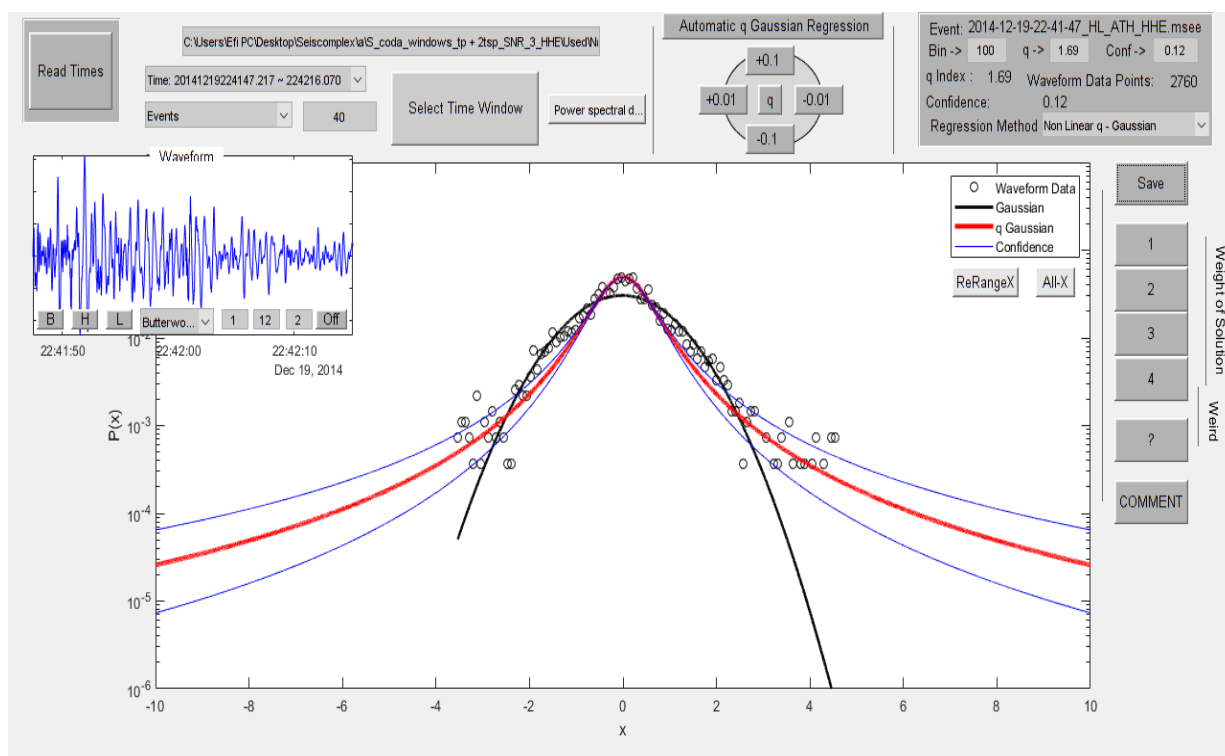


Figure 8.2.47

In figure 8.2.48 the time origin of the earthquake is 13/04/2015 at 03:49:02, latitude 39.13, longitude 24.46, depth 17 km, magnitude 4.1 at 26.6 km NNW of Skyros. The value of the index  $q$  is 1.68.

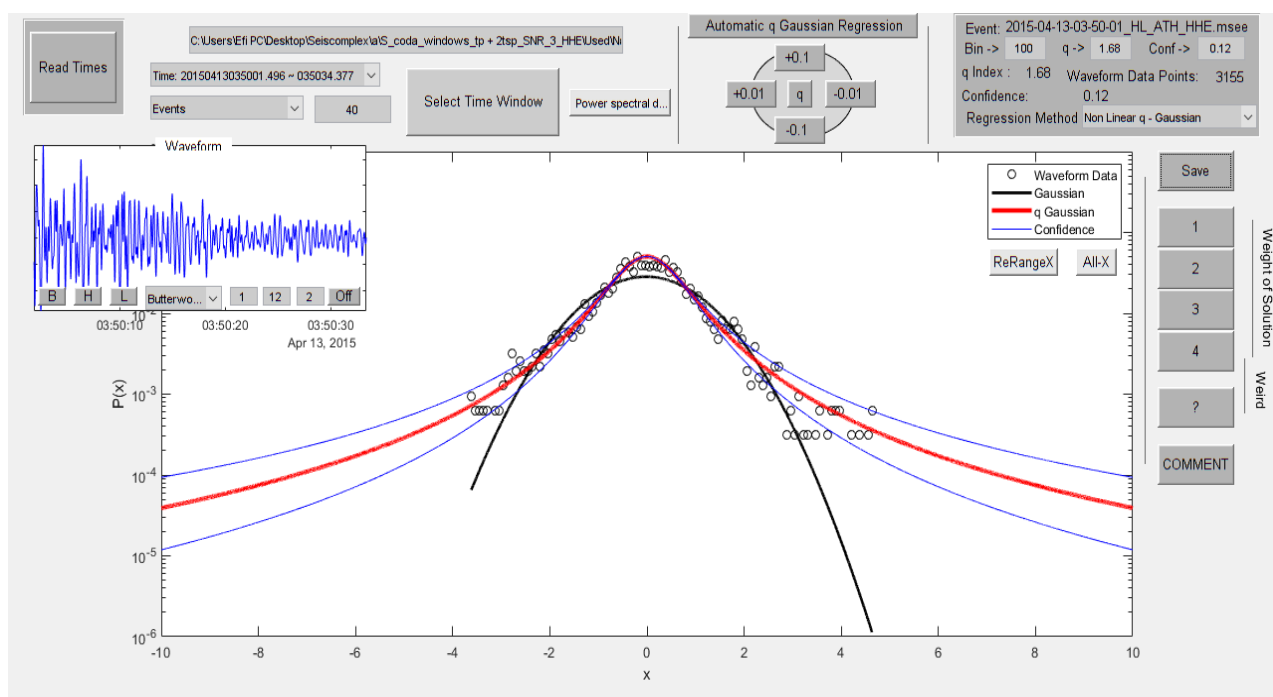


Figure 8.2.48

In figure 8.2.49 the time origin of the earthquake is 11/12/2019 at 02:29:27, latitude 37.5504, longitude 24.0079, depth 142 km, magnitude 4.1 at 53.9 km SSE of Athens. The value of the index  $q$  is 1.8.

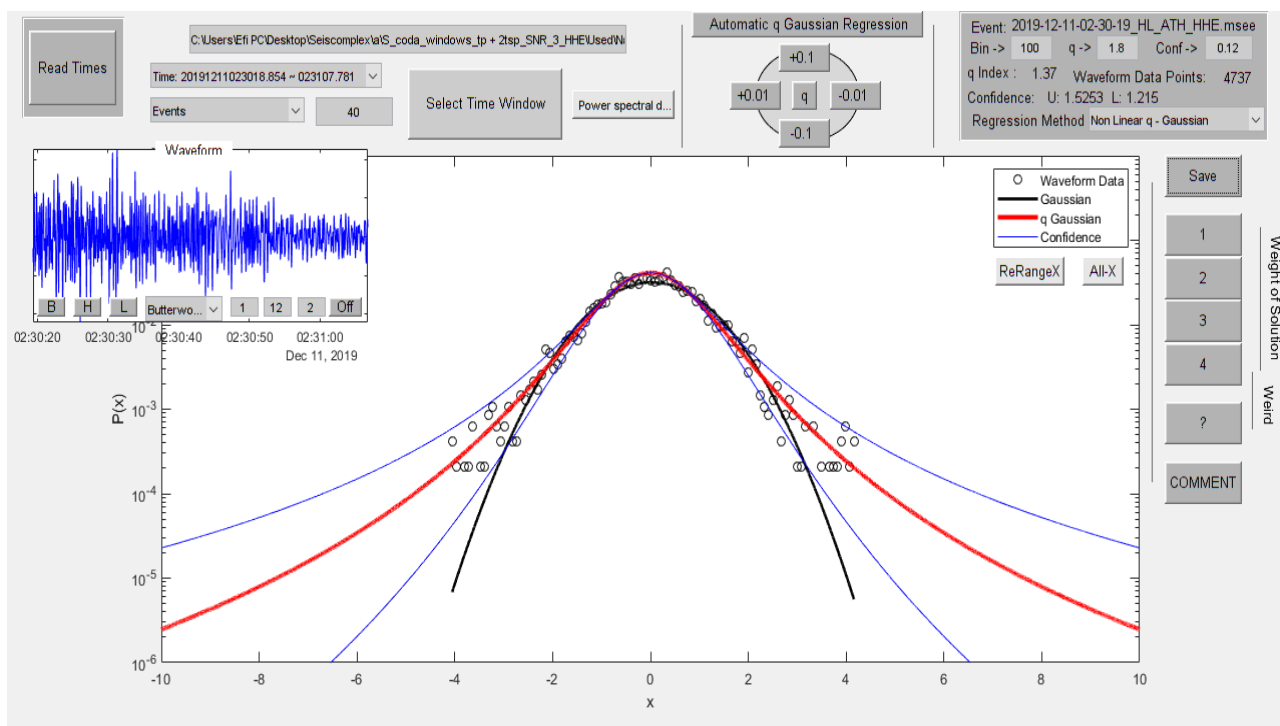


Figure 8.2.49

In figure 8.2.50 the time origin of the earthquake is 14/07/2011 at 08:41:55, latitude 37.83, longitude 22.62, depth 82 km, magnitude 4 at 29.9 km WSW of Korinthos. The value of the index  $q$  is 1.45.

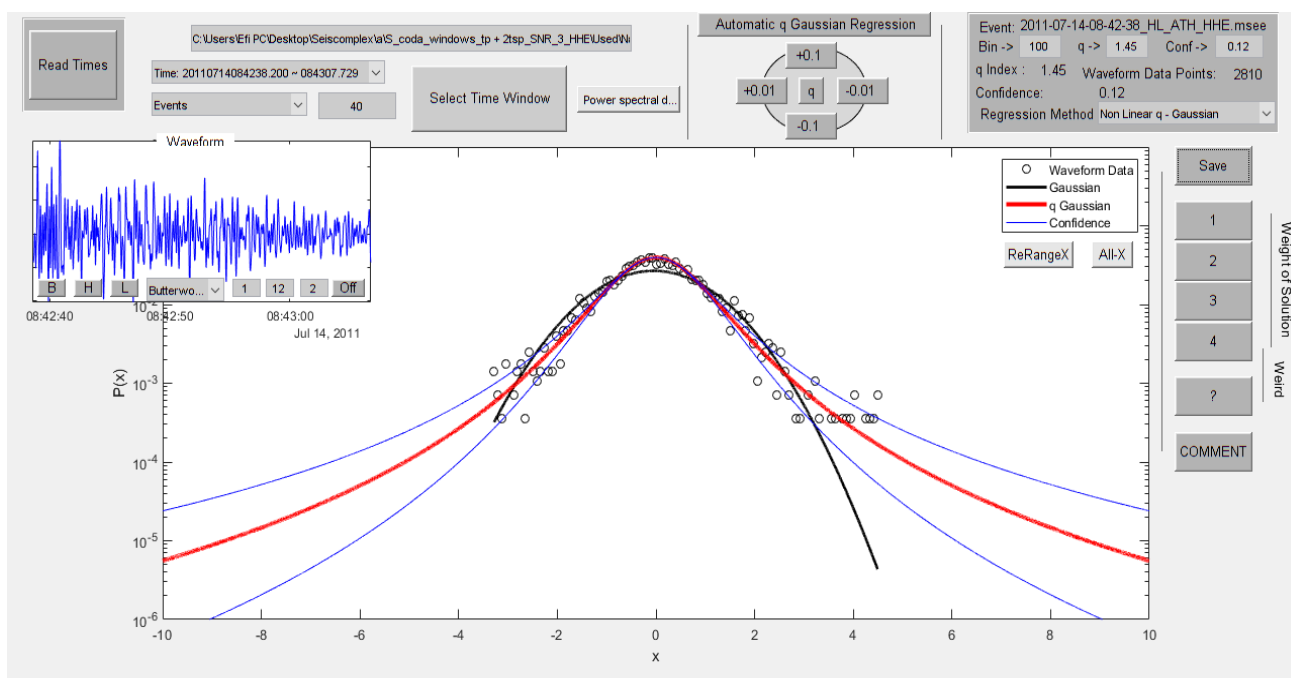


Figure 8.2.50

In figure 8.2.51 the time origin of the earthquake is 30/01/2013 at 04:27:25, latitude 38.78, longitude 23.37, depth 22 km, magnitude 4 at 35.2 km ENE of Atalanti. The value of the index  $q$  is 1.8.

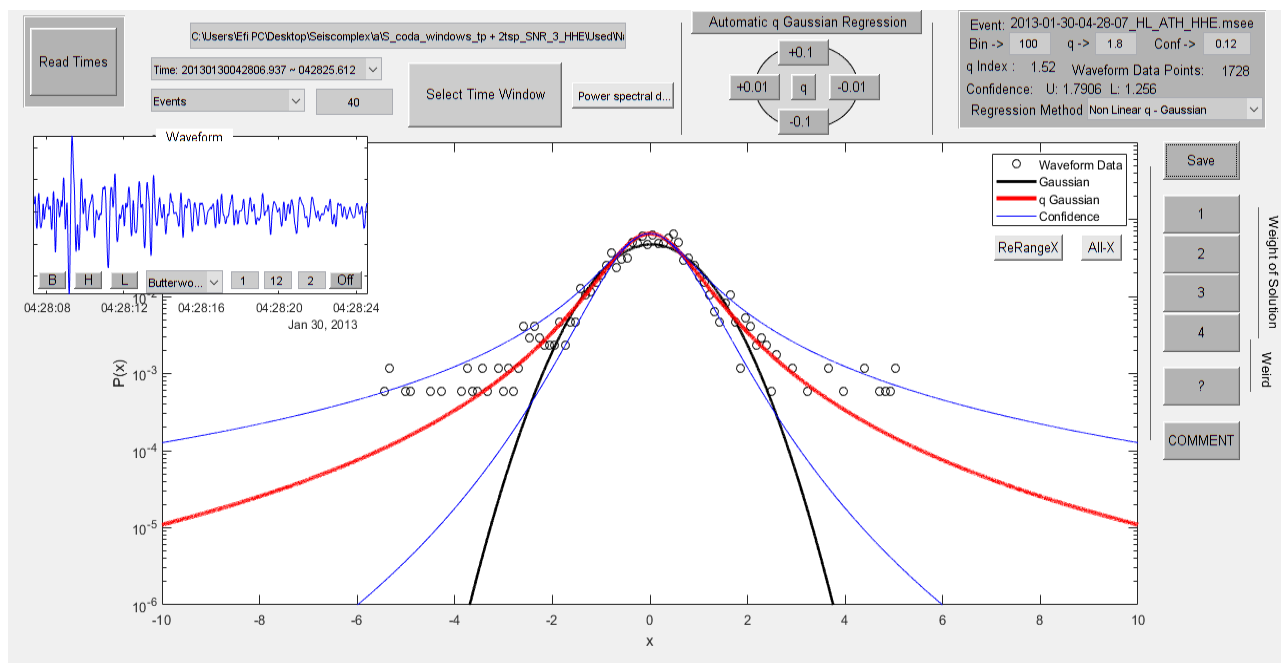


Figure 8.2.51

In figure 8.2.52 the time origin of the earthquake is 16/09/2016 at 06:55:13, latitude 38.89, longitude 23.33, depth 25 km, magnitude 4 at 33.5 km SSW of Skiathos. The value of the index  $q$  is 1.82.

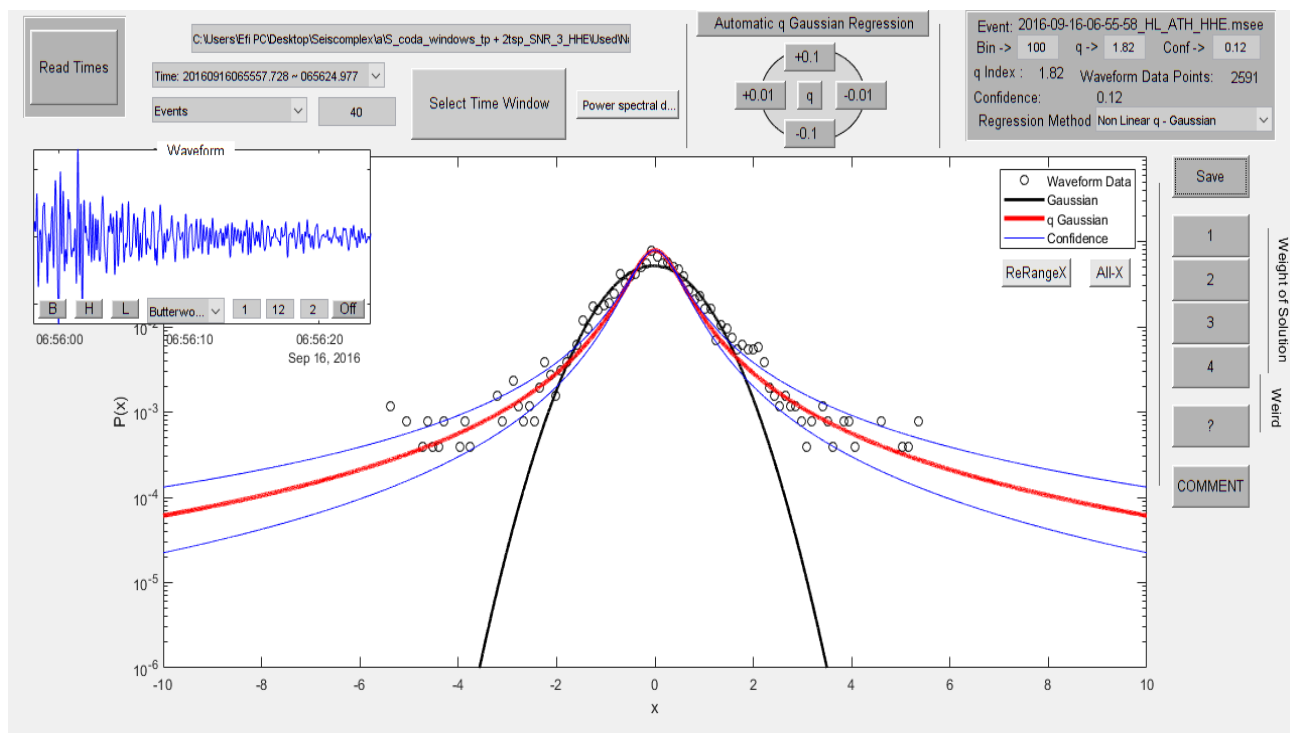


Figure 8.2.52

In figure 8.2.53 the time origin of the earthquake is 29/09/2016 at 01:17:36, latitude 39.53, longitude 24.1, depth 30 km, magnitude 4 at 66.7 km NE of Skiathos. The value of the index  $q$  is 1.59.

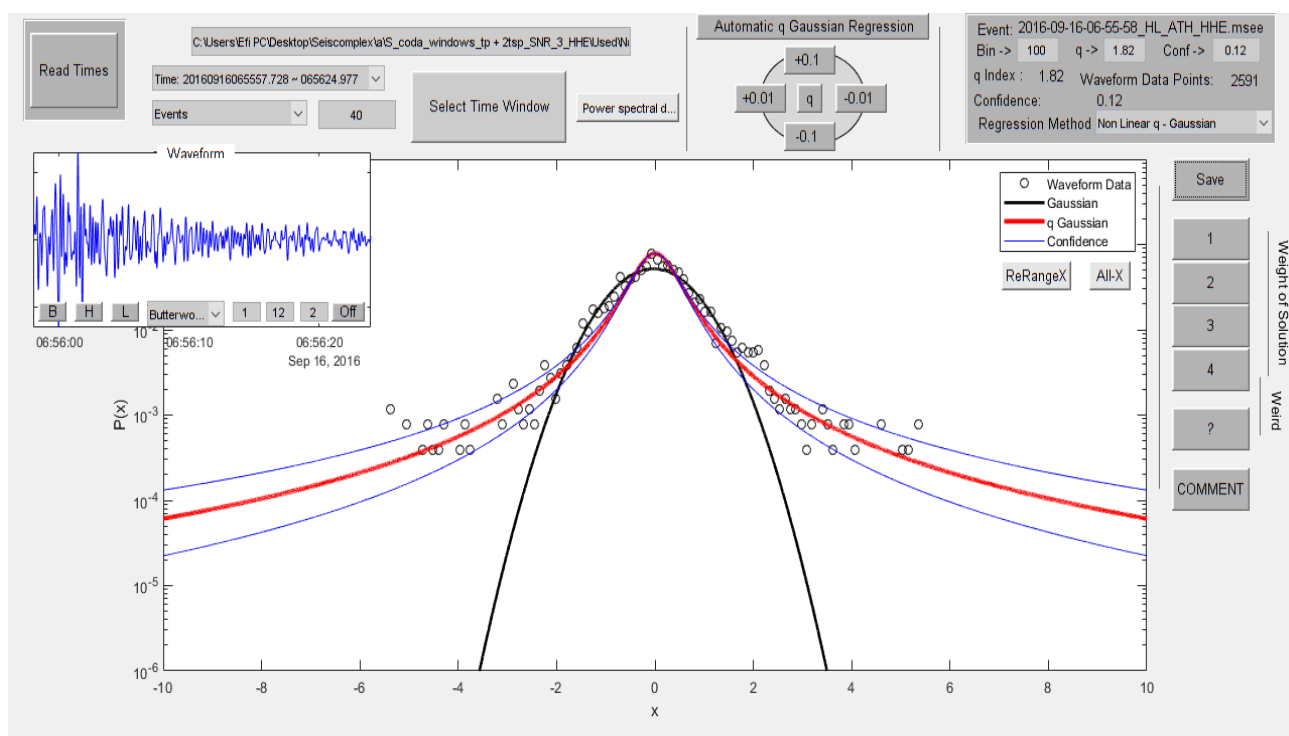


Figure 8.2.53

In figure 8.2.54 the time origin of the earthquake is 22/04/2011 at 01:20:24, latitude 38.37, longitude 23.62, depth 23 km, magnitude 3.9 at 10.6 km S of Chalkida. The value of the index  $q$  is 1.7.

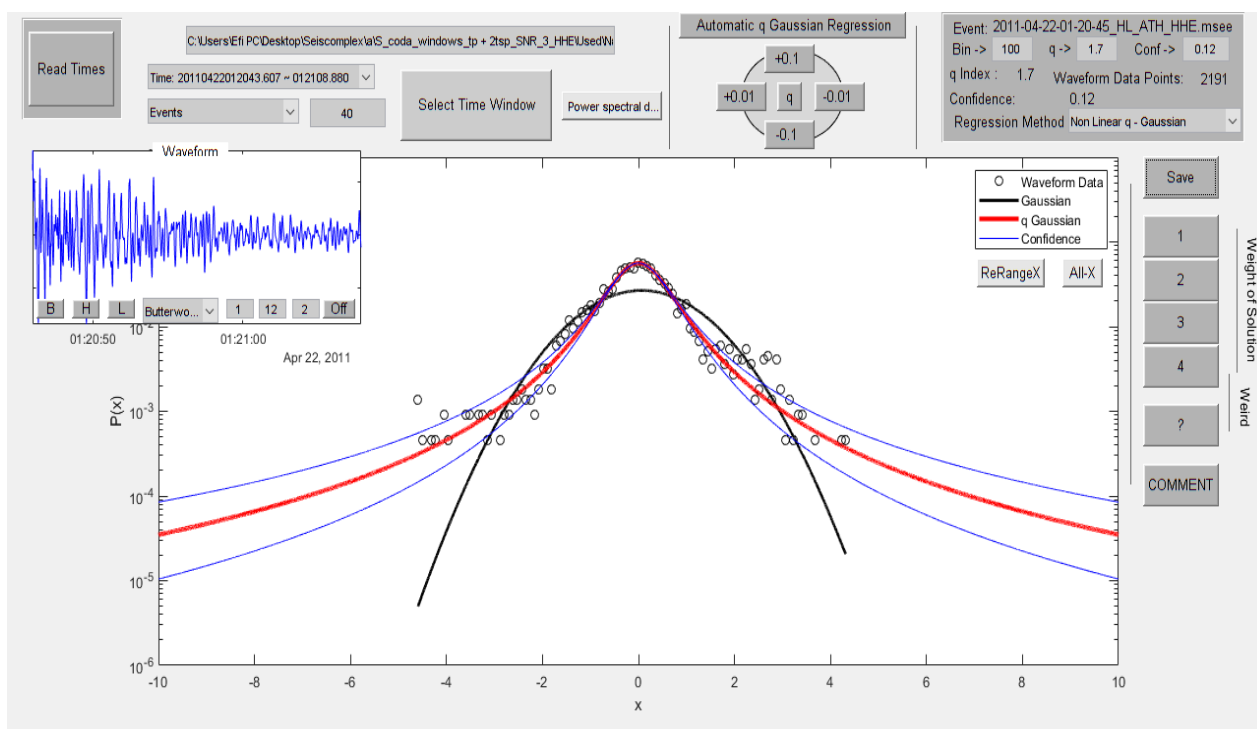


Figure 8.2.54

In figure 8.2.55 the time origin of the earthquake is 24/09/2012 at 19:18:37, latitude 39.03, longitude 23.16, depth 23 km, magnitude 3.9 at 31.8 km WSW of Skiathos. The value of the index  $q$  is 1.5.

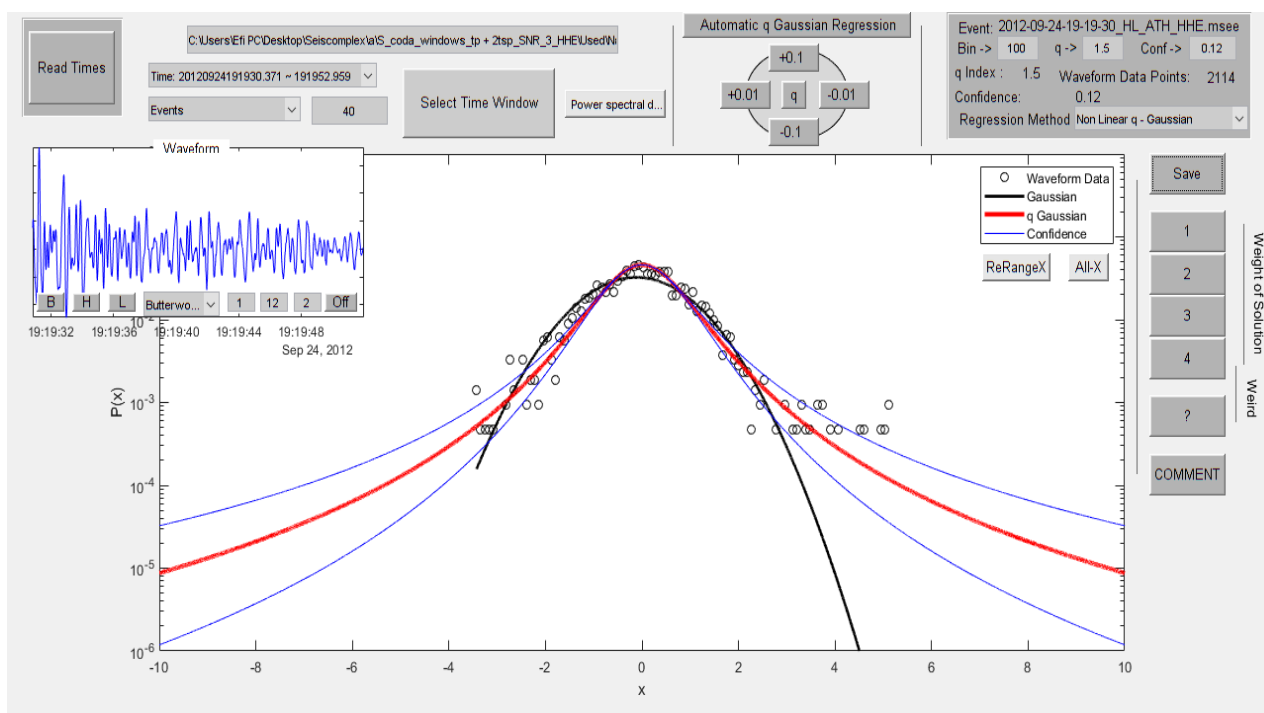


Figure 8.2.55

In figure 8.2.56 the time origin of the earthquake is 17/09/2013 at 05:46:52, latitude 38.72, longitude 22.77, depth 17 km, magnitude 3.9 at 21.3 km WNW of Atalanti. The value of the index  $q$  is 1.79.

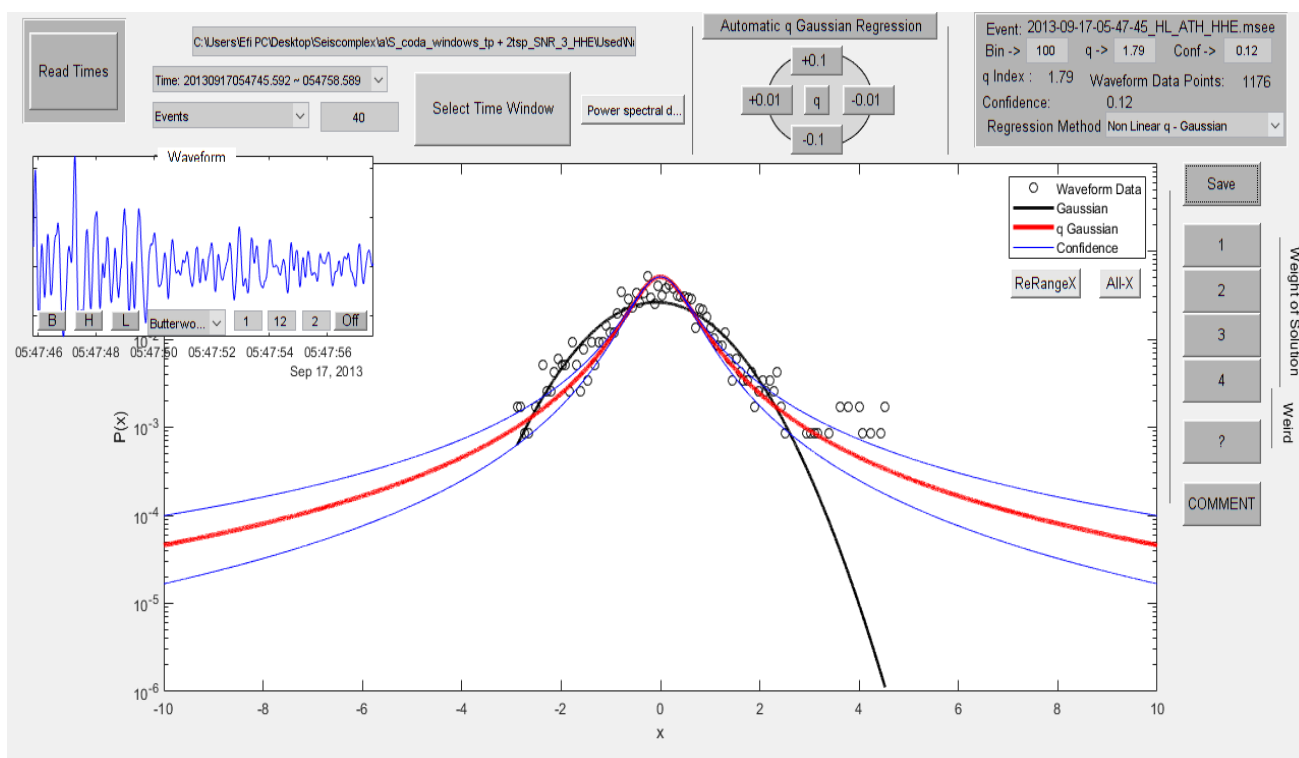


Figure 8.2.56

In figure 8.2.57 the time origin of the earthquake is 04/11/2013 at 22:09:17, latitude 38.91, longitude 23.1, depth 23km, magnitude 3.9 at 30.1 km NNE of Atalanti. The value of the index  $q$  is 1.57.

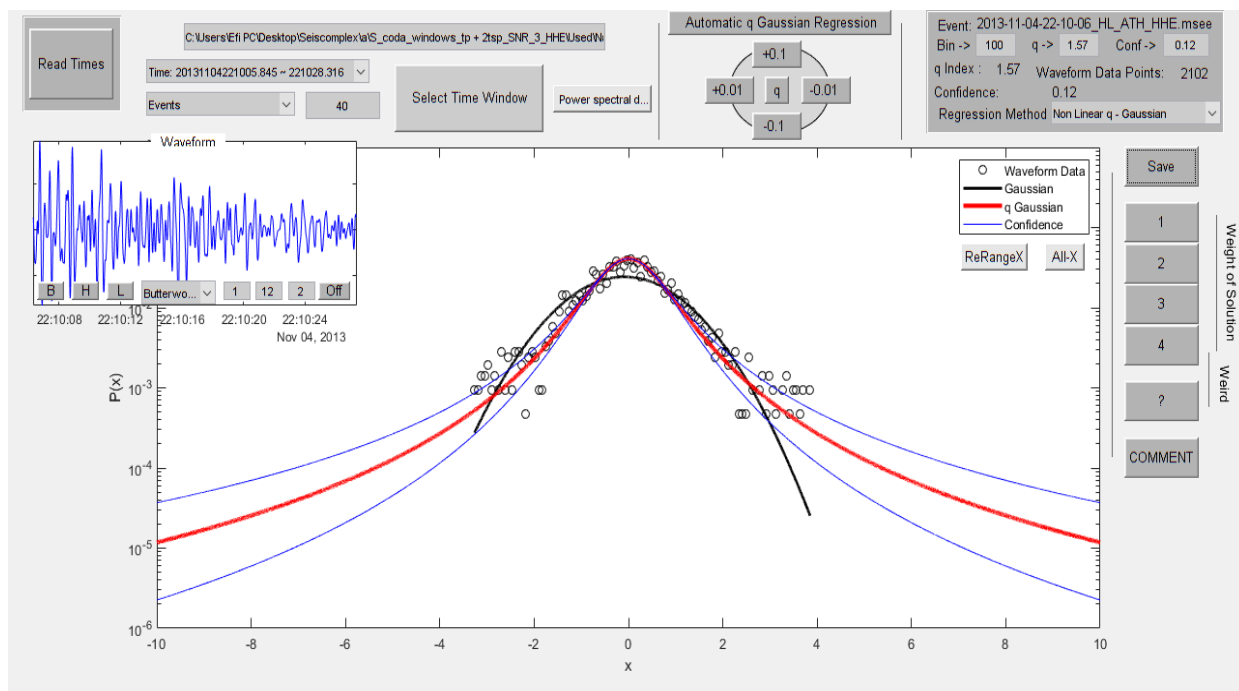


Figure 8.2.57

In figure 8.2.58 the time origin of the earthquake is 29/09/2014 at 08:15:07, latitude 39.31, longitude 24.04, depth 32km, magnitude 3.9 at 50.5 km ENE of Skiathos. The value of the index  $q$  is 1.43.

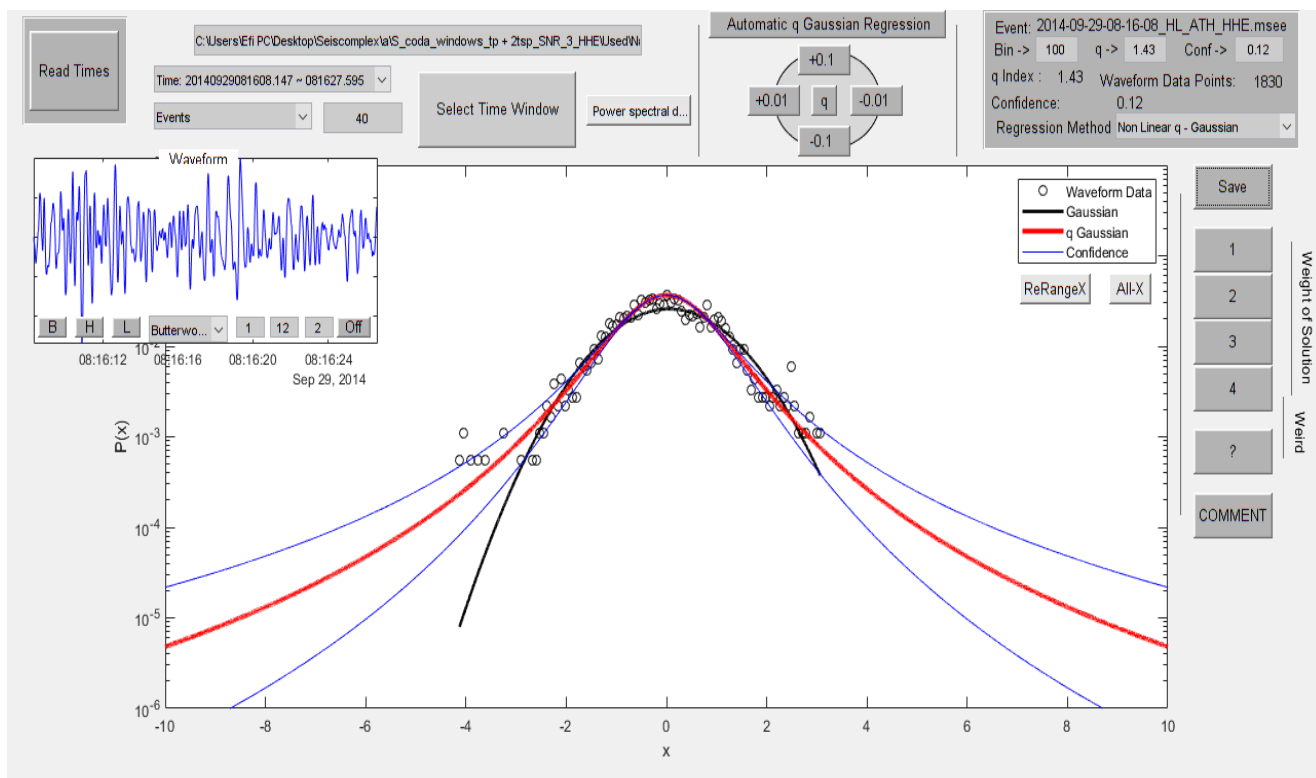


Figure 8.2.58

In figure 8.2.59 the time origin of the earthquake is 18/11/2014 at 01:13:47, latitude 38.64, longitude 23.41, depth 23km, magnitude 3.9 at 25.6 km NW of Chalkida. The value of the index  $q$  is 1.52.

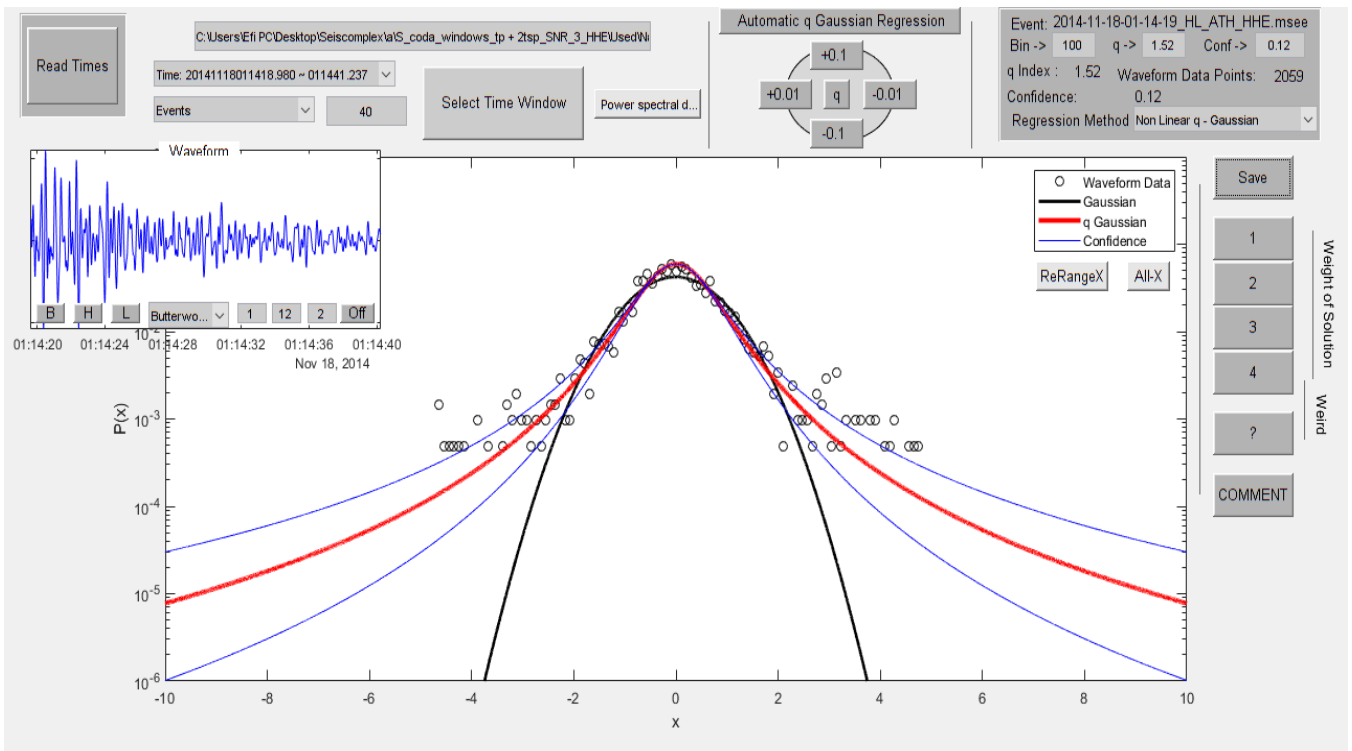


Figure 8.2.59

In figure 8.2.60 the time origin of the earthquake is 19/11/2014 at 00:37:26, latitude 38.64, longitude 23.42, depth 24km, magnitude 3.9 at 25.1 km NW of Chalkida. The value of the index  $q$  is 1.8.

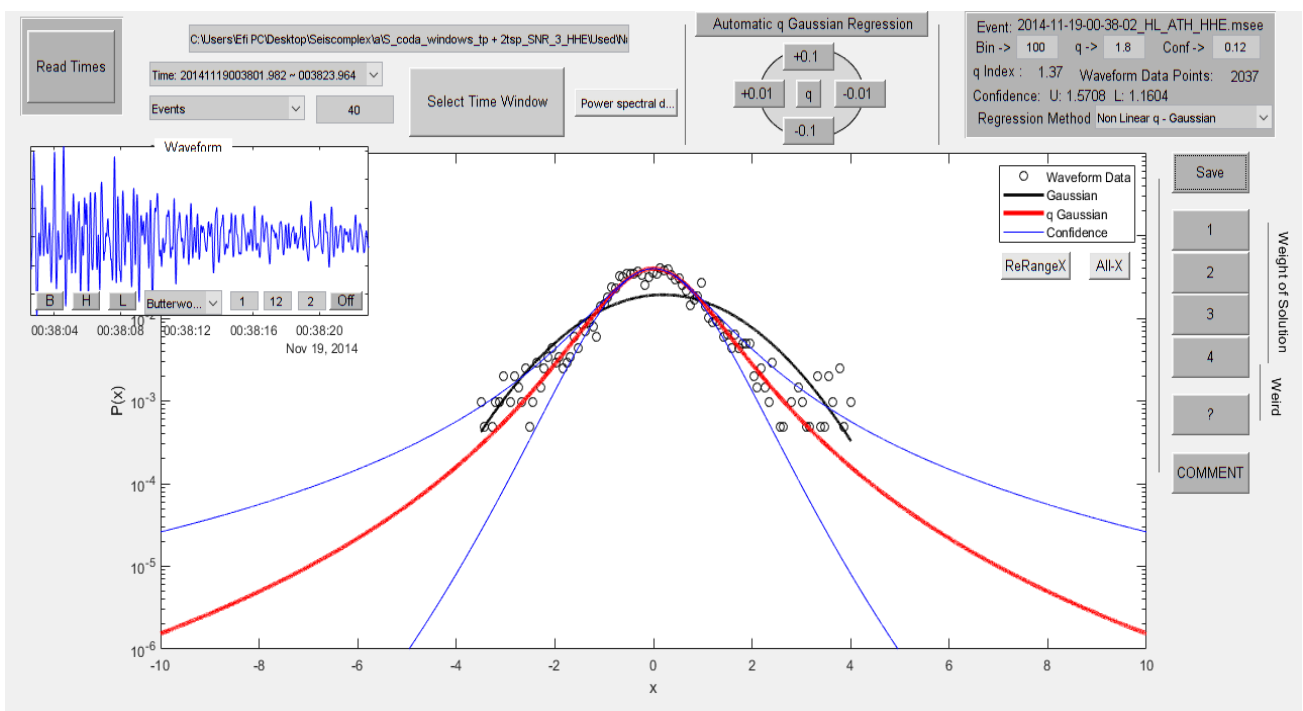


Figure 8.2.60

In figure 8.2.61 the time origin of the earthquake is 31/12/2014 at 04:49:58, latitude 38.19, longitude 22.51, depth 20km, magnitude 3.9 at 38.0 km E of Aegion. The value of the index  $q$  is 1.48.

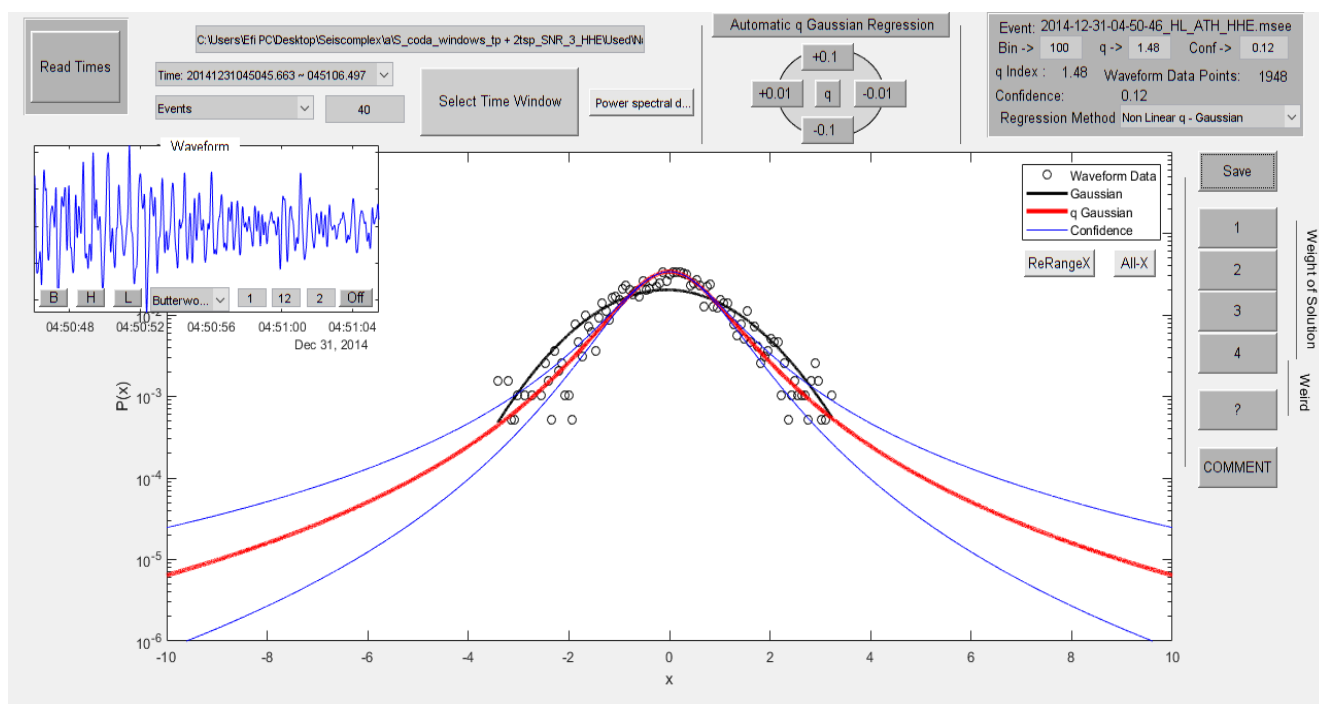


Figure 8.2.61

In figure 8.2.62 the time origin of the earthquake is 17/11/2015 at 03:00:09, latitude 39.51, longitude 24.07, depth 43km, magnitude 3.9 at 63.3 km NE of Skiathos. The value of the index  $q$  is 1.8.

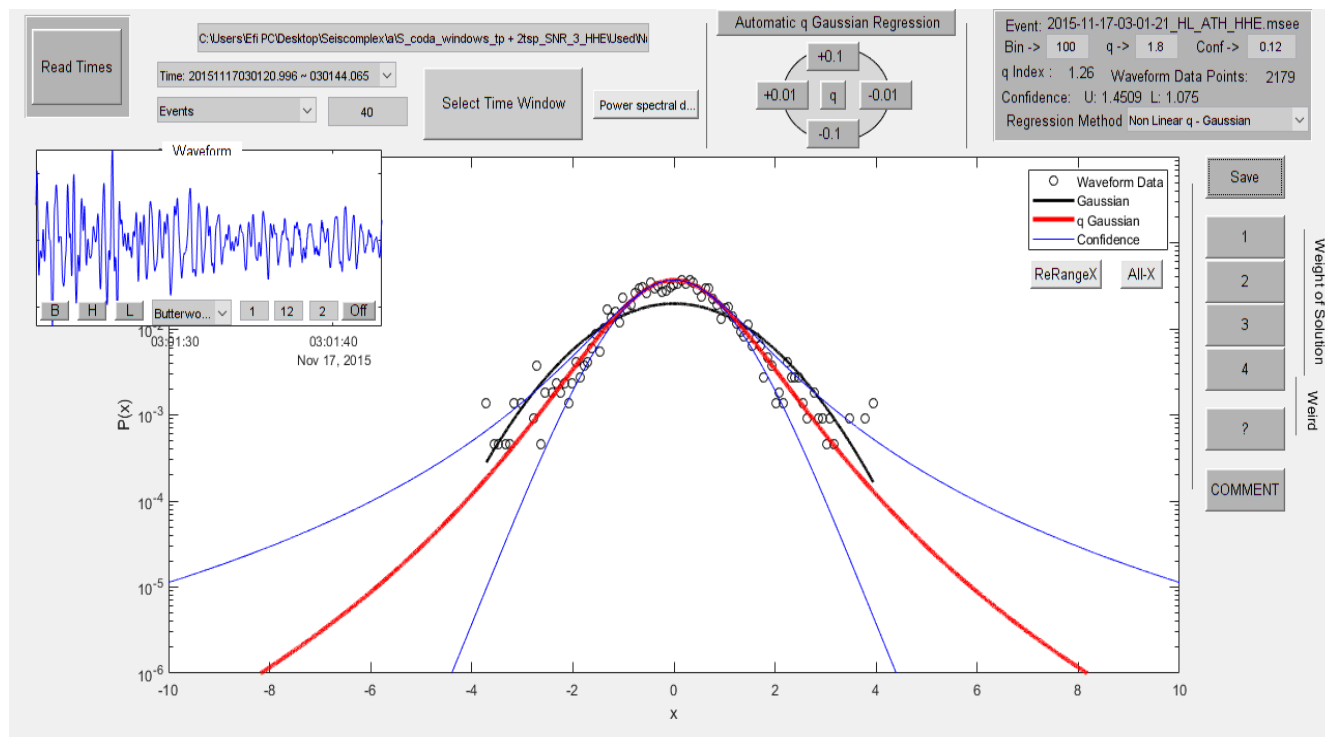


Figure 8.2.62

In figure 8.2.63 the time origin of the earthquake is 20/05/2016 at 20:00:20, latitude 38.59, longitude 24.47, depth 15km, magnitude 3.9 at 5.9 km SSW of Skyros. The value of the index  $q$  is 1.98.

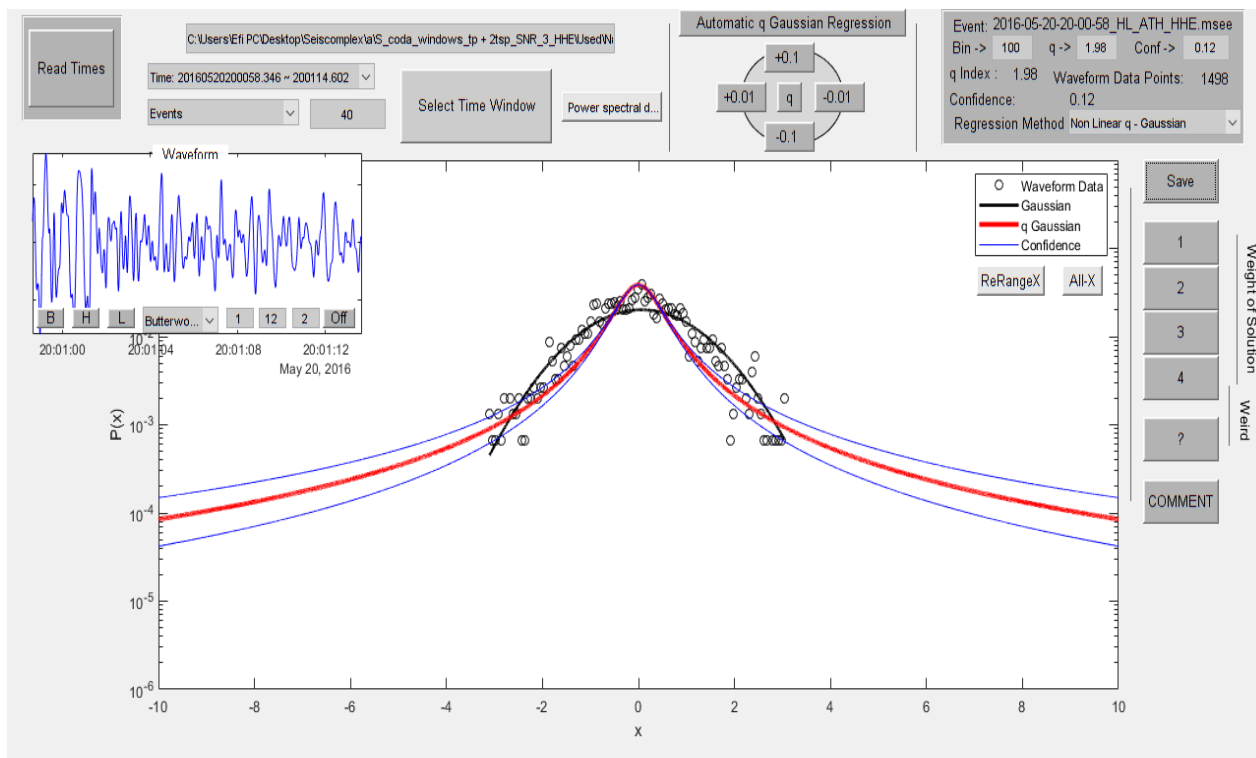


Figure 8.2.63

In figure 8.2.64 the time origin of the earthquake is 19/01/2018 at 10:10:07, latitude 37.5118, longitude 23.7805, depth 137km, magnitude 3.9 at 52.6 km S of Athens. The value of the index  $q$  is 1.96.

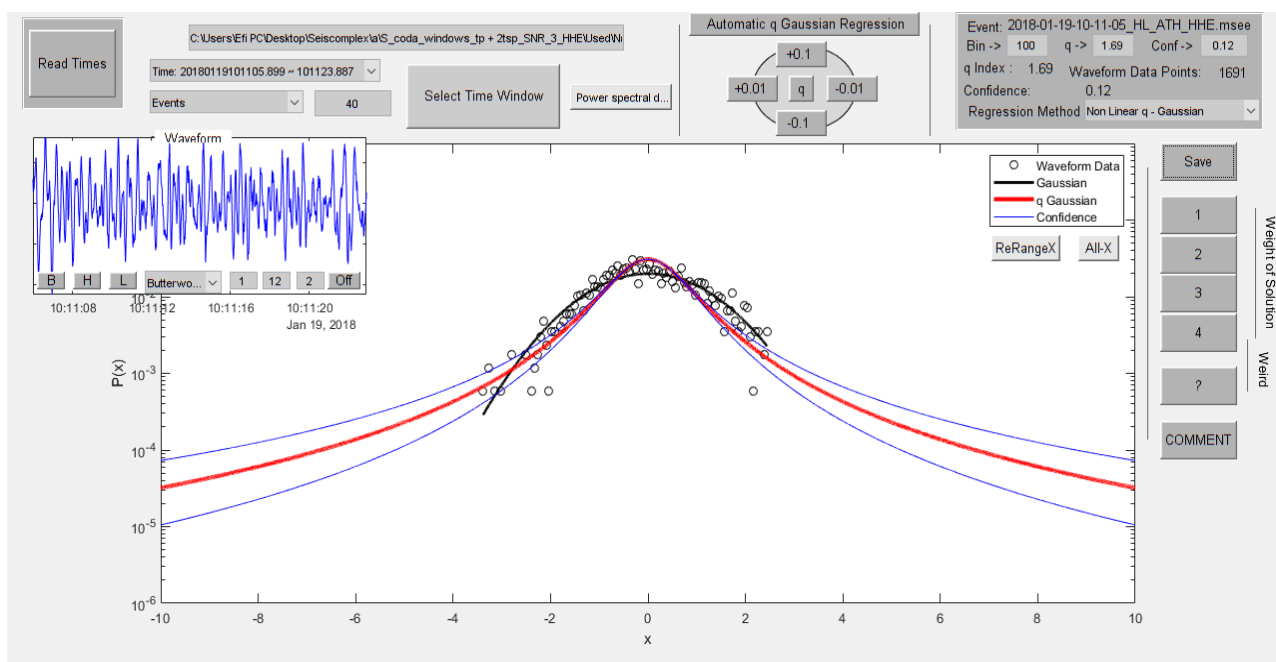


Figure 8.2.64

In figure 8.2.65 the time origin of the earthquake is 12/03/2010 at 03:34:37, latitude 38.12, longitude 22.63, depth 20km, magnitude 3.8 at 33.3 km NW of Korinthos. The value of the index  $q$  is 1.72.

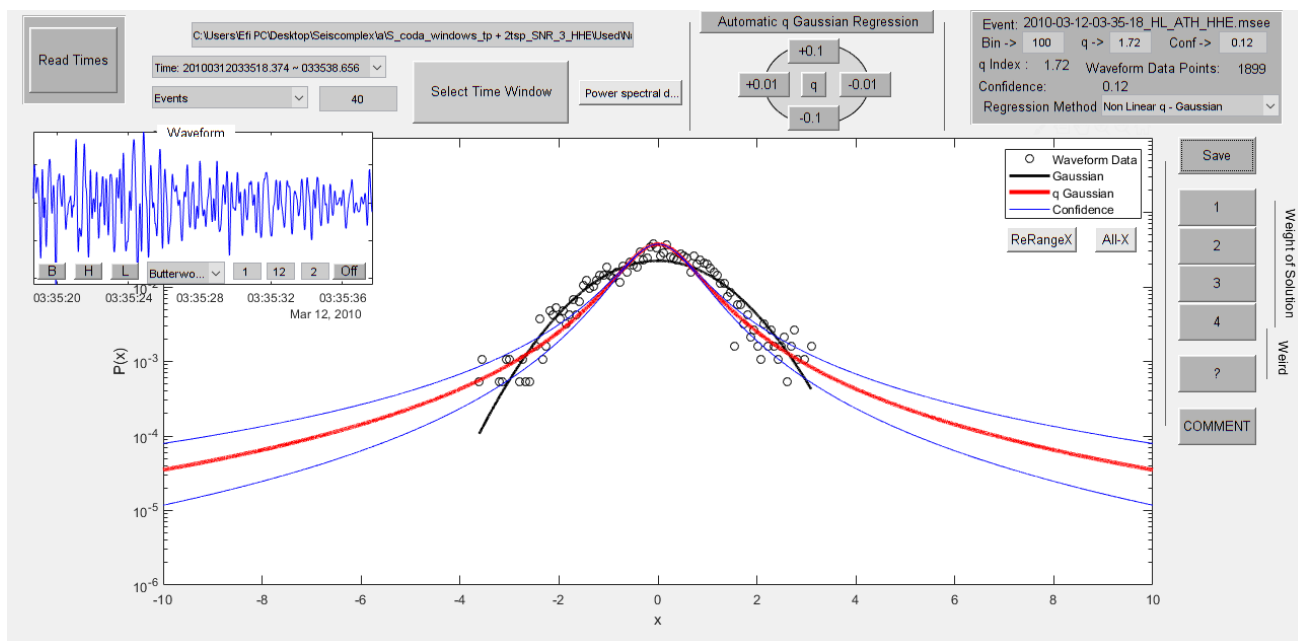


Figure 8.2.65

In figure 8.2.66 the time origin of the earthquake is 17/01/2011 at 22:27:10, latitude 38.78, longitude 23.45, depth 23km, magnitude 3.8 at 37.5 km NNW of Chalkida. The value of the index  $q$  is 1.61.

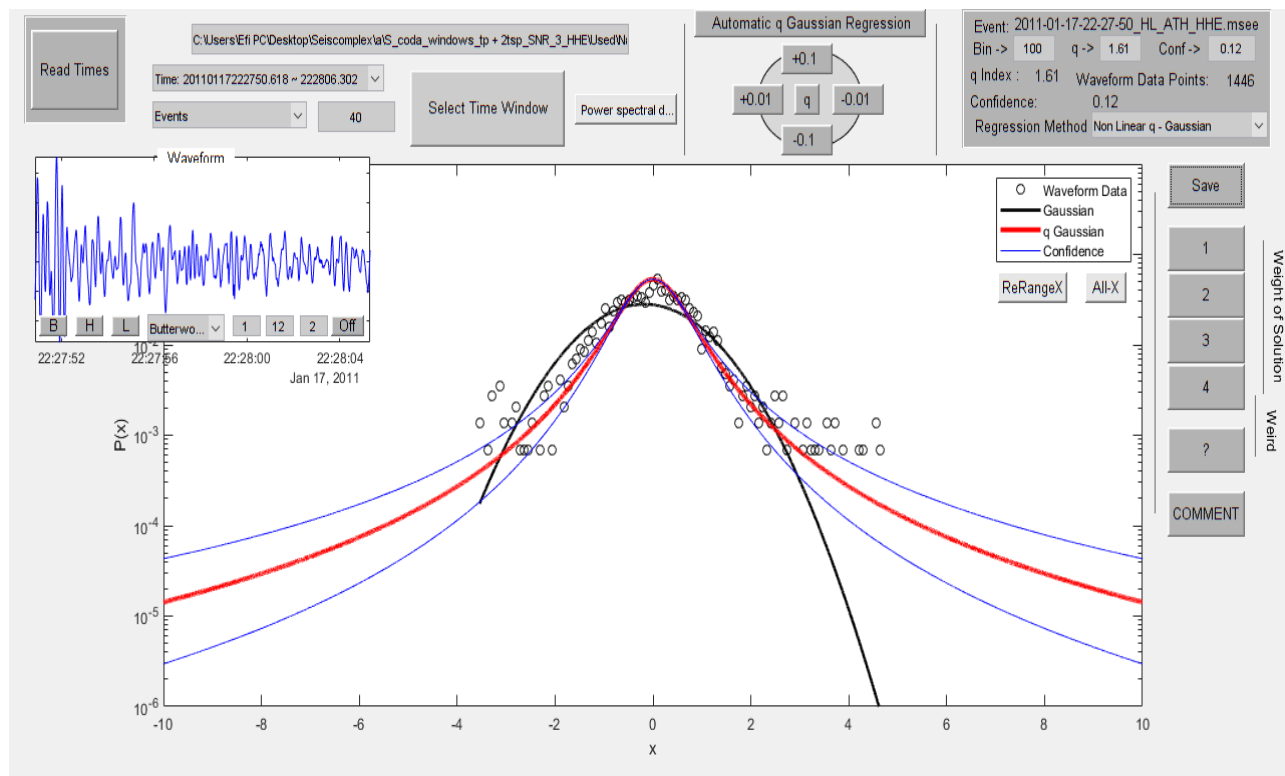


Figure 8.2.66

In figure 8.2.67 the time origin of the earthquake is 09/02/2011 at 08:13:10, latitude 38.63, longitude 22.49, depth 21km, magnitude 3.8 at 15.5 km NE of Amfissa. The value of the index  $q$  is 1.94.

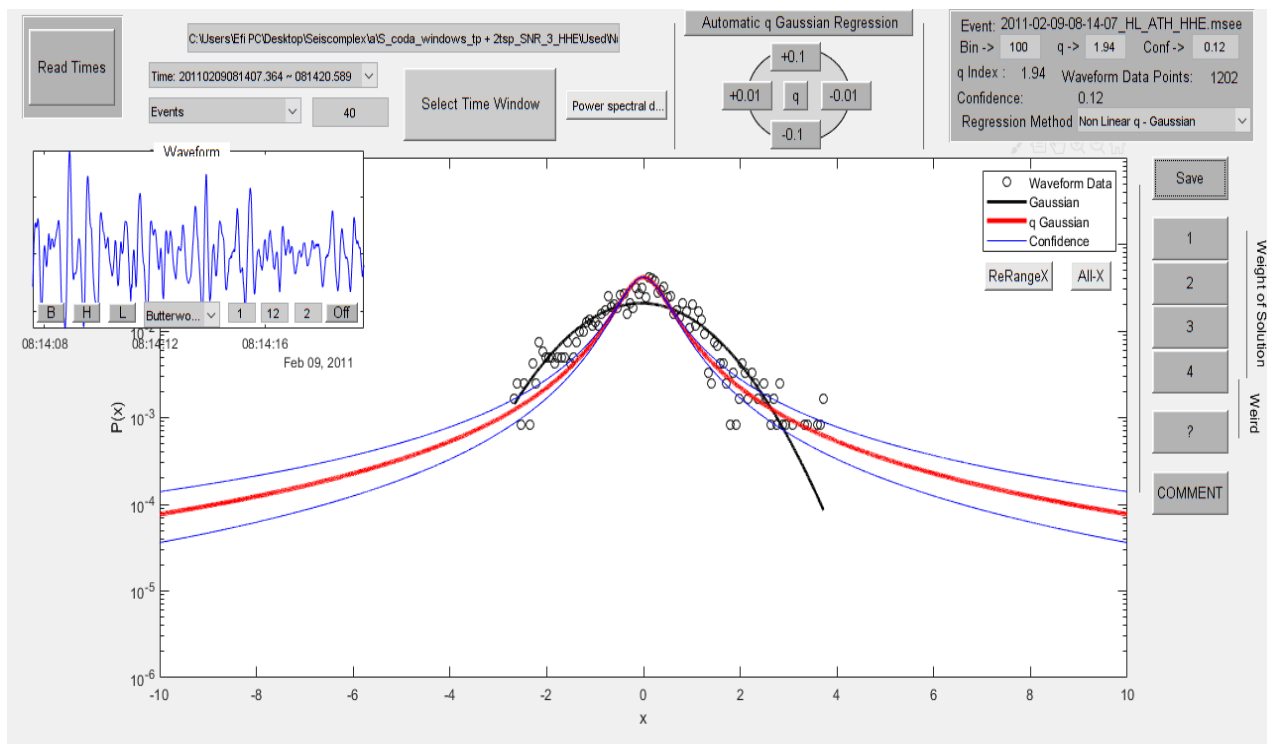


Figure 8.2.67

In figure 8.2.68 the time origin of the earthquake is 19/05/2011 at 09:05:38, latitude 38.43, longitude 23.86, depth 24km, magnitude 3.8 at 23.0 km E of Chalkida. The value of the index  $q$  is 1.75.

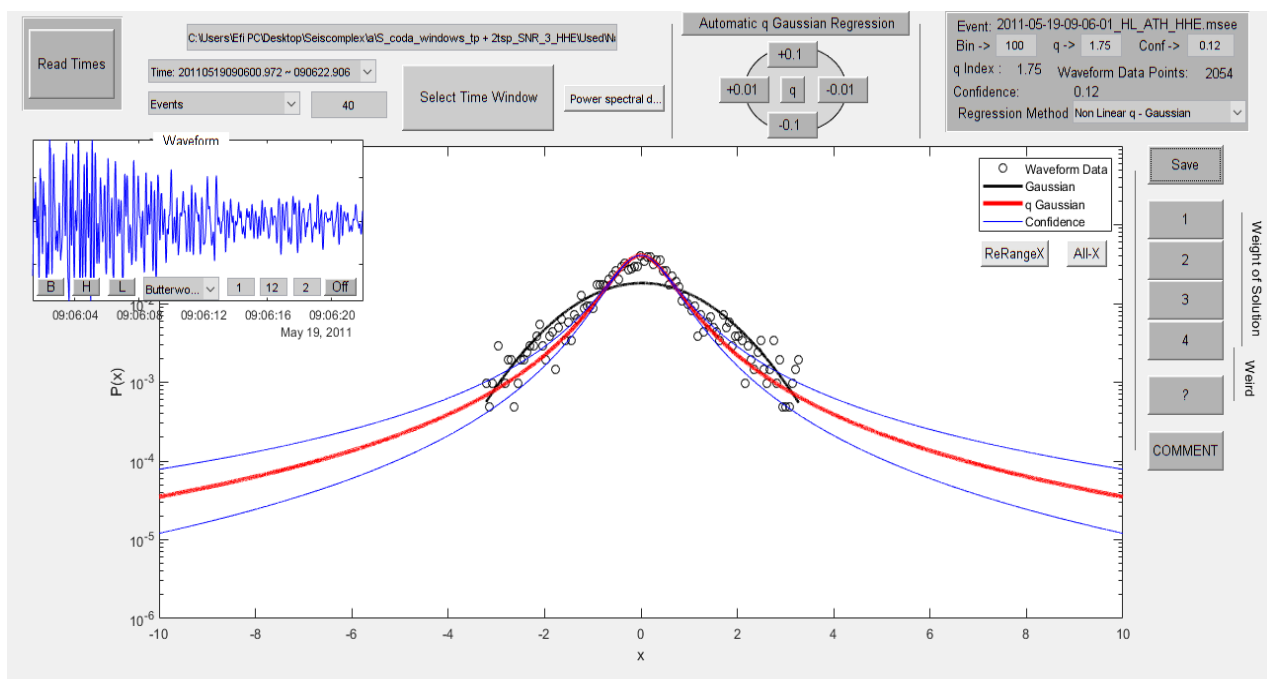


Figure 8.2.68

In figure 8.2.69 the time origin of the earthquake is 25/08/2012 at 06:17:44, latitude 38.89, longitude 23.22, depth 25km, magnitude 3.8 at 32.7 km NE of Atalanti. The value of the index  $q$  is 1.75.

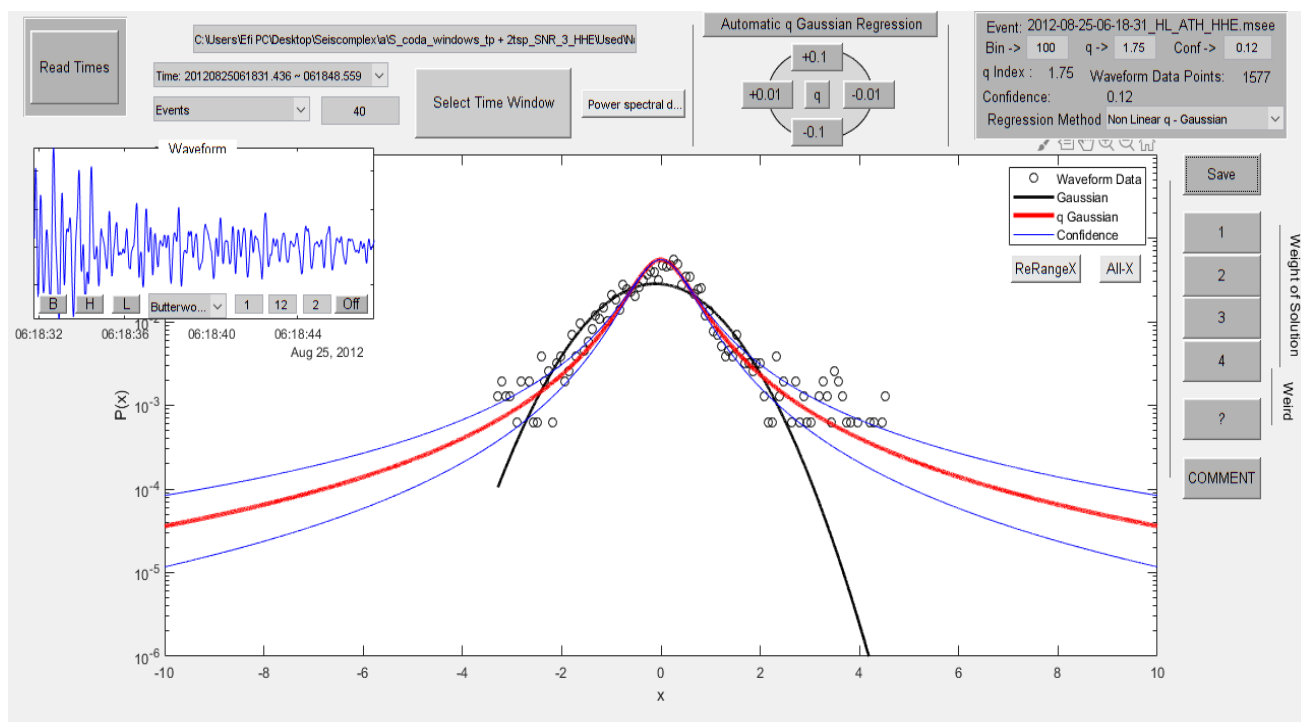


Figure 8.2.69

In figure 8.2.70 the time origin of the earthquake is 13/05/2014 at 01:24:10, latitude 38.24, longitude 25.13, depth 32km, magnitude 3.8 at 48.4 km NNE of Andros. The value of the index  $q$  is 1.51.

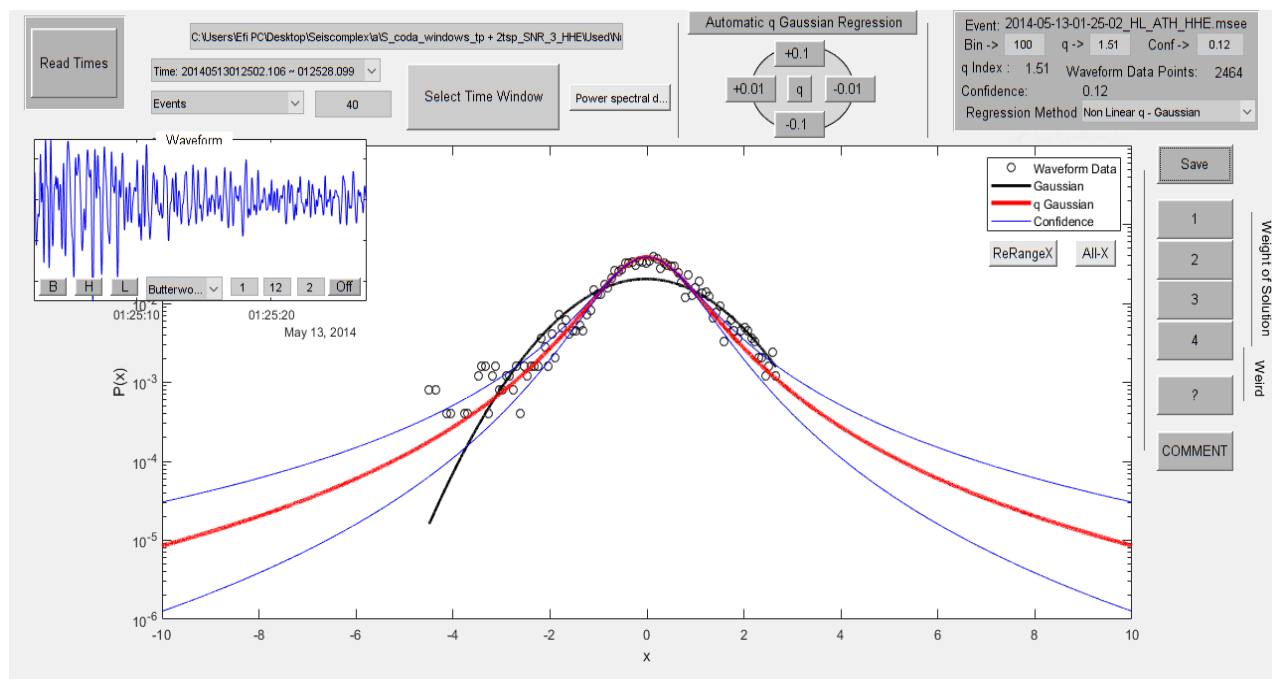


Figure 8.2.70

In figure 8.2.71 the time origin of the earthquake is 27/05/2014 at 11:21:30, latitude 37.54, longitude 22.86, depth 78km, magnitude 3.8 at 5.3 km ESE of Nafplio. The value of the index  $q$  is 1.61.

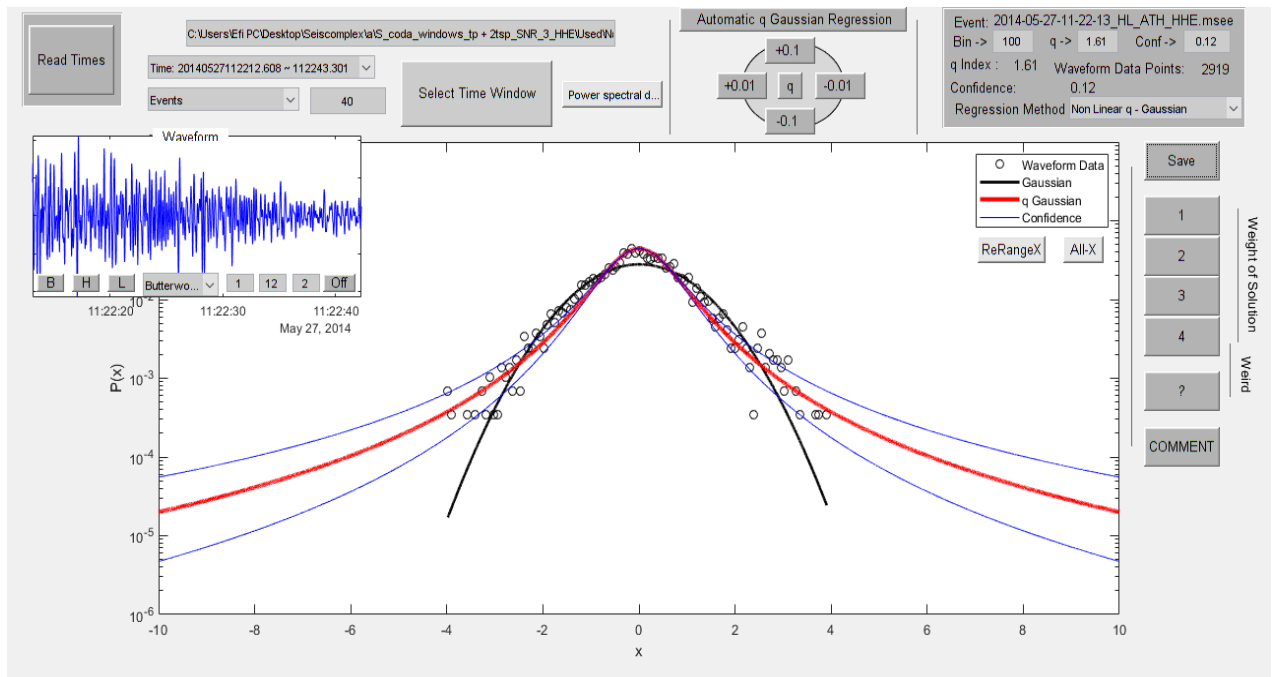


Figure 8.2.71

In figure 8.2.72 the time origin of the earthquake is 17/11/2014 at 23:40:36, latitude 38.65, longitude 23.37, depth 21 km, magnitude 3.8 at 28.8 km NW of Chalkida. The value of the index  $q$  is 1.6.

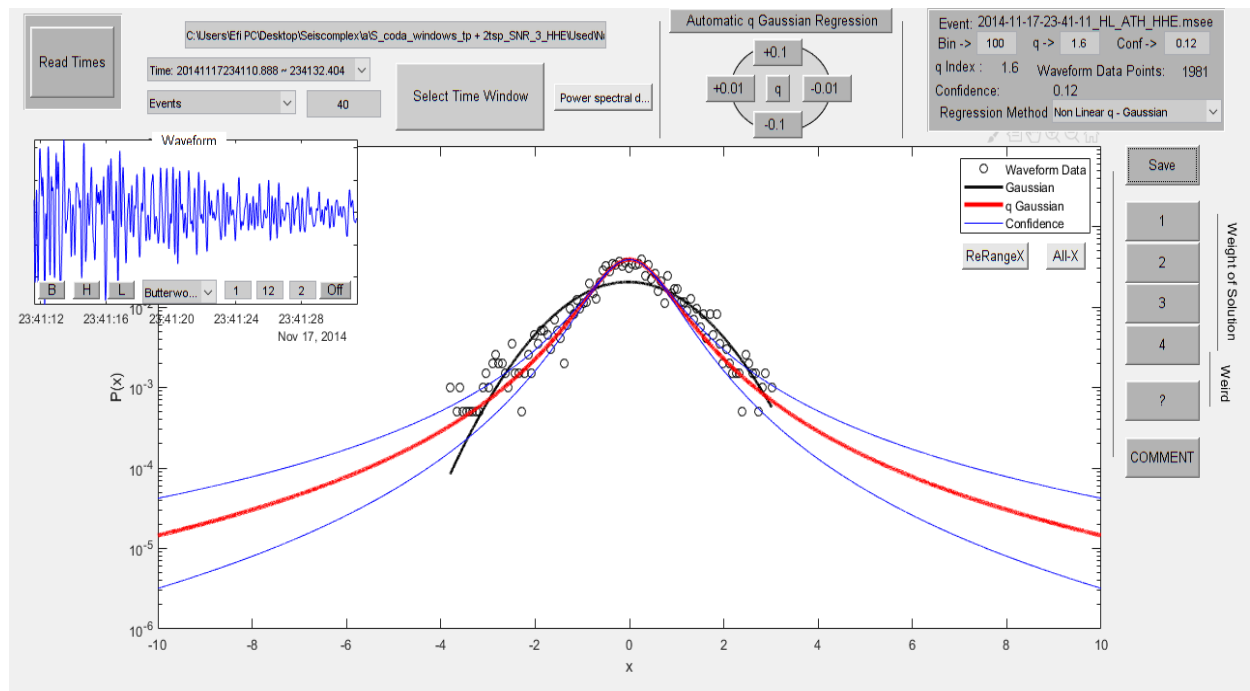


Figure 8.2.72

In figure 8.2.73 the time origin of the earthquake is 09/04/2016 at 01:36:11, latitude 38.63, longitude 24.45, depth 26km, magnitude 3.8 at 32.0 km SSW of Skyros. The value of the index  $q$  is 1.8.

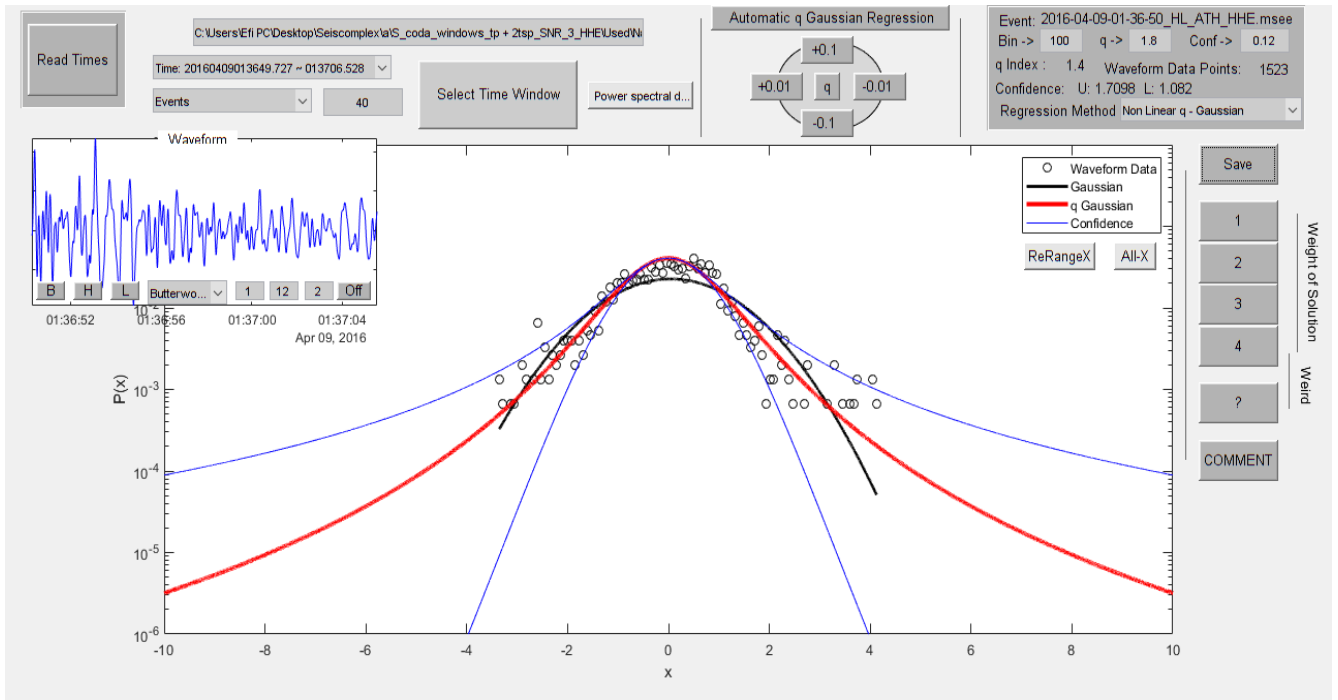


Figure 8.2.73

In figure 8.2.74 the time origin of the earthquake is 09/05/2016 at 17:29:19, latitude 38.85, longitude 23.62, depth 19km, magnitude 3.8 at 37.1 km SSE of Skiathos. The value of the index  $q$  is 1.74.

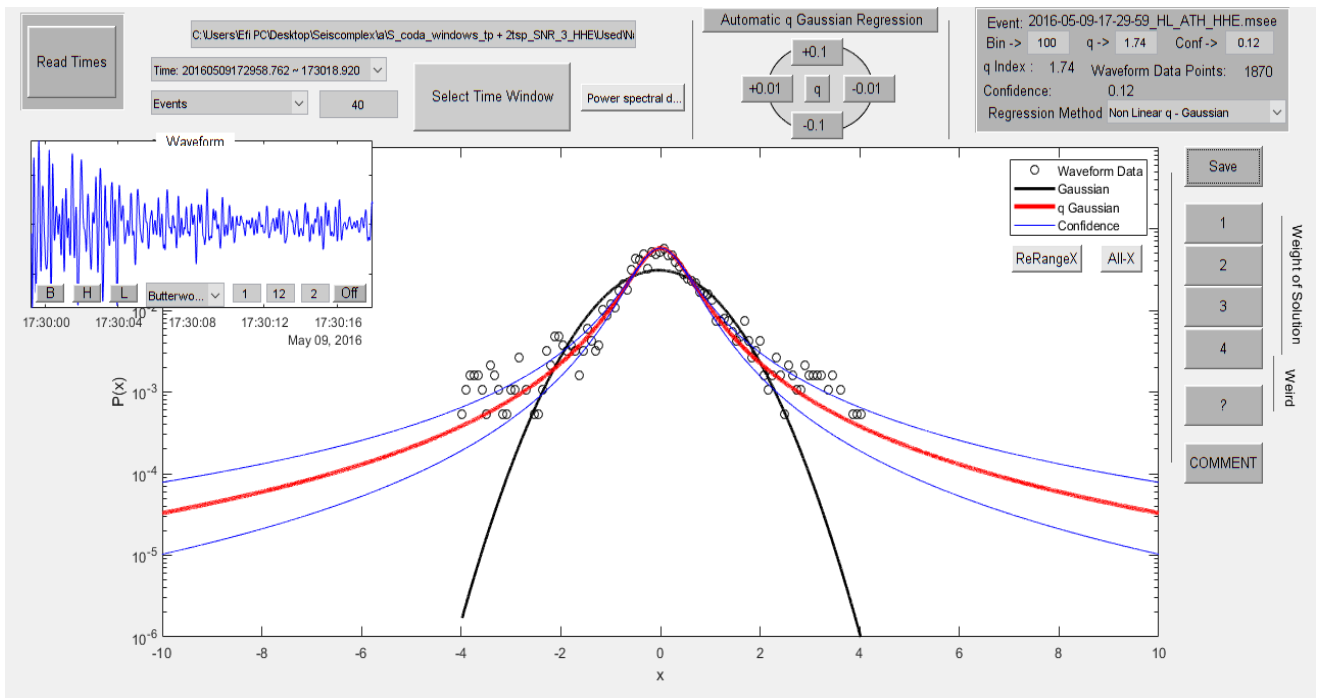


Figure 8.2.74

In figure 8.2.75 the time origin of the earthquake is 09/05/2016 at 22:57:01, latitude 39.14, longitude 24.15, depth 15km, magnitude 3.8 at 44.3 km NW of Skyros. The value of the index  $q$  is 1.74.

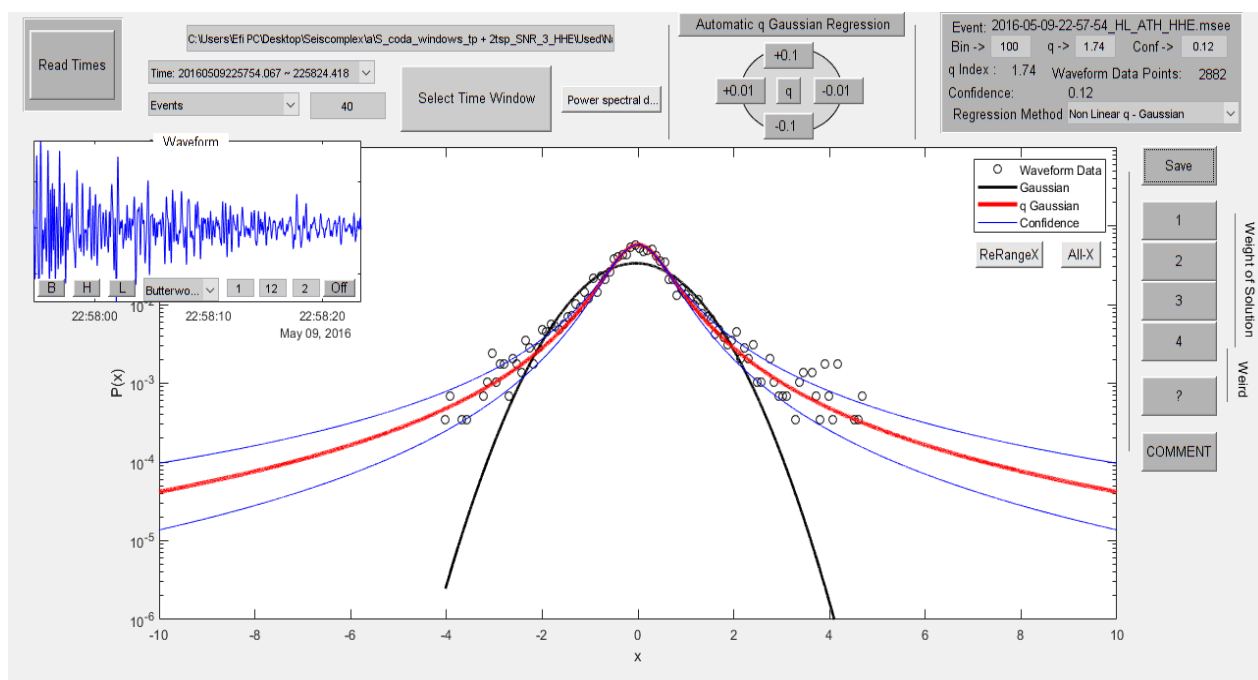


Figure 8.2.75

In figure 8.2.76 the time origin of the earthquake is 23/12/2018 at 22:34:10, latitude 37.3258, longitude 23.945, depth 28km, magnitude 3.8 at 50.4 km WNW of Seriphos. The value of the index  $q$  is 1.51.

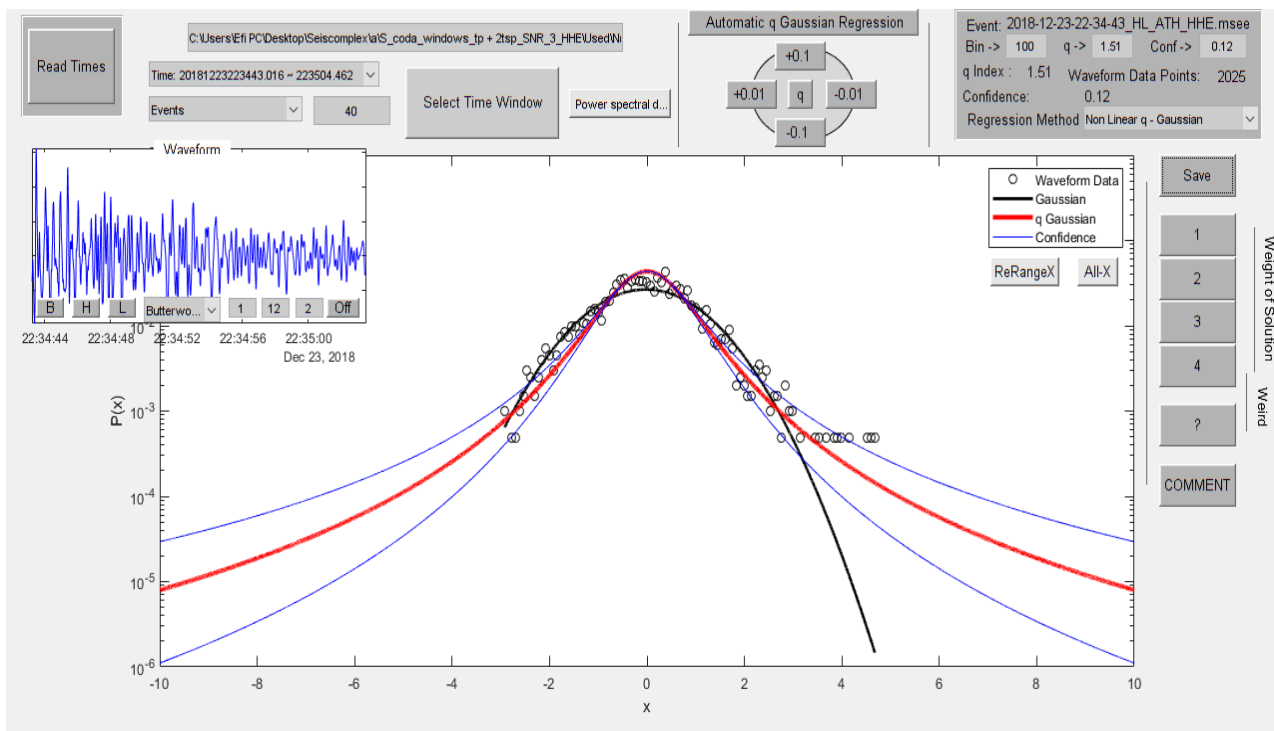


Figure 8.2.76

In figure 8.2.77 the time origin of the earthquake is 24/11/2019 at 18:34:57, latitude 39.4579, longitude 24.0852, depth 15km, magnitude 3.8 at 61.1 km ENE of Skiathos. The value of the index  $q$  is 1.6.

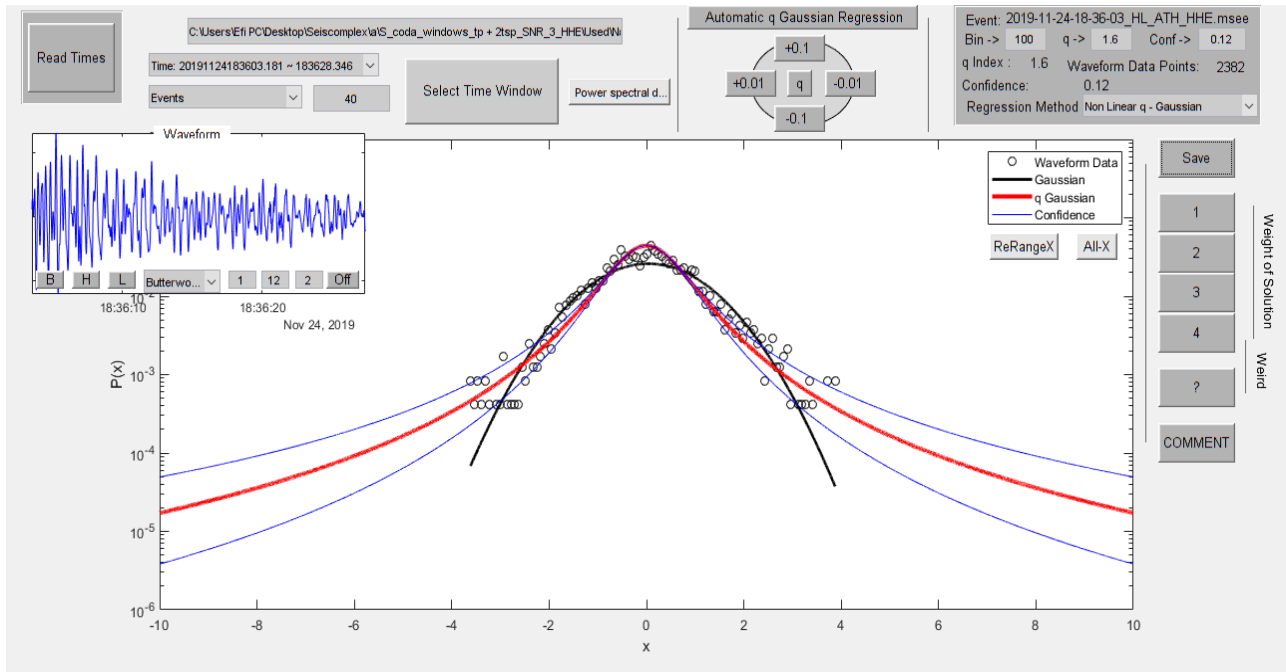


Figure 8.2.77

In figure 8.2.78 the time origin of the earthquake is 11/01/2011 at 15:46:45, latitude 38.75, longitude 22.2, depth 23km, magnitude 3.7 at 26.2 km SW of Lamia. The value of the index  $q$  is 1.3.

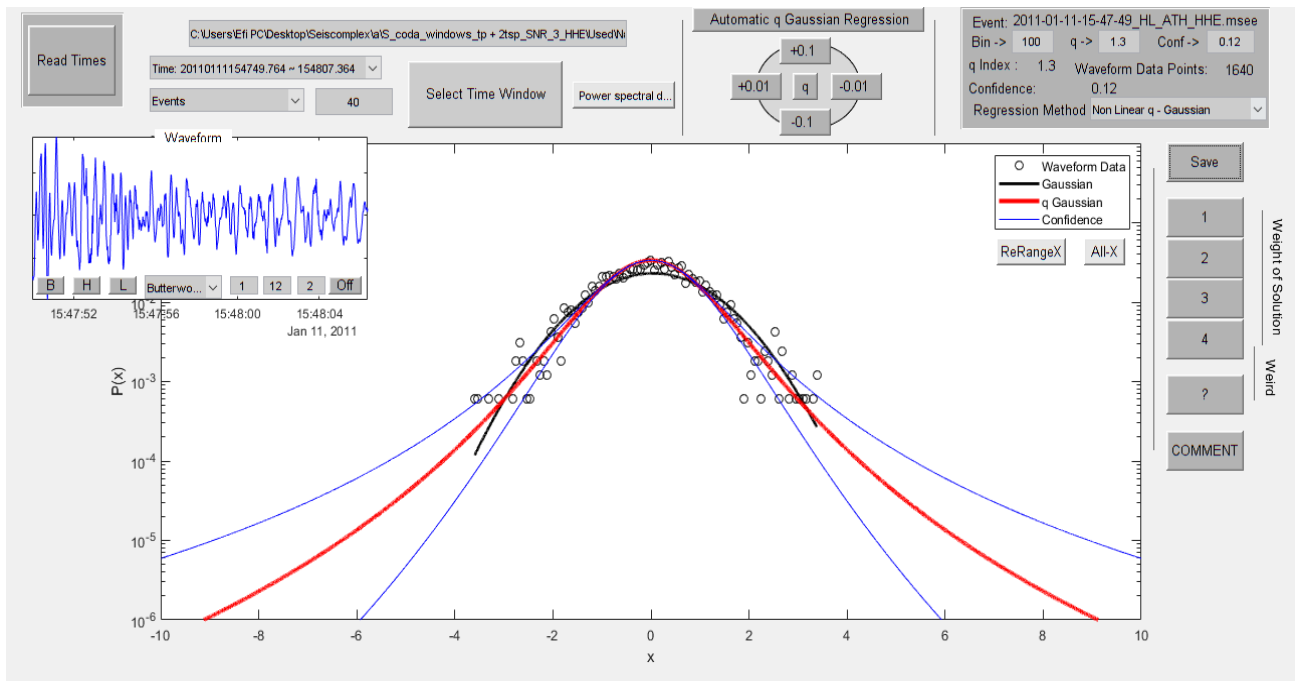


Figure 8.2.78

In figure 8.2.79 the time origin of the earthquake is 13/02/2011 at 00:17:22, latitude 38.71, longitude 22.81, depth 17km, magnitude 3.7 at 17.7 km WNW of Atalanti. The value of the index  $q$  is 1.69.

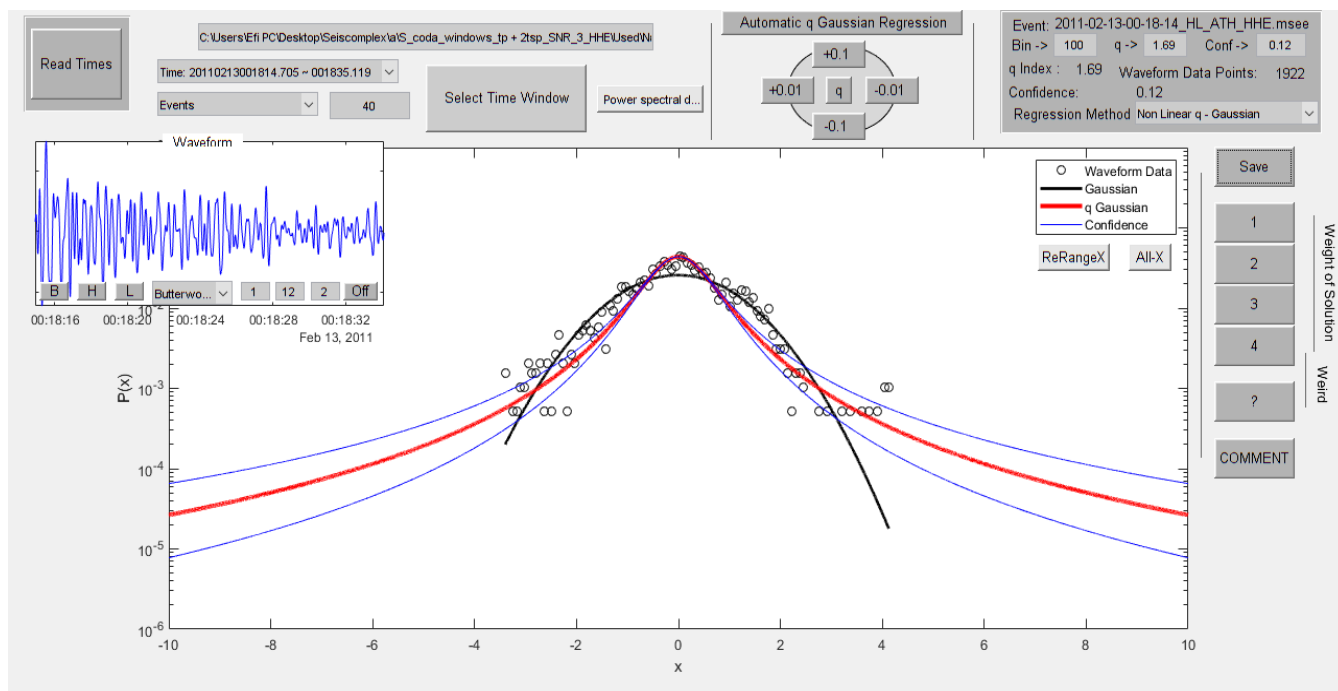


Figure 8.2.79

In figure 8.2.80 the time origin of the earthquake is 12/09/2011 at 14:29:22, latitude 38.72, longitude 23.39, depth 21km, magnitude 3.7 at 33.8 km NNW of Chalkida. The value of the index  $q$  is 1.55.

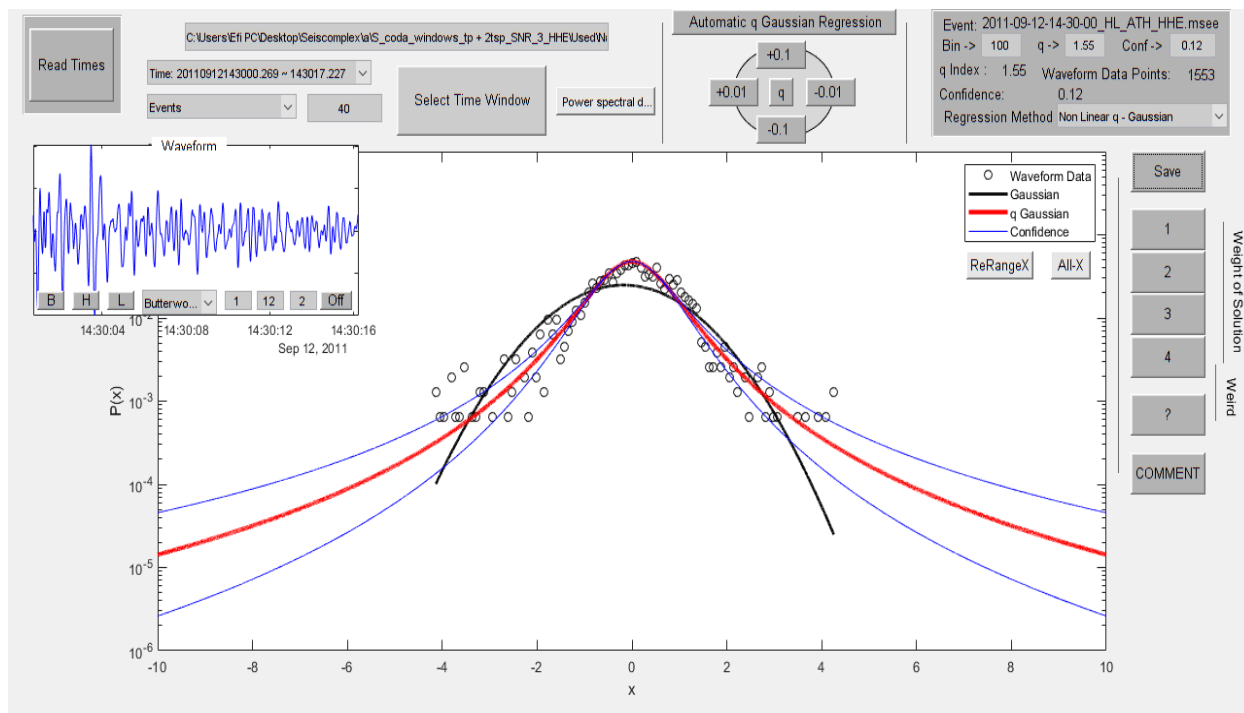


Figure 8.2.80

In figure 8.2.81 the time origin of the earthquake is 13/03/2013 at 23:09:01, latitude 39.19, longitude 23.47, depth 15km, magnitude 3.7 at 2.8 km NNW of Skiathos. The value of the index  $q$  is 1.6.

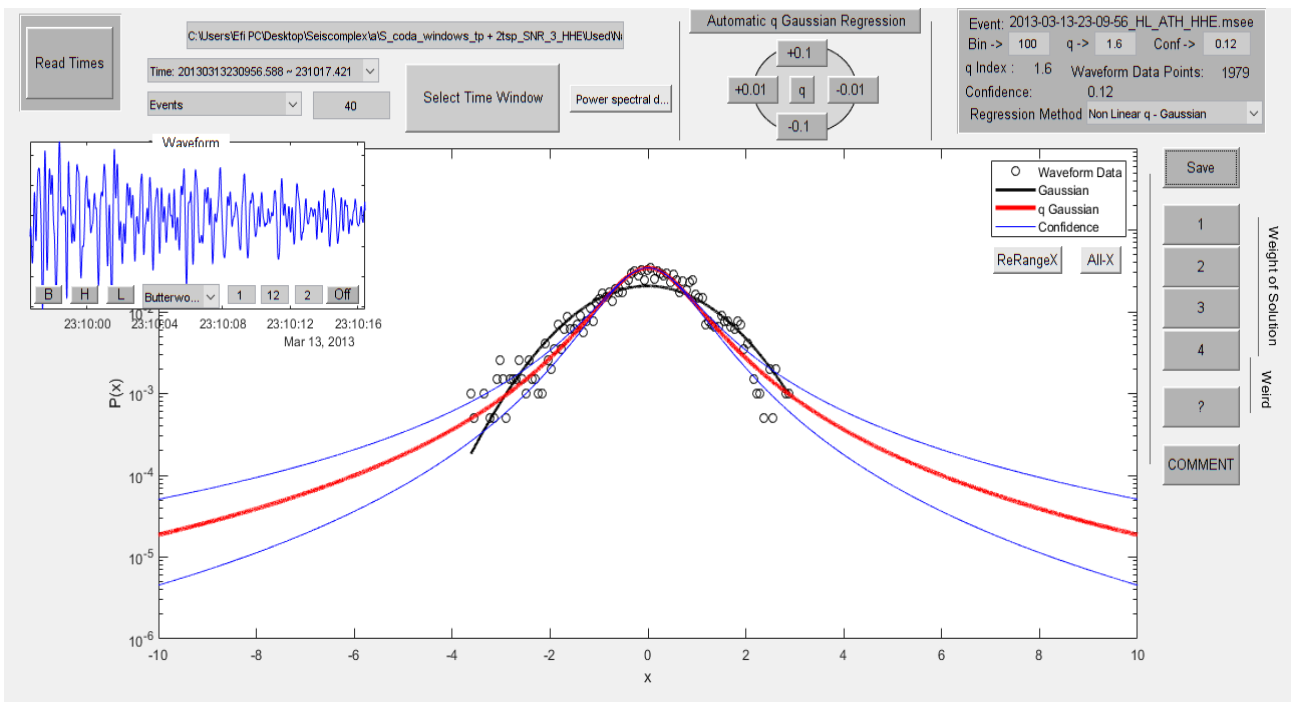


Figure 8.2.81

In figure 8.2.82 the time origin of the earthquake is 28/04/2014 at 03:49:50, latitude 38.69, longitude 22.81, depth 23km, magnitude 3.7 at 17.0 km WNW of Atalanti. The value of the index  $q$  is 1.77.

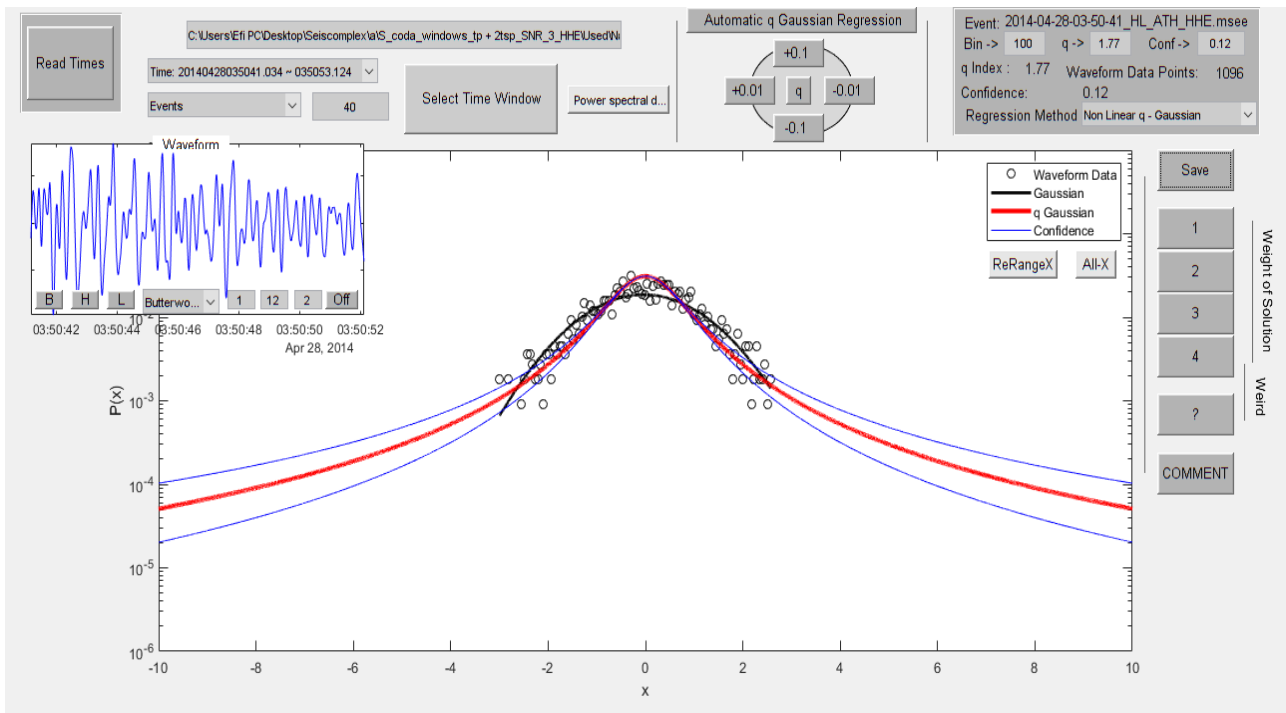


Figure 8.2.82

In figure 8.2.83 the time origin of the earthquake is 28/06/2014 at 19:09:47, latitude 37.46, longitude 22.85, depth 20km, magnitude 3.7 at 12.1 km SSE of Nafplio. The value of the index  $q$  is 1.66.

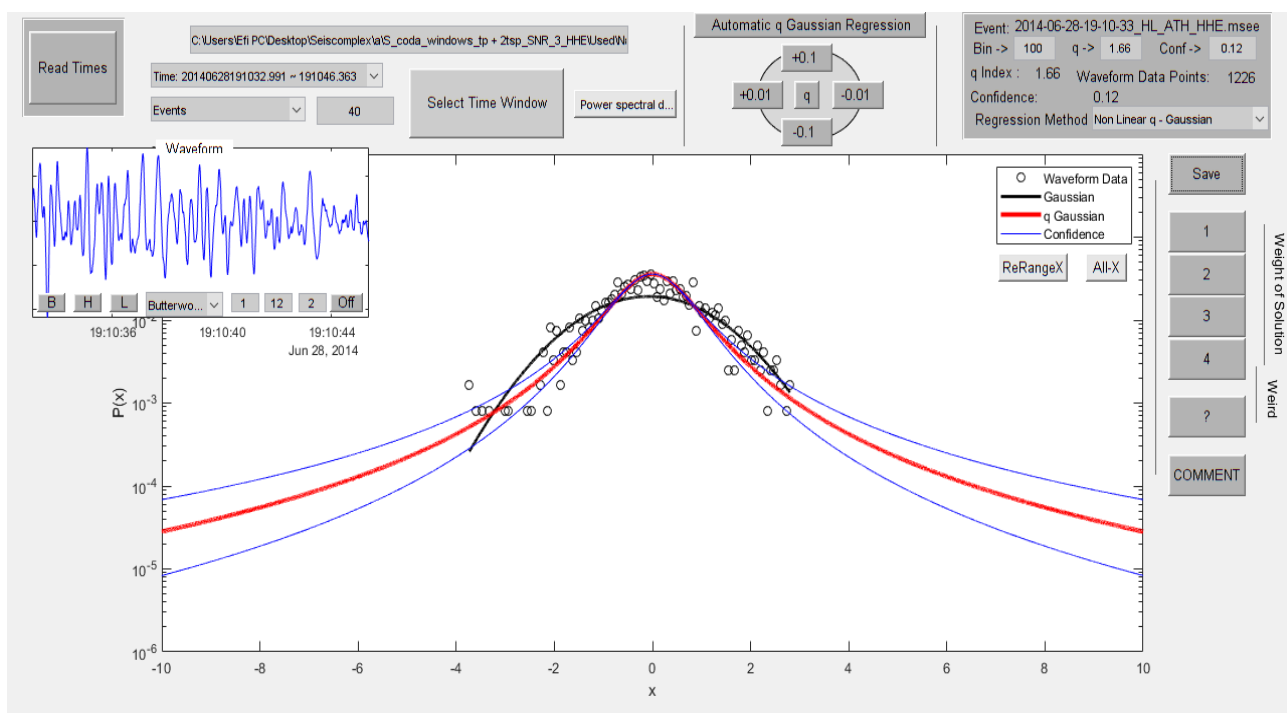


Figure 8.2.83

In figure 8.2.84 the time origin of the earthquake is 30/10/2014 at 06:09:08, latitude 38.14, longitude 22.63, depth 15km, magnitude 3.7 at 34.7 km NW of Korinthos. The value of the index  $q$  is 1.45.

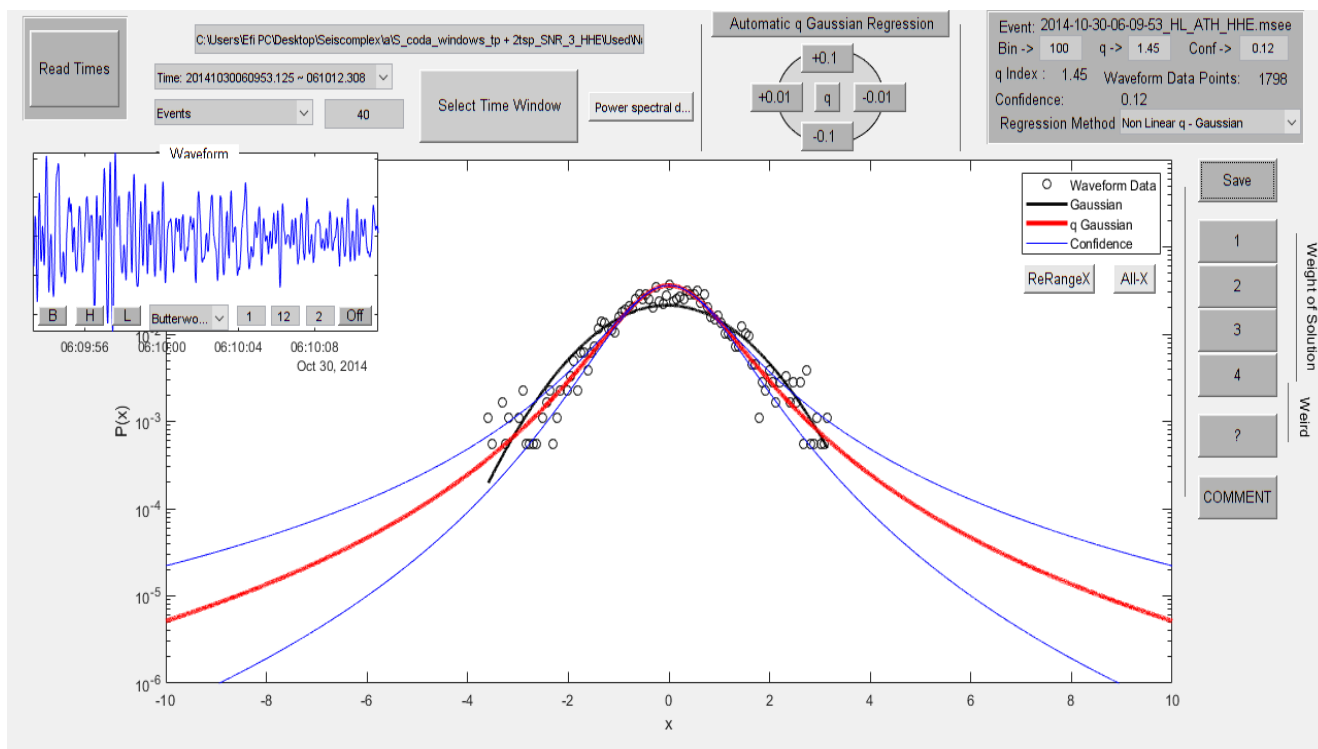


Figure 8.2.84

In figure 8.2.85 the time origin of the earthquake is 05/11/2014 at 20:51:39, latitude 39.14, longitude 24.19, depth 25km, magnitude 3.7 at 41.5 km NW of Skyros. The value of the index  $q$  is 1.81.

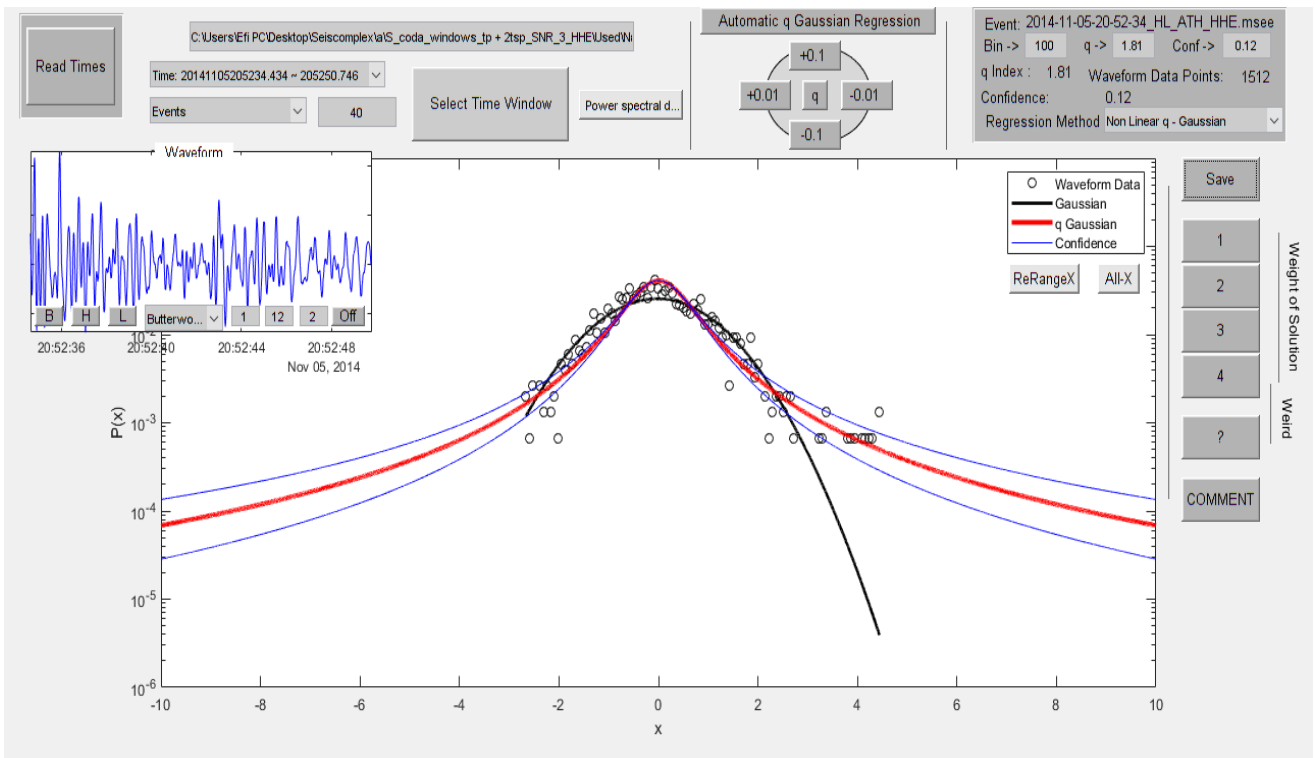


Figure 8.2.85

In figure 8.2.86 the time origin of the earthquake is 15/11/2014 at 08:11:31, latitude 38.99, longitude 23.7, depth 24km, magnitude 3.7 at 27.1 km SE of Skiathos. The value of the index  $q$  is 1.64.

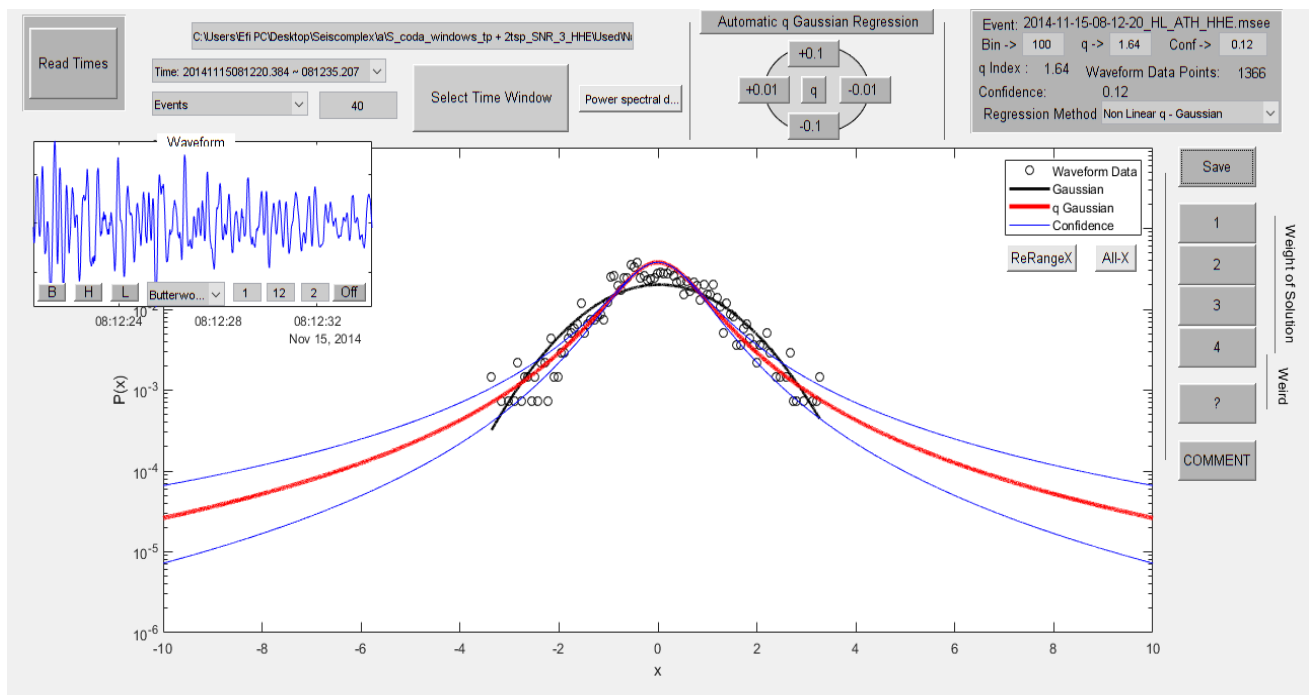


Figure 8.2.86

In figure 8.2.87 the time origin of the earthquake is 18/11/2014 at 00:53:59, latitude 38.63, longitude 23.43, depth 23km, magnitude 3.7 at 23.7 km NW of Chalkida. The value of the index  $q$  is 1.73.

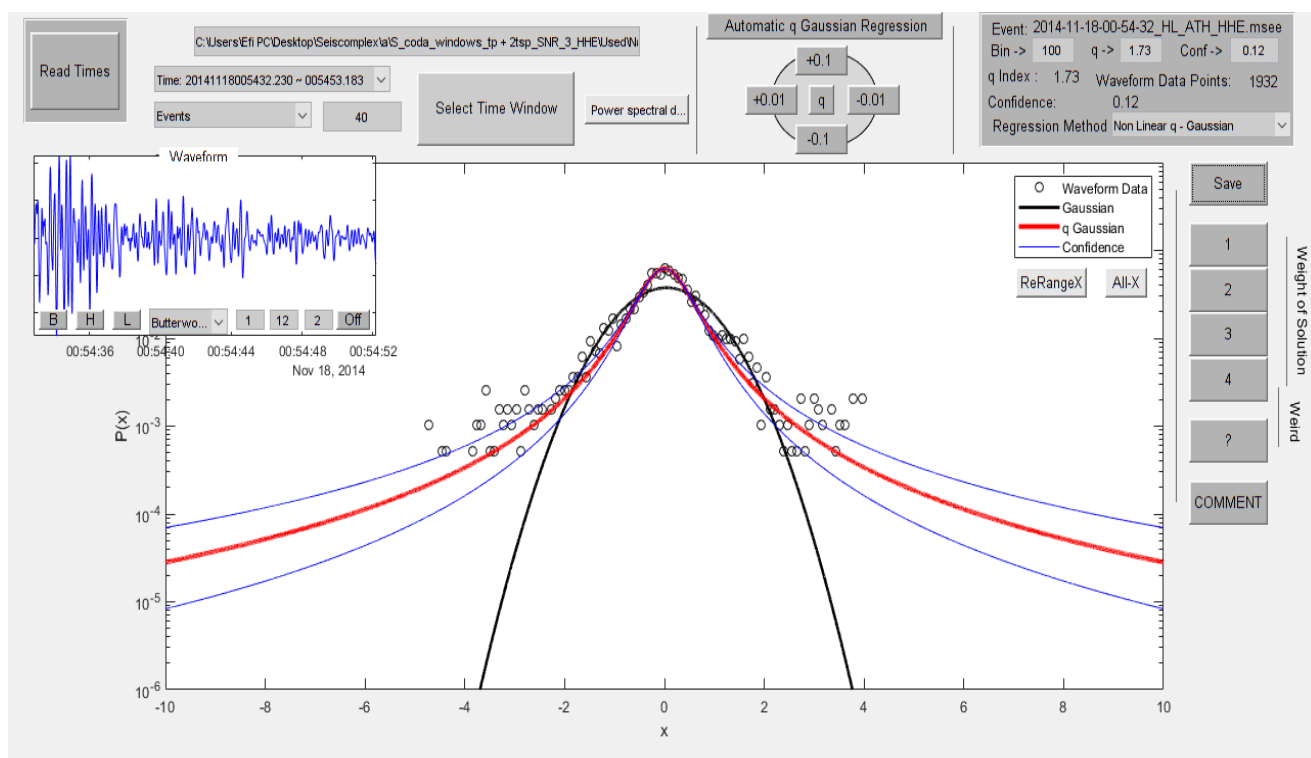


Figure 8.2.87

In figure 8.2.88 the time origin of the earthquake is 14/12/2014 at 08:16:33, latitude 38.62, longitude 22.88, depth 18km, magnitude 3.7 at 10.9 km WSW of Atalanti. The value of the index  $q$  is 1.59.

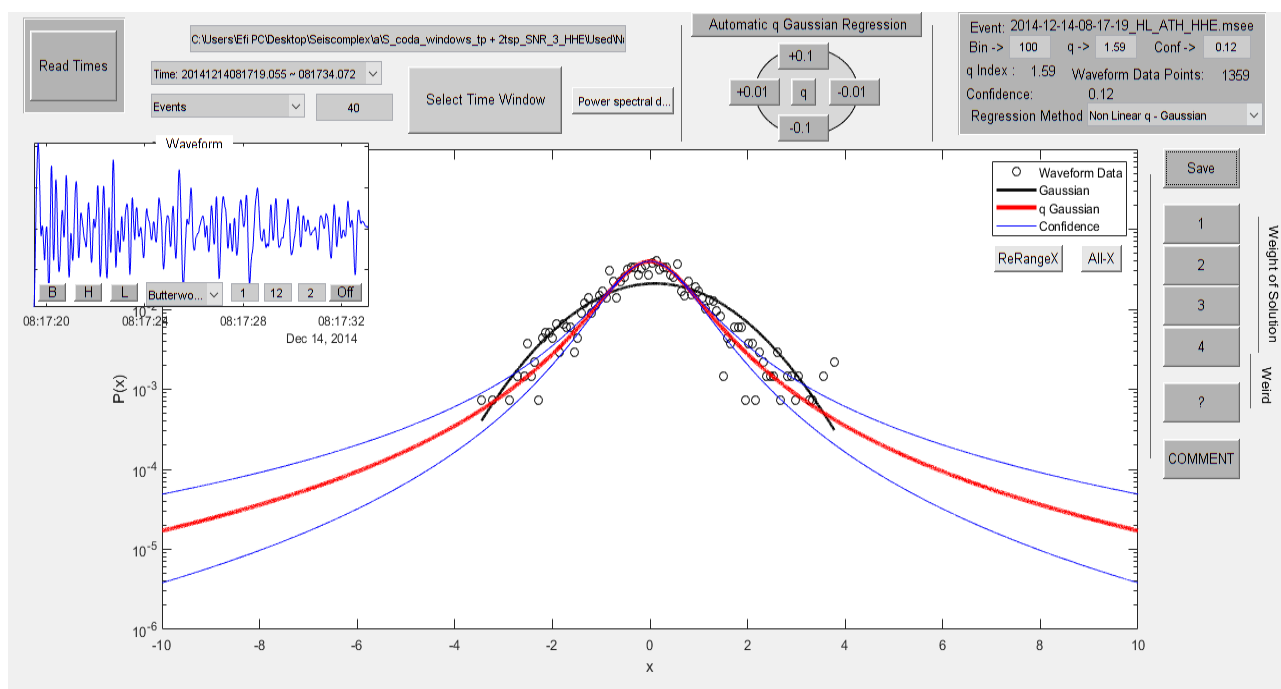


Figure 8.2.88

In figure 8.2.89 the time origin of the earthquake is 09/03/2015 at 03:24:41, latitude 39.31, longitude 24.02, depth 16km, magnitude 3.7 at 48.9 km ENE of Skiathos. The value of the index  $q$  is 1.63.

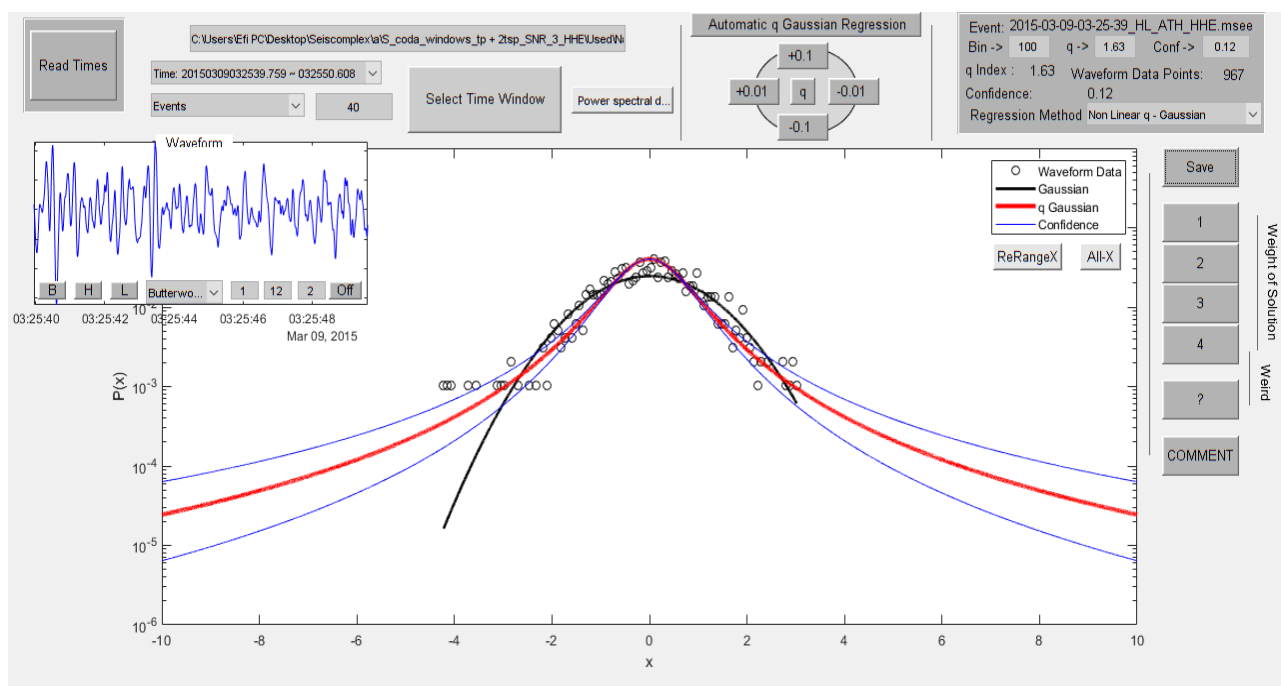


Figure 8.2.89

In figure 8.2.90 the time origin of the earthquake is 28/07/2016 at 16:17:29, latitude 38.17, longitude 22.94, depth 15km, magnitude 3.7 at 25.8 km N of Korinthos. The value of the index  $q$  is 1.8.

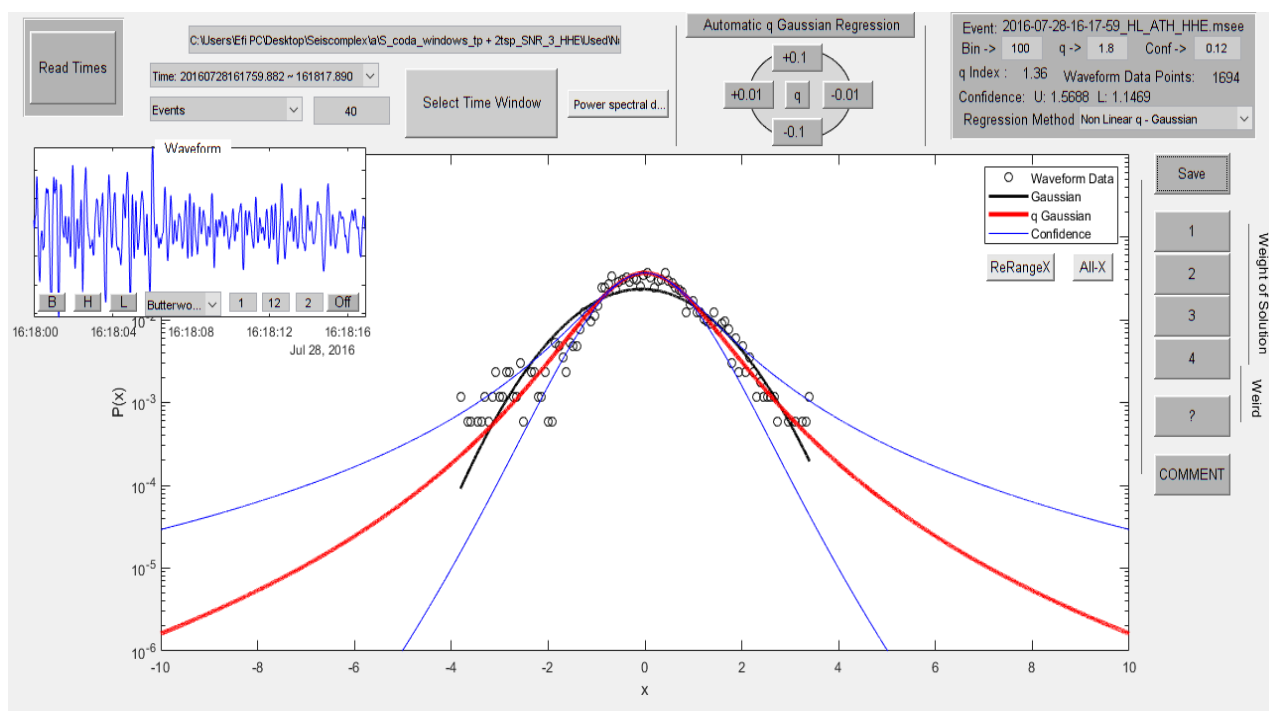


Figure 8.2.90

In figure 8.2.91 the time origin of the earthquake is 11/03/2010 at 09:54:08, latitude 38.12, longitude 23.26, depth 21km, magnitude 3.6 at 35.1 km NE of Korinthos. The value of the index  $q$  is 1.49.

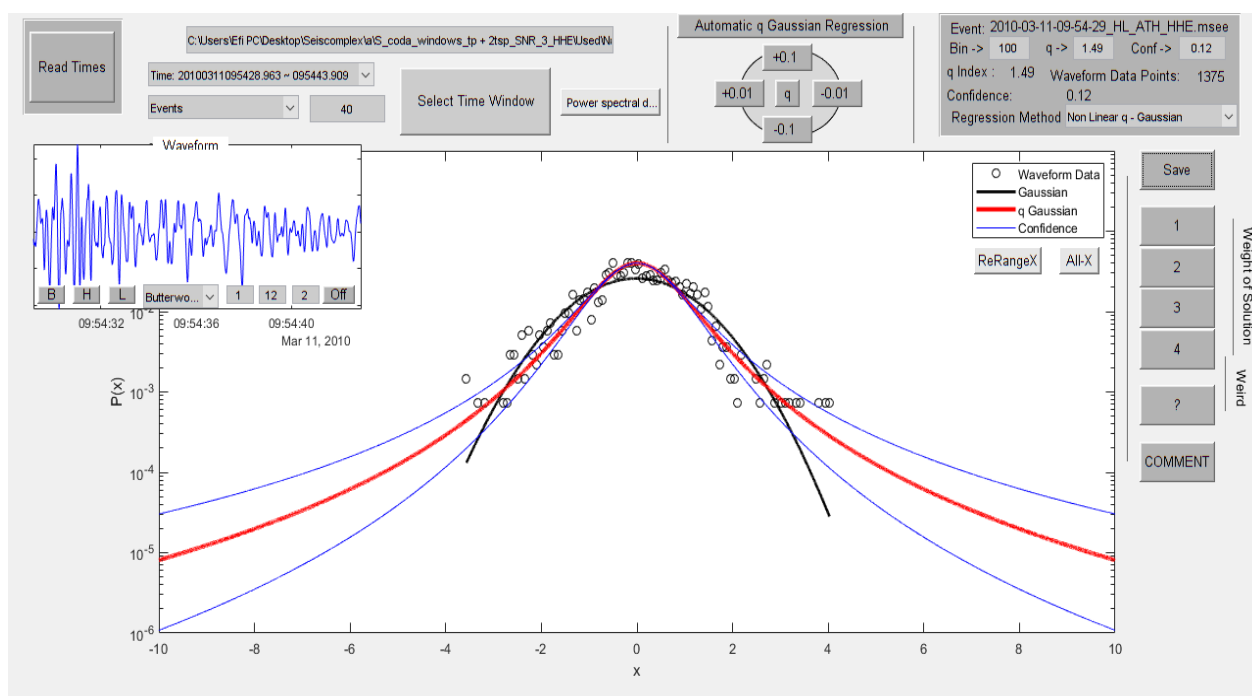


Figure 8.2.91

In figure 8.2.92 the time origin of the earthquake is 12/05/2010 at 06:59:22, latitude 38.62, longitude 23.78, depth 25km, magnitude 3.6 at 23.4 km NE of Chalkida. The value of the index  $q$  is 1.67.

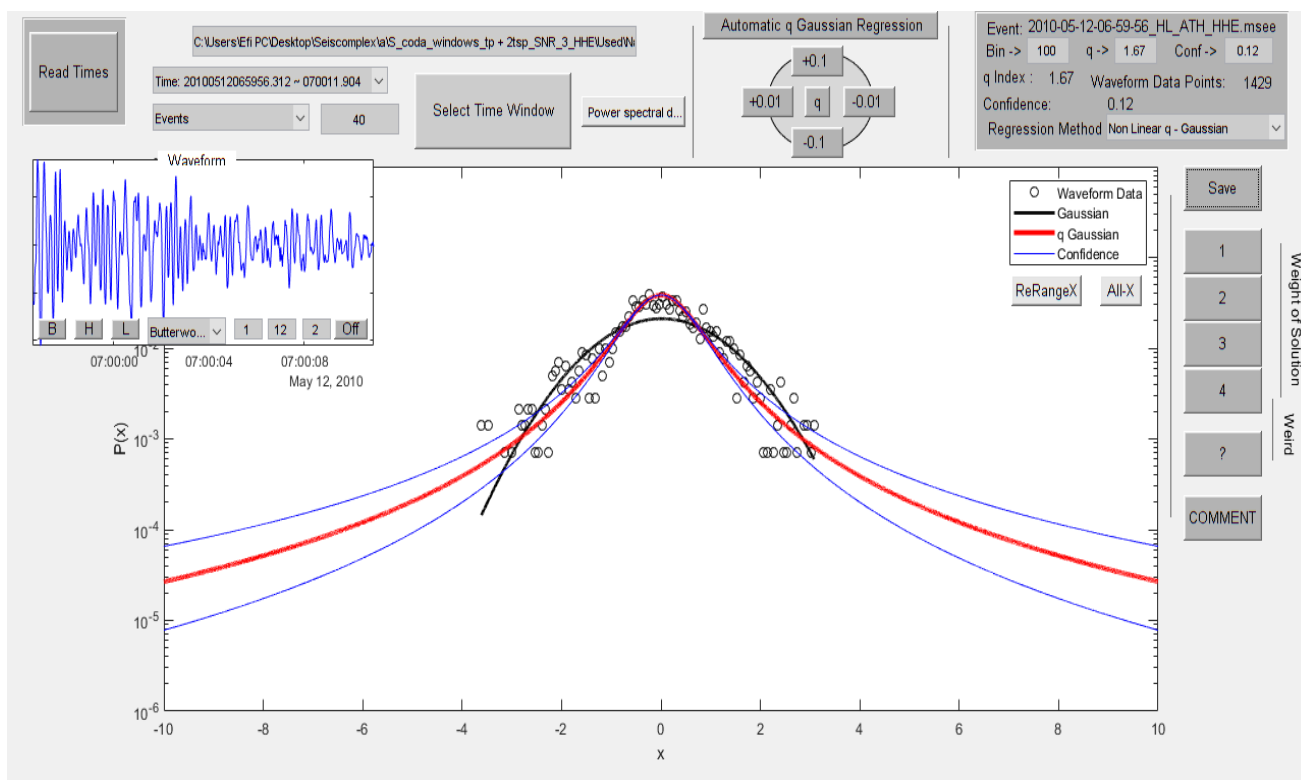


Figure 8.2.92

In figure 8.2.93 the time origin of the earthquake is 28/07/2010 at 13:55:27, latitude 37.47, longitude 23.32, depth 29km, magnitude 3.6 at 46.4 km ESE of Nafplio. The value of the index  $q$  is 2.17.

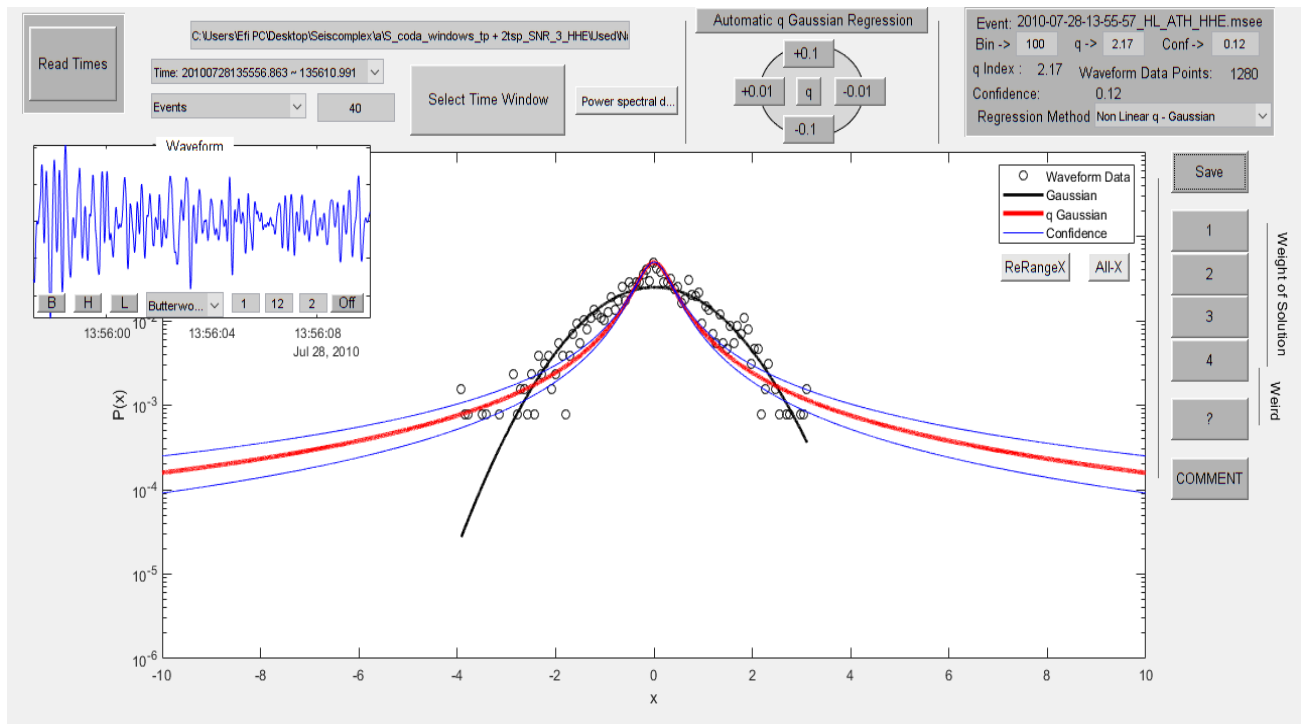


Figure 8.2.93

In figure 8.2.94 the time origin of the earthquake is 06/09/2010 at 19:20:42, latitude 37.59, longitude 22.61, depth 56km, magnitude 3.6 at 17.7 km W of Nafplio. The value of the index  $q$  is 1.6.

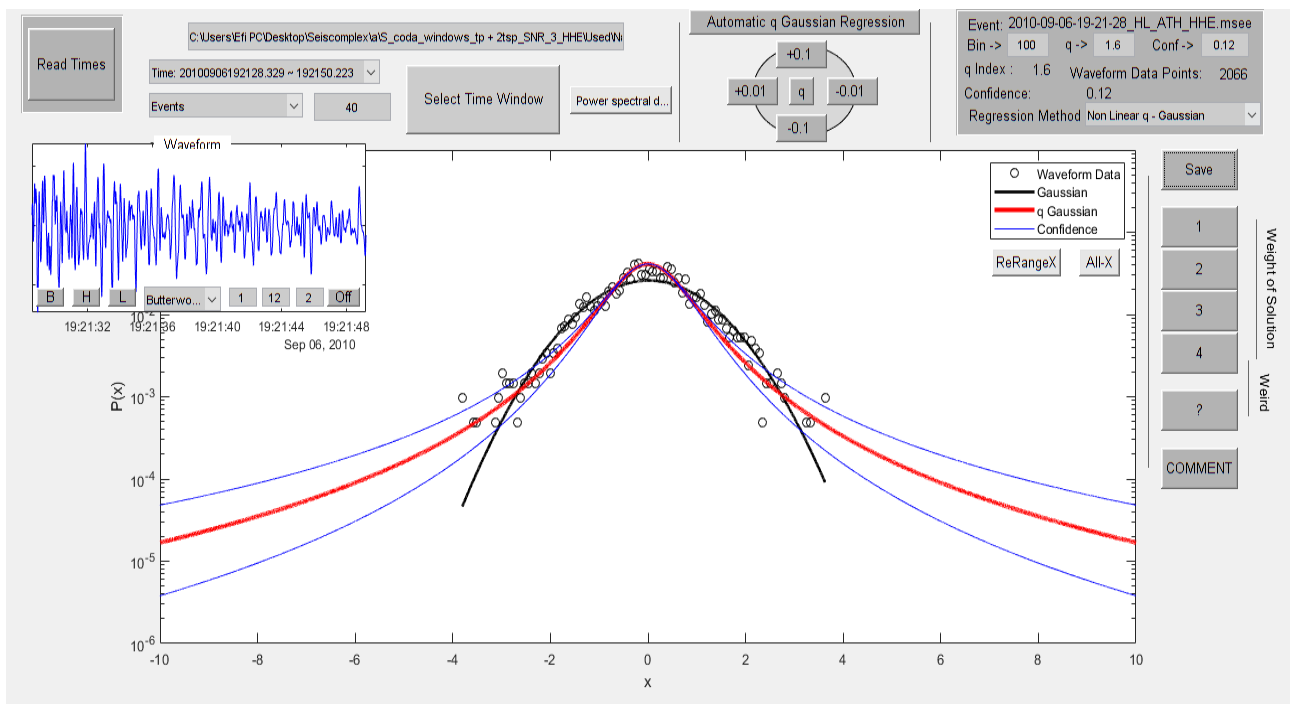


Figure 8.2.94

In figure 8.2.95 the time origin of the earthquake is 28/10/2010 at 04:04:46, latitude 38.36, longitude 22.25, depth 20km, magnitude 3.6 at 19.2 km NE of Aegion. The value of the index  $q$  is 1.72.

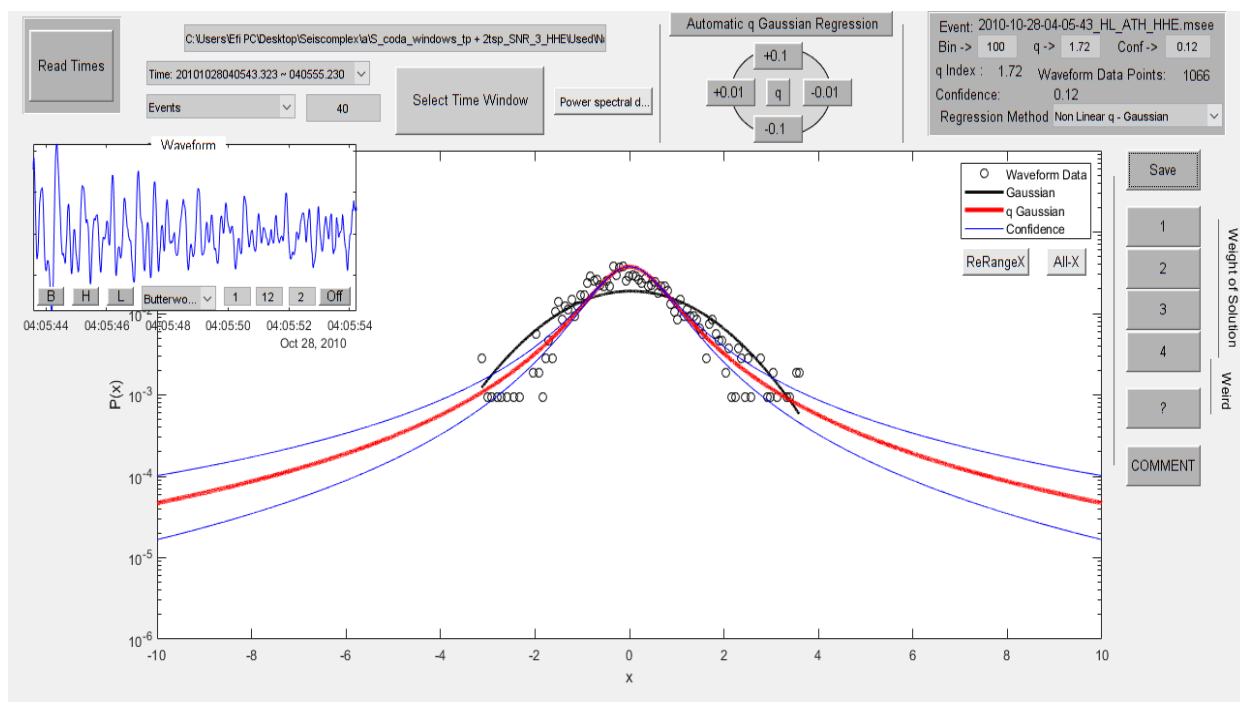


Figure 8.2.95

In figure 8.2.96 the time origin of the earthquake is 14/12/2010 at 13:58:52, latitude 38.06, longitude 22.78, depth 19km, magnitude 3.6 at 19.0 km NW of Korinthos. The value of the index  $q$  is 1.76.

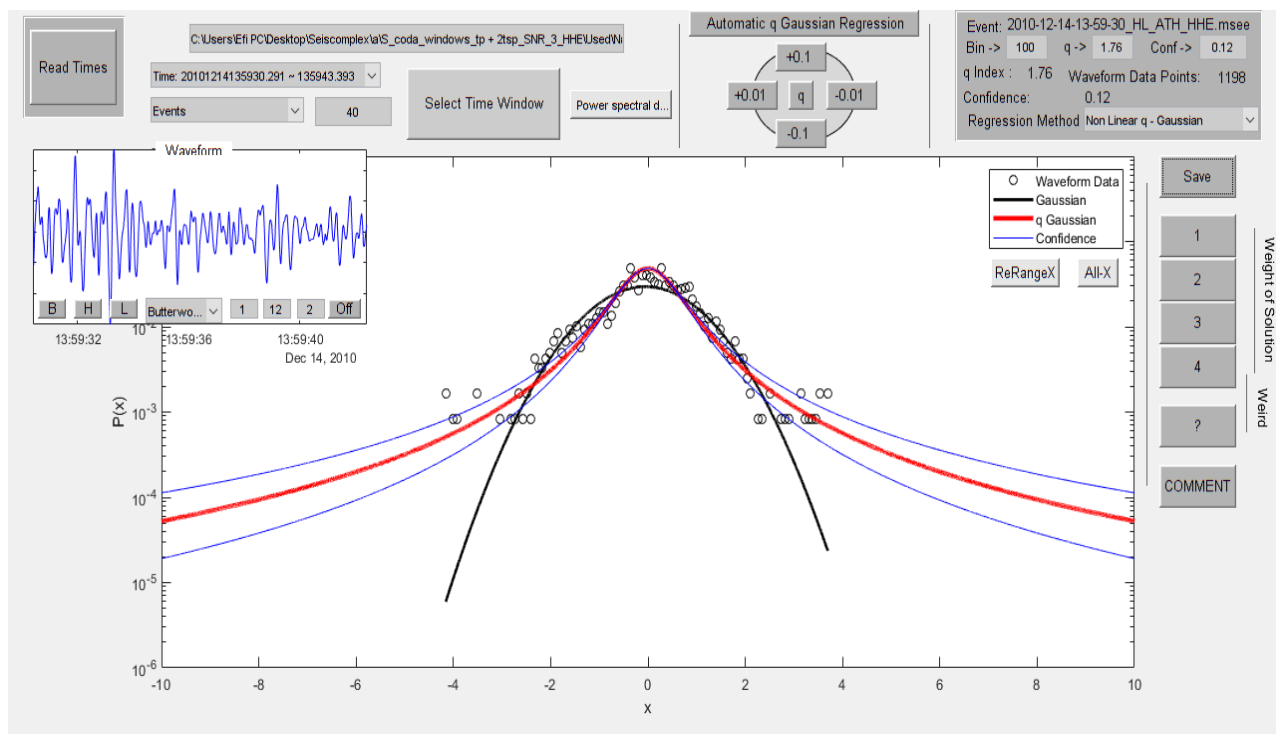


Figure 8.2.96

In figure 8.2.97 the time origin of the earthquake is 31/01/2011 at 17:23:13, latitude 37.87, longitude 22.7, depth 26km, magnitude 3.6 at 21.7 km WSW of Korinthos. The value of the index  $q$  is 1.42.

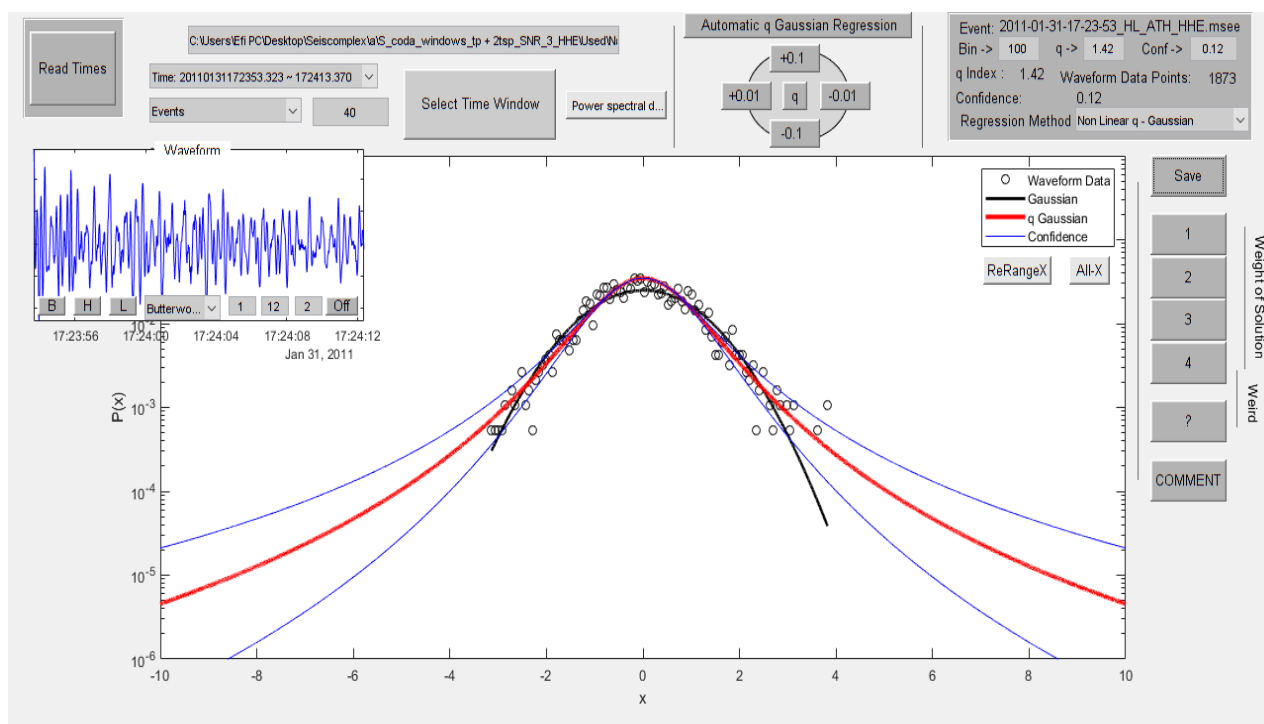


Figure 8.2.97

In figure 8.2.98 the time origin of the earthquake is 16/08/2012 at 21:22:53, latitude 38.28, longitude 22.55, depth 24km, magnitude 3.6 at 31.3 km SSE of Amfissa. The value of the index  $q$  is 1.66.

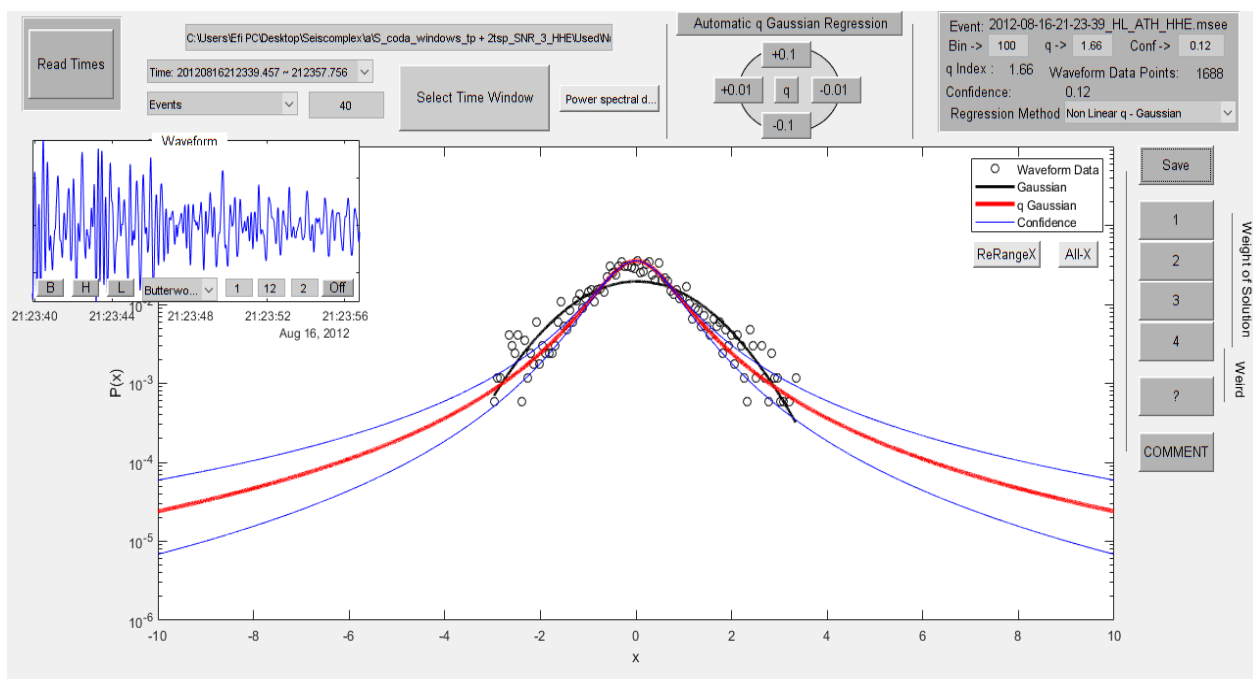


Figure 8.2.98

In figure 8.2.99 the time origin of the earthquake is 08/09/2013 at 06:22:10, latitude 38.59, longitude 23.76, depth 23km, magnitude 3.6 at 19.8 km NE of Chalkida. The value of the index  $q$  is 1.77.

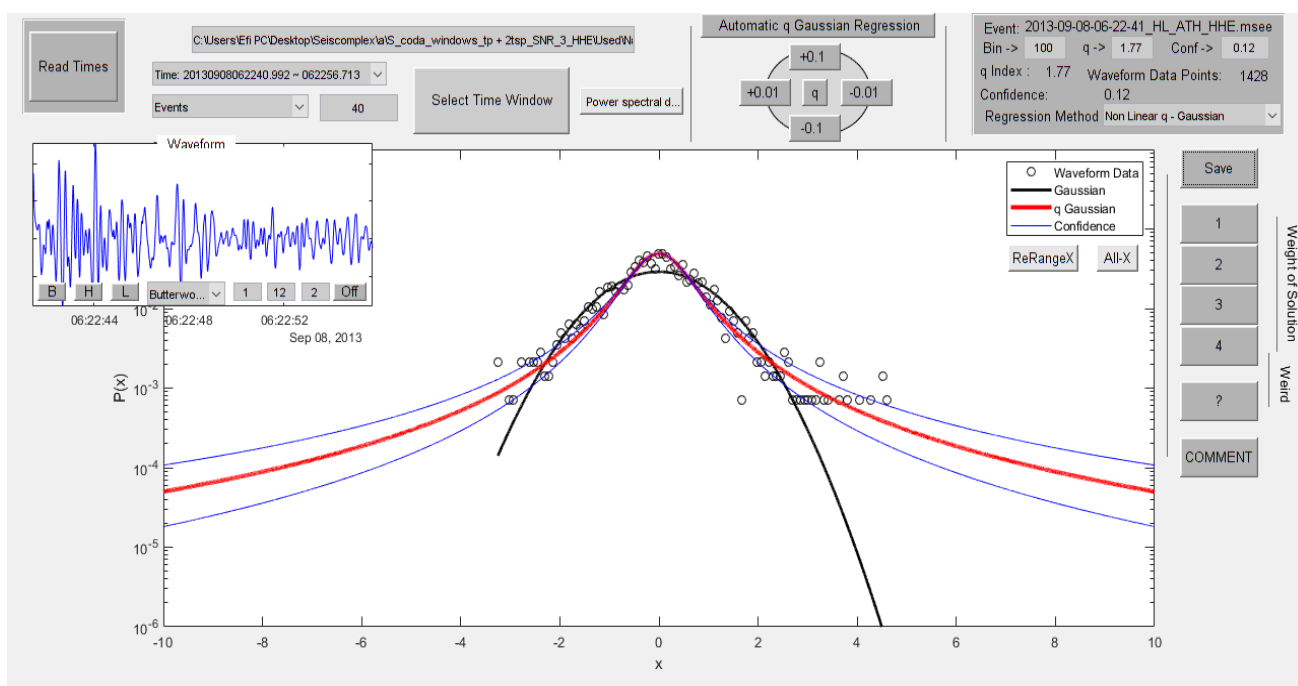


Figure 8.2.99

In figure 8.2.100 the time origin of the earthquake is 12/02/2014 at 07:41:00, latitude 37.93, longitude 22.6, depth 16km, magnitude 3.6 at 29.1 km W of Korinthos. The value of the index  $q$  is 1.58.

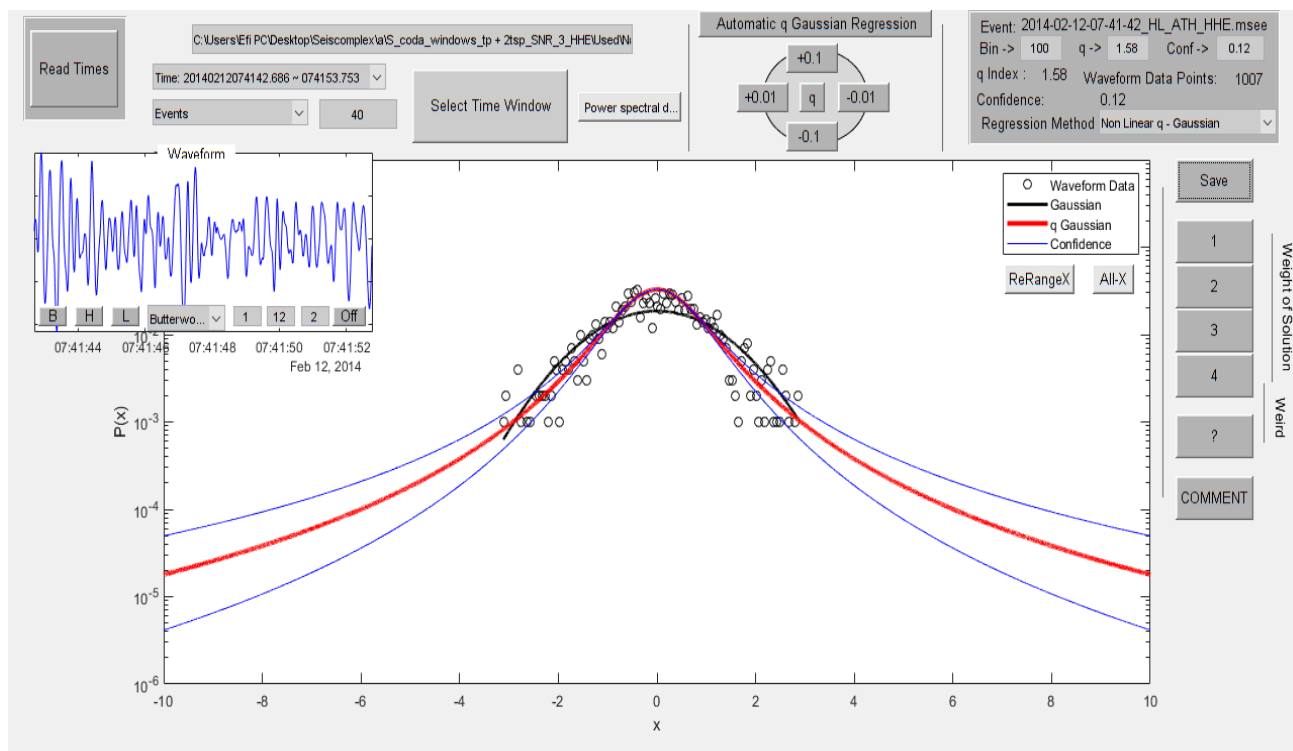


Figure 8.2.100

In figure 8.2.101 the time origin of the earthquake is 09/06/2014 at 22:02:57, latitude 39.17, longitude 23.75, depth 24km, magnitude 3.6 at 23.0 km E of Skiathos. The value of the index  $q$  is 1.73.

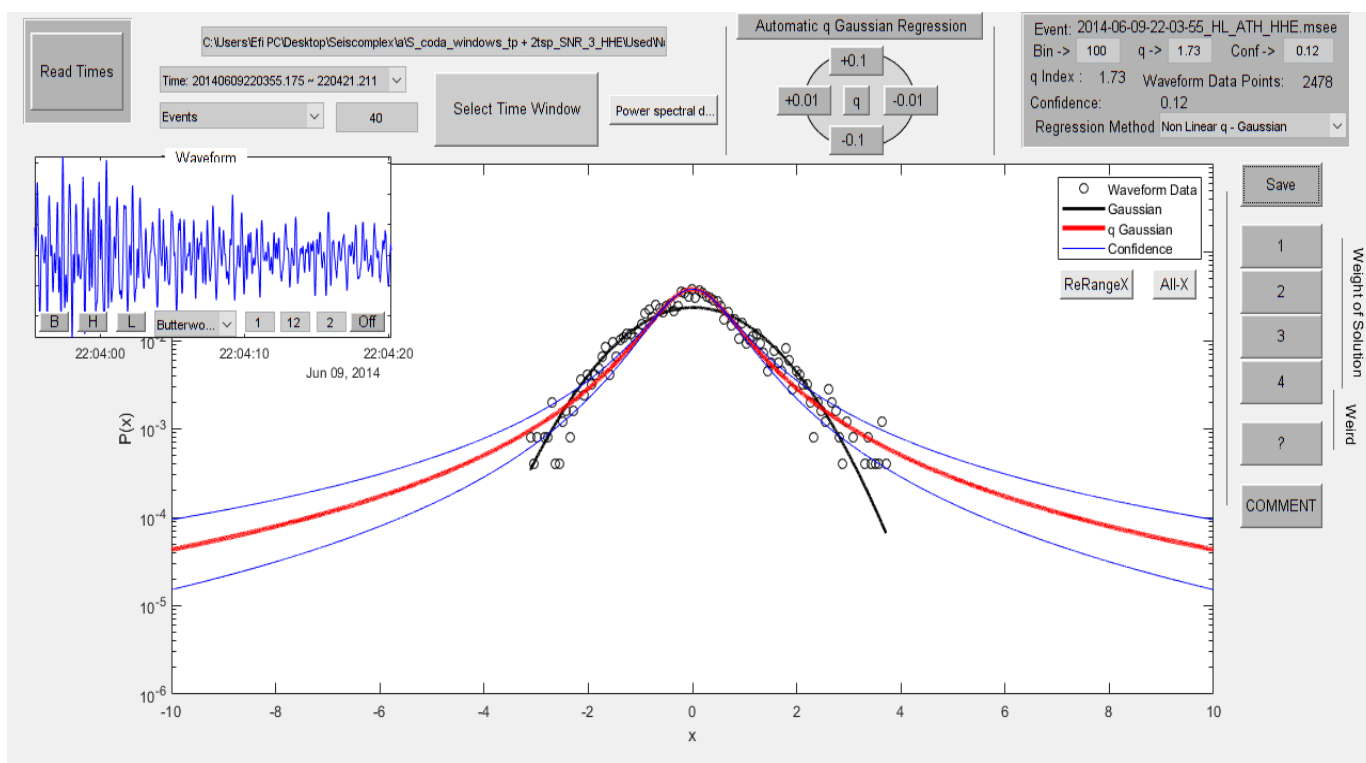


Figure 8.2.101

In figure 8.2.102 the time origin of the earthquake is 30/07/2014 at 00:55:04, latitude 38.04, longitude 24.12, depth 19km, magnitude 3.6 at 34.5 km E of Athens. The value of the index  $q$  is 1.85.

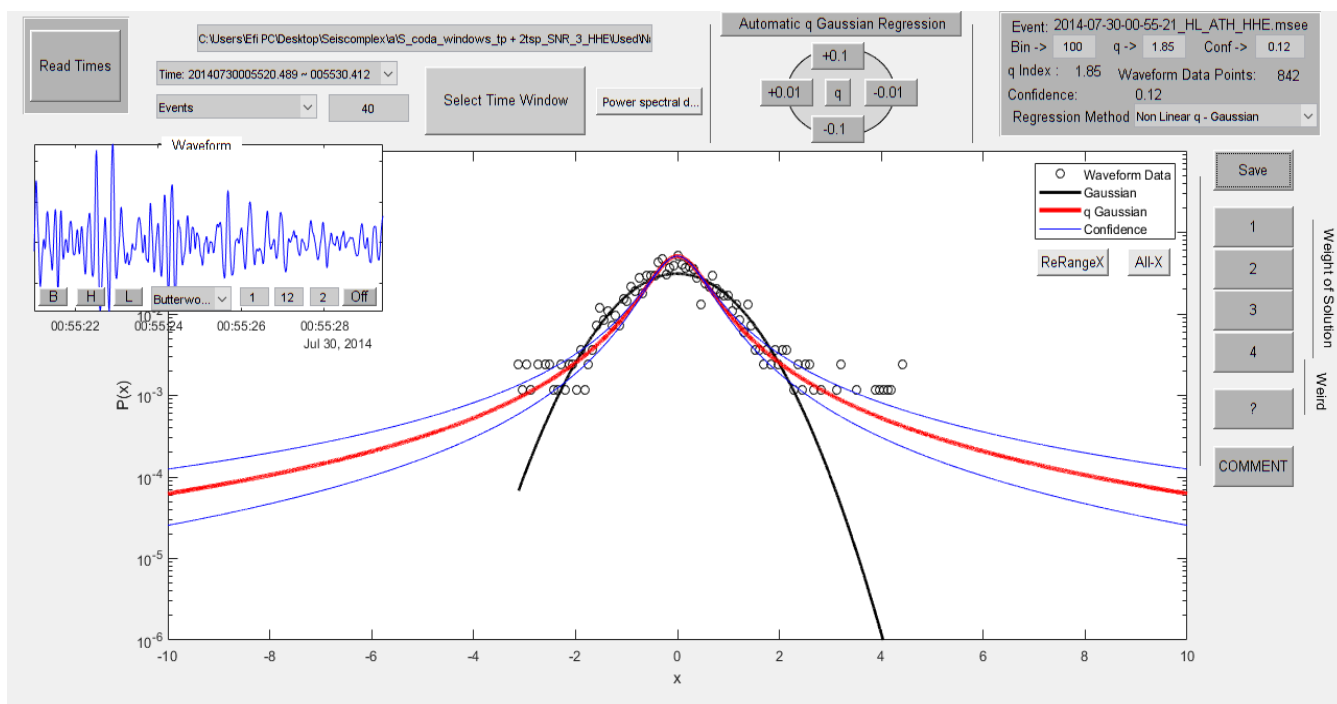


Figure 8.2.102

In figure 8.2.103 the time origin of the earthquake is 26/07/2016 at 16:59:47, latitude 37.63, longitude 23.5, depth 15km, magnitude 3.6 at 44.3 km SSW of Athens. The value of the index  $q$  is 1.8.

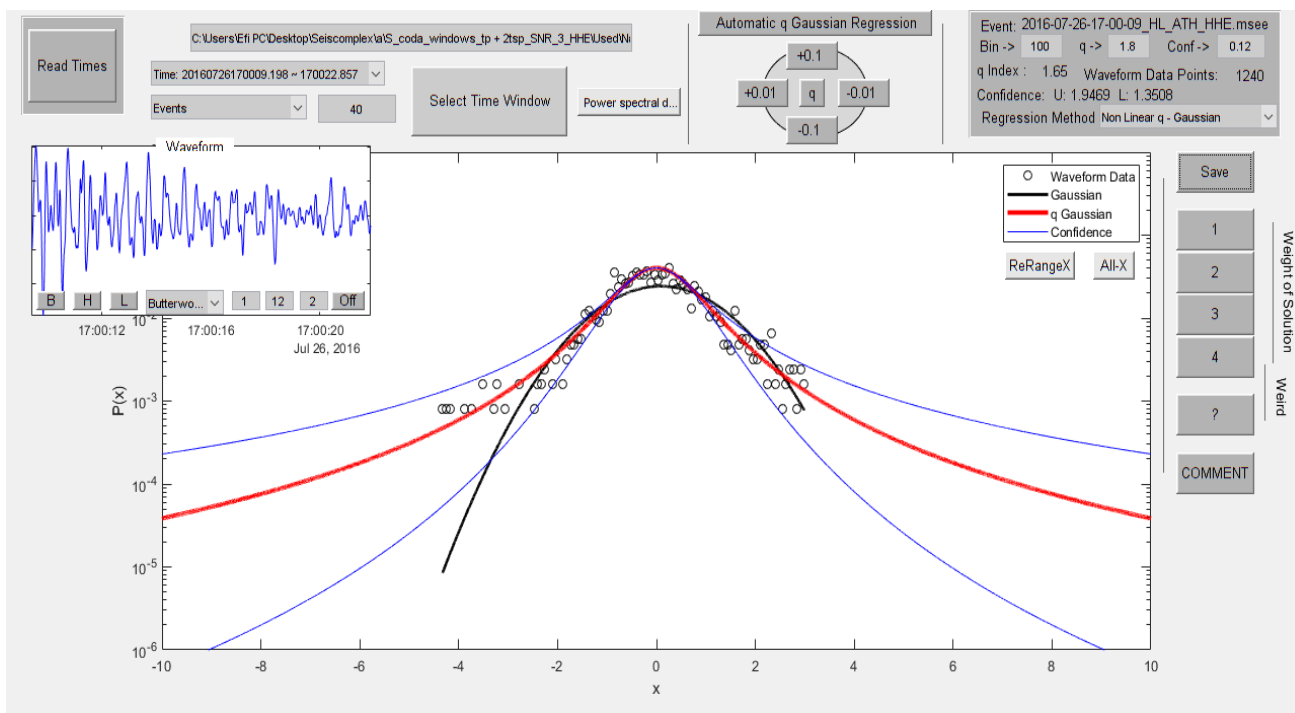


Figure 8.2.103

In figure 8.2.104 the time origin of the earthquake is 26/08/2016 at 07:47:24, latitude 38.6, longitude 24.47, depth 21km, magnitude 3.6 at 34.8 km SSW of Skyros. The value of the index  $q$  is 1.8.

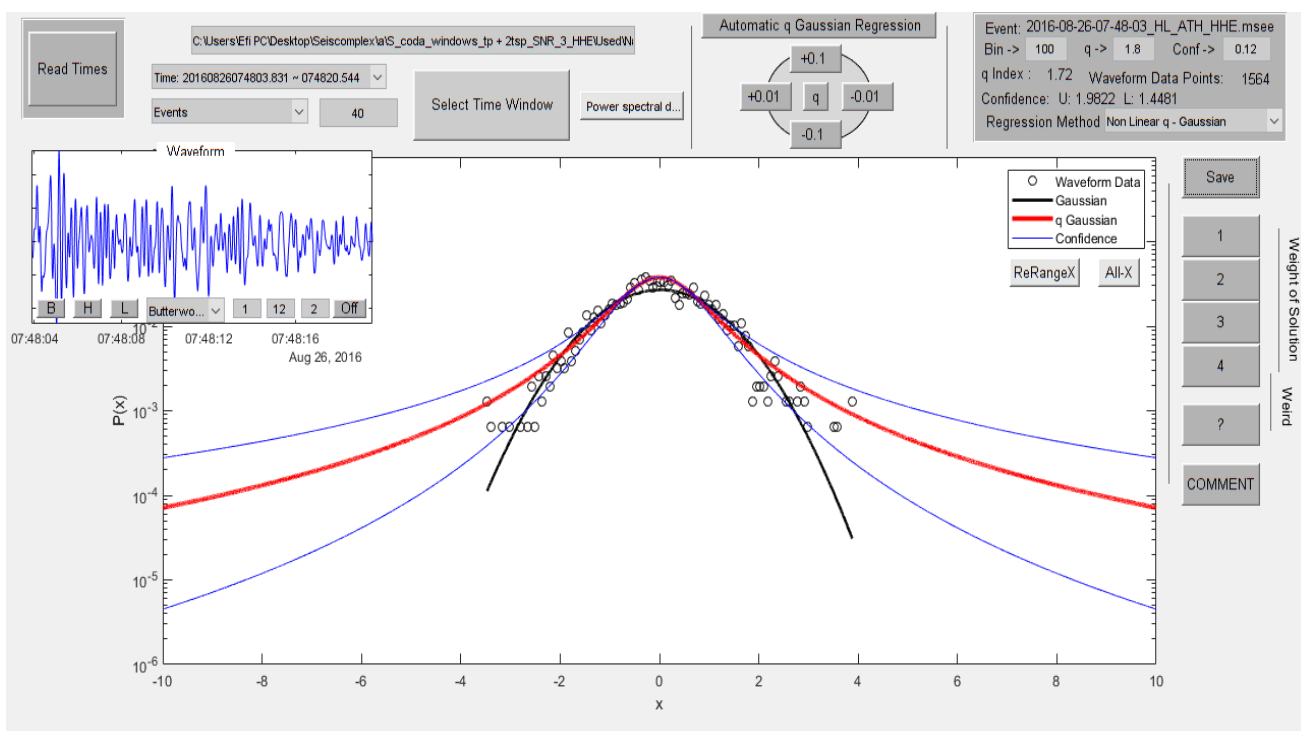


Figure 8.2.104

In figure 8.2.105 the time origin of the earthquake is 23/06/2017 at 22:26:17, latitude 38.4549, longitude 23.53, depth 17km, magnitude 3.6 at 6.1 km W of Chalkida. The value of the index  $q$  is 1.78.

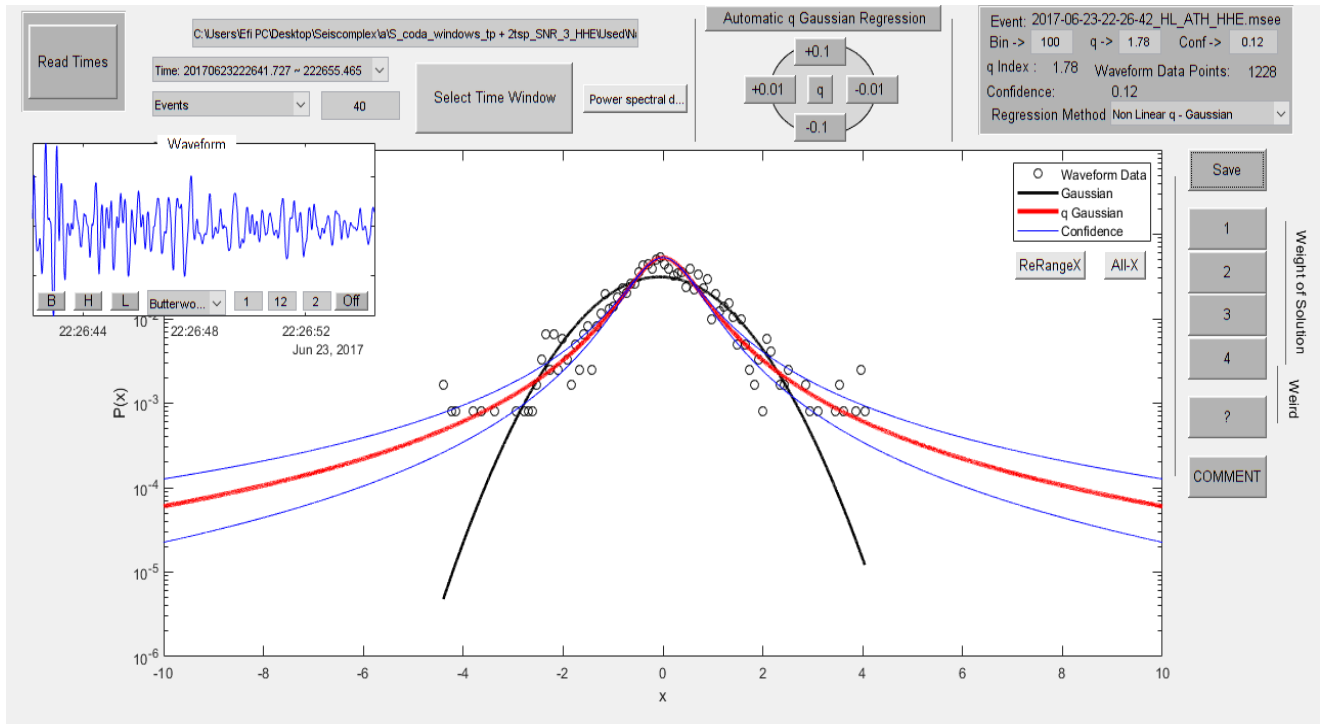


Figure 8.2.105

In figure 8.2.106 the time origin of the earthquake is 03/08/2019 at 17:17:09, latitude 38.1404, longitude 22.7019, depth 15km, magnitude 3.6 at 30.2 km NW of Korinthos. The value of the index  $q$  is 1.77.

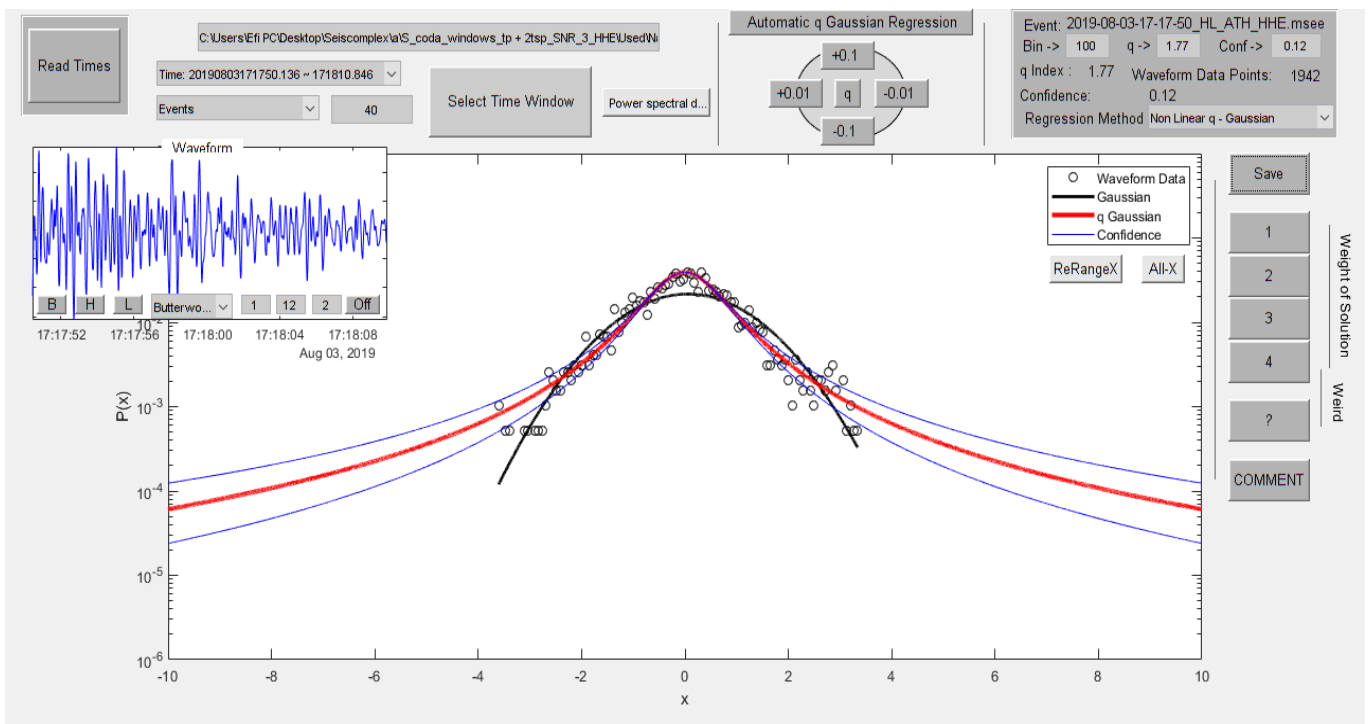


Figure 8.2.106

In figure 8.2.107 the time origin of the earthquake is 05/06/2010 at 05:12:40, latitude 38.13, longitude 23.18, depth 18km, magnitude 3.5 at 30.5 km NE of Korinthos. The value of the index  $q$  is 1.85.

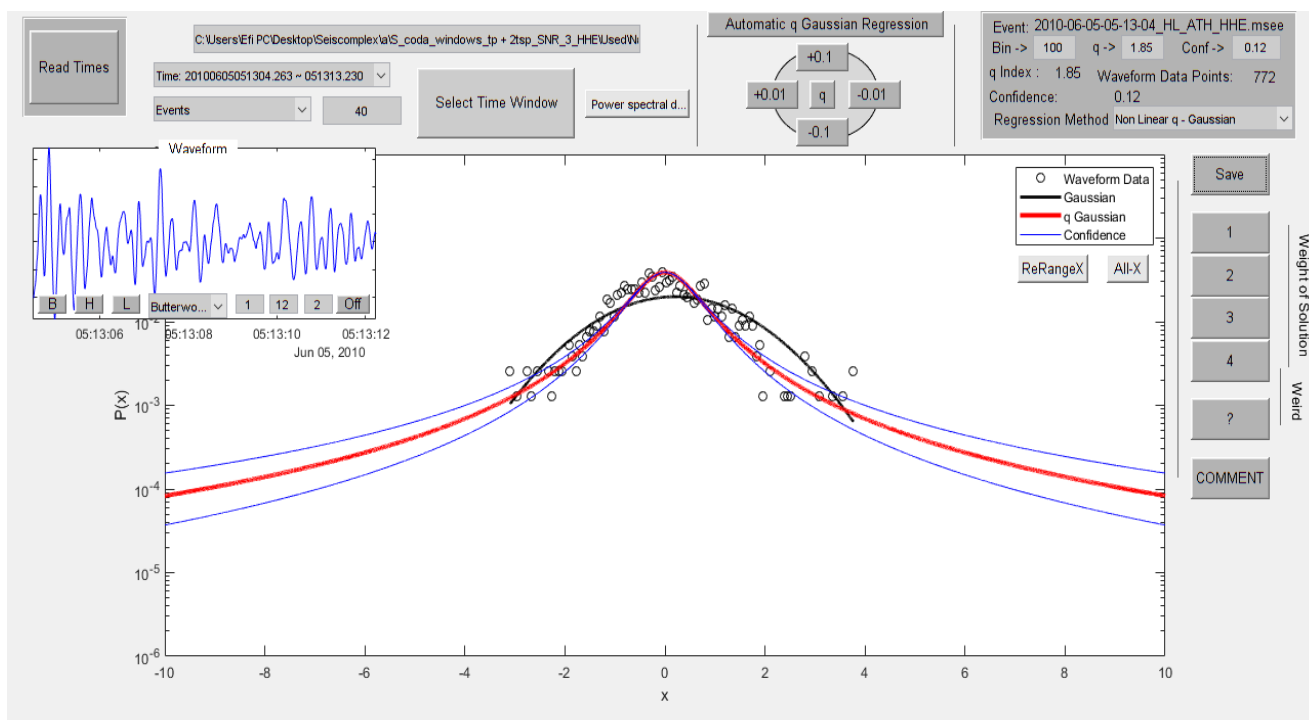


Figure 8.2.107

In figure 8.2.108 the time origin of the earthquake is 16/06/2010 at 15:11:21, latitude 37.41, longitude 23.58, depth 28km, magnitude 3.5 at 65.2 km SSW of Athens. The value of the index  $q$  is 1.74.

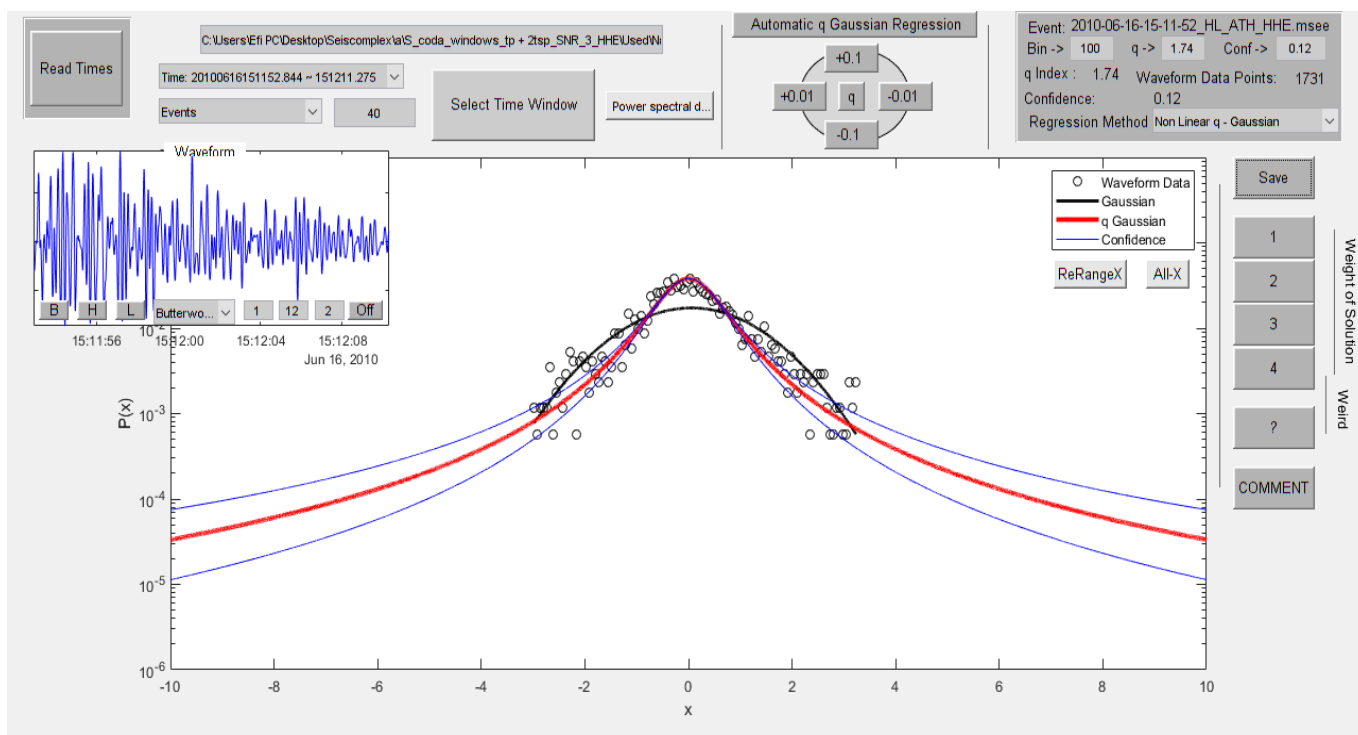


Figure 8.2.108

In figure 8.2.109 the time origin of the earthquake is 07/03/2011 at 17:10:53, latitude 38.25, longitude 22.55, depth 15km, magnitude 3.5 at 34.2 km SSE of Amfissa. The value of the index  $q$  is 1.93.

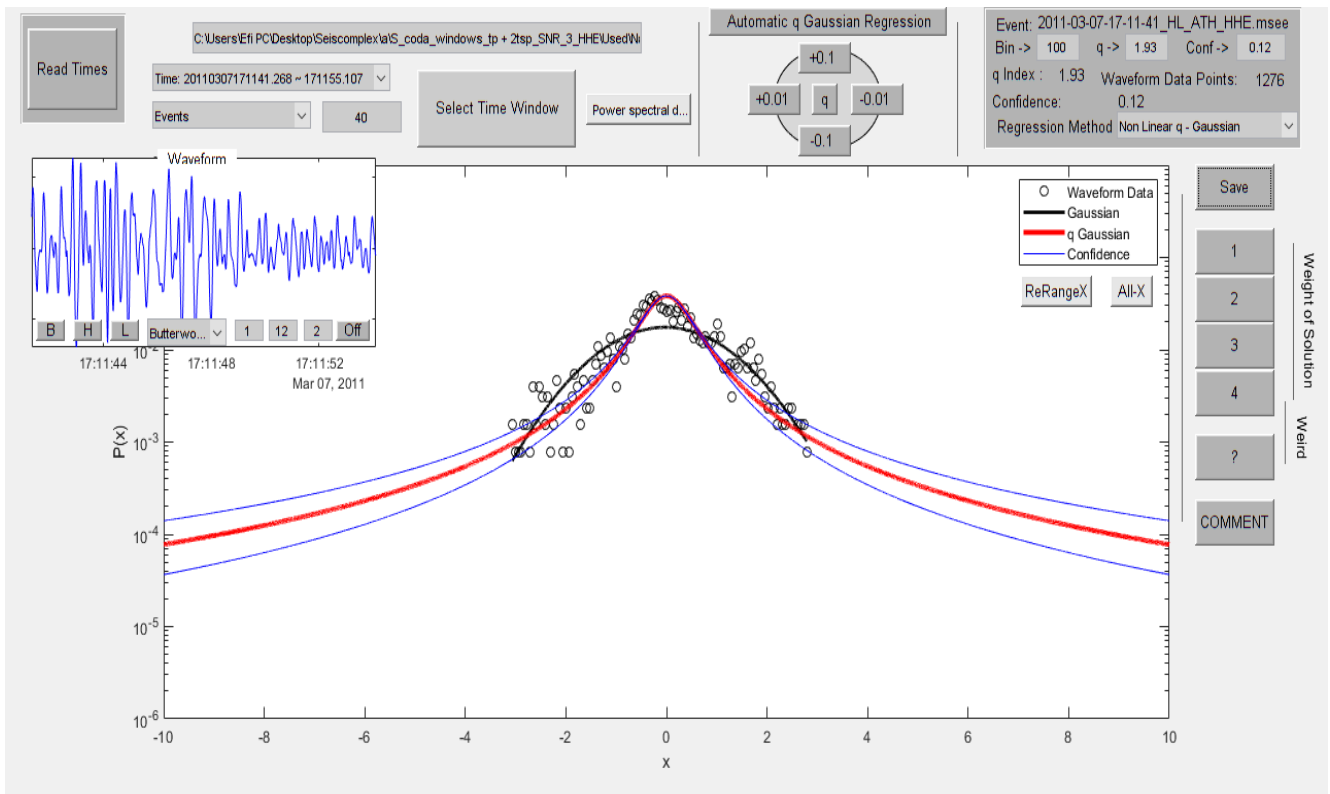


Figure 8.2.109

In figure 8.2.110 the time origin of the earthquake is 16/08/2011 at 20:22:22, latitude 38.15, longitude 22.71, depth 22km, magnitude 3.5 at 30.6 km NW of Korinthos. The value of the index  $q$  is 1.83.

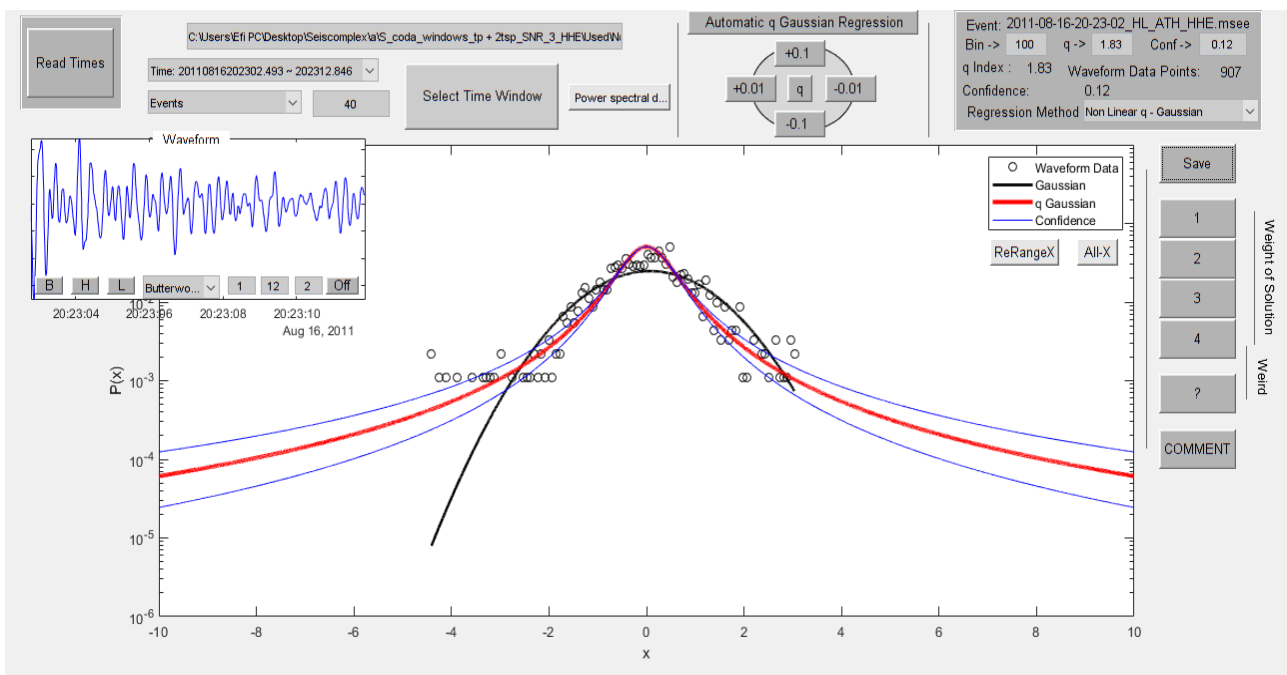


Figure 8.2.110

In figure 8.2.111 the time origin of the earthquake is 24/10/2011 at 09:24:37, latitude 37.61, longitude 23.51, depth 27km, magnitude 3.5 at 45.9 km SSW of Athens. The value of the index  $q$  is 1.76.

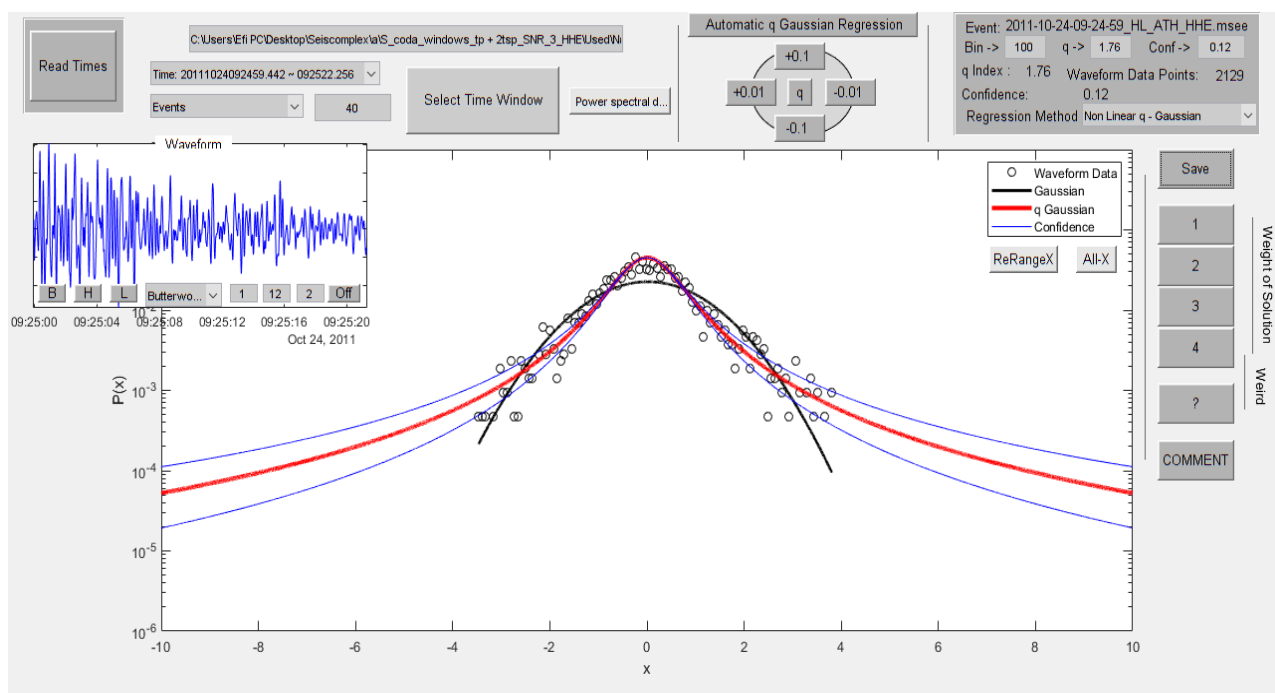


Figure 8.2.111

In figure 8.2.112 the time origin of the earthquake is 20/11/2011 at 22:14:14, latitude 38.17, longitude 22.56, depth 21km, magnitude 3.5 at 40.2 km SW of Levadhia. The value of the index  $q$  is 1.6.

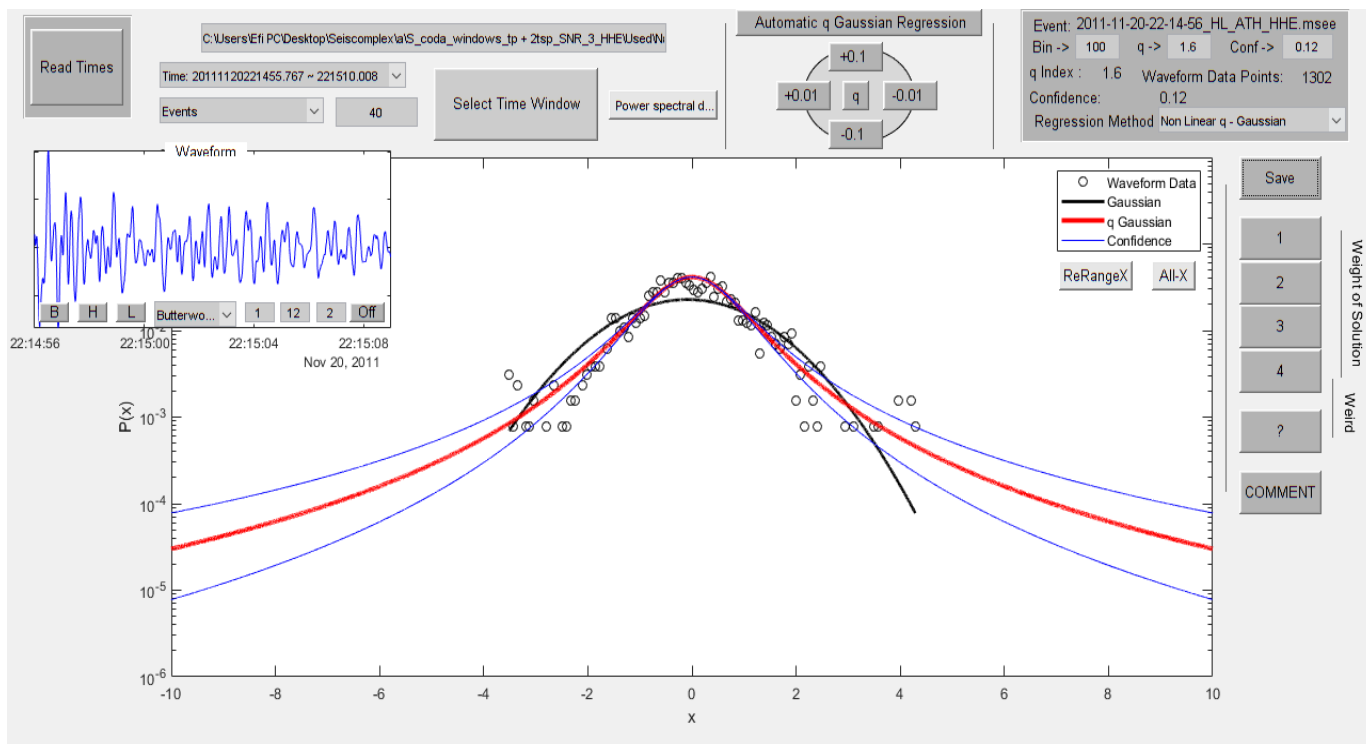


Figure 8.2.112

In figure 8.2.113 the time origin of the earthquake is 11/06/2013 at 19:36:16, latitude 38.17, longitude 23.23, depth 23km, magnitude 3.5 at 36.7 km NE of Korinthos. The value of the index  $q$  is 1.63.

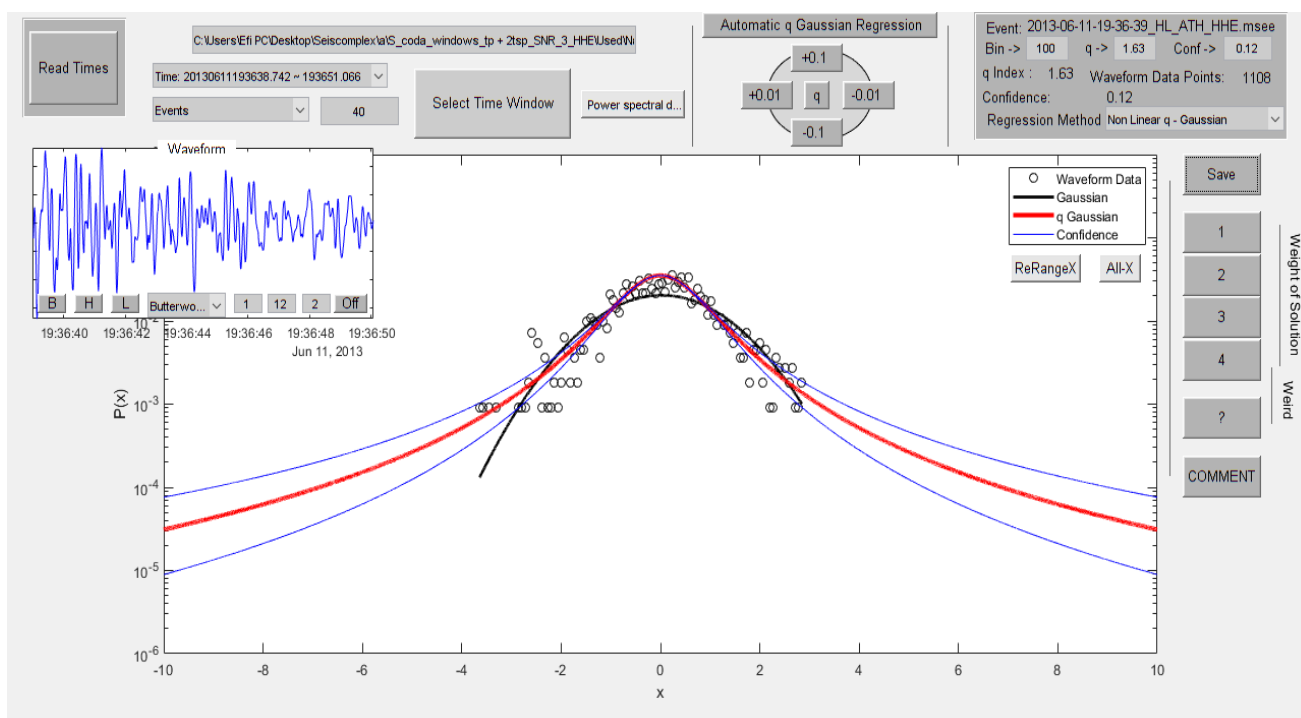


Figure 8.2.113

In figure 8.2.114 the time origin of the earthquake is 27/10/2013 at 13:53:37, latitude 38.64, longitude 23.61, depth 22km, magnitude 3.5 at 19.6 km N of Chalkida. The value of the index  $q$  is 1.8.

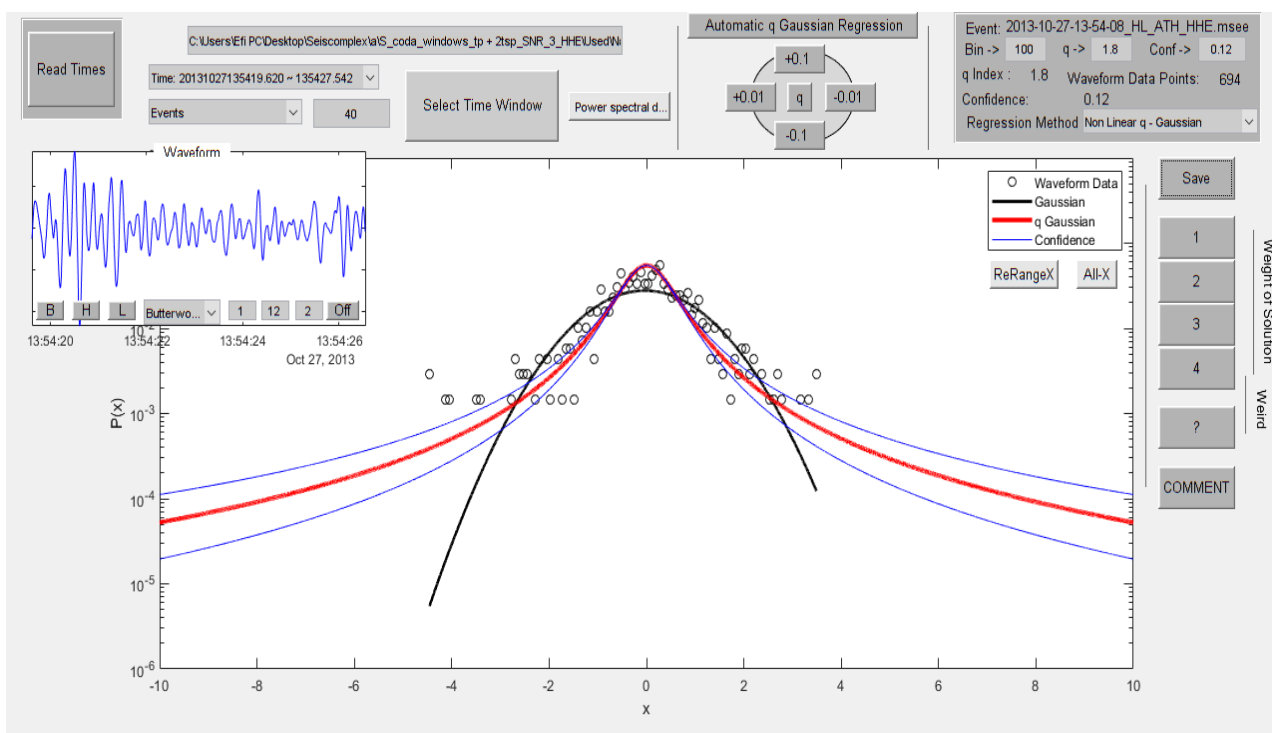


Figure 8.2.114

In figure 8.2.115 the time origin of the earthquake is 22/12/2013 at 18:04:02, latitude 37.85, longitude 22.76, depth 27km, magnitude 3.5 at 18.0 km WSW of Korinthos. The value of the index  $q$  is 1.5.

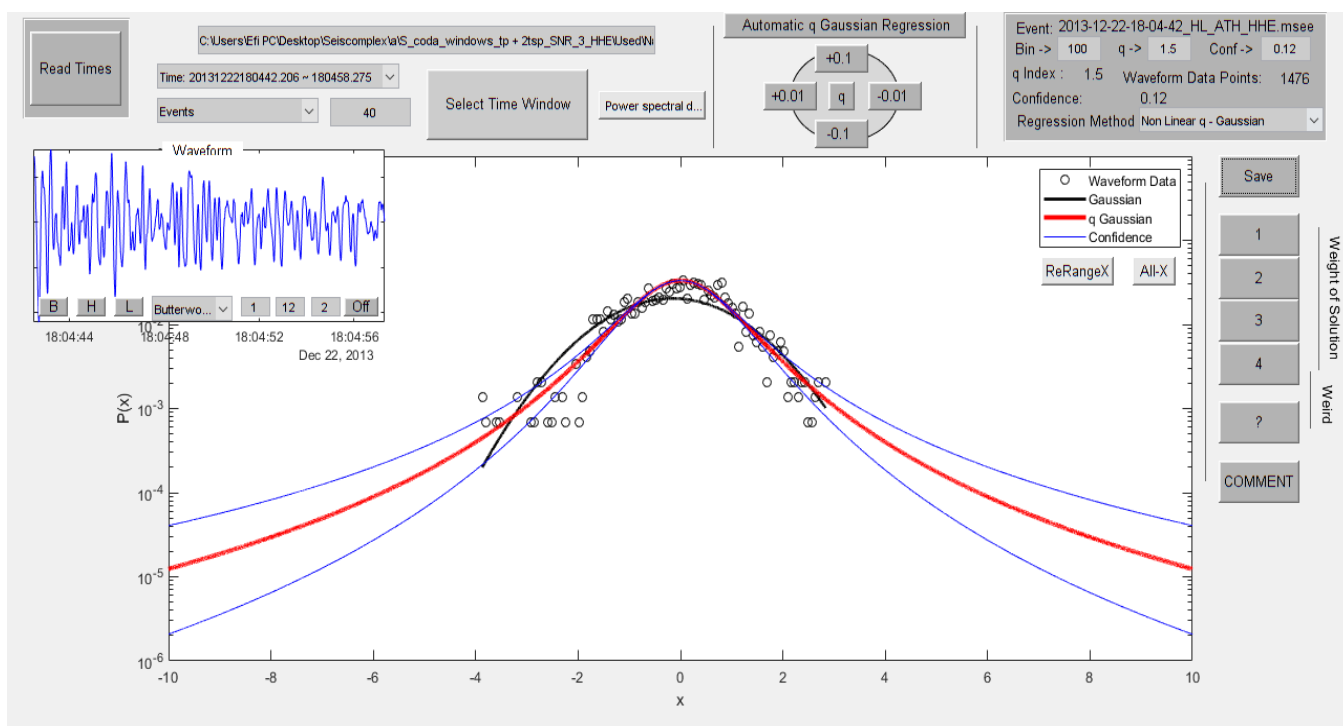


Figure 8.2.115

In figure 8.2.116 the time origin of the earthquake is 10/04/2014 at 17:40:44, latitude 37.93, longitude 22.61, depth 24 km, magnitude 3.5 at 28.3 km W of Korinthos. The value of the index  $q$  is 1.65.

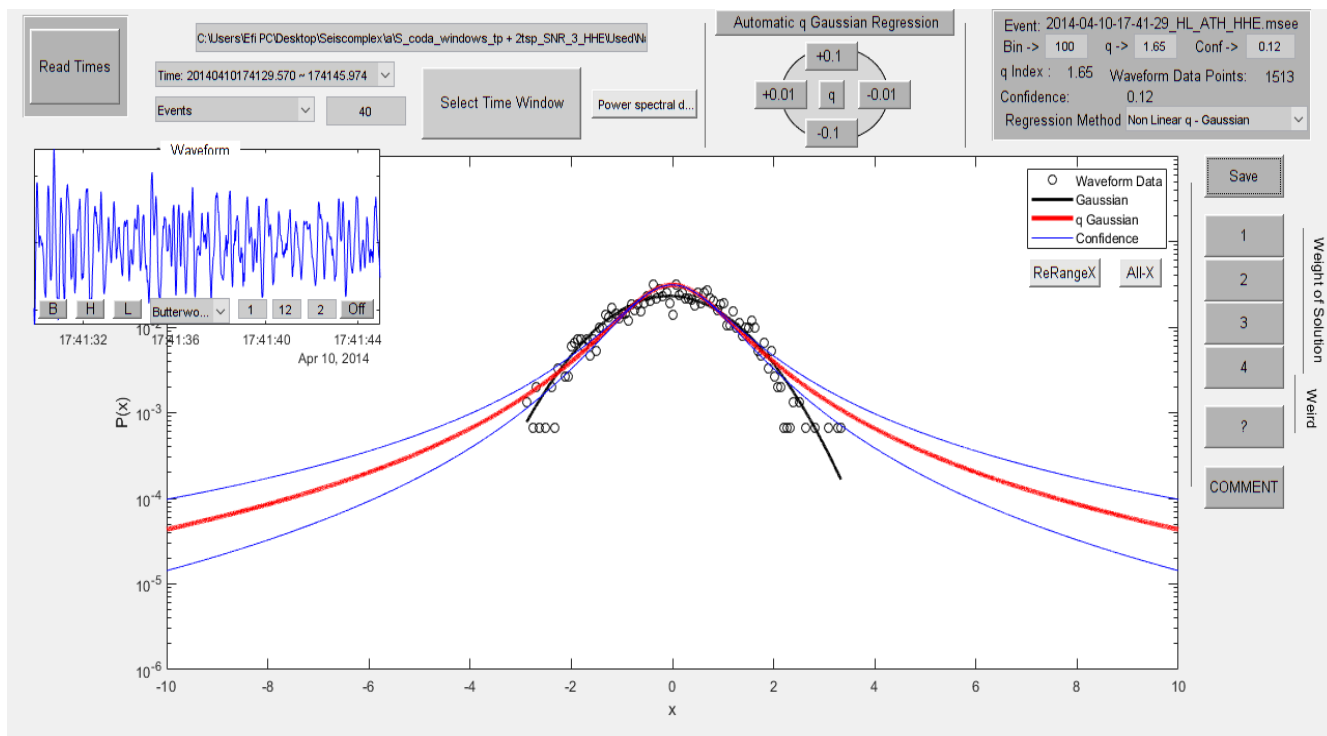


Figure 8.2.116

In figure 8.2.117 the time origin of the earthquake is 17/11/2014 at 23:18:45, latitude 38.66, longitude 23.4, depth 23 km, magnitude 3.5 at 27.9 km NW of Chalkida. The value of the index  $q$  is 1.86.

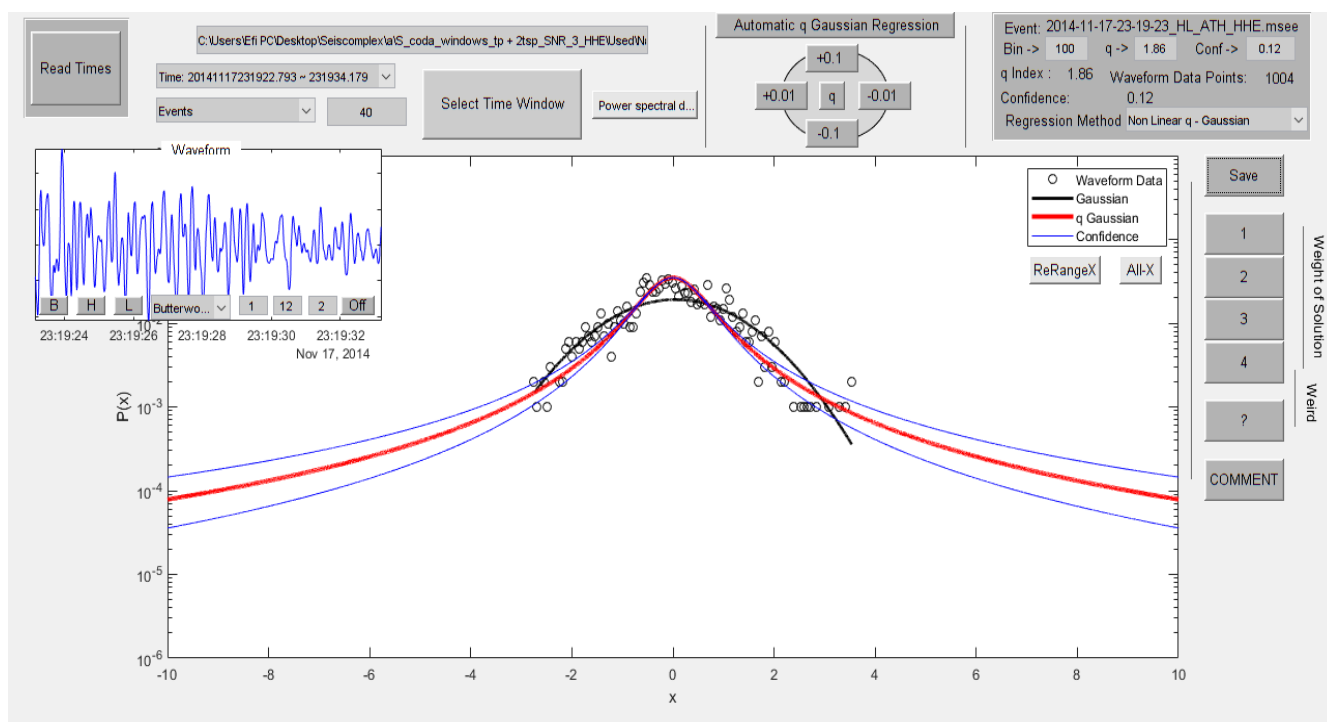


Figure 8.2.117

In figure 8.2.118 the time origin of the earthquake is 20/11/2014 at 16:26:22, latitude 38.65, longitude 23.36, depth 24 km, magnitude 3.5 at 29.4 km NW of Chalkida. The value of the index  $q$  is 1.51.

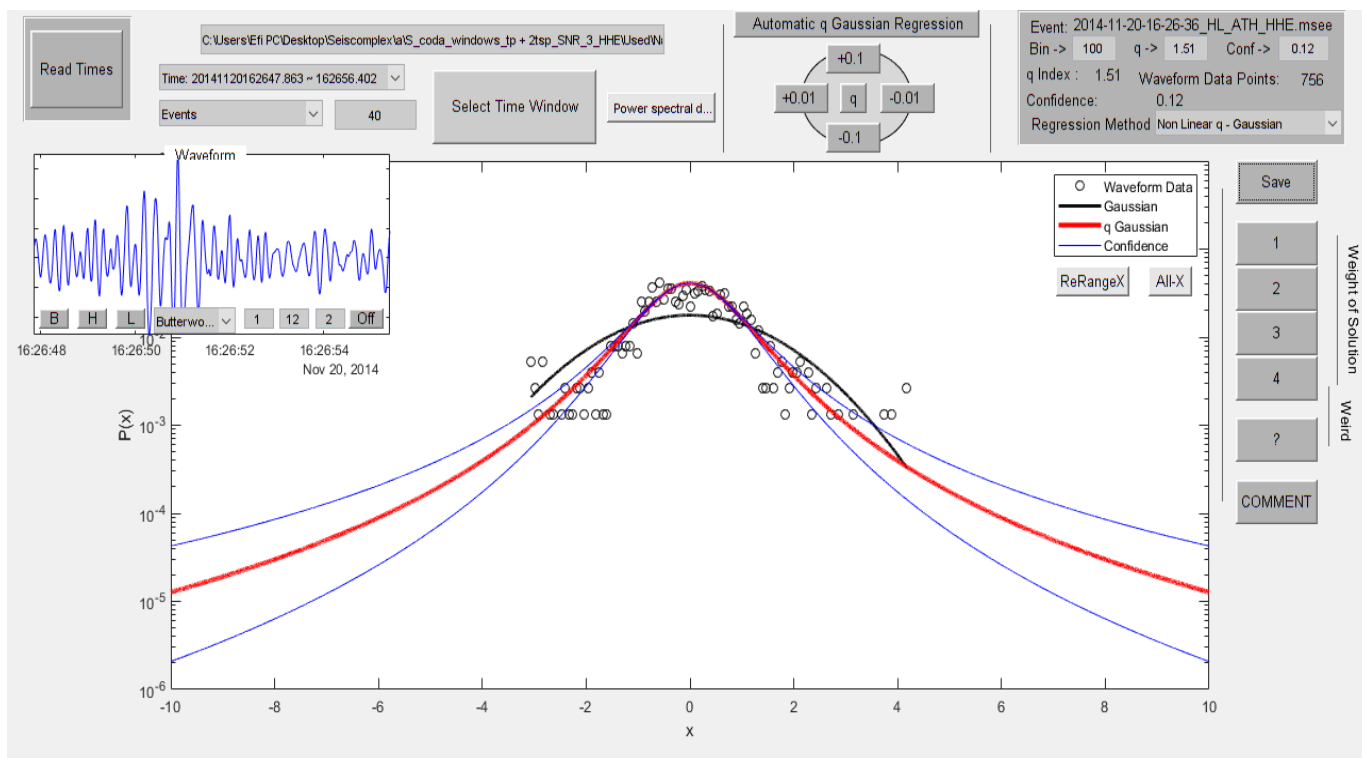


Figure 8.2.118

In figure 8.2.119 the time origin of the earthquake is 09/06/2015 at 02:13:27, latitude 38.63, longitude 23.4, depth 16 km, magnitude 3.5 at 25.4 km NW of Chalkida. The value of the index  $q$  is 1.78.

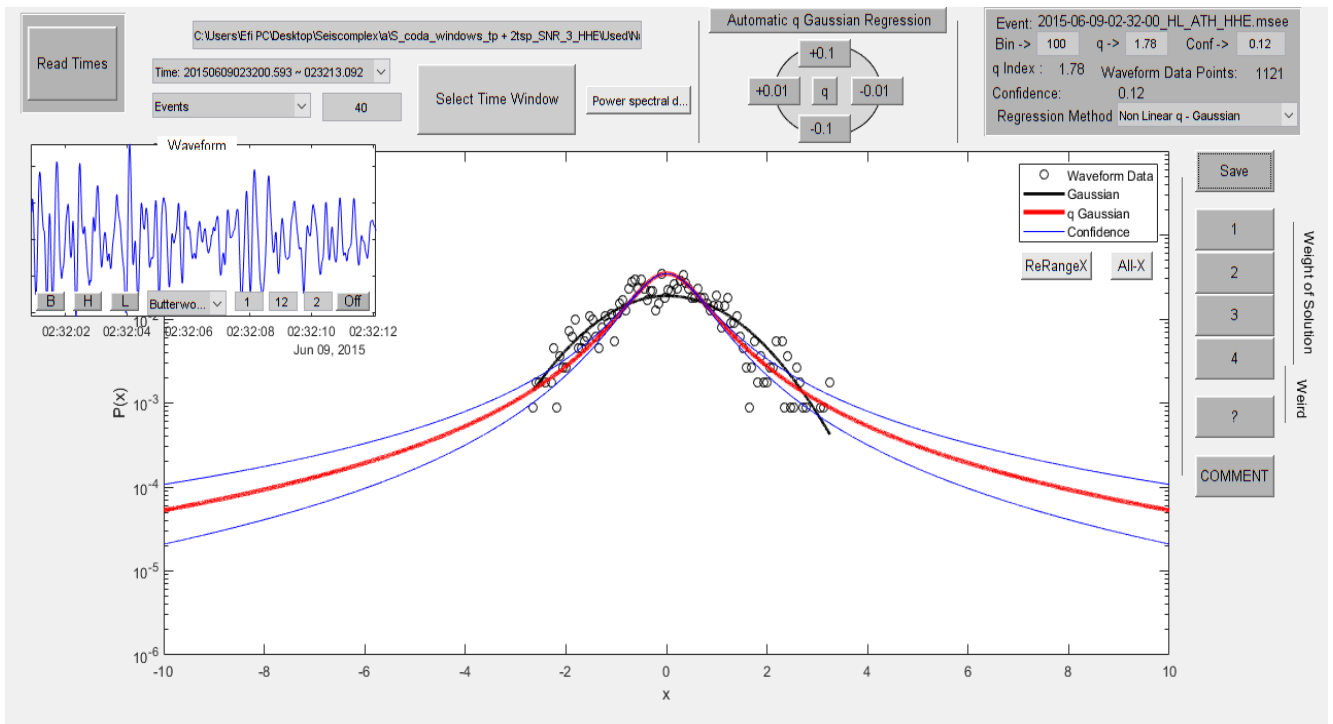


Figure 8.2.119

In figure 8.2.120 the time origin of the earthquake is 09/06/2015 at 03:04:41, latitude 38.63, longitude 23.42, depth 15 km, magnitude 3.5 at 24.2 km NW of Chalkida. The value of the index  $q$  is 1.71.

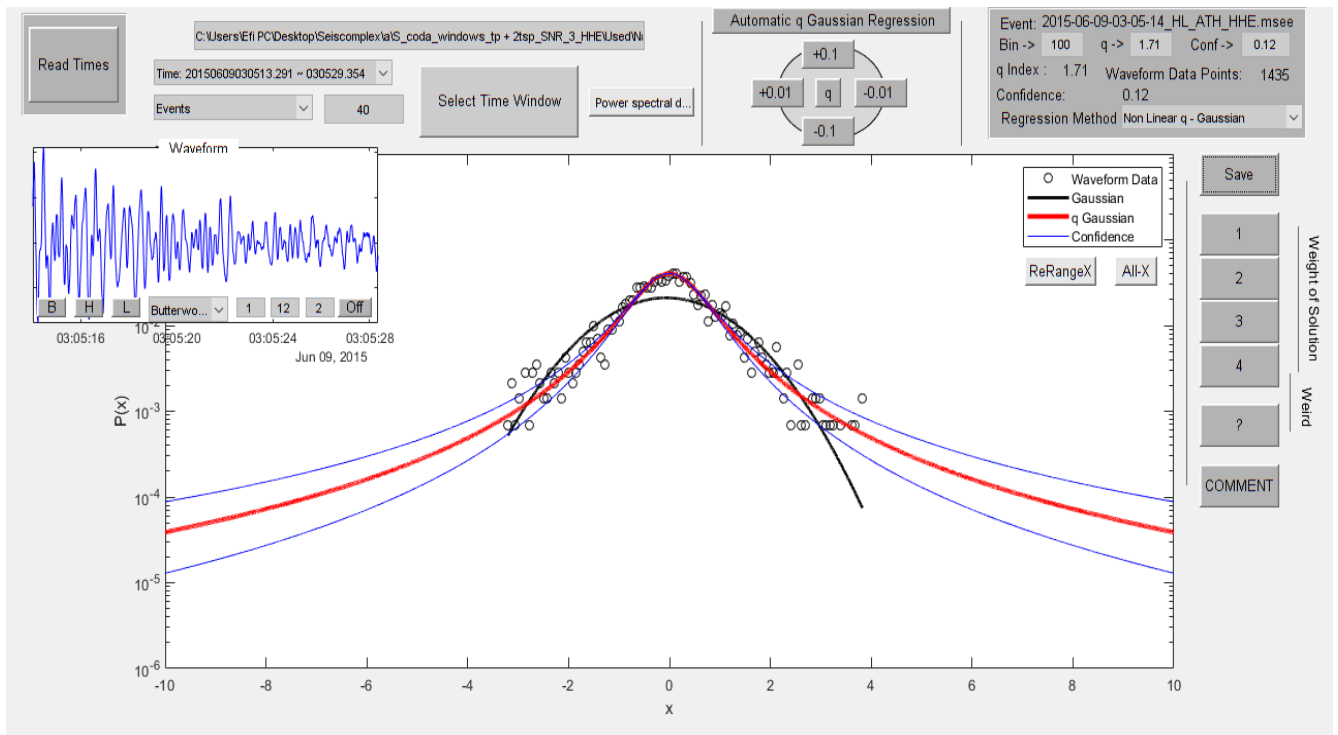


Figure 8.2.120

In figure 8.2.121 the time origin of the earthquake is 28/05/2016 at 21:00:10, latitude 37.57, longitude 23.57, depth 16 km, magnitude 3.5 at 48.1 km SSW of Athens. The value of the index  $q$  is 1.92.

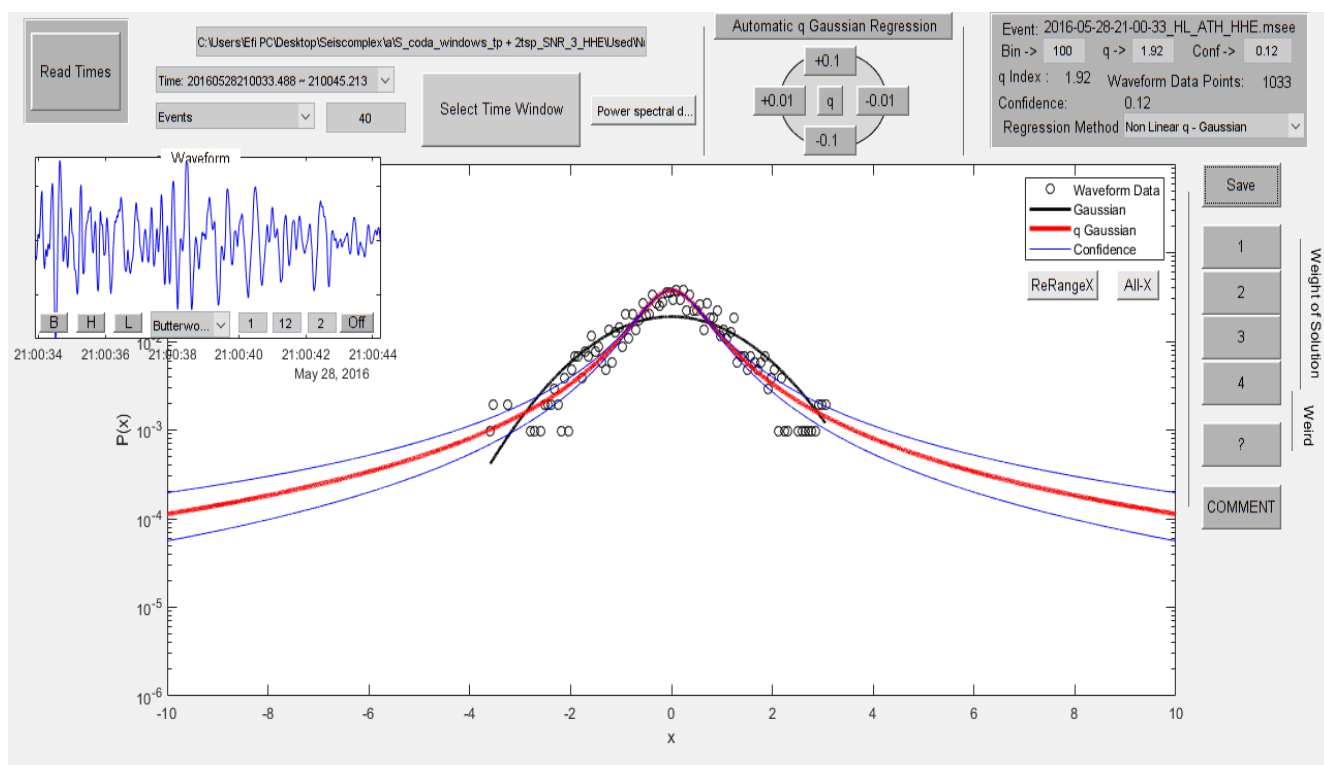


Figure 8.2.121

In figure 8.2.122 the time origin of the earthquake is 03/06/2016 at 01:28:49, latitude 38.62, longitude 24.45, depth 16 km, magnitude 3.5 at 33.1 km SSW of Skyros. The value of the index  $q$  is 1.54.

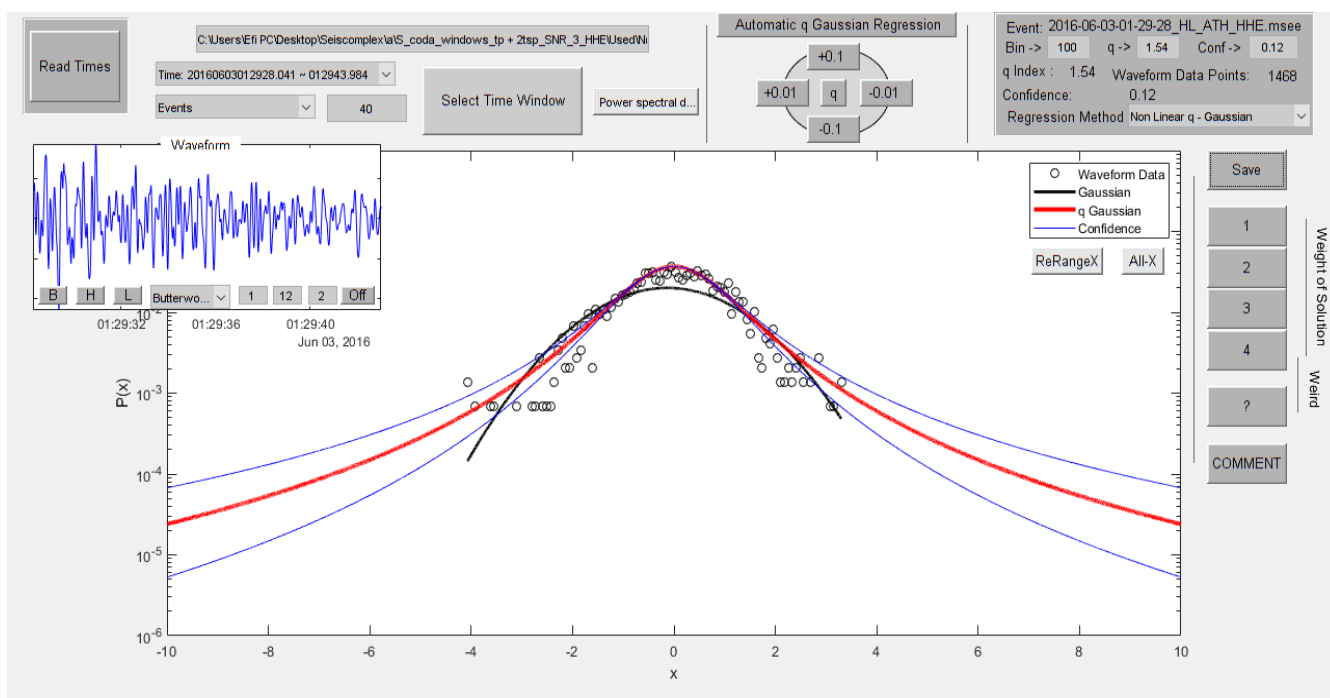


Figure 8.2.122

In figure 8.2.123 the time origin of the earthquake is 19/07/2019 at 11:42:19, latitude 38.1248, longitude 23.5158, depth 16 km, magnitude 3.5 at 24.7 km NW of Athens. The value of the index  $q$  is 1.75.

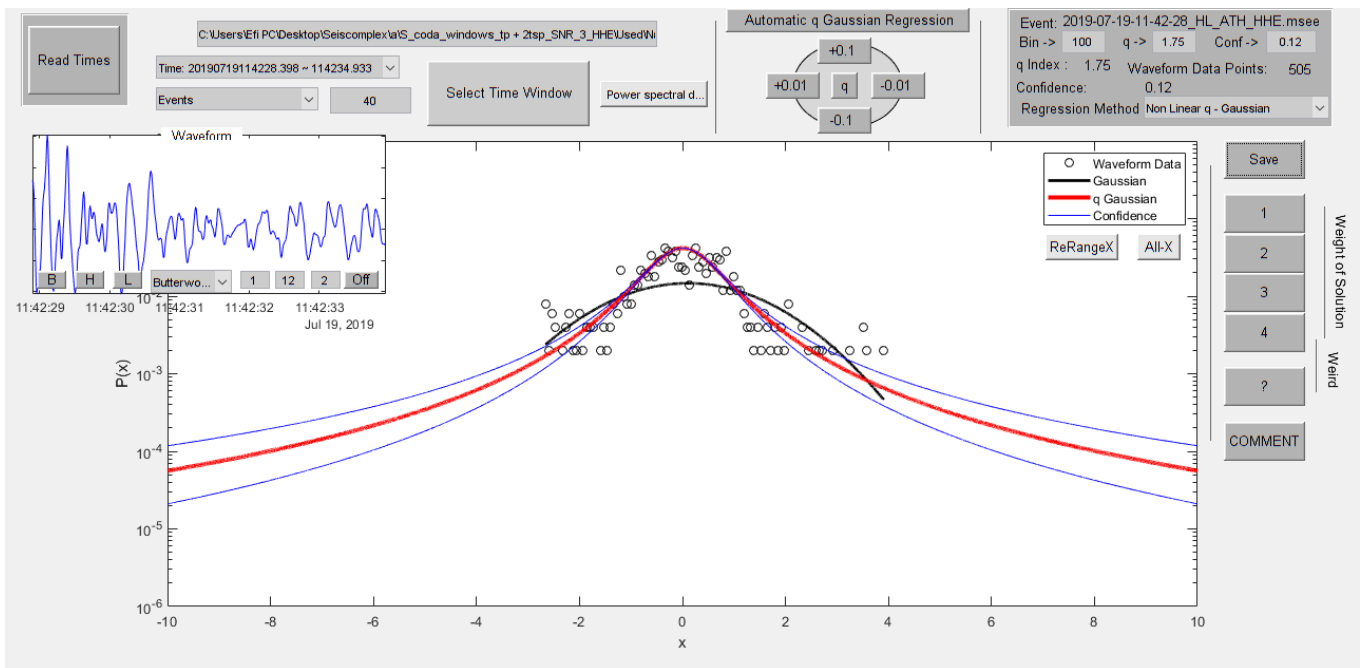


Figure 8.2.123

In figure 8.2.124 the time origin of the earthquake is 27/08/2010 at 11:23:20, latitude 37.86, longitude 22.98, depth 19 km, magnitude 3.4 at 9.6 km SSE of Korinthos. The value of the index  $q$  is 1.79.

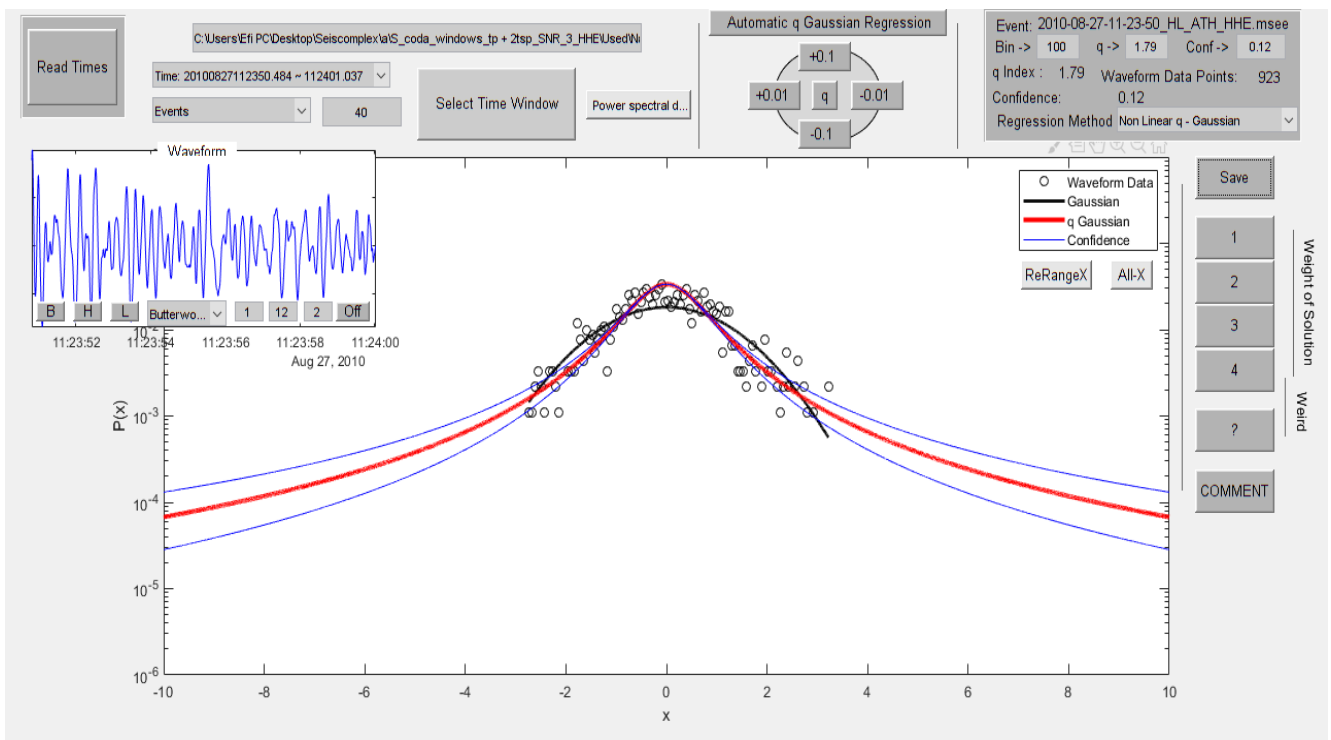


Figure 8.2.124

In figure 8.2.125 the time origin of the earthquake is 21/09/2010 at 08:02:11, latitude 38.15, longitude 23.32, depth 24 km, magnitude 3.4 at 40.7 km WNW of Athens. The value of the index  $q$  is 1.79.

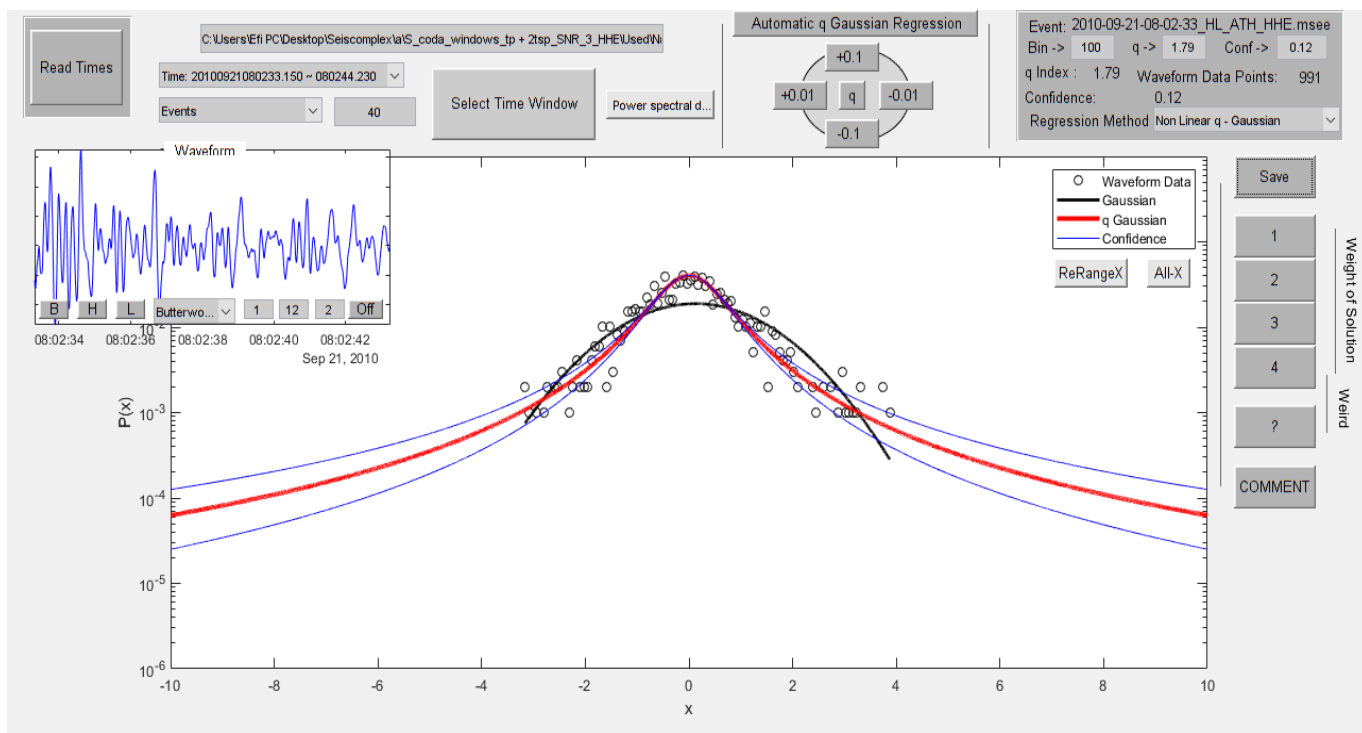


Figure 8.2.125

In figure 8.2.126 the time origin of the earthquake is 12/12/2010 at 08:19:31, latitude 38.11, longitude 23.55, depth 18 km, magnitude 3.4 at 21.4 km NW of Athens. The value of the index  $q$  is 2.14.

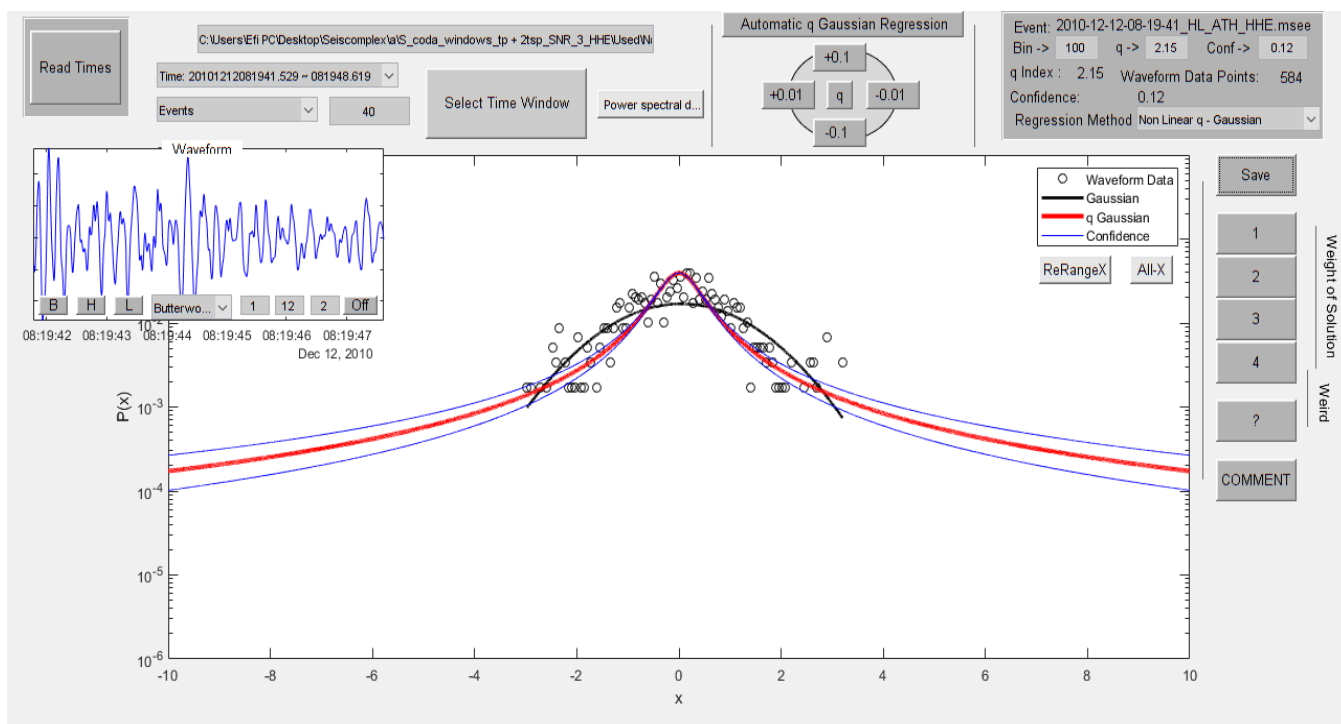


Figure 8.2.126

In figure 8.2.127 the time origin of the earthquake is 26/06/2011 at 06:31:10, latitude 38.88, longitude 23.69, depth 22 km, magnitude 3.4 at 36.5 km SSE of Skiathos. The value of the index  $q$  is 1.75.

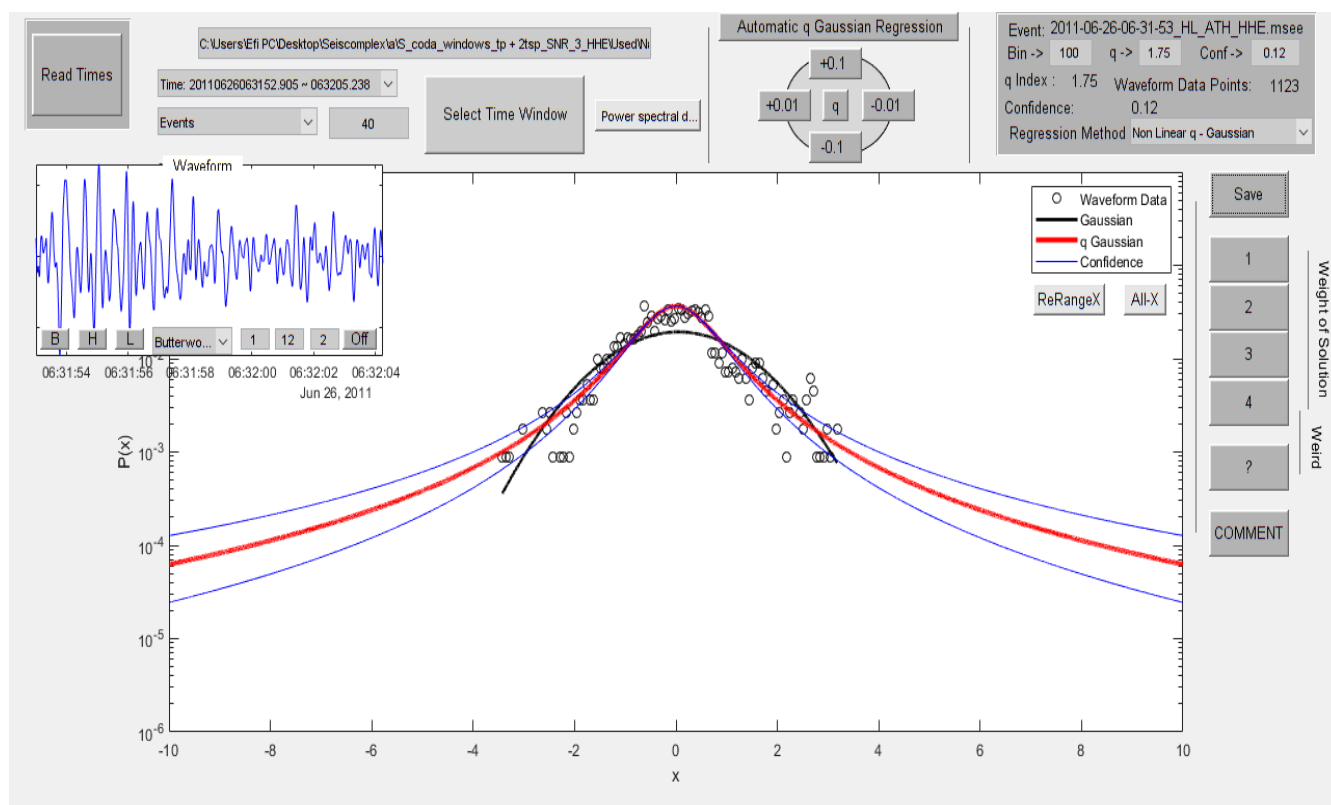


Figure 8.2.127

In figure 8.2.128 the time origin of the earthquake is 01/12/2011 at 01:17:43, latitude 38.76, longitude 23.44, depth 25 km, magnitude 3.4 at 35.8 km NNW of Chalkida. The value of the index  $q$  is 1.96.

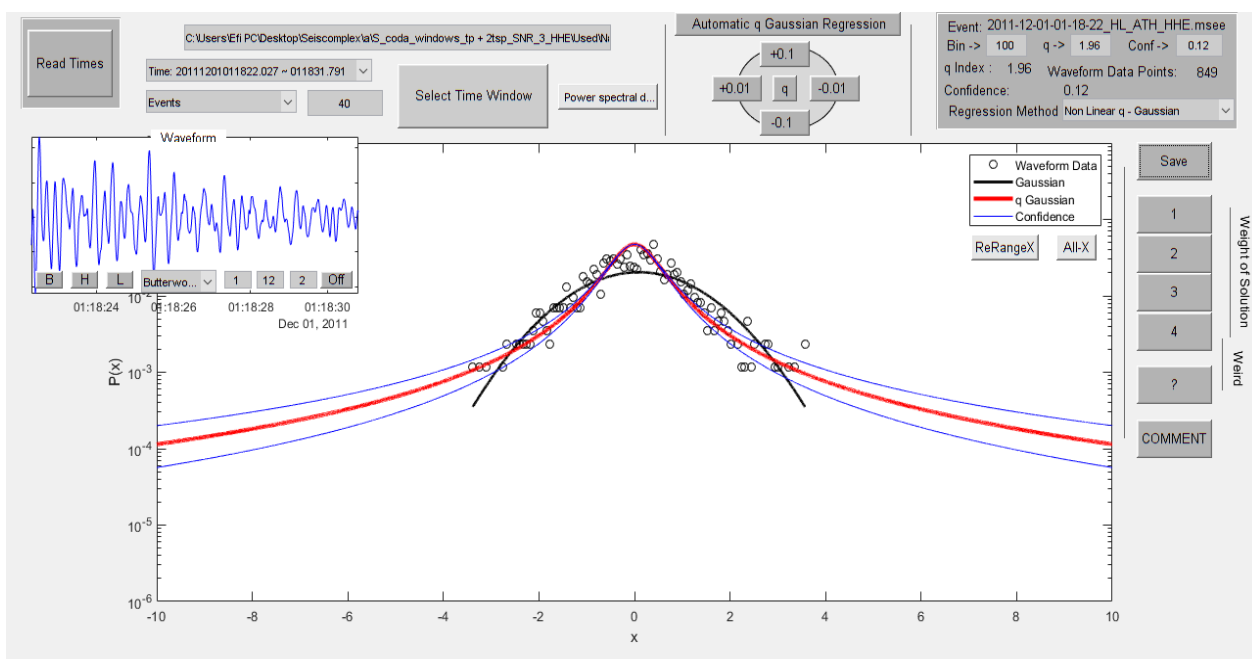


Figure 8.2.128

In figure 8.2.129 the time origin of the earthquake is 15/08/2013 at 01:03:30, latitude 38.7, longitude 22.67, depth 19 km, magnitude 3.4 at 29.1 km W of Atalanti. The value of the index  $q$  is 1.94.

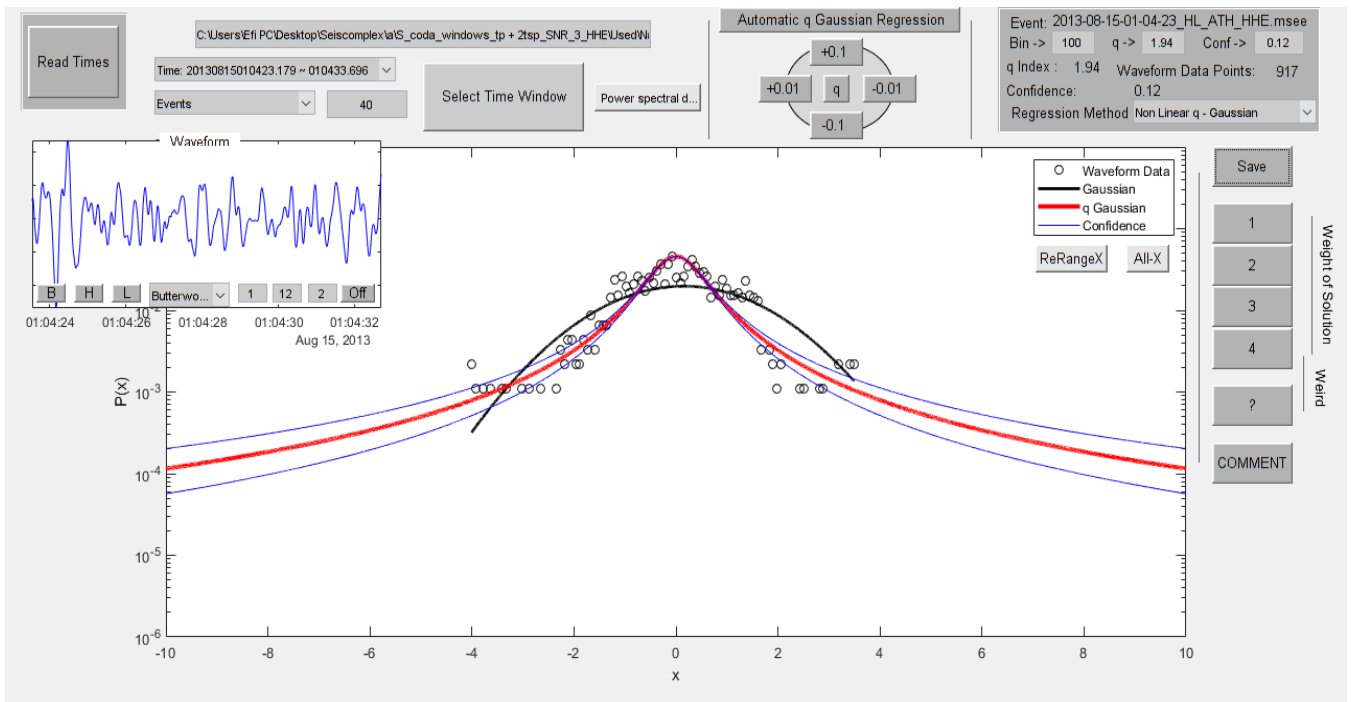


Figure 8.2.129

In figure 8.2.130 the time origin of the earthquake is 21/12/2013 at 05:50:39, latitude 38.23, longitude 22.21, depth 50 km, magnitude 3.4 at 11.4 km E of Aegion. The value of the index  $q$  is 1.63.

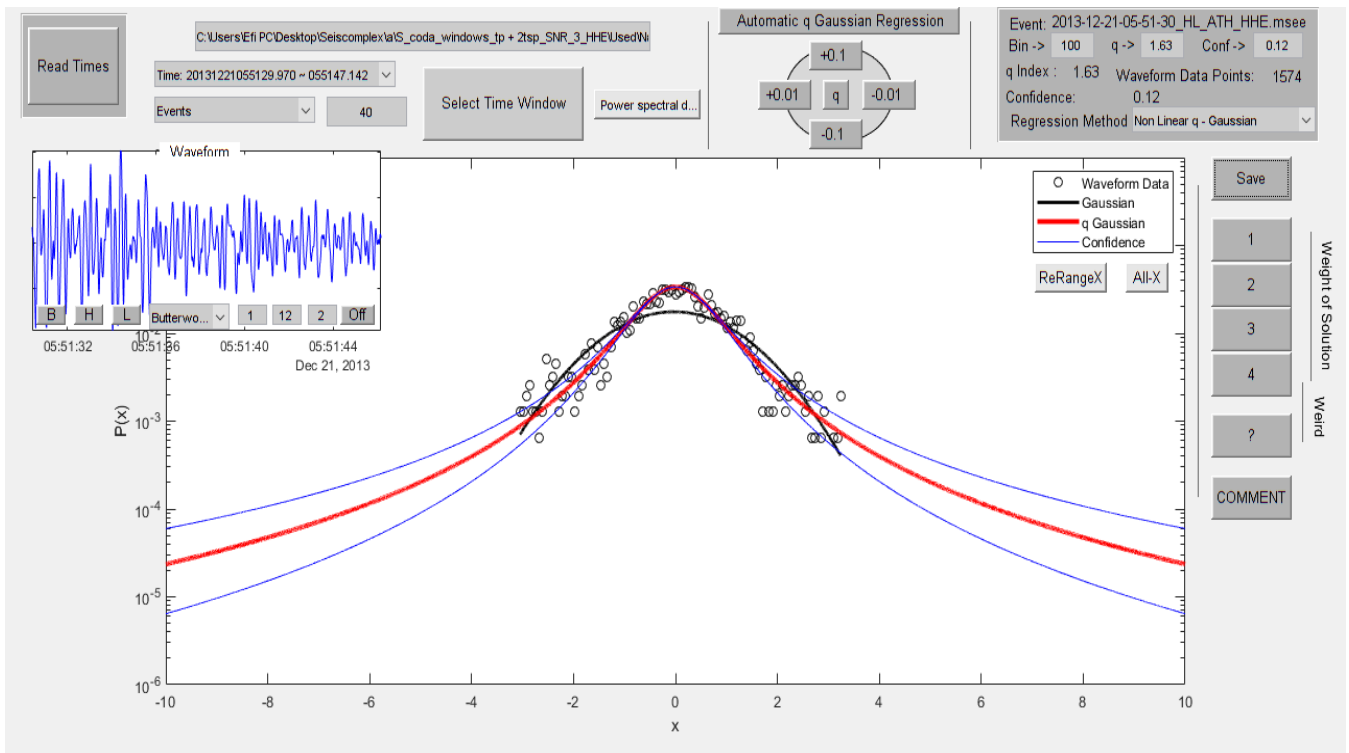


Figure 8.2.130

In figure 8.2.131 the time origin of the earthquake is 28/02/2014 at 22:13:54, latitude 38.2, longitude 22.53, depth 21 km, magnitude 3.4 at 38.6 km SSE of Amfissa. The value of the index  $q$  is 1.48.

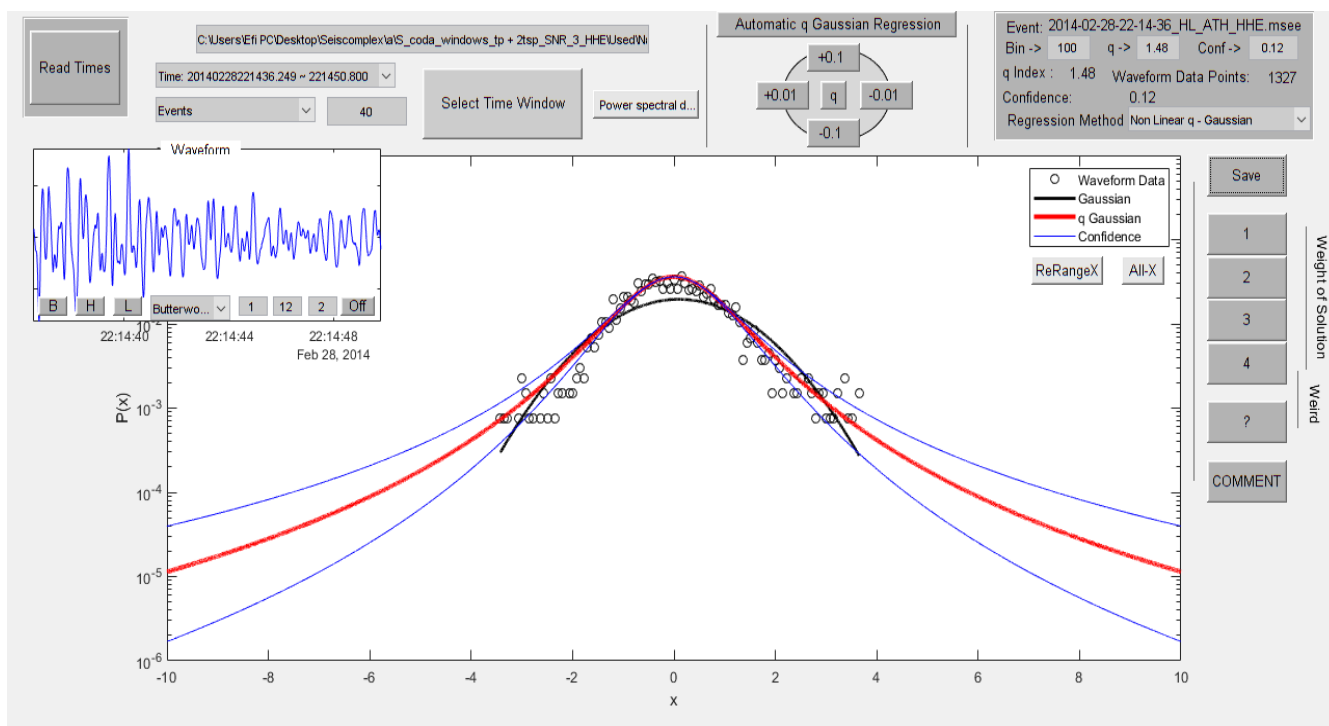


Figure 8.2.131

In figure 8.2.132 the time origin of the earthquake is 30/03/2014 at 20:31:03, latitude 37.58, longitude 23.45, depth 20 km, magnitude 3.4 at 51.3 km SSW of Athens. The value of the index  $q$  is 1.5.

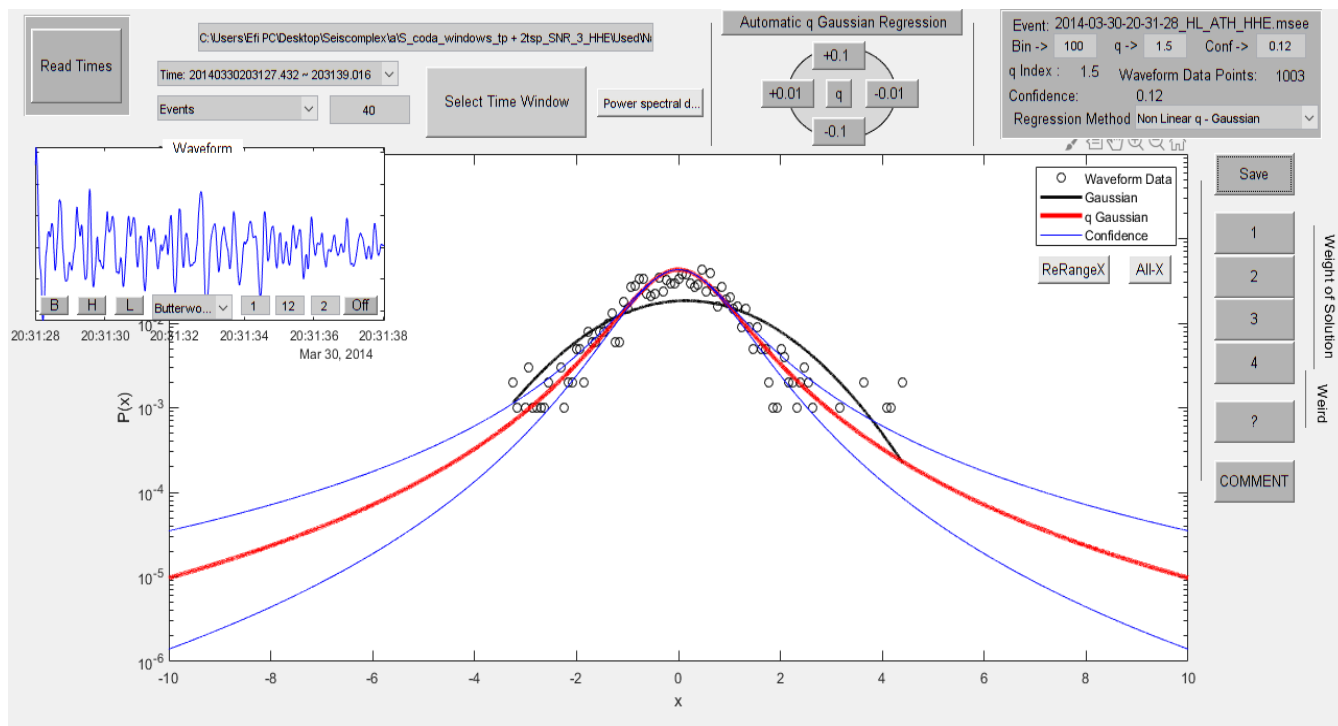


Figure 8.2.132

In figure 8.2.133 the time origin of the earthquake is 18/11/2014 at 01:16:19, latitude 38.63, longitude 23.4, depth 19 km, magnitude 3.4 at 25.4 km NW of Chalkida. The value of the index  $q$  is 1.81.

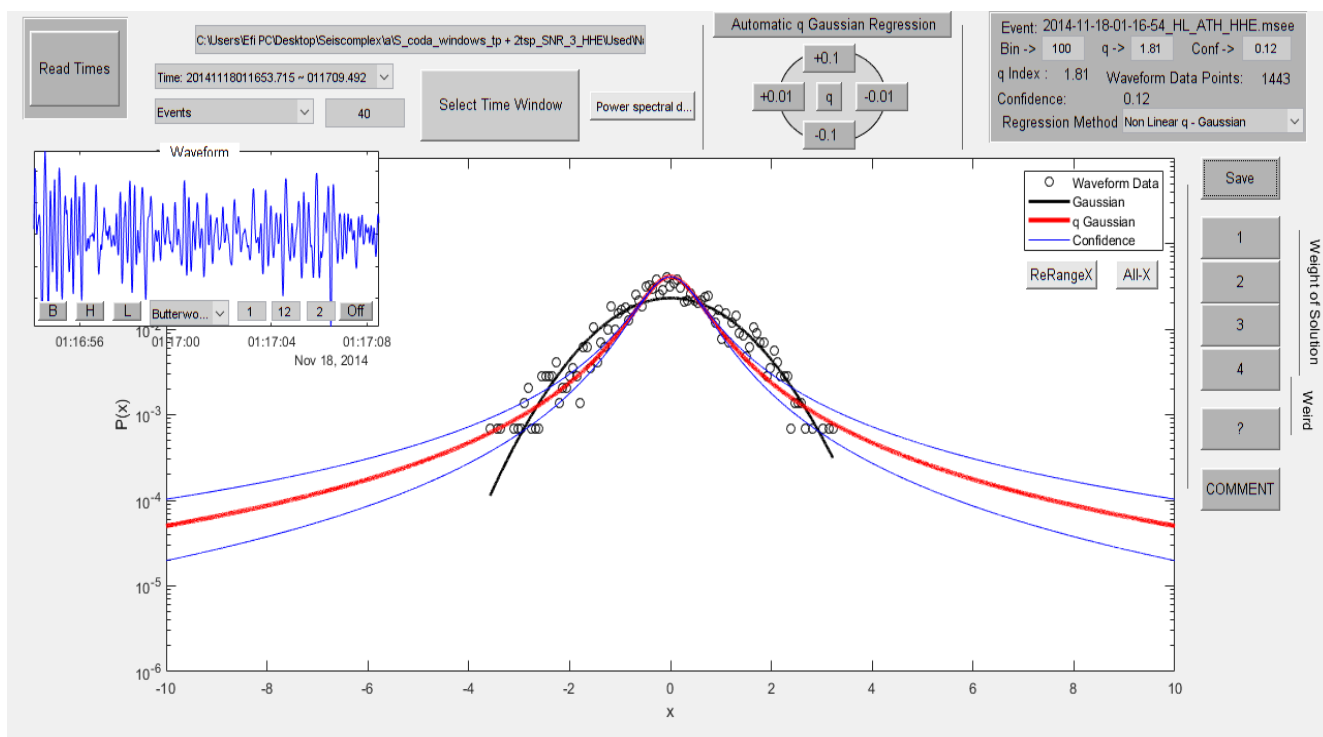


Figure 8.2.133

In figure 8.2.134 the time origin of the earthquake is 18/11/2014 at 03:18:49, latitude 38.64, longitude 23.41, depth 23 km, magnitude 3.4 at 25.6 km NW of Chalkida. The value of the index  $q$  is 1.84.

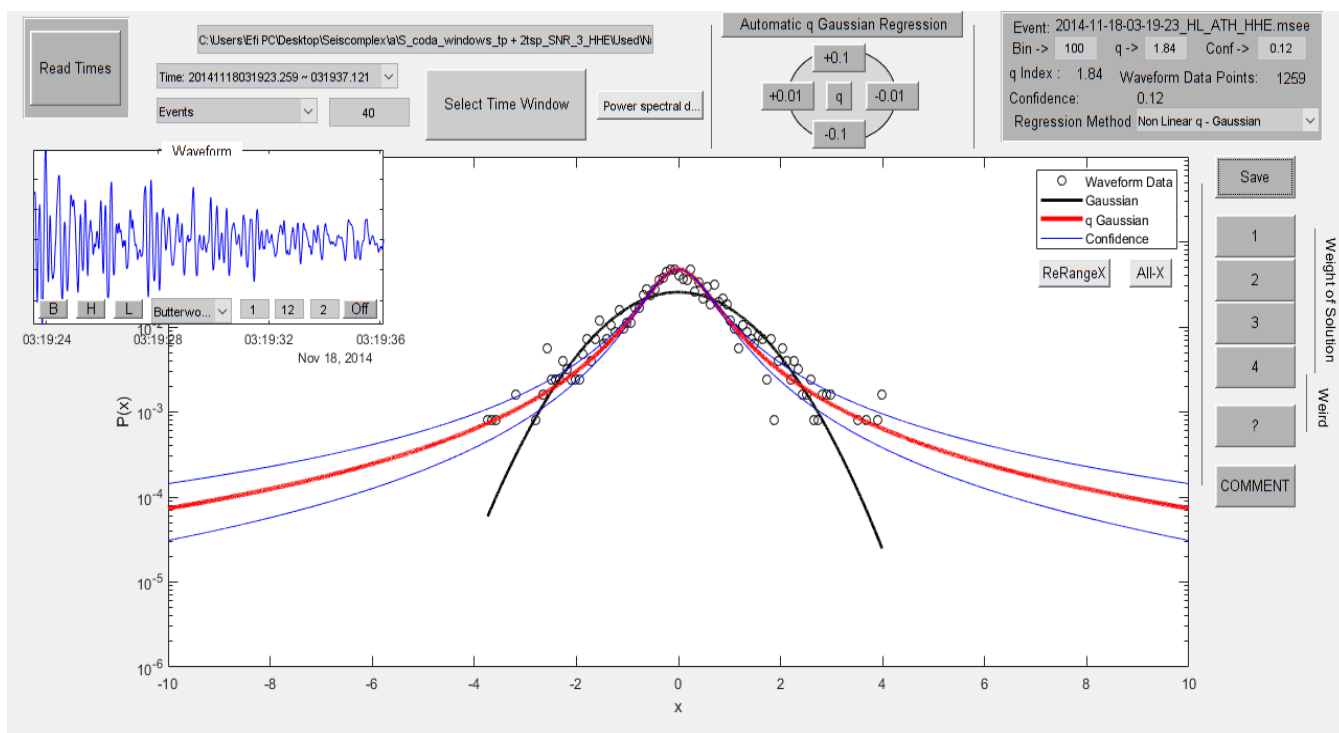


Figure 8.2.134

In figure 8.2.135 the time origin of the earthquake is 18/11/2014 at 23:44:40, latitude 38.64, longitude 23.36, depth 21 km, magnitude 3.4 at 28.6 km NW of Chalkida. The value of the index  $q$  is 1.56.

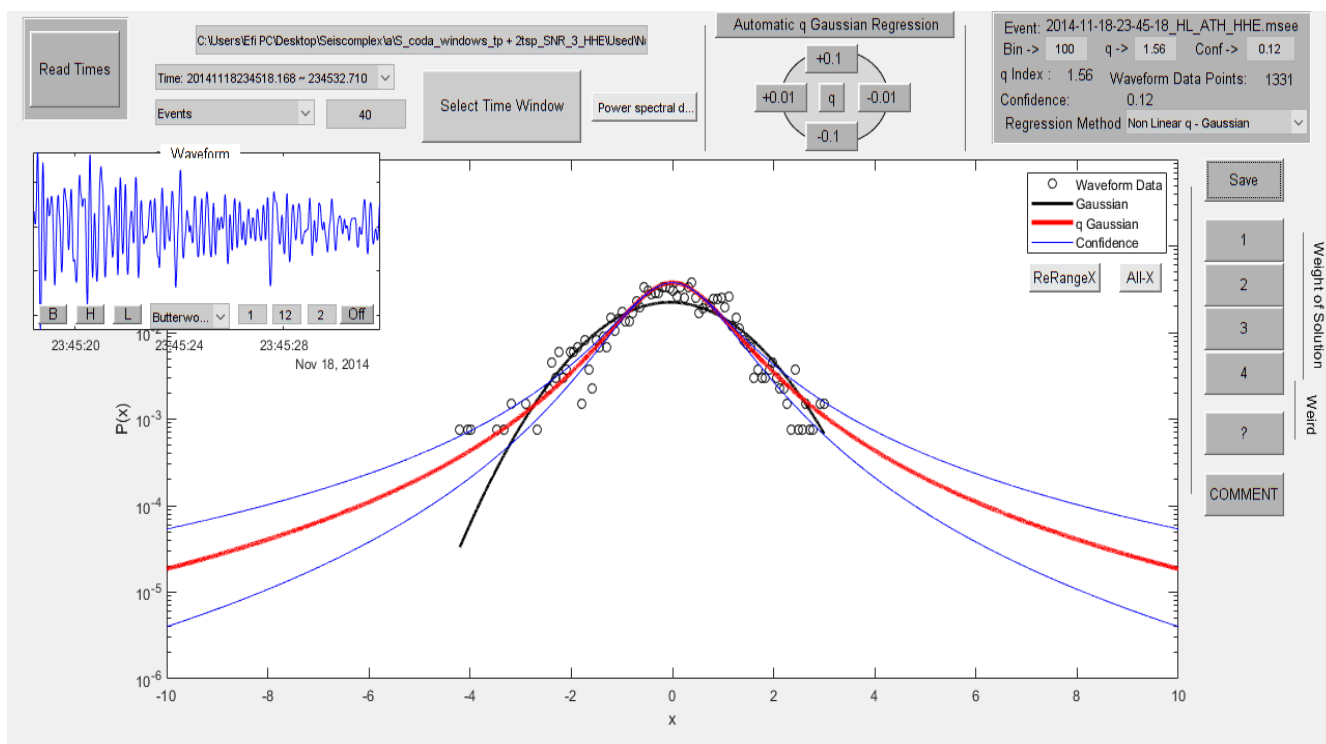


Figure 8.2.135

In figure 8.2.136 the time origin of the earthquake is 27/10/2015 at 01:52:29, latitude 38.94, longitude 24.3, depth 16 km, magnitude 3.4 at 23.1 km W of Skyros. The value of the index  $q$  is 2.

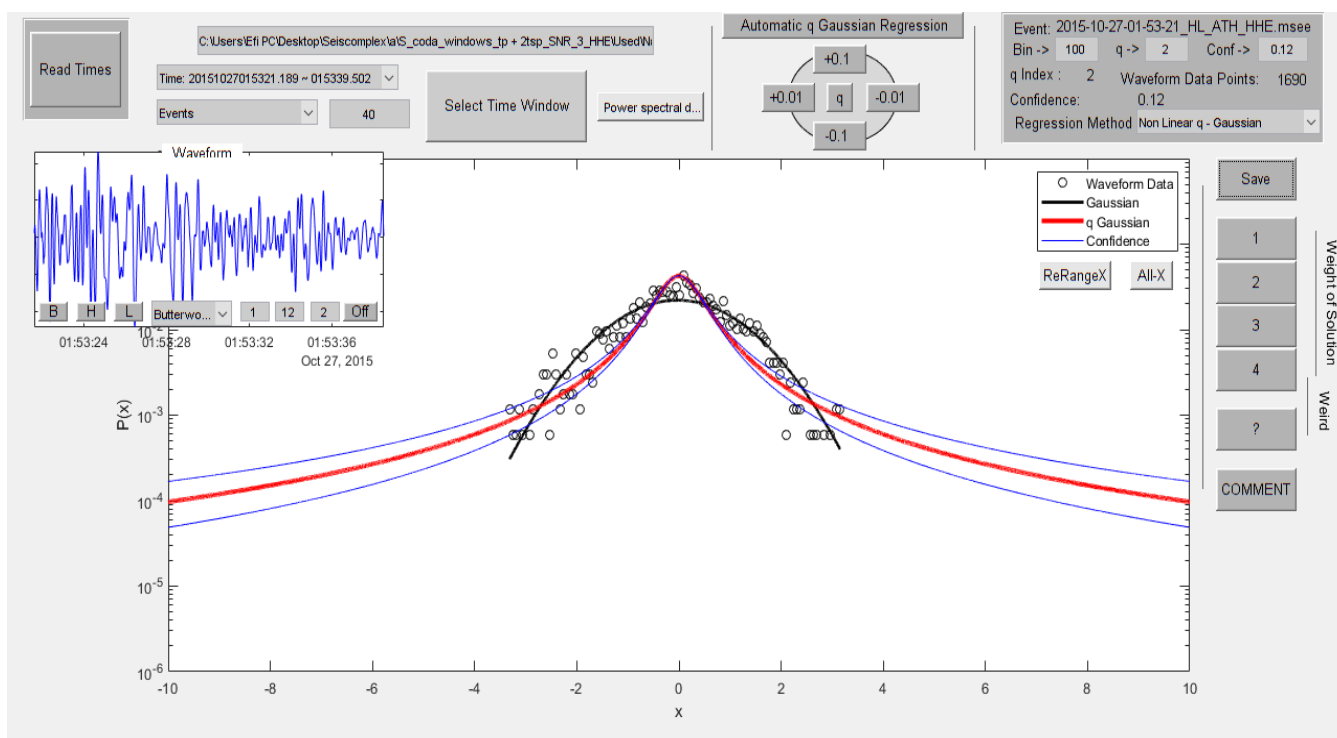


Figure 8.2.136

In figure 8.2.137 the time origin of the earthquake is 14/01/2016 at 00:27:57, latitude 38.95, longitude 24.08, depth 16 km, magnitude 3.4 at 42.1 km W of Skyros. The value of the index  $q$  is 1.57.

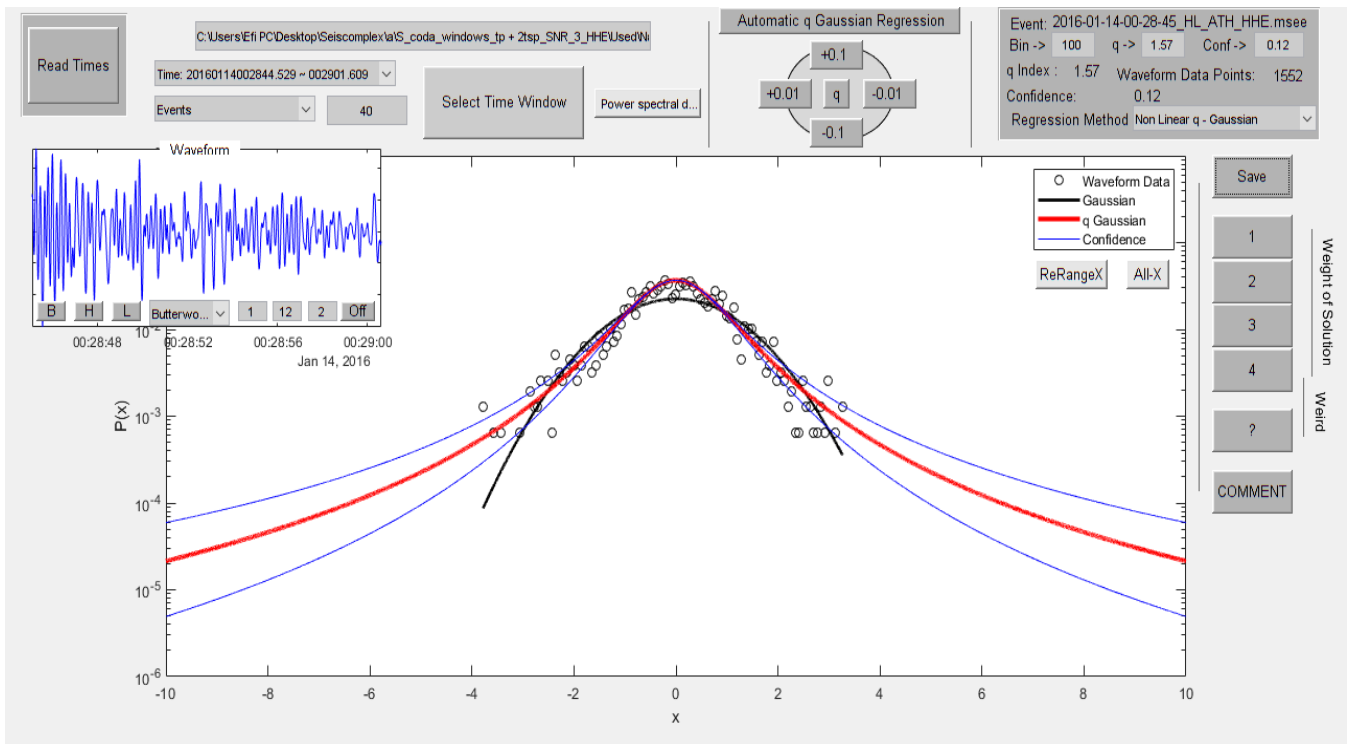


Figure 8.2.137

In figure 8.2.138 the time origin of the earthquake is 06/02/2016 at 02:23:31, latitude 38.42, longitude 23.99, depth 26 km, magnitude 3.4 at 34.4 km E of Chalkida. The value of the index  $q$  is 1.5.

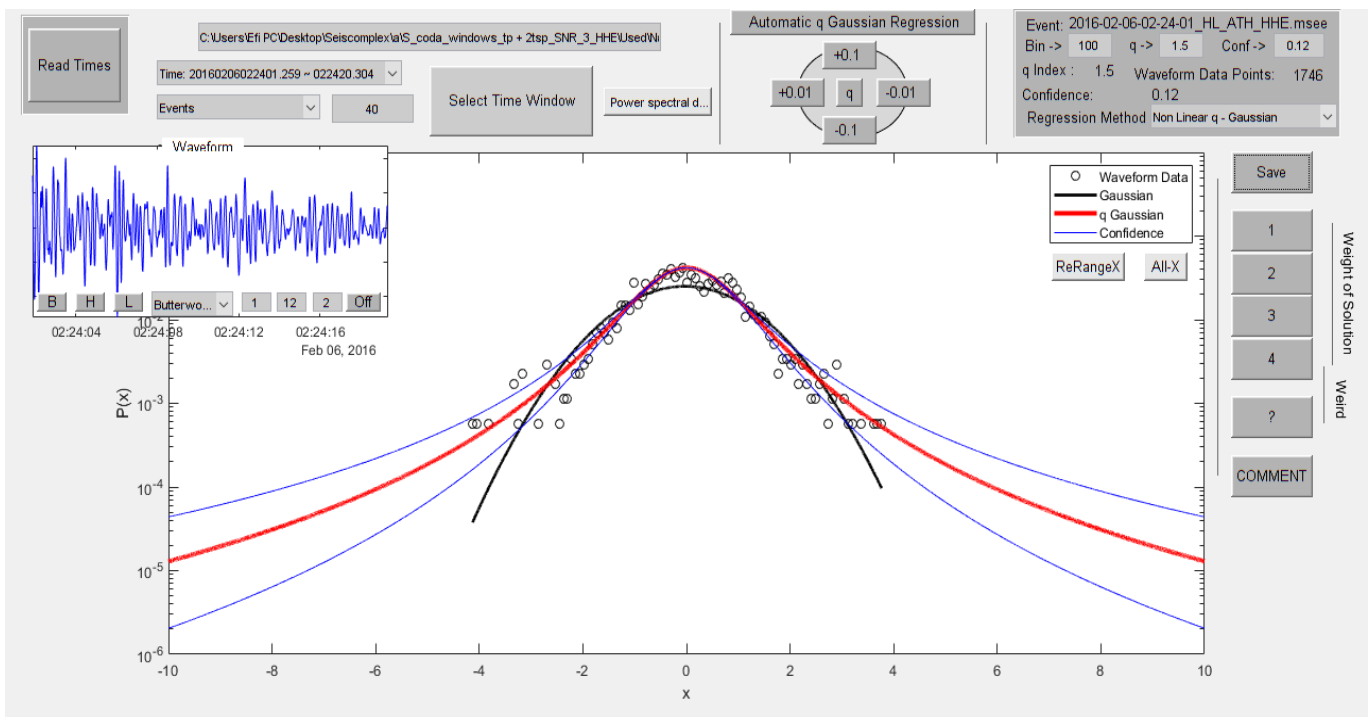


Figure 8.2.138

In figure 8.2.139 the time origin of the earthquake is 22/08/2016 at 13:24:10, latitude 38.33, longitude 24.06, depth 15 km, magnitude 3.4 at 42.8 km ESE of Chalkida. The value of the index  $q$  is 1.63.

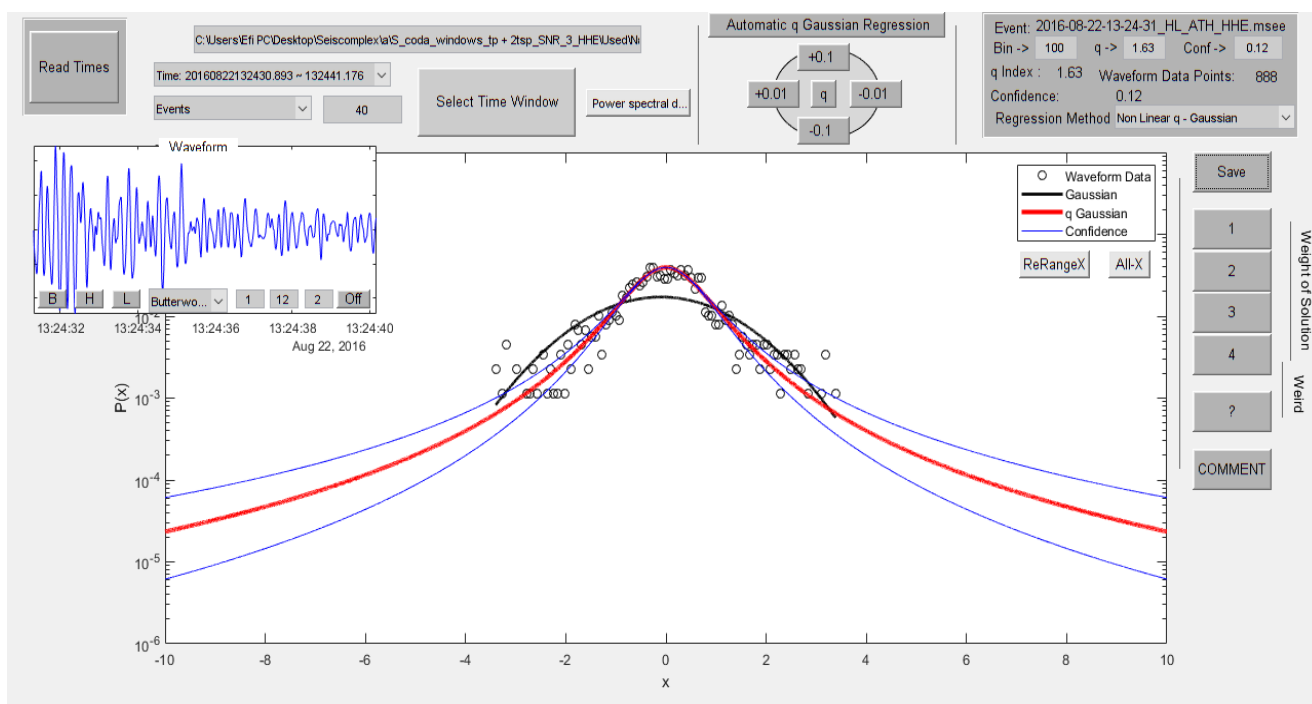


Figure 8.2.139

In figure 8.2.140 the time origin of the earthquake is 09/09/2016 at 14:07:49, latitude 37.57, longitude 23.58, depth 17 km, magnitude 3.4 at 47.9 km SSW of Athens. The value of the index  $q$  is 2.01.

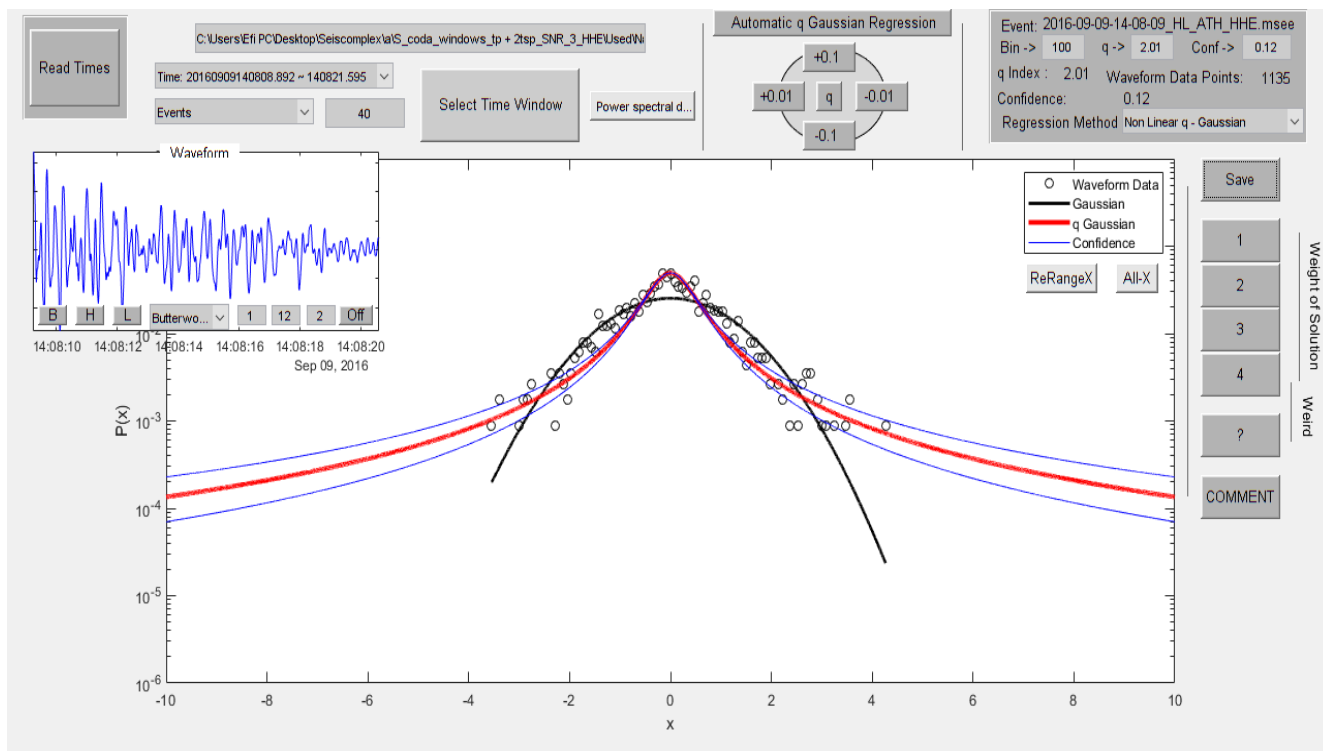


Figure 8.2.140

In figure 8.2.141 the time origin of the earthquake is 04/06/2017 at 00:07:21, latitude 38.1495, longitude 24.0802, depth 20 km, magnitude 3.4 at 35.5 km ENE of Athens. The value of the index  $q$  is 1.5.

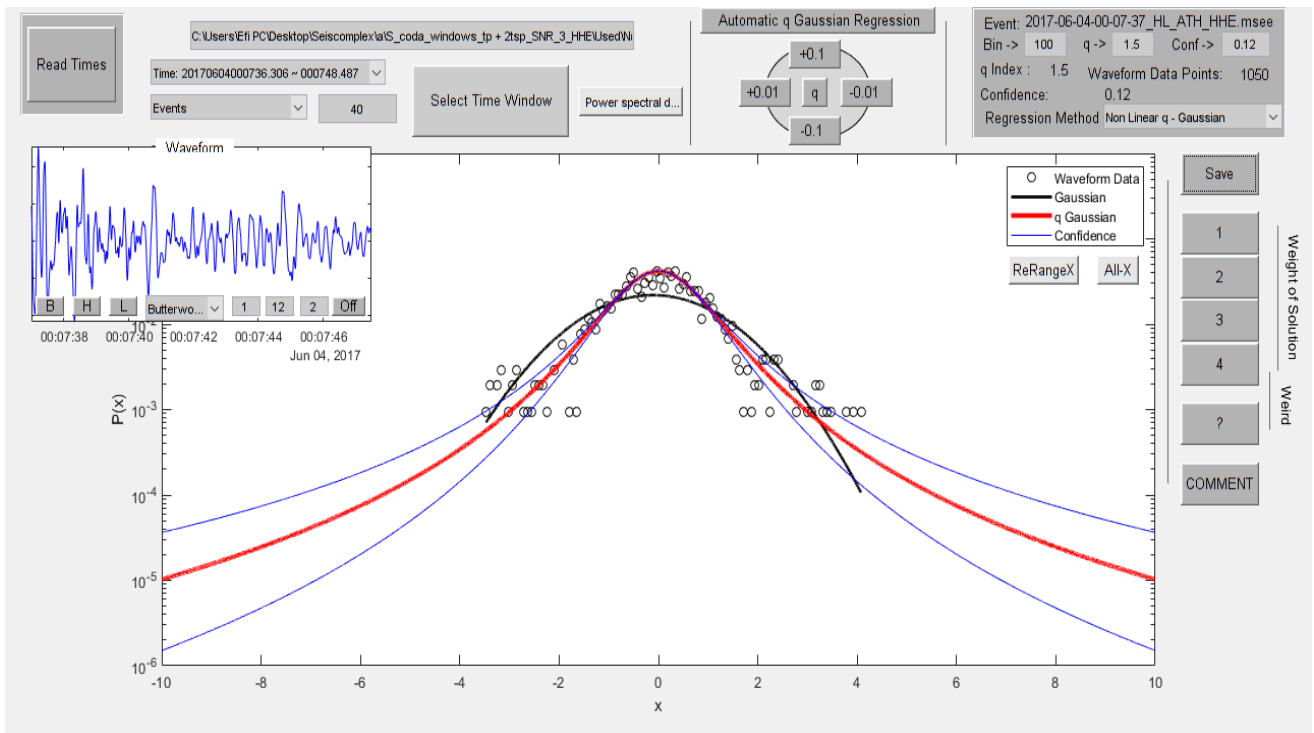


Figure 8.2.141

In figure 8.2.142 the time origin of the earthquake is 02/09/2017 at 04:21:05, latitude 38.4229, longitude 23.5107, depth 23 km, magnitude 3.4 at 9.0 km WSW of Chalkida. The value of the index  $q$  is 1.62.

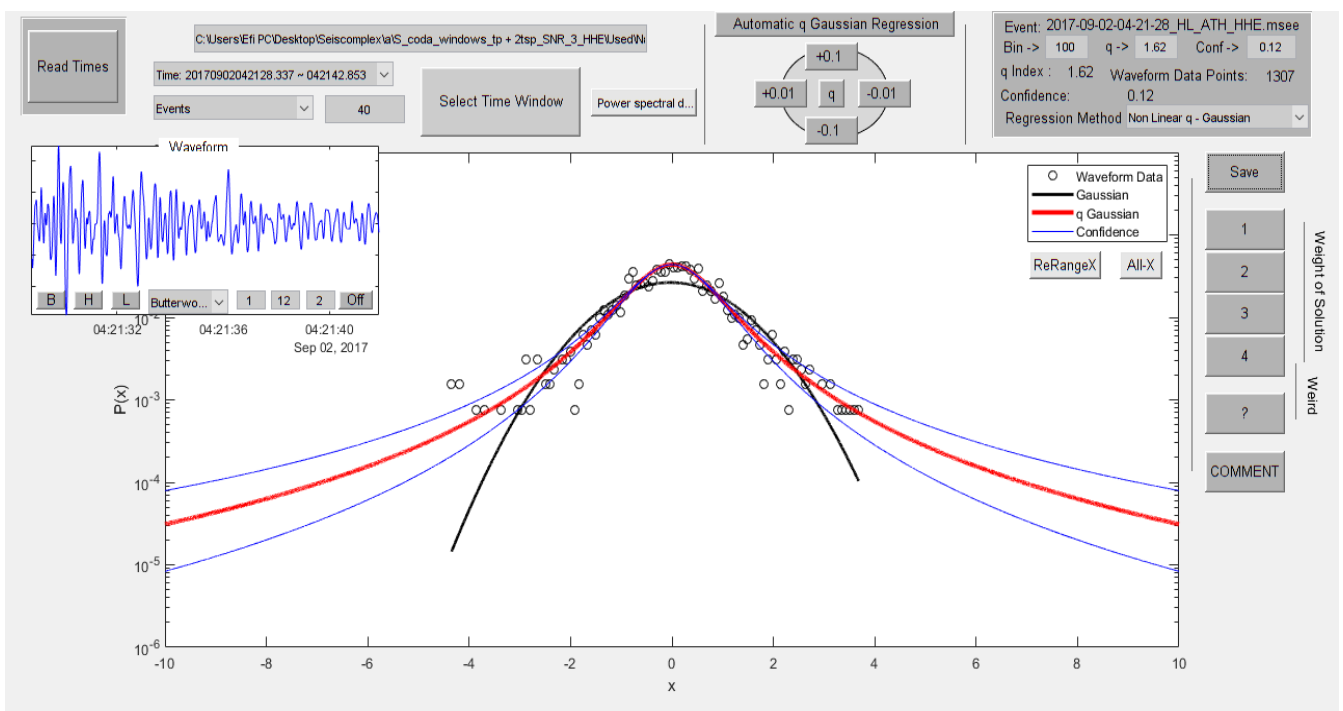


Figure 8.2.142

In figure 8.2.143 the time origin of the earthquake is 29/10/2017 at 20:35:32, latitude 37.5146, longitude 22.6611, depth 30 km, magnitude 3.4 at 14.0 km WSW of Nafplio. The value of the index  $q$  is 1.79.

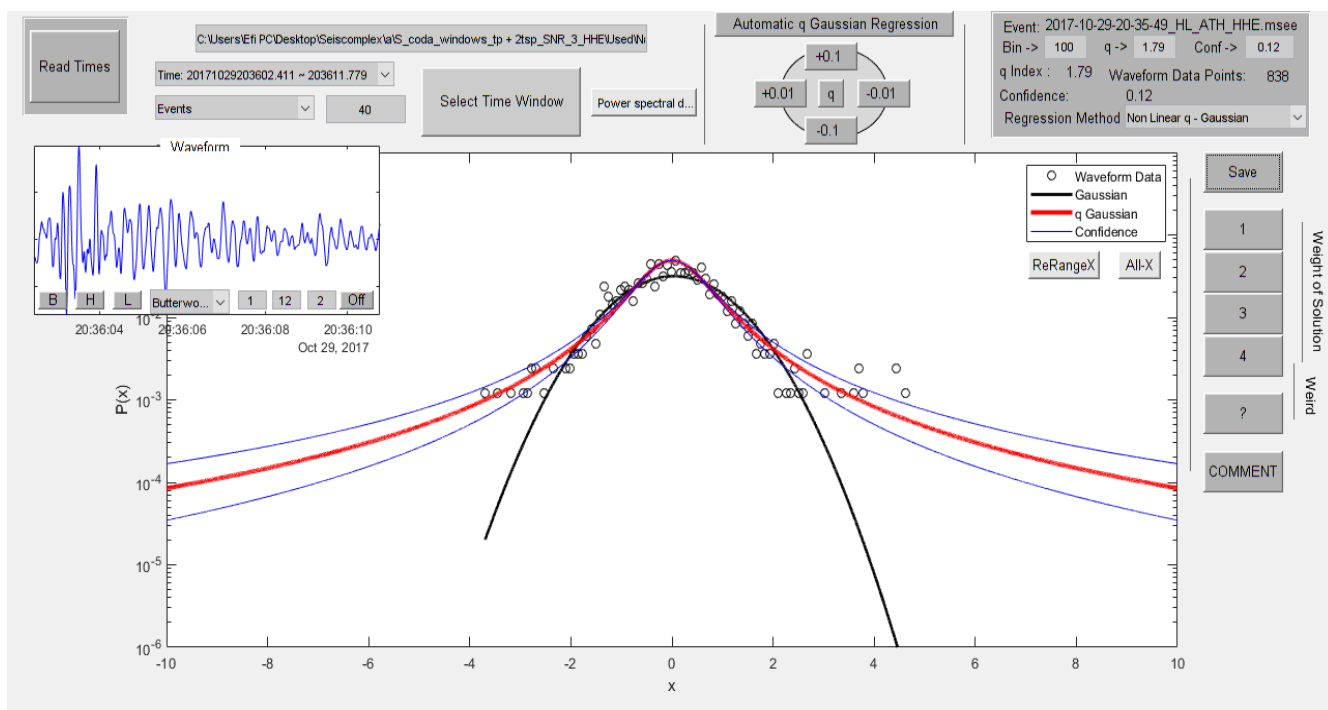


Figure 8.2.143

In figure 8.2.144 the time origin of the earthquake is 15/03/2012 at 23:47:48, latitude 38.14, longitude 22.67, depth 20 km, magnitude 3.3 at 32.1 km NW of Korinthos. The value of the index  $q$  is 1.67.

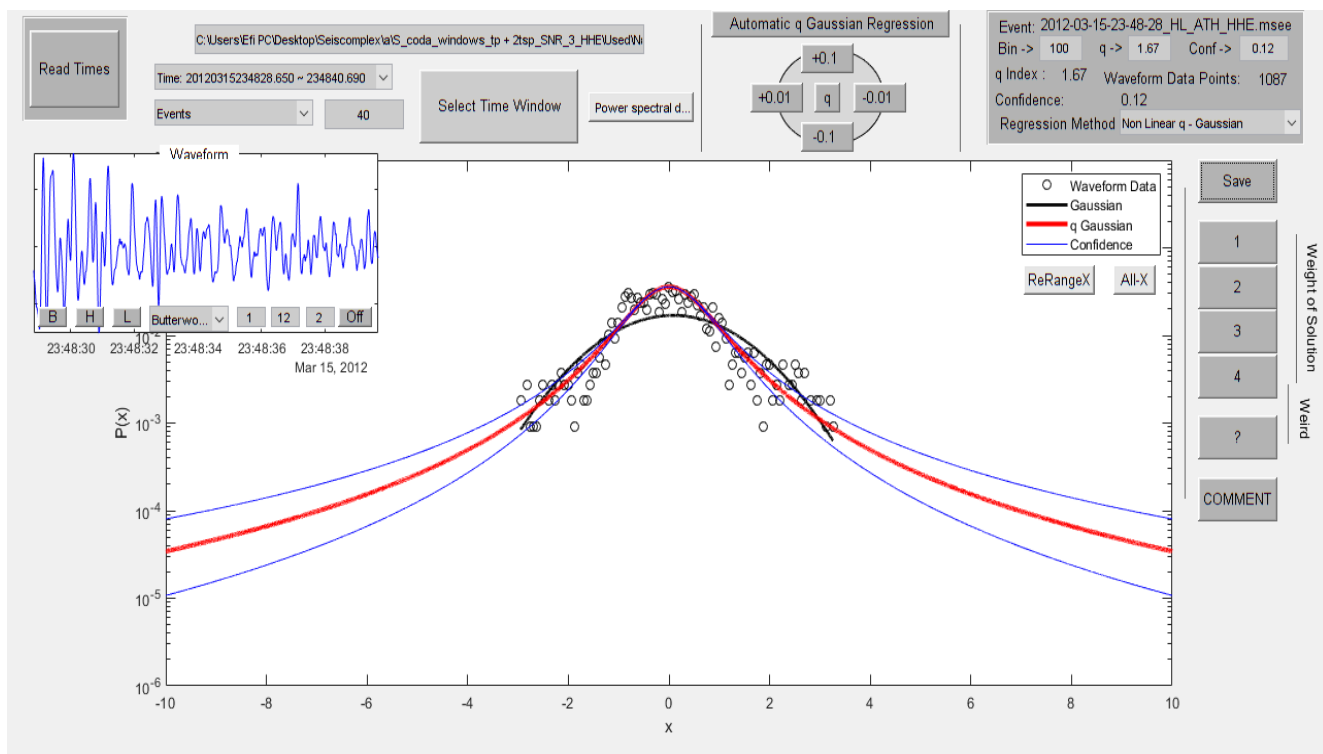


Figure 8.2.144

In figure 8.2.145 the time origin of the earthquake is 14/04/2012 at 20:19:18, latitude 38.11, longitude 22.71, depth 15 km, magnitude 3.3 at 27.3 km NW of Korinthos. The value of the index  $q$  is 1.65.

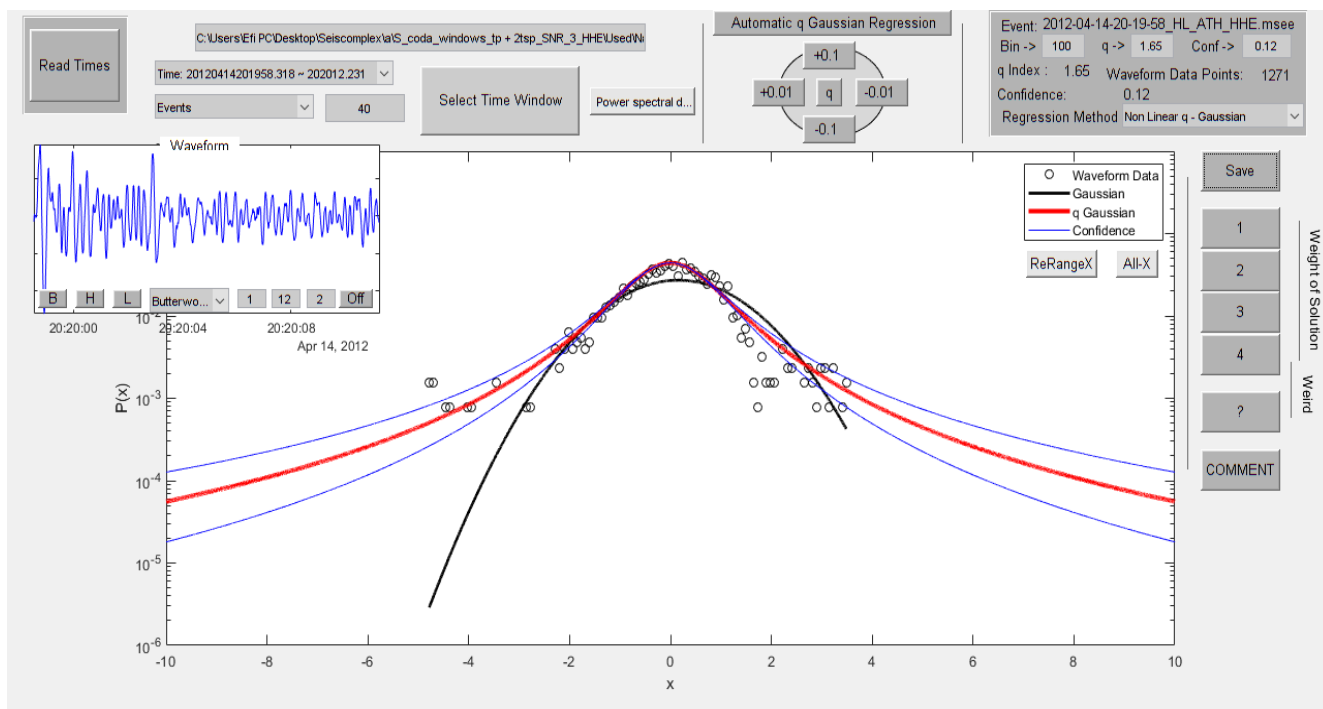


Figure 8.2.145

In figure 8.2.146 the time origin of the earthquake is 30/09/2012 at 05:19:37, latitude 38.1, longitude 22.7, depth 15 km, magnitude 3.3 at 27.2 km NW of Korinthos. The value of the index  $q$  is 2.1.

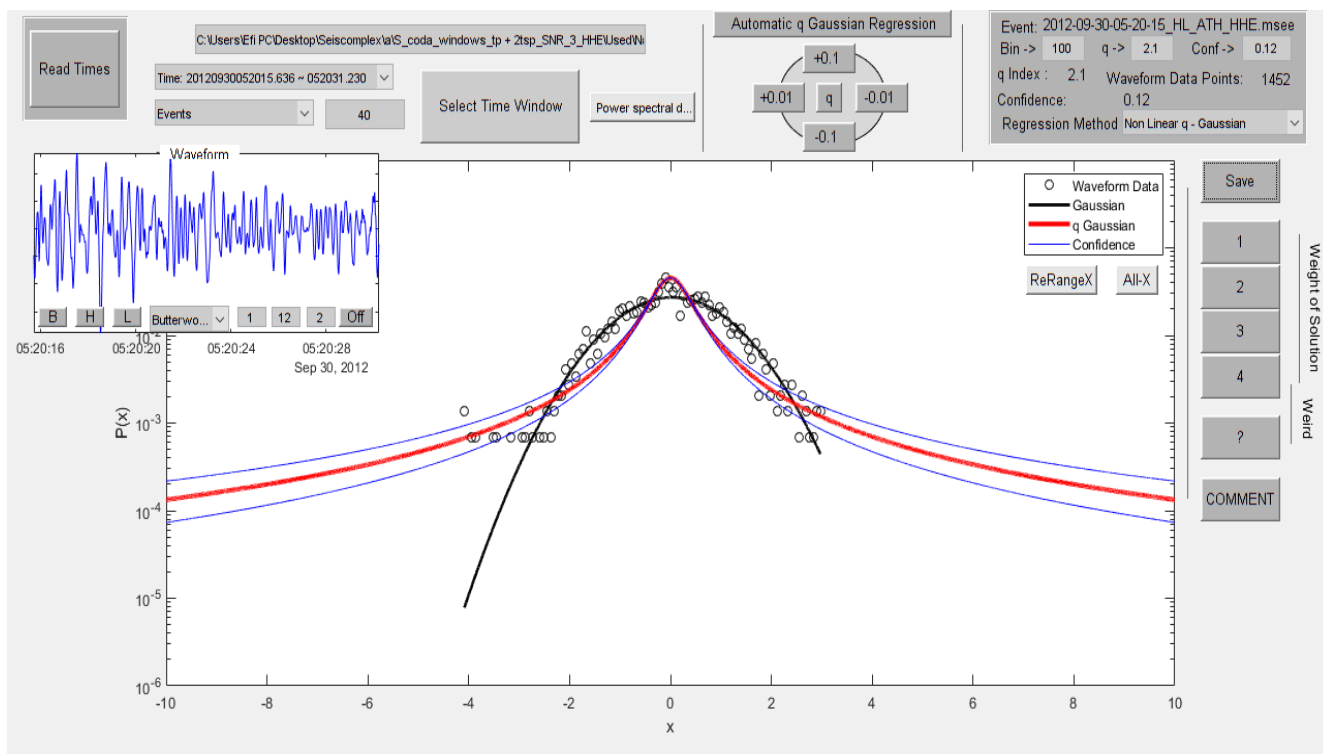


Figure 8.2.146

In figure 8.2.147 the time origin of the earthquake is 26/09/2013 at 00:49:53, latitude 38.44, longitude 23.81, depth 24 km, magnitude 3.3 at 18.5 km E of Chalkida. The value of the index  $q$  is 1.97.

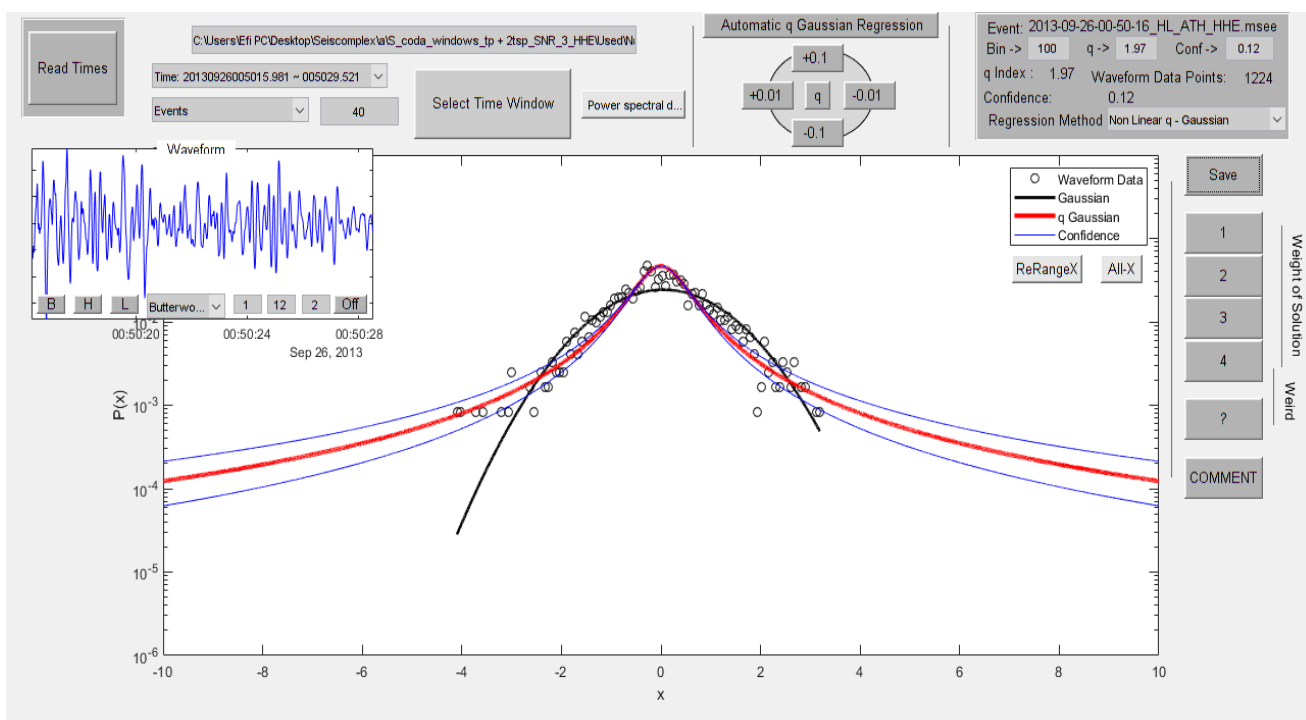


Figure 8.2.147

In figure 8.2.148 the time origin of the earthquake is 26/12/2013 at 13:51:58, latitude 38.6, longitude 23.95, depth 28 km, magnitude 3.3 at 34.1 km ENE of Chalkida. The value of the index  $q$  is 1.76.

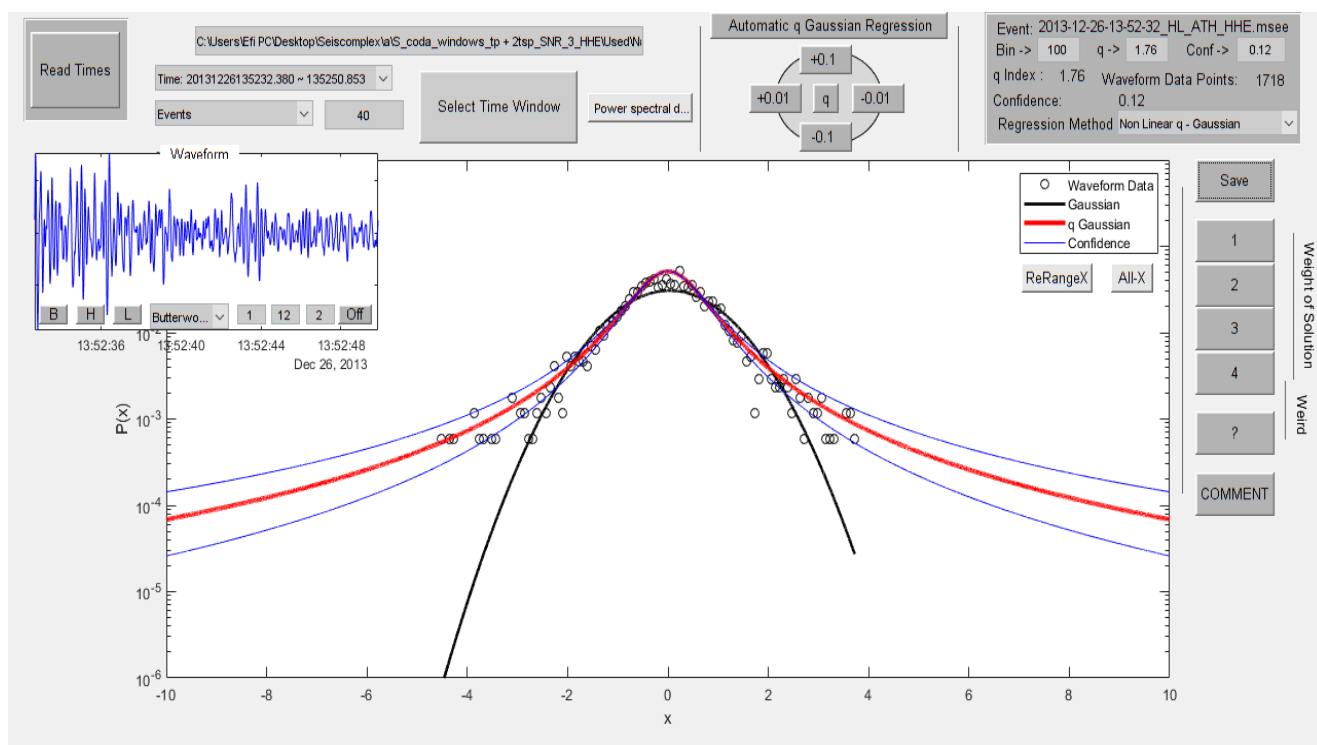


Figure 8.2.148

In figure 8.2.149 the time origin of the earthquake is 13/01/2014 at 03:08:12, latitude 38.86, longitude 23.39, depth 24 km, magnitude 3.3 at 35.0 km SSW of Skiathos. The value of the index  $q$  is 1.66.

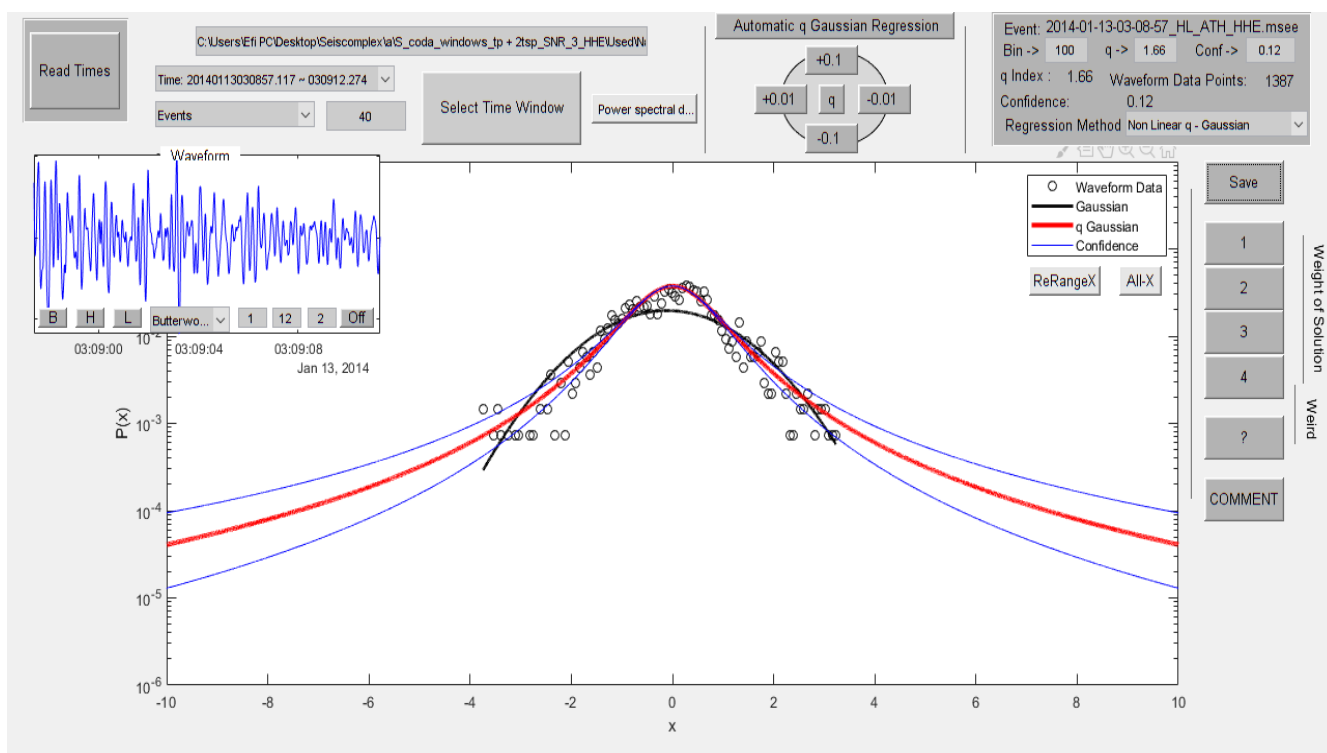


Figure 8.2.149

In figure 8.2.150 the time origin of the earthquake is 23/06/2014 at 01:47:01, latitude 38.69, longitude 23.56, depth 15 km, magnitude 3.3 at 25.4 km N of Chalkida. The value of the index  $q$  is 1.75.

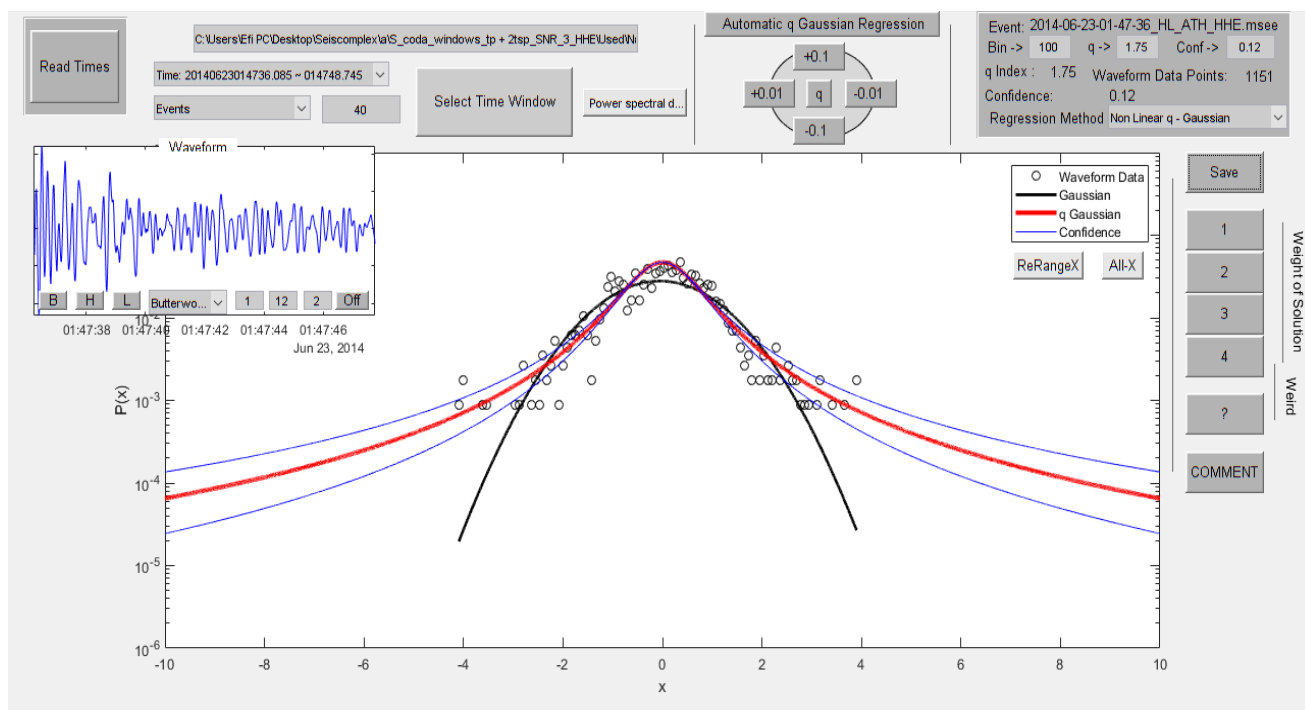


Figure 8.2.150

In figure 8.2.151 the time origin of the earthquake is 18/11/2014 at 00:35:38, latitude 38.65, longitude 23.41, depth 21 km, magnitude 3.3 at 26.5 km NW of Chalkida. The value of the index  $q$  is 1.71.

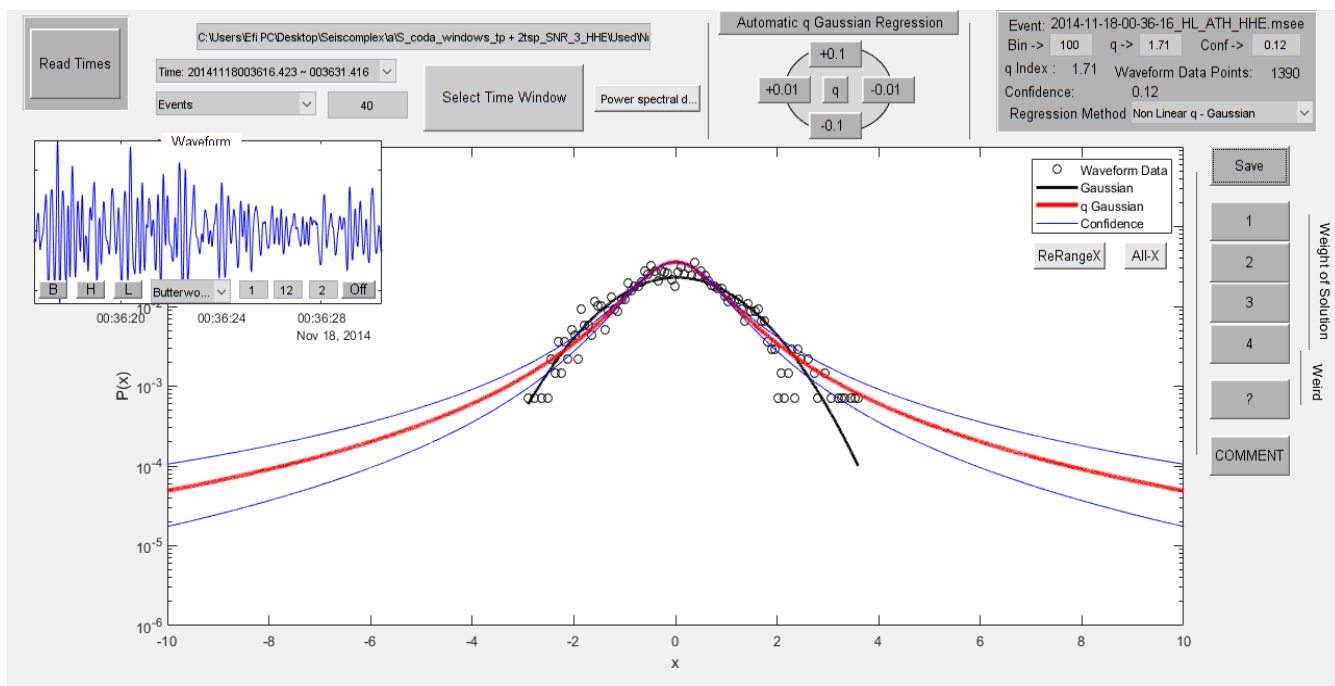


Figure 8.2.151

In figure 8.2.152 the time origin of the earthquake is 18/11/2014 at 00:47:48, latitude 38.66, longitude 23.41, depth 24 km, magnitude 3.3 at 27.4 km NW of Chalkida. The value of the index  $q$  is 2.17.

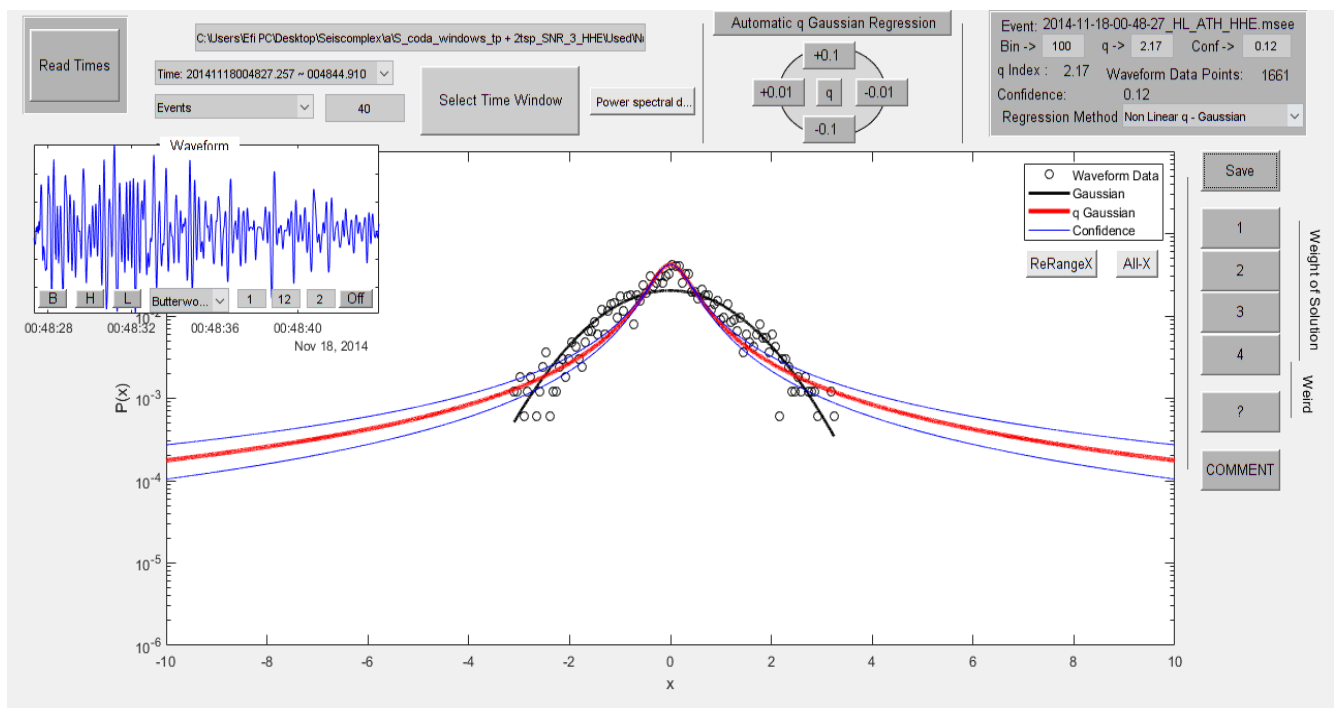


Figure 8.2.152

In figure 8.2.153 the time origin of the earthquake is 06/05/2015 at 19:05:01, latitude 38.43, longitude 23.9, depth 17 km, magnitude 3.3 at 26.4 km E of Chalkida. The value of the index  $q$  is 1.63.

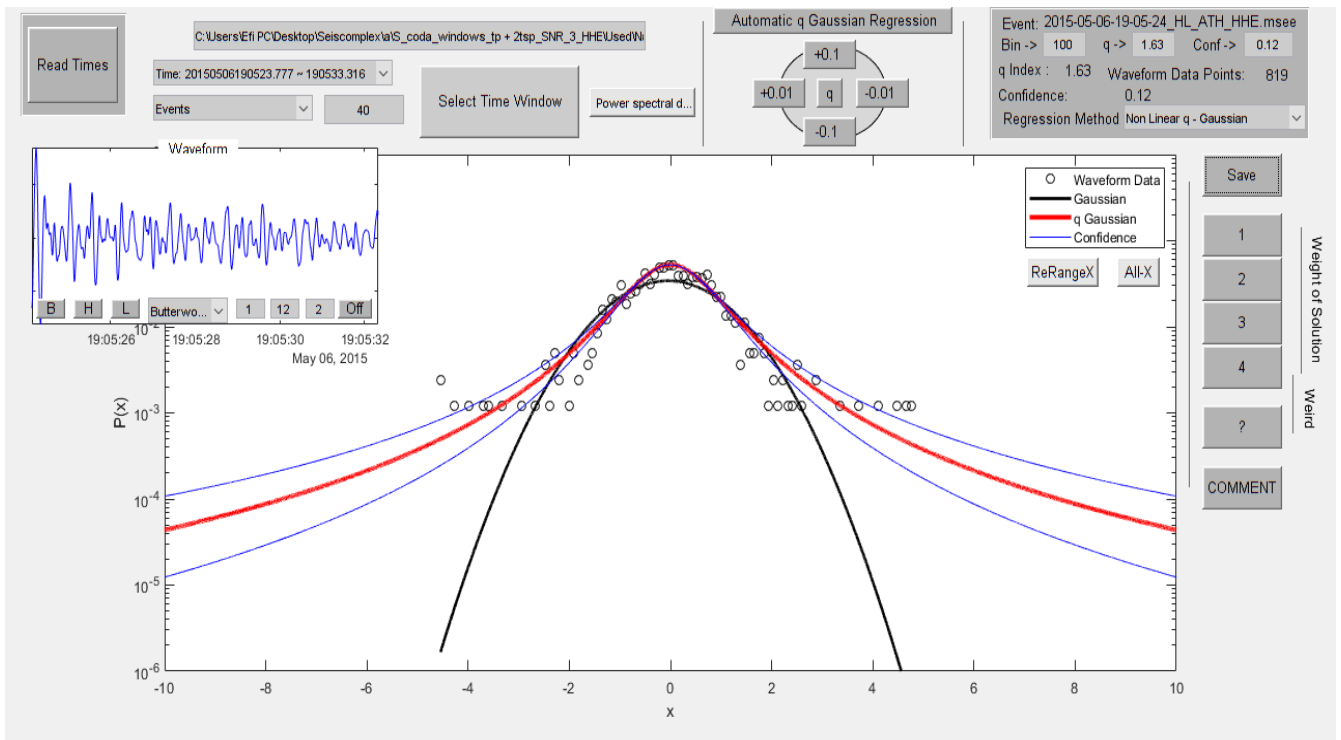


Figure 8.2.153

In figure 8.2.154 the time origin of the earthquake is 10/06/2015 at 18:46:41, latitude 38.66, longitude 23.42, depth 17 km, magnitude 3.3 at 26.8 km NW of Chalkida. The value of the index  $q$  is 1.83.

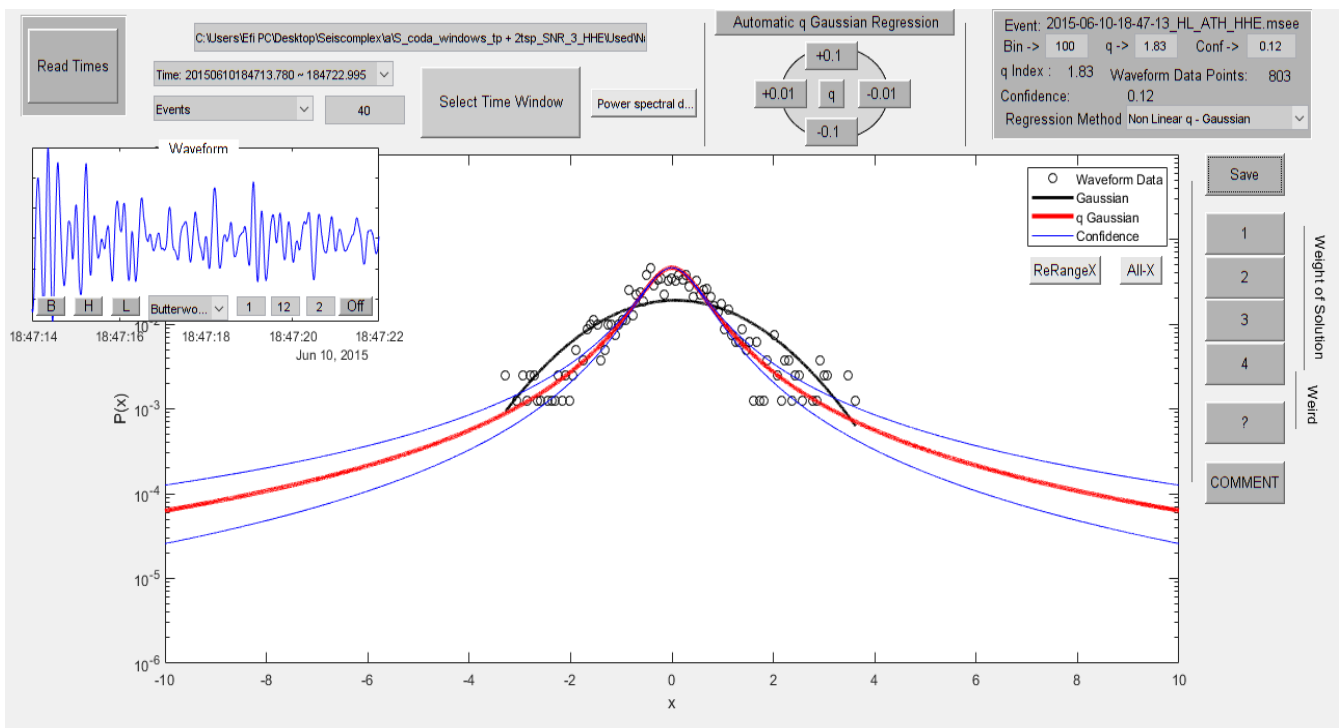


Figure 8.2.154

In figure 8.2.155 the time origin of the earthquake is 23/06/2016 at 12:10:57, latitude 38.16, longitude 22.68, depth 16 km, magnitude 3.3 at 33.1 km NW of Korinthos. The value of the index  $q$  is 1.69.

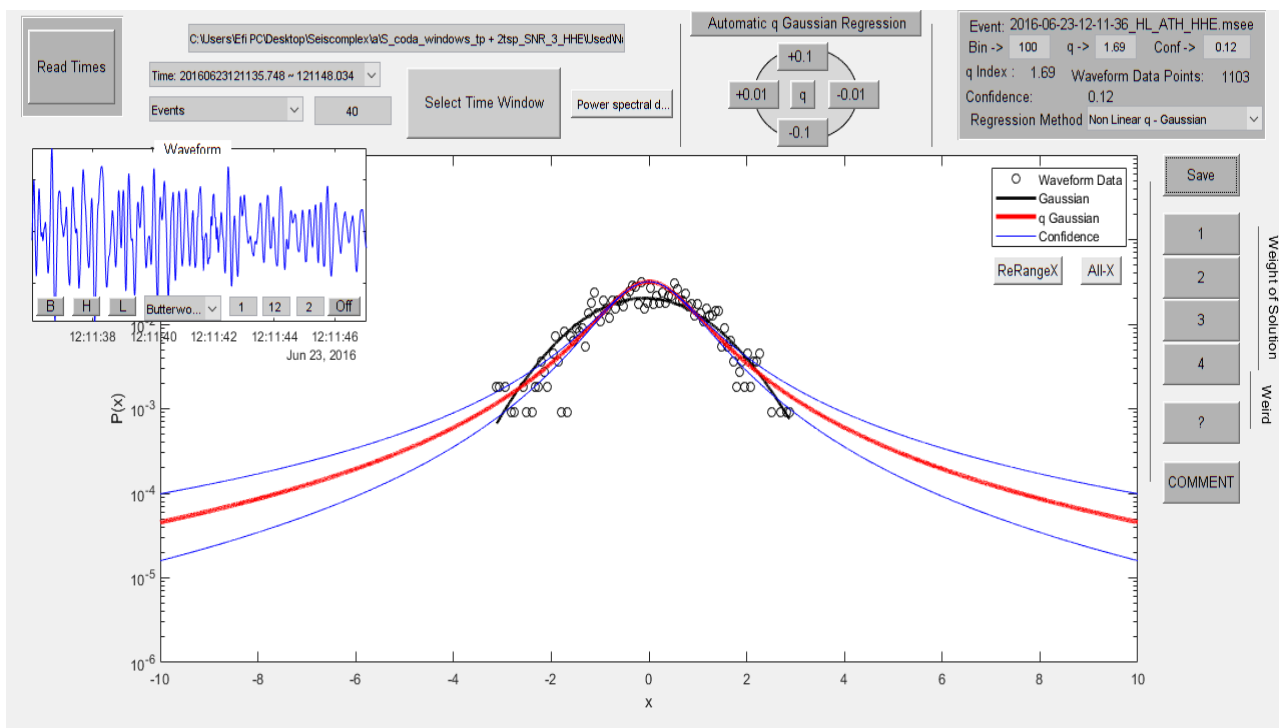


Figure 8.2.155

In figure 8.2.156 the time origin of the earthquake is 04/07/2016 at 05:42:46, latitude 37.54, longitude 23.63, depth 16 km, magnitude 3.3 at 50.1 km S of Athens. The value of the index  $q$  is 2.05.

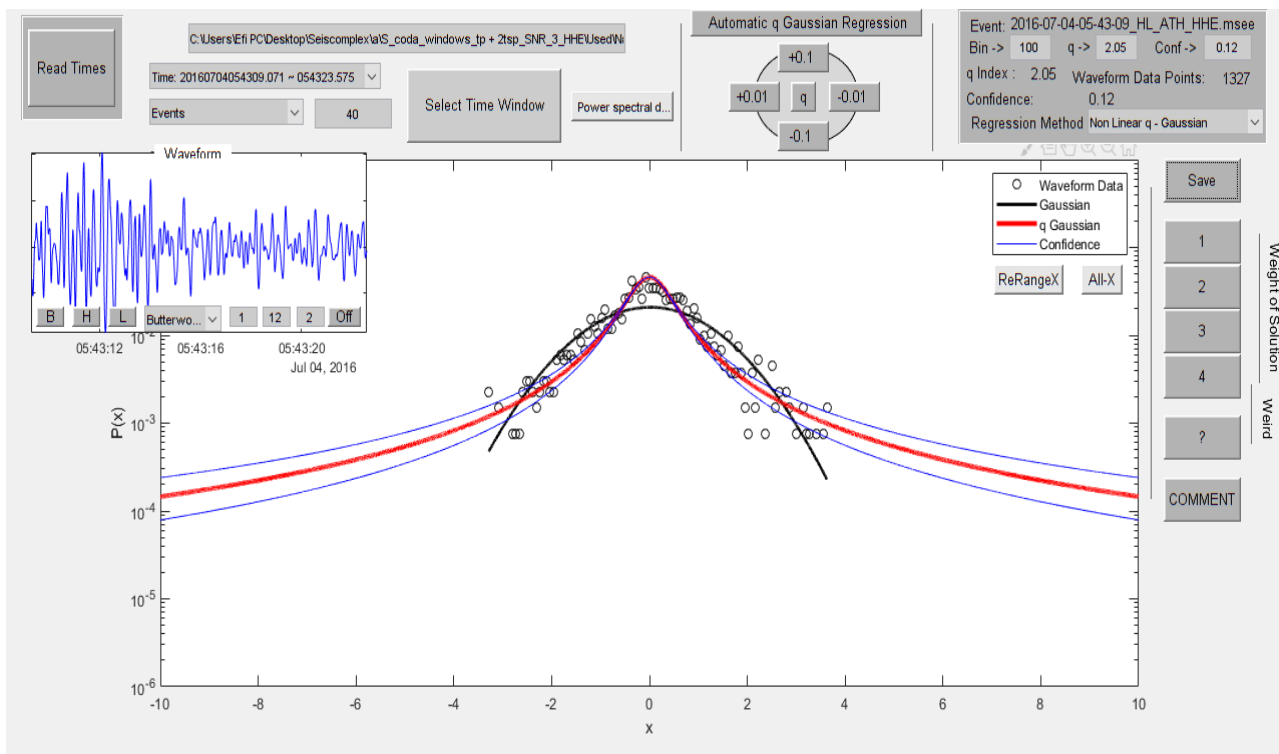


Figure 8.2.156

In figure 8.2.157 the time origin of the earthquake is 07/09/2016 at 09:34:15, latitude 38.4, longitude 23.92, depth 18 km, magnitude 3.3 at 28.8 km ESE of Chalkida. The value of the index  $q$  is 1.82.

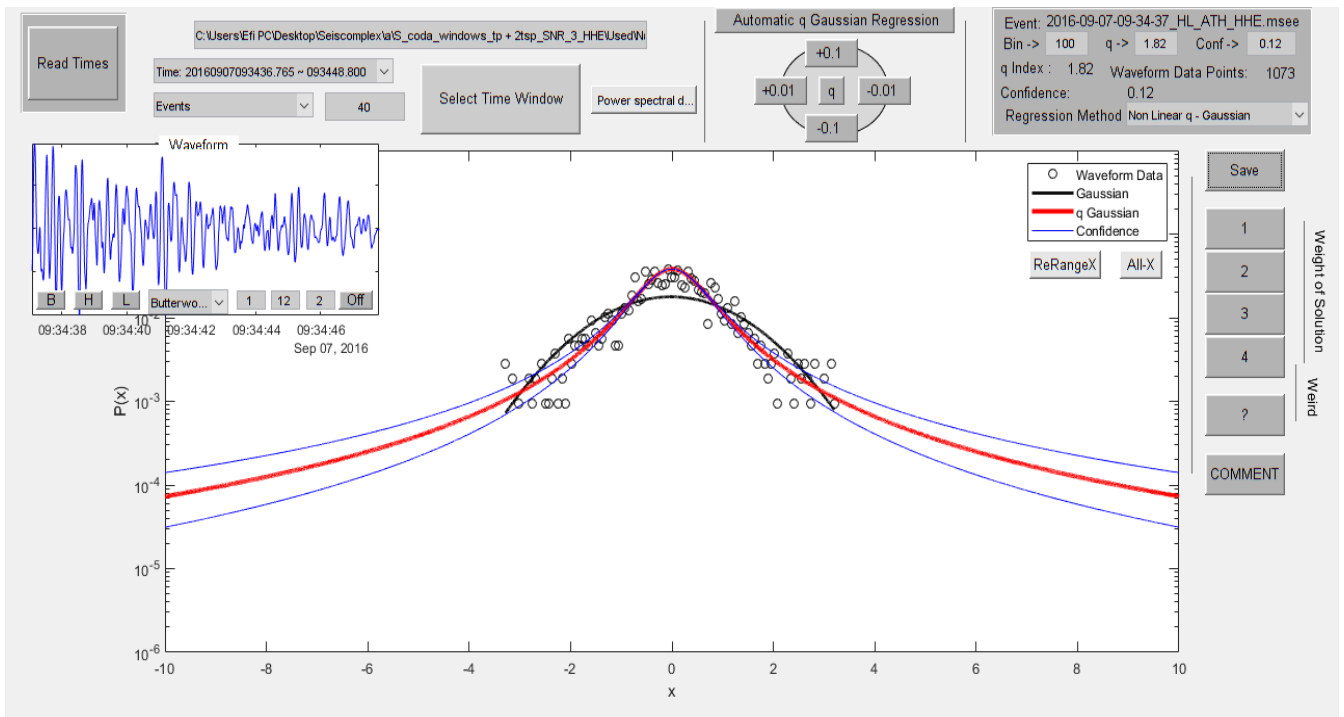


Figure 8.2.157

In figure 8.2.158 the time origin of the earthquake is 01/10/2019 at 01:23:57, latitude 39.521, longitude 23.5826, depth 17 km, magnitude 3.3 at 40.3 km NNE of Skiathos. The value of the index  $q$  is 1.46.

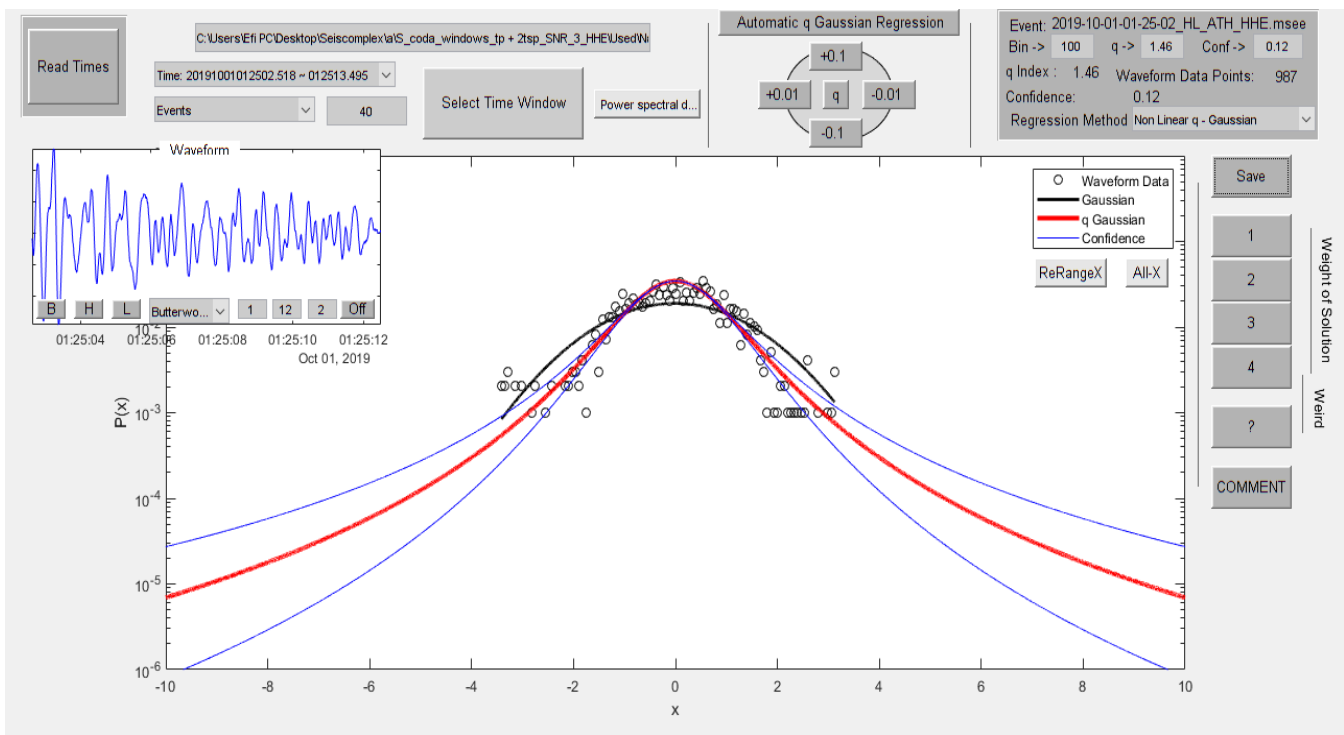


Figure 8.2.158

In figure 8.2.159 the time origin of the earthquake is 29/05/2011 at 22:23:19, latitude 38.16, longitude 23.95, depth 18 km, magnitude 3.2 at 27.3 km NE of Athens. The value of the index  $q$  is 1.8.

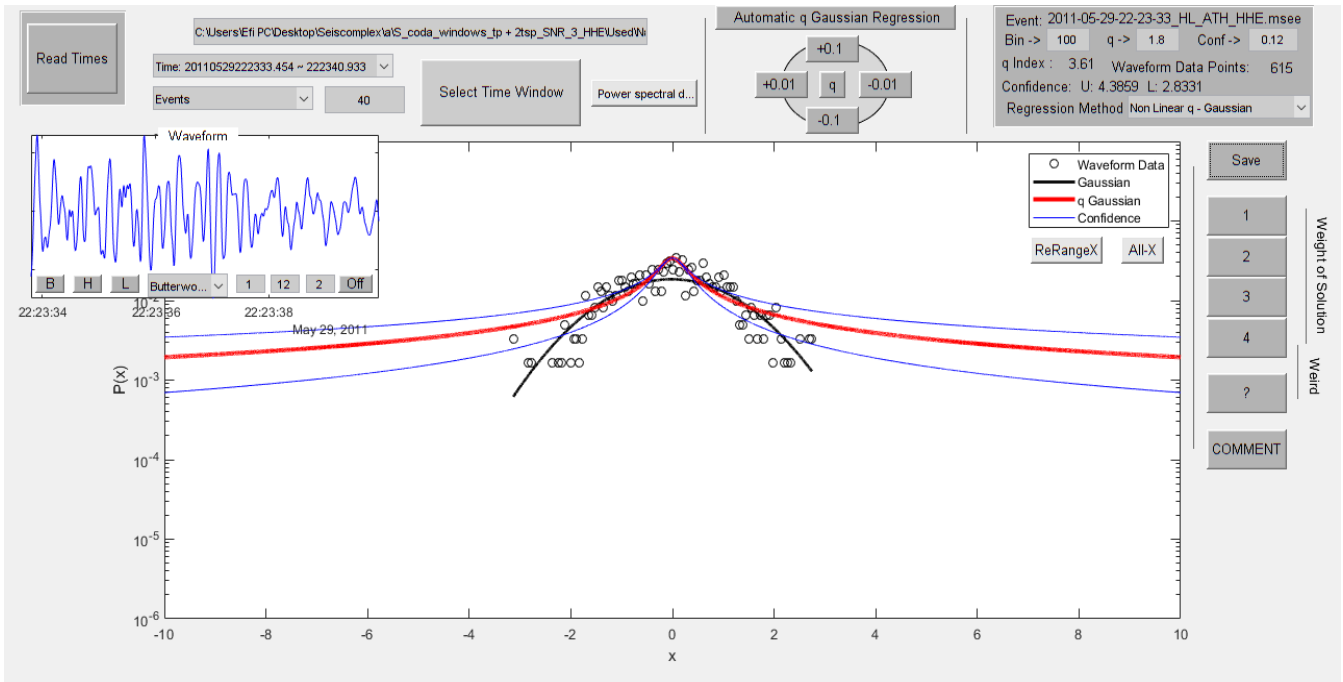


Figure 8.2.159

In figure 8.2.160 the time origin of the earthquake is 05/08/2011 at 05:49:59, latitude 38.72, longitude 23.71, depth 25 km, magnitude 3.2 at 30.1 km NNE of Chalkida. The value of the index  $q$  is 1.73.

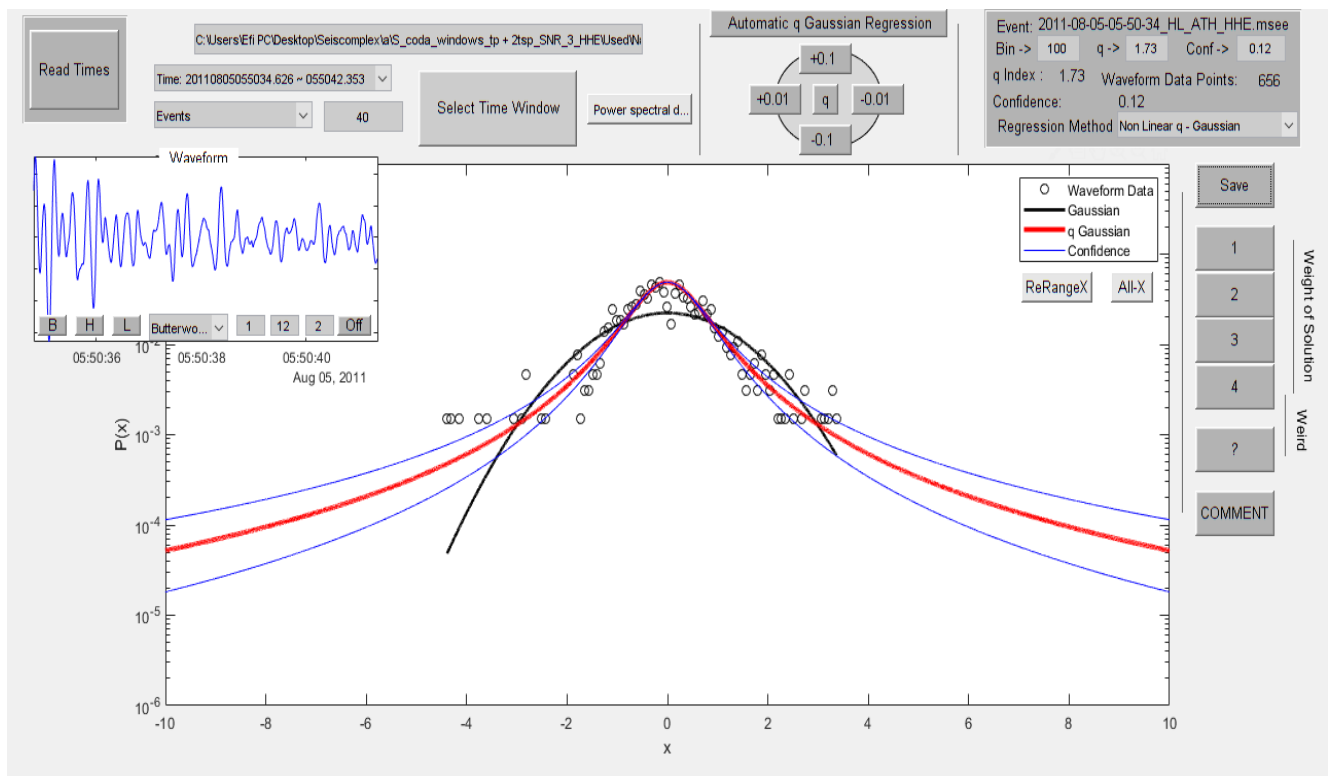


Figure 8.2.160

In figure 8.2.161 the time origin of the earthquake is 30/09/2012 at 02:41:34, latitude 38.11, longitude 22.7, depth 20 km, magnitude 3.2 at 27.9 km NW of Korinthos. The value of the index  $q$  is 1.91.

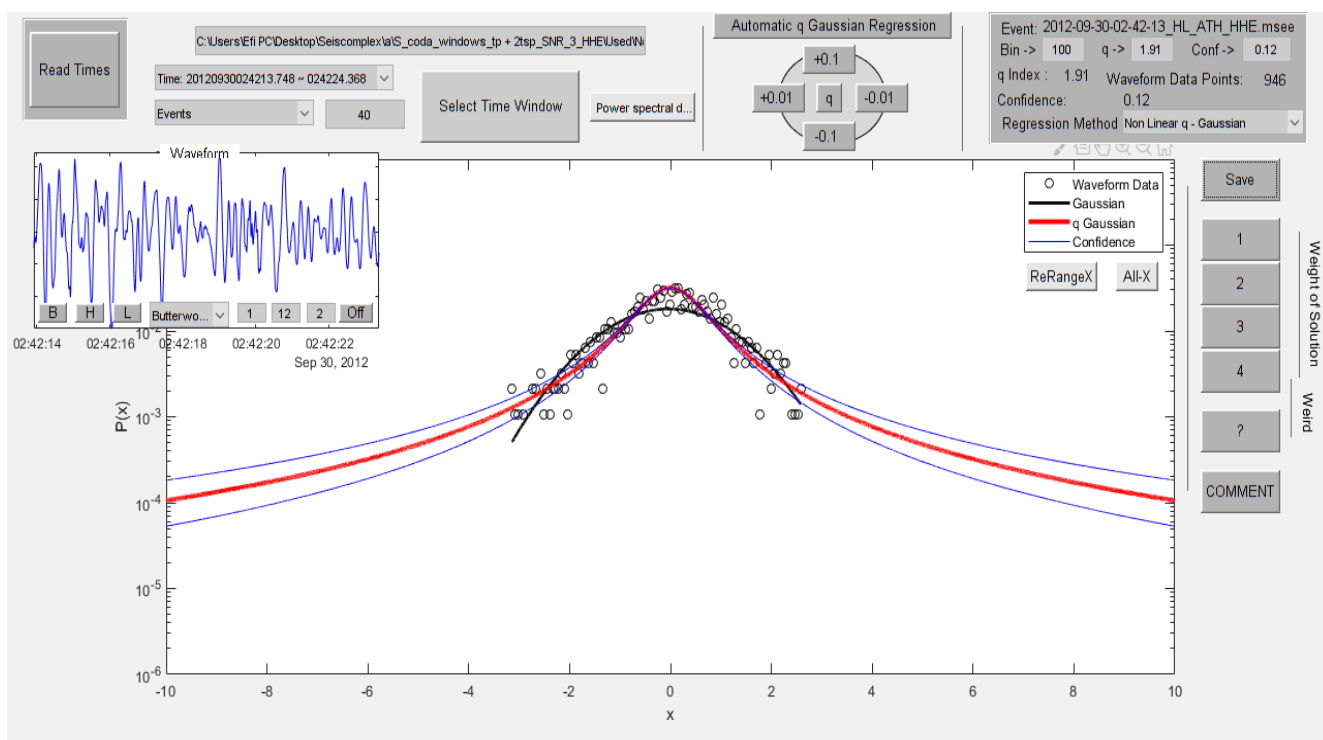


Figure 8.2.161

In figure 8.2.162 the time origin of the earthquake is 27/07/2013 at 06:46:52, latitude 38.6, longitude 23.94, depth 28 km, magnitude 3.2 at 33.3 km ENE of Chalkida. The value of the index  $q$  is 1.76.

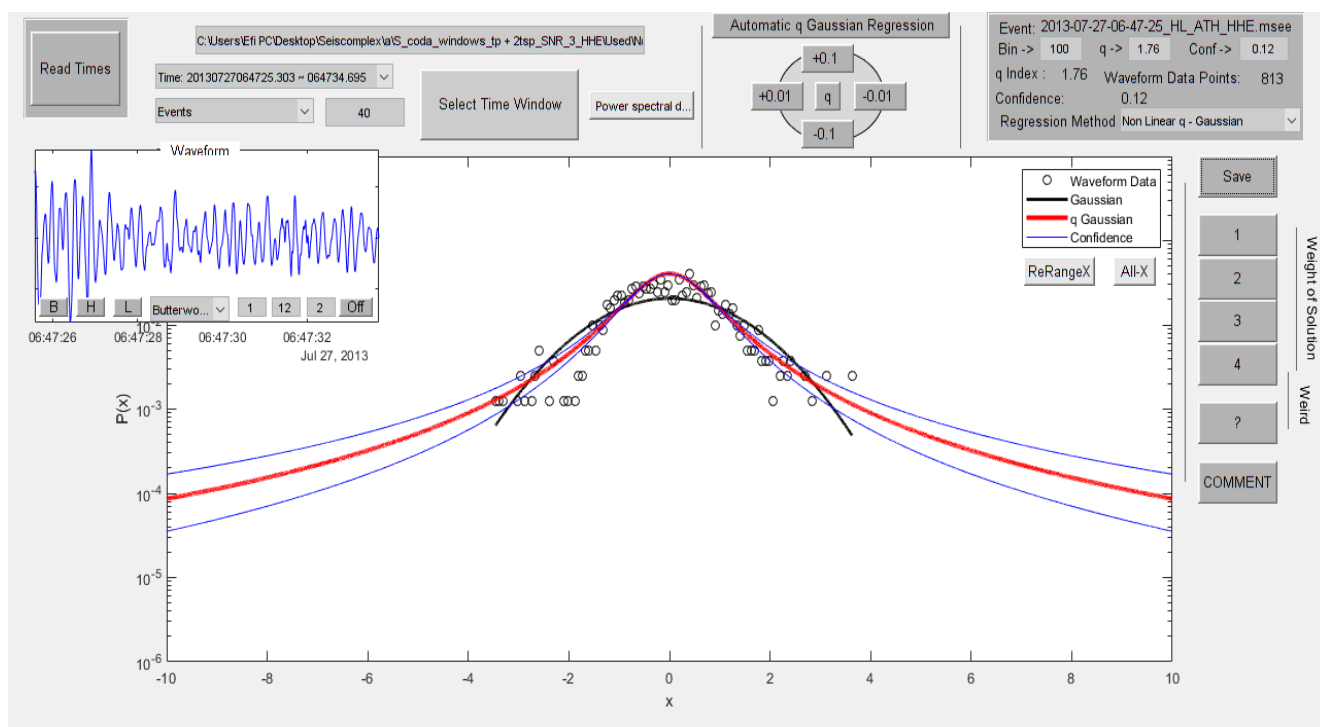


Figure 8.2.162

In figure 8.2.163 the time origin of the earthquake is 15/11/2013 at 18:11:03, latitude 37.54, longitude 22.9, depth 76 km, magnitude 3.2 at 8.6 km ESE of Nafplio. The value of the index  $q$  is 1.95.

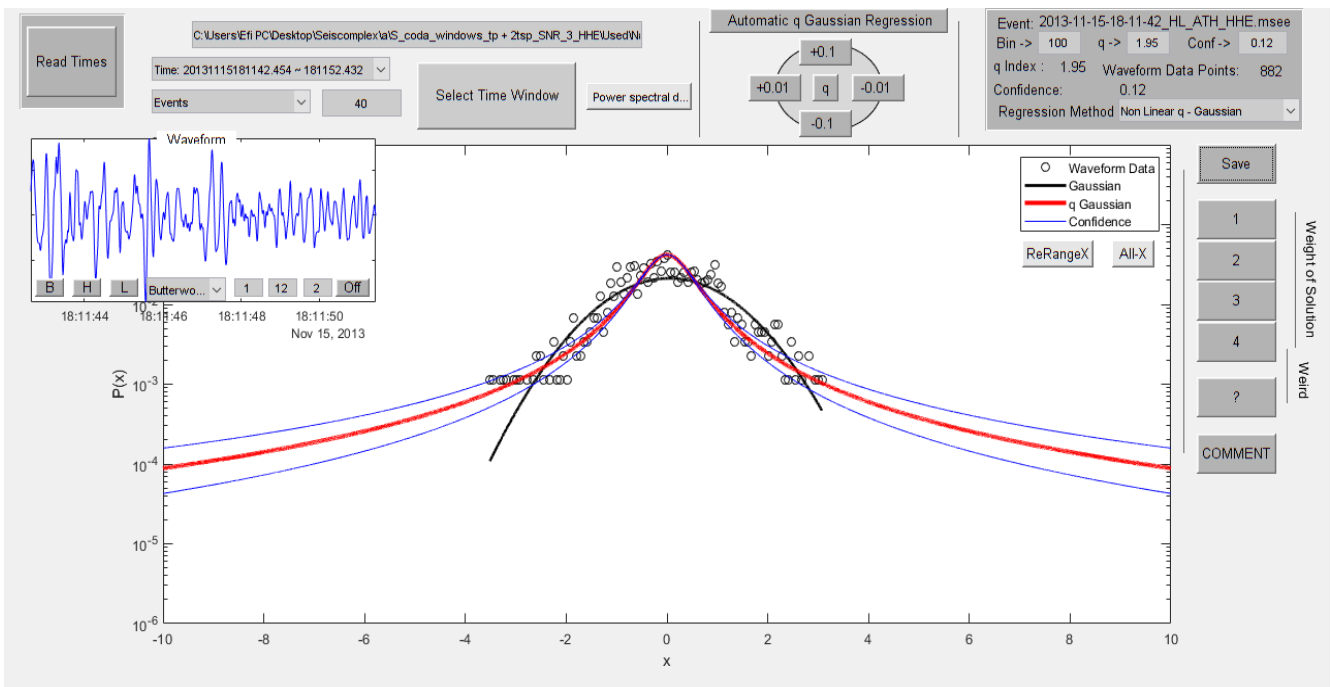


Figure 8.2.163

In figure 8.2.164 the time origin of the earthquake is 11/10/2014 at 01:53:35, latitude 37.88, longitude 22.55, depth 19 km, magnitude 3.2 at 34.1 km W of Korinthos. The value of the index  $q$  is 1.44.

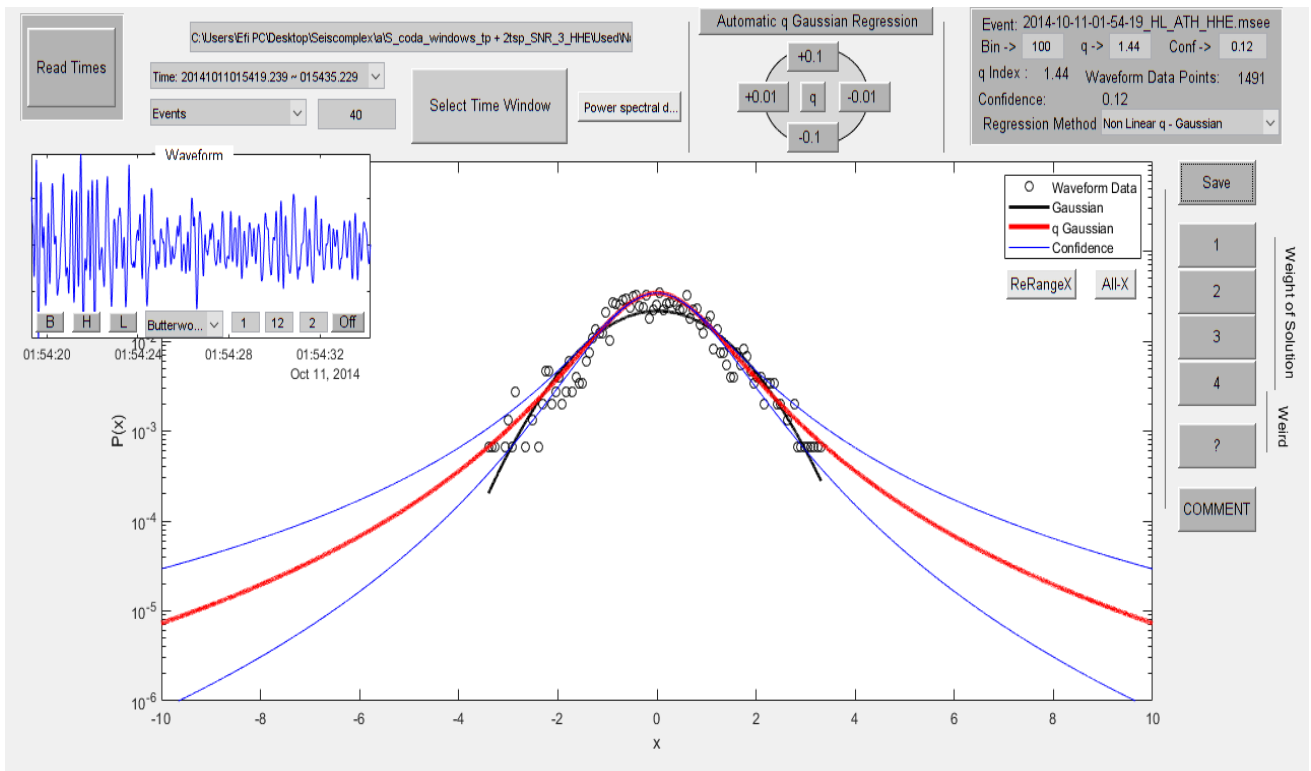


Figure 8.2.164

In figure 8.2.165 the time origin of the earthquake is 21/10/2014 at 17:46:25, latitude 38.59, longitude 22.99, depth 23 km, magnitude 3.2 at 6.8 km S of Atalanti. The value of the index  $q$  is 1.6.

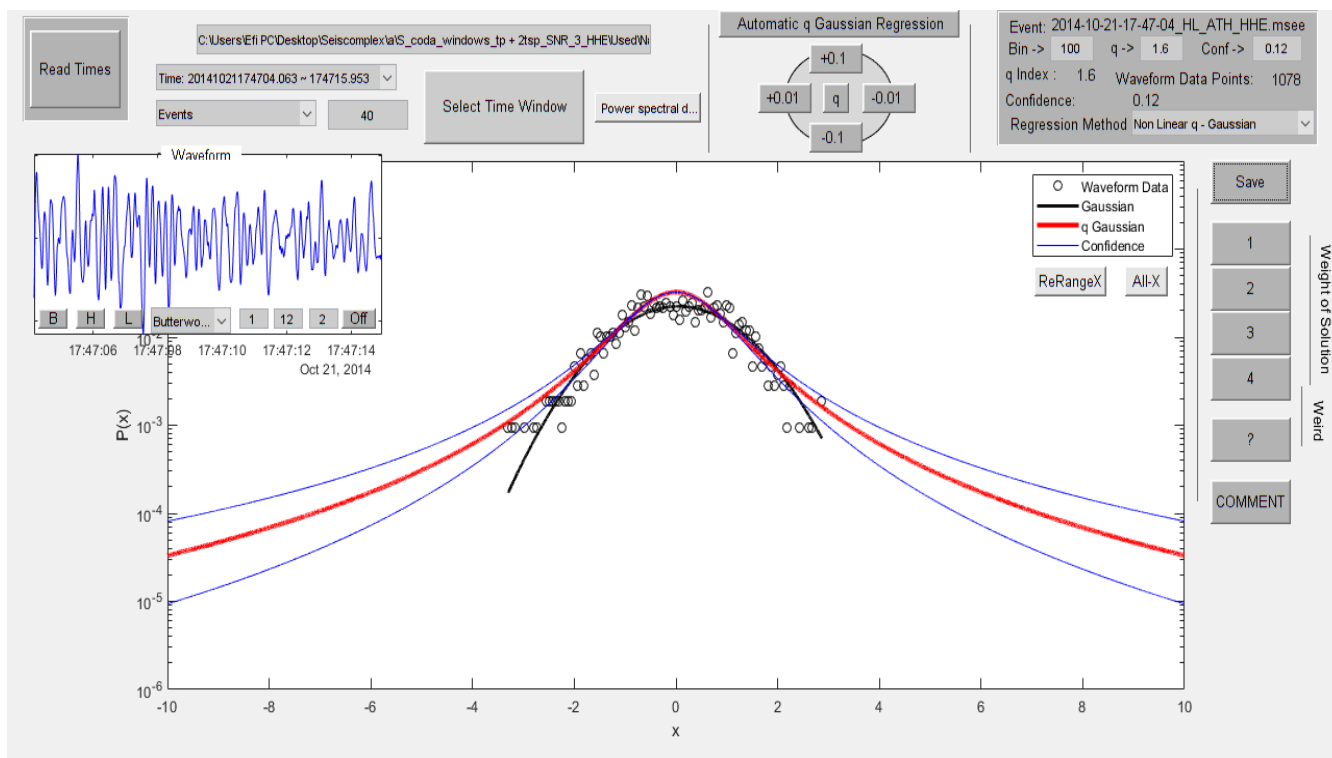


Figure 8.2.165

In figure 8.2.166 the time origin of the earthquake is 19/11/2014 at 16:32:28, latitude 38.65, longitude 23.42, depth 24 km, magnitude 3.2 at 25.9 km NW of Chalkida. The value of the index  $q$  is 1.76.

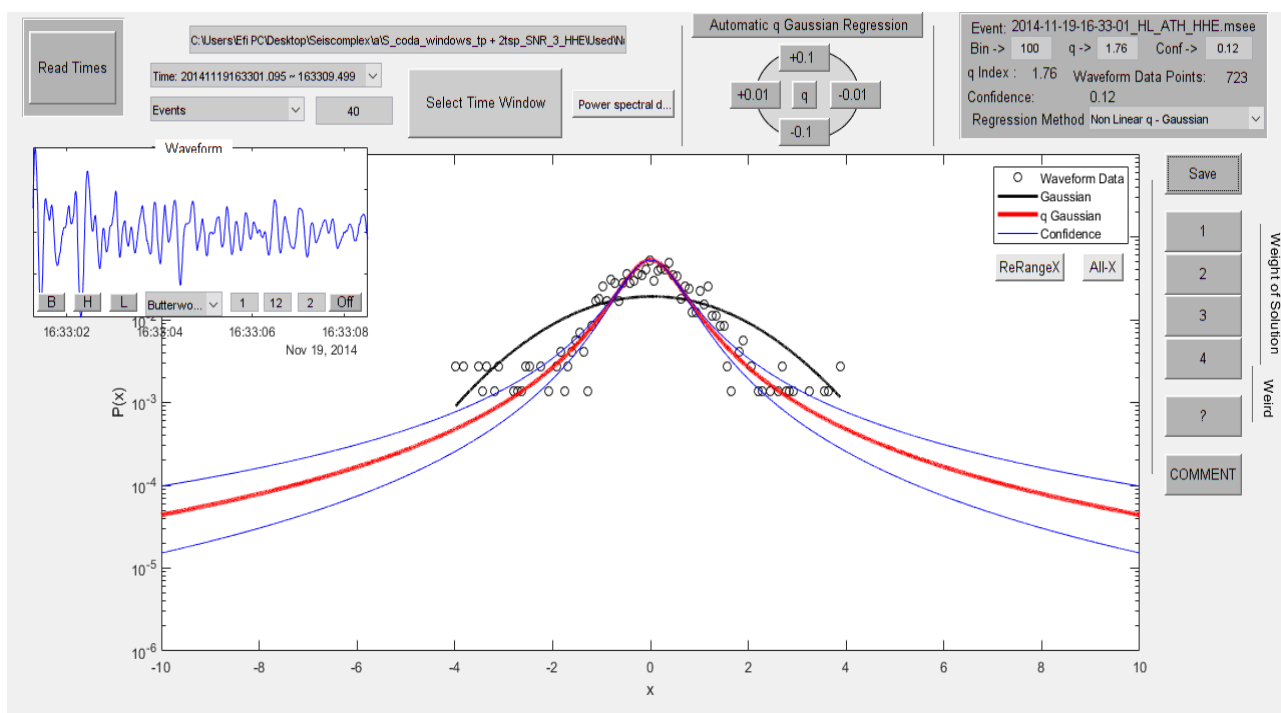


Figure 8.2.166

In figure 8.2.167 the time origin of the earthquake is 06/05/2015 at 18:05:31, latitude 38.43, longitude 23.9, depth 16 km, magnitude 3.2 at 26.4 km E of Chalkida. The value of the index  $q$  is 1.85.

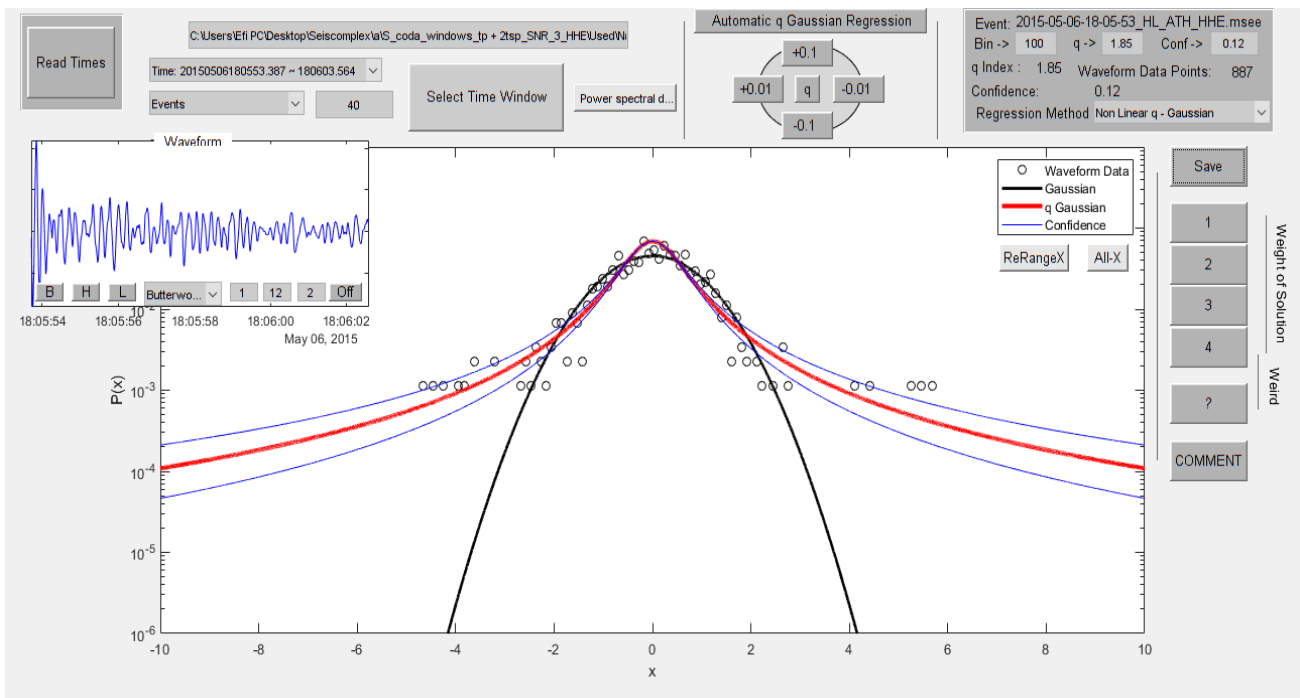


Figure 8.2.167

In figure 8.2.168 the time origin of the earthquake is 05/11/2015 at 14:27:53, latitude 38.62, longitude 24.46, depth 24 km, magnitude 3.2 at 32.8 km SSW of Skyros. The value of the index  $q$  is 1.85.

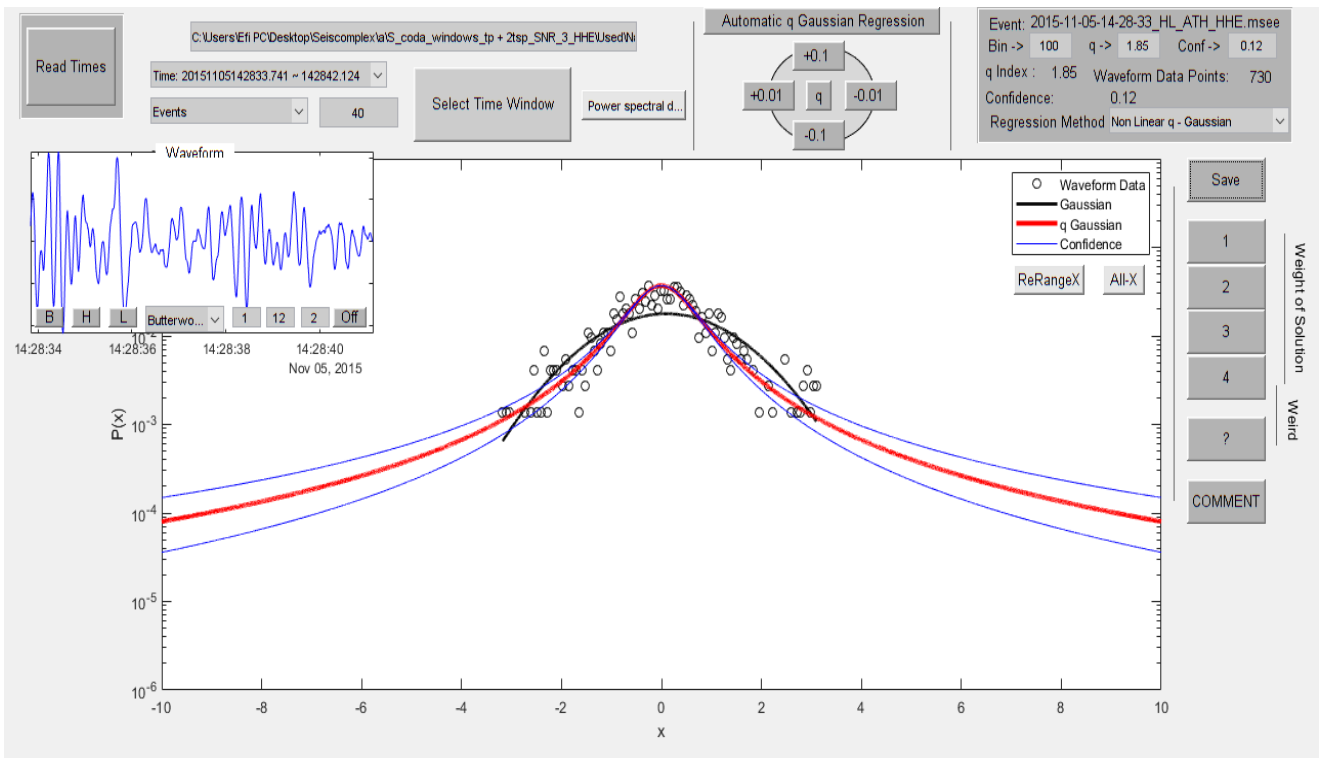


Figure 8.2.168

In figure 8.2.169 the time origin of the earthquake is 31/03/2016 at 04:43:29, latitude 37.54, longitude 23.57, depth 21 km, magnitude 3.2 at 51.3 km SSW of Athens. The value of the index  $q$  is 1.8.

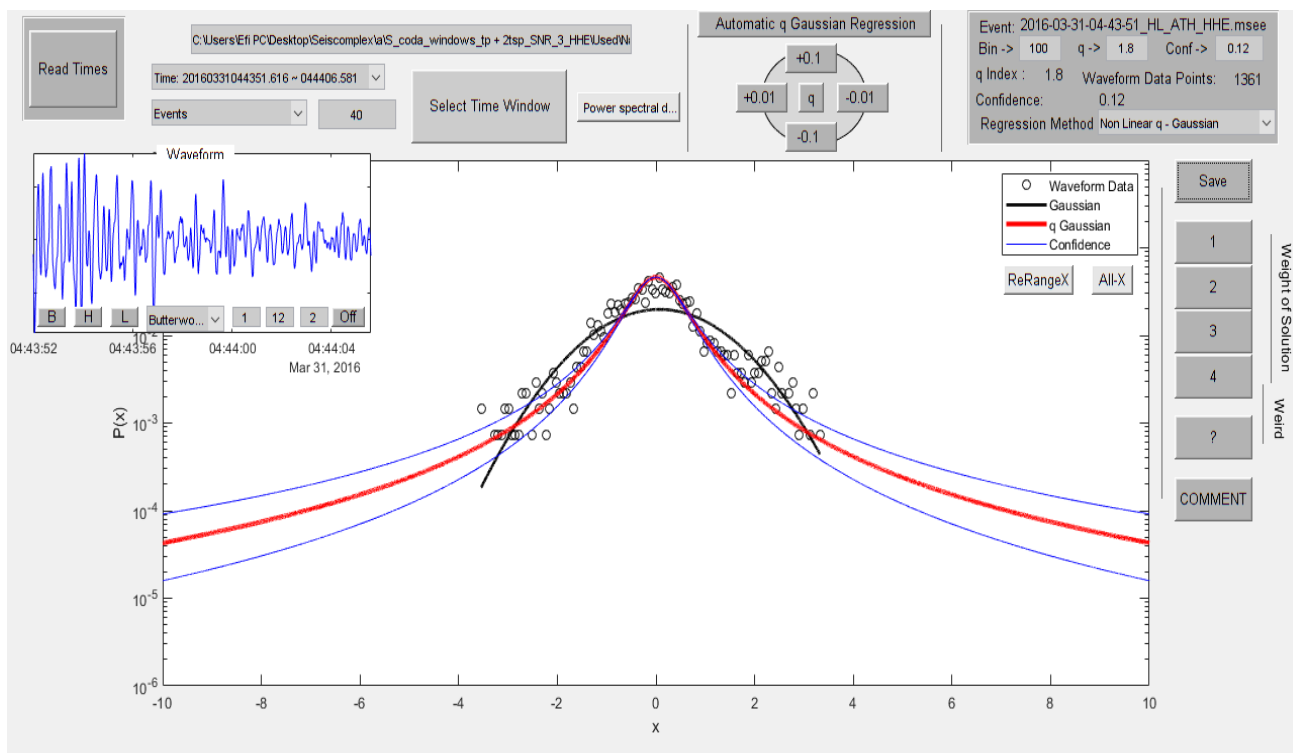


Figure 8.2.169

In figure 8.2.170 the time origin of the earthquake is 04/05/2016 at 23:03:37, latitude 37.53, longitude 23.58, depth 15 km, magnitude 3.2 at 52.2 km SSW of Athens. The value of the index  $q$  is 1.76.

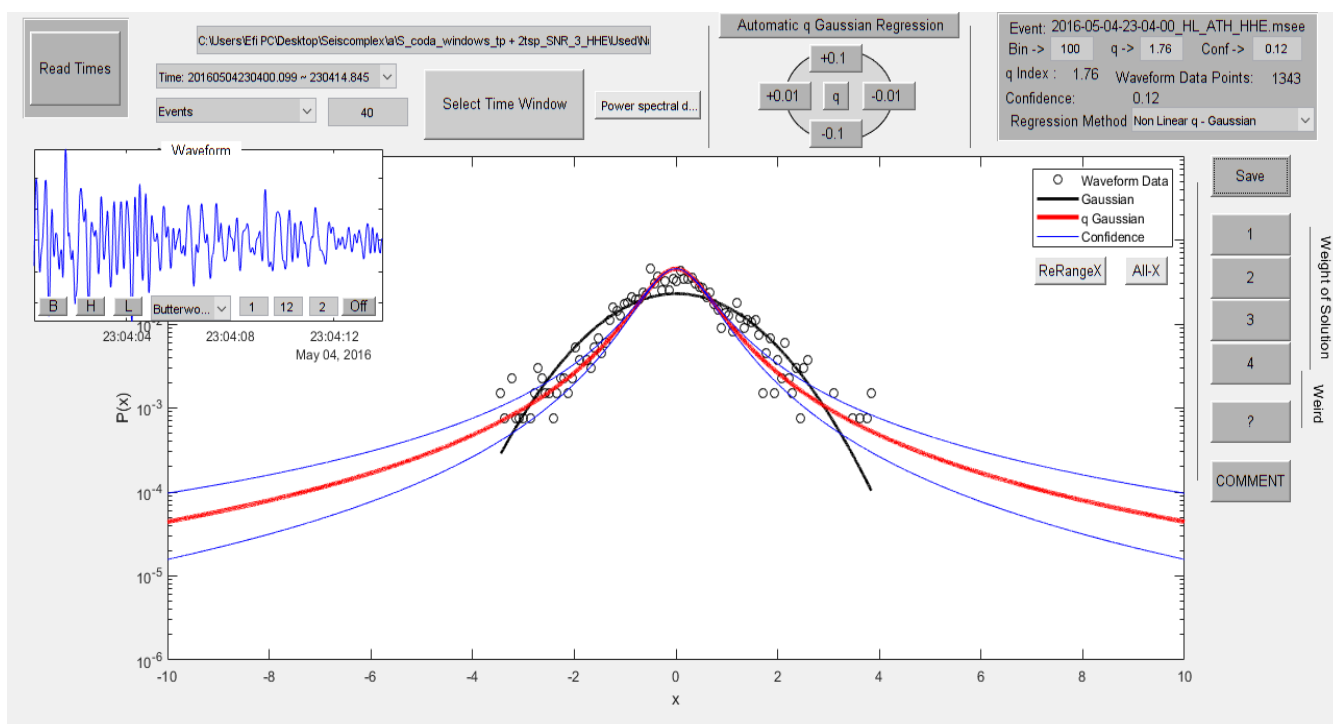


Figure 8.2.170

In figure 8.2.171 the time origin of the earthquake is 02/07/2016 at 23:46:09, latitude 37.55, longitude 23.59, depth 15 km, magnitude 3.2 at 49.8 km SSW of Athens. The value of the index  $q$  is 1.78.

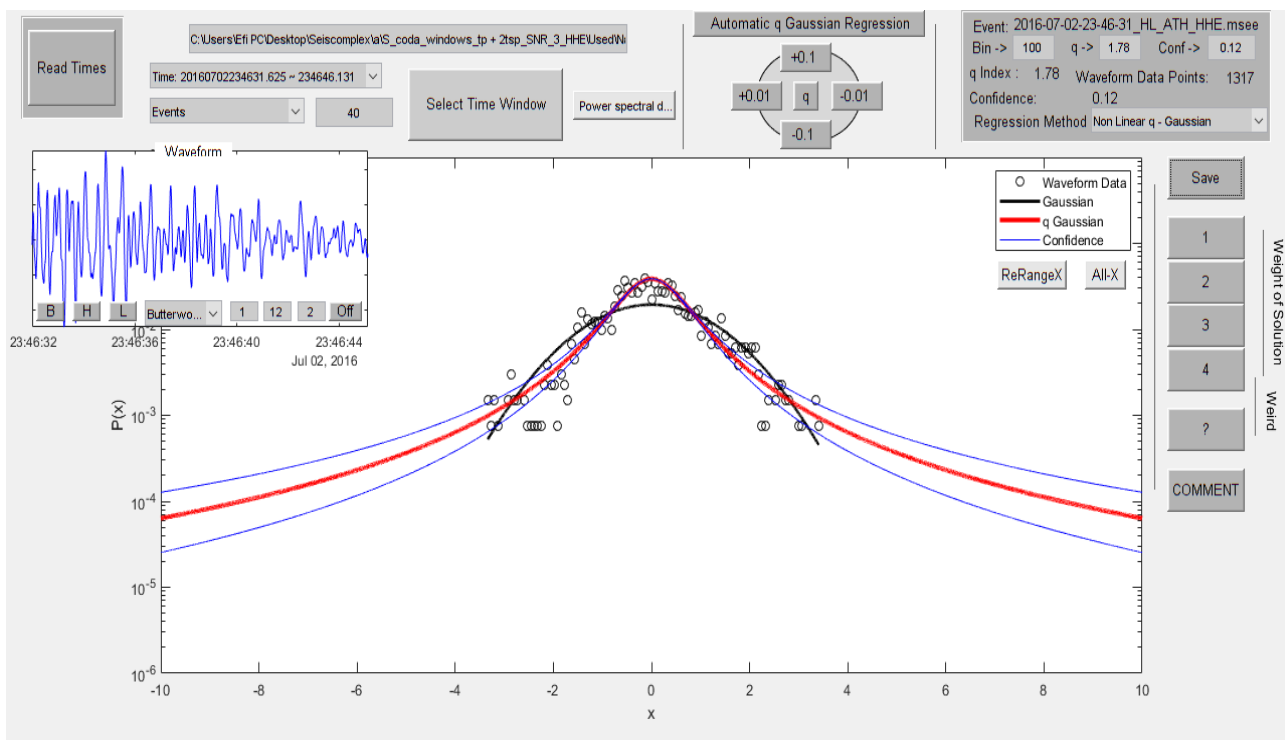


Figure 8.2.171

In figure 8.2.172 the time origin of the earthquake is 29/10/2016 at 11:52:42, latitude 38.91, longitude 23.92, depth 26 km, magnitude 3.2 at 47.3 km SE of Skiathos. The value of the index  $q$  is 1.67.

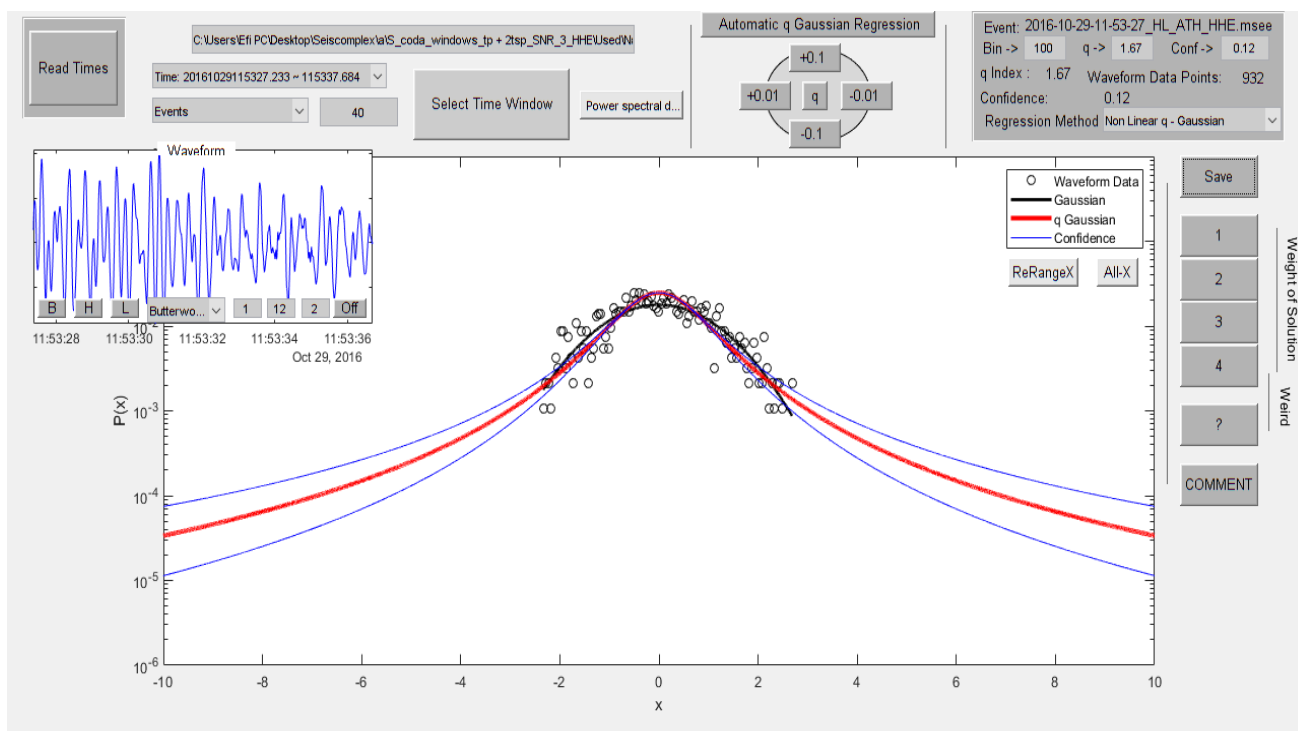


Figure 8.2.172

In figure 8.2.173 the time origin of the earthquake is 10/05/2017 at 12:44:01, latitude 38.7763, longitude 23.358, depth 25 km, magnitude 3.2 at 34.1 km ENE of Atalanti. The value of the index  $q$  is 1.72.

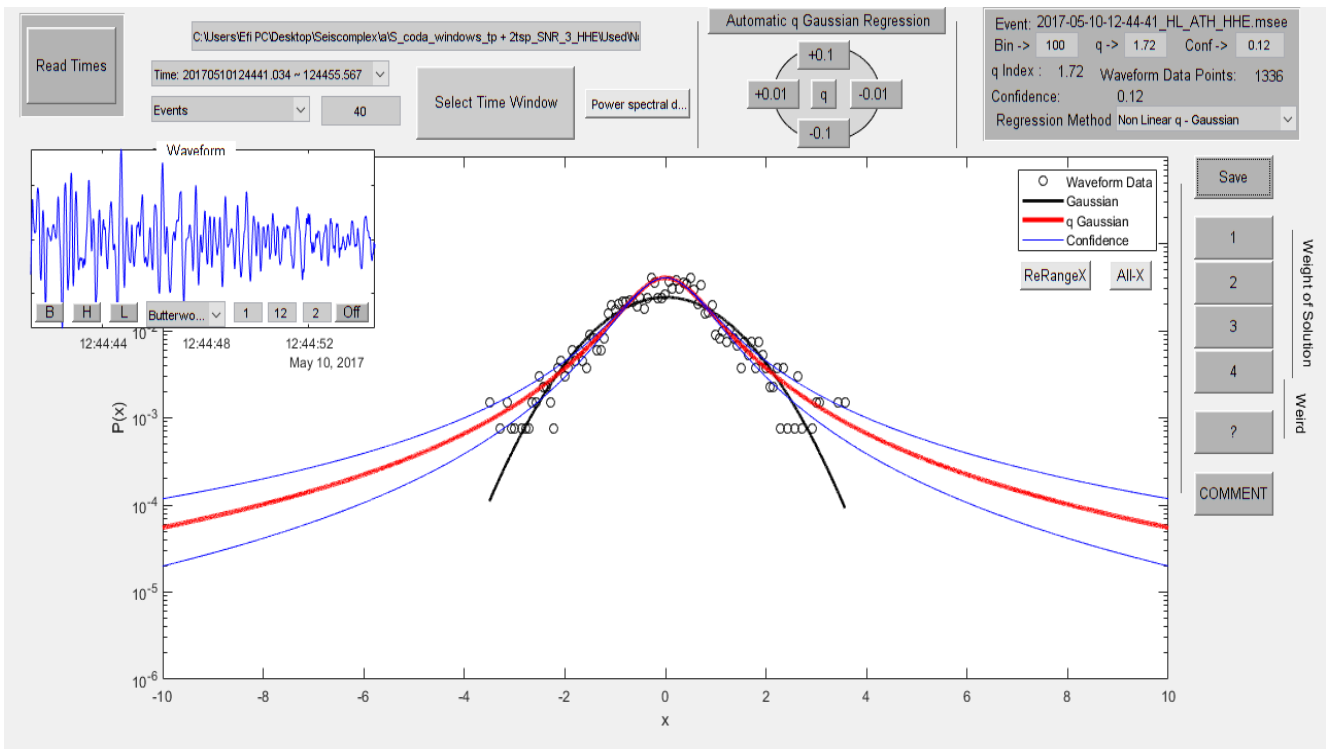


Figure 8.2.173

In figure 8.2.174 the time origin of the earthquake is 24/03/2010 at 20:15:18, latitude 38.87, longitude 23.63, depth 21 km, magnitude 3.1 at 35.3 km SSE of Skiathos. The value of the index  $q$  is 1.83.

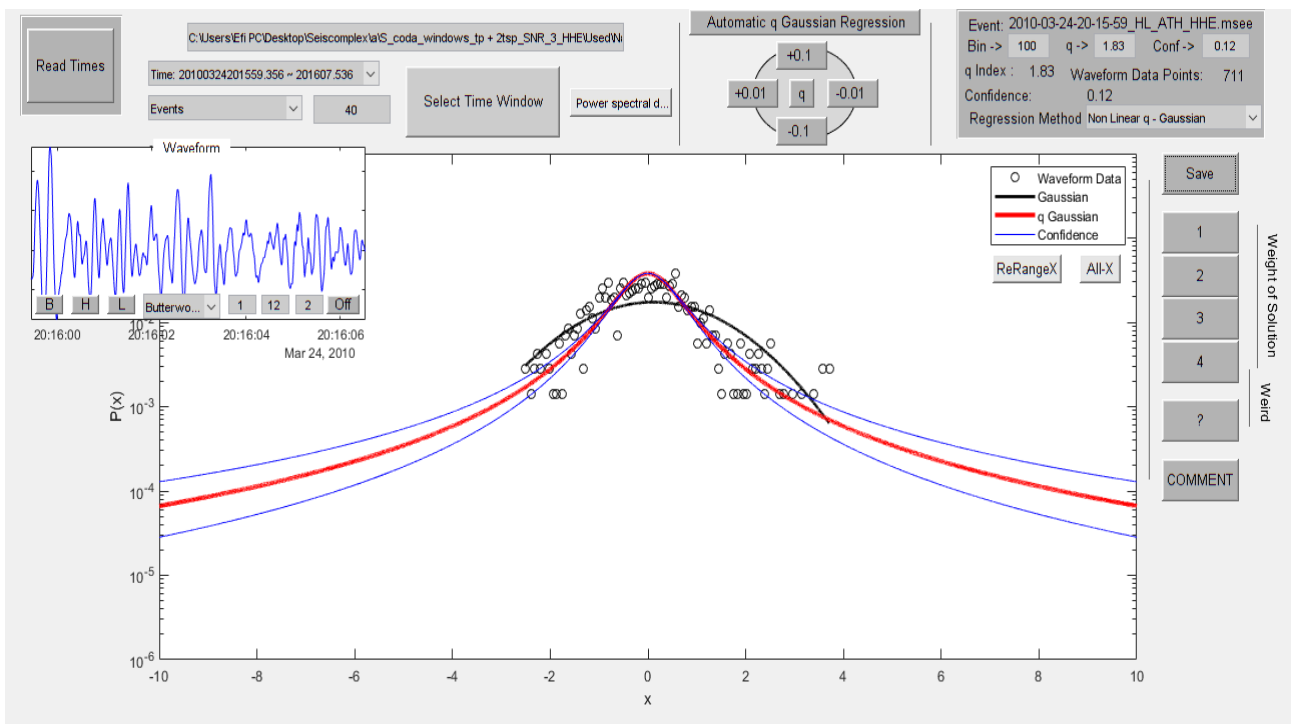


Figure 8.2.174

In figure 8.2.175 the time origin of the earthquake is 15/05/2010 at 12:10:02, latitude 38.13, longitude 23.17, depth 19 km, magnitude 3.1 at 29.8 km NE of Korinthos. The value of the index  $q$  is 1.96.

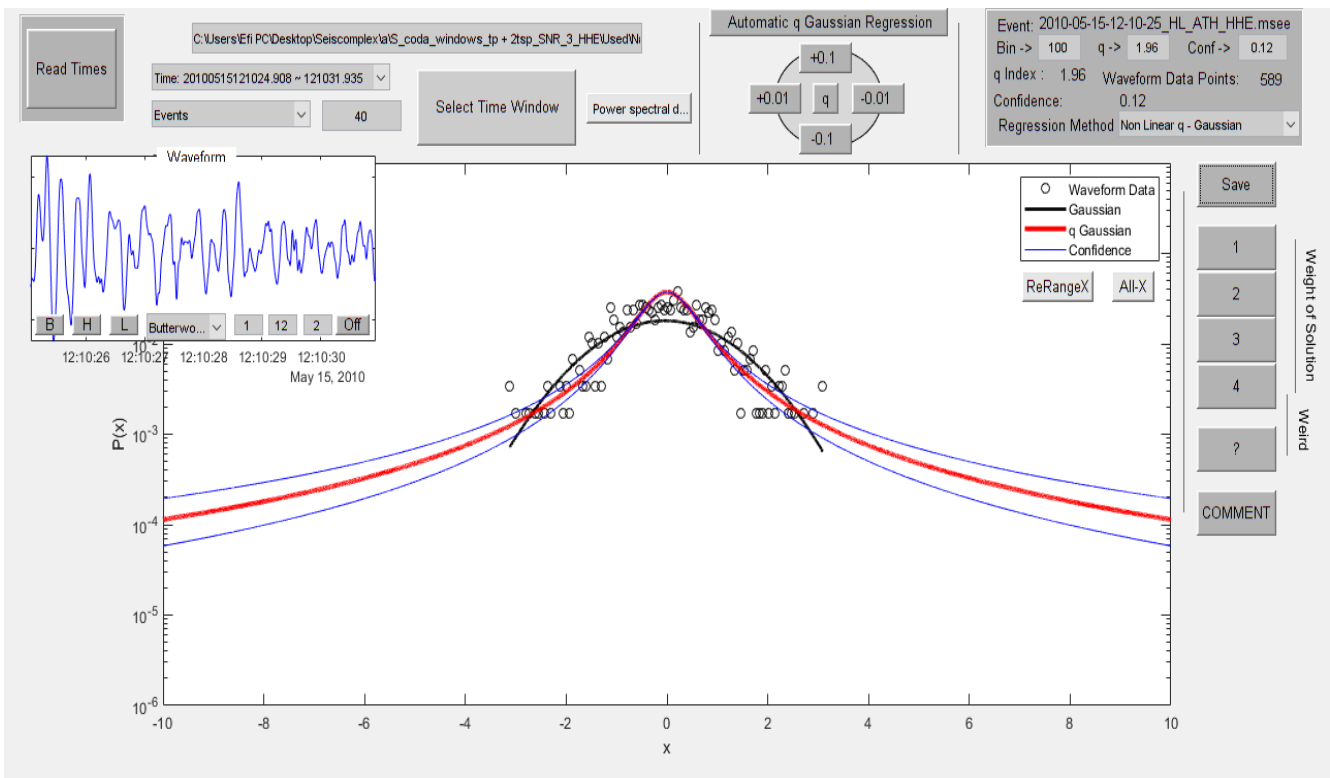


Figure 8.2.175

In figure 8.2.176 the time origin of the earthquake is 28/01/2011 at 01:36:06, latitude 38.21, longitude 23.16, depth 17 km, magnitude 3.1 at 35.3 km SE of Levadhia. The value of the index  $q$  is 1.66.

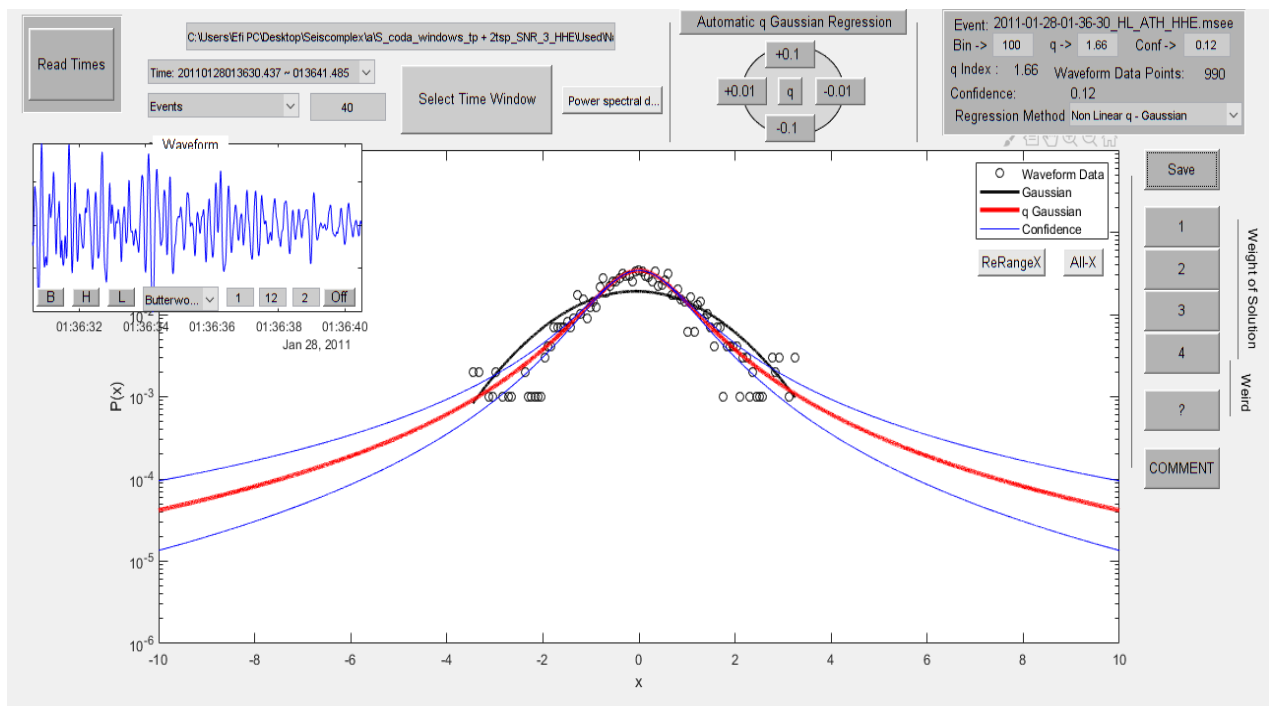


Figure 8.2.176

In figure 8.2.177 the time origin of the earthquake is 20/05/2011 at 23:36:21, latitude 38.44, longitude 23.88, depth 24 km, magnitude 3.1 at 24.6 km E of Chalkida. The value of the index  $q$  is 1.8.

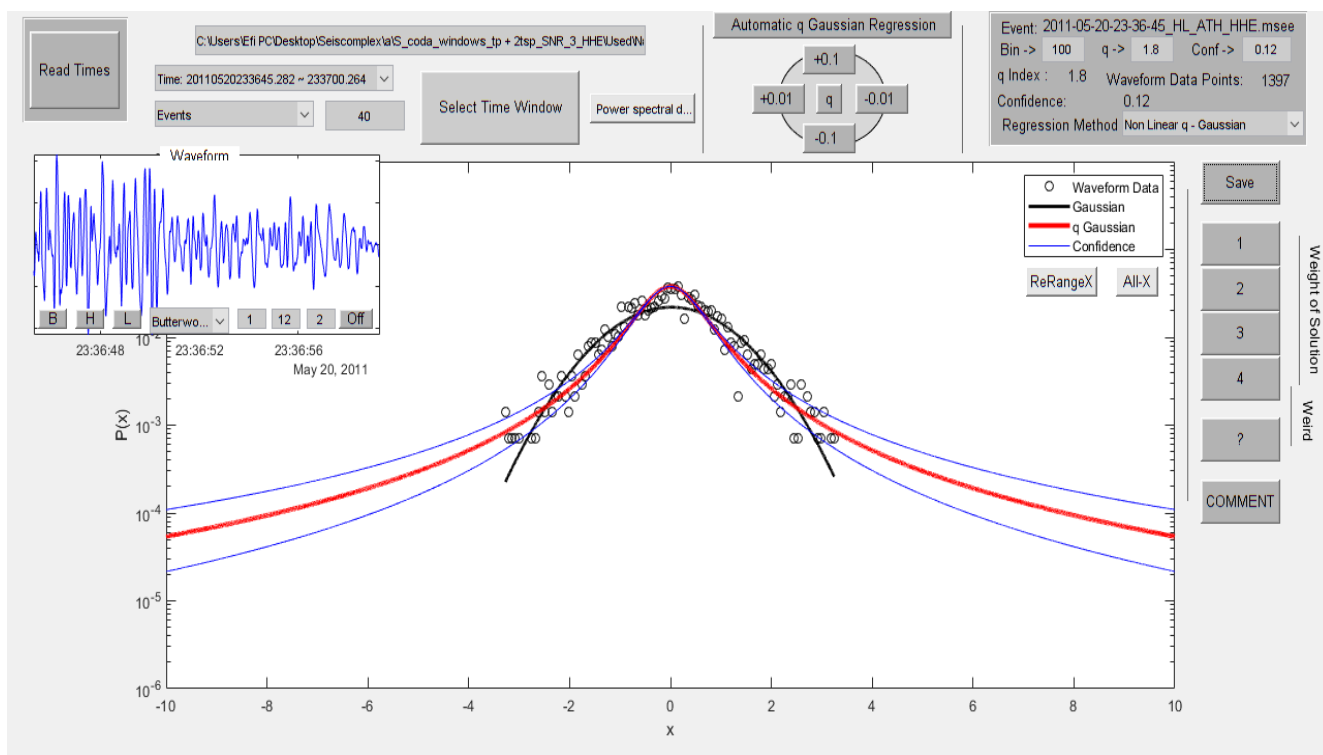


Figure 8.2.177

In figure 8.2.178 the time origin of the earthquake is 24/05/2011 at 10:27:50, latitude 37.88, longitude 22.98, depth 16 km, magnitude 3.1 at 7.7 km SSE of Korinthos. The value of the index  $q$  is 1.99.

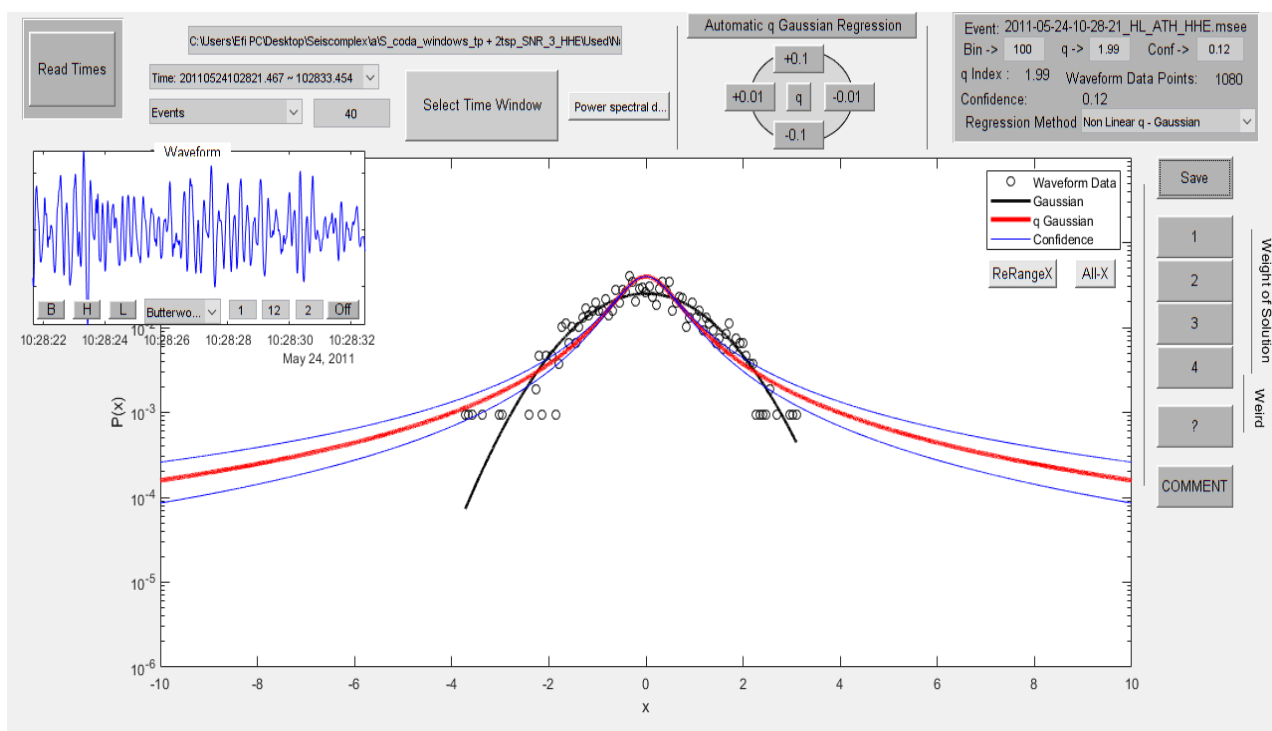


Figure 8.2.178

In figure 8.2.179 the time origin of the earthquake is 13/09/2011 at 02:13:33, latitude 38.72, longitude 23.38, depth 22 km, magnitude 3.1 at 33.9 km ENE of Atalanti. The value of the index  $q$  is 1.8.

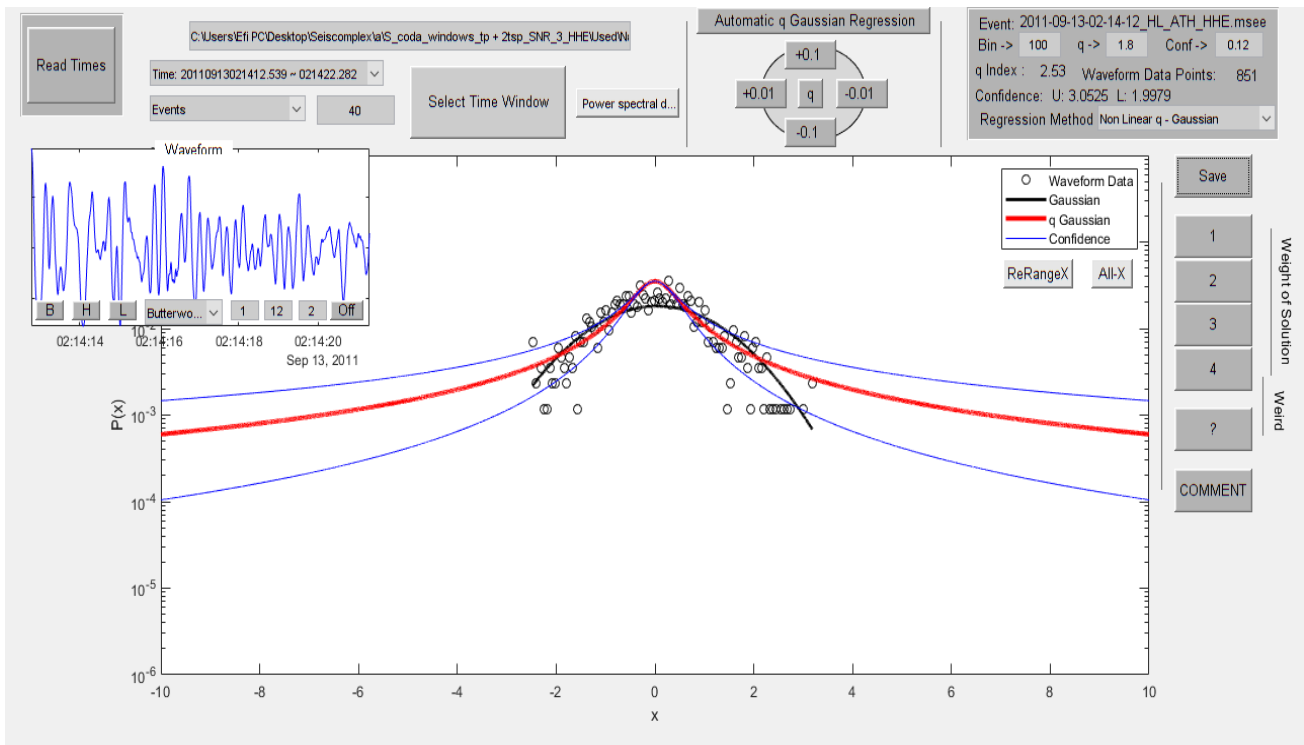


Figure 8.2.179

In figure 8.2.180 the time origin of the earthquake is 06/11/2011 at 07:38:21, latitude 39.1, longitude 23.28, depth 22 km, magnitude 3.1 at 19.0 km WSW of Skiathos. The value of the index  $q$  is 1.76.

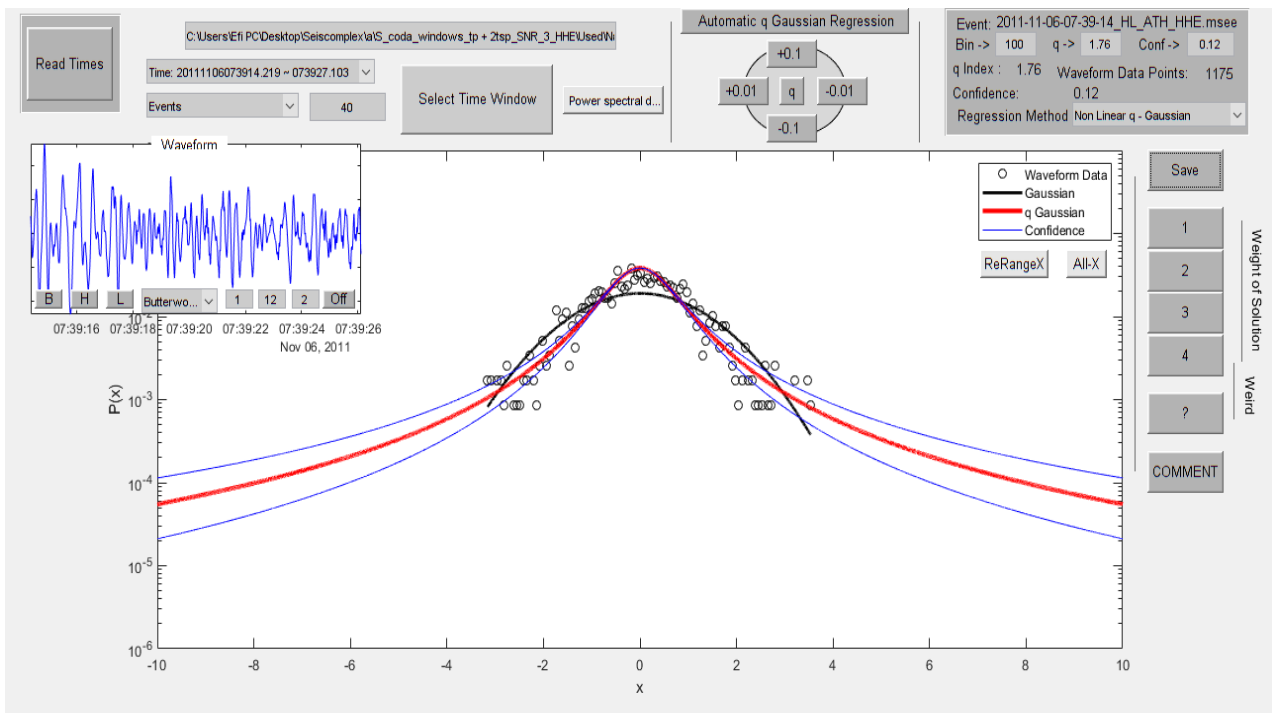


Figure 8.2.180

In figure 8.2.181 the time origin of the earthquake is 18/01/2012 at 17:53:18, latitude 37.72, longitude 23.04, depth 24 km, magnitude 3.1 at 26.0 km SSE of Korinthos. The value of the index  $q$  is 1.85.

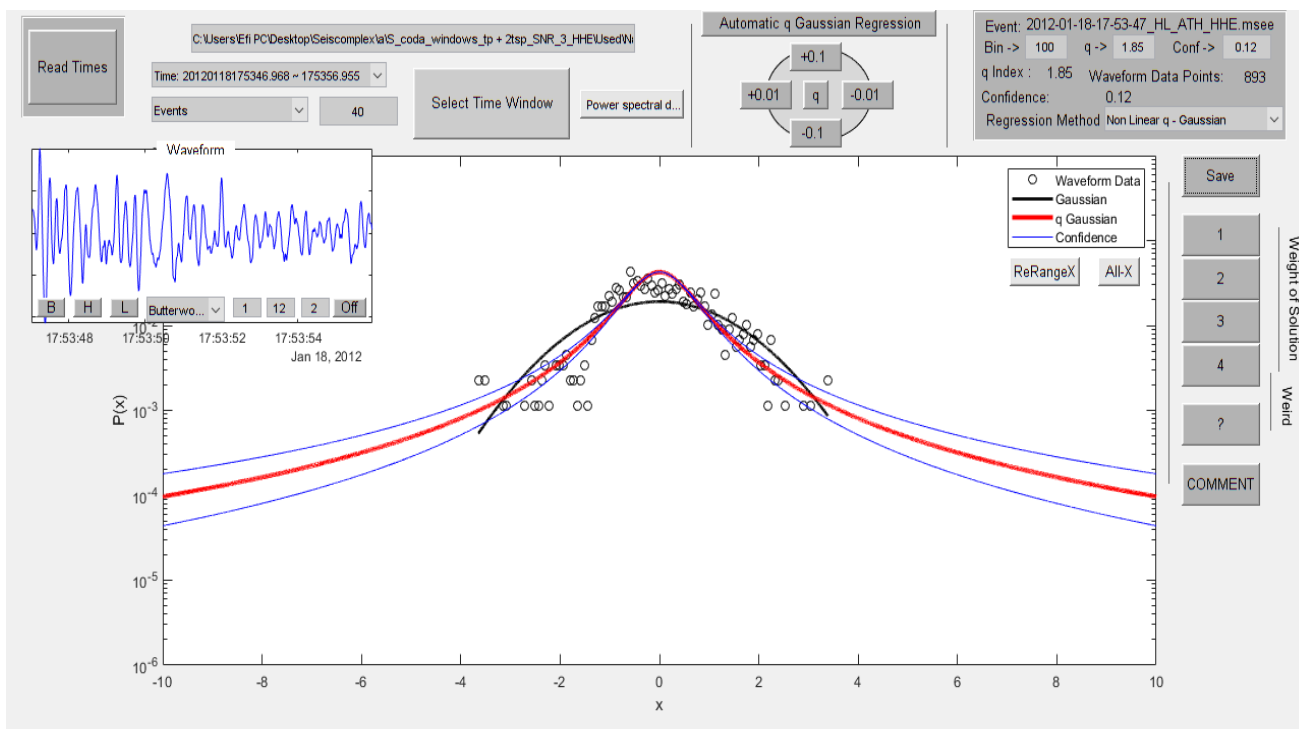


Figure 8.2.181

In figure 8.2.182 the time origin of the earthquake is 20/02/2012 at 00:51:46, latitude 38.19, longitude 24.1, depth 21 km, magnitude 3.1 at 39.5 km NE of Athens. The value of the index  $q$  is 1.99.

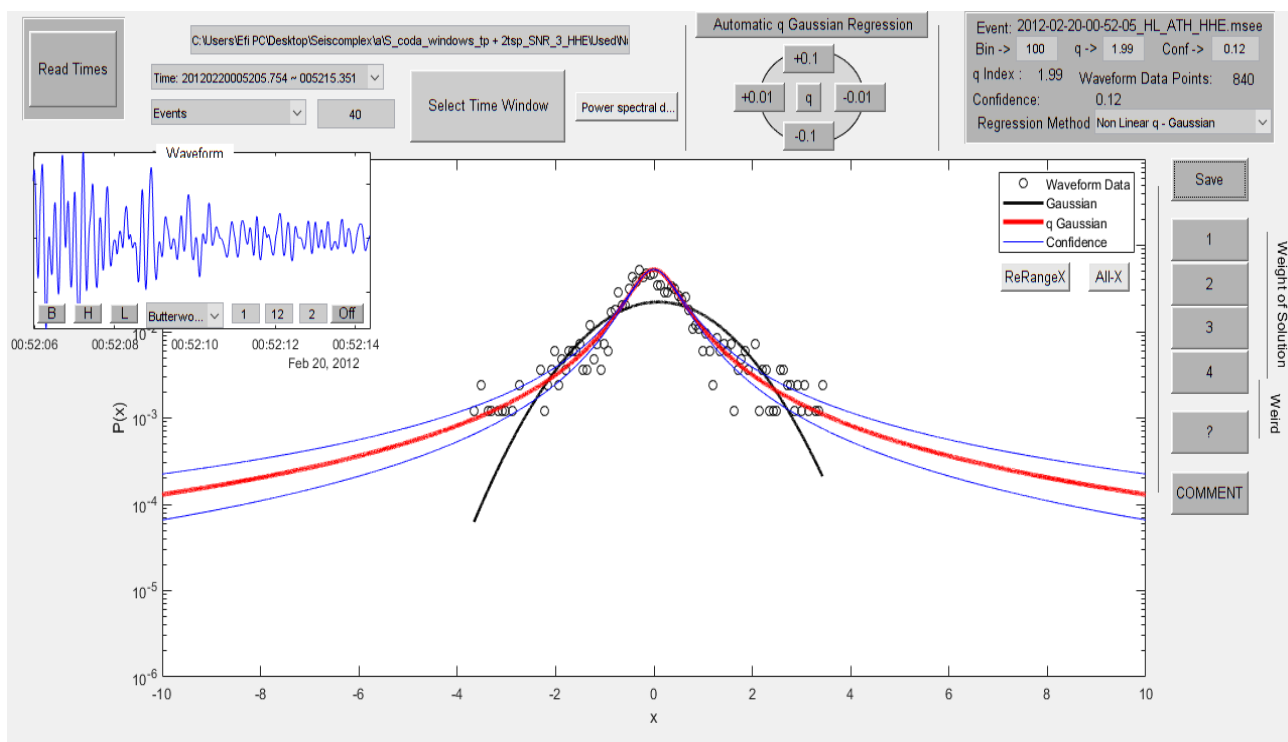


Figure 8.2.182

In figure 8.2.183 the time origin of the earthquake is 16/05/2012 at 00:51:46, latitude 37.81, longitude 22.91, depth 22 km, magnitude 3.1 at 14.3 km S of Korinthos. The value of the index  $q$  is 1.75.

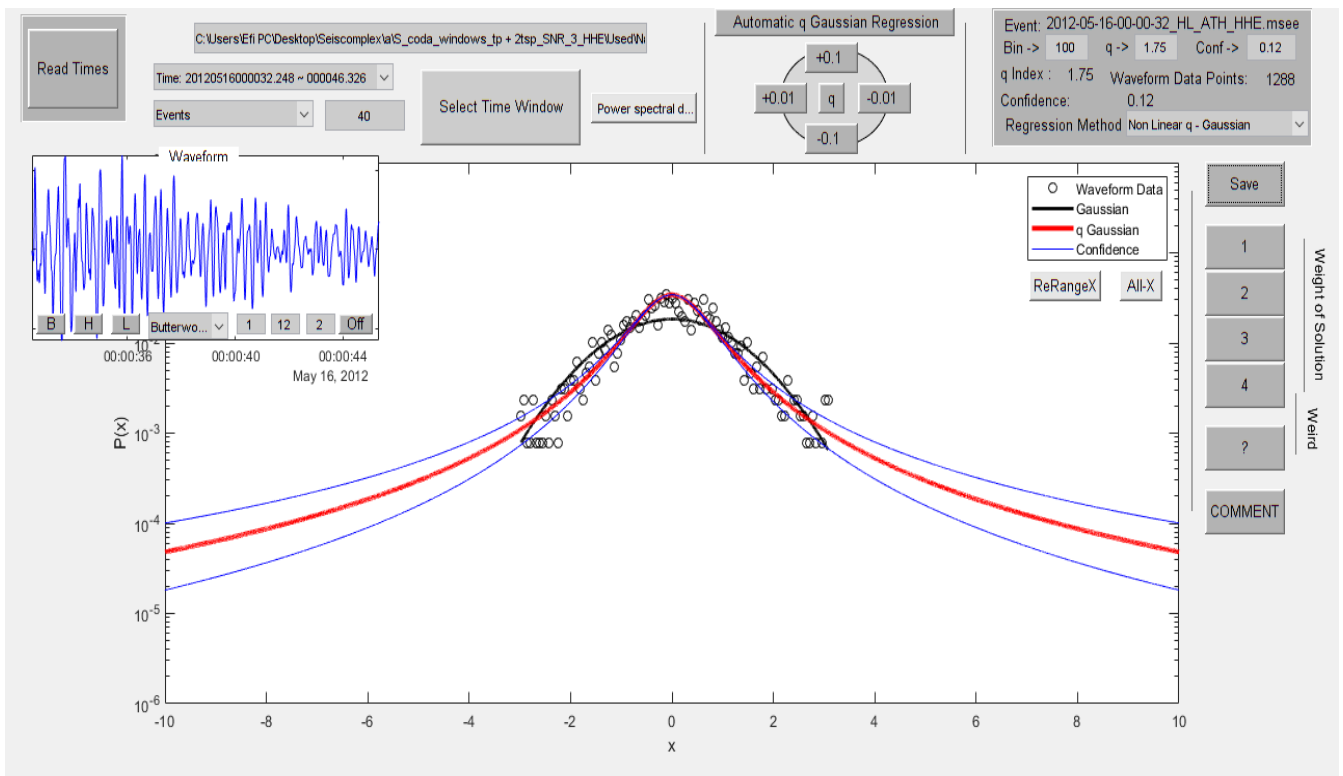


Figure 8.2.183

In figure 8.2.184 the time origin of the earthquake is 25/06/2013 at 20:25:24, latitude 38.17, longitude 23.22, depth 15 km, magnitude 3.1 at 36.1 km NE of Korinthos. The value of the index  $q$  is 1.86.

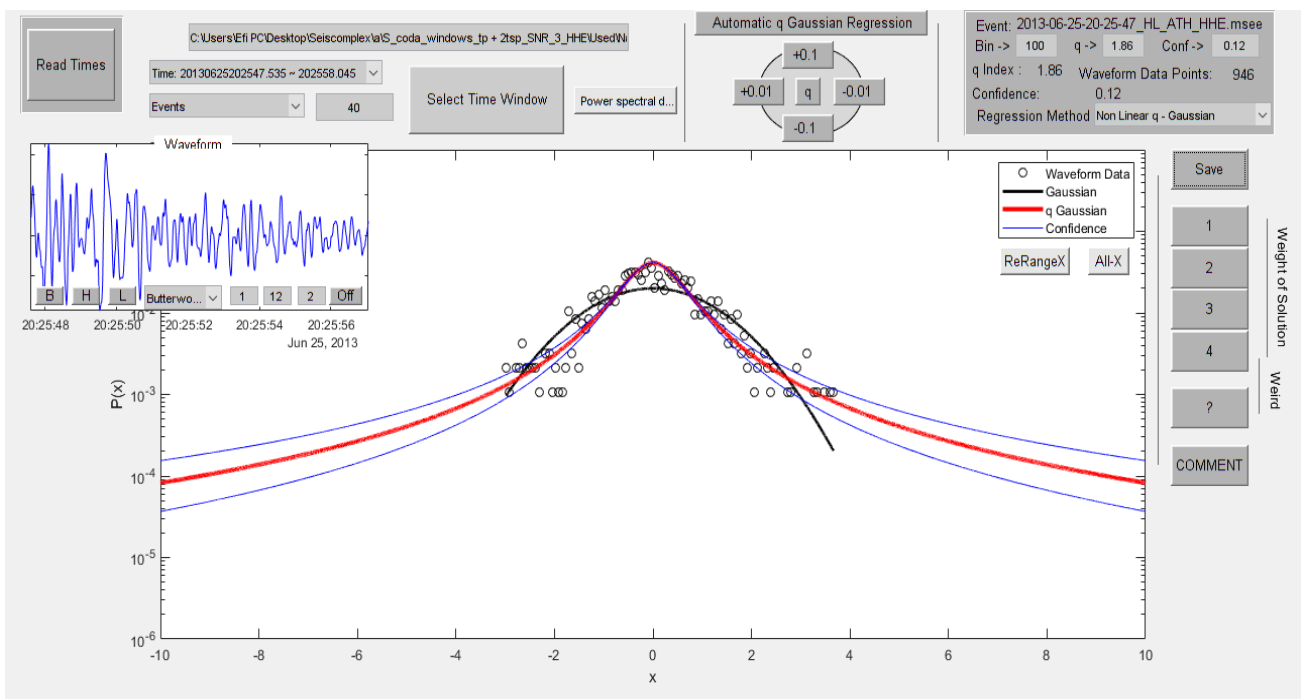


Figure 8.2.184

In figure 8.2.185 the time origin of the earthquake is 08/09/2013 at 06:28:10, latitude 38.61, longitude 23.76, depth 24 km, magnitude 3.1 at 21.4 km NE of Chalkida. The value of the index  $q$  is 1.89.

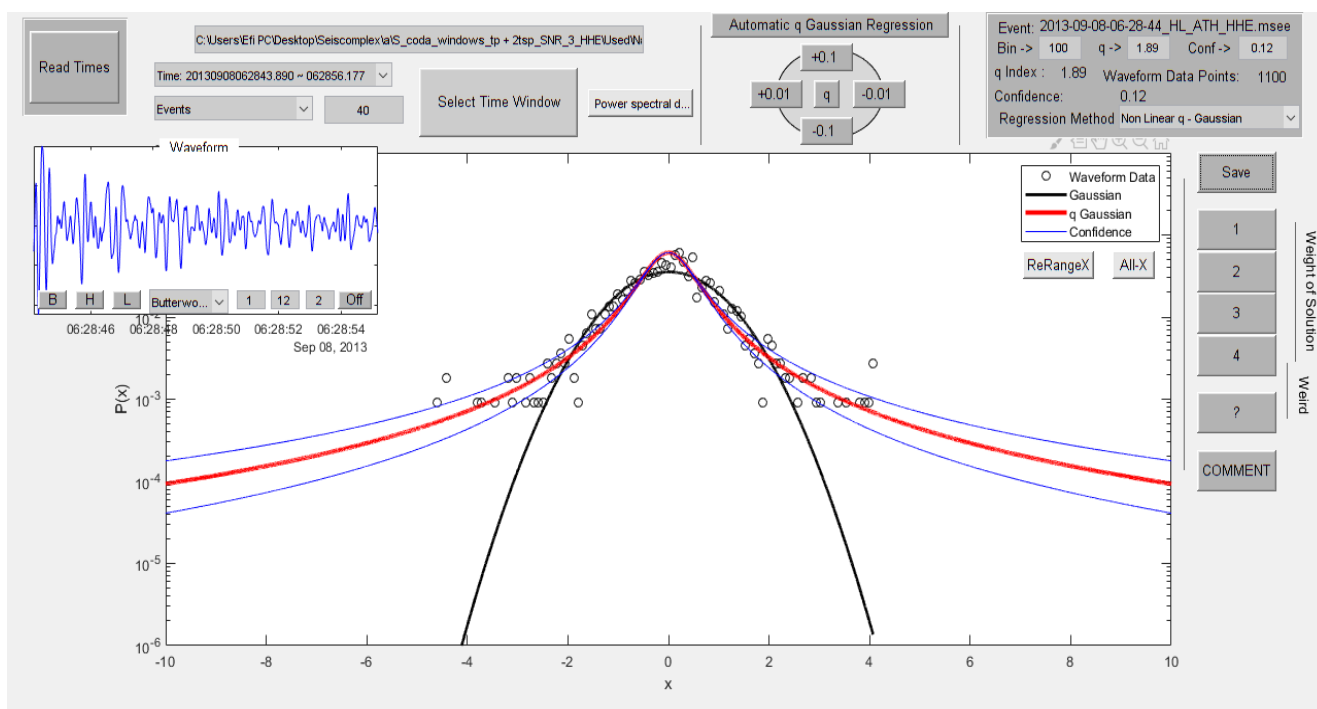


Figure 8.2.185

In figure 8.2.186 the time origin of the earthquake is 08/11/2013 at 20:01:57, latitude 38.65, longitude 24.61, depth 26 km, magnitude 3.1 at 28.6 km S of Skyros. The value of the index  $q$  is 1.81.

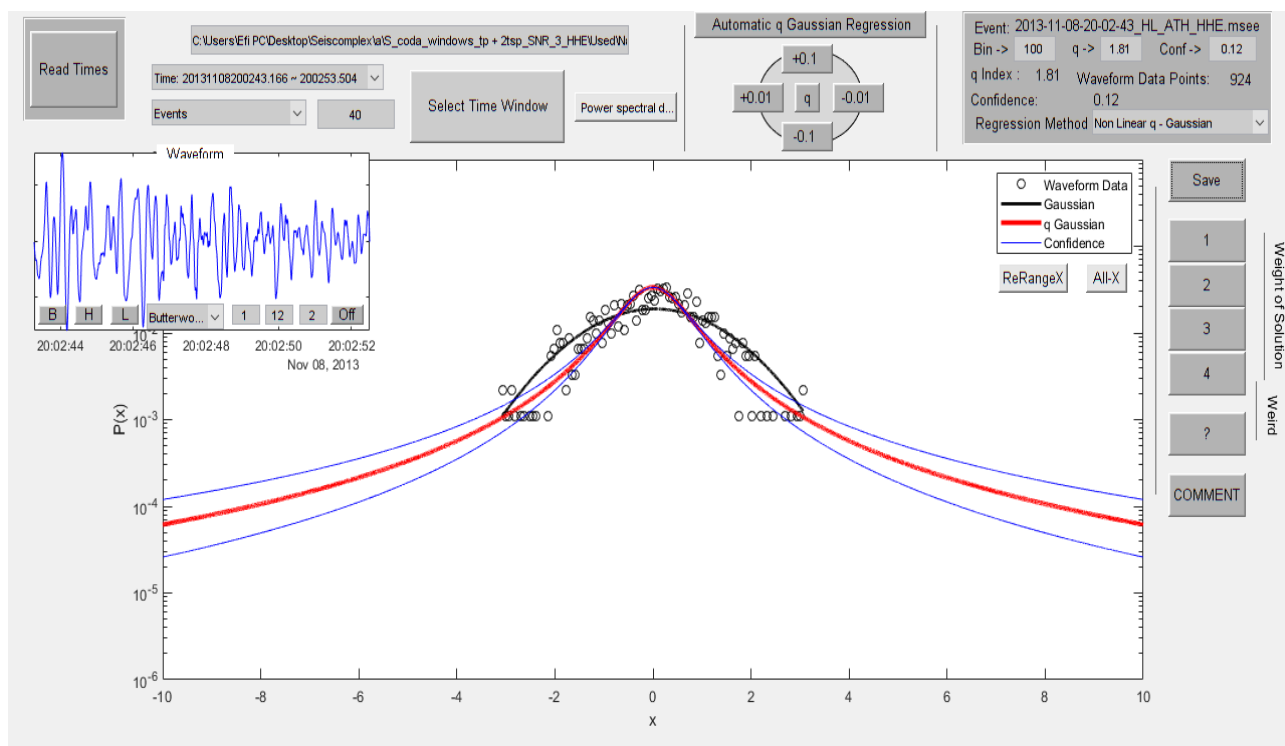


Figure 8.2.186

In figure 8.2.187 the time origin of the earthquake is 11/08/2014 at 00:25:29, latitude 38.41, longitude 22.5, depth 19 km, magnitude 3.1 at 16.9 km SE of Amfissa. The value of the index  $q$  is 1.85.

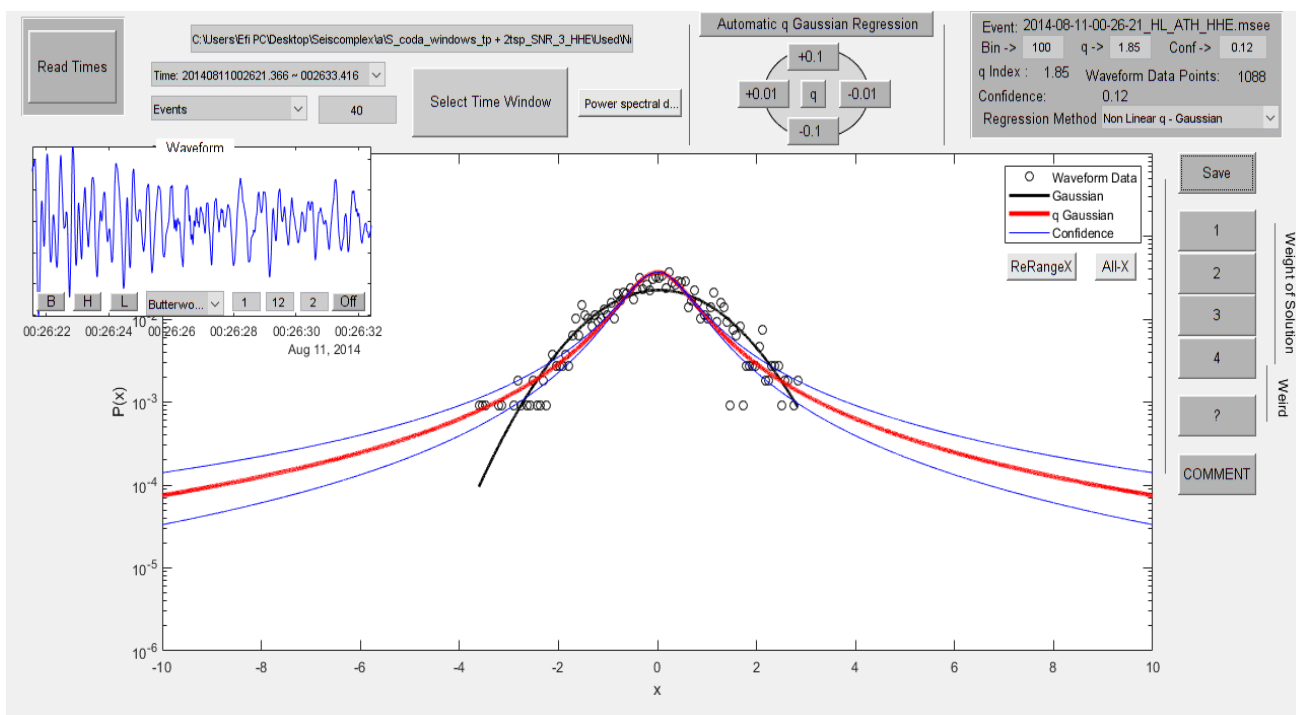


Figure 8.2.187

In figure 8.2.188 the time origin of the earthquake is 18/11/2014 at 01:19:37, latitude 38.65, longitude 23.41, depth 25 km, magnitude 3.1 at 26.5 km NW of Chalkida. The value of the index  $q$  is 1.85.

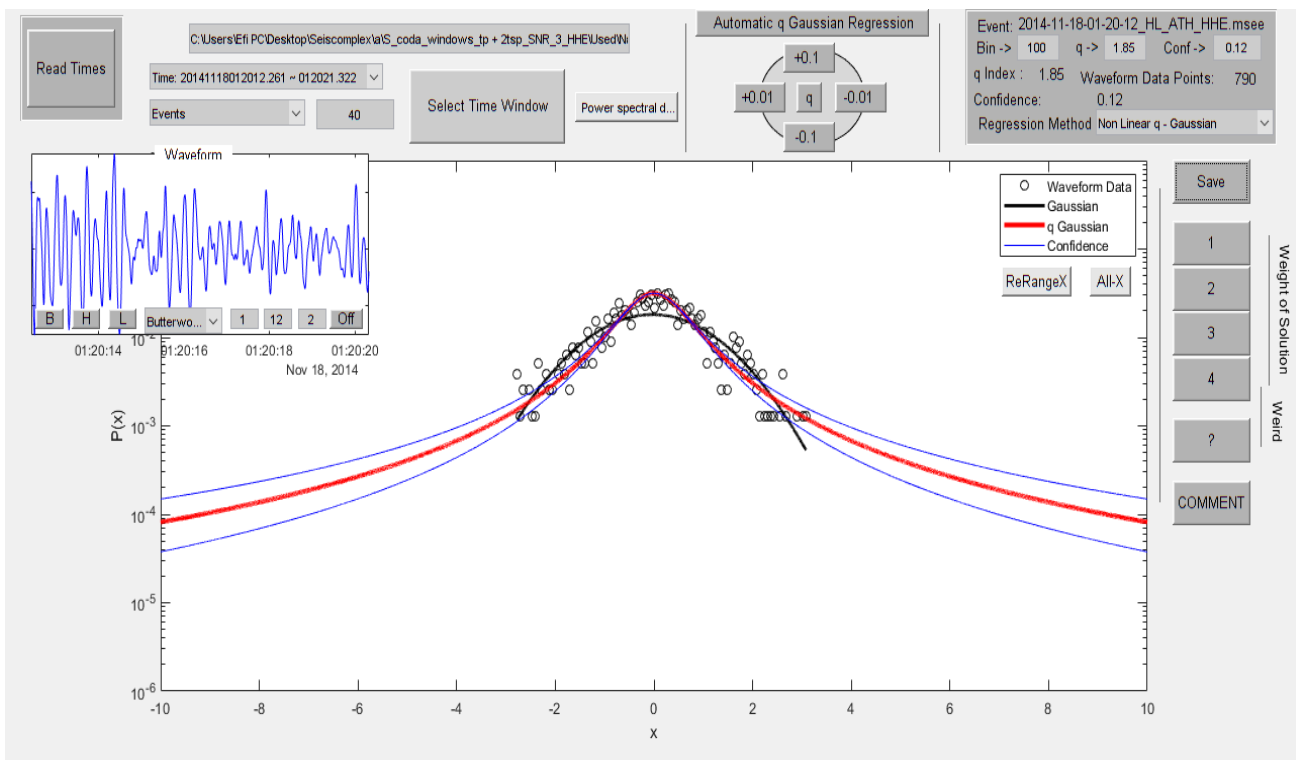


Figure 8.2.188

In figure 8.2.189 the time origin of the earthquake is 21/11/2014 at 10:37:59, latitude 38.66, longitude 23.39, depth 25 km, magnitude 3.1 at 28.4 km NW of Chalkida. The value of the index  $q$  is 1.8.

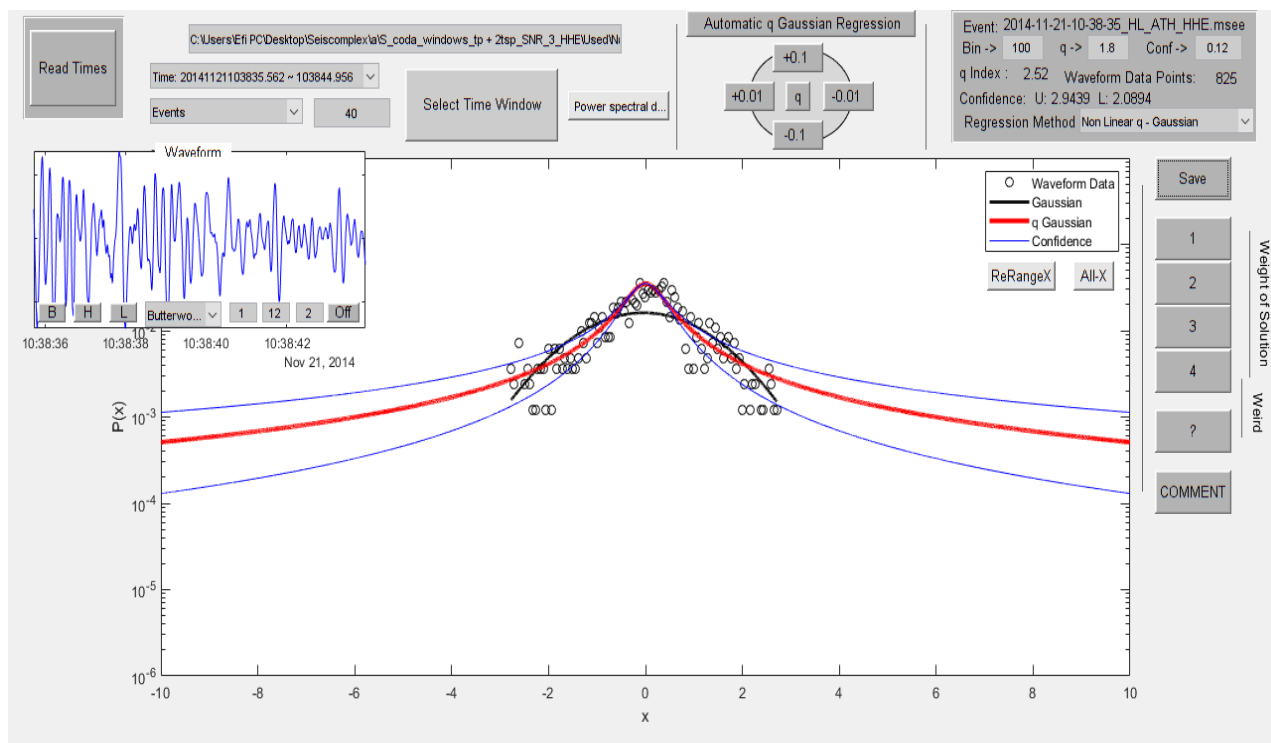


Figure 8.2.189

In figure 8.2.190 the time origin of the earthquake is 06/06/2015 at 00:40:19, latitude 38.79, longitude 23.46, depth 15 km, magnitude 3.1 at 38.3 km NNW of Chalkida. The value of the index  $q$  is 1.8.

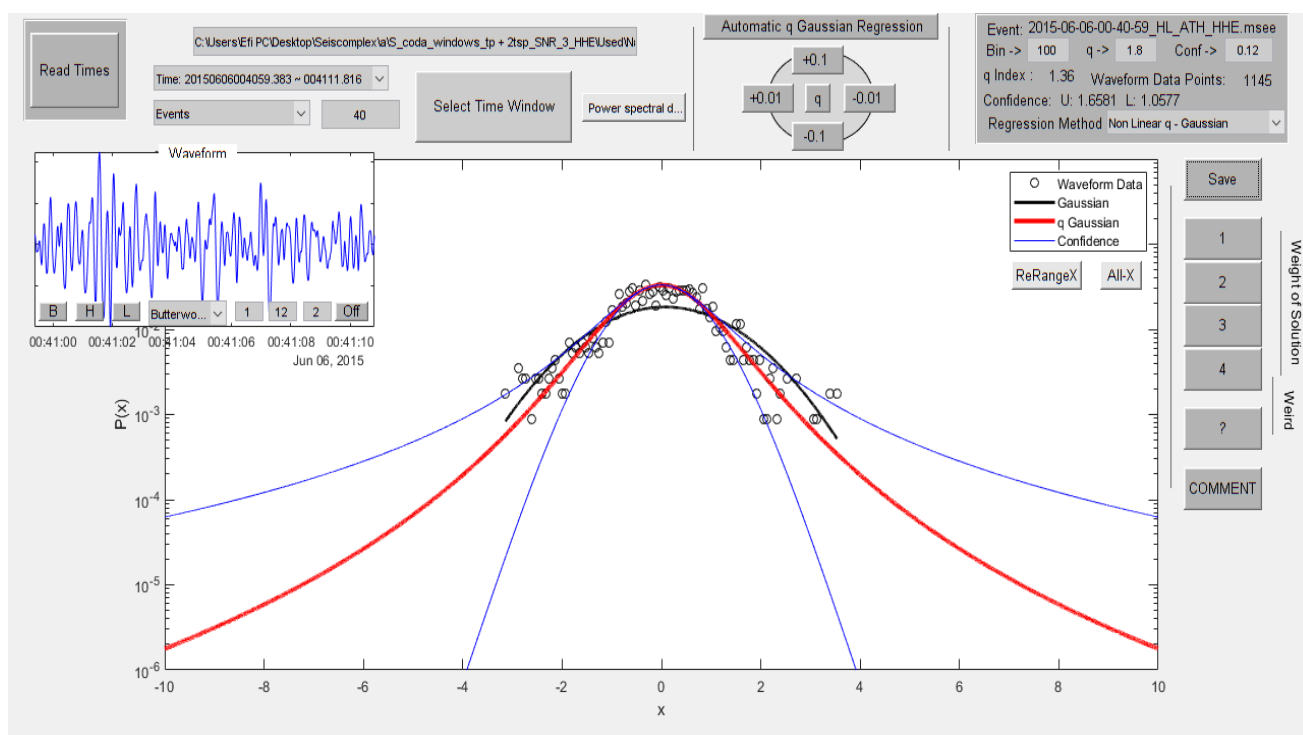


Figure 8.2.190

In figure 8.2.191 the time origin of the earthquake is 23/07/2015 at 16:05:50, latitude 38.6, longitude 23.42, depth 15 km, magnitude 3.1 at 21.8 km NW of Chalkida. The value of the index  $q$  is 1.62.

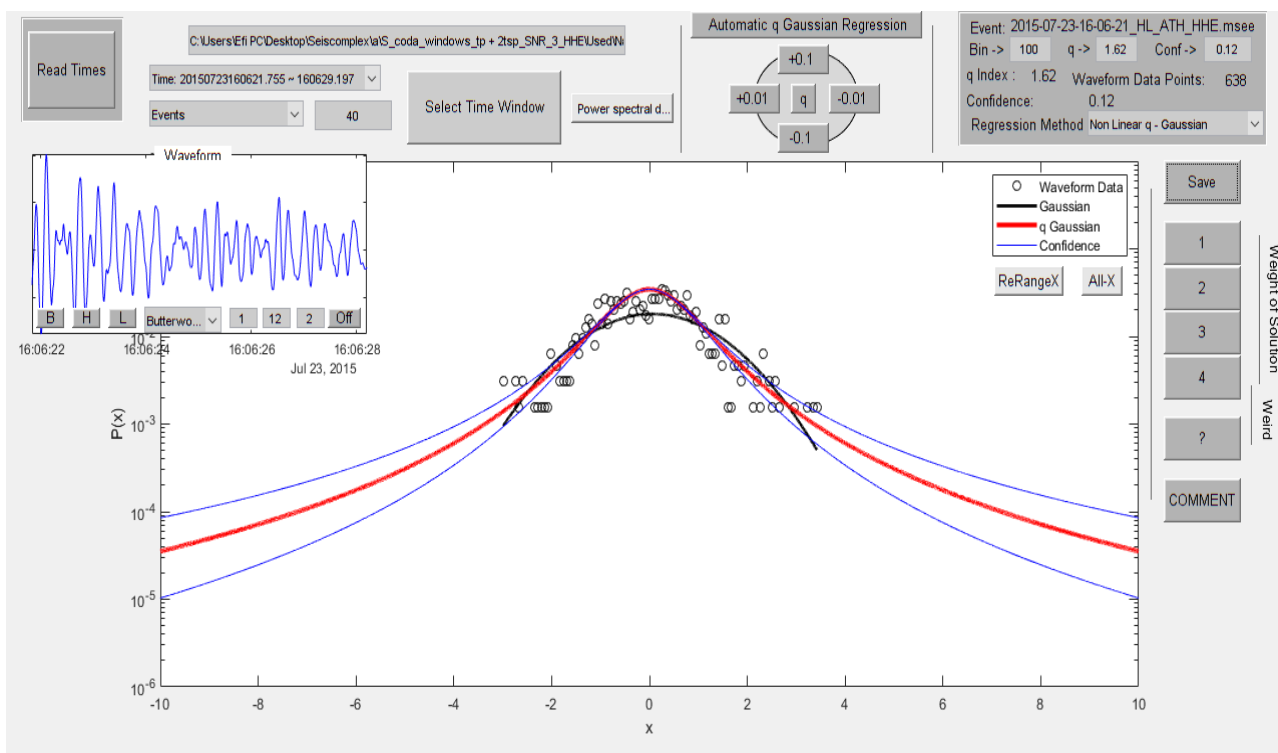


Figure 8.2.191

In figure 8.2.192 the time origin of the earthquake is 21/01/2016 at 03:14:49, latitude 37.51, longitude 22.62, depth 76 km, magnitude 3.1 at 17.6 km WSW of Nafplio. The value of the index  $q$  is 1.54.

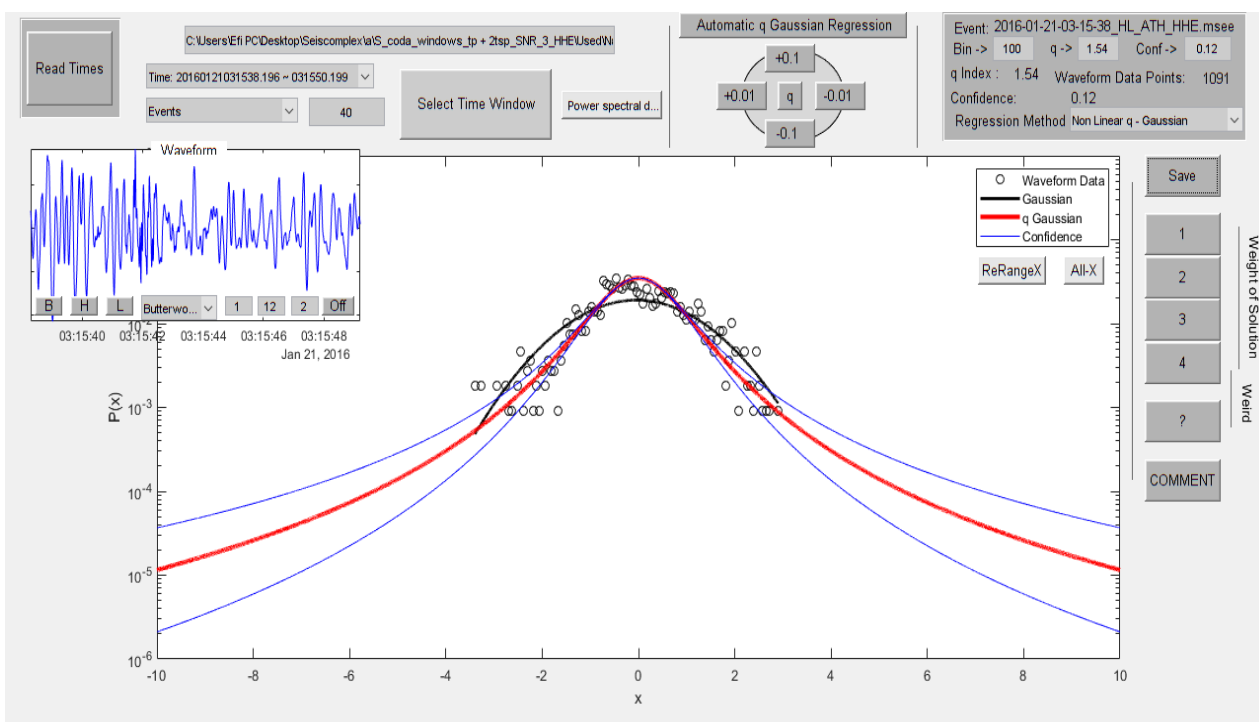


Figure 8.2.192

In figure 8.2.193 the time origin of the earthquake is 19/03/2016 at 08:17:32, latitude 37.52, longitude 23.61, depth 18 km, magnitude 3.1 at 52.6 km SSW of Athens. The value of the index  $q$  is 1.92.

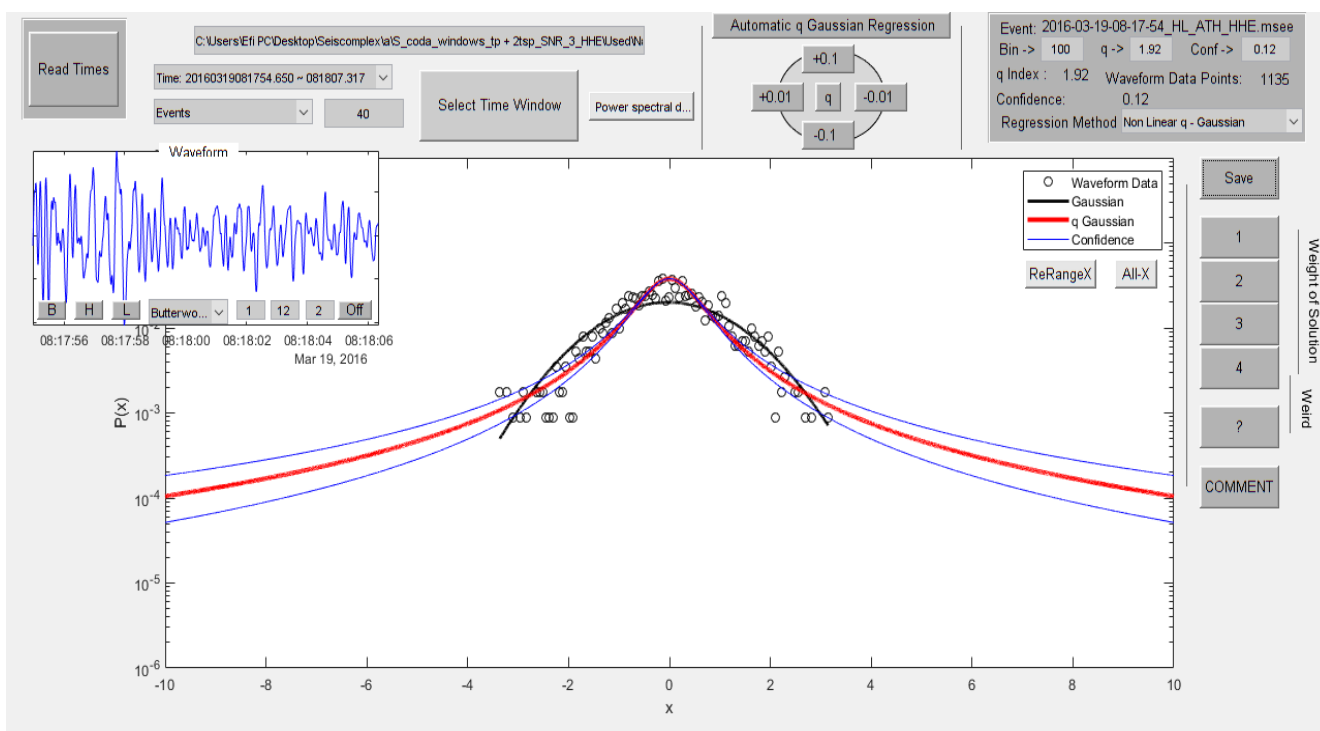


Figure 8.2.193

In figure 8.2.194 the time origin of the earthquake is 22/04/2016 at 13:33:20, latitude 37.54, longitude 23.6, depth 19 km, magnitude 3.1 at 50.7 km SSW of Athens. The value of the index  $q$  is 1.88.

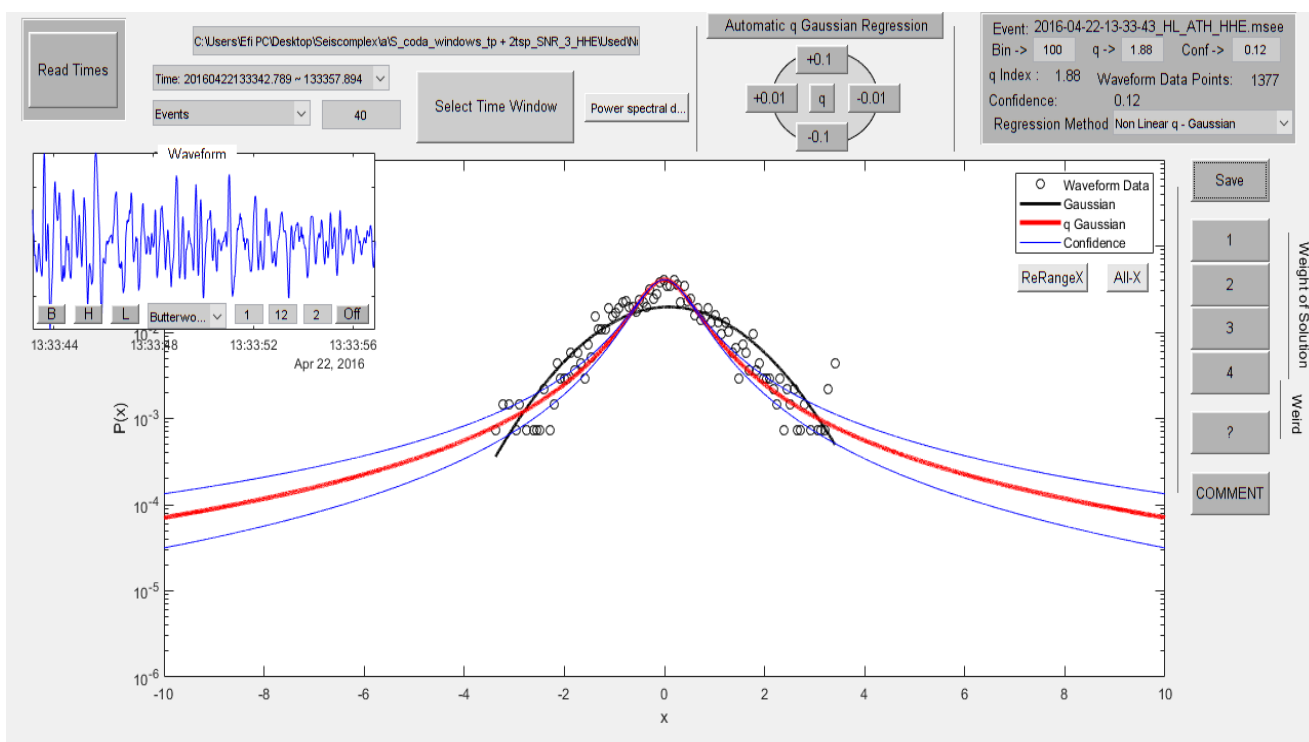


Figure 8.2.194

In figure 8.2.195 the time origin of the earthquake is 28/05/2016 at 20:18:58, latitude 37.56, longitude 23.57, depth 15 km, magnitude 3.1 at 49.2 km SSW of Athens. The value of the index  $q$  is 1.57.

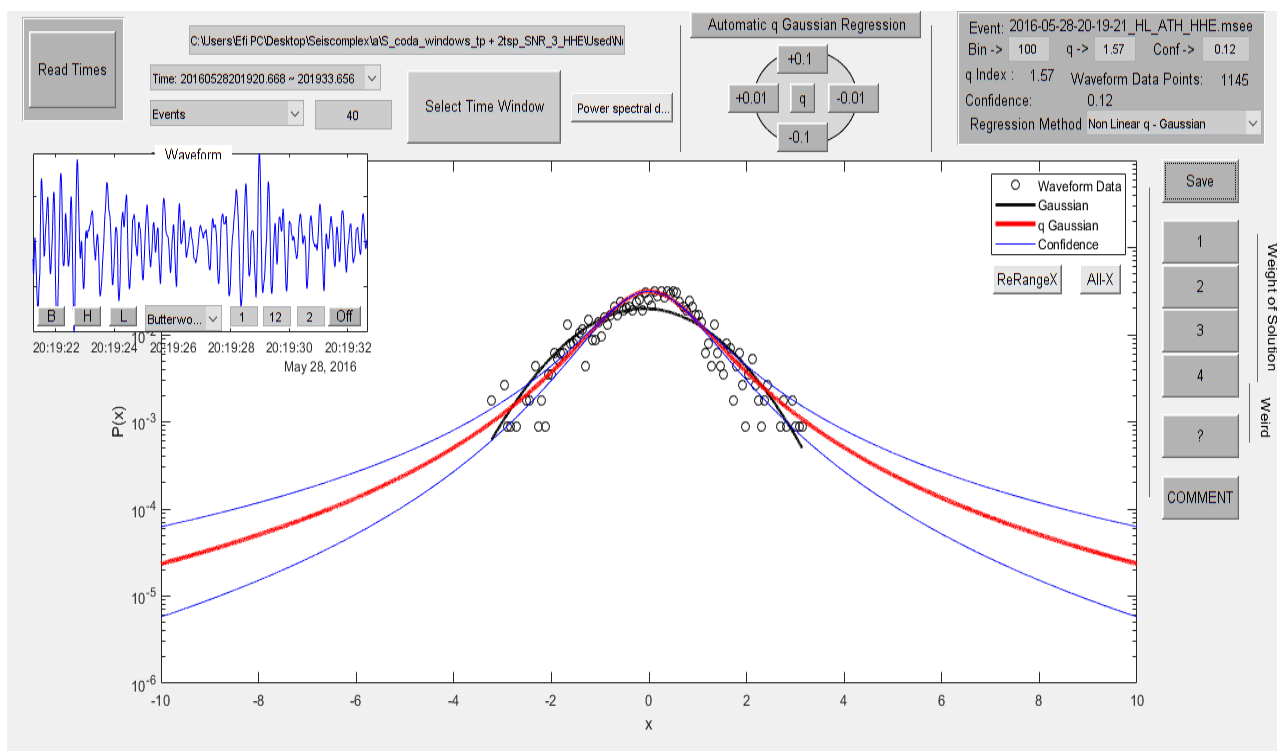


Figure 8.2.195

In figure 8.2.196 the time origin of the earthquake is 06/07/2016 at 16:26:12, latitude 37.55, longitude 23.6, depth 15 km, magnitude 3.1 at 49.6 km SSW of Athens. The value of the index  $q$  is 1.87.

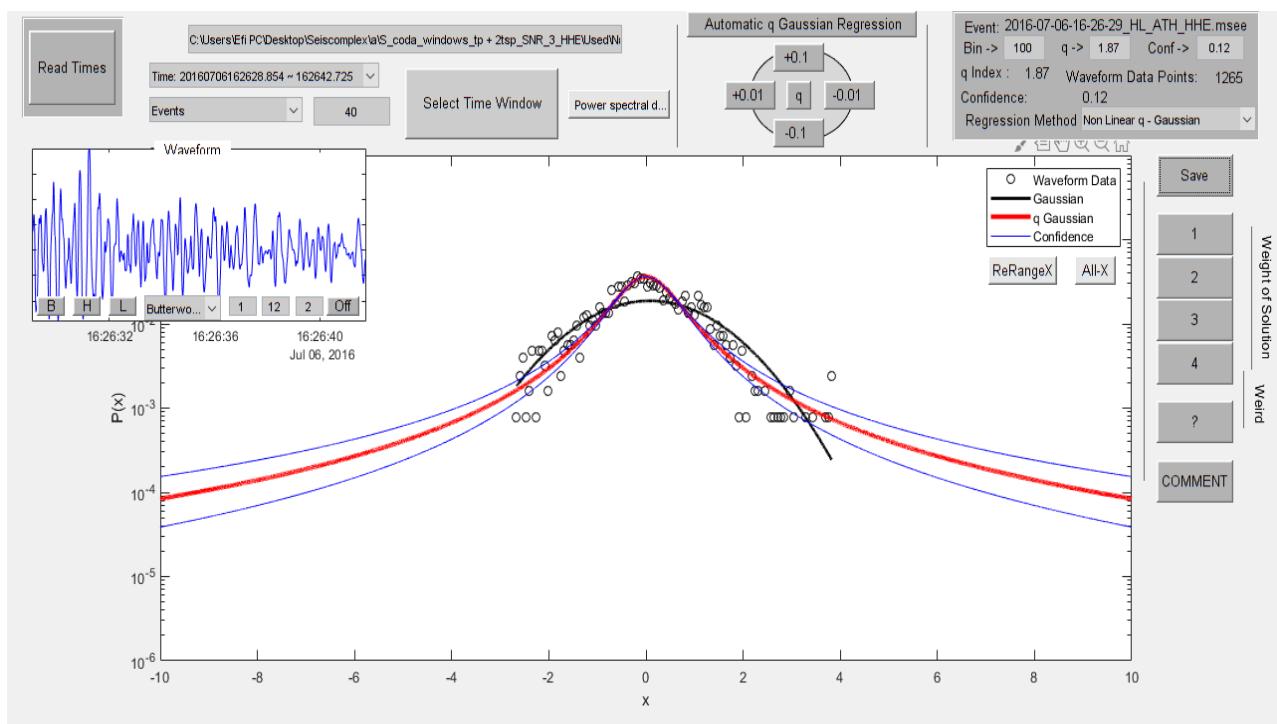


Figure 8.2.196

In figure 8.2.197 the time origin of the earthquake is 18/05/2017 at 08:14:16, latitude 38.0013, longitude 23.9545, depth 17 km, magnitude 3.1 at 19.5 km E of Athens. The value of the index  $q$  is 1.79.

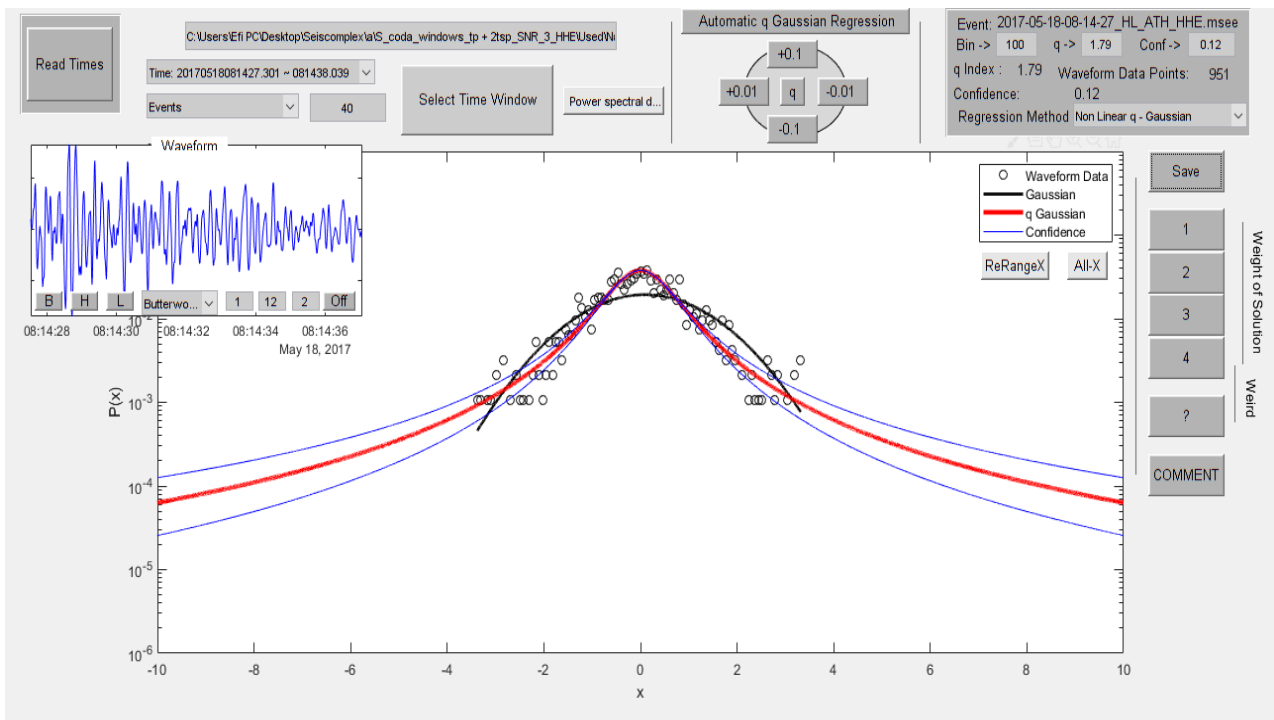


Figure 8.2.197

In figure 8.2.198 the time origin of the earthquake is 06/06/2017 at 08:01:33, latitude 38.4808, longitude 23.3872, depth 20 km, magnitude 3.1 at 18.6 km W of Chalkida. The value of the index  $q$  is 1.65.

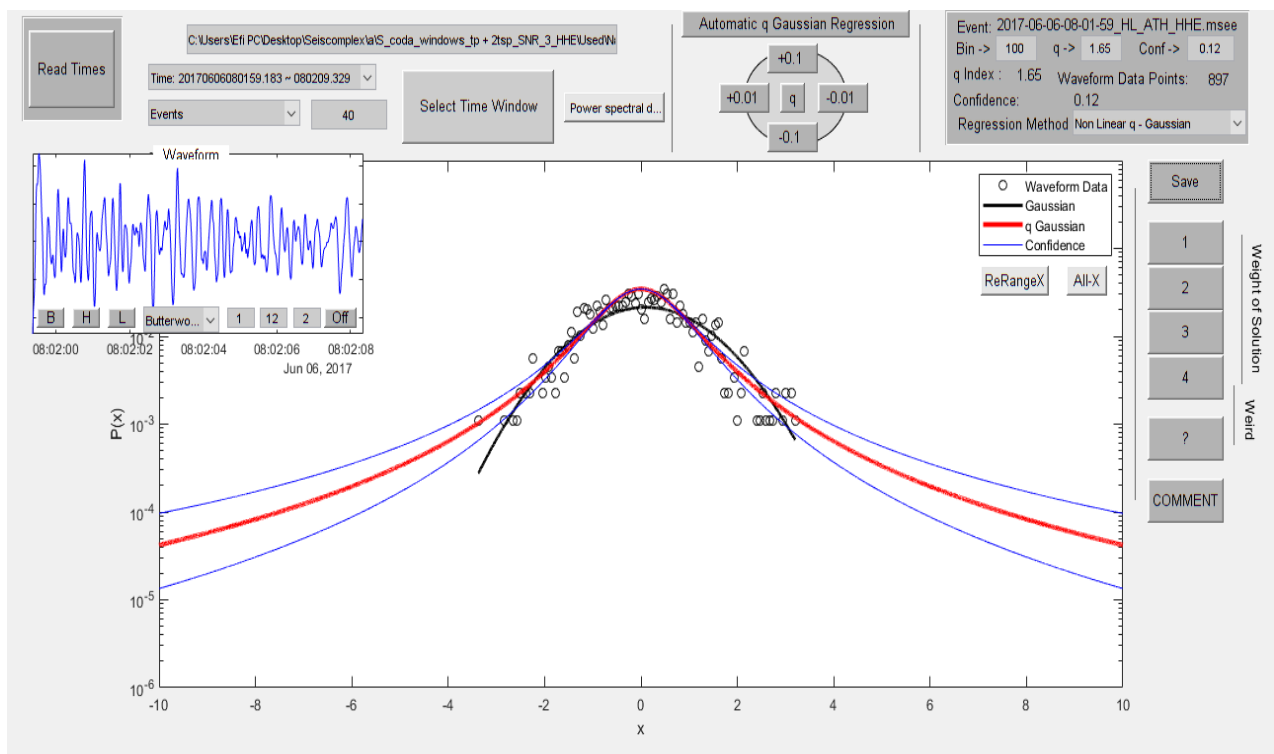


Figure 8.2.198

In figure 8.2.199 the time origin of the earthquake is 23/08/2018 at 02:30:42, latitude 37.5758, longitude 22.626, depth 64 km, magnitude 3.1 at 16.1 km W of Nafplio. The value of the index  $q$  is 1.87.

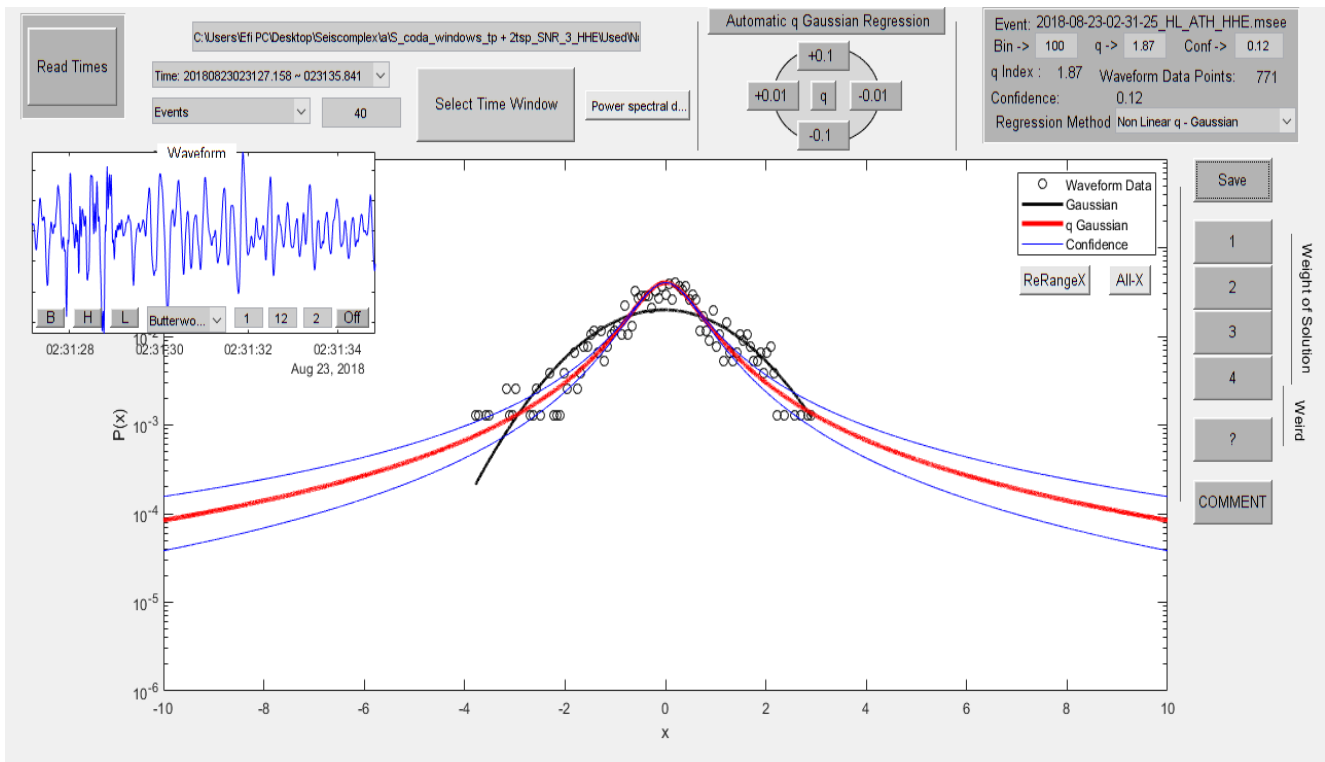


Figure 8.2.199

In figure 8.2.200 the time origin of the earthquake is 15/07/2019 at 20:28:24, latitude 37.9047, longitude 22.6447, depth 16 km, magnitude 3.1 at 25.5 km W of Korinthos. The value of the index  $q$  is 1.95.

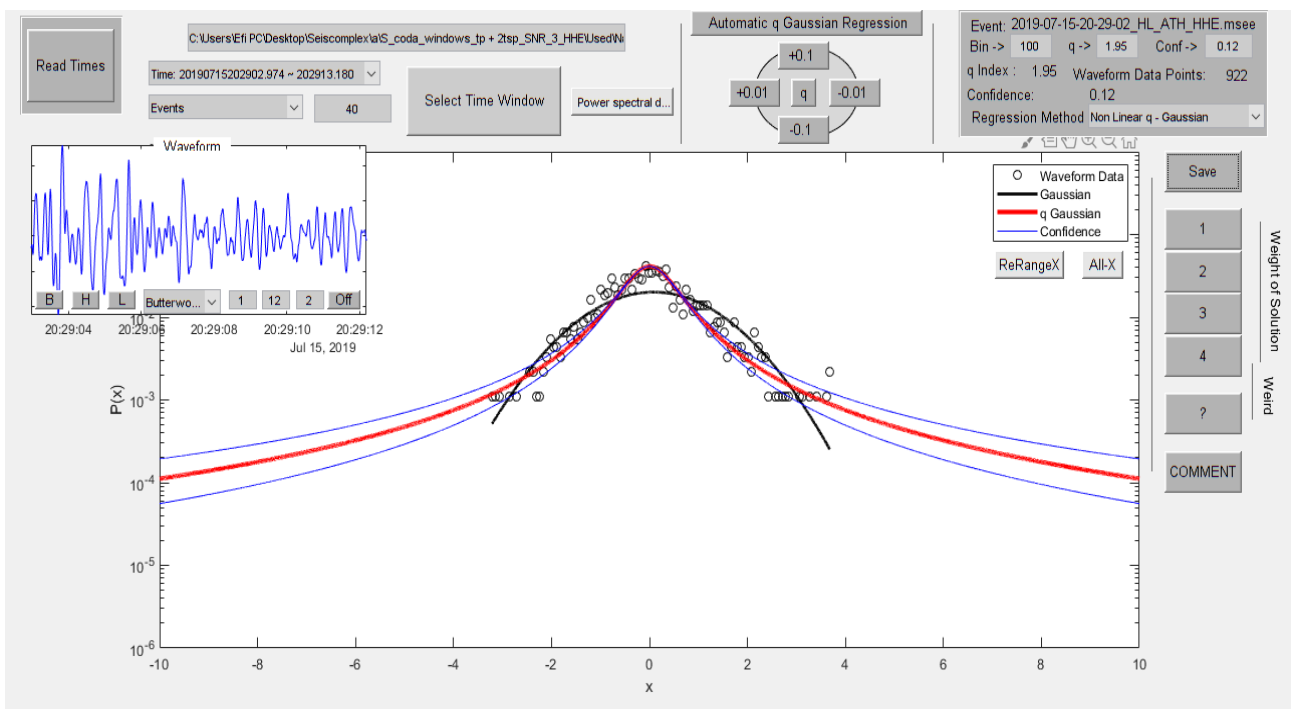


Figure 8.2.200

## References

- Sato, H., Fehler, M. C. & Maeda, T., (2012): Seismic Wave Propagation and Scattering in the Heterogeneous Earth. Springer-Verlag, Berlin, Heidelberg, 2nd edition, 2012.
- Sato, H. & Fukushima, R., (2013): Radiative transfer theory for the fractal structure and power-law decay characteristics of short-period seismograms, *Geophys. J. Int.* (2013) **195**, 1831–1842
- Wu, R. S. & Aki, K., (1985): The Fractal Nature of the Inhomogeneities in the Lithosphere Evidenced from Seismic Wave Scattering, *PAGEOPH*, Vol **123** (1985)
- Sato, H. & Fehler, M. C., (2007): Synthesis of Seismogram Envelopes in Heterogeneous Media, *Advances in Geophysics*, VOL. **48**, CHAPTER 10
- Sato, H., (2019): Power spectra of random heterogeneities in the solid earth, *Solid Earth*, **10**, 275–292, 2019
- Sato, H., (1982): Coda Wave Excitation due to Nonisotropic Scattering and Nonspherical Source Radiation, *Journal of Geophysical Research*, VOL. **87**, NO. B10, PAGES 8665-8674, OCTOBER 10, 1982
- Sato, H., (2019): Isotropic scattering coefficient of the solid earth, *Geophys. J. Int.* (2019) **218**, 2079–2088
- Sato, H., (1988): Is the Single Scattering Model Invalid for the Coda Excitation at Long Lapse Time?, *PAGEOPH*, Vol. **128**, Nos. 1/2 (198)
- Douma, H. & Kabir, R. C., (2001): Amplitude effects due to multiscale impedance contrasts and multiple scattering: implications for Ivrea-type continental lower crust, *Geophys. J. Int.* (2001) **147**, 435-448
- Shapiro, S. A., (1992): Elastic waves scattering and radiation by fractal inhomogeneity of a medium, *Geophys. J. Int.* (1992) **110**, 591-600
- Matsumoto, S., (1995): Characteristics of Coda Waves and Inhomogeneity of the Earth, *J. Phys. Earth*, **43**, 279-299, 1995
- Aki, K. & Chouet, B., (1975): Origin of coda waves: source, attenuation and scattering effects, *J. geophys. Res.*, **80**, 3322–3342
- Gusev, A.A. & Abubakirov, I.R., (1996): Simulated envelopes of nonisotropically scattered body waves as compared to observed ones: another manifestation of fractal heterogeneity, *Geophys. J.*, **1001** (127), 9–60
- Lee, W. & Sato, H., (2006): Power-law decay characteristic of coda envelopes revealed from the analysis of regional earthquakes, *Geophys. Res. Lett.*, **33**, L07317, doi:10.1029/2006GL025840
- Sato, H., (1977): Energy propagation including scattering effects: single isotropic scattering approximation, *J. Phys. Earth*, **25**, 27–41
- Zeng, Y., Su, F. & Aki, K., (1991): Scattering wave energy propagation in a random isotropic scattering medium 1. Theory, *J. geophys. Res.*, **96**, 607–619

Kilias, A., Tranos, M., Papadimitriou, E. & Karakostas, V., (2008): The recent crustal deformation of the Hellenic orogen in Central Greece; the Kremasta and Sperchios Fault Systems and their relationship with the adjacent large structural features, *Z. dt. Ges. Geowiss.*, **159**/3, p. 533–547, 8 figs., 1 tab., Stuttgart, September 2008

Nikolaev, A.V. & Troitskiy, P.A., (1987): Lithospheric studies based on array analysis of P-coda and microseisms, *Tectonophysics* **140**, 103

Fountain, D.M. & Christensen, N.I., (1989): Composition of the continental crust and upper mantle; a review, in: L.C. Pakiser and W.D. Mooney (eds.), *Geophysical Framework of the Continental United States, Geol. Soc. Am. Mem.* **172**, pp. 711–742

Mandelbrot, B.B., (1977): *Fractals: forms, chance and dimension*. Freeman, San Francisco

Berry, J. W., (1979b): "Acculturation as varieties of adaptation." Presented in symposium "Psychological Dimensions in the Acculturation Process," *American Association for the Advancement of Science*, Houston, January

Aki, K., (1969): Analysis of the seismic coda of local earthquakes as scattered waves, *J. geophys. Res.* **74**, *J. R. Astron. Soc.* **76**, 147–156

Rautian, T. G. & Khalturin, V. I., (1978): The use of coda for determination of the earthquake source spectrum, *Bull. Seismol. Soc. Amer.* **68**, 923–948

Aki, K. & Tsujiura, M., (1959): Correlational study of near earthquake waves, *Earthquake Research Institute*, Vol. 37 (1959), pp. 207-232

Spudich, P. & Bostwick, T., (1987): Studies of the seismic coda using an earthquake cluster as a deeply buried seismograph array, *J. Geophys. Res.* **92**, 10,526–10, 546

Kuwahara, Y. et al., (1985): Effects of the fault surface roughness on unstable slip and a scaling law of slip, *Annu. Mtg. Seismol. Soc. Jpn., Progr. Abstr.* (1985)

Scherbaum, F. & Sato, H., (1991): Inversion of full seismogram envelopes based on the parabolic approximation: Estimation of randomness and attenuation in southeast Honshu, Japan, *J. geophys. Res. : Solid Earth*

Matsumoto, S., Tsumura, M., Hasegawa, A. & Horiuchi, S., (2000): Three-dimensional attenuation structure beneath the northeastern Japan arc estimated from spectra of small earthquakes, *Tectonophysics* Vol. 319, Issue 4, 20 April 2000, Pages 241-260

Gusev, A. A. & Lemzikov, V. K., (1985): Properties of scattered elastic waves in the lithosphere of Kamchatka: Parameters and temporal variations. *Tectonophysics.* **112**, 137–153

Aki, K., (1980): Scattering and attenuation of shear waves in the lithosphere, *J. Geophys. Res.* **85**, 6496–6504

Gao, L., Lee, L. C., Biswas, N. N. & Aki, K., (1983): Comparison of the effects between single and multiple scattering on coda waves for local earthquakes. *Bull. Seismol. Soc. Amer.* **73**, 377–389

Jin, A. & Aki, K., (1986): Temporal change in coda Q before the Tangshan earthquake of 1976 and the Haicheng earthquake of 1975. *J. Geophys. Res.* **91**, 665–673

- Wu, R. S., (1982): Attenuation of short period seismic waves due to scattering. *Geophys. Res. Lett.* **9**, 9–12
- Kanao, M. & Ito, K., (1990): Attenuation of Coda Waves in the Source Area of the 1990 July 16 Luzon Earthquake, Philippines, *Bull. Disas. Prey. Res. Inst., Kyoto Univ.*, Vol. 42, Part 2, No. 365, June, 1992
- Sadovskiy, M. A., Golubeva, T. V., Pisarenko, V.F. & Shnirman, M.G., (1984): Characteristic Dimensions of Rock and Hierarchical Properties of Seismicity, *Izv. Acad. Sci. USSR Phys. Solid Earth*, **20**, **87**, 1984
- Kagan, Y. & Knopoff, L., (1980): Spatial distribution of earthquakes: the two-point correlation function, *Geophysical Journal International*, Volume 62, Issue 2, August 1980, Pages 303–320
- Hirata, T., Satoh, T. & Ito, K., (1987): Fractal structure of spatial distribution of microfracturing in rock, *Geophysical Journal International*, Volume 90, Issue 2, August 1987, Pages 369–374
- Frankel, A. & Wennerberg, L., (1987): Energy-flux model of seismic coda: Separation of scattering and intrinsic attenuation. *Bulletin of the Seismological Society of America*, **77**, 1223-1251
- Benites, R., Aki, K. & Yomogida, K., (1997): Coda Q in two-layer random media, *Geophysical Journal International*, Volume 128, Issue 2, February 1997, Pages 425–433
- Hirata, T. & Imoto, M., (1991): Multifractal analysis of spatial distribution of microearthquakes in the Kanto region, *Geophysical Journal International*, 1991
- Godano, C., Pezzo, E. D. & Martino, M., (1994): Dependence of the apparent seismic quality factor on epicentral distance: an interpretation in terms of fractal structure of the seismic medium, *Physics of the Earth and Planetary Interiors*, Volume 82, Issues 3–4, March 1994, Pages 271-276
- Rastogi, P. K. & Scheucher, K. F., (1990): Range dependence of volume scattering from a fractal medium: Simulation results, *Radio Science*, 1990
- Roecker, S. W., Tucker, B., King, J. & Hatzfeld, D., (1982): Estimates of Q in central Asia as a function of frequency and depth using the coda of locally recorded earthquakes, *Bulletin of the Seismological Society of America* (1982) **72** (1): 129–149
- Hoshiya, M., (1997): Seismic coda wave envelope in depth-dependent S wave velocity structure, *Physics of the Earth and Planetary Interiors*, Volume 104, Issues 1–3, 30 November 1997, Pages 15-22
- Frankel, A. & Clayton, R. W., (1986): Finite Difference Simulations of Seismic Scattering' Implications for the Propagation of Short-Period Seismic Waves in the Crust and Models of Crustal Heterogeneity, *Journal of Geophysical Research*, VOL. 91, NO. B6, Pages 6465-6489, MAY 10, 1986
- Tsallis, C., (1988): Possible generalization of Boltzmann-Gibbs statistics. *Journal of statistical physics*, 1988, 52.1-2: 479-487
- Galanakis, D., (1997): Neotectonic and stratigraphic of the neogene-quaternary sediments of Almyros-Pagasetikos, Pilio, Oreoi-Trikeri and Maliakos basins, Aristotle University of Thessaloniki, 1997